Research Topics

Model organisms in embryonic development

Edited by
Michael Schubert, Gabriella Lania, Alice Jouneau
and Denhi Schnabel

Published in
Frontiers in Cell and Developmental Biology

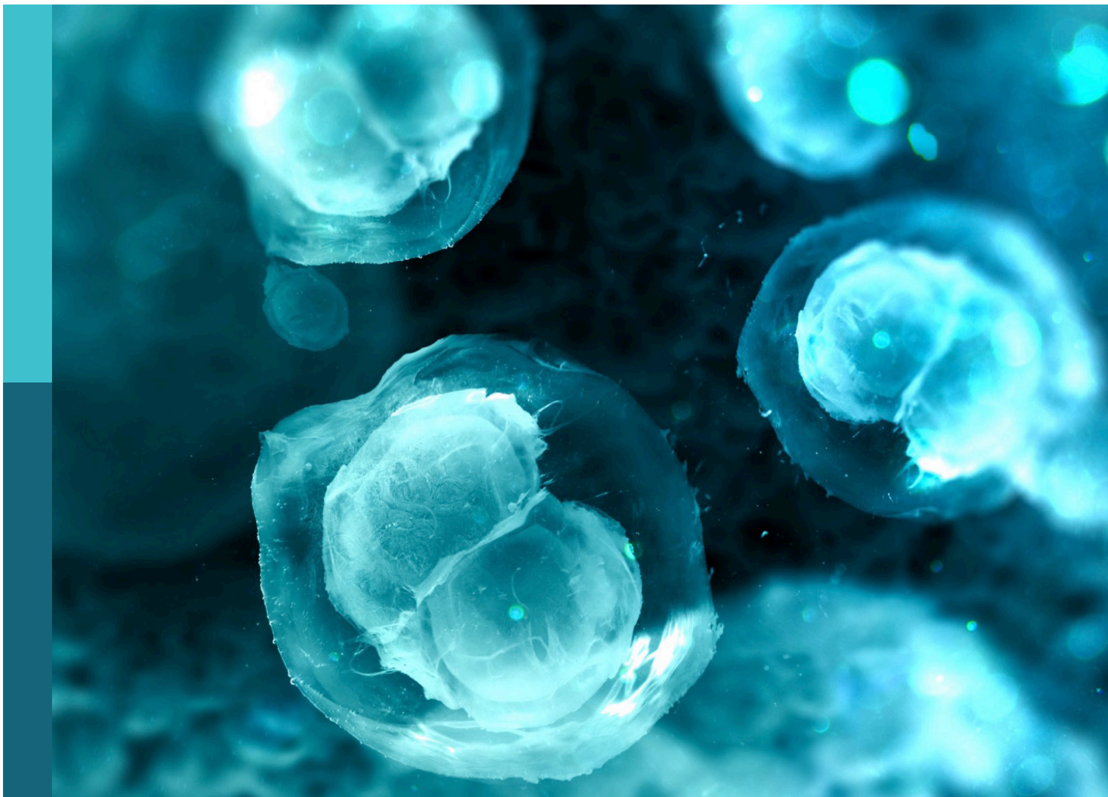

ISSN 1664-8714
ISBN 978-2-8325-6639-8
DOI 10.3389/978-2-8325-6639-8

Generative AI statement
Any alternative text (Alt text) provided alongside figures in the articles in this ebook has been generated by Frontiers with the support of artificial intelligence and reasonable efforts have been made to ensure accuracy, including review by the authors wherever possible. If you identify any issues, please contact us.

About Frontiers

Frontiers is more than just an open access publisher of scholarly articles: it is a pioneering approach to the world of academia, radically improving the way scholarly research is managed. The grand vision of Frontiers is a world where all people have an equal opportunity to seek, share and generate knowledge. Frontiers provides immediate and permanent online open access to all its publications, but this alone is not enough to realize our grand goals.

Frontiers journal series

The Frontiers journal series is a multi-tier and interdisciplinary set of open-access, online journals, promising a paradigm shift from the current review, selection and dissemination processes in academic publishing. All Frontiers journals are driven by researchers for researchers; therefore, they constitute a service to the scholarly community. At the same time, the *Frontiers journal series* operates on a revolutionary invention, the tiered publishing system, initially addressing specific communities of scholars, and gradually climbing up to broader public understanding, thus serving the interests of the lay society, too.

Dedication to quality

Each Frontiers article is a landmark of the highest quality, thanks to genuinely collaborative interactions between authors and review editors, who include some of the world's best academicians. Research must be certified by peers before entering a stream of knowledge that may eventually reach the public - and shape society; therefore, Frontiers only applies the most rigorous and unbiased reviews. Frontiers revolutionizes research publishing by freely delivering the most outstanding research, evaluated with no bias from both the academic and social point of view. By applying the most advanced information technologies, Frontiers is catapulting scholarly publishing into a new generation.

What are Frontiers Research Topics?

Frontiers Research Topics are very popular trademarks of the *Frontiers journals series*: they are collections of at least ten articles, all centered on a particular subject. With their unique mix of varied contributions from Original Research to Review Articles, Frontiers Research Topics unify the most influential researchers, the latest key findings and historical advances in a hot research area.

Find out more on how to host your own Frontiers Research Topic or contribute to one as an author by contacting the Frontiers editorial office: frontiersin.org/about/contact

Model organisms in embryonic development

Topic editors
Michael Schubert — UMR7009 Laboratoire de Biologie du Développement de Villefranche sur Mer, France
Gabriella Lania — Institute of Genetics and Biophysics Adriano Buzzati-Traverso, Department of Biomedical Sciences, National Research Council (CNR), Italy
Alice Jouneau — Institut National de recherche pour l'agriculture, l'alimentation et l'environnement (INRAE), France
Denhi Schnabel — National Autonomous University of México, Mexico

Citation
Schubert, M., Lania, G., Jouneau, A., Schnabel, D., eds. (2025). *Model organisms in embryonic development*. Lausanne: Frontiers Media SA.
doi: 10.3389/978-2-8325-6639-8

Table of contents

frontiers | Frontiers in Cell and Developmental Biology

TYPE Editorial
PUBLISHED 10 July 2025
DOI 10.3389/fcell.2025.1649186

Editorial: Model organisms in embryonic development

Gabriella Lania[1], Denhi Schnabel[2] and Michael Schubert[3]*

[1]Istituto di Genetica e Biofisica (IGB) Adriano Buzzati-Traverso, Consiglio Nazionale delle Ricerche (CNR), Naples, Italy, [2]Instituto de Biotecnología, Universidad Nacional Autónoma de México, Cuernavaca, Mexico, [3]Laboratoire de Biologie du Développement de Villefranche-sur-Mer, Institut de la Mer de Villefranche, Centre National de la Recherche Scientifique (CNRS), Sorbonne Université, Villefranche-sur-Mer, France

OPEN ACCESS

EDITED AND REVIEWED BY
Beate Emmi Margarete Brand-Saberi,
Ruhr University Bochum, Germany

*CORRESPONDENCE
Michael Schubert,
✉ michael.schubert@imev-mer.fr

RECEIVED 18 June 2025
ACCEPTED 27 June 2025
PUBLISHED 10 July 2025

CITATION
Lania G, Schnabel D and Schubert M (2025) Editorial: Model organisms in embryonic development.
Front. Cell Dev. Biol. 13:1649186.
doi: 10.3389/fcell.2025.1649186

KEYWORDS

embryology, animal model systems, classical model species, alternative model species, evolution of development

Editorial on the Research Topic
Model organisms in embryonic development

> "Our real teacher has been and still is the embryo, who is, incidentally, the only teacher who is always right." — Viktor Hamburger.

Evolution has produced a vast diversity of organisms, and, in order to understand the inner workings of their biology, scientists use model organisms. Findings obtained in model organisms are usually extrapolated and applied to other species, including humans (Nadeau and Auwerx, 2019; Patton et al., 2021; Yamamoto et al., 2024). This practice is possible because the molecular and genetic mechanisms controlling the main biological functions share at least a certain degree of conservation between species (Hall, 2003; Pai and Gilad, 2014; Mosby et al., 2024). Experimental animal model systems have thus been essential not only for uncovering the mechanisms of animal development, metabolism and physiology, but also for advancing agricultural science, biomedical research and the development of treatments for human diseases (Nadeau and Auwerx, 2019; Smith and Rhodes, 2000; Patton et al., 2021; Yamamoto et al., 2024).

Classical animal model systems widely used in developmental studies include the fruit fly *Drosophila melanogaster*, the roundworm *Caenorhabditis elegans* as well as several vertebrates, such as the zebrafish (*Danio rerio*), the clawed frog (*Xenopus laevis*/*Xenopus tropicalis*), the chicken (*Gallus gallus*) and the mouse (*Mus musculus*). While the zebrafish has gained immense popularity in the course of the last few decades, most original discoveries on the biological processes characterizing the earliest stages of development have come from studies using the clawed frog, and groundbreaking experiments in the chicken have revealed how cells and tissues interact during embryogenesis. Regarding the mouse, the fruit fly and the roundworm, they have been instrumental for detailing the spatiotemporal functions of genes during animal development (Barresi and Gilbert, 2023). Despite being incredibly powerful from an experimental point of view, the limited number and restricted phylogenetic coverage of classical animal model systems have proven largely insufficient to describe the diversity of animal developmental mechanisms (Raff, 1992; Haen Whitmer, 2018; Nakamura and Huang, 2025). Recent efforts have therefore focused on the exploration of alternative model organisms, often located at key phylogenetic positions within the animal tree of life, to establish links between the deployment of novel genetic modules during development and the emergence of biological novelties (Stolfi et al., 2010; Steinmetz et al., 2012; Musser et al., 2021).

This Research Topic features examples from both classical and alternative animal models to illustrate the power of established classical models and the usefulness of alternative models for understanding how the evolution of developmental mechanisms drove animal diversification.

Classical model systems featured in articles of this Research Topic include the mouse, which is used by An et al. Their study focuses on blastocyst hatching and its role in implantation of the fetus. Using a high throughput sequencing approach, the authors identify transcriptomic patterns in developing mouse blastocysts that they use to develop a gene expression-based model for predicting implantation success of the blastocyst. Lv et al. use the mouse to assess the role of FGF18 during craniofacial development. In their paper, the authors describe a mouse model allowing the specific increase of FGF18 signaling activity in cranial neural crest cells. The resulting abnormalities in mice are like those of the human Pierre Robin syndrome, a rare congenital birth defect. This work thus demonstrates the need of a tight control of endogenous FGF signaling levels during craniofacial development.

A different classical vertebrate model organism, the clawed frog, is used by Castro Colabianchi et al. to examine the establishment of the embryonic dorsoventral axis. This publication shows that molecules required for ventral patterning of the embryo are asymmetrically distributed in the unfertilized egg, which suggests that the frog egg is prepatterned dorsoventrally prior to fertilization. The establishment of asymmetries is an important feature of body axis formation and found in different animal species and developmental contexts. The work by Guichard et al. provides another example for this, focusing on the emergence of left-right asymmetries during brain development of the lamprey, a jawless vertebrate and an alternative vertebrate model organism. The authors are interested in asymmetric development of the habenula, a bilateral epithalamic structure. Using a transcriptomic approach, they first identify novel markers of different habenular territories and subsequently characterize the development of the lamprey habenula, allowing them to describe a significant asymmetric temporal regulation of habenular territories. Altogether, this article highlights the importance of the lamprey as a model for understanding the evolution of brain asymmetries in vertebrates.

One article of the Research Topic addresses brain development in the fruit fly *D. melanogaster*, a classical invertebrate model organism. More specifically, Barthel et al. study the role of two components of the transcriptional elongation machinery, Spt4 and Spt5, during mushroom body development. The mushroom body is a paired structure in the fruit fly brain required for processing sensory inputs. Taking advantage of the genetic tools available for this model, the authors demonstrate that, in the developing fruit fly mushroom body, Spt4 and Spt5 control both cell proliferation of neural progenitors and remodeling of certain axonal projections. The cephalochordate amphioxus (*Branchiostoma floridae*), an invertebrate chordate model, is used by Kozmik and Kozmikova to study the function of Pax6 during nervous system development. They show that deletion of two amino acids in the conserved paired domain of Pax6 using the CRISPR/Cas9 approach is sufficient for reducing the ability of Pax6 to activate target genes. In these Pax6 mutants, gene expression is altered in the anterior central nervous system, which is consistent with a conserved role for Pax6 in chordate brain regionalization. Mikula Mrstakova and Kozmik use an alternative vertebrate model system for their work, the medaka fish (*Oryzias latipes*), to test the hypothesis of a quasi-universal requirement for Pax6 during animal eye development. Their results reveal significant functional differences between medaka and mouse Pax6 genes, which allows the authors to retrace the evolutionary history of the roles of Pax6 during vertebrate eye development.

The Research Topic further includes studies using alternative animal models covering a wide variety of different animal taxa. Romanova et al., for example, report on long-term cultures of placozoans, early-branching metazoans characterized by an extremely simple body plan. Detailed analyses of the placozoan *Trichoplax adherens* reared for several years in the laboratory reveal surprisingly complex population dynamics and provide evidence that placozoans might have magnetoreception. This work thus reveals novel aspects of placozoan biology and further establishes these animals as alternative model systems in ecology, systems biology and evolution. Wanninger and Schwarze have contributed a review focusing on the usefulness of the quagga mussel (*Dreissena rostriformis*) as an alternative model system in ecology and evolutionary biology. The article discusses the resources currently available for this bivalve mollusk and covers recent advances of our understanding of quagga mussel biology, with special focus on the morphology and molecular biology of development as well as on the molecular and cellular mechanisms underlying physiological adaptations. Anselmi et al. use different invertebrate chordate models, namely tunicates, for a comparative study of developing solitary (*Ciona robusta*) and colonial (*Botryllus schlosseri*) species. While solitary tunicates are oviparous with fertilization and development taking place outside the parent body, colonial tunicates are ovoviviparous with adults retaining the embryos inside their body. The authors thus first describe a method for *in vitro* culturing of *B. schlosseri* embryos and subsequently characterize the development of this colonial tunicate. Finally, they compare the time courses of *C. robusta* and *B. schlosseri* embryology and identify significant heterochronic shifts between the two tunicate species.

Taken together, the articles of this Research Topic nicely illustrate how the combination of classical and alternative model organisms enrich our understanding of animal development. It is thus important to keep pushing the boundaries by both expanding the experimental toolkit and enlarging the species sampling to more comprehensively cover the true diversity of life.

Author contributions

GL: Writing – review and editing. DS: Writing – review and editing. MS: Writing – original draft, Writing – review and editing.

Funding

The author(s) declare that financial support was received for the research and/or publication of this article. MS is funded by the

Agence Nationale de la Recherche, contract ANR-21-CE340006-02, and by the Centre National de la Recherche Scientifique. DS is supported by the Programa de Apoyo a Proyectos de Investigacióne Innovación Tecnológica No. IN222325.

Acknowledgments

We thank all authors and reviewers for their respective contributions to this Research Topic and Alice Jouneau for supporting its coordination.

Conflict of interest

The authors declare that the research was conducted in the absence of any commercial or financial relationships that could be construed as a potential conflict of interest.

The author(s) declared that they were an editorial board member of Frontiers, at the time of submission. This had no impact on the peer review process and the final decision.

Generative AI statement

The author(s) declare that no Generative AI was used in the creation of this manuscript.

Publisher's note

References

Barresi, M. J., and Gilbert, S. F. (2023). *Developmental Biology*. 13th Edition. Oxford, UK: Oxford University Press.

Haen Whitmer, K. M. (2018). Model systems for exploring the evolutionary origins of the nervous system. *Results Probl. Cell Differ.* 65, 185–196. doi:10.1007/978-3-319-92486-1_10

Hall, B. K. (2003). Descent with modification: the unity underlying homology and homoplasy as seen through an analysis of development and evolution. *Biol. Rev. Camb. Philos. Soc.* 78, 409–433. doi:10.1017/s1464793102006097

Mosby, L. S., Bowen, A. E., and Hadjivasiliou, Z. (2024). Morphogens in the evolution of size, shape and patterning. *Development* 151, dev202412. doi:10.1242/dev.202412

Musser, J. M., Schippers, K. J., Nickel, M., Mizzon, G., Kohn, A. B., Pape, C., et al. (2021). Profiling cellular diversity in sponges informs animal cell type and nervous system evolution. *Science* 374, 717–723. doi:10.1126/science.abj2949

Nadeau, J. H., and Auwerx, J. (2019). The virtuous cycle of human genetics and mouse models in drug discovery. *Nat. Rev. Drug Discov.* 18, 255–272. doi:10.1038/s41573-018-0009-9

Nakamura, M., and Huang, G. N. (2025). Why some hearts heal and others don't: the phylogenetic landscape of cardiac regenerative capacity. *Semin. Cell Dev. Biol.* 170, 103609. doi:10.1016/j.semcdb.2025.103609

Pai, A. A., and Gilad, Y. (2014). Comparative studies of gene regulatory mechanisms. *Curr. Opin. Genet. Dev.* 29, 68–74. doi:10.1016/j.gde.2014.08.010

Patton, E. E., Zon, L. I., and Langenau, D. M. (2021). Zebrafish disease models in drug discovery: from preclinical modelling to clinical trials. *Nat. Rev. Drug Discov.* 20, 611–628. doi:10.1038/s41573-021-00210-8

Raff, R. A. (1992). Evolution of developmental decisions and morphogenesis: the view from two camps. *Development* 116 (Supplement), 15–22. doi:10.1242/dev.116.Supplement.15

Smith, R. C., and Rhodes, S. J. (2000). Applications of developmental biology to medicine and animal agriculture. *Prog. Drug Res.* 54, 213–256. doi:10.1007/978-3-0348-8391-7_7

Steinmetz, P. R., Kraus, J. E., Larroux, C., Hammel, J. U., Amon-Hassenzahl, A., Houliston, E., et al. (2012). Independent evolution of striated muscles in cnidarians and bilaterians. *Nature* 487, 231–234. doi:10.1038/nature11180

Stolfi, A., Gainous, T. B., Young, J. J., Mori, A., Levine, M., and Christiaen, L. (2010). Early chordate origins of the vertebrate second heart field. *Science* 329, 565–568. doi:10.1126/science.1190181

Yamamoto, S., Kanca, O., Wangler, M. F., and Bellen, H. J. (2024). Integrating non-mammalian model organisms in the diagnosis of rare genetic diseases in humans. *Nat. Rev. Genet.* 25, 46–60. doi:10.1038/s41576-023-00633-6

frontiers | Frontiers in Cell and Developmental Biology

TYPE Original Research
PUBLISHED 20 March 2024
DOI 10.3389/fcell.2024.1365705

Check for updates

OPEN ACCESS

EDITED BY
Alice Jouneau,
Institut National de recherche pour l'agriculture, l'alimentation et l'environnement (INRAE), France

REVIEWED BY
Jiawei Sun,
Massachusetts General Hospital and Harvard Medical School, United States
Sally Ann Moody,
George Washington University, United States
Laurent Kodjabachian,
UMR7288 Institut de Biologie du Développement de Marseille (IBDM), France

*CORRESPONDENCE
Silvia L. López,
slopez@fmed.uba.ar,
silvialopez.emol@gmail.com

RECEIVED 04 January 2024
ACCEPTED 07 March 2024
PUBLISHED 20 March 2024

CITATION
Castro Colabianchi AM, González Pérez NG, Franchini LF and López SL (2024), A maternal dorsoventral prepattern revealed by an asymmetric distribution of ventralizing molecules before fertilization in *Xenopus laevis*. *Front. Cell Dev. Biol.* 12:1365705.
doi: 10.3389/fcell.2024.1365705

A maternal dorsoventral prepattern revealed by an asymmetric distribution of ventralizing molecules before fertilization in *Xenopus laevis*

Aitana M. Castro Colabianchi [1,2], Nicolás G. González Pérez [1,2], Lucía F. Franchini [3] and Silvia L. López [1,2]*

[1]Universidad de Buenos Aires, Facultad de Medicina, Departamento de Biología Celular e Histología / 1° U.A. Departamento de Histología, Embriología, Biología Celular y Genética, Laboratorio de Embriología Molecular "Prof. Dr. Andrés E. Carrasco", Buenos Aires, Argentina, [2]CONICET–Universidad de Buenos Aires, Instituto de Biología Celular y Neurociencias "Prof. E. De Robertis" (IBCN), Buenos Aires, Argentina, [3]Instituto de Investigaciones en Ingeniería Genética y Biología Molecular (INGEBI) "Dr. Héctor N. Torres", Consejo Nacional de Investigaciones Científicas y Técnicas (CONICET), Buenos Aires, Argentina

The establishment of the embryonic dorsoventral axis in *Xenopus* occurs when the radial symmetry around the egg's animal-vegetal axis is broken to give rise to the typical symmetry of Bilaterians. We have previously shown that the Notch1 protein is ventrally enriched during early embryogenesis in *Xenopus laevis* and zebrafish and exerts ventralizing activity through β-Catenin destabilization and the positive regulation of ventral center genes in *X. laevis*. These findings led us to further investigate when these asymmetries arise. In this work, we show that the asymmetrical distribution of Notch1 protein and mRNA precedes cortical rotation and even fertilization in *X. laevis*. Moreover, we found that in unfertilized eggs transcripts encoded by the ventralizing gene *bmp4* are also asymmetrically distributed in the animal hemisphere and *notch1* transcripts accumulate consistently on the same side of the eccentric maturation point. Strikingly, a Notch1 asymmetry orthogonal to the animal-vegetal axis appears during *X. laevis* oogenesis. Thus, we show for the first time a maternal bias in the distribution of molecules that are later involved in ventral patterning during embryonic axialization, strongly supporting the hypothesis of a dorsoventral prepattern or intrinsic bilaterality of *Xenopus* eggs before fertilization.

KEYWORDS

bilateral symmetry, axialization, maternal determinants, maternal asymmetries, bilaterians, notch

Introduction

Amphibian eggs bear an animal-vegetal polarity that roughly predicts the future array of presumptive germ layers, with germ cell determinants accumulating in the vegetal pole from the earliest stages of oogenesis (Dale and Slack, 1987; Moody, 1987; Card, 1995; Houston, 2022). So far, it was described that before fertilization in *Xenopus*, maternal asymmetries in the distribution of transcripts only exist along the animal-vegetal axis (Figure 1A, left). They appear during oogenesis (Kloc and Etkin, 1995; Kloc et al., 2001; Sindelka et al., 2018) and

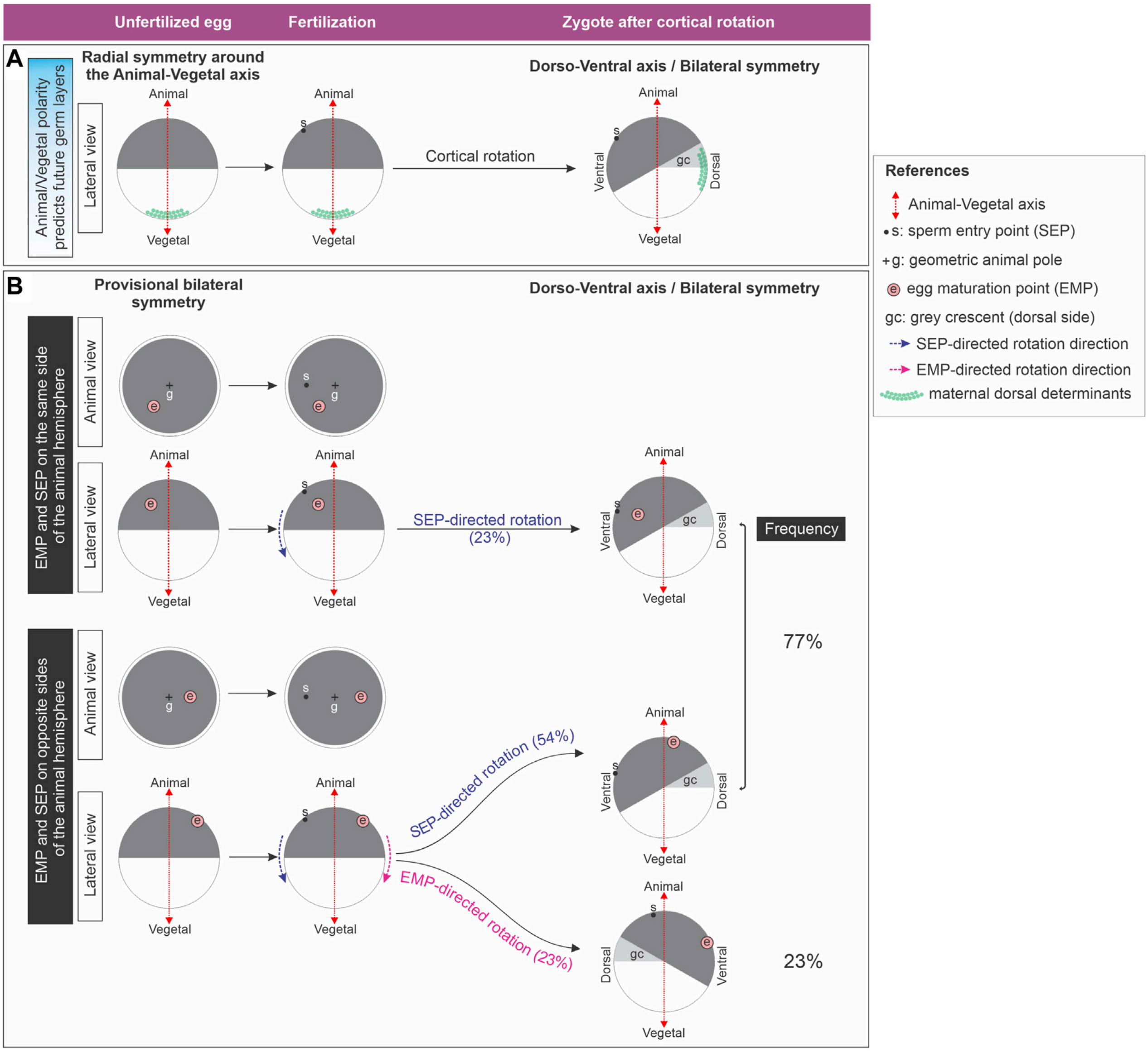

FIGURE 1
(A) Classic model which considers that the *Xenopus* unfertilized egg is radially symmetric around the animal-vegetal axis. Radial symmetry is broken shortly after fertilization by cortical rotation through relocation of maternal dorsal determinants from the vegetal pole to the future dorsal side. **(B)** *Xenopus* unfertilized eggs bear an intrinsic bilateral symmetry related to the position of the eccentric EMP, which can direct dorsoventral axialization if the SEP-oriented cues fail. Diagram representing the results obtained by Brown et al. (1994) (Brown et al., 1994), who analyzed the direction of yolk mass rotation in eggs with the cortex artificially immobilized, here illustrated as cortical rotation for simplicity. Only in eggs in which the sperm entered the animal hemisphere on the opposite side of the EMP, the later can override the SEP to direct rotation. Global frequencies for either SEP- or EMP- directed rotation were calculated from the results presented on Figure 6 of (Brown et al., 1994) and are shown as percentage of the total number of eggs analyzed (n = 31) in the right column. From the same dataset we also calculated the frequencies for SEP- or EMP- directed rotation for the eggs with the EMP and SEP on the same or on opposite sides of the animal hemisphere (percentages between brackets).

are also present during early cleavage stages (De Domenico et al., 2015). This radial symmetry around the animal-vegetal axis (Figure 1A, left) is considered to be broken shortly after fertilization because the embryonic dorsoventral axis is established on the meridian passing through the animal pole and the site where the gastrula organizer (the dorsal blastopore lip) will appear (Figure 1A, right). Since this initial dorsoventral axis sets the position of the future body midline, the embryo acquires the typical symmetry of Bilaterians relative to the plane of bilateral symmetry, with the concomitant emergence of anterior-posterior and mediolateral dimensions (Gerhart et al., 1989; Ubbels, 1997). In *Xenopus*, this dorsoventral polarity is generated by cortical rotation, a process normally triggered by fertilization, with the sperm entering the egg's animal hemisphere (Figure 1A). Cortical rotation starts around the mid-first cell cycle and concludes shortly before first cleavage, shifting the zygote's vegetal cortex in relation to the cytoplasmic core 30° away from the sperm entry point (SEP) towards the future dorsal side (Gerhart et al., 1989) (Figure 1A). If the egg's cortex is artificially immobilized, the cytoplasmic core, along with the yolk mass, rotates towards the SEP, also relocating the vegetal cortex to the future dorsal side (Gerhart et al., 1989; Brown et al., 1994).

Maternal dorsal determinants like *wnt11b* mRNA and Dishevelled protein move during this rotation from the vegetal pole to the future dorsal side (Figure 1A). During early cleavage stages, Wnt11b activates Dishevelled, leading to Glycogen synthase kinase-3 (GSK3) degradation dorsally and β-Catenin stabilization. Then, nuclearized β-Catenin activates dorsal genes, whereas in the ventral side, GSK3 continues tagging β-Catenin for degradation in a destruction complex involving Axin1 (Molenaar et al., 1996; Miller et al., 1999; Wessely et al., 2001; Weaver et al., 2003; Weaver and Kimelman, 2004; Wessely et al., 2004; Tao et al., 2005; Ishibashi et al., 2008; Verheyen and Gottardi, 2010; Houston, 2017; Tassan et al., 2017). β-Catenin's dorsal stabilization by a Wnt ligand is nowadays debated, and it was reported that maternal Wnt11b rather is required for robust cortical rotation (Houston, 2022; Houston et al., 2022). The maternal mRNA *huluwa* (*hwa*) is vegetally deposited in *Xenopus* oocytes and becomes dorsally enriched in early cleavage embryos. In zebrafish, it moves from the vegetal pole towards the animal region along one side of the yolk cell during early cleavage. Hwa protein localizes dorsally and promotes Axin1 degradation, stabilizing β-Catenin. It is essential for dorsal development in both species, operating independently of a Wnt ligand (Yan et al., 2018). Lysosome activation on the dorsal side is crucial for dorsal axial development in *Xenopus* (Tejeda-Muñoz and De Robertis, 2022). It was proposed that, in the ventral region, Hwa protein is ubiquitinated and undergoes lysosomal degradation, whereas dorsally, non-ubiquitinated Hwa requires intact lysosomal trafficking for its dorsalizing activity (Zhu et al., 2021; Tejeda-Muñoz and De Robertis, 2022).

Strikingly, in approximately 30% of cases, the dorsal blastopore lip does not appear opposite to the SEP side in *Xenopus*. The most accurate predictor for the position of the future dorsoventral axis is the direction of cortical rotation, which can occur in the absence of sperm, after activating the egg by parthenogenesis. The microtubules of the sperm aster are not necessary for cortical rotation, but they polarize its direction (Black and Vincent, 1988; Gerhart et al., 1989; Ubbels, 1997; Tassan et al., 2017). Moreover, several amphibian eggs have some degree of latent dorsoventral asymmetry which reveals signs of bilateral symmetry. Some authors consider that the assumption that unfertilized amphibian eggs have perfect radial symmetry around the animal-vegetal axis should be revised (Brachet, 1977; Brown et al., 1994; Ubbels, 1997). During maturation of *Xenopus* stage VI oocytes, transition to metaphase II occurs, with the breakdown of the nucleus and the extrusion of the first polar body, leaving a white spot in the pigmented animal hemisphere. This "egg maturation point" (EMP) is eccentric in relation to the geometric center or geometric animal pole (GAP) of the animal hemisphere in about 70% of the spawned eggs (Brown et al., 1994) (Figure 1B). Remarkably, an intrinsic asymmetry of the unfertilized egg, termed "provisional bilateral symmetry" by Brown et al. (Brown et al., 1994), dictates the direction of yolk mass rotation after activation by parthenogenesis. Here, the EMP serves as a reliable positional predictor, because the yolk mass consistently rotates towards the EMP side. Since in most fertilized eggs the yolk mass rotates towards the SEP side, the sperm generally overrides the egg's provisional bilateral symmetry, providing a new directional cue. Strikingly, this is not always the case. For unknown reasons, some fertilized eggs (23% in the study of Brown et al.) (Brown et al., 1994) escape the directionality imposed by the sperm, and the yolk mass rotates guided by their intrinsic asymmetry. Notably, this EMP-directed rotation can only occur if the EMP and the SEP are on opposite sides (Brown et al., 1994) (Figure 1B). Thus, the *Xenopus* unfertilized egg bears an intrinsic bilateral symmetry which can direct dorsoventral axialization if the SEP-oriented cues fail. The molecular basis underlying this intrinsic bilateral symmetry is unknown.

The embryo's dorsal center, induced by β-Catenin, acts in concert with a ventral center to regulate the dorsoventral and anterior-posterior embryonic axes. Their reciprocal antagonistic relationship, extensively studied in amphibians and fish, involves the ventral center secreting BMP4 and Wnt8a morphogens to induce ventral-posterior fates. Meanwhile, the dorsal center expresses antagonists and transcriptional repressors of ventral morphogens, safeguarding the dorsal region from ventralization and posteriorization (De Robertis, 2009; Thisse and Thisse, 2015). It remained unclear if an event of asymmetric distribution of ventralizing molecules occurs at the beginning of embryogenesis. *Xenopus* transplantation experiments suggest local influences on ventral cell fates start from at least the 16-cell stage (Gallagher et al., 1991). While previous studies demonstrated the dorsalizing activity of polyA + mRNA from dorsal-animal blastomeres (Pandur et al., 2002) and dorsal accumulation of *wnt11b* transcripts at early cleavage stages (Castro Colabianchi et al., 2018; Schroeder et al., 1999; Tao et al., 2005), an enrichment of *wnt8b* mRNA in ventral-animal blastomeres at the 16-cell stage was also observed (Pandur et al., 2002). This hints at an early appearance of an asymmetric distribution of dorsally and ventrally enriched molecules. Strikingly, RNAseq analysis of total (4 embryos) or polyadenylated mRNA (1 embryo) did not find significant differences in transcriptomes between *Xenopus* dorsal and ventral cells at the 8-cell stage (De Domenico et al., 2015). However, mass spectrometry assays showed significant differences between dorsal and ventral proteomes at the 16-cell stage (Lombard-Banek et al., 2016) and in the metabolome at the 8 and 16-cell stage (Onjiko et al., 2015; Onjiko et al., 2017), with some proteins and small metabolites differentially enriched in the dorsal or the ventral side. This highlights that, from a molecular perspective, ventral is not equivalent to dorsal without dorsal molecules.

Our previous research revealed that Notch1 protein and mRNA are ventrally enriched in the animal hemisphere of 1-cell *Xenopus laevis* embryos, maintaining this asymmetry through cleavage stages. Employing gain- and loss-of-function approaches, we demonstrated that Notch1 contributes to the formation of the initial *Xenopus laevis* dorsoventral axis. This involves two ventralizing activities: 1) positive regulation of ventral center genes, mainly through the canonical pathway; 2) confining the blastula dorsal center through a non-canonical pathway, which promotes the destabilization of β-Catenin that escapes from the GSK3β-dependent degradation in the ventral side (Acosta et al., 2011; Castro Colabianchi et al., 2018). This local enrichment of Notch1, a molecule with proven ventralizing properties, represents the earliest sign of ventral development described so far in vertebrates, since it is evident from the 1-cell stage. Notably, mass spectrometry identified Nrarp (NOTCH regulated ankyrin repeat protein) as ventrally enriched in animal-ventral blastomeres of the 16-cell embryo, whereas GAPDH is homogeneously distributed, as expected for a housekeeping gene product (Lombard-Banek et al., 2016). This supports the idea that the Notch pathway is active at the ventral side of early cleaving embryos, since *nrarp* is regulated by canonical, RBPJ-dependent Notch signaling (Lamar et al., 2001).

Our previous findings raised the important question of whether ventralizing molecules are asymmetrically enriched at the same time or even earlier than maternal dorsal determinants. In this work, we aimed to establish when Notch1 asymmetry first arises in *X. laevis*. Surprisingly, we found that it is already present in the animal hemisphere prior to cortical rotation in zygotes and even in unfertilized eggs, both at the protein and mRNA levels. Moreover, *notch1* mRNA is not randomly distributed in unfertilized eggs, but consistently accumulates on the same side of the eccentric EMP. Strikingly, we found that the asymmetric distribution of Notch1 protein in an axis orthogonal to the animal-vegetal axis is already present in oocytes from the earliest stages of oogenesis. In addition, unfertilized eggs also show an asymmetric distribution of *bmp4* transcripts in the animal hemisphere. Our findings reveal a maternal bias in the distribution of molecules in the unfertilized egg that are known to control ventral patterning during embryonic axialization. This indicates that *X. laevis* eggs bear a latent, dorsoventral prepattern before fertilization, lending support for the first time at the molecular level to the hypothesis of their intrinsic bilaterality previously proposed by other authors (Brown et al., 1994; Ubbels, 1997). In addition, *notch1* asymmetry at the mRNA level is conserved in early zebrafish embryos from the zygote stage, supporting evidence of Notch pathway asymmetries during the earliest steps of development in Bilaterians.

Materials and methods

Animals and oocytes

Albino and wild-type *X. laevis* embryos were obtained by natural mating from adult males and females obtained from Nasco (Wisconsin), according to standard protocols (Sive et al., 2010). Adult animals were hormonally stimulated by injection of human chorionic gonadotrophin (Pregnyl, MSD, Argentina) (Sive et al., 2010). Eggs were obtained by gently squeezing hormonally stimulated females. Oocytes were donated by Dr. Karina Alleva´s laboratory and obtained from ovaries surgically removed from anesthetized pigmented *X. laevis* females. Ovaries lobes were transferred to ND96 buffer (96 mM NaCl; 2 mM KCl; 1.8 mM $CaCl_2$; 1 mM $MgCl_2$; 5 mM HEPES, pH 7.4) and oocytes were separated in smaller clumps with forceps. Oocyte clumps were incubated for 2 hs. with 1 mg/mL collagenase type I (GIBCO) in ND96, with gentle rotation (200 r.p.m). Every 15 min, oocytes were dispersed in the collagenase solution by gently pipetting them up and down through a wide tip Pasteur pipette. Once completely defolliculated, oocytes were extensively washed with ND96 buffer and fixed.

X. laevis embryos were staged according to Nieuwkoop and Faber (Nieuwkoop and Faber, 1994) and oocytes were staged according to Dumont (Dumont, 1972). *Danio rerio* (zebrafish) embryos were obtained as previously described (Kamm et al., 2013) and staged according to Kimmel et al. (Kimmel et al., 1995). The cortical rotation period in *X. laevis* spans from around 0.4 to 0.8 of the first cell cycle (Gerhart et al., 1989), corresponding approximately from 33 to 66 min post-fertilization (mpf) at 22°C–24°C, which is the temperature at which zygotes were collected.

In situ hybridization and immunolocalization

In situ hybridization (ISH) probes for zebrafish *notch1a* (Ke et al., 2008) and *X. laevis bmp4* (Fainsod et al., 1994), *hes4* (previously known as *hairy2a*) (Schmidt et al., 1995), *dll1* (previously known as *delta-1*) (Chitnis et al., 1995), *notch1* (Coffman et al., 1990), *wnt11b* (Tada and Smith, 2000) were previously described.

For cloning *pou5f3.1* cDNA (previously known as *oct91*), total RNA was isolated from *X. laevis* embryos with TRIzol reagent (ThermoFisher, Cat. #15596018), reverse transcribed with oligodT and SuperScript II reverse transcriptase (TermoFisher, Cat. #18064014). *Pou5f3.1* cDNA was amplified with Pfx DNA polymerase (Invitrogen, Cat. #11708013) with specific PCR primers containing linkers with restriction enzyme sites for cloning. Their sequences were as follows: *pou5f3.1*-F, CGGGATCCCCGGCAACTTAGGTAGGATT (BamHI site underlined); *pou5f3.1*-R, GGATCGATCGAAGTCTAGTTG CCTTGGT (ClaI site underlined). The PCR product was cut with BamHI and ClaI and inserted in pBluescript II SK+ with T4 DNA ligase. Identity was confirmed by sequencing. The plasmid was linearized with BamHI and the antisense probe was transcribed with T7 RNA polymerase.

Since it is not possible to distinguish the animal-vegetal axis in whole albino or bleached wild-type *X. laevis* oocytes, unfertilized eggs and zygotes, or in early stages of oogenesis in wild type oocytes, we adopted two strategies to determine if there are asymmetries in the distribution of Notch1 in the animal hemisphere: 1) For wild-type eggs, after fixation and rehydration, we isolated animal hemispheres by dissection through the equatorial plane, guided by the animal-vegetal pigmentation asymmetry. These animal hemispheres were further processed for ISH or Notch1 immunofluorescence as previously described, including a bleaching step to avoid quenching of the immunofluorescence signal by the pigment (Castro Colabianchi et al., 2018) (see below). 2) Albino eggs, albino zygotes, and bleached wild-type oocytes were processed for *notch1* ISH or Notch immunofluorescence combined with ISH for vegetal markers as spatial reference (*gdf1* for zygotes, *wnt11b* for eggs and oocytes), following the procedures described before (Castro Colabianchi et al., 2018).

The preparation of digoxigenin-labeled antisense RNA probes and the whole-mount ISH procedure for *Xenopus* were performed as previously described (Pizard et al., 2004), except that the proteinase K step was omitted. Double ISH was performed as previously described (López et al., 2005). Zebrafish embryos were fixed and processed for whole-mount ISH in the same conditions as *X. laevis* embryos, except that, after rehydration, they were dechorionated with sharp forceps pre-treated with 0.5 NaOH before proceeding to ISH. For immunofluorescence of endogenous Notch1 and GAPDH proteins, *X. laevis* oocytes, eggs, and embryos were fixed for 90 min with MEMPFA, transferred to Dent's fixative (80% methanol, 20% DMSO) for 72 h at −20°C, and permeabilized with pre-hybridization solution in the same conditions as for ISH. For revealing the ISH, we used the following reagents: a combination of 5-bromo-4-chloro-3-indoxyl phosphate (BCIP, Biosynth, B-7500) with p-Nitroblue Tetrazolium Chloride (NBT, Biosynth, N-8100), which gives a purplish/blueish color; BCIP, which gives a turquoise color, or Magenta Phosphate (Biosynth, B-7550), which gives a magenta color.

For Notch1 immunofluorescence combined with ISH of vegetal markers, specimens were fixed with MEMPFA overnight at 4°C and, the following day, they were subjected to the standard ISH protocol. After stringency washings, they were washed with TBSE, TBSET, and TBSET + BSA as described (Acosta et al., 2011), and were incubated overnight at 4°C simultaneously with the anti-digoxigenin-alkaline phosphatase antibody for ISH (Roche, 11093274910, 1/2000) and the Notch1 antibody for immunofluorescence. After washing 4 times with TBSET for 45 min and 1 h with TBSET + BSA, specimens were incubated with the secondary antibodies overnight at 4°C. Then, they were washed three times with TBSET and processed for revealing the *wnt11b* or the *gdf1* ISH. The pattern of the vegetal marker was correlated with the immunofluorescence image for Notch1 of the same specimen.

For preparing samples for cryosections, animal hemispheres of wild-type eggs obtained and treated as previously described were impregnated in 15% sucrose in PBS for 30 min at room temperature and were then kept overnight in 30% sucrose in PBS at 4°C. The following day, specimens were incubated in 15% gelatin (Sigma, G9391) in PBS for 30 min at 37°C, in tubes of 2 mL capacity. Embedding was performed in the same solution, and specimens were oriented in such a way that the internal, equatorial surface of animal hemispheres was laid on the bottom. In this way, serial sections were obtained, with the first section being the most internal one. Embedded specimens were snap-frozen by immersion for 1 min in an isopropanol/dry ice bath at −40°C or below, and immediately transferred to −70°C overnight. Before sectioning, specimens were transferred to −20°C for 1 h. Sections of 20 µm thickness were obtained with a cryostat (Leica, CM 1850) and collected on positively charged glass slides (Fisherbrand, Superfrost Plus). Sections were dried overnight at room temperature. Immunofluorescence was performed in general as previously described for whole-mount specimens (Acosta et al., 2011), except that for sections, incubations were carried out with 0.2 mL of each solution per slide and the slides were covered with Parafilm. Antibody incubations were performed overnight at 4°C in a wet chamber, and the antibodies were washed four times for 30 min with 50 mL of PBS each. Slides were mounted with Vectashield (Vector Laboratories, H-1200).

The commercially available Notch1 intra rabbit polyclonal antibody (N1 intra Ab) (Abcam, ab8387) was raised against a peptide from the human intracellular domain of NOTCH1, which has 93% identity with the protein encoded by *X. laevis notch1* and was validated in *X. laevis* in previous work (Castro Colabianchi et al., 2018). Primary and secondary antibodies were diluted in blocking buffer as follows: N1 intra Ab (1/200), GAPDH (Ambion, AM4300, 1/100), anti-α-tubulin (DSHB, 12G10, 1/100), anti-rabbit IgG-Alexa 594 (Thermo Fisher Scientific, A-11012, 1/100), anti-mouse IgG F(ab′)2-Alexa Fluor 488 (Thermo Fisher Scientific, A-11017, 1/200). For double immunofluorescence for Notch1 and GAPDH or α-tubulin in cryosections, the comparison of both patterns was restricted to those eggs in which GAPDH or α-tubulin showed a regular expression along the section.

Specimens were bleached at the end of the ISH procedure or after the permeabilization step with pre-hybridization buffer during the immunofluorescence procedure. The bleaching step was performed in 1% H_2O_2, 5% Formamide, 0.5X SSC, over a fluorescent light source.

All specimens were photographed in a MVX10 fluorescence microscope (Olympus) equipped with a DP72 camera (Olympus). For visual consistency to facilitate comprehension for the reader, all images in the figures were oriented with the Notch1+ side to the left, except for the bleached animal hemisphere shown in animal view in Figure 4A″ and the morphometric analysis shown in Figure 5, where the ISH images were oriented following the polar coordinates criterion described below, with the EMP upwards.

Results are expressed as the number of specimens showing an asymmetric distribution of the analyzed marker in relation to the total number of specimens analyzed (n) and are indicated in the Supplementary Tables. Biological replicates represent batches of embryos, eggs, or oocytes from different females, and their number (N) is indicated in the Supplementary Tables. In the case of double ISH or immunofluorescence combined with ISH with the reference markers *gdf1* or *wnt11b*, analysis of the other markers was restricted to those specimens showing a vegetal signal for the reference markers.

Image analysis for Notch1 immunofluorescence in unfertilized eggs

Notch1 and GAPDH immunofluorescence was quantified in cryosections of animal hemispheres from 15 independent unfertilized eggs (n = 15). Measurements were performed with ImageJ by defining two circular regions of interest (ROI), one on the region of visually maximum Notch1 immunofluorescence intensity (ROIa) and the other, on the opposite side (ROIb), for both, Notch1 and GAPDH immunofluorescence (Figure 3D). These ROIs comprised a portion of the egg's membrane (where Notch1 immunofluorescence intensity is visually highest) and the adjacent cytoplasmatic area (Figure 3D). We measured the gray value per pixel, which quantifies how far from the darkness (lack of fluorescence) the measured pixels are. Therefore, this variable represents the fluorescence intensity per pixel and indirectly represents the "protein level". For each ROI, we computed the mean pixel intensity (mpi). Statistical analysis was carried out using GraphPad Prism. As each sample always comprised a pair of measurements (as defined by ROIa and ROIb), paired t-tests (two-tailed) were performed; the difference between means was considered statistically significant when $p < 0.05$.

TABLE 1 Parameters for the morphometric analysis of ISH domains.

Parameter	Abbreviation	Definition
GAP centroid	GAPc	Centroid of the adjusted ellipse corresponding to the animal hemisphere outline. It represents a geometric animal pole (GAP) estimate
Egg's maturation point	EMP	White spot left in the pigmented egg's animal hemisphere after the extrusion of the first polar body during the transition to meiotic metaphase II.
y-axis length	YL	Measured length of the y-axis comprised by the egg's outline (px)
Circle radius	CR	Calculated length (px): $CR = 0.5 \times YL$
ISHc angle	ISHc ϴ	Angle between the radius passing through the ISHc and the radius on the y-axis passing through the EMP, with the vertex in the GAPc
EMP-GAPc distance	EGD	Measured distance between the EMP and the GAPc (px)
ISHc-GAPc distance	IGD	Measured distance between the ISHc and the GAPc (px)
Relative EGD diametrical distance	$rEGD_{diam}$ (%)	Calculated relative distance: expressed as % of YL. $rEGDdiam = \frac{EGD}{YL} \times 100$
Relative IGD diametrical distance	$rIGD_{diam}$ (%)	Calculated relative distance: expressed as % of YL. $rIGDdiam = \frac{IGD}{YL} \times 100$
Relative EGD radial distance	$rEGD_{rad}$ (%)	Calculated relative distance: expressed as % of CR. $rEGDrad = \frac{EGD}{YL} \times 100$
Relative IGD radial distance	$rIGD_{rad}$ (%)	Calculated relative distance: expressed as % of CR. $rIGDrad = \frac{IGD}{YL} \times 100$
ISH area per quadrant	ISHa q_n	Measured area of the ISH domain for each quadrant (q1 to q4) (px^2)
Relative ISH area per quadrant	rISHa q_n (%)	Calculated relative area: expressed as % of total ISH area. $rISHa\,qn = \frac{ISHa\,qn}{ISHa\,q1+ISHa\,q2+ISHa\,q3+ISHa\,q4} \times 100$

Morphometric analysis of the spatial relationship between *notch1* mRNA distribution and the EMP position

Animal hemispheres dissected from unfertilized pigmented eggs that were cut in the equatorial plane and hybridized with *notch1* or *pou5f3.1* probes as described above were subjected to a morphometric analysis with FIJI/ImageJ as follows (Supplementary Figure S1). For determining the positions of the animal hemisphere's and the ISH domain's centroids, measurements were set to fit an ellipse. External views (animal view face images) of the egg's animal hemisphere were used to obtain the animal hemisphere's outline, the adjusted ellipse, and the centroid position through the Analyze Particles tool, as shown in Supplementary Figure S1. This centroid was named GAPc, as an estimate of the GAP position. Particles were added to the ROI Manager, and measurements gave us the GAPc coordinates, which were used to mark its position with the overlay brush. Then, the EMP was also marked with the overlay brush. The overlay containing the egg's outline, the GAPc, and the EMP was flattened and saved with.png format. This image was then processed with Adobe Photoshop. After unlocking layers, an overlay with transparent background was generated by deleting everything (after selection with the magic wand or the lasso tool), except for the egg's outline, the GAPc, and the EMP. To overlap this image to the ISH image (equatorial face) of the same egg, both were imported to CorelDRAW. The ISH image was digitally inverted to put it in register with the animal face view. In this way, all further measurements performed on the inverted ISH image are indeed projections on the animal view face, from which the egg's outline, the GAPc, and the EMP positions were obtained. Then, the transparent overlay containing these landmarks was reoriented until the egg's outline in the overlay matched the egg's contour on the inverted ISH image. Both objects were then grouped and reoriented on a polar coordinates graph representing the animal view of the egg, with the y-axis corresponding to the egg's meridian passing through the GAPc and the EMP, with the GAPc centered at $x,y = 0$, and the EMP in the positive ray of the y-axis. The x-axis corresponds to the meridian perpendicular to the GAPc-EMP meridian. We defined four quadrants around the GAPc, with boundaries at the x and y-axes. They were numbered clockwise, from q1 to q4 (Supplementary Figures S1–S4; Figure 5F). The CorelDRAW image generated in such a way was exported to.tif and cut with Adobe Photoshop to 15 cm × 15 cm at 300 ppi. This image was opened with FIJI/ImageJ and made binary to define a region of interest (ROI) encompassing the whole ISH domain (ISH ROI), while synchronizing the binary and the RGB image to trace the ISH ROI. After measuring to obtain the ISH ROI centroid, which we designated as ISH centroid (ISHc), this was marked in the overlay of the RGB image, together with the radius passing through the ISHc. A flattened image was created in tif format to proceed for further measurements, which were performed using the ObjectJ Plugin in FIJI/ImageJ, available at: https://sils.fnwi.uva.nl/bcb/objectj/. For this purpose, we created an ObjectJ project (Supplementary Methods) to measure the parameters listed in Table 1.

The ISHc angle serves as an estimate of the position of the ISH domain in relation to the EMP. This angle may be in theory between 0° and 180°, with positive and negative values at the right and the left sides of the y-axis, respectively (Supplementary Figures S1–S4; Figure 5F). Those ISHc forming an angle between ± 89° and 0° were considered to be located on the same side of the EMP, whereas those forming an angle between ± 91° and 180° were considered to be located on the opposite side of the EMP.

Assuming a spheric egg shape, YL would represent the egg's diameter if the egg were cut exactly at the equatorial plane. Then, one-half of this length would represent the egg's radius (or circle radius, CR, at the equatorial plane). As it is impossible to ascertain if the eggs were cut exactly at the equatorial plane, to compensate for small deviations between samples, all measured distances were normalized by dividing them by the corresponding measured YL or calculated CR. For expressing results in the graphs, we used normalizations relative to the CR, thus representing relative radial distances, as they more clearly show the grade of eccentricity with respect to the GAPc.

It is obvious that the *y*-axis cannot be defined in eggs with a central EMP, i.e., those in which the EMP position coincides with the GAPc position. Moreover, we surmise that as the GAPc is an estimate of the GAP position and is subject to error, the orientation of the *y*-axis might be wrongly determined in eggs with an EMP very close to the GAPc. Therefore, a cut-off level for the distance between the EMP and the GAPc was assumed to minimize the error of orienting the egg along an ambiguous *y*-axis. Hence, for analyzing the spatial relationship between the EMP and the ISH domain, we excluded those eggs with a $rEGD_{rad} < 10\%$, even if they showed an asymmetric *notch1* mRNA or a central *pou5f3.1* distribution when visually observed, although they are included in the qualitative analysis shown in Supplementary Table S3. We also excluded from this morphometric analysis those eggs included in Supplementary Table S3 in which the EMP was not visible because it was masked by the ISH staining.

For each frog and ISH marker, EMP and ISHc positions for the analyzed eggs were represented using CorelDRAW on a polar coordinates graph representing the animal view of an egg as a circle with a *y*-axis length and CR length of 100% on the equatorial plane, as described above (Supplementary Figures S1–S2; Figure 5; Supplementary Table S4). To construct the graphs in Supplementary Figures S2–S4, each point was positioned in the polar graphs using the relative radial distance to the GAPc ($rEGD_{rad}$ and $rIGD_{rad}$) and the ISHc angle (being the EMP positioned on the positive ray of the *y*-axis, by definition) (Supplementary Figure S1B). Then, the three polar graphs of Supplementary Figures S2–S4 were overlapped to construct the polar graph in Figure 5F containing the ISH centroids from all the analyzed eggs and both ISH markers. In this figure, to avoid overcrowding the graph with dots and to clearly show the position of the ISHc, we deleted the individual EMPs and instead represented the mean EMP position for all the analyzed eggs. This is a *bonafide* simplification, as there were no significant differences between the mean $rEGD_{rad}$ of eggs analyzed for *notch1* and *pou5f3.1* nor between the mean $rEGD_{rad}$ of eggs from the two frogs analyzed (two-tailed *t*-test, $p < 0.05$).

Statistical analysis was performed with GraphPad Prism. The employed tests are indicated in the figure legends or the main text. The difference between means was considered statistically significant when $p < 0.05$.

Results

Notch1 is asymmetrically distributed in *Xenopus laevis* zygotes before the onset of cortical rotation

From our previous findings and given the well-known relocation of maternal dorsal determinants through cortical rotation, we wondered if the early asymmetric location of Notch1 precedes or appears during cortical rotation. For this purpose, we analyzed the distribution of Notch1 protein and mRNA through immunofluorescence and *in situ* hybridization (ISH) in albino embryos at different post-fertilization timepoints, before the onset of cortical rotation, which begins around 30 min post-fertilization (mpf), and at the end of this process. Because the animal-vegetal axis cannot be assigned in albino embryos by means of pigment distribution, we revealed *gdf1* mRNA in the same embryos, as this marker (previously known as *vg1*) is uniformly located in the vegetal hemisphere of oocytes and eggs, and is inherited by the vegetal cells of early embryos without being translocated to the dorsal side (Weeks and Melton, 1987; Alarcón and Elinson, 2001). Surprisingly, we found that both Notch1 protein (Figures 2A–C) and mRNA (Figure 2D) are asymmetrically distributed in the animal hemisphere before cortical rotation takes place (Supplementary Table S1), even as early as at 3 mpf (Figure 2A). This *notch1* mRNA asymmetry was maintained by the end of cortical rotation (Figure 2E). Our results demonstrate that an early asymmetric Notch1 distribution exists in the zygote's animal hemisphere, and it is independent of cortical rotation.

Notch1 protein is asymmetrically distributed before fertilization in an axis orthogonal to the animal-vegetal axis of *Xenopus laevis* eggs

The asymmetric distribution of *notch1* gene products in the animal hemisphere of zygotes preceding cortical rotation might be due to an inherited maternal asymmetry. Therefore, we addressed if such asymmetries could be present prior to fertilization in eggs.

We dissected animal hemispheres (where Notch1 protein and mRNA are found during the early embryonic stages) from fixed, unfertilized *X. laevis* eggs obtained from pigmented females and processed them for immunofluorescence. Notch1 asymmetries in the animal hemisphere were observed in 96 out of 99 eggs obtained from three different pigmented females (Supplementary Table S2; Figure 3A,A′-C; Supplementary Figure S5A–C). We also fixed unfertilized eggs from albino females and combined Notch1 immunofluorescence with *wnt11b* ISH to orient the unpigmented eggs in the animal-vegetal axis since *wnt11b* transcripts are localized in a gradient from the vegetal pole to the equator before fertilization (Kataoka et al., 2005). Notch1 was asymmetrically distributed in the animal hemisphere of eggs from two different albino females (Figure 3C,C′; Supplementary Table S2).

A potential problem with immunofluorescence in egg halves or whole eggs might be that deformations could arise, resulting in an apparent asymmetric signal due to the unequal accumulation of material. Therefore, we performed double immunofluorescence for Notch1 and the ubiquitously expressed proteins GAPDH or α-Tubulin in cryosections obtained from pigmented hemispheres in a plane perpendicular to the animal-vegetal axis. In this way, we could observe the same density of material throughout the entire sample. Again, we found a very clear asymmetric distribution of Notch1 immunofluorescence (Figure 3B), while GAPDH (Figure 3B′) or α-Tubulin immunofluorescence (Supplementary Figure S5D, E) in the same sections was ubiquitous, as expected.

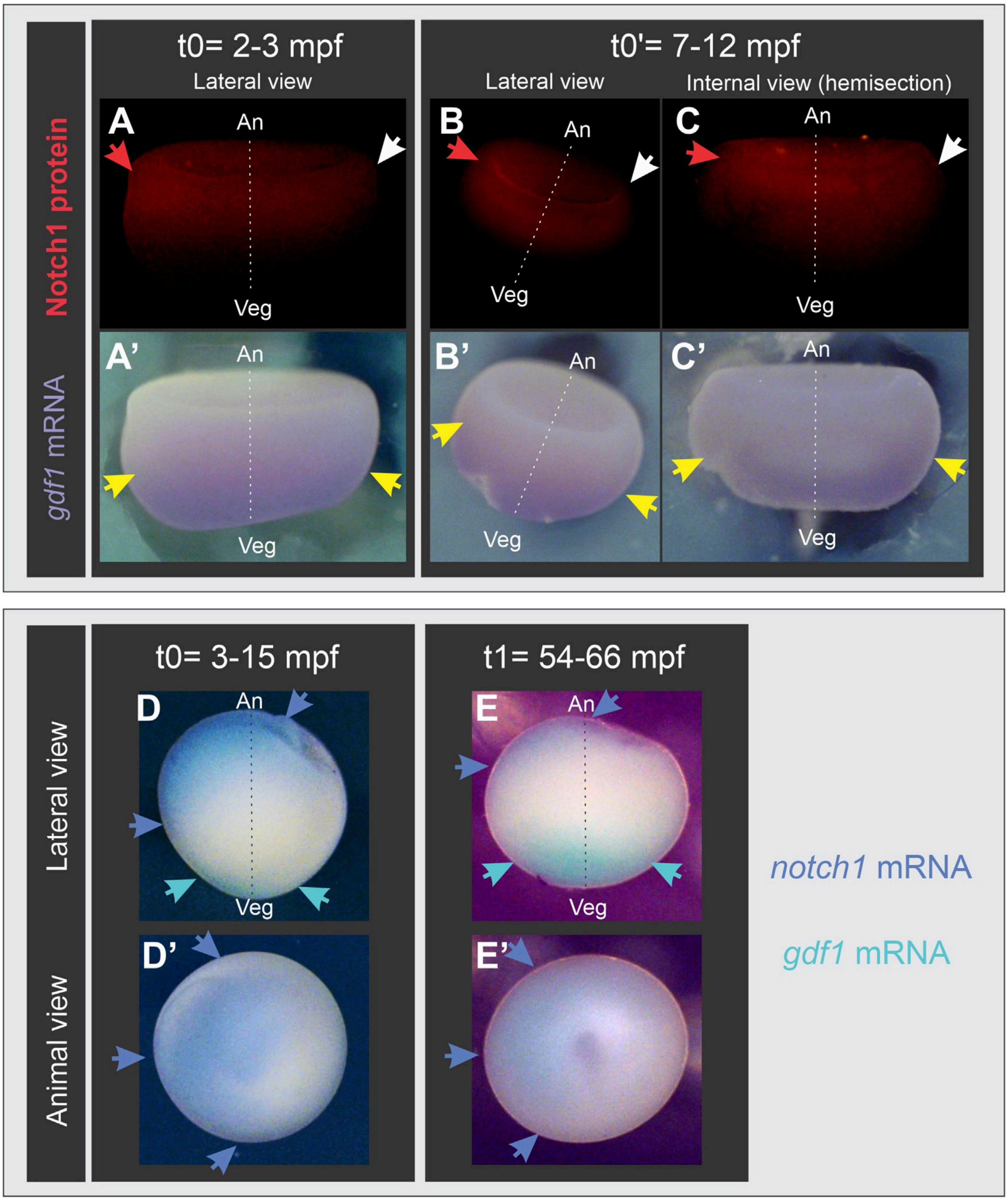

FIGURE 2
Notch1 protein and mRNA are asymmetrically distributed in the animal hemisphere of *Xenopus laevis* zygotes before the onset of cortical rotation. Albino embryos at s1 fixed before (t0, t0′) or at the end (t1) of cortical rotation; mpf, minutes post-fertilization. **(A′–E′)** are the same embryos shown in **(A–E)**, respectively. **(A–C′)** combined Notch1 immunofluorescence **(A–C)** and *gdf1 (vg1)* ISH **(A′–C′)**. Red and white arrows respectively point to the highest and lowest immunofluorescence signal, indicating that Notch1 protein is asymmetrically distributed in the animal hemisphere before and after cortical rotation, while *gdf1 (vg1)* mRNA is uniformly distributed in the vegetal region (yellow arrows), as expected. **(D–E′)** double ISH for *notch1* (blue) and *gdf1 (vg1)* (turquoise). Blue arrows point to the asymmetric distribution of *notch1* mRNA in the animal hemisphere before **(D,D′)** and at the end of cortical rotation **(E,E′)**. Embryo's orientation was verified by *gdf1* (*vg1*) mRNA location (turquoise arrows) as reference since it is uniformly distributed in the vegetal cortex. An, animal pole; Veg, vegetal pole; broken line, animal-vegetal axis.

These asymmetries in cryosections were observed in 21 out of 22 eggs obtained from two different females (Supplementary Table S2), confirming that Notch1 protein is asymmetrically distributed in the animal hemisphere of *X. laevis* unfertilized eggs in an axis orthogonal to the animal-vegetal axis. Overall, this asymmetric Notch1 protein distribution was observed in 96% of the eggs analyzed by either experimental approach (n = 130; 6 independent biological replicates; Supplementary Table S2).

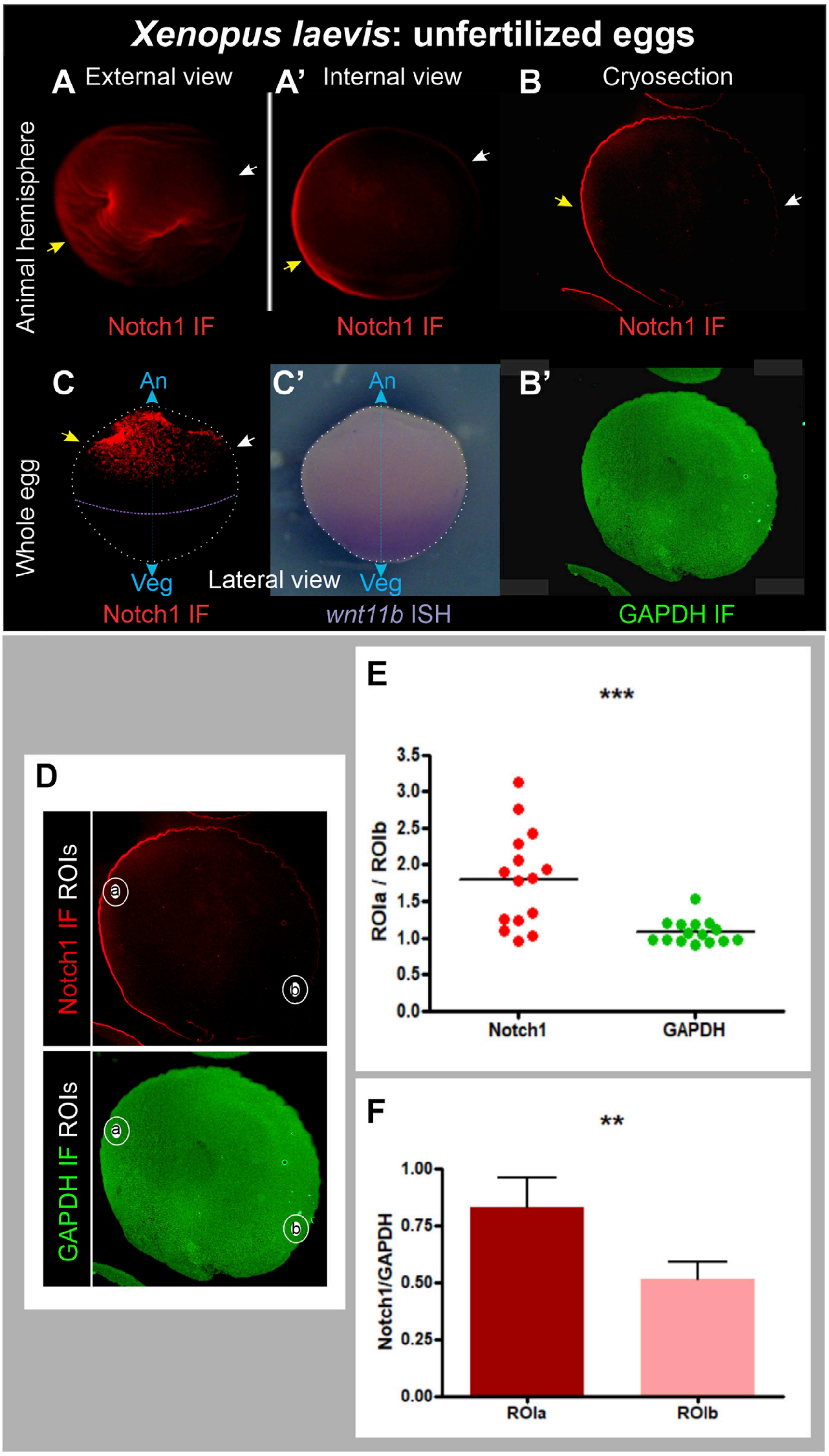

FIGURE 3
Asymmetric distribution of Notch1 protein in the animal hemisphere of unfertilized *Xenopus laevis* eggs. **(A–B')** Pigmented animal hemispheres were dissected by cutting them away through the equatorial plane, bleached, and directly processed for Notch1 immunofluorescence **(A,A')** or cryosections followed by Notch1 immunofluorescence combined with GAPDH immunofluorescence as ubiquitous reference protein **(B,B')**. **(C,C')** Whole albino egg, Notch1 immunofluorescence **(C')** combined with *wnt11b* ISH as reference to verify the orientation of the animal-vegetal axis **(C')**, since *wnt11b* mRNA is uniformly distributed in the vegetal region. Yellow and white arrows respectively point to the highest and lowest Notch1 immunofluorescence signal, indicating that Notch1 protein is asymmetrically distributed in the animal hemisphere in unfertilized eggs. An, animal pole; Veg, vegetal pole; IF, immunofluorescence; cyan double arrow, animal-vegetal axis. **(D–F)** Quantification of Notch1 and GAPDH immunofluorescence in cryosections of animal hemispheres obtained from pigmented, unfertilized eggs, bleached before immunofluorescence. The images shown in **(D)** are the same as in **(B,B')**, but here, the selected ROIs are demarcated. **(E)** Dispersion graph comparing the relative mean pixel intensity (mpi) between ROIa and ROIb for Notch1 and GAPDH immunofluorescence in animal hemisphere cryosections from 15 independent unfertilized eggs. The mean ROIa/ROIb ratio was

(*Continued*)

FIGURE 3 (Continued)
significantly higher for Notch1 than for GAPDH immunofluorescence, which was close to 1, as expected for a protein of homogeneous distribution ($p = 0.0008$, two-tailed paired *t*-test). **(F)** Comparison of relative Notch1/GAPDH mpi levels between ROIa and ROIb in the same set of eggs shown in **(E)**. The Notch1/GAPDH ratio was significantly higher in ROIa than in ROIb ($p = 0.0016$, two-tailed paired *t*-test, n = 15). Since each sample always comprised a pair of measurements (as defined by ROIa and ROIb), paired t-tests (two-tailed) were performed; the difference between means was considered statistically significant when $p < 0.05$.

For further verification, Notch1 and GAPDH immunofluorescence were quantified in cryosections of animal hemispheres from 15 independent unfertilized eggs by measuring the mean pixel intensity (mpi) in two circular regions of interest (ROI), one in the region of visually maximum Notch1 immunofluorescence (ROIa) and the other, in the opposite side (ROIb) (Figure 3D). Figure 3E shows a dispersion graphic comparing the ROIa/ROIb mpi ratios between Notch1 and GAPDH. For GAPDH immunofluorescence, these ratios were consistently distributed around a mean close to 1 (mean = 1.079 ± 0.04231, n = 15), as expected for a protein of homogeneous distribution. In contrast, for Notch1 immunofluorescence, ROIa/ROIb mpi ratios were distributed around a significantly higher mean (1.801 ± 0.1699, n = 15; $p = 0.0008$, two-tailed paired *t*-test) (Figure 3E), confirming that Notch1 protein is asymmetrically distributed in the animal hemisphere, whereas GAPDH is homogeneously distributed, as expected. Moreover, when we normalized Notch1 in relation to GAPDH immunofluorescence levels, the Notch1/GAPDH ratio for ROIa was significantly higher than the Notch1/GAPDH ratio for ROIb ($p = 0.0016$, two-tailed paired *t*-test, n = 15) (Figure 3F). In conclusion, Notch1 protein is asymmetrically distributed in the animal hemisphere of *X. laevis* unfertilized eggs.

notch1 mRNA is asymmetrically distributed in the animal hemisphere of unfertilized *Xenopus laevis* eggs and it is not the only maternal transcript with asymmetric distribution

Next, we wondered if *notch1* transcripts and other mRNAs encoded by genes involved in Notch signaling (*dll1, hes4*) (Turner and Weintraub, 1994; Chitnis et al., 1995; Davis et al., 2001; Tsuji et al., 2003; López et al., 2005; Sakano et al., 2010), embryonic dorsoventral patterning (*bmp4*) (Hemmati-Brivanlou and Thomsen, 1995; Bell et al., 2003; Reversade et al., 2005; Kirmizitas et al., 2017), or maintenance of pluripotency (*pou5f3.1*) (Morrison and Brickman, 2006) showed asymmetric patterns in unfertilized eggs in an axis different from the animal-vegetal one. Single ISH for each marker was performed in dissected animal hemispheres from pigmented eggs, or double ISH for *notch1* and *wnt11b* as reference marker for the vegetal pole was performed in albino eggs. We also performed double ISH for *notch1* and *pou5f3.1* in albino eggs.

notch1 mRNA was asymmetrically distributed in the animal hemispheres (Figure 4A–A″,B-F; 97%, n = 70 unfertilized eggs obtained from a total of seven different females; Supplementary Table S3). Surprisingly, the same was observed for *bmp4* (Figure 4G,G′), *dll1* (Figure 4H,H′), and, although weakly, also with *hes4* transcripts (Figure 4I,I′) (Supplementary Table S3). In contrast, we observed a central, non-asymmetric distribution of *pouf5f3.1* mRNA (Figures 4C–F, J,J′; Supplementary Table S3), probably representing accumulation in the egg's nuclear region below the animal pole. Eggs processed in parallel without adding the ISH probe did not show any staining (Figure 4K,K′), confirming that the patterns shown here were not due to non-specific color reaction. These results demonstrate that in unfertilized eggs, there is a prepattern of asymmetric distribution of some maternal mRNAs, some of them with known ventralizing properties, such as *notch1* and *bmp4*, in an axis different from the animal-vegetal axis. Asymmetric distribution of *bmp4* transcripts in the egg's animal hemisphere as shown in the present work was not previously recognized, even when the ISH image in Figure 2A in Bell et al. (Bell et al., 2003) suggests being so.

notch1 mRNA preferentially locates on the EMP side in *Xenopus laevis* unfertilized eggs

Next, we aimed to determine if the asymmetric distribution of *notch1* mRNA bears a spatial correlation with the EMP location since it was previously established that this point is generally eccentric in relation to the GAP and predicts the direction of yolk mass rotation in activated eggs (Brown et al., 1994). For this purpose, we performed a morphometric analysis of the ISH domains in pigmented animal hemispheres from unfertilized eggs, comparing *notch1* and *pou5f3.1* mRNA distributions as detailed in the Materials and Methods section (see Table 1; Supplementary Figure S1). The animal hemisphere centroid was considered as an estimate of the GAP and was named GAP centroid (GAPc). We represented the egg's animal hemisphere in animal view as a circle in a polar coordinates graph with the EMP-GAPc axis as the *y*-axis, the GAPc in the center (at the origin of coordinates x,y), and projected the ISH domain into this template. Then, we measured the relative radial distance of the ISH domains centroids (ISHc) to the GAPc and their angular deviation from the EMP-GAPc axis (*y*-axis). We also measured the total ISH area and the relative ISH area contributed by each of the four quadrants defined around the GAPc (q1 to q4, in clockwise direction). Results are presented in Figure 5, Supplementary Figures S2–S4, Supplementary Movie S1; Supplementary Table S4.

The *pou5f3.1* centroids were found very closely around the GAPc (mean relative radial distance = 5.7%, n = 7; Figure 5A-A″,F,G; Supplementary Figure S2, Supplementary Movie S1), consistent with a central location for this marker. In contrast, the distribution of *notch1* centroids clearly did not overlap that of the *pou5f3.1* centroids (Figures 5B–F; Supplementary Figure S3; Supplementary Figure S4, Supplementary Movie S1). Moreover, they were significantly farther away from the GAPc (mean

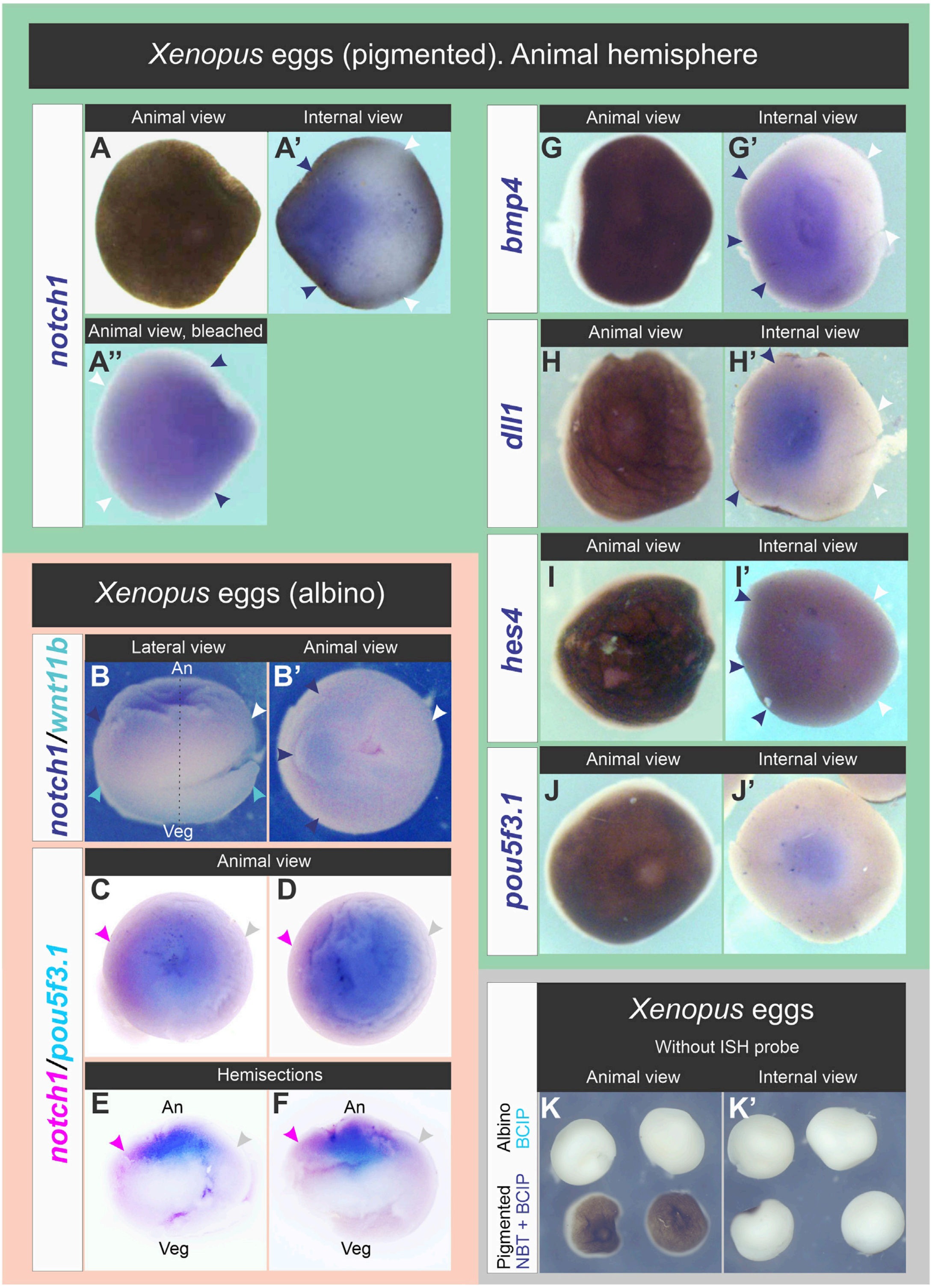

FIGURE 4
Distribution of *notch1* mRNA and other transcripts in the animal hemisphere of unfertilized *Xenopus laevis* eggs. **(A–A'')**, **(G–J')** Pigmented eggs were cut through the equatorial plane. Animal hemispheres were processed for ISH for the following markers: *notch1* **(A–A'')**, *bmp4* **(G,G')**, *dll1* **(H,H')**, *hes4* **(I,I')**, and *pou5f3.1* **(J,J')**. Animal hemispheres in **(A,G–J)** were photographed in animal view, then turned 180° to the right of the observer to photograph their internal side (equatorial face of the animal hemisphere; internal views in **(A',G'-J')**. The animal hemisphere processed for *notch1* ISH was photographed before **(A,A')** and after bleaching **(A'')** in animal **(A,A')** and internal views **(A')**. **(B,B')** Albino egg processed for double ISH for *notch1* (blue) and *wnt11b* (turquoise) shown in lateral **(B)** and animal views **(B')**. Dark blue and white arrowheads respectively point to the highest and lowest *notch1* ISH signal, indicating that its transcripts are asymmetrically distributed in the animal hemisphere. The egg's orientation was verified by the location of *wnt11b* mRNA as reference (turquoise arrowheads), which is uniformly distributed in the vegetal cortex **(B)**. **(C–F)** Whole albino eggs processed for double ISH for *notch1* (magenta) and *pou5f3.1* (turquoise). Animal **(C,D)** and internal views of hemisections cut in the animal-vegetal plane **(E,F)**. Magenta and gray arrowheads respectively point to the highest and lowest *notch1* ISH signal, indicating that its transcripts are enriched on one side of the animal

(Continued)

FIGURE 4 (Continued)
hemisphere, while *pou5f3.1* does not show such asymmetry. An, animal pole; Veg, vegetal pole; broken line, animal-vegetal axis. Dark blue and white arrowheads in **(A′-A″,G′–I′)** respectively point to the highest and lowest levels of *notch1, bmp4, dll1,* and *hes4* transcripts in the animal hemisphere. Notice the central location of *pou5f3.1* transcripts in the animal hemisphere, most likely related to accumulation in the nuclear region. **(K,K′)** Absence of non-specific staining in whole albino eggs (upper row) and animal hemispheres from pigmented eggs (lower row) that were processed for ISH but without adding probes, in parallel with albino eggs processed for double ISH (as those shown in B,B′) and revealed with BCIP and with eggs processed for *notch1* ISH (as shown in A-A″) and revealed with NBT + BCIP. After the ISH procedure, albino eggs were bisected to show the internal face (K′, upper row).

relative radial distance = 31.5%, n = 15, $p < 0.05$; two-tailed *t*-test; Figure 5G), implying that they are consistently eccentric (i.e., 5.5 times more eccentric than the central marker *pou5f3.1*), hence reflecting *notch1* mRNA asymmetric distribution in the animal hemisphere. Notably, 13 out of the 15 analyzed eggs showed the *notch1* centroid on the same side of the EMP (Figure 5F; Supplementary Figures S3, S4; Supplementary Table S4), being distributed at both sides of the EMP-GAPc axis. Overall, the mean deviation angle of the *notch1* ISHc from the EMP-GAPc axis was +9.2° (Figure 5F, Supplementary Movie S1; Supplementary Table S4). Morphometric analysis of the *notch1* ISH area showed that both quadrants on the same side of the EMP (q1 and q4) mostly contribute to the ISH domain in the analyzed population of eggs in equal proportions, with significantly lower contribution from both quadrants on the opposite side of the EMP (q2 and q3) (paired, two-tailed *t*-test, $p < 0.05$; n = 15) (Figure 5H; Supplementary Table S4). These results confirm the asymmetric distribution of *notch1* transcripts in the animal hemisphere and strongly argue in favor of a bias of *notch1* mRNA distribution towards the EMP side in unfertilized eggs.

Notch1 is asymmetrically distributed in *Xenopus laevis* oocytes

The results shown above prompt the question about the distribution of Notch1 during oogenesis. In the ovary of adult *X. laevis* females, oocytes are found in meiotic prophase I at different growing stages classified from I to VI (Dumont, 1972). Stage VI oocytes (sVI) represent their terminal stage. They are competent for maturation (during which resumption of meiosis from prophase I to metaphase II occurs) and subsequent ovulation, which proceed under the stimulus of pituitary and ovarian hormones (Rasar and Hammes, 2006).

To address when Notch1 expression and asymmetry in the animal hemisphere first arise, defolliculated sI to sVI oocytes obtained from pigmented females were processed for *wnt11b* ISH, as reference marker of the vegetal pole throughout oogenesis (Kloc and Etkin, 1995), followed by Notch1 immunofluorescence. After the ISH staining, a bleaching step was included to avoid quenching of the immunofluorescence by the pigment.

We found that Notch1 is asymmetrically distributed towards one side of the animal-vegetal axis from the earliest stages of oogenesis (Figure 6; Supplementary Table S5). We often observed Notch1 immunofluorescence in the vegetal region with variable intensity during earlier stages, but expression appears to be more restricted towards one side of the animal hemisphere by stage VI (Figure 6). Therefore, Notch1 asymmetry in an axis orthogonal to the animal-vegetal axis emerges with oogenesis.

Notch1 mRNA is asymmetrically distributed in zebrafish during early embryogenesis

We have previously shown that *notch1* transcripts are enriched on the ventral side during early *X. laevis* embryogenesis (Castro Colabianchi et al., 2018) and we wondered if the same occurs in another anamniote model, like the zebrafish, in which we also showed an asymmetric Notch1 distribution at the protein level (Castro Colabianchi et al., 2018). *D. rerio* has four *notch* genes: *notch1a, notch1b, notch2* and *notch3*. The two *notch1* genes appeared in teleosts at a recent duplication event, after they diverged from tetrapods. Among them, *notch1a* transcripts are the only ones that can be detected by ISH as maternal mRNA (Favarolo and López, 2018), but no attention has been paid to whether it shows an asymmetric distribution. Therefore, we analyzed the expression of *notch1a* by ISH in zebrafish embryos and found that there is also a consistent enrichment of *notch1* transcripts in a region of the animal hemisphere, from the zygote stage until the last analyzed stage (sphere) (100% of embryos, n = 134; Figure 7; Supplementary Table S6). This result indicates that the early asymmetry in the distribution of *notch1* transcripts is conserved between fish and amphibians.

Discussion

Molecular asymmetries support the hypothesis of a latent dorsoventral prepattern in unfertilized *Xenopus laevis* eggs

In the present work, we found that the asymmetric distribution of Notch1 protein in an axis orthogonal to the animal-vegetal axis is already present from the earliest stages of oogenesis. This asymmetry is maintained and even more pronounced in mature, unfertilized eggs, in which a marked enrichment of Notch1 protein is observed towards one side of the animal hemisphere. Strikingly, in mature, unfertilized eggs, *notch1* mRNA is consistently enriched on the EMP side. After fertilization, *notch1* mRNA and its encoded protein are asymmetrically distributed in the zygote's animal hemisphere before and after cortical rotation, and we have previously demonstrated that ventrally accumulated Notch1 normally plays a ventralizing role in the establishment of the embryonic dorsoventral axis (Acosta et al., 2011; Castro Colabianchi et al., 2018). Importantly, both phosphorothioate-modified antisense DNA oligonucleotides and antisense morpholino oligonucleotides have been previously used to block *notch1* function in oocytes by other authors (Mir et al., 2008) and early embryos in our previous work (Acosta et al., 2011; Castro Colabianchi et al., 2018). Since maternal mRNAs can be

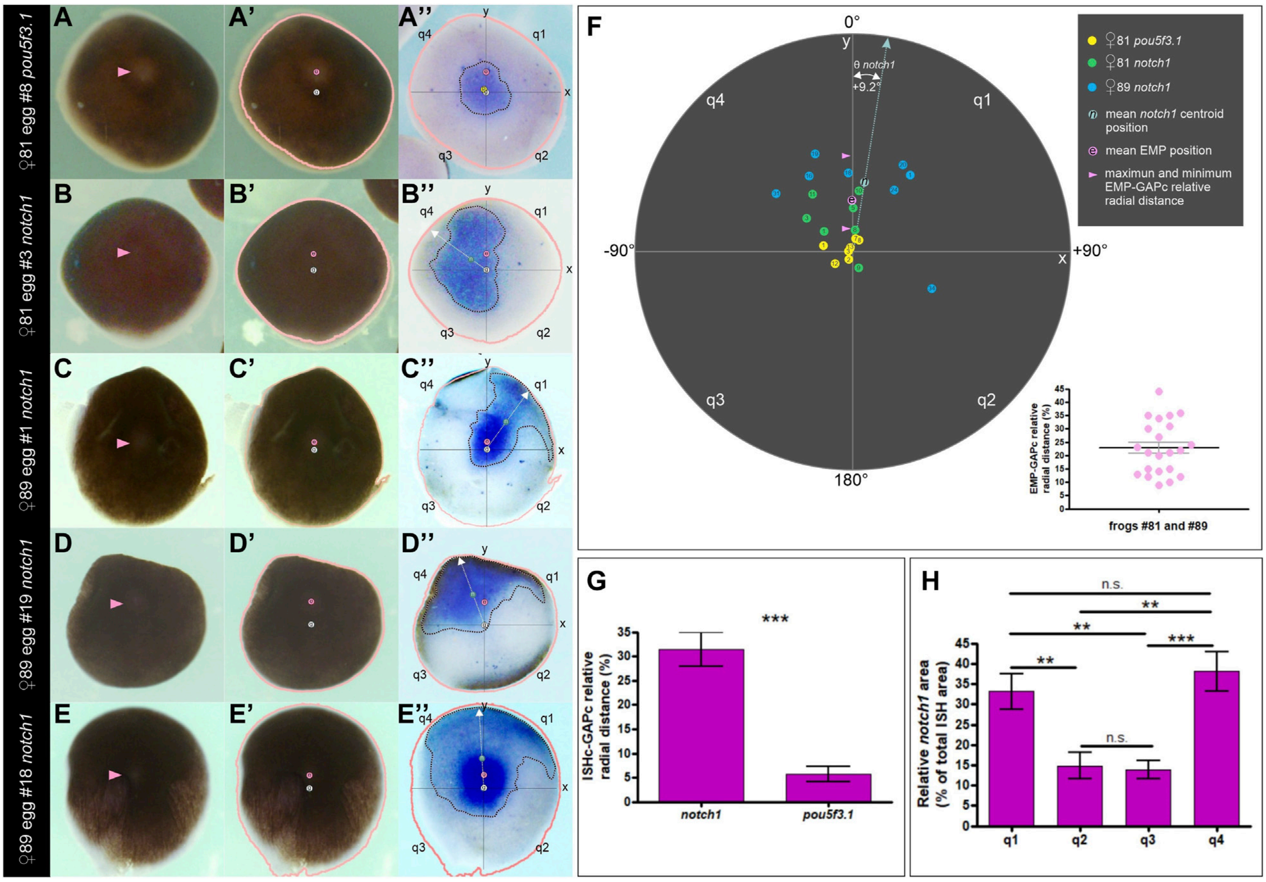

FIGURE 5
Morphometric analysis showing that the distribution of *notch1* mRNA is biased towards the EMP side in unfertilized *Xenopus laevis* eggs. **(A–E″)** Examples of animal hemispheres obtained from pigmented eggs that were analyzed by morphometry. **(A–A″)** *pou5f3.1* ISH. **(B–E″)** *notch1* ISH in four different animal hemispheres. The first column shows the external, animal views; pink arrowheads point to the EMP. The second column shows the same animal views labeled with the EMP (e, pink circles) and GAPc (g, white circles) locations, and a salmon line corresponding to the egg's outline drawn by the Analize Particle tools with FIJI. In the third column, these landmarks were overlapped as an overlay to the inverted internal views (equatorial face) showing the ISH domains of the corresponding eggs. Axes and quadrants were labeled as described in the text. Dotted black lines demarcate the ISH ROIs; their centroids are labeled with a yellow circle for *pou5f3.1* (p) and a green circle for *notch1* (n). The white dotted arrow lines correspond to the radius containing the ISH centroids (ISHc). Eggs in **(A–A″,D–D″)** are the same as Figure 4F, F′ and A-A″, respectively, but here, their images are oriented for the morphometric analysis and labeled with the landmarks. **(F)** Polar coordinates graph showing the distribution of ISH centroids for *pou5f3.1* and *notch1* (color-coded circles, see references in the upper right corner of the figure) for all the analyzed eggs, according to their relative radial distances to the GAPc and their deviation angle from the EMP-GAPc axis (*y*-axis). Inside the circles, numbers indicate the individual egg# (see Supplementary Table S4 for the corresponding measurements). For *notch1* ISH centroids, the mean deviation angle ϴ from the EMP-GAPc axis is indicated. The pink circle shows the mean EMP relative radial distance to the GAPc for all analyzed eggs; pink arrowheads show the range of EMP relative positions of the analyzed eggs. Notice that the inferior range limit is the cut-off level assumed for performing the morphometric analysis. The inset in the lower right corner shows a dispersion diagram representing the EMP relative radial distance to the GAPc for all the analyzed eggs. Mean±SEM values are indicated (black and grey lines, respectively). Their spatial distribution is displayed in the polar coordinates graphs of Supplementary Figures S2–S4 and measurements are shown in Supplementary Table S4. See Supplementary Movie S1 showing the transitions between images. **(G)** ISH centroids for *notch1* mRNA are significantly eccentric in relation to the central marker *pou5f3.1* (unpaired, two-tailed *t*-test; $p < 0.0001$). Bars indicate mean±SEM. **(H)** Spatial composition of the *notch1* ISH domain. Both quadrants on the same side of the EMP (q1, q4) show a significantly higher contribution to the ISH area than the opposite quadrants (q2, q3) in the analyzed eggs (two-tailed, paired *t*-test; q1,q2: $p = 0.0052$; q1,q3: $p = 0.0083$; q1,q4: $p = 0.5519$; q2,q3: $p = 0.7671$; q2,q4: $p = 0.0089$; q3,q4: $p = 0.0003$); n.s., non-significant differences. Bars indicate mean±SEM. *notch1* ISH, n = 15, two independent females; *pou5f3.1* ISH, n = 7, one female.

efficiently depleted from oocytes (but not from fertilized eggs) using phosphorothioate-modified antisense DNA oligonucleotides that trigger specific RNAse-H-mediated degradation, this technique is useful to assess maternal but not zygotic functions, whereas antisense morpholino oligonucleotides that block translation impair both maternal and zygotic functions (Hulstrand et al., 2010). The antisense *notch1* phosphorothioate-modified oligonucleotide efficiently depleted the endogenous *notch1* mRNA from oocytes and when they were transferred to host females, they could be fertilized. Endogenous *notch1* mRNA remained depleted in the resulting embryos through mid-blastula and at least until early gastrula. Noteworthy, when analyzed at the blastula stage, these embryos showed a remarkable expansion of the dorsal marker *foxi1* towards the ventral side (Mir et al., 2008), much similar to the ventral expansion of *bonafide* markers of the dorsal center that we observed after blocking *notch1* translation by means of morpholino injections in early embryos (Acosta et al., 2011), which also suppressed *bonafide* markers of the ventral center (Castro

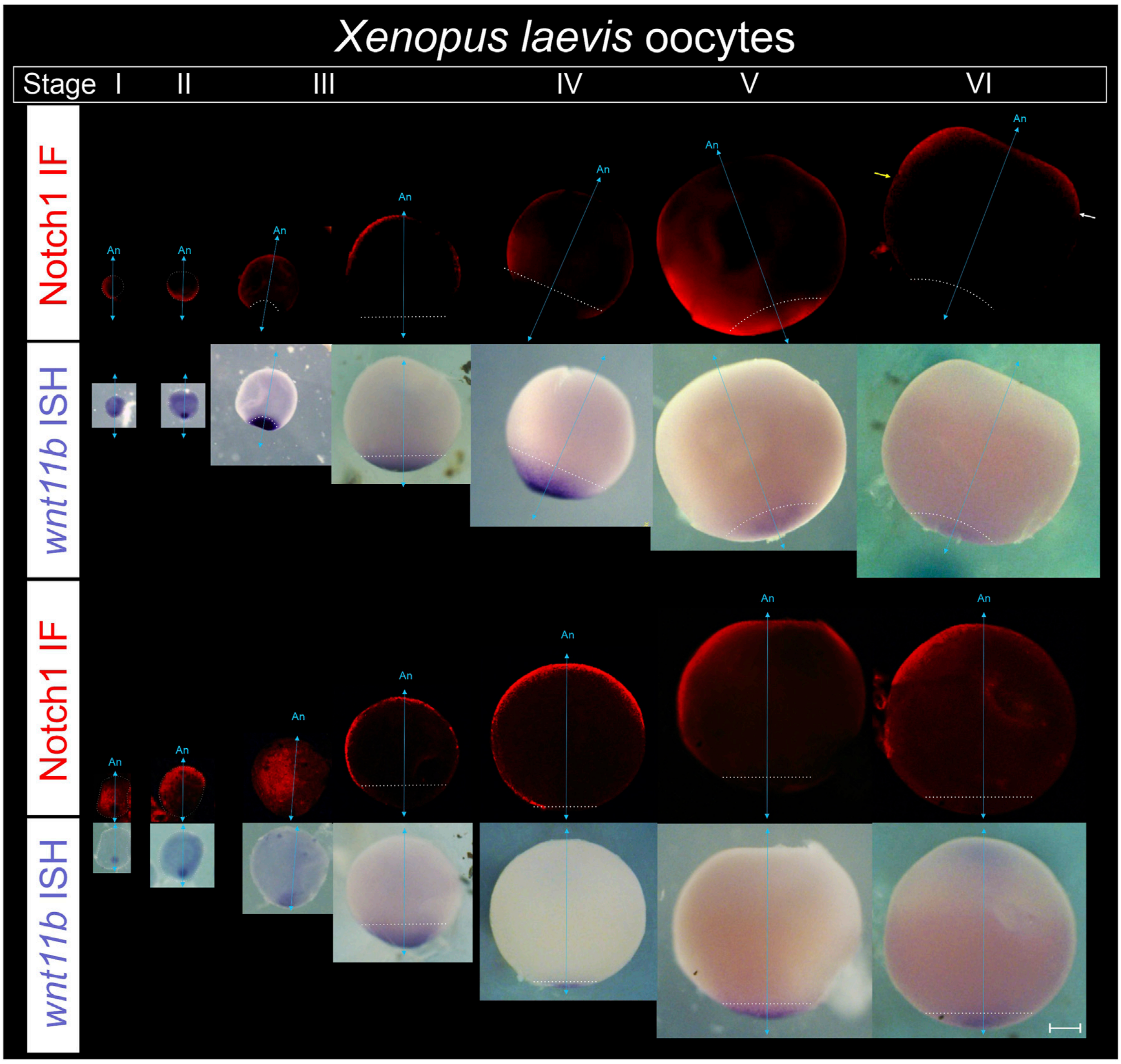

FIGURE 6
Notch1 protein becomes asymmetrically distributed in an orthogonal axis with respect to the animal-vegetal axis during *Xenopus laevis* oogenesis. Defolliculated oocytes obtained from pigmented females were fixed, bleached, and processed for combined immunofluorescence for Notch1 protein and ISH for *wnt11b* mRNA as reference marker of the vegetal pole to orient the oocytes in their animal-vegetal axis. From left to right, successive stages of oogenesis are shown in two representative series. Oocytes were classified according to the stages (s) described by (Dumont, 1972). For each series, the upper tier shows Notch1 immunofluorescence. The same oocytes are shown in bright field in the lower tier, with *wnt11b* mRNA located in the vegetal pole throughout oogenesis and also on the cytoplasm of early sI oocytes, as previously described (Kloc and Etkin, 1995). An, animal pole; cyan double arrow, animal-vegetal axis, as determined by *wnt11b* mRNA location; the white dotted line demarcates the contour of sI and sII oocytes and the *wnt11b* domain from sIII to sVI. Yellow and white arrows on the sVI oocyte point to the vegetal boundary of Notch1 protein expression in the animal hemisphere, which is more vegetal on one side (yellow arrow) than on the other side of the picture (white arrow), thus showing an asymmetric domain in the animal hemisphere. Scale bar: 200 μm. See data in Supplementary Table S5.

Colabianchi et al., 2018). Therefore, both depletion of *notch1* mRNA specifically from oocytes and inhibition of *notch1* translation in early embryos produced dorsalized phenotypes. We surmise that if *notch1* mRNA is destroyed before fertilization, there will not be a post-fertilization *notch1* mRNA asymmetry, because there simply will be no *notch1* mRNA to construct such asymmetry at the zygote stage. All this evidence indicates that sustained maternal *notch1* mRNA asymmetry, already established before fertilization, is necessary for the correct establishment of the initial dorsoventral patterning.

We have previously performed *notch1* gain-of-function and knock-down experiments in *X. laevis* zygotes and obtained a range of ventralized and dorso-anteriorized phenotypes, respectively, at tailbud stages (Acosta et al., 2011). These results were consistent with the changes we observed in the expression of dorsal and ventral markers at late blastula (Acosta et al., 2011; Castro Colabianchi et al., 2018). In the future, it will be interesting to perform *notch1* overexpression and knock-down experiments with phosphorothioate-modified antisense DNA oligonucleotides and antisense morpholinos in oocytes, *in vitro* mature them, and perform the host-transfer technique to obtain embryos (Mir and Heasman, 2008; Schneider et al., 2010). This will allow us to compare the phenotypes in tailbud stages with those previously

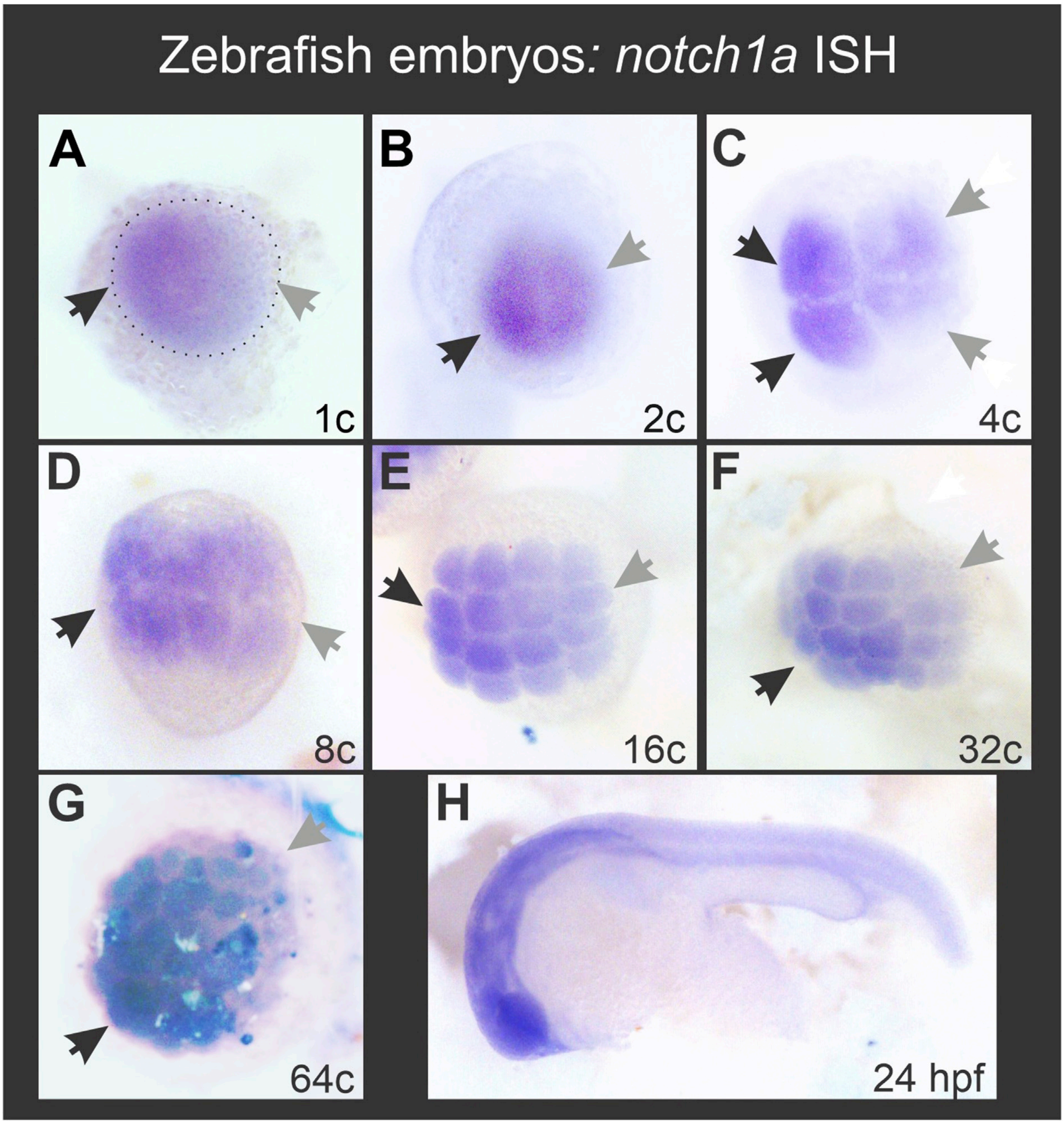

FIGURE 7
Zebrafish *notch1a* mRNA is asymmetrically distributed during early embryogenesis in the animal hemisphere from the 1-cell stage. Black and grey arrows in **(A–G)** respectively point to the regions with the highest and lowest *notch1a* ISH signal. The dotted ellipse in **(A)** demarcates the blastodisc. **(H)** ISH performed in parallel with the same *notch1a* probe in a 24 hpf embryo, showing typical expression for this transcript.

obtained. A higher severity or penetrance would further support the maternal contribution of *notch1* to dorsoventral patterning.

The conclusion that Notch1 mRNA and protein are asymmetrically distributed along an axis orthogonal to the animal-vegetal axis before fertilization and cortical rotation are based on the uneven distribution of the immunofluorescence signal and colorimetric staining along the animal hemispheres. One potential caveat about this interpretation is that this uneven distribution might be due to technical issues. Since there is no marker currently available that could label the prospective ventral or dorsal sides at these stages to validate our results, several approaches were employed to gain robustness and consistency. First, we have analyzed large sample sizes with independent biological replicates and performed statistical analyses whenever possible. Then, we have also used double staining with known vegetal markers to confidently orient the animal-vegetal axis or with double immunofluorescence for the ubiquitously expressed proteins GAPDH or α-Tubulin in pigmented animal hemispheres, both in whole-mount and in cryosections to rule-out the possibility of observing an uneven distribution of Notch1 due to the unequal accumulation of material across the specimens.

In a recent RNA seq study along the animal-vegetal axis in *X. laevis* eggs, *notch1* transcripts were found within the animal group of maternal mRNAs (Supplementary Dataset S1 in Sindelka et al.) (Sindelka et al., 2018). However, the RNAseq study did not address the possibility of uneven distribution of transcripts in an axis orthogonal to the animal-vegetal one. While the mechanisms that control mRNA location in the vegetal pole of *Xenopus* oocytes and eggs were studied quite deeply and involve motifs in their 3′UTR sequences, those controlling animal mRNA locations are largely unknown (Sindelka et al., 2018).

In addition to *notch1*, *bmp4, dll1, and hes4* transcripts (although weakly for the latter) also showed a bias towards one side of the animal hemisphere in unfertilized eggs. Therefore, mRNAs corresponding to two pathways involved in ventral polarization are already asymmetrically distributed in an axis orthogonal to the animal-vegetal one before fertilization. They might be the source for localized translation during early embryogenesis before the beginning of zygotic transcription. So far, asymmetries of RNA or maternal proteins distribution have not been previously shown in *Xenopus* unfertilized eggs in an axis other than the animal-vegetal one.

The EMP/*notch1* side likely predicts the provisional ventral side in unfertilized eggs, because 1) in unfertilized, activated eggs with an eccentric EMP, the yolk mass rotates towards the EMP side whereas in fertilized eggs, the yolk mass rotates in most of them towards the SEP, which generally predicts the ventral side (Brown et al., 1994); 2) if they are provided with a diploid nucleus and a centrosome, activated eggs can parthenogenetically develop into an embryo with the position of the dorsal midline predicted by the direction of rotation (Black and Vincent, 1988; Gerhart et al., 1989; Ubbels, 1997; Tassan et al., 2017); 3) *notch1* mRNA and protein are ventrally enriched in 1-cell embryos through cleavage stages and at least, until mid-blastula transition (Castro Colabianchi et al., 2018); 4) *notch1* has ventralizing properties in embryos and normally contributes to the establishment of a well-balanced dorsoventral axis. It is necessary for the expression of ventral center genes and prevents the expression of dorsal genes in the ventral side (Mir et al., 2008; Acosta et al., 2011; Castro Colabianchi et al., 2018). If *notch1* mRNA marks the provisional ventral side before fertilization (Figure 8B), then, its distribution should be conserved when the sperm cues fail to direct cortical rotation and the EMP-dependent directionality is used as a backup mechanism (Figure 8B, row B3) or when the EMP and SEP happen to be on the same side of the animal hemisphere (Figure 8B, row B1), but should be reorganized when the sperm redirects the cortical rotation cues if the EMP happens to be on the opposite side of the SEP and cannot counteract the SEP driving force (Figure 8B, row B2).

In conclusion, the discussion of whether an intrinsic bilaterality of the egg exists and participates in the axialization of the body plan is still active. The classic model of axis formation only considers relocation of maternal dorsal determinants from the vegetal pole to the future dorsal side as a consequence of sperm-directed cortical rotation but does not take into account the influence of early localized ventralizing molecules (Figure 8A). The molecular asymmetries shown in this work support the hypothesis that *X. laevis* unfertilized eggs possess inherent bilaterality. We propose that a maternal prepattern involving the asymmetric distribution of ventralizing molecules like Notch1 and *bmp4* acts in concert with the directionality of cortical rotation imposed by sperm entry to set the initial dorsoventral molecular asymmetries that lead to embryonic axialization. In addition, it is also possible that this intrinsic egg bilaterality or latent dorsoventral prepattern is available as a backup mechanism for directionality of cortical rotation in case of failure of the mechanism directed by sperm entry, which occurs more frequently. The maternal bias in the distribution of molecules of known ventralizing properties before fertilization does not exclude that their spatial levels could be additionally controlled in relation to the fertilization-oriented cortical rotation. Nevertheless, our results imply that any control in the distribution of ventralizing molecules during or after fertilization might trigger mechanisms related to embryonic axialization that take their asymmetric prepattern in the unfertilized egg as a departure platform (Figure 8B).

Further experimental work is needed to study if the asymmetric maternal supply of molecules in an axis orthogonal to the animal-vegetal axis like those described here is providing ventralizing cues before fertilization. As discussed above, the expansion of a dorsal marker after maternal depletion of *notch1* mRNA in *Xenopus* (Mir et al., 2008) supports this hypothesis, at least for *notch1*. Although at lower levels than after zygotic genome activation, maternal *bmp4* transcripts were detected in *X. laevis* eggs by RNAseq (Session et al., 2016) and by ISH with a pattern that, although not commented by the authors, suggests an uneven distribution of transcripts in the animal hemisphere (Bell et al., 2003). In zebrafish embryos, maternal *bmp4* transcripts were detected in 2/8-cell or 64/128-cell by Northern blot and transcriptomics, respectively (Dick et al., 2000; Yang et al., 2013). In zebrafish, BMP4 signaling was proposed to be rather involved during late gastrulation in dorsoventral patterning, weakly contributing to ventralization, whereas BMP2b and BMP7a are mainly involved in early dorsoventral patterning (Stickney et al., 2007). Homozygous zebrafish embryos for a null *bmp4* allele (*bmp4*^{st72}) show a weak dorsalized phenotype in 73% of the cases, whereas heterozygous embryos look normal (Stickney et al., 2007), indicating that the null mutation results in a recessive dorsalized phenotype to which both, the maternal and the paternal allele, contribute. Strikingly, mating of adult females homozygous for this null *bmp4* allele with wild-type males produced 90% of heterozygous zebrafish embryos with a wild-type phenotype, while the remaining 10% showed a weak dorsalized phenotype. The authors concluded that there is no strict maternal requirement for BMP4 (Stickney et al., 2007), but in our view, their results do not rule out a subtle maternal effect with only 10% penetrance.

Regardless of the possible differences across species about gene contributions to early dorsoventral polarization, time-demanding loss-of-function experiments involving gene editing in *Xenopus* would help to illuminate if the asymmetric distribution of determinants in the egg have a significant impact on embryonic dorsoventral polarization. Functional experiments with the tools available for *Xenopus* until now could not discriminate between maternal and zygotic contributions. Addressing this issue would require generational intercrosses to study the effect of maternally/egg-derived mutant alleles or zygotically/sperm derived mutant alleles, as recently described for *wnt11b* loss-of-function in *X. laevis*, where this gene is present as singleton (Houston et al.,

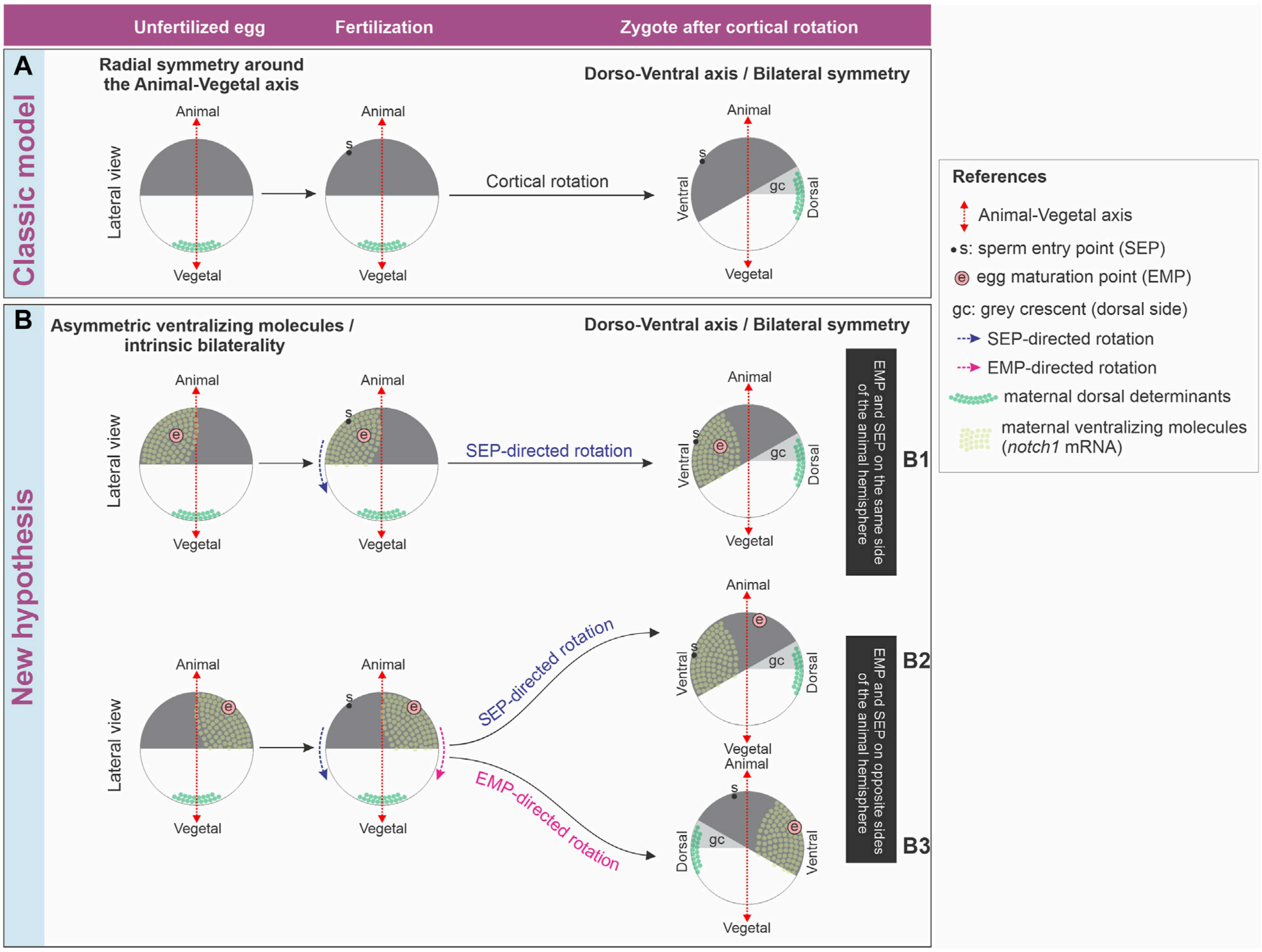

FIGURE 8
(A) Classic model of axis formation in *Xenopus*, which only considers relocation of maternal dorsal determinants after fertilization. **(B)** New hypothesis for axis formation in *Xenopus*, which considers both relocation of maternal dorsal determinants after fertilization and an intrinsic bilaterality of unfertilized eggs harboring an asymmetric distribution of ventralizing molecules in the animal hemisphere. See main text for additional details.

2022). A detailed analysis of the range and penetrance of phenotypes obtained should follow, because, for example, strong or weak phenotypes might be either zygotically- or maternally-related, or *vice versa*. This kind of analysis would be relatively more straightforward in the diploid species *Xenopus tropicalis* but might be complicated by the possibility that homozygous null mutations were embryonic lethal. This would require rescuing of homozygous embryos with injection of wild-type mRNA to obtain homozygous progenitors mutant for the gene under study, as previously done in the past for zebrafish mutants (Kishimoto et al., 1997; Dick et al., 2000).

Possible mechanisms underlying Notch1 polarization

The development of the main embryonic axis in amphibians, fish, and birds is sensitive to gravity, but it is unlikely that gravity influences the specification of the animal-vegetal axis (Gerhart, 1980). Pigment always concentrates in the animal hemisphere, where the germinal vesicle is located, and yolk platelets in the vegetal region, where the mitochondrial clouds are first observed, regardless of the orientation of the oocytes in the follicle in relation to gravity. Therefore, it is thought that oocytes intrinsically build the animal-vegetal axis (Gerhart, 1980), whose development was better studied from sI to sVI and appears to be prefigured in oogonia, in the germline cyst (Kloc et al., 2004; Bilinski et al., 2017). Notably, Gerhart also discussed the observations of Wittek (1952) (quoted by Gerhart, 1980) in other amphibian species (*R. temporaria* and *T. alpestris*) where a precocious bilateral symmetry is apparent after oocyte maturation, with eccentric maturation spots in the pigmented animal hemisphere. This precocious bilateral symmetry could be traced back to a more lateral position of the germinal vesicle and the mitochondrial cloud at previtellogenic stages (Gerhart, 1980). After Gerhart discussed in 1980 all these important aspects, it was reported that the EMP's eccentricity in *X. laevis* eggs might be related to the position held by the oocytes in the gravity field during maturation. Oocytes that were held during *in vitro* maturation with the GAP tipped 90° or 135° off axis in relation to the gravitational field showed maturation points with stronger eccentricity than oocytes that were held on axis, whose maturation points revealed very low or no eccentricity (Brown et al., 1994). Notably, in the process of *Xenopus* axialization, two periods of sensitivity to the centrifugal force were recognized during the first cell cycle (Black and Gerhart, 1985). Although the reason for this temporal change remains unexplained, it is striking that the centrifugal force could change the site of dorsalization from the centrifugal equatorial region before 40% of the cycle (i.e., before the onset of cortical rotation) to the opposite side (centripetal) between 40% and 70% of the cycle (i.e., during cortical rotation), when the only other variable was the position of the SEP, towards or away from the center of the rotor, as shown by these authors. Since the SEP usually marks the future ventral side, applying centrifugal force during the second period of sensitivity with the SEP towards the center of the rotor would completely reverse the directionality of cortical rotation and the displacement of maternal dorsal determinants from the vegetal cortex. A possible explanation for the first period of sensitivity might perhaps involve the relocation of ventralizing molecules already asymmetrically distributed before cortical rotation, related to the intrinsic bilateral symmetry or latent dorsoventral prepattern of the egg.

If the animal-vegetal axis were not influenced by gravity, the asymmetry of Notch1 immunofluorescence that we observe in an axis orthogonal to the animal-vegetal one, with variability of the immunofluorescence signal in the vegetal region during oogenesis might be related to gravity. Additional cues related to the resumption of meiosis during maturation, which appear to be also influenced by gravity, might refine this pattern. Although we have not attempted to demonstrate if Notch1 immunofluorescence correlates with the position of the EMP because this is technically more challenging, we have found that the asymmetrical *notch1* mRNA domain correlates with the EMP region.

Remarkably, it was earlier reported that *znf330 (Xnoa36)* and *α-spectrin* mRNAs and α-Spectrin protein are transiently segregated to a lateral half of mid-sI oocytes in a domain parallel to the animal-vegetal axis. This expression domain is opposite to the site from where the oocyte pends from the ovarian epithelium, which the authors called "hylum" (Vaccaro et al., 2010; Carotenuto and Tussellino, 2018) but would be better designated as "ovulation site" (Dumont and Brummett, 1978). Since these authors strictly adhered to the traditional view of dorsoventral axis formation being triggered after fertilization and did not contemplate the possibility of an intrinsic maternal bilateral symmetry which we thoroughly discuss in the present work, they doubted that the asymmetry they observed could anticipate a dorsoventral polarity (Vaccaro et al., 2010). Notwithstanding their interpretation, the results shown by these authors, which were overlooked in the literature, are in line with those described in the present work. They strongly support the idea of asymmetrical distribution of molecules along an axis orthogonal to the animal-vegetal one during *Xenopus* oogenesis.

Interestingly, Vaccaro et al. noticed that, apart from the mitochondrial cloud, which marks the future vegetal side of the oocyte, the only other asymmetry of the oocyte is relative to the position it occupies within the ovary (Vaccaro et al., 2010). The oocyte is completely surrounded by the follicular cells and the theca layer. The follicle is wrapped by the inner ovarian epithelium, except at the side facing the ovulation site, which instead contacts the outer ovarian epithelium (Dumont and Brummett, 1978). Both are squamous epithelia, but the outer one, lining the coelomic cavity, is composed of monociliated cells, whereas the inner one, lining the ovarian lumen, consists of a layer of nonciliated cells (Dumont and Brummett, 1978). It is known that primary cilia have a key role in the transduction of several morphogen pathways (Oh and Katsanis, 2012) and they are present in the outer ovarian epithelium in mammals (Teilmann and Christensen, 2005). Since the domain expressing *znf330 (Xnoa36)* and *α-spectrin* mRNAs and α-Spectrin protein in mid-sI oocytes is in the antipode of the ovulation site, the question arises if the developing oocyte is under the influence of differential signaling from these distinct epithelia which might polarize the oocyte in an axis different from the animal-vegetal one. If such differential signaling exists, it might contribute to developing the asymmetric Notch1 distribution we observed throughout oogenesis.

Further experimentation is needed to understand how the asymmetric Notch1 distribution described here arises and is maintained. Several aspects need to be considered in the future. For example, does this expression pattern bear any correlation with the ovulation site? Could it be influenced by gravity during oogenesis and oocyte maturation? Other aspects include examining the role of the cytoskeleton and whether mechanisms of transport, local stabilization or decay are involved. Cytoskeletal reorganization occurs during oogenesis (Carotenuto and Tussellino, 2018) and throughout the oocyte during maturation, the most conspicuous one related to germinal vesicle breakdown, meiotic spindle assembly and first polar body extrusion. During oocyte maturation, several important changes affect the three major filament systems of the cytoplasm (actin filaments, intermediate filaments, and microtubules) (Bement and Capco, 1990; Gard, 1992). Intriguingly, we notice that in unfertilized eggs, Gard observed an important variability regarding the orientation of the M2 spindle (which is assembled after polar body extrusion). In unfertilized eggs, the M2 spindle was either aligned with or transverse to the animal-vegetal axis. However, in *in vitro* matured oocytes, nearly all the M2 spindles became aligned with the animal-vegetal axis (Gard, 1992). We surmise that unfertilized eggs naturally matured in different orientations within the gravity field, whereas the *in vitro* matured oocytes mostly went through this process with the animal-vegetal axis aligned with the gravity field. Although this remains speculative, perhaps the grade of EMP eccentricity, which is influenced by gravity, is related to meiotic spindle orientation in this specialized asymmetric cell division that extrudes the first polar body. It remains to be elucidated if these processes are related with the Notch asymmetry we observed in this work. Experiments perturbing the cytoskeleton during oogenesis, oocyte maturation, and in eggs might clarify if cytoskeletal components are necessary for the establishment, refinement, or maintenance of the molecular asymmetries we describe here.

Notch asymmetries during axis formation in bilaterians

We previously showed that Notch1 and β-Catenin proteins are asymmetrically and oppositely distributed during early embryogenesis in zebrafish as early as from the zygote stage (Castro Colabianchi et al., 2018). Now, we show that *notch1a* transcripts are also asymmetrically distributed in zebrafish embryos from the zygote stage. This conservation between fish and amphibians suggests that the control of the distribution of Notch1 on the dorsoventral axis is executed at the transcripts level, but we cannot rule out additional controls in the distribution of the protein for the maintenance of the asymmetry.

Our previous work showed that, in *X. laevis* embryos, Notch1 promotes β-Catenin destabilization through a non-canonical mechanism, independent of the DNA-binding protein RBPJ, which is the transcription factor that mediates canonical Notch, nuclear activity (Acosta et al., 2011). This non-canonical pathway explains part of Notch1 ventralizing activity (Castro Colabianchi et al., 2018) and was also described in *Drosophila* and in mammalian embryonic stem cells, where membrane-bound Notch associates to β-Catenin, promoting its degradation through the endocytic/lysosomal pathway (Hayward et al., 2005; Hayward et al., 2008; Sanders et al., 2009; Muñoz-Descalzo et al., 2010). Therefore, the early membrane-bound Notch1 asymmetry that we detected in this work before and immediately after cortical rotation might be relevant in destabilizing β-Catenin. More research is needed to demonstrate if Notch1 is already promoting β-Catenin degradation at these time points. In addition, we could detect ventral accumulation of Notch1 in nuclei at least from stage 7 in *X. laevis* embryos (i.e., before mid-blastula transition) (Castro Colabianchi et al., 2018).

Notably, a recent work described an asymmetry in the distribution of *notch1* transcripts in chicken embryos at early cleavage stages (Hwang et al., 2018). Although its functional significance was not studied, this points to the conservation of early *notch1* asymmetries in vertebrate embryos. Moreover, an antibody against the transcriptionally active Notch1 intracellular domain showed nuclear immunofluorescence in the outer cells but not in the inner cell mass of the mouse blastocyst, and Notch1 favors the specification of the trophectoderm lineage, disfavoring the inner cell mass lineage (Rayon et al., 2014). Therefore, this asymmetric Notch1 distribution is related to the earliest cell-fate choice in mammalian development, suggesting an active role in the polarity of the embryonic-abembryonic axis. More recently a reporter gene study revealed that an asymmetric Notch activity already exists as early as in the 4-cell stage mouse conceptus (Menchero et al., 2019). Symmetry breaking mechanisms are the subject of ongoing debate in mouse development. It was proposed that in most conceptus, the blastocyst's axis of bilateral symmetry is parallel to the zygote's animal-vegetal axis, whereas the blastocyst's plane of bilateral symmetry and the embryonic-abembryonic axis are orthogonal to the first cleavage's plane (Gardner, 2001; Johnson, 2009; Graham and Zernicka-Goetz, 2016). The body axes (dorsoventral and anterior-posterior) are definitively established in the period from implantation to pre-gastrulation. While the dorsoventral axis is indirectly inherited from the embryonic-abembryonic axis, the anterior-posterior axis of the embryo-fetus was proposed to correlate with the blastocyst's axis of bilateral symmetry (Johnson, 2009; Zhang and Hiiragi, 2018).

In invertebrates like insects and cephalopods, eggs already show an obvious bilateral symmetry (Gardner, 1998; Houston, 2017). In *Drosophila melanogaster*, anterior-posterior and dorsoventral body axes are defined during oogenesis through the asymmetrical distribution of maternal determinants (Johnston and Nüsslein-Volhard, 1992; Stein and Stevens, 2014; Ma et al., 2016; Schüpbach, 2019). During *Drosophila* oogenesis, interactions between germline and somatic cells, involving Delta in the germline/oocyte and Notch in follicle cells participate in the establishment of the oocyte's anterior-posterior axis, which determines the embryo's anterior-posterior axis. Activation of the Notch pathway by Delta signaling from the oocyte is necessary for establishing the oocyte's posterior pole (Ruohola et al., 1991; González-Reyes and St Johnston, 1998; López-Schier, 2003; Torres et al., 2003; Poulton and Deng, 2007; Sun et al., 2011; Schüpbach, 2019). In the nematode *Caenorhabditis elegans*, *glp-1* encodes one of the two *notch* orthologues present in this worm and is necessary for developing anterior cell fates. Maternal *glp-1* mRNA is uniformly distributed in zygotes and all blastomeres until the 8-cell stage. However, Glp-1 protein is asymmetrically distributed at the 2-cell stage, being localized in the blastomere fated to give rise to anterior tissues. This asymmetric distribution is controlled by translational repression and requires specific sequences in the 3′ UTR of *glp-1* mRNA (Evans et al., 1994).

Altogether, our findings, together with those from other animal models, point to the conservation of the involvement of the Notch pathway in establishing molecular asymmetries related to axis formation in Bilaterians.

Data availability statement

The original contributions presented in the study are included in the article/Supplementary Material, further inquiries can be directed to the corresponding author.

Ethics statement

The animal study was approved by the Laboratory Animal Welfare and Research Committees (Comisión Institucional para el Cuidado y Uso de Animales de Laboratorio -CICUAL) from Facultad de Medicina-UBA, Facultad de Farmacia y Bioquímica-UBA, and INGEBI-CONICET. The study was conducted in accordance with the local legislation and institutional requirements.

Author contributions

AC: Validation, Investigation, Writing–review and editing, Writing–original draft, Visualization, Methodology, Formal Analysis, Conceptualization. NG: Writing–review and editing, Investigation. LF: Writing–review and editing, Writing–original draft, Resources. SL: Writing–review and editing, Writing–original draft, Visualization, Supervision, Resources, Project administration, Methodology, Funding acquisition, Formal Analysis, Conceptualization.

Funding

The author(s) declare that financial support was received for the research, authorship, and/or publication of this article. Research was supported by Agencia I+D+i, Argentina (PICT 2019-#01439) and Consejo Nacional de Investigaciones Cientıficas y Técnicas, Argentina (PIP 2021-2023 #11220200101818CO).

Acknowledgments

We acknowledge the following colleagues for kindly providing us with the constructs for probes: Eddy De Robertis (*bmp4*); Douglas Melton (*gdf1*); Tomas Pieler (*dll1, notch1*); Dave Turner (*hes4*); J. S. Smith (*wnt11b*); Vladimir Korzh (zebrafish *notch1a*). We also are grateful to Karina Alleva, for defolliculated *X. laevis* oocytes; Cecilia Aguirre, for cloning *pou5f3.1*; Marianela Ceol Retamal, Andrea Pecile, Manuel Ponce, and Ezequiel Yamus, for animal husbandry; Leonel Cruces, for help with experiments; and Marıa Cecilia Cirio, for reagents. We are also indebted to Dr. Marcelo Rubinstein, for his constant support and advice.

Conflict of interest

The authors declare that the research was conducted in the absence of any commercial or financial relationships that could be construed as a potential conflict of interest.

The reviewer LK declared a past collaboration with the authors AC, LF, SL to the handling editor.

Publisher's note

Supplementary material

The Supplementary Material for this article can be found online at: https://www.frontiersin.org/articles/10.3389/fcell.2024.1365705/full#supplementary-material

References

Acosta, H., López, S. L., Revinski, D. R., and Carrasco, A. E. (2011). Notch destabilises maternal beta-catenin and restricts dorsal-anterior development in Xenopus. *Development* 138, 2567–2579. doi:10.1242/dev.061143

Alarcón, V. B., and Elinson, R. P. (2001). RNA anchoring in the vegetal cortex of the Xenopus oocyte. *J. Cell Sci.* 114, 1731–1741. doi:10.1242/jcs.114.9.1731

Bell, E., Muñoz-Sanjuán, I., Altmann, C. R., Vonica, A., and Brivanlou, A. H. (2003). Cell fate specification and competence by Coco, a maternal BMP, TGFbeta and Wnt inhibitor. *Development* 130, 1381–1389. doi:10.1242/dev.00344

Bement, W. M., and Capco, D. G. (1990). Transformation of the amphibian oocyte into the egg: structural and biochemical events. *J. Electron Microsc. Tech.* 16, 202–234. doi:10.1002/JEMT.1060160303

Bilinski, S. M., Kubiak, J. Z., and Kloc, M. (2017). Asymmetric divisions in oogenesis. *Results Probl. Cell Differ.* 61, 211–228. doi:10.1007/978-3-319-53150-2_9

Black, S. D., and Gerhart, J. C. (1985). Experimental control of the site of embryonic axis formation in *Xenopus laevis* eggs centrifuged before first cleavage. *Dev. Biol.* 108, 310–324. doi:10.1016/0012-1606(85)90035-1

Black, S. D., and Vincent, J. P. (1988). The first cleavage plane and the embryonic axis are determined by separate mechanisms in *Xenopus laevis*. II. Experimental dissociation by lateral compression of the egg. *Dev. Biol.* 128, 65–71. doi:10.1016/0012-1606(88)90267-9

Brachet, J. (1977). Chapter 5 an old enigma: the gray crescent of Amphibian eggs. *Curr. Top. Dev. Biol.* 11, 133–186. doi:10.1016/S0070-2153(08)60745-0

Brown, E. E., Margelot, K. M., and Danilchik, M. V. (1994). Provisional bilateral symmetry in Xenopus eggs is established during maturation. *Zygote* 2, 213–220. doi:10.1017/s0967199400002008

Card, D. L. (1995). 7 Axis formation during Amphibian oogenesis: reevaluating the role of the cytoskeleton. *Curr. Top. Dev. Biol.* 30, 215–252. doi:10.1016/S0070-2153(08)60568-2

Carotenuto, R., and Tussellino, M. (2018). *Xenopus laevis* oocyte as a model for the study of the cytoskeleton. *C. R. Biol.* 341, 219–227. doi:10.1016/J.CRVI.2018.04.001

Castro Colabianchi, A. M., Revinski, D. R., Encinas, P. I., Baez, M. V., Monti, R. J., Rodríguez Abinal, M., et al. (2018). Notch1 is asymmetrically distributed from the beginning of embryogenesis and controls the ventral center. *Development* 145, dev159368. doi:10.1242/dev.159368

Chitnis, A., Henrique, D., Lewis, J., Ish-Horowicz, D., and Kintner, C. (1995). Primary neurogenesis in Xenopus embryos regulated by a homologue of the Drosophila neurogenic gene Delta. *Nature* 375, 761–766. doi:10.1038/375761a0

Coffman, C., Harris, W., and Kintner, C. (1990). Xotch, the Xenopus homolog of Drosophila notch. *Science* 249, 1438–1441. doi:10.1126/science.2402639

Dale, L., and Slack, J. M. (1987). Fate map for the 32-cell stage of *Xenopus laevis*. *Development* 99, 527–551. doi:10.1242/dev.99.4.527

Davis, R. L., Turner, D. L., Evans, L. M., and Kirschner, M. W. (2001). Molecular targets of vertebrate segmentation: two mechanisms control segmental expression of Xenopus hairy2 during somite formation. *Dev. Cell* 1, 553–565. doi:10.1016/s1534-5807(01)00054-5

De Domenico, E., Owens, N. D. L., Grant, I. M., Gomes-Faria, R., and Gilchrist, M. J. (2015). Molecular asymmetry in the 8-cell stage Xenopus tropicalis embryo described by single blastomere transcript sequencing. *Dev. Biol.* 408, 252–268. doi:10.1016/j.ydbio.2015.06.010

De Robertis, E. M. (2009). Spemann's organizer and the self-regulation of embryonic fields. *Mech. Dev.* 126, 925–941. doi:10.1016/j.mod.2009.08.004

Dick, A., Hild, M., Bauer, H., Imai, Y., Maifeld, H., Schier, A. F., et al. (2000). Essential role of Bmp7 (snailhouse) and its prodomain in dorsoventral patterning of the zebrafish embryo. *Development* 127, 343–354. doi:10.1242/DEV.127.2.343

Dumont, J. N. (1972). Oogenesis in *Xenopus laevis* (Daudin). I. Stages of oocyte development in laboratory maintained animals. *J. Morphol.* 136, 153–179. doi:10.1002/jmor.1051360203

Dumont, J. N., and Brummett, A. R. (1978). Oogenesis in *Xenopus laevis* (Daudin). V. Relationships between developing oocytes and their investing follicular tissues. *J. Morphol.* 155, 73–97. doi:10.1002/jmor.1051550106

Evans, T. C., Crittenden, S. L., Kodoyianni, V., and Kimble, J. (1994). Translational control of maternal glp-1 mRNA establishes an asymmetry in the *C. elegans* embryo. *Cell* 77, 183–194. doi:10.1016/0092-8674(94)90311-5

Fainsod, A., Steinbeisser, H., and De Robertis, E. M. (1994). On the function of BMP-4 in patterning the marginal zone of the Xenopus embryo. *EMBO J.* 13, 5015–5025. doi:10.1002/j.1460-2075.1994.tb06830.x

Favarolo, M. B., and López, S. L. (2018). Notch signaling in the division of germ layers in bilaterian embryos. *Mech. Dev.* 154, 122–144. doi:10.1016/j.mod.2018.06.005

Gallagher, B. C., Hainski, A. M., and Moody, S. A. (1991). Autonomous differentiation of dorsal axial structures from an animal cap cleavage stage blastomere in Xenopus. *Development* 112, 1103–1114. doi:10.1242/dev.112.4.1103

Gard, D. L. (1992). Microtubule organization during maturation of Xenopus oocytes: assembly and rotation of the meiotic spindles. *Dev. Biol.* 151, 516–530. doi:10.1016/0012-1606(92)90190-R

Gardner, R. L. (1998). Axial relationships between egg and embryo in the mouse. *Curr. Top. Dev. Biol.* 39, 35–71. doi:10.1016/s0070-2153(08)60452-4

Gardner, R. L. (2001). Specification of embryonic axes begins before cleavage in normal mouse development. *Development* 128, 839–847. doi:10.1242/dev.128.6.839

Gerhart, J., Danilchik, M., Doniach, T., Roberts, S., Rowning, B., and Stewart, R. (1989). Cortical rotation of the Xenopus egg: consequences for the anteroposterior pattern of embryonic dorsal development. *Development* 107, 37–51. Suppl. doi:10.1242/dev.107.Supplement.37

Gerhart, J. C. (1980). Mechanisms regulating pattern formation in the Amphibian egg and early embryo. *Biol. Regul. Dev.*, 133–316. doi:10.1007/978-1-4684-9933-9_4

González-Reyes, A., and St Johnston, D. (1998). Patterning of the follicle cell epithelium along the anterior-posterior axis during Drosophila oogenesis. *Development* 125, 2837–2846. doi:10.1242/dev.125.15.2837

Graham, S. J. L., and Zernicka-Goetz, M. (2016). The acquisition of cell fate in mouse development: how do cells first become heterogeneous? *Curr. Top. Dev. Biol.* 117, 671–695. doi:10.1016/bs.ctdb.2015.11.021

Hayward, P., Brennan, K., Sanders, P., Balayo, T., DasGupta, R., Perrimon, N., et al. (2005). Notch modulates Wnt signalling by associating with Armadillo/beta-catenin and regulating its transcriptional activity. *Development* 132, 1819–1830. doi:10.1242/dev.01724

Hayward, P., Kalmar, T., and Martinez Arias, A. (2008). Wnt/Notch signalling and information processing during development. *Development* 135, 411–424. doi:10.1242/dev.000505

Hemmati-Brivanlou, A., and Thomsen, G. H. (1995). Ventral mesodermal patterning in Xenopus embryos: expression patterns and activities of BMP-2 and BMP-4. *Dev. Genet.* 17, 78–89. doi:10.1002/dvg.1020170109

Houston, D. W. (2017). "Vertebrate axial patterning: from egg to asymmetry," in *Advances in experimental medicine and Biology* (New York: Springer New York LLC), 209–306. doi:10.1007/978-3-319-46095-6_6

Houston, D. W. (2022). "Maternal mRNAs and the making of cell lineages in the early Xenopus embryo," in *Xenopus. From basic Biology to disease models in the genomic era*. Editors A. Fainsod, and S. A. Moody (Boca Raton: CRC Press), 25–42. doi:10.1201/9781003050230-4

Houston, D. W., Elliott, K. L., Coppenrath, K., Wlizla, M., and Horb, M. E. (2022). Maternal Wnt11b regulates cortical rotation during Xenopus axis formation: analysis of maternal-effect wnt11b mutants. *Development* 149, dev200552. doi:10.1242/dev.200552

Hulstrand, A. M., Schneider, P. N., and Houston, D. W. (2010). The use of antisense oligonucleotides in Xenopus oocytes. *Methods* 51, 75–81. doi:10.1016/j.ymeth.2009.12.015

Hwang, Y. S., Seo, M., Lee, B. R., Lee, H. J., Park, Y. H., Kim, S. K., et al. (2018). The transcriptome of early chicken embryos reveals signaling pathways governing rapid asymmetric cellularization and lineage segregation. *Development* 145, dev157453. doi:10.1242/dev.157453

Ishibashi, H., Matsumura, N., Hanafusa, H., Matsumoto, K., De Robertis, E. M., and Kuroda, H. (2008). Expression of Siamois and Twin in the blastula Chordin/Noggin signaling center is required for brain formation in *Xenopus laevis* embryos. *Mech. Dev.* 125, 58–66. doi:10.1016/j.mod.2007.10.005

Johnson, M. H. (2009). From mouse egg to mouse embryo: polarities, axes, and tissues. *Annu. Rev. Cell Dev. Biol.* 25, 483–512. doi:10.1146/annurev.cellbio.042308.113348

Johnston, D. S., and Nüsslein-Volhard, C. (1992). The origin of pattern and polarity in the Drosophila embryo. *Cell* 68, 201–219. doi:10.1016/0092-8674(92)90466-P

Kamm, G. B., Pisciottano, F., Kliger, R., and Franchini, L. F. (2013). The developmental brain gene NPAS3 contains the largest number of accelerated regulatory sequences in the human genome. *Mol. Biol. Evol.* 30, 1088–1102. doi:10.1093/molbev/mst023

Kimmel, C. B., Ballard, W. W., Kimmel, S. R., Ullmann, B., and Schilling, T. F. (1995). Stages of embryonic development of the zebrafish. *Dev. Dyn.* 203, 253–310. doi:10.1002/aja.1002030302

Kirmizitas, A., Meiklejohn, S., Ciau-Uitz, A., Stephenson, R., and Patient, R. (2017). Dissecting BMP signaling input into the gene regulatory networks driving specification of the blood stem cell lineage. *Proc. Natl. Acad. Sci. U. S. A.* 114, 5814–5821. doi:10.1073/pnas.1610615114

Kishimoto, Y., Lee, K. H., Zon, L., Hammerschmidt, M., and Schulte-Merker, S. (1997). The molecular nature of zebrafish swirl: BMP2 function is essential during early dorsoventral patterning. *Development* 124, 4457–4466. doi:10.1242/DEV.124.22.4457

Kloc, M., Bilinski, S., Chan, A. P., Allen, L. H., Zearfoss, N. R., and Etkin, L. D. (2001). RNA localization and germ cell determination in Xenopus. *Int. Rev. Cytol.* 203, 63–91. doi:10.1016/S0074-7696(01)03004-2

Kloc, M., Bilinski, S., Dougherty, M. T., Brey, E. M., and Etkin, L. D. (2004). Formation, architecture and polarity of female germline cyst in Xenopus. *Dev. Biol.* 266, 43–61. doi:10.1016/J.YDBIO.2003.10.002

Kloc, M., and Etkin, L. D. (1995). Two distinct pathways for the localization of RNAs at the vegetal cortex in Xenopus oocytes. *Development* 121, 287–297. doi:10.1242/dev.121.2.287

Lamar, E., Deblandre, G., Wettstein, D., Gawantka, V., Pollet, N., Niehrs, C., et al. (2001). Nrarp is a novel intracellular component of the Notch signaling pathway. *Genes Dev.* 15, 1885–1899. doi:10.1101/gad.908101

Lombard-Banek, C., Moody, S. A., and Nemes, P. (2016). Single-cell mass spectrometry for discovery proteomics: quantifying translational cell heterogeneity in the 16-cell frog (Xenopus) embryo. *Angew. Chem. Int. Ed. Engl.* 55, 2454–2458. doi:10.1002/anie.201510411

López, S. L., Rosato-Siri, M. V., Franco, P. G., Paganelli, A. R., and Carrasco, A. E. (2005). The Notch-target gene hairy2a impedes the involution of notochordal cells by promoting floor plate fates in Xenopus embryos. *Development* 132, 1035–1046. doi:10.1242/dev.01659

López-Schier, H. (2003). The polarisation of the anteroposterior axis in Drosophila. *BioEssays* 25, 781–791. doi:10.1002/bies.10309

Ma, J., He, F., Xie, G., and Deng, W. M. (2016). Maternal AP determinants in the Drosophila oocyte and embryo. *Wiley Interdiscip. Rev. Dev. Biol.* 5, 562–581. doi:10.1002/wdev.235

Menchero, S., Rollan, I., Lopez-Izquierdo, A., Andreu, M. J., Sainz de Aja, J., Kang, M., et al. (2019). Transitions in cell potency during early mouse development are driven by Notch. *Elife* 8, e42930. doi:10.7554/eLife.42930

Miller, J. R., Rowning, B. A., Larabell, C. A., Yang-Snyder, J. A., Bates, R. L., and Moon, R. T. (1999). Establishment of the dorsal-ventral axis in Xenopus embryos coincides with the dorsal enrichment of dishevelled that is dependent on cortical rotation. *J. Cell Biol.* 146, 427–437. doi:10.1083/jcb.146.2.427

Mir, A., and Heasman, J. (2008). How the mother can help: studying maternal Wnt signaling by anti-sense-mediated depletion of maternal mRNAs and the host transfer technique. *Methods Mol. Biol.* 469, 417–429. doi:10.1007/978-1-60327-469-2_26

Mir, A., Kofron, M., Heasman, J., Mogle, M., Lang, S., Birsoy, B., et al. (2008). Long- and short-range signals control the dynamic expression of an animal hemisphere-specific gene in Xenopus. *Dev. Biol.* 315, 161–172. doi:10.1016/j.ydbio.2007.12.022

Molenaar, M., van de Wetering, M., Oosterwegel, M., Peterson-Maduro, J., Godsave, S., Korinek, V., et al. (1996). XTcf-3 transcription factor mediates beta-catenin-induced axis formation in Xenopus embryos. *Cell* 86, 391–399. doi:10.1016/s0092-8674(00)80112-9

Moody, S. A. (1987). Fates of the blastomeres of the 32-cell-stage Xenopus embryo. *Dev. Biol.* 122, 300–319. doi:10.1016/0012-1606(87)90296-x

Morrison, G. M., and Brickman, J. M. (2006). Conserved roles for Oct4 homologues in maintaining multipotency during early vertebrate development. *Development* 133, 2011–2022. doi:10.1242/dev.02362

Muñoz-Descalzo, S., Sanders, P. G. T., Montagne, C., Johnson, R. I., Balayo, T., and Martinez Arias, A. (2010). Wingless modulates the ligand independent traffic of Notch through Dishevelled. *Fly. (Austin)* 4, 182–193. doi:10.4161/fly.4.3.11998

Nieuwkoop, P. D., and Faber, J. (1994). *Normal table of* Xenopus laevis *(daudin)*. New York and London: Garland Publishing.

Oh, E. C., and Katsanis, N. (2012). Cilia in vertebrate development and disease. *Development* 139, 443–448. doi:10.1242/dev.050054

Onjiko, R. M., Moody, S. A., and Nemes, P. (2015). Single-cell mass spectrometry reveals small molecules that affect cell fates in the 16-cell embryo. *Proc. Natl. Acad. Sci. U. S. A.* 112, 6545–6550. doi:10.1073/pnas.1423682112

Onjiko, R. M., Plotnick, D. O., Moody, S. A., and Nemes, P. (2017). Metabolic comparison of dorsal versus ventral cells directly in the live 8-cell frog embryo by microprobe single-cell CE-ESI-MS. *Anal. Methods* 9, 4964–4970. doi:10.1039/C7AY00834A

Pandur, P. D., Sullivan, S. A., and Moody, S. A. (2002). Multiple maternal influences on dorsal-ventral fate of Xenopus animal blastomeres. *Dev. Dyn.* 225, 581–587. doi:10.1002/dvdy.10181

Pizard, A., Haramis, A., Carrasco, A. E., Franco, P., López, S., and Paganelli, A. (2004). Whole-mount *in situ* hybridization and detection of RNAs in vertebrate embryos and isolated organs. *Curr. Protoc. Mol. Biol.* Chapter 14, Unit 9. doi:10.1002/0471142727.mb1409s66

Poulton, J. S., and Deng, W. M. (2007). Cell-cell communication and axis specification in the Drosophila oocyte. *Dev. Biol.* 311, 1–10. doi:10.1016/j.ydbio.2007.08.030

Rasar, M. A., and Hammes, S. R. (2006). The physiology of the *Xenopus laevis* ovary. *Methods Mol. Biol.* 322, 17–30. doi:10.1007/978-1-59745-000-3_2

Rayon, T., Menchero, S., Nieto, A., Xenopoulos, P., Crespo, M., Cockburn, K., et al. (2014). Notch and hippo converge on Cdx2 to specify the trophectoderm lineage in the mouse blastocyst. *Dev. Cell* 30, 410–422. doi:10.1016/j.devcel.2014.06.019

Reversade, B., Kuroda, H., Lee, H., Mays, A., and De Robertis, E. M. (2005). Depletion of Bmp2, Bmp4, Bmp7 and Spemann organizer signals induces massive brain formation in Xenopus embryos. *Development* 132, 3381–3392. doi:10.1242/dev.01901

Ruohola, H., Bremer, K. A., Baker, D., Swedlow, J. R., Jan, L. Y., and Jan, Y. N. (1991). Role of neurogenic genes in establishment of follicle cell fate and oocyte polarity during oogenesis in Drosophila. *Cell* 66, 433–449. doi:10.1016/0092-8674(81)90008-8

Sakano, D., Kato, A., Parikh, N., McKnight, K., Terry, D., Stefanovic, B., et al. (2010). BCL6 canalizes Notch-dependent transcription, excluding Mastermind-like1 from selected target genes during left-right patterning. *Dev. Cell* 18, 450–462. doi:10.1016/j.devcel.2009.12.023

Sanders, P. G. T., Muñoz-Descalzo, S., Balayo, T., Wirtz-Peitz, F., Hayward, P., and Martinez Arias, A. (2009). Ligand-independent traffic of Notch buffers activated Armadillo in Drosophila. *PLoS Biol.* 7, e1000169. doi:10.1371/journal.pbio.1000169

Schmidt, J. E., Suzuki, A., Ueno, N., and Kimelman, D. (1995). Localized BMP-4 mediates dorsal/ventral patterning in the early Xenopus embryo. *Dev. Biol.* 169, 37–50. doi:10.1006/dbio.1995.1124

Schneider, P. N., Hulstrand, A. M., and Houston, D. W. (2010). Fertilization of Xenopus oocytes using the host transfer method. *JoVE J. Vis. Exp.*, e1864. doi:10.3791/1864

Schroeder, K. E., Condic, M. L., Eisenberg, L. M., and Yost, H. J. (1999). Spatially regulated translation in embryos: asymmetric expression of maternal Wnt-11 along the dorsal-ventral axis in Xenopus. *Dev. Biol.* 214, 288–297. doi:10.1006/dbio.1999.9426

Schüpbach, T. (2019). Genetic screens to Analyze pattern formation of egg and embryo in Drosophila: a personal history. *Annu. Rev. Genet.* 53, 1–18. doi:10.1146/annurev-genet-112618-043708

Session, A. M., Uno, Y., Kwon, T., Chapman, J. A., Toyoda, A., Takahashi, S., et al. (2016). Genome evolution in the allotetraploid frog *Xenopus laevis*. *Nature* 538, 336–343. doi:10.1038/nature19840

Sindelka, R., Abaffy, P., Qu, Y., Tomankova, S., Sidova, M., Naraine, R., et al. (2018). Asymmetric distribution of biomolecules of maternal origin in the *Xenopus laevis* egg and their impact on the developmental plan. *Sci. Rep.* 8, 8315. doi:10.1038/s41598-018-26592-1

Sive, H. L., Grainger, R. M., and Harland, R. M. (2010). *Early development of* Xenopus laevis. *A laboratory manual*. Cold Spring Harbor: Cold Spring Harbor Laboratory Press.

Stein, D. S., and Stevens, L. M. (2014). Maternal control of the Drosophila dorsal-ventral body axis. *Wiley Interdiscip. Rev. Dev. Biol.* 3, 301–330. doi:10.1002/wdev.138

Stickney, H. L., Imai, Y., Draper, B., Moens, C., and Talbot, W. S. (2007). Zebrafish bmp4 functions during late gastrulation to specify ventroposterior cell fates. *Dev. Biol.* 310, 71–84. doi:10.1016/J.YDBIO.2007.07.027

Sun, Y., Yan, Y., Denef, N., and Schüpbach, T. (2011). Regulation of somatic myosin activity by protein phosphatase 1β controls Drosophila oocyte polarization. *Development* 138, 1991–2001. doi:10.1242/dev.062190

Tada, M., and Smith, J. C. (2000). Xwnt11 is a target of Xenopus Brachyury: regulation of gastrulation movements via Dishevelled, but not through the canonical Wnt pathway. *Development* 127, 2227–2238. doi:10.1242/dev.127.10.2227

Tao, Q., Yokota, C., Puck, H., Kofron, M., Birsoy, B., Yan, D., et al. (2005). Maternal wnt11 activates the canonical wnt signaling pathway required for axis formation in Xenopus embryos. *Cell* 120, 857–871. doi:10.1016/j.cell.2005.01.013

Tassan, J.-P., Wühr, M., Hatte, G., and Kubiak, J. (2017). Asymmetries in cell division, cell size, and furrowing in the *Xenopus laevis* embryo. *Results Probl. Cell Differ.* 61, 243–260. doi:10.1007/978-3-319-53150-2_11

Teilmann, S. C., and Christensen, S. T. (2005). Localization of the angiopoietin receptors Tie-1 and Tie-2 on the primary cilia in the female reproductive organs. *Cell Biol. Int.* 29, 340–346. doi:10.1016/J.CELLBI.2005.03.006

Tejeda-Muñoz, N., and De Robertis, E. M. (2022). Lysosomes are required for early dorsal signaling in the Xenopus embryo. *Proc. Natl. Acad. Sci. U. S. A.* 119, e2201008119. doi:10.1073/pnas.2201008119

Thisse, B., and Thisse, C. (2015). Formation of the vertebrate embryo: moving beyond the Spemann organizer. *Semin. Cell Dev. Biol.* 42, 94–102. doi:10.1016/j.semcdb.2015.05.007

Torres, I. L., López-Schier, H., and St Johnston, D. (2003). A Notch/Delta-dependent relay mechanism establishes anterior-posterior polarity in Drosophila. *Dev. Cell* 5, 547–558. doi:10.1016/s1534-5807(03)00272-7

Tsuji, S., Cho, K. W. Y., and Hashimoto, C. (2003). Expression pattern of a basic helix-loop-helix transcription factor Xhairy2b during *Xenopus laevis* development. *Dev. Genes Evol.* 213, 407–411. doi:10.1007/s00427-003-0338-4

Turner, D. L., and Weintraub, H. (1994). Expression of achaete-scute homolog 3 in Xenopus embryos converts ectodermal cells to a neural fate. *Genes Dev.* 8, 1434–1447. doi:10.1101/gad.8.12.1434

Ubbels, G. A. (1997). Establishment of polarities in the oocyte of *Xenopus laevis*: the provisional axial symmetry of the full-grown oocyte of *Xenopus laevis*. *Cell. Mol. Life Sci.* 53, 382–409. doi:10.1007/pl00000613

Vaccaro, M. C., Gigliotti, S., Graziani, F., Carotenuto, R., De Angelis, C., Tussellino, M., et al. (2010). A transient asymmetric distribution of XNOA 36 mRNA and the associated spectrin network bisects *Xenopus laevis* stage I oocytes along the future A/V axis. *Eur. J. Cell Biol.* 89, 525–536. doi:10.1016/j.ejcb.2009.12.007

Verheyen, E. M., and Gottardi, C. J. (2010). Regulation of Wnt/beta-catenin signaling by protein kinases. *Dev. Dyn.* 239, 34–44. doi:10.1002/dvdy.22019

Weaver, C., Farr, G. H., Pan, W., Rowning, B. A., Wang, J., Mao, J., et al. (2003). GBP binds kinesin light chain and translocates during cortical rotation in Xenopus eggs. *Development* 130, 5425–5436. doi:10.1242/dev.00737

Weaver, C., and Kimelman, D. (2004). Move it or lose it: axis specification in Xenopus. *Development* 131, 3491–3499. doi:10.1242/dev.01284

Weeks, D. L., and Melton, D. A. (1987). A maternal mRNA localized to the vegetal hemisphere in Xenopus eggs codes for a growth factor related to TGF-beta. *Cell* 51, 861–867. doi:10.1016/0092-8674(87)90109-7

Wessely, O., Agius, E., Oelgeschläger, M., Pera, E. M., and De Robertis, E. M. (2001). Neural induction in the absence of mesoderm: beta-catenin-dependent expression of secreted BMP antagonists at the blastula stage in Xenopus. *Dev. Biol.* 234, 161–173. doi:10.1006/dbio.2001.0258

Wessely, O., Kim, J. I., Geissert, D., Tran, U., and De Robertis, E. M. (2004). Analysis of Spemann organizer formation in Xenopus embryos by cDNA macroarrays. *Dev. Biol.* 269, 552–566. doi:10.1016/j.ydbio.2004.01.018

Yan, L., Chen, J., Zhu, X., Sun, J., Wu, X., Shen, W., et al. (2018). Maternal Huluwa dictates the embryonic body axis through β-catenin in vertebrates. *Science* 362, eaat1045. doi:10.1126/science.aat1045

Yang, H., Zhou, Y., Gu, J., Xie, S., Xu, Y., Zhu, G., et al. (2013). Deep mRNA sequencing analysis to capture the transcriptome landscape of zebrafish embryos and larvae. *PLoS One* 8, e64058. doi:10.1371/JOURNAL.PONE.0064058

Zhang, H. T., and Hiiragi, T. (2018). Symmetry breaking in the mammalian embryo. *Annu. Rev. Cell Dev. Biol.* 34, 405–426. doi:10.1146/annurev-cellbio-100617-062616

Zhu, X., Wang, P., Wei, J., Li, Y., Zhai, J., Zheng, T., et al. (2021). Lysosomal degradation of the maternal dorsal determinant Hwa safeguards dorsal body axis formation. *EMBO Rep.* 22, e53185. doi:10.15252/embr.202153185

Frontiers in Cell and Development Biology

TYPE Original Research
PUBLISHED 17 April 2024
DOI 10.3389/fcell.2024.1376814

OPEN ACCESS

EDITED BY
Denhi Schnabel,
National Autonomous University of México,
Mexico

REVIEWED BY
Chengjie Zhou,
Boston Children's Hospital and Harvard Medical School, United States
Jiawei Sun,
Massachusetts General Hospital and Harvard Medical School, United States

*CORRESPONDENCE
Xuefeng Hu,
✉ bioxfh@fjnu.edu.cn

†These authors have contributed equally to this work

RECEIVED 26 January 2024
ACCEPTED 05 April 2024
PUBLISHED 17 April 2024

CITATION
Lv Y, Wang Q, Lin C, Zheng X, Zhang Y and Hu X (2024), Overexpression of *Fgf18* in cranial neural crest cells recapitulates Pierre Robin sequence in mice.
Front. Cell Dev. Biol. 12:1376814.
doi: 10.3389/fcell.2024.1376814

Overexpression of *Fgf18* in cranial neural crest cells recapitulates Pierre Robin sequence in mice

Yi Lv†, Qian Wang†, Chensheng Lin, Xi Zheng, Yanding Zhang and Xuefeng Hu*

Fujian Key Laboratory of Developmental and Neural Biology, College of Life Sciences, Fujian Normal University, Fuzhou, China

The pivotal role of FGF18 in the regulation of craniofacial and skeletal development has been well established. Previous studies have demonstrated that mice with deficiency in *Fgf18* exhibit severe craniofacial dysplasia. Recent clinical reports have revealed that the duplication of chromosome 5q32-35.3, which encompasses the *Fgf18* gene, can lead to cranial bone dysplasia and congenital craniosynostosis, implicating the consequence of possible overdosed FGF18 signaling. This study aimed to test the effects of augmented FGF18 signaling by specifically overexpressing the *Fgf18* gene in cranial neural crest cells using the *Wnt1-Cre; pMes-Fgf18* mouse model. The results showed that overexpression of *Fgf18* leads to craniofacial abnormalities in mice similar to the Pierre Robin sequence in humans, including abnormal tongue morphology, micrognathia, and cleft palate. Further examination revealed that elevated levels of *Fgf18* activated the Akt and Erk signaling pathways, leading to an increase in the proliferation level of tongue tendon cells and alterations in the contraction pattern of the genioglossus muscle. Additionally, we observed that excessive FGF18 signaling contributed to the reduction in the length of Meckel's cartilage and disrupted the development of condylar cartilage, ultimately resulting in mandibular defects. These anomalies involve changes in several downstream signals, including Runx2, p21, Akt, Erk, p38, Wnt, and Ihh. This study highlights the crucial role of maintaining the balance of endogenous FGF18 signaling for proper craniofacial development and offers insights into potential formation mechanisms of the Pierre Robin sequence.

KEYWORDS

FGF18, cranial neural crest cells, cleft palate, mandible, condylar cartilage, Pierre Robin sequence

1 Introduction

Normal craniofacial development is a precise process that involves the spatiotemporal coordination of multiple cellular signals, and any interruption of this process may result in abnormal craniofacial structures (Li et al., 2022). Pierre Robin sequence (PRS) is a congenital craniofacial defect, estimated to occur in approximately 1:8500 births, and is typified by mandibular hypoplasia, glossoptosis, cleft palate, and upper airway obstruction (Tan et al., 2013). These structural anomalies contribute to various degrees of airway obstruction and feeding difficulties, which are concomitant with a high mortality rate in infancy (Hsieh and Woo, 2019). The mandibular compression theory suggests that mandibular growth restriction inhibits the downward and forward movement of the tongue, thereby hindering the lift and fusion of the palatal shelves, which is considered a major cause of PRS (Giudice et al., 2018).

The fibroblast growth factor (FGF) signaling plays an important role in craniofacial development by influencing cellular proliferation, differentiation, and survival via multiple signaling cascades, such as RAS-MAPK, P13K-AKT, and PLCγ-PKC (Lee et al., 2018). Studies have shown that mutations in genes encoding FGFR are associated with craniosynostosis in patients (Moosa and Wollnik, 2016). In addition to FGFR, FGF2, FGF3, FGF4, and FGF9 also play a critical role during cranial suture development (Zhao et al., 2023). The loss of FGF10 function affects the process of palatal closure, resulting in abnormal tongue morphology and cleft palate (Prochazkova et al., 2018). Genome-wide analysis has shown that mutations in *Fgf8* were associated with the development of cleft lip and palate (Hao et al., 2019). Further studies have shown that *Fgf8* has dose-dependent effects on jaw shape, size, and symmetry (Zbasnik et al., 2022).

FGF18 is a member of the FGF8 subfamily and is highly conserved between humans and mice. Studies have shown that *Fgf18*$^{-/-}$ mice survived embryonic development but died in early neonatal life, meanwhile, mostly exhibiting cleft palate and mandibular malformations (Liu et al., 2002). Specific inactivation of *Fgf18* in neural crest-derived craniofacial mesenchyme results in mandibular shortening and reduced ossification of the frontal, nasal, and anterior cranial base skeletal elements (Yue et al., 2021). This piece of evidence suggests that *Fgf18* expression in neural crest-derived mesenchyme plays a critical role in mandibular and multi-craniofacial bone development. Further studies have shown that FGF18 is necessary for cell proliferation and differentiation during osteogenesis and chondrogenesis (Liu et al., 2002; Ohbayashi et al., 2002). Of note, targeting *Fgf18* in calvarial bone development delayed the process of suture closure (Ohbayashi et al., 2002). It has been demonstrated that FGF18 signals partly via FGFR3 to promote osteogenesis and chondrogenesis (Davidson et al., 2005). We accessed the ClinVar database and identified a duplication of chromosome 5q32-35.3, which encompasses the FGF18 gene and causes cranial bone dysplasia and congenital craniosynostosis, implicating a possible consequence of overdosed FGF18 signaling.

In this study, we used a conditionally activated *Fgf18* mouse model to investigate the possible effects of overdosed *Fgf18* in craniofacial bone development. We activated a conditional *Fgf18* transgenic allele in cranial neural crest cells (CNCCs) by crossing *Wnt1-Cre* mice with *pMes-Fgf18* mice generated in our laboratory. Our results demonstrated that *Wnt1-Cre;pMes-Fgf18* mice exhibited the characteristic features of the PRS, such as cleft palate, abnormal tongue placement, micrognathia, and skull malformations. Additionally, we have provided evidence that maintaining a proper balance of endogenous FGF18 signaling is crucial for normal craniofacial development. Dysregulation of FGF18 signals alters the downstream signaling pathways such as Akt, Erk, p38, β-catenin, Ihh, Runx2, and p21, thus affecting the normal proliferation and ossification of craniofacial cells.

2 Materials and methods

2.1 Animals

The *pMes-Fgf18* transgenic mice were produced by pronuclear injection of the *pMes-Ires-Egfp* vector, which contains the complete cDNA of mouse *Fgf18*. This transgenic vector was created by integrating the *Fgf18* sequence between a *LoxP*-flanked STOP cassette controlled by the *β-actin* promoter and the *Ires-Egfp* sequences. The *Wnt1-Cre* (JAX Stock No. 007807) and *R26R*^{mTmG} (JAX Stock No.007576) transgenic mice used in this study were obtained from the Jackson Laboratory and have been described in previous reports (Zhang et al., 2021). To specifically activate the *Fgf18* transgenic allele in the neural crest-derived mesenchyme, we utilized *Wnt1-Cre* mice and bred them with *pMes-Fgf18* mice to generate *Wnt1-Cre;pMes-Fgf18* mice. Subsequently, these mice were mated with *pMes-Fgf18;R26R*^{mTmG} mice to obtain *Wnt1-Cre;pMes-Fgf18;R26R*^{mTmG} mice. These experimental procedures were approved by the Institutional Animal Care and Use Committee at Fujian Normal University.

2.2 Organ culture of palates

For *in vitro* palate fusion assay, paired palatal shelves were carefully dissected from E13.5 *Wnt1-Cre;pMes-Fgf18* mutant and wild-type embryos. Paired palatal shelves were placed on a filter paper in Trowell-type organ culture and were oriented and juxtaposed with the MEE facing each other closely, as described previously (Chen et al., 2019). Samples were cultured in DMEM culture medium containing 20% fetal bovine serum, and incubated at 37° and 5% CO_2 for 72 h. The medium was changed every 24 h in culture. After culture, samples were collected for fixation and histological analysis.

2.3 Rotational explant culture

E13.5 embryos of *Wnt1-Cre;pMes-Fgf18* mutant and wild-type mice were collected and decapitated in sterile cold PBS. The heads, minus the tongue and mandible, were placed in a 20-mL glass bottle filled with 2 mL of DMEM medium supplemented with 20% fetal calf serum. Samples were incubated on a rotary apparatus rotating at a speed of 4 rpm in a vertical position for 24 h at 37°C and 5% CO_2. After this period, the samples were washed with PBS for fixation and histological analysis.

2.4 Skeletal staining

The skulls of *Wnt1-Cre;pMes-Fgf18* and control mice were fixed in 100% ethanol for 1-2 days and soaked in acetone for 3 days. Samples were then washed three times with water and transferred to the Alcian blue-alizarin red mixture for 5 days. Then soaked samples with 95% alcohol solution for 30 min, followed by 2% KOH for hydrolysis and gradient glycerol clearing.

2.5 Histology and immunofluorescence

Mouse embryos were harvested from timed pregnant females. Skulls of collected embryos were fixed in 4% Paraformaldehyde at 4°C for 24 h, then decalcified with formic acid for 14 days. Heads were sectioned (7 μm thickness) and stained with hematoxylin and eosin (H&E) or Azan. Immunofluorescence was performed in PBS/10% bovine serum albumin using the following antibodies: anti-Runx2 (Abcam,ab76956), anti-Sox9 (Abcam, ab3697; 1:50), anti-Ki67 (BD, 550609; 1:50), anti-Sp7/Osterix (Abcam, ab22552; 1:100), anti-Caspase3 (Bioss, bs-0081R), anti-GFP (Abcam, ab13970), anti-COLX (Abcam, ab58632), anti-COLII (Abcam, ab34712), anti-Caspase3 (Abcam, ab44976), anti-Scleraxis (Santa Cruz, sc-518082), Anti-FGF18 (Santa Cruz, sc-393471), anti-Collagen Type I (Proteintech, 14695-1-AP), anti-IHH (Proteintech, 13388-1-AP), anti-β-catenin (CST, #8480), anti-pErk1/2 (CST, #4370), anti-pP38 (CST, #4511), anti-pJNK (Santa Cruz, sc-6254). For immunofluorescence staining, an appropriate secondary antibody conjugated to a fluorescence probe was added. This was then incubated at room temperature for 1 h, followed by rinsing in PBS. Finally, the samples were mounted in an anti-fading mounting media. Results were obtained using an Olympus BX51 upright microscope (Olympus Optical, Tokyo, Japan).

2.6 *In situ* hybridization

Whole-mount *in situ* hybridization was performed according to published protocols (Zhang et al., 2021). At least three embryos of each genotype were hybridized to the *Shh* probe and only probes that detected consistent patterns of expression in all samples were considered valid results.

2.7 Statistical analysis

Data are expressed as the mean ± standard deviation (SD). A comparison of means between the two groups was performed using the Student's t-test. Differences between multiple groups were compared using one-way ANOVA. $p < 0.05$ was considered statistically significant.

3 Results

3.1 *Fgf18* overexpression in CNCCs causes severe craniofacial defects

Expression of *Fgf18* has been documented in the paraxial mesoderm of mice at E8.0 (Maruoka et al., 1998; Hagan et al., 2019). To explore the function of FGF18 in craniofacial development, we conducted an analysis of FGF18 expression in the developing palate and mandibular condyle at E13.5 to E18.5 mice. The results have revealed that FGF18 was weakly expressed in the anterior, middle, and posterior regions of the palatal shelves at E13.5 (Supplementary Figures S1A–C). At E14.5, the expression of FGF18 remained at a low level in these regions (Supplementary Figures S1D–F). However, at E15.5, a relatively higher expression level of FGF18 was observed in the palatal shelves (Supplementary Figures S1G–I). By E16.5, FGF18 expression was dramatically increased (Supplementary Figures S1J–L). Additionally, FGF18 was expressed at the onset of condyle primordium formation in E14.5. From E15.5 to E18.5, the expression of FGF18 was restricted to the fibrous/polymorphic progenitor cell layer of the condyle (Supplementary Figures S1M–P). These results suggest that the FGF18 signaling pathway is involved in the regulation of the development of the palate and mandibular condyle.

Previous studies have shown that *Fgf18*$^{-/-}$ mutant mice die shortly after birth, most with severe craniofacial deformities such as skull bone defects, micrognathia, and cleft palates (Liu et al., 2002; Ohbayashi et al., 2002). To gain deeper insights into the impacts of upregulated FGF18 signaling in craniofacial development, we employed the *Wnt1-Cre* allele to activate a conditional *Fgf18* transgenic allele in CNCCs by compounding it with the *pMes-Fgf18* allele (Supplementary Figure S2A). The fluorescence analysis of *Wnt1-Cre; R26R*^{mTmG} mice revealed specific expression of Cre recombinase in CNCCs, indicating precise targeting of the transgene in the desired cell population (Supplementary Figures S2B, C). Meanwhile, results from E10.5 *Wnt1-Cre;pMes-Fgf18* showed elevated FGF18 in the branchial arch, verifying successful overexpression of the *Fgf18* allele in CNCCs (Supplementary Figures S2D, E). Intriguingly, *Wnt1-Cre;pMes-Fgf18* mouse embryos also died at birth and exhibited multiple craniofacial malformations, including micrognathia and cleft palate (Figures 1A–D). Skeletal preparations of *Wnt1-Cre;pMes-Fgf18* mice at P0 further confirmed severe craniofacial bone defects, including significantly shortened basisphenoid, maxillary, and mandibular bones (Figures 1E–H).

To understand the developmental changes of the palatal shelves, we examined the histology of the developing palatal shelves in the transgenic mice. Histological analyses revealed that *Wnt1-Cre;pMes-Fgf18* embryos exhibited a similar localization of the palatal shelves at E13.5 compared to control littermates (Figures 2A–F). However, at E14.5, while palatal shelves had already elevated and initiated fusion in control littermates, *Wnt1-Cre;pMes-Fgf18* mouse embryos still had vertically oriented palatal shelves with the tongue wedged in between (Figures 2G–L). Furthermore, all *Wnt1-Cre;pMes-Fgf18* mouse embryos examined from E16.5 to P0 exhibited a failure of palatal shelf elevation (Figures 2M–R). Collectively, conditional *Fgf18* overexpression in the CNCCs disrupted craniofacial development and affected the elevation of palatal shelves, resembling the phenotype of human PRS.

3.2 *Fgf18* overexpression altered the direction of genioglossus muscle contraction

FGF transduction signals regulate diverse cellular activities, including cell proliferation and survival (Xie et al., 2020). To investigate whether the cleft palate in *Wnt1-Cre;pMes-Fgf18* mice is caused by changes in cell proliferation and survival, we examined the expression of Ki67 and Caspase3 in the palatal shelves. However, no significant difference was observed in the number of Ki67^{+} and Caspase3^{+} cells within the palatal shelves (Figures 3A–F) (Supplementary Figure S3). These results suggest that the overexpression of *Fgf18* in the CNCCs does not lead to cleft palate by influencing the proliferation and apoptosis of palatal frame cells. However, the cleft palate defects in mouse models are often secondary to defects in tongue movement and mandible. To investigate whether the failure of palatal shelves

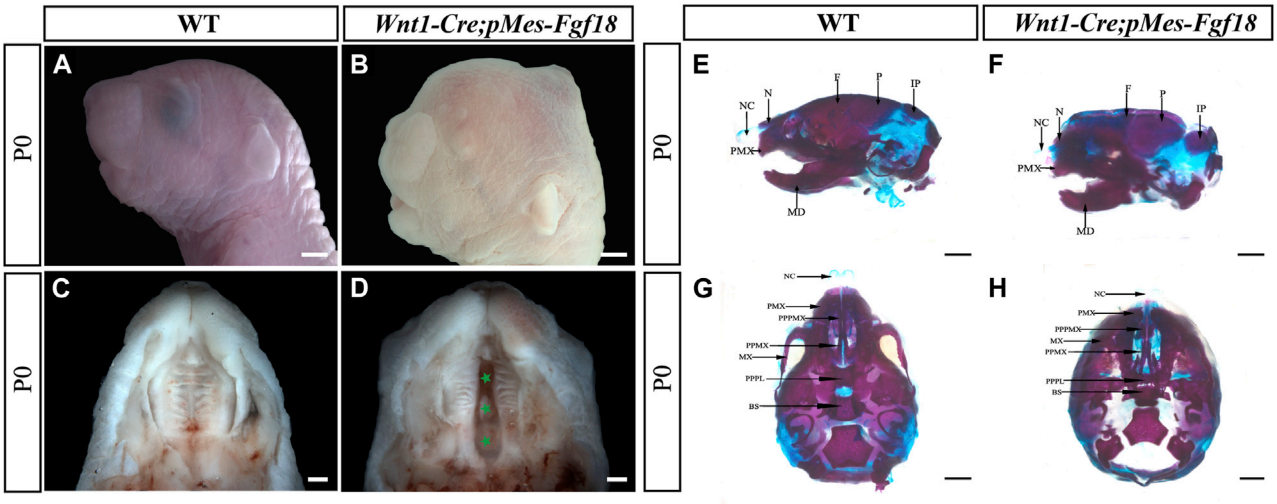

FIGURE 1
Gross craniofacial phenotype of *Wnt1-Cre;pMes-Fgf18* mice. **(A,B)** Lateral view of the mouse's head at P0. **(C,D)** Intraoral view of the mice palate at P0. **(E,F)** Lateral view of the mice heads at P0 staining by Alcian Blue-Alizarin Red. **(G,H)** Top view of the mice head at P0 staining by Alcian Blue-Alizarin Red. N, nasal; NC, nasal capsule; P, parietal bone; F, frontal bone; IP, interparietal; MD, mandible; PMX, premaxilla; BS, basisphenoid; MX, maxilla; PPMX, the palatal process of maxilla; PPPL, the palatal process of palatine; PPPMX, the palatal process of the premaxilla. Scale bar = 1,000 μm **(A,B,E–H)**; Scale bar = 500 μm **(C,D)**.

elevation in *Wnt1-Cre;pMes-Fgf18* embryos were associated with mandible and tongue malformations, we established organotypic cultures of embryos after removing the mandible and tongue. Our findings revealed that the palatal shelves from both E13.5 control and *Wnt1-Cre;pMes-Fgf18* mice were able to elevate and fuse after 72 h in culture (Figure 3G–L). These results suggested that the cleft palate observed in *Wnt1-Cre;pMes-Fgf18* mice is due to physical obstruction caused by the malformed mandible/tongue.

The genioglossus muscle, located in the face, is crucial for controlling tongue movement (Kouskoura et al., 2016). To explore the impact of genioglossus contraction direction on tongue movement, we performed histological analysis on the tongues of E13.5 embryos. Our findings revealed that, in contrast to controls, the fibers of the genioglossus in *Wnt1-Cre;pMes-Fgf18* mice displayed a distinct shift in orientation, adopting a more acute angle relative to the horizontal plane (Figures 4A–D). Immunofluorescence staining of Acta2, a marker of myofibroblasts, further supports the observed alteration in genioglossus fiber orientation (Figures 4E, F) (Supplementary Figure S3G). To determine whether the altered direction of genioglossus muscle contraction was attributed to abnormal genioglossus muscle attachment, we evaluated the expression of Scx, a marker for tendons, in E13.5 *Wnt1-Cre;pMes-Fgf18* mice. The findings revealed a significant increase in the number of Scx-positive cells in the tongues of *Wnt1-Cre;pMes-Fgf18* mice compared to control animals (Figures 4G, H).

To further investigate the underlying mechanism responsible for the elevated Scx^+ cell population, we conducted an analysis of cell proliferation and survival in the tongue at E13.5. Immunofluorescence staining revealed a significant increase in the number of Ki67 and Scx double-positive cells in *Wnt1-Cre;pMes-Fgf18* mice at E13.5, while apoptosis levels remained unaltered (Figures 4I, J, O) (Supplementary Figures S3E, F, K). Previous research has suggested that FGF signaling plays a crucial role in the development, repair, and injury of tendons (Eloy-Trinquet et al., 2009). To investigate the influence of overdosed FGF18 on the proliferation of tongue tendon cells, we evaluated the expression of FGF downstream signaling molecules Akt and Erk in E13.5 *Wnt1-Cre;pMes-Fgf18* mice. Immunofluorescence analysis indicated that *Wnt1-Cre;pMes-Fgf18* mice exhibited elevated protein levels of Akt and Erk in tongue tendon cells compared to the control group (Figures 4K–N) (Supplementary Figure S3H). In summary, overexpression of *Fgf18* increases the proliferation of tongue tendon cells and modulates the direction of genoglossus muscle contraction by upregulating the expression of signaling molecules such as Akt and Erk.

3.3 Excessive *Fgf18* signaling in CNCCs led to mandibular deformation

Mandibular dysplasia is a primary etiology of cleft palate. We conducted a comprehensive investigation on the development of the mandible in *Wnt1-Cre;pMes-Fgf18* mice during the stages of E14.5 to P0. Osteogenic staining revealed that the total mandibular length of *Wnt1-Cre;pMes-Fgf18* mice were significantly reduced, and other regions such as the condylar process, condylar cartilage, and angular process also exhibited abnormalities (Supplementary Figures S4A–H). Histological analysis revealed a significant increase in the sectional area of the mandibular coronal and Meckel's cartilage in *Wnt1-Cre;pMes-Fgf18* mice at E14.5 to E16.5, as compared to the control group (Supplementary Figures S4I–N). Consistent with increased coronal area of the mandible phenotype, immunostaining for Sp7, a marker for osteogenic progenitor cells, revealed a significant increase in the number of positive cells in *Wnt1-Cre;*

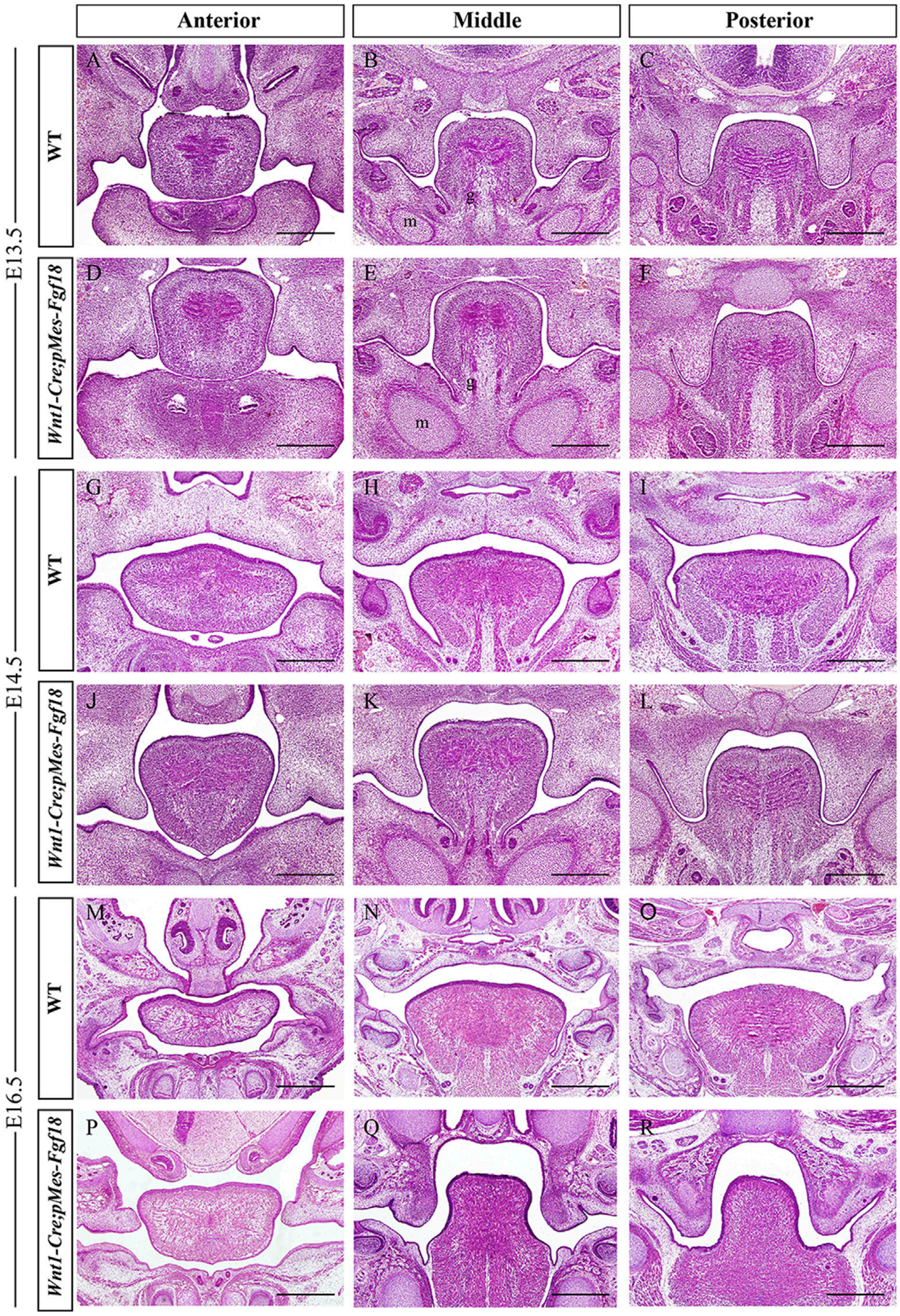

FIGURE 2
Wnt1-Cre;pMes-Fgf18 mouse embryos exhibited cleft palate. **(A–I)** Hematoxylin and eosin (HE) stained coronal sections of control and *Wnt1-Cre;pMes-Fgf18* mouse embryos at E13.5 **(A–F)**, E14.5 **(G–L)**, and E16.5 **(M–R)**. m: Meckel cartilage, g: genioglossus, Scale bar = 400 μm.

pMes-Fgf18 mice (Figures 5A, B). Immunostaining for Ki67 and Caspase3 revealed that the number of apoptotic cells in mutants was similar to that of controls, however, the percentage of Ki67-positive cells was significantly higher in the mandible of *Wnt1-Cre;pMes-Fgf18* mice at E13.5 (Figures 5C–H), suggesting that the increased mandibular size in the coronal plane is at least partially due to an increase in proliferation in *Wnt1-Cre;pMes-Fgf18* embryos.

Previous research has indicated that abnormalities in Meckel's cartilage can result in defects in the development and growth of the mandible (Biosse Duplan et al., 2016). To explore Meckel's cartilage phenotype in *Wnt1-Cre;pMes-Fgf18* mice, we conducted a

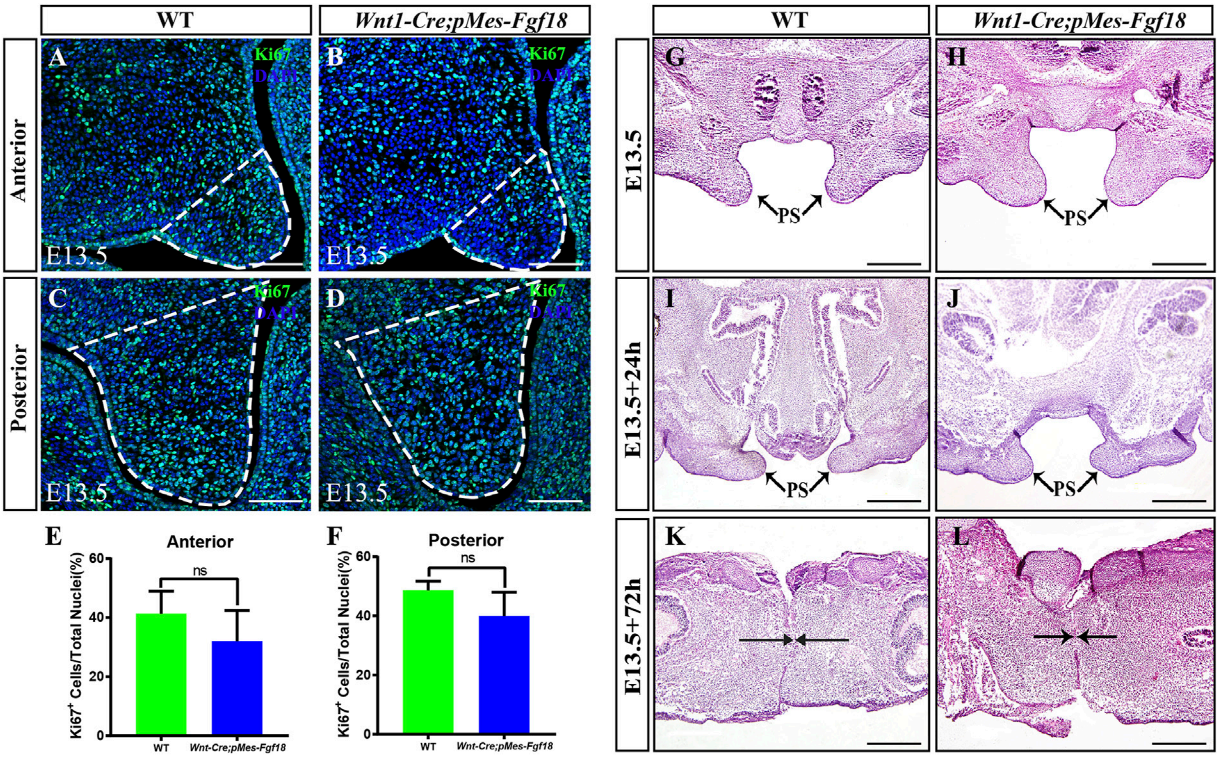

FIGURE 3
Overexpression of *Fgf18* inhibited the elevation and fusion of palate. **(A–D)** Immunostaining with antibodies against Ki67 was performed on the anterior and posterior regions of mouse embryos palate at E13.5. **(E, F)** Quantification analysis of the percentage of Ki67-positive cells in the anterior and posterior of palate. **(G–L)** After 24 h and 72 h of organ culture, the palatal shelve of E13.5 mouse embryos was stained with hematoxylin and eosin (HE). Scale bar = 100 μm **(A–D)**, Scale bar = 400 μm **(G–J)**, Scale bar = 200 μm **(K, L)**.

histological examination on embryonic sections ranging from E14.5 to E16.5. Our findings showed that the degeneration in the cartilage's middle region is disrupted in mutants (Figures 5J–M). Additionally, Meckel's cartilage in these mice exhibits a decreased length and is severely distorted (Figures 5I, N–Q). Immunofluorescence analysis of Sox9 expression, a critical gene for chondrocyte fate determination, revealed a significant increase in Sox9-positive cells in the Meckel's cartilages of E13.5 *Wnt1-Cre; pMes-Fgf18* embryos when compared to controls (Supplementary Figures S5A, B). Furthermore, Ki67 staining indicated an increase in cell proliferation in mutant embryos' Meckel's cartilages, while the rate of cell apoptosis in *Wnt1-Cre;pMes-Fgf18* mice was similar to that of controls (Supplementary Figures S5C–H). These findings suggest that the deformation of Meckel's cartilages is likely linked to the substantial rise in cell proliferation within Sox9-positive cells.

3.4 Conditional activation of *Fgf18* induced condylar cartilage defects

The condylar cartilage, undergoing endochondral ossification, is crucial for mandible growth and development. Defects in this cartilage can cause dental and facial issues like mandibular hypoplasia and dysmorphogenesis (Xu et al., 2022). Histological analyses revealed that during the initial stages of condylar primordia formation at E14.5, the size of the condyle in *Wnt1-Cre;pMes-Fgf18* mice was noticeably larger than that of the control group (Figures 6A, B). This suggested that alterations in the condylar cartilage may play a crucial role in the development of mandibular dysplasia. During the embryonic stages of E15.5 to E18.5, the chondrocytes in the control mice exhibited a well-organized structure, comprising of a superficial cell layer, a polymorphic progenitor cell layer, a zone of flattened chondrocytes, and a zone of hypertrophic chondrocytes that extended from the superficial to the deep cartilage of the condyle. In contrast, *Wnt1-Cre;pMes-Fgf18* mice demonstrated cellular derangement in the condyle (Figures 6C–H). Furthermore, Azan staining results indicated that the intensity of anilin blue staining is significantly lower in the condylar cartilage of *Wnt1-Cre;pMes-Fgf18* mice (Supplementary Figure S6), suggesting that collagen expression was reduced in mutant mice, which is probably caused by changes in cell types.

To evaluate the alterations in cell types and their distribution within the condylar cartilage of *Wnt1-Cre;pMes-Fgf18* mice, we utilized immunofluorescence analysis to identify distinct cell markers. Our findings demonstrate that collagen type 10 (Col10), a biomarker for hypertrophic chondrocytes, is highly expressed in the hypertrophic zone of control E16.5 mice. Conversely, this expression is significantly reduced in *Wnt1-Cre;pMes-Fgf18* mice, suggesting that hypertrophy is disrupted at this stage (Figures 6I, J). The obtained result implied that the activation of FGF18 signaling may cause chondrocyte hypertrophy defects. Subsequently, we conducted experiments to examine the expression of Sox9, Col2,

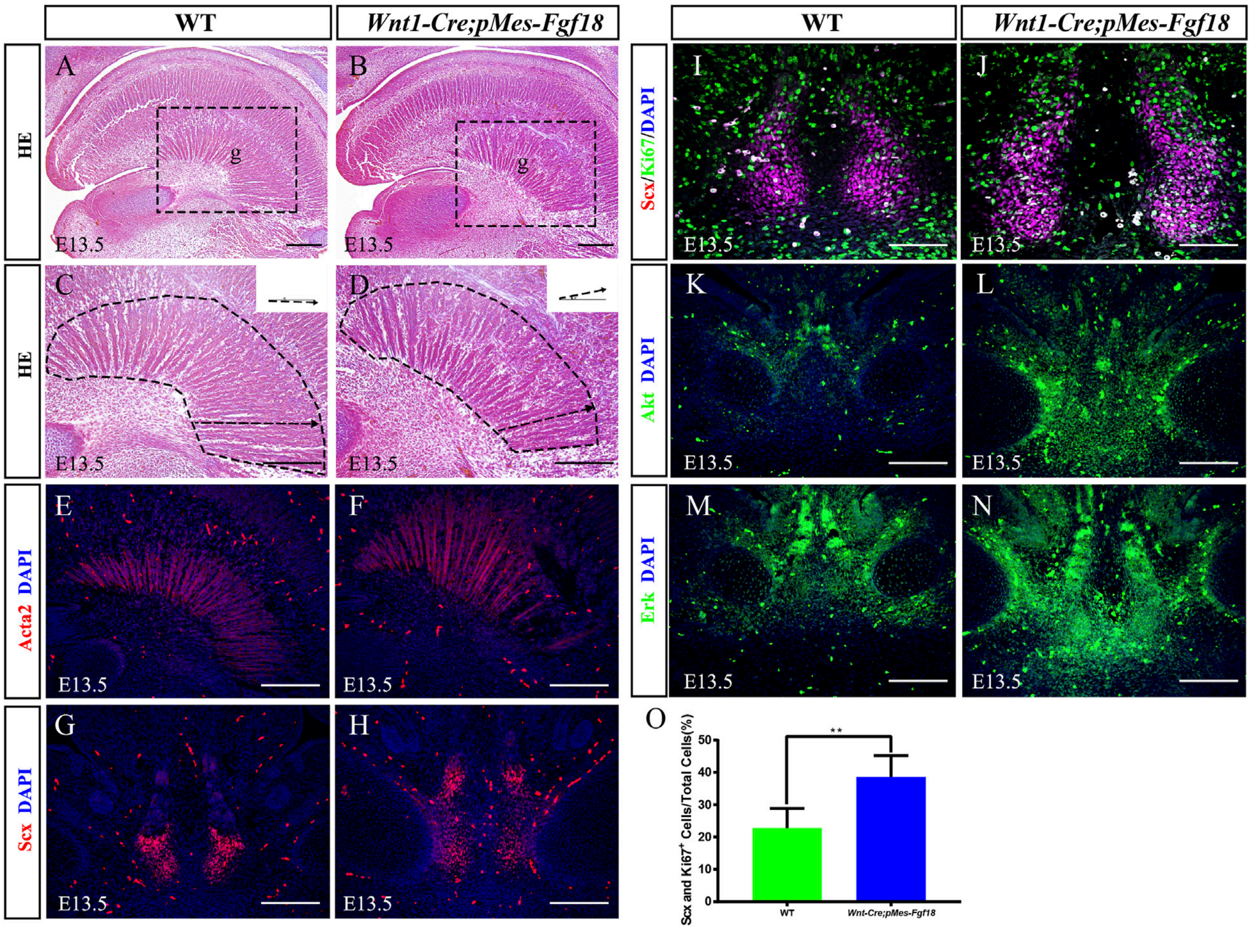

FIGURE 4
Overexpression of *Fgf18* changed the direction of genioglossus muscle contraction. **(A–D)** Azon staining of sagittal sections of the genioglossus muscle in mice at E13.5. **(E, F)** Immunostaining with antibodies against Acta2 was performed on the sagittal sections of the E13.5 mouse embryos tongue. **(G, H)** Immunostaining with antibodies against Scx was performed on the tongue of mouse embryos at E13.5. **(I, J)** Immunostaining was performed on genioglossus muscle attachment sites of E13.5 mouse embryos using antibodies against Scx and Ki67. **(K–N)** Immunostaining with antibodies against Akt and Erk was performed on the tongue of mouse embryos at E13.5. **(O)** Quantification analysis of the percentage of Scx and Ki67 double-positive cells in the tongue tendon cells. m: Meckel cartilage, g: genioglossus, Scale bar = 200 μm **(A–H, L–O)**, Scale bars = 100 μm **(I, J)**. $^{**}p < 0.01$.

Col1, and Sp7 in the condylar cartilage of *Wnt1-Cre;pMes-Fgf18* mice during the earlier stages of chondrocyte differentiation, prior to the onset of hypertrophy. The immunofluorescence results indicated that in comparison to the control group, the expressions of Sox9 and Col2 were significantly downregulated in *Wnt1-Cre;pMes-Fgf18* mice, whereas the expressions of Sp7 and Col1 were elevated (Figures 6K–R). These results indicated that overdosed FGF18 signaling may accelerate chondrocyte maturation and differentiation towards hypertrophic condyles, ultimately resulting in disparities in the expression of these markers between the two groups.

Runx2 is a crucial transcription factor for skeletal development and plays a role in determining whether chondrocytes become transient cartilage or permanent cartilage. Immunofluorescence results demonstrated that Runx2 was highly expressed in prehypertrophic chondrocytes, while its expression was significantly reduced in other regions of the control mice's condylar cartilage. Interestingly, in the *Wnt1-Cre;pMes-Fgf18* mice, we observed a significant increase in the number of Runx2-positive cells, particularly in the polymorphic layer cells of the condyle (Figures 6S, T). This finding suggests that the differentiation of condylar chondrocytes is disrupted by the abnormal activation of Runx2 in the polymorphic layer cells of *Wnt1-Cre;pMes-Fgf18* mice.

3.5 Excessive FGF18 signaling altered cell proliferation and ossification in the condyle

To determine whether *Fgf18* overexpression in CNCCs modulates condylar endochondral ossification by influencing cell proliferation and apoptosis, we evaluated the expression of Ki67 and Caspase3 in the condyle at E16.5. In control mice, Ki67 staining revealed a high presence of proliferating cells in the polymorphic progenitor cell layer and the zone of flattened chondrocytes. Conversely, in *Wnt1-Cre;pMes-Fgf18* mice, there was a significant increase in Ki67-positive cells throughout the entire condylar cartilage (Figures 7A, B). However, the Caspase3 assay showed

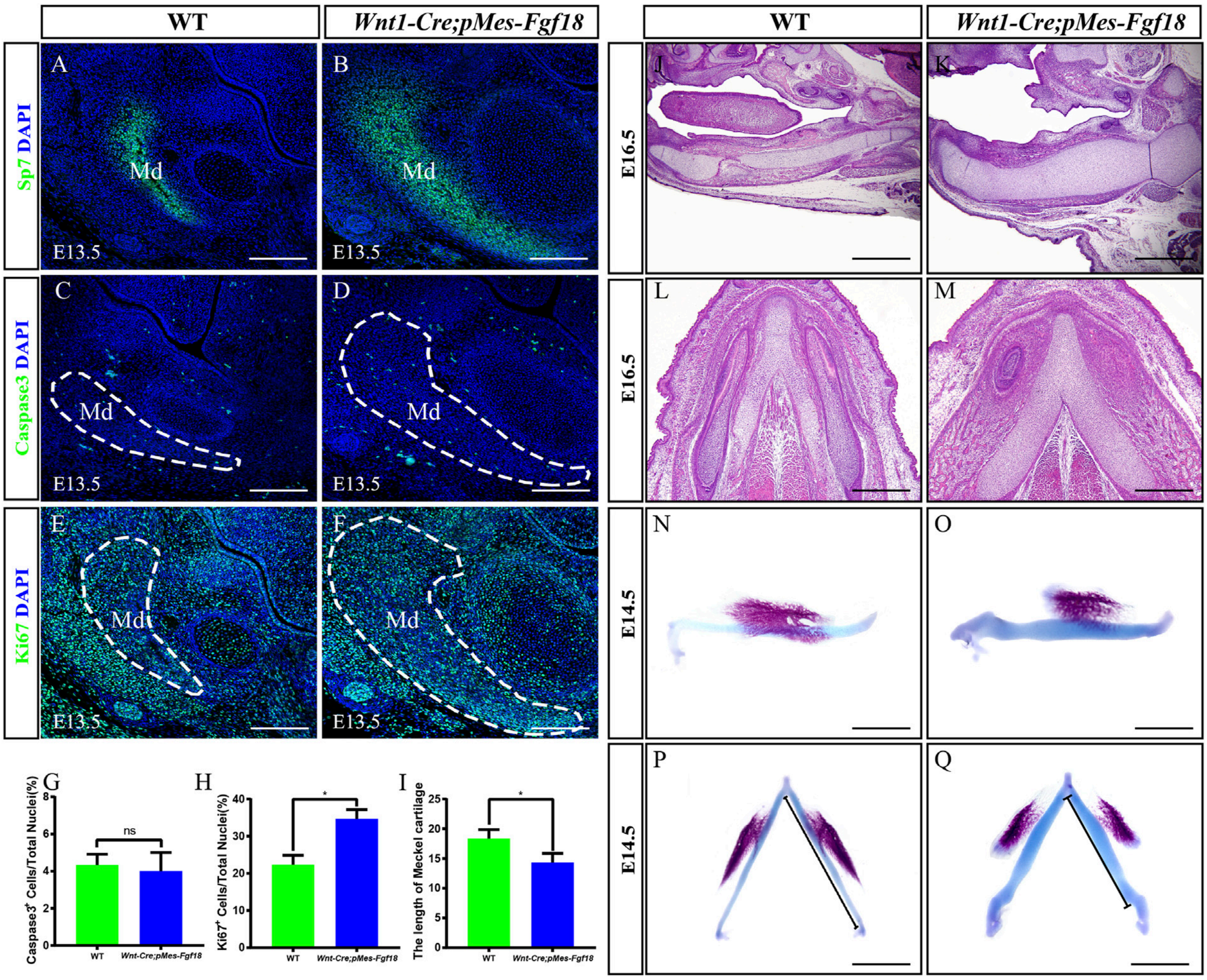

FIGURE 5
Wnt1-Cre;pMes-Fgf18 embryos exhibited severely hypoplastic Meckel's cartilages. **(A–F)** Immunostaining was performed on coronal sections of the mandible at E13.5 with antibodies against Sp7 **(A,B)**, Caspase 3 **(C,D)**, and Ki67 **(E,F)**. **(G,H)** Quantification analysis of the percentage of Caspase 3-positive cells and Ki67-positive cells in the mandible at E13.5. **(I)** Statistical analysis of the length of Meckel's cartilage. **(J–M)** Hematoxylin and eosin (HE) staining of Meckel's cartilage of embryos at E16.5. **(N–Q)** The top and side macroscopic views of the lower jaw of mouse embryos at E14.5, following Alcian Blue-Alizarin Red staining. Scale bar = 200 μm **(A–F)**, Scale bar = 400 μm **(J–Q)**, $^*p < 0.05$.

no significant difference in cell apoptosis in the condyle of *Wnt1-Cre;pMes-Fgf18* mice compared to control mice (Supplementary Figure S7). Previous research has demonstrated that FGF signaling promotes cell proliferation by suppressing p21 expression through activation of the Akt signaling pathway (Lu et al., 2020). To explore whether FGF18 signaling promoted chondrocyte proliferation in the condyle by inhibiting p21 expression, we evaluated the expression levels of p21 in the condyle of *Wnt1-Cre;pMes-Fgf18* mice. Our findings revealed that the expression of p21 was significantly reduced in the condyle of these mice compared to control mice at E16.5 (Figures 7C, D). These findings suggest that the overexpression of *Fgf18* disrupts chondrocyte proliferation, partly due to the abnormal distribution of p21 in the condylar cartilage.

To elucidate the fundamental process of abnormal endochondral ossification, we examined the expression of crucial proteins involved in the FGF signaling pathway within the condylar process of *Wnt1-Cre;pMes-Fgf18* mice. The results indicated that phosphor-p38 and phosphor-Erk1/2 were primarily expressed in the surface cell layer and polymorphic progenitor cell layer of the E16.5 wild-type mouse condyle. However, in mutant mice, their expression was observed to extend to the zone of flattened chondrocytes. Furthermore, most of these proteins were found to be localized in the nucleus, indicating their activation (Figures 7E–H). However, despite the presence of phosphor-JNK in the condyle of the mutant mice, its expression range was expanded to the zone of flattened chondrocytes. Nevertheless, it primarily localized in the cytoplasm, indicating an inactive state (Figures 7I–L). When compared to wild-type mice, the condyle of *Wnt1-Cre;pMes-Fgf18* mice displayed phosphorylation of Akt in almost all cells, indicating that FGF18 may stimulate the proliferation of pre-flattened chondrocytes by activating the Akt signaling pathway (Figures 7K, L).

The Wnt and Hedgehog (Hh) signaling pathways play crucial roles in the development and growth of organs and tissues, as they regulate cell proliferation, differentiation, and migration (Guzzetta et al., 2020; Oichi et al., 2020). To investigate the effect of overdosed

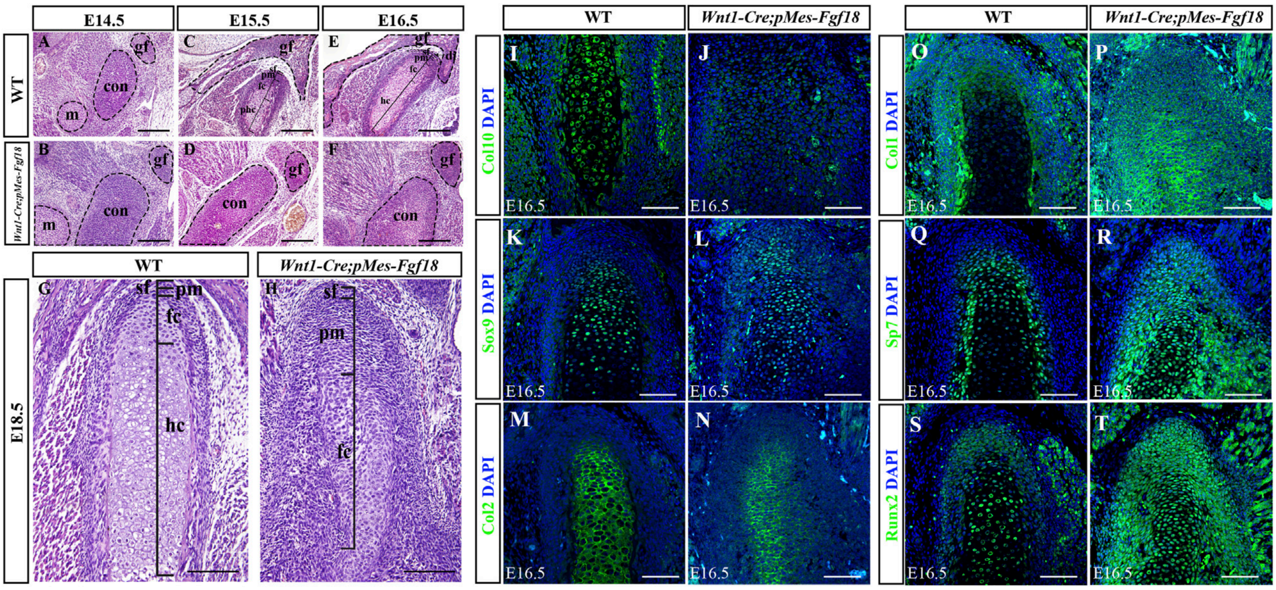

FIGURE 6
Conditional activation of *Fgf18* resulted in condylar cartilage defects. **(A–F)** Hematoxylin and eosin (HE) stained the condyles of mouse embryos at E14.5~E18.5. **(I–T)** Immunostaining assays were performed to detect the expression of Col10, Sox9, Col2, Col1, Sp7, and Runx2 proteins in the condylar of mice at E16.5. sf: superficial layer, pm: polymorphic, fc: flattened chondrocyte zone, hc: hypertrophic chondrocyte zone, gf: glenoid fossa, con: condylar cartilage, m: Meckel cartilage, Scale bar = 200 μm **(A–H)**, Scale bar = 100 μm **(I–T)**.

Fgf18 in CNCCs on Wnt and Hh signaling, we examined the expression of β-catenin and Ihh in condyle at E16.5. In comparison to wild-type mice, the condyle of *Wnt1-Cre;pMes-Fgf18* mice exhibited a significant increase in β-catenin, particularly in the area where flattened chondrocytes. This suggests that the canonical Wnt signaling pathway is activated in the condyle of these mutant mice (Figures 7M, N). However, when compared to the control group, the expression of Ihh was noticeably reduced in the condylar cartilage of *Wnt1-Cre;pMes-Fgf18* mice. Ihh expression was robust in the hypertrophic chondrocyte region of the condyle, with no detectable expression observed in the polymorphic progenitor layer of wild-type mice. (Figures 7O, P). These findings suggest that Hh signaling may facilitate the differentiation of flat chondrocytes into pre-hypertrophic chondrocytes. Together, excessive FGF18 in CNCCs induced the abnormality of FGF-related signals and disturbed the normal development of condyle.

4 Discussion

PRS is a congenital craniofacial structural defect characterized by mandibular hypoplasia, glossoptosis, cleft palate, and upper airway obstruction (Cote et al., 2015). While the underlying pathogenesis of PRS remains to be fully understood, it is believed that the core problems include failure of mandibular outgrowth or muscle defect with incomplete tongue descent (Tan et al., 2013; Juge et al., 2022). Previous research has shown that conditional knockout of *Fgf18* in CNCCs results in mice with cleft palate and micrognathism (Yue et al., 2021). To further explore the mechanisms of FGF18, we utilized a *Wnt1-Cre;pMes-Fgf18* mouse model to specifically activate the conditional *Fgf18* transgenic allele in CNCCs. Our findings reveal that *Wnt1-Cre;pMes-Fgf18* mice exhibited cleft palate, mandibular deformation, and tongue malposition, indicating that a precise equilibrium of endogenous FGF18 signaling is essential for normal craniofacial development. Furthermore, an *in vitro* assay of roller culture showed that mutant palatal shelves elevate normally when the tongue and mandible are removed, suggesting that FGF18 is not a crucial intrinsic factor for regulating palate elevation. This is consistent with previous research that demonstrated that the specific knockout of *Fgf18* in CNCCs does not impact palatal shelf elevation and fusion (Yue et al., 2021). We propose that the FGF18 paradox should not be solely determined by the signaling amplitude, but rather by the cascade that FGF18 transactivates. Here, we have successfully generated an animal model of *Wnt1-Cre;pMes-Fgf18* mice that exhibit a phenotype similar to the human PRS, providing a valuable tool for further elucidating its pathogenesis. However, it is noteworthy that concerns have been raised about the Wnt1-Cre strain, which is widely used, possessing the capability to function as a general gene delete (Dinsmore et al., 2022). Hence, caution and meticulousness are necessary when employing this strain in research.

The mandibular cartilage is known to play a crucial role in the growth and development of the mandible (Xu et al., 2022; Zhang et al., 2022). Our observations revealed that the mandibular morphology of *Wnt1-Cre;pMes-Fgf18* mice was severely shortened, with noticeable abnormalities in Meckel's cartilage and deformities in condylar cartilage. The defects observed are consistent with previous research reports, which have demonstrated that the overexpression of *Fgf10* or gain-of-function mutations in FGFR3 can lead to changes in the size and shape of Meckel's cartilage and abnormal condyle, ultimately resulting in mandibular dysmorphogenesis (Mina et al., 2007; Terao et al., 2011). The normal morphogenesis of the mandible relies on two types of ossification: intramembranous ossification and

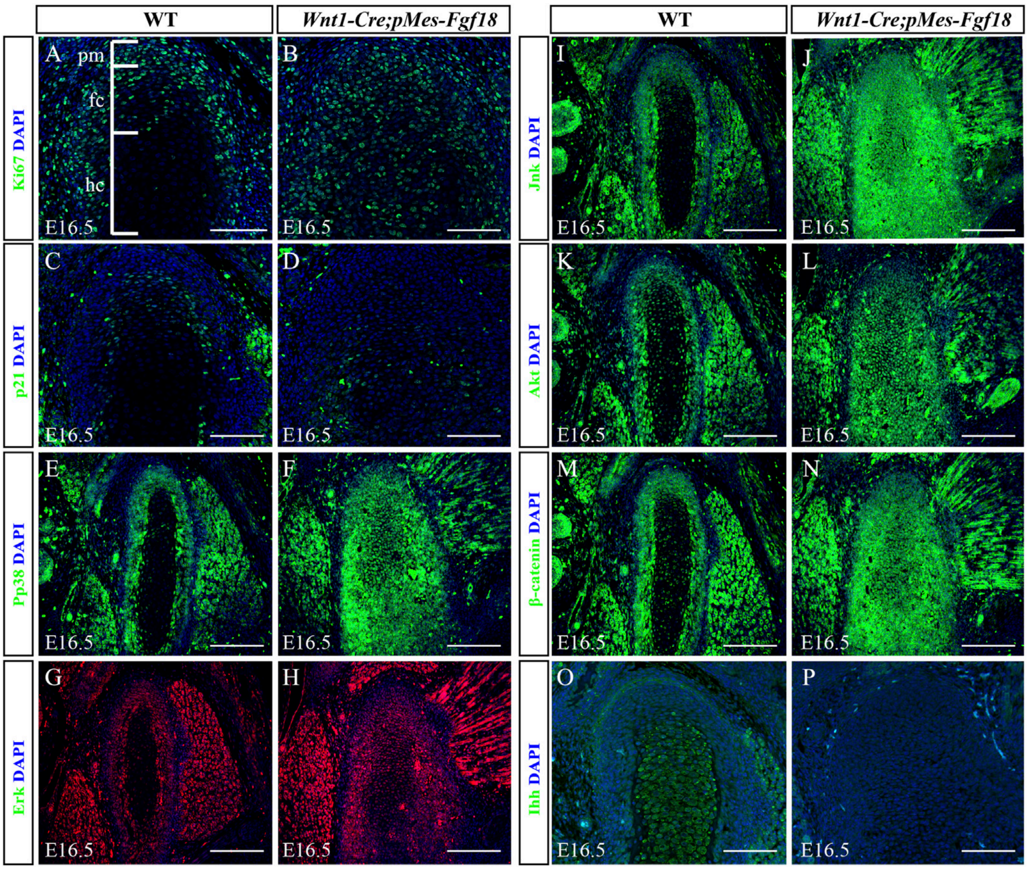

FIGURE 7
Overexpression of *Fgf18* disrupted downstream signals in condyle. **(A–P)** Immunostaining was performed on the condylar cartilage at E16.5 with antibodies against Ki67 **(A,B)**, p21**(C,D)**, pp38 **(E,F)**, Erk **(G,H)**, Jnk **(I,J)**, Akt **(K, L)**, β-catenin **(M, N)** and Ihh **(O, P)**. pm: polymorphic, fc: flattened chondrocyte zone, hc: hypertrophic chondrocyte zone, Scale bar = 200 μm.

endochondral ossification (Sugito et al., 2011). Previous studies have shown that congenital deficiency of FGF18 or FGFR3 led to similar expansion of growth plates in fetal mice, and the addition of FGF18 can stimulate the repair of damaged cartilage by enhancing proliferation and matrix production (Davidson et al., 2005; Moore et al., 2005). The expression of Sp7 in the mandibular primordium of E13.5 *Wnt1-Cre;pMes-Fgf18* mice was significantly upregulated, indicating that the FGF18 signaling pathway has a crucial impact on the early osteogenic differentiation program. However, the precise impact of FGF18 overexpression on earlier embryonic stages prior to E13.5 remains enigmatic and warrants further investigation.

Studies have shown that FGF plays a crucial role in embryonic development and adult tissue homeostasis by regulating multiple cellular activities such as proliferation, survival, migration, differentiation, and angiogenesis through the modulation of Akt, Erk, P38, p21, Jnk, Wnt, Ihh, and Runx2 signaling pathways (Chen et al., 2017; Zhai et al., 2017; Yao et al., 2019; Hayes et al., 2022). Our findings indicate that overexpression of *Fgf18* in CNCCs disrupts the downstream signals, which subsequently causes abnormalities in cell proliferation and cartilage ossification. These modifications result in alterations in the direction of genioglossus muscle contraction and mandibular deformation. Akt and Erk are crucial components of the BMP, TGFβ, FGF, and EGF signaling pathways. Studies have revealed that mice with disabled ERK or BMP2 signaling in neural crest cells display a phenotype that is comparable to human PRS (Parada et al., 2015; Chen et al., 2019). Additionally, the osteogenic differentiation effects of FGF18 are confirmed in part by increased levels of BMP2 and BMP4 (Jeon et al., 2012; Nagayama et al., 2013). Paradoxically, conditional overexpression of Bmp4 in CNCCs results in a shorter, more pointed mandible compared to controls (Bonilla-Claudio et al., 2012). Meanwhile, we observed abnormalities in the temporomandibular joint (TMJ) of *Wnt1-Cre; pMes-Fgf18 mice.* In comparison to wild-type mice, mutant mice exhibited a suppression in glenoid fossa differentiation, and the articular disc structure was absent at E16.5 (Figure 6). Ihh plays an important role in promoting the development of TMJ (Lu et al., 2022). Our findings indicate that an overdosed FGF18 hinders the expression of Ihh in condylar cartilage, which may be the cause of abnormal TMJ development in mutant mice. The tissue-specific defects observed can be attributed to the unique patterns of FGF18 receptor expression in each tissue, which explains the distinct phenotypic outcomes observed in different tissues when FGF18 is dysregulated. Additionally, the intricate interplay among downstream signaling pathways, such as Akt, Erk, p38, β-catenin, Ihh, Runx2, and p21, is crucial in determining the tissue-specific phenotypic outcomes observed upon dysregulation of FGF18. Given that FGF18 is a secreted protein, its overexpression can potentially disrupt the delicate interaction among different organs. Altered FGF18 expression might affect the endocrine system, thereby modulating hormone secretion and regulation. The specific mechanism underlying the tissue-specific response to FGF18 dysregulation caused by this complex network of signaling molecules remains unclear. Hence, further research is needed to understand the precise mechanisms by which FGF18 regulates these processes and how it contributes to the development of local craniofacial structures.

In summary, our study has shown that overexpression of Fgf18 signaling in CNCCs disrupts the development and growth of the mandible, leading to structural anomalies in the Meckel's and condylar cartilages. These anomalies are likely caused by significant increases in cell proliferation, defective cell differentiation, and abnormal distribution of correlation signals in the orofacial regions. These findings enhance our understanding of the potential mechanisms underlying the Pierre Robin sequence. However, further research is necessary to fully comprehend the role of FGF18 in craniofacial development and to identify potential therapeutic targets for treating craniofacial disorders caused by FGF18 signaling dysregulation.

Data availability statement

The datasets presented in this study can be found in online repositories. The names of the repository/repositories and accession number(s) can be found in the article/Supplementary Material.

Ethics statement

The animal study was approved by the Institutional Animal Care and Use Committee at Fujian Normal University. The study was conducted in accordance with the local legislation and institutional requirements.

Author contributions

YL: Data curation, Formal Analysis, Visualization, Writing–original draft. QW: Formal Analysis, Project administration, Visualization, Writing–original draft. CL: Methodology, Software, Writing–original draft. XZ: Data curation, Project administration, Writing–original draft. YZ: Conceptualization, Resources, Supervision, Writing–review and editing. XH: Funding acquisition, Resources, Supervision, Writing–review and editing.

Funding

The author(s) declare that financial support was received for the research, authorship, and/or publication of this article. This study was supported by the National Natural Science Foundation of China (Nos 81771034 and 82170917) and Foundation of Stomatological Key Laboratory of Fujian College and University, School and Hospital of Stomatology, Fujian Medical University (Grant Nos 2022GXA01 and 2023GCB01).

Conflict of interest

The authors declare that the research was conducted in the absence of any commercial or financial relationships that could be construed as a potential conflict of interest.

Publisher's note

Supplementary material

The Supplementary Material for this article can be found online at: https://www.frontiersin.org/articles/10.3389/fcell.2024.1376814/full#supplementary-material

References

Biosse Duplan, M., Komla-Ebri, D., Heuze, Y., Estibals, V., Gaudas, E., Kaci, N., et al. (2016). Meckel's and condylar cartilages anomalies in achondroplasia result in defective development and growth of the mandible. *Hum. Mol. Genet.* 25, 2997–3010. doi:10.1093/hmg/ddw153

Bonilla-Claudio, M., Wang, J., Bai, Y., Klysik, E., Selever, J., and Martin, J. F. (2012). Bmp signaling regulates a dose-dependent transcriptional program to control facial skeletal development. *Development* 139, 709–719. doi:10.1242/dev.073197

Chen, T., Gong, W., Tian, H., Wang, H., Chu, S., Ma, J., et al. (2017). Fibroblast growth factor 18 promotes proliferation and migration of H460 cells via the ERK and p38 signaling pathways. *Oncol. Rep.* 37, 1235–1242. doi:10.3892/or.2016.5301

Chen, Y., Wang, Z., Chen, Y., and Zhang, Y. (2019). Conditional deletion of Bmp2 in cranial neural crest cells recapitulates Pierre Robin sequence in mice. *Cell Tissue Res.* 376, 199–210. doi:10.1007/s00441-018-2944-5

Cote, A., Fanous, A., Almajed, A., and Lacroix, Y. (2015). Pierre Robin sequence: review of diagnostic and treatment challenges. *Int. J. Pediatr. Otorhinolaryngol.* 79, 451–464. doi:10.1016/j.ijporl.2015.01.035

Davidson, D., Blanc, A., Filion, D., Wang, H., Plut, P., Pfeffer, G., et al. (2005). Fibroblast growth factor (FGF) 18 signals through FGF receptor 3 to promote chondrogenesis. *J. Biol. Chem.* 280, 20509–20515. doi:10.1074/jbc.M410148200

Dinsmore, C. J., Ke, C. Y., and Soriano, P. (2022). The Wnt1-Cre2 transgene is active in the male germline. *Genesis* 60, e23468. doi:10.1002/dvg.23468

Eloy-Trinquet, S., Wang, H., Edom-Vovard, F., and Duprez, D. (2009). Fgf signaling components are associated with muscles and tendons during limb development. *Dev. Dyn.* 238, 1195–1206. doi:10.1002/dvdy.21946

Giudice, A., Barone, S., Belhous, K., Morice, A., Soupre, V., Bennardo, F., et al. (2018). Pierre Robin sequence: a comprehensive narrative review of the literature over time. *J. Stomatol. Oral Maxillofac. Surg.* 119, 419–428. doi:10.1016/j.jormas.2018.05.002

Guzzetta, A., Koska, M., Rowton, M., Sullivan, K. R., Jacobs-Li, J., Kweon, J., et al. (2020). Hedgehog-FGF signaling axis patterns anterior mesoderm during gastrulation. *Proc. Natl. Acad. Sci. U. S. A.* 117, 15712–15723. doi:10.1073/pnas.1914167117

Hagan, A. S., Boylan, M., Smith, C., Perez-Santamarina, E., Kowalska, K., Hung, I. H., et al. (2019). Generation and validation of novel conditional flox and inducible Cre alleles targeting fibroblast growth factor 18 (Fgf18). *Dev. Dyn.* 248, 882–893. doi:10.1002/dvdy.85

Hao, Y., Tang, S., Yuan, Y., Liu, R., and Chen, Q. (2019). Roles of FGF8 subfamily in embryogenesis and oral-maxillofacial diseases (Review). *Int. J. Oncol.* 54, 797–806. doi:10.3892/ijo.2019.4677

Hayes, A. J., Whitelock, J., and Melrose, J. (2022). Regulation of FGF-2, FGF-18 and transcription factor activity by perlecan in the maturational development of transitional rudiment and growth plate cartilages and in the maintenance of permanent cartilage homeostasis. *Int. J. Mol. Sci.* 23, 1934. doi:10.3390/ijms23041934

Hsieh, S. T., and Woo, A. S. (2019). Pierre Robin sequence. *Clin. Plast. Surg.* 46, 249–259. doi:10.1016/j.cps.2018.11.010

Jeon, E., Yun, Y. R., Kang, W., Lee, S., Koh, Y. H., Kim, H. W., et al. (2012). Investigating the role of FGF18 in the cultivation and osteogenic differentiation of mesenchymal stem cells. *PLoS One* 7, e43982. doi:10.1371/journal.pone.0043982

Juge, L., Knapman, F. L., Humburg, P., Burke, P. G. R., Lowth, A. B., Brown, E., et al. (2022). The relationship between mandibular advancement, tongue movement, and treatment outcome in obstructive sleep apnea. *Sleep* 45, zsac044. doi:10.1093/sleep/zsac044

Kouskoura, T., El Fersioui, Y., Angelini, M., Graf, D., Katsaros, C., and Chiquet, M. (2016). Dislocated tongue muscle attachment and cleft palate formation. *J. Dent. Res.* 95, 453–459. doi:10.1177/0022034515621869

Lee, K. K. L., Peskett, E., Quinn, C. M., Aiello, R., Adeeva, L., Moulding, D. A., et al. (2018). Overexpression of Fgfr2c causes craniofacial bone hypoplasia and ameliorates craniosynostosis in the Crouzon mouse. *Dis. Model Mech.* 11, dmm035311. doi:10.1242/dmm.035311

Li, K., Fan, L., Tian, Y., Lou, S., Li, D., Ma, L., et al. (2022). Application of zebrafish in the study of craniomaxillofacial developmental anomalies. *Birth Defects Res.* 114, 583–595. doi:10.1002/bdr2.2014

Liu, Z., Xu, J., Colvin, J. S., and Ornitz, D. M. (2002). Coordination of chondrogenesis and osteogenesis by fibroblast growth factor 18. *Genes Dev.* 16, 859–869. doi:10.1101/gad.965602

Lu, H., Yin, M., Wang, L., Cheng, J., Cheng, W., An, H., et al. (2020). FGF13 interaction with SHCBP1 activates AKT-GSK3α/β signaling and promotes the proliferation of A549 cells. *Cancer Biol. Ther.* 21, 1014–1024. doi:10.1080/15384047.2020.1824512

Lu, K., Ma, F., Yi, D., Yu, H., Tong, L., and Chen, D. (2022). Molecular signaling in temporomandibular joint osteoarthritis. *J. Orthop. Transl.* 32, 21–27. doi:10.1016/j.jot.2021.07.001

Maruoka, Y., Ohbayashi, N., Hoshikawa, M., Itoh, N., Hogan, B. L., and Furuta, Y. (1998). Comparison of the expression of three highly related genes, Fgf8, Fgf17 and Fgf18, in the mouse embryo. *Mech. Dev.* 74, 175–177. doi:10.1016/s0925-4773(98)00061-6

Mina, M., Havens, B., and Velonis, D. A. (2007). FGF signaling in mandibular skeletogenesis. *Orthod. Craniofac Res.* 10, 59–66. doi:10.1111/j.1601-6343.2007.00385.x

Moore, E. E., Bendele, A. M., Thompson, D. L., Littau, A., Waggie, K. S., Reardon, B., et al. (2005). Fibroblast growth factor-18 stimulates chondrogenesis and cartilage repair in a rat model of injury-induced osteoarthritis. *Osteoarthr. Cartil.* 13, 623–631. doi:10.1016/j.joca.2005.03.003

Moosa, S., and Wollnik, B. (2016). Altered FGF signalling in congenital craniofacial and skeletal disorders. *Semin. Cell Dev. Biol.* 53, 115–125. doi:10.1016/j.semcdb.2015.12.005

Nagayama, T., Okuhara, S., Ota, M. S., Tachikawa, N., Kasugai, S., and Iseki, S. (2013). FGF18 accelerates osteoblast differentiation by upregulating Bmp2 expression. *Congenit. Anom. (Kyoto)* 53, 83–88. doi:10.1111/cga.12012

Ohbayashi, N., Shibayama, M., Kurotaki, Y., Imanishi, M., Fujimori, T., Itoh, N., et al. (2002). FGF18 is required for normal cell proliferation and differentiation during osteogenesis and chondrogenesis. *Genes Dev.* 16, 870–879. doi:10.1101/gad.965702

Oichi, T., Otsuru, S., Usami, Y., Enomoto-Iwamoto, M., and Iwamoto, M. (2020). Wnt signaling in chondroprogenitors during long bone development and growth. *Bone* 137, 115368. doi:10.1016/j.bone.2020.115368

Parada, C., Han, D., Grimaldi, A., Sarrion, P., Park, S. S., Pelikan, R., et al. (2015). Disruption of the ERK/MAPK pathway in neural crest cells as a potential cause of Pierre Robin sequence. *Development* 142, 3734–3745. doi:10.1242/dev.125328

Prochazkova, M., Prochazka, J., Marangoni, P., and Klein, O. D. (2018). Bones, glands, ears and more: the multiple roles of FGF10 in craniofacial development. *Front. Genet.* 9, 542. doi:10.3389/fgene.2018.00542

Sugito, H., Shibukawa, Y., Kinumatsu, T., Yasuda, T., Nagayama, M., Yamada, S., et al. (2011). Ihh signaling regulates mandibular symphysis development and growth. *J. Dent. Res.* 90, 625–631. doi:10.1177/0022034510397836

Tan, T. Y., Kilpatrick, N., and Farlie, P. G. (2013). Developmental and genetic perspectives on Pierre Robin sequence. *Am. J. Med. Genet. C Semin. Med. Genet.* 163C, 295–305. doi:10.1002/ajmg.c.31374

Terao, F., Takahashi, I., Mitani, H., Haruyama, N., Sasano, Y., Suzuki, O., et al. (2011). Fibroblast growth factor 10 regulates Meckel's cartilage formation during early mandibular morphogenesis in rats. *Dev. Biol.* 350, 337–347. doi:10.1016/j.ydbio.2010.11.029

Xie, Y., Su, N., Yang, J., Tan, Q., Huang, S., Jin, M., et al. (2020). FGF/FGFR signaling in health and disease. *Signal Transduct. Target Ther.* 5, 181. doi:10.1038/s41392-020-00222-7

Xu, M., Zhang, X., and He, Y. (2022). An updated view on temporomandibular joint degeneration: insights from the cell subsets of mandibular condylar cartilage. *Stem Cells Dev.* 31, 445–459. doi:10.1089/scd.2021.0324

Yao, X., Zhang, J., Jing, X., Ye, Y., Guo, J., Sun, K., et al. (2019). Fibroblast growth factor 18 exerts anti-osteoarthritic effects through PI3K-AKT signaling and mitochondrial fusion and fission. *Pharmacol. Res.* 139, 314–324. doi:10.1016/j.phrs.2018.09.026

Yue, M., Lan, Y., Liu, H., Wu, Z., Imamura, T., and Jiang, R. (2021). Tissue-specific analysis of Fgf18 gene function in palate development. *Dev. Dyn.* 250, 562–573. doi:10.1002/dvdy.259

Zbasnik, N., Dolan, K., Buczkowski, S. A., Green, R. M., Hallgrimsson, B., Marcucio, R. S., et al. (2022). Fgf8 dosage regulates jaw shape and symmetry through pharyngeal-cardiac tissue relationships. *Dev. Dyn.* 251, 1711–1727. doi:10.1002/dvdy.501

Zhai, F., Song, N., Ma, J., Gong, W., Tian, H., Li, X., et al. (2017). FGF18 inhibits MC3T3-E1 cell osteogenic differentiation via the ERK signaling pathway. *Mol. Med. Rep.* 16, 4127–4132. doi:10.3892/mmr.2017.7088

Zhang, J., Lin, C., Song, Y., and Chen, J. (2022). BMP4/ALK3 deficiency leads to Meckel's cartilage truncation mimicking the mandible Tessier 30 cleft. *Oral Dis.* 28, 1215–1227. doi:10.1111/odi.13855

Zhang, J., Lin, C., Song, Y., Zhang, Y., and Chen, J. (2021). Augmented BMP4 signal impairs tongue myogenesis. *J. Mol. Histol.* 52, 651–659. doi:10.1007/s10735-021-09987-9

Zhao, X., Erhardt, S., Sung, K., and Wang, J. (2023). FGF signaling in cranial suture development and related diseases. *Front. Cell Dev. Biol.* 11, 1112890. doi:10.3389/fcell.2023.1112890

frontiers | Frontiers in Cell and Developmental Biology

TYPE Original Research
PUBLISHED 25 July 2024
DOI 10.3389/fcell.2024.1431337

OPEN ACCESS

EDITED BY
Michael Schubert,
UMR7009 Laboratoire de Biologie du Développement de Villefranche sur Mer, France

REVIEWED BY
Guang Li,
Xiamen University, China
Jian Sun,
University of Delaware, United States
David McClay,
Duke University, United States
Nicholas Holland,
University of California, San Diego, United States

*CORRESPONDENCE
Iryna Kozmikova,
✉ kozmikova@img.cas.cz

RECEIVED 11 May 2024
ACCEPTED 10 July 2024
PUBLISHED 25 July 2024

CITATION
Kozmik Z and Kozmikova I (2024), Ancestral role of Pax6 in chordate brain regionalization.
Front. Cell Dev. Biol. 12:1431337.
doi: 10.3389/fcell.2024.1431337

Ancestral role of Pax6 in chordate brain regionalization

Zbynek Kozmik and Iryna Kozmikova*

Laboratory of Transcriptional Regulation, Institute of Molecular Genetics of the Czech Academy of Sciences, Prague, Czechia

The *Pax6* gene is essential for eye and brain development across various animal species. Here, we investigate the function of *Pax6* in the development of the anterior central nervous system (CNS) of the invertebrate chordate amphioxus using CRISPR/Cas9-induced genome editing. Specifically, we examined Pax6 mutants featuring a 6 bp deletion encompassing two invariant amino acids in the conserved paired domain, hypothesized to impair Pax6 DNA-binding capacity and gene regulatory functions. Although this mutation did not result in gross morphological changes in amphioxus larvae, it demonstrated a reduced ability to activate Pax6-responsive reporter gene, suggesting a hypomorphic effect. Expression analysis in mutant larvae revealed changes in gene expression within the anterior CNS, supporting the conserved role of *Pax6* gene in brain regionalization across chordates. Additionally, our findings lend support to the hypothesis of a zona limitans intrathalamica (ZLI)-like region in amphioxus, suggesting evolutionary continuity in brain patterning mechanisms. ZLI region, found in both hemichordates and vertebrates, functions as a key signaling center and serves as a restrictive boundary between major thalamic regions.

KEYWORDS

evolution, brain, eye, amphioxus, chordates, genome editing, pax6

Introduction

Pax6 is a member of the homeobox gene family, which also contains a DNA-binding paired-box motif originally identified in *Drosophila* (Bopp et al., 1986). The paired domains of Pax6 proteins exhibit a high degree of sequence conservation; vertebrate Pax6 proteins display nearly identical paired domains, whereas invertebrate Pax6 proteins show more than 90% sequence homology with their mouse Pax6 (Callaerts et al., 1997). Since its discovery in 1991 (Walther and Gruss, 1991), studies on *Pax6* lead to the transformative thinking regarding the genetic programs orchestrating eye morphogenesis as well as the origin and evolution of diverse visual systems. The uncovering of the *Pax6* gene as an essential factor in eye development within both mice (Hill et al., 1991; Grindley et al., 1995) and *Drosophila* (Quiring et al., 1994; Czerny et al., 1999) has given rise to the concept of a “master control gene for eye morphogenesis and evolution,” alongside the hypothesis of a monophyletic origin of eyes in metazoans (Gehring and Ikeo, 1999). This idea presented a stark contrast to the perspective originally posited by Salvini-Plawen and Mayr, which suggested a diverse, independent origin of photoreceptor organs across numerous species (von Salvini-Plawen and Mayr, 1977). The theory about a “master control gene,” has propelled a wave of scientific investigation into the expression and function of Pax6 across diverse animal species (Kozmik, 2005).

Pax6 is a typical pleiotropic transcription factor that has been implicated in diverse biological processes, and it is known to regulate expression of a broad range of molecules, including transcription factors, cell adhesion and cell signaling molecules, hormones, and structural proteins [reviewed in Simpson and Price (2002); Cvekl and Callaerts (2017)]. *Pax6* function is not restricted to the visual system as it is also essential for the development of the central nervous system and endocrine glands of vertebrates and invertebrates. The expression patterns of *Pax6* in the developing nervous systems of vertebrates, eyes included, show significant similarity (Carriere et al., 1993; Goulding et al., 1993; Grindley et al., 1995; Hirsch and Harris, 1997; Pan J. et al., 2023).

Heterozygous mice carrying the Small eye (Sey) *Pax6* gene mutation (Hill et al., 1991), which involves a premature stop codon, display a range of eye deficits including aniridia, which is a condition also observed in humans, as well as lens size (Hogan et al., 1986; Hogan et al., 1988). These mice also exhibit abnormalities in the telencephalon, diencephalon, and metencephalon (Schmahl et al., 1993). Homozygous Sey mutants are not viable; the embryos exhibit profound brain and olfactory malformations (Grindley et al., 1995). *Pax6* plays a role in establishing boundaries between regions of the central nervous system in the anteroposterior axis, at least in part, due to the regulation of homeobox-containing genes such as *En1*, *Pax2*, and *Lhx1* (Mastick et al., 1997; Warren and Price, 1997; Matsunaga et al., 2000). The boundary between cortical and striatal regions of the telencephalon is dramatically altered in Sey mutants: radial glial fascicles do not form at the border, and the normal expression of R-cadherin and tenascin-C at the border is lost suggesting that *Pax6* regulates boundary formation between developing forebrain regions (Stoykova et al., 1997). Paired domain is necessary for the regulation of neurogenesis, cell proliferation and patterning effects of Pax6, since these aspects are severely affected in the developing forebrain of the Pax6Aey18 mice with a deletion in the PD but intact homeodomain and transactivation domain (Haubst et al., 2004).

In *Xenopus*, mutations that result in truncated Pax6 proteins affect forebrain regionalization but do not completely eliminate eyes; rather, they lead to the formation of eye-like structures without lenses (Nakayama et al., 2015). It is hypothesized that an additional *Pax6.2* gene may compensate for these phenotypic alterations. In medaka, mutations in the individual *Pax6.1* or *Pax6.2* genes do not completely eliminate eyes either (Pan K. et al., 2023; Pan J. et al., 2023). Despite the shift away from the “master control gene” concept, *Pax6* central role in eye and brain development is undeniable, continuing to make it an intriguing subject for evolutionary studies.

The cephalochordate amphioxus, owing to its unique phylogenetic position as the presumed closest living relative to the common ancestor of chordates, serves as a pivotal model for exploring chordate evolution and vertebrate innovations. In amphioxus, *Pax6* expression initiates during neurulation in the surface anterior ectoderm and neural plate. As neurulation progresses, strong expression becomes localized in the anterior ectoderm and the developing cerebral vesicle, the presumptive homolog of the vertebrate brain (Glardon et al., 1998). Previous studies, utilizing electron microscopy and gene expression analysis, have suggested that the brain’s anterior part corresponding to the frontal eye, may represent a potential homolog of the vertebrate paired eyes (Vopalensky et al., 2012; Pergner and Kozmik, 2017; Pergner et al., 2020). More recently, in light of new experimental evidence (Albuixech-Crespo et al., 2017) it has been proposed that the molecular signature of the frontal eye exhibits similarities to both the vertebrate retina and hypothalamus (Lacalli, 2022). Our research investigates the impact of a mutation in the most conserved region of the *Pax6* gene on the anterior central nervous system of amphioxus.

Results

Targeted mutagenesis of *Branchiostoma floridae Pax6* gene

To determine the functional role of *Pax6* gene in amphioxus central nervous system development we analyzed mutants generated by CRISPR/Cas9 genome editing, methodology applied previously in amphioxus (Su et al., 2020). Targeting 5’end of the exon encoding the N-terminal half of paired domain produced an allele carrying a 6 bp deletion (Figure 1A) that was transmitted to F1 generation, and was designated Pax6ΔQL. Progeny of genetic crosses between Pax6ΔQL F1 (and F2) animals was genotyped to identify wild type, heterozygote, and homozygote embryos (Figure 1B). No significant morphological changes were observed in the homozygote mutant amphioxus larvae at 4 days of development (Figure 1C). The 6 bp deletion results in the elimination of the two evolutionarily conserved amino acids found in both bilaterian and cnidarian Pax proteins. Our analysis (Figure 1D) has shown that the respective QL amino acids are conserved in all nine human paralogues (PAX1-PAX9), in *Drosophila* Pax6, and even in the cnidarian PaxB that was previously characterized as a structural hybrid between a typical bilaterian Pax6 and Pax2 (Kozmik et al., 2003).

We reasoned that elimination of two invariant amino acids of paired domain might compromise DNA binding ability of Pax6 and as a result diminish its ability to regulate target genes. This notion was further supported by the published structure of the Pax6 paired domain–DNA complex showing DNA contacts of the mutagenized amino acids with the phosphate backbone (Xu et al., 1999). To test the hypothesis we performed luciferase reporter gene assays using either wild type Pax6 or mutant Pax6ΔQL. Reporter gene assay revealed a strongly reduced capacity of the mutated protein to activate the Pax6 responsive promoter (Figure 1E). However, the observed residual activity of Pax6ΔQL as compared to the empty expression vector (Figure 1E) strongly suggests that the mutant allele generated by us here using CRISPR/Cas9 genome editing is hypomorhic. To exclude the possibility that the effect observed in reporter gene assays is not due to the reduced DNA binding of Pax6ΔQL as compared to the wild type protein but rather due to the reduced protein level we performed Western blotting following the transfection assay. As shown in Figure 1F, comparable levels of wild type Pax6 and mutant Pax6ΔQL proteins were detected in transfected cells.

Pax6 mutation affects the molecular organization and regionalization in the brain of amphioxus larvae

The results demonstrating the reduced activity of the mutated Pax6 protein encouraged us to closely examine the expression of marker genes in the region referred to as the frontal eye by Pergner et al. (2020), or as the retina and hypothalamus according to Lacalli (2022), as well as the proto-tectum and primary motor center, or

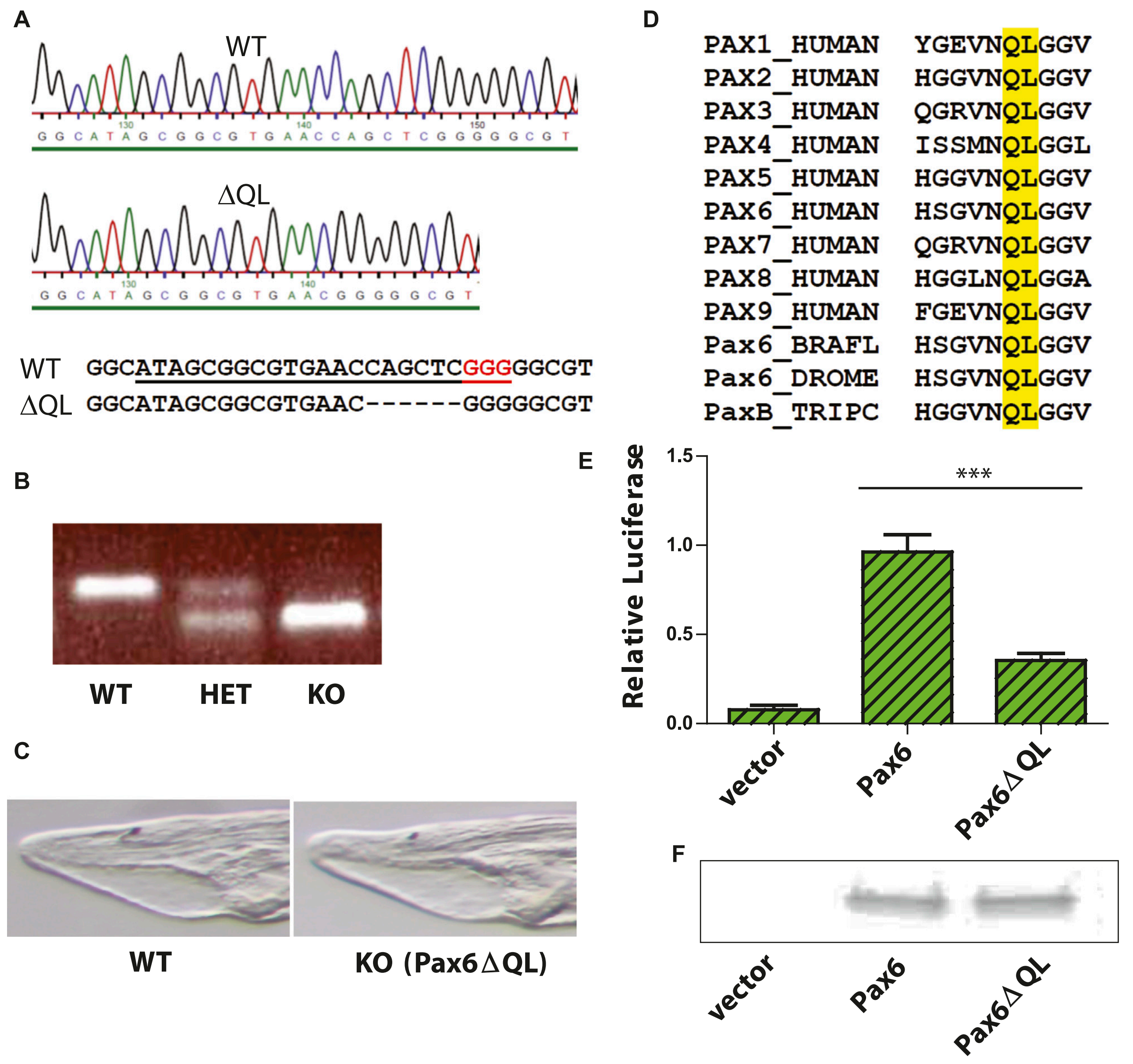

FIGURE 1
Targeted mutagenesis of *Branchiostoma floridae* Pax6 gene and characterization of the Pax6ΔQL mutant protein. **(A)** DNA sequencing results validating the 6 bp deletion in the *Branchiostoma floridae* Pax6 gene. sgRNA used for CRISPR/Cas9 genome editing is underlined and PAM sequence highlighted red. **(B)** A representative PCR based genotyping of amphioxus embryos carrying wild type and Pax6ΔQL alleles **(C)** Bright field images of the anterior part of the four-day-old wild type and KO (Pax6ΔQL homozygote mutant) larvae. **(D)** Amino acid sequence alignment of paired domain region for selected Pax genes. Amino acids QL deleted in mutant allele of *Branchiostoma floridae* Pax6 described here are highlighted by the yellow box. BRAFL, *Branchiostoma floridae*; DROME, *Drosophila melanogaster*; TRIPC, *Tripedalia cystophora*. **(E)** Reporter gene assays were performed by co-transfecting the indicated Pax6-encoding expression vector or empty expression vector with Pax6-responsive promoter construct. Triplicate assays were performed to obtain standard deviations and transfection efficiency was normalized by co-transfection of β-galactosidase expression plasmid. **(F)** Comparable levels of wild type Pax6 and mutant Pax6ΔQL proteins are detected in transfected cells by Western blotting.

dien-mesencephalon (suggested counterpart of vertebrate thalamus, pretectum, and midbrain). Up to now, it is not completely clear which concept should prevail, and for clarity, we will maintain the terminology proposed by Pergner et al. (2020).

We analyzed the expression of Six3/6, Otx, and Brn3 (Figure 2), which are found in photoreceptors of wild type larva (Figures 2A–2as3; Figures 2Bd–bd; Figures 2C–Cs1’ and 2c–cs1’). These genes showed no significant change in expression in these cells (Figure 4), indicating that the photoreceptors were likely unaffected. However, we did notice alterations in the expression of Six3/6, Brn1/2/4, Lhx3, and Pax6 in other regions of the frontal eye. Specifically, Six3/6 expression, seen at the boundary of the frontal eye with the proto-tectum in wild type larvae, was reduced in this region (Figures 2A–A’ and Figures 2a–a’; Figure 2As3 and 2as3; Figure 4). Conversely, Brn1/2/4 expression extended into the anterior frontal eye, affecting Row3, Row2, and even the photoreceptors (Figure 2D–ds2). Lhx3 expression was significantly diminished in Row4 but not in Row3 cells, and Pax6 showed reduced expression in

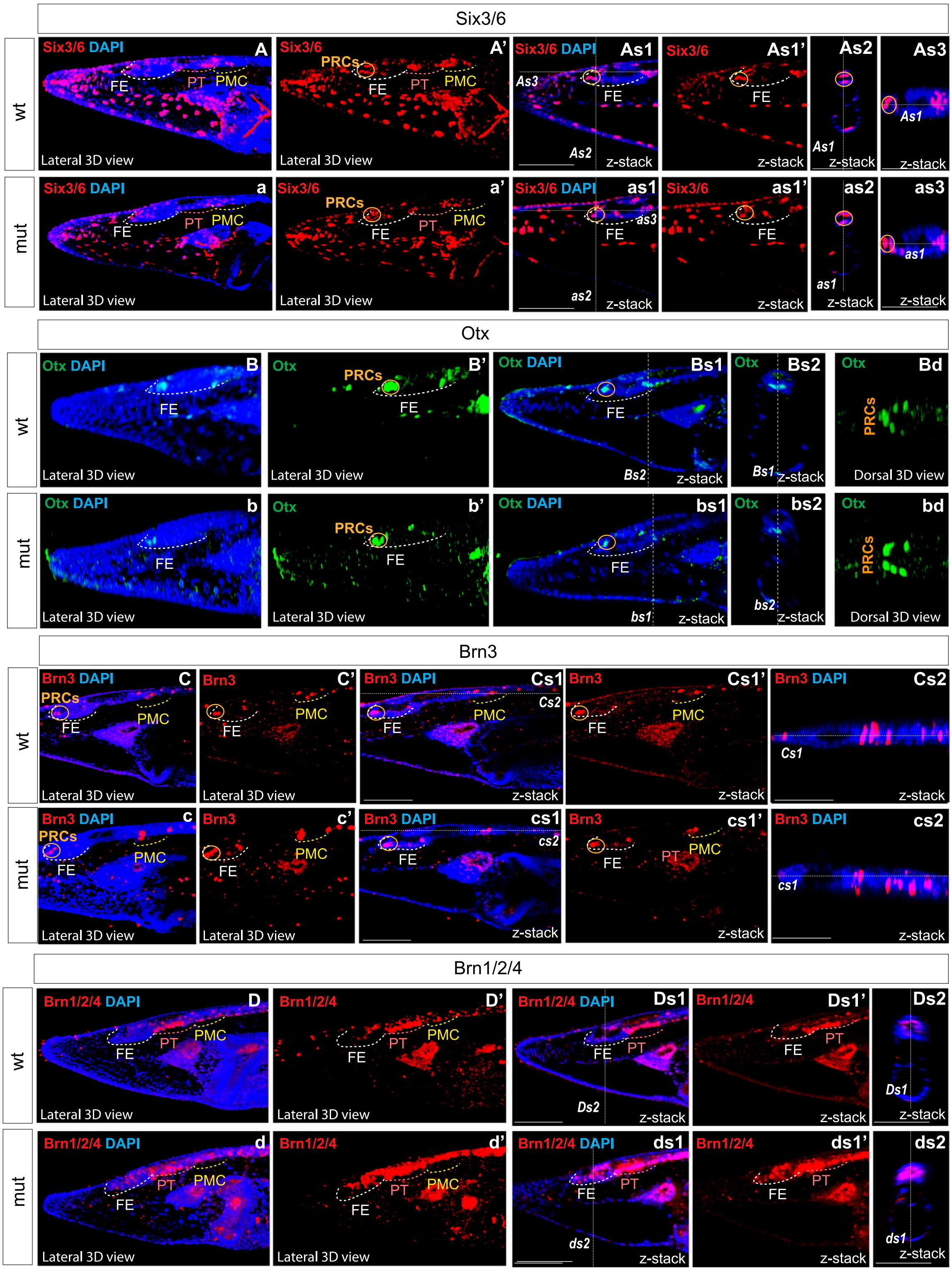

FIGURE 2
Expression of individual genes in amphioxus wild type **(A)**–As3, **(B)**–Bd, **(C)**–Cs2, **(D)**–Ds2 and Pax6ΔQL mutant embryos (a–as3, b–bd, c–cs2, d–ds2). Wt-wild type embryos. Mut – mutant embryos FE – frontal eye. PT – proto-tectum PMC – primary motor center. PRCs and an orange circle – photoreceptors. The positions of individual z-slices (As2, As1, As3, as1, as2, as3, Bs1, Bs2, bs1, bs2 Cs1, Cs2, cs1, cs2, Ds1, Ds2, ds1, ds2) from complete z-stacks are indicated with dashed lines (As2, As1, As3, as1, as2, as3, Bs1, Bs2, bs1, bs2 Cs1, Cs2, cs1, cs2, Ds1, Ds2, ds1, ds2).

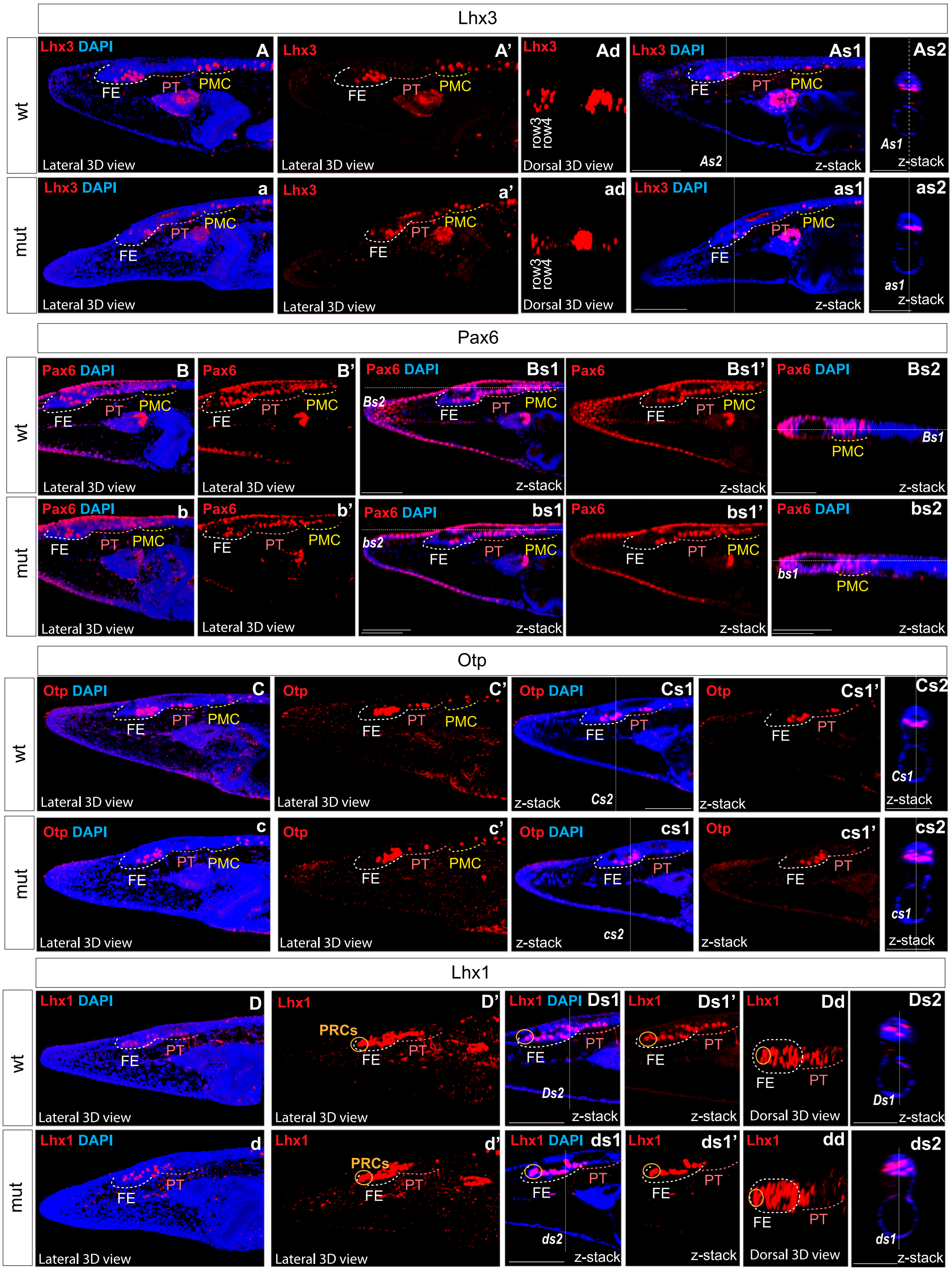

FIGURE 3
Expression of individual genes in amphioxus wild type **(A)**–As2, **(B)**–Bs2, **(C)**–Cs2, **(D)**–Ds2 and Pax6ΔQL mutant embryos (a–as3, b–bs2, c–cs2, d–ds2). Wt-wild type embryos. Mut – mutant embryos FE – frontal eye. PT – proto-tectum PMC – primary motor center. PRCs and an orange circle – photoreceptors. The positions of individual z-slices (As2, As1, as1, as2, Bs1, Bs2, bs1, bs2 Cs1, Cs2, cs1, cs2, Ds1, Ds2, ds1, ds2) from complete z-stacks are indicated with dashed lines (As2, As1, as1, as2, Bs1, Bs2, bs1, bs2 Cs1, Cs2, cs1, cs2, Ds1, Ds2, ds1, ds2).

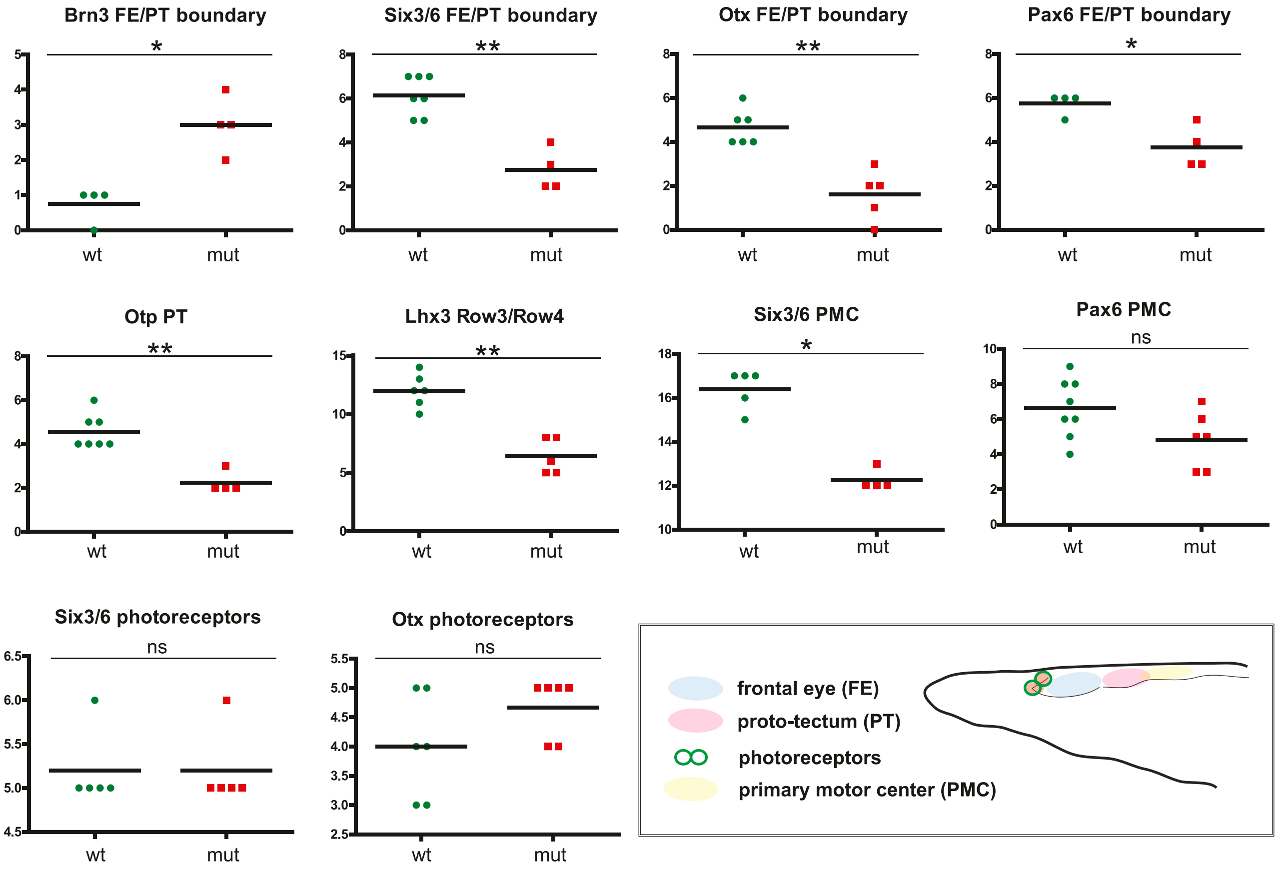

FIGURE 4
Difference in cell numbers between wild type and Pax6ΔQL mutant animals for the indicated regional markers. Mann-Whitney two tailed test was used for calculation of statistical significance. FE, frontal eye; PT, proto-tectum; PMC, primary motor center.

Row4 and at the boundary of the frontal eye with the proto-tectum (Figures 3B–bs2; Figure 4). Notably, there were no marked changes in the expression of Otp and Lhx1 in Row4 (Figures 3C–cs2; Figure 3D–ds2). However, both these genes, along with Brn3, were downregulated in the proto-tectum (Figures 3C–cs2; Figures 3D–Dd, Figures 3d–dd; Figure 4). Additionally, Brn3 and Lhx1 expression was slightly elevated at the boundary of the frontal eye with the proto-tectum (Figures 2C–Cs1' and 2c–cs1'; Figures 3D–ds2; Figure 4). Conversely, Pax6 and Otx expression was reduced in this area (Figures 3B–bs2; Figures 2B–Bs2 and 2b–bs2; Figure 4). Apart from Otp, several genes expressed in the primary motor center, including Lhx3, Brn3, and Six3/6, were downregulated (Figures 2A–as3; Figures 2C–cs2; Figures 3A–as2; Figure 4). In summary, our data suggest that the most significant changes due to the *Pax6* mutation occur in the posterior frontal eye, proto-tectum, and primary motor center (Figure 5A).

Discussion

Genotype-phenotype correlation and hypomorphic mutations

The relationship between genotype and phenotype is generally intricate and multi-dimensional. Developmental pathways, behavioral changes, genetic networks, and gene expression patterns all contribute to the final phenotypic outcomes, often in ways that are not linear or directly correlated (Huang, 2012). Homology, a central concept in evolutionary biology, further complicates this relationship as homologous traits can arise from different genetic and developmental contexts (Tautz, 1998; Wray and Abouheif, 1998). Previous work underscores the importance of considering both genetic and epigenetic factors, as well as the potential for phenotypic plasticity and evolutionary innovation, in understanding the genotype-phenotype correlation (Wagner and Zhang, 2011). Finally, the nature of a particular mutation adds another level of complexity to a genetic study. For example, hypomorphic mutations typically produce a protein that retains some activity but is less effective than the wild-type (normal) version (Wilkie, 1994; St Johnston, 2002). This reduced functionality can lead to milder phenotypic effects compared to null mutations, which completely eliminate gene function (McLean et al., 2011). Hypomorphs are often useful in studying gene function because they can reveal the consequences of decreasing, but not entirely eliminating, the activity of a particular gene (Spradling et al., 1999).

Functional assays performed by us strongly argue that Pax6ΔQL protein maintains partial activity, and so the allele of *Pax6* described here represents a hypomorphic mutation. We anticipate that the complete elimination of *Pax6* gene in amphioxus would result in a more severe phenotype, especially in patterning and differentiation

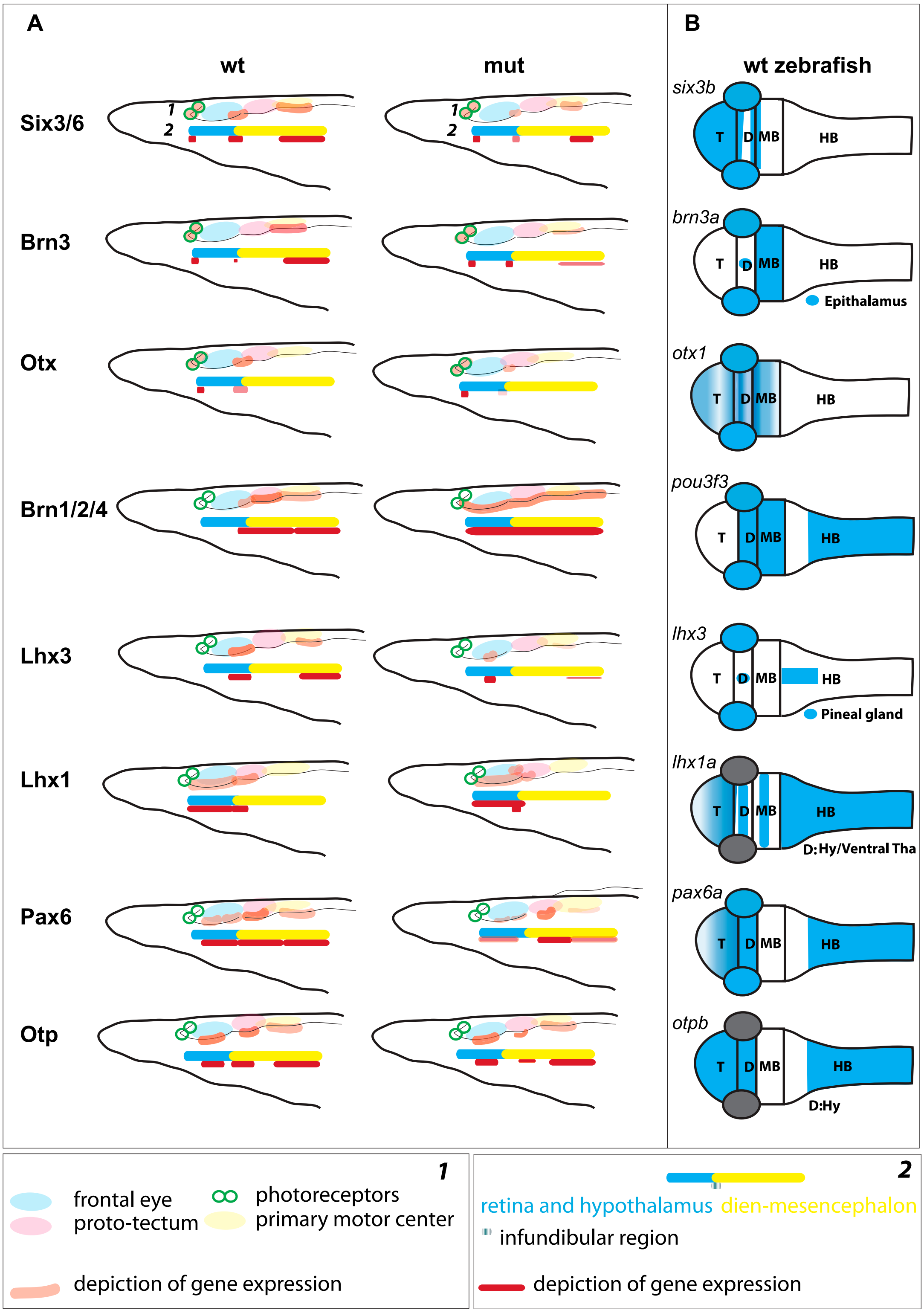

FIGURE 5
(A) Schematic illustration of gene expression in the anterior central nervous system of amphioxus, which is regionalized according to Pergner et al. (schematics ***1***) or Lacalli (schematics ***2***), for both wild type (**wt**) and Pax6ΔQL mutants (mut). **(B)** Schematic illustration of the orthologous gene expression (*six3b* (Kobayashi et al., 1998), *brn3a* (Halluin et al., 2016), *otx1* (Scholpp et al., 2007), *brn1/2/4* (*pou3f3*, http://zfin.org), *lhx3* (Glasgow et al., 1997), *lhx1a* (Swanhart et al., 2010), *pax6a* (Scholpp et al., 2007), *otpb* (Del Giacco et al., 2006)) in the wild type pharyngula stage zebrafish. T – telencephalon; D –Diencephalon; MB – Midbrain; HB – Hindbrain; Hy – Hypothalamus; Tha – Thalamus.

of the anterior neural tube. Since *Pax6* is crucial for the differentiation of neural progenitor cells (Gotz and Huttner, 2005) its absence might result in a failure of these progenitor cells to properly differentiate, leading to a reduction or absence of specific neural cell types. In addition, *Pax6* gene loss could lead to widespread defects in neural circuitry, affecting amphioxus sensory processing and motor functions. We found the hypomorphic *Pax6* mutation to be highly informative and somewhat advantageous. In fact, it is plausible that a severe, more pleiotropic phenotype resulting from a complete loss-of-function allele of *Pax6* would hinder the identification of the regional patterning defects described here.

Composite structure of the chordate brain

It has been argued that the central nervous system of chordates is intricately regionalized, characterized by a complex, gene-specific configuration of the rostral brain as defined by various studies (Holland, 2009; Vopalensky et al., 2012; Holland et al., 2013; Tosches and Arendt, 2013; Albuixech-Crespo et al., 2017; Pergner et al., 2020; Lacalli, 2022). At least two regions of the brain, the anterior and posterior, are recognized (Albuixech-Crespo et al., 2017; Holland, 2020; Lacalli, 2022). These regions are separated from each other by the junction that resembles *zona limitans intrathalamica* (ZLI), a feature molecularly defined in hemichordates and thought to correspond to the infundibular region located at the border between frontal eye and proto-tectum in amphioxus (Figure 5A) (Lacalli et al., 1994; Lacalli, 2022).

In four-day-old larvae of *Branchiostoma floridae*, we observed the presence of Six3/6 and Otx in putative photoreceptors, consistent with previous findings from two-day-old larvae of *B. floridae* (Vopalensky et al., 2012) and four-day-old larvae of *Branchiostoma lanceolatum* (Pergner et al., 2020). We did not detect Pax6 in the photoreceptors of our samples, consistent with similar observations in *B. lanceolatum* larvae (Pergner et al., 2020). However, this contrasts with the weak expression of Pax6 observed in photoreceptors of two-day-old larvae (Vopalensky et al., 2012), suggesting that the role for *Pax6* is limited to early photoreceptor development. In amphioxus *Pax6* mutants, the anterior frontal eye, including photoreceptors, appeared unaffected. No examinations of possible changes in the photoreceptors have been conducted in *Xenopus* and medaka *Pax6* knockouts (Nakayama et al., 2015; Pan K. et al., 2023; Pan J. et al., 2023). In *Xenopus Pax6* mutants, the retina is present but disorganized (Nakayama et al., 2015). In mice, retina-specific *Pax6* gene ablation disrupts normal differentiation program leading to the complete absence of all mature retina neurons (Klimova and Kozmik, 2014).

A somewhat unexpected finding of our study is the conspicuous expression of Brn3 in ciliary photoreceptors, an apparent divergence from the situation in vertebrate retinas where *Brn3* is typically absent from photoreceptors and is found in ganglion cells (Liu et al., 2000). A specialized subset of the vertebrate *Brn3*-positive retinal ganglion cells is intrinsically photosensitive due to the expression of the rhabdomeric type opsin (Opn4, melanopsin) (Berson et al., 2002; Hattar et al., 2002). The presence of Brn3 in amphioxus ciliary photoreceptors lends support to the hypothesis of a shared ancestral origin between photoreceptors and retina interneurons (Arendt, 2003; Arendt et al., 2016).

The notion of homologizing row 2, row 3, and row 4 of the amphioxus frontal eye with the interneuron organization of the vertebrate retina (Pergner et al., 2020) apparently warrants further investigation. The previously proposed homology appears less convincing due to the widespread presence of genes in these rows that are also found in other brain regions of vertebrates (Figure 5B). For example, we identified Otp expression in rows 3 and 4, the proto-tectum, and the primary motor center, a gene not typically expressed in the developing vertebrate eye but a marker of the vertebrate hypothalamus, crucial for neurosecretory cell differentiation (Wang and Lufkin, 2000; Fernandes et al., 2013). The presence of Otp expression in the frontal eye, which is believed to coincide with both the retina and hypothalamus, aligns with the brain regionalization scheme previously suggested (Albuixech-Crespo et al., 2017; Lacalli, 2022). Additionally, we discovered Pax6 expression in the proto-tectum, this contrasts with previous findings (Vopalensky et al., 2012; Pergner et al., 2020). In vertebrates, *Pax6* shows weak expression in the mesencephalon only during early neurula stages, ceasing at the diencephalon-mesencephalon border in later stages (Callaerts et al., 1997; Nakayama et al., 2015; Albuixech-Crespo et al., 2017; Pan K. et al., 2023; Pan J. et al., 2023). However, the expression of Otp in the proto-tectum and primary motor center complicates the comparison of this region, called dien-mesencephalon, with the pretectum, thalamus and mesencephalon in vertebrates.

In the border region between the posterior frontal eye and the anterior proto-tectum, which likely corresponds to the infundibular region, we observed elevated expression of Otx. In zebrafish, *Otx2* is expressed in the presumptive ZLI region at earlier stages and in the ZLI region at later stages, serving as one of the key factors in establishing this area (Scholpp et al., 2007). Contrary to the findings of Albuixech-Crespo et al. (2017), some researchers propose that the ZLI is present in the developing brain of amphioxus (Holland, 2020) and the infundibular region might represent this (Lacalli, 2022). Our findings lend support to this hypothesis. *Otx*, along with *Wnt8*, *FoxA*, *Hh*, and *Ptch* genes, is expressed in the ZLI-like region of hemichordates (Pani et al., 2012). We were interested in whether the expression of amphioxus *Otx* in the boundary between the posterior frontal eye and the anterior proto-tectum could be observed at earlier stages. We observed the expression of Otx and FoxA in this region at the tailbud neurula stage (Figure 6A a–f). Moreover, we detected elevated expression of *Ptch* specifically in this region (Figure 6A g–i). *Ptch* is a target gene which indicates where Hh signaling is active in amphioxus (Hu et al., 2017). These data suggest that Hh signaling operates in this region similarly to that in vertebrates and hemichordates. Our findings lend support to the hypothesis that a ZLI-like region is present in cephalochordate amphioxus (Figure 6B c).

Conserved role of *Pax6* in the brain regionalization

In our study, we examined amphioxus *Pax6* mutants exhibiting a significant decrease in protein activity (measured as transcriptional output), apparently due to impaired binding of the paired domain to

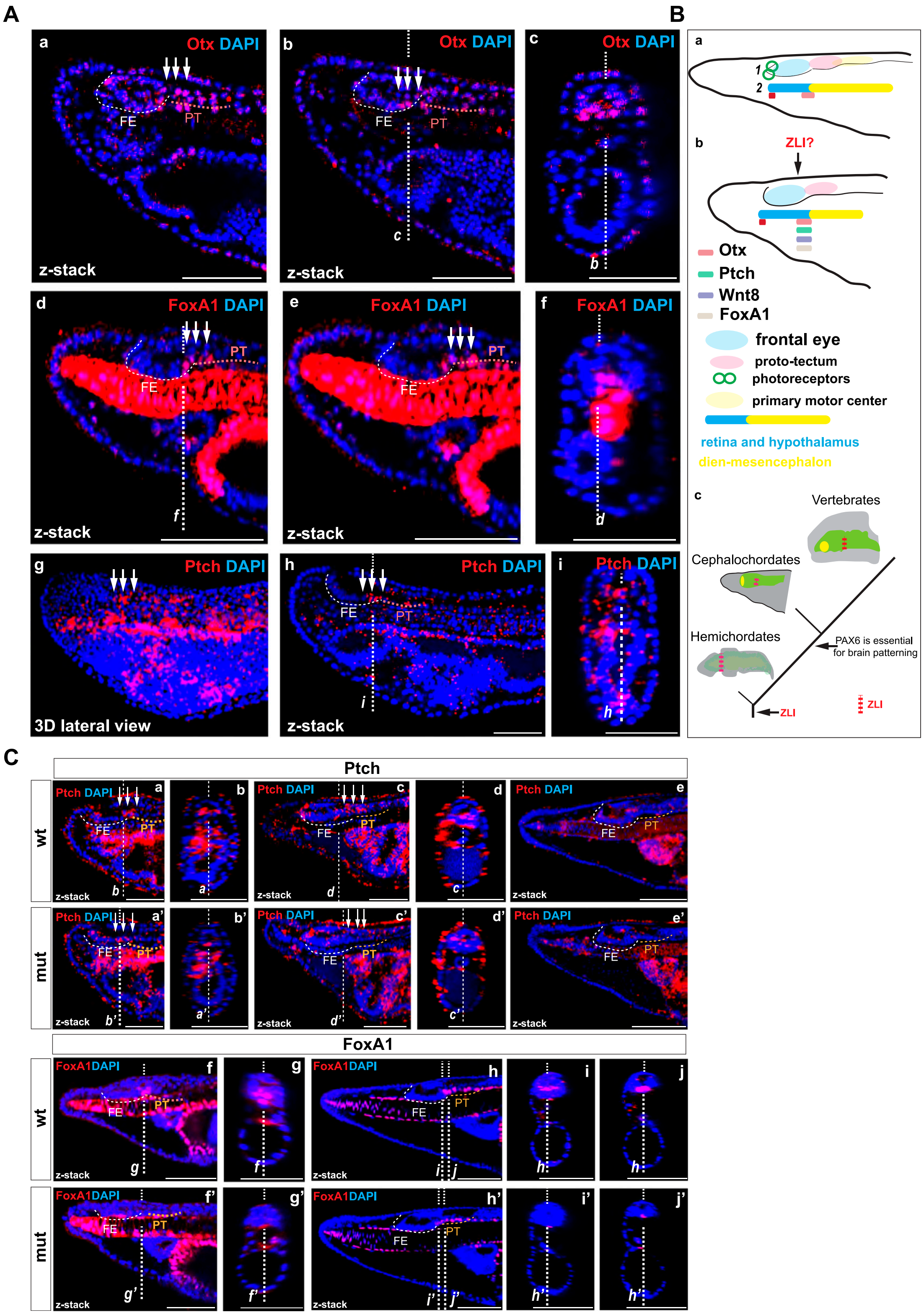

FIGURE 6
(A) The expression of Otx and FoxA1 proteins (a–c) and *Ptch* mRNA (d–e) in amphioxus tailbud neurula. The positions of individual z-slices (b–c, d, f, i–h) from complete zstacks are indicated with dashed lines (*c–b, f, d, i–h*). **(B)** Schematic illustration of gene expression in the anterior central nervous system of amphioxus, which is regionalized according to Pergner et al. (2020) (schematics ***1***) or Lacalli (schematics ***2***) for *Otx* at the amphioxus four-day-old larvae (a) and *Otx, Ptch, FoxA,* and *Wnt8* (Schubert et al., 2000; Somorjai et al., 2018) at the tailbud neurula (b). Proposed scenario of brain patterning in deuterostomes (c). **(C)** The expression of *Ptch* mRNA in the wild type and Pax6ΔQL mutant animals at the T0 (a–b and a'–b'), two-day-old larva (c–d and c'–d'), and four-day-old larva (e and e'). The expression of FoxA1 protein in the wild type and Pax6ΔQL mutant animals at the two-day-old larva (c–d and c'–d') and four-day-old larva (e and e').

its DNA recognition site. In the case of heterozygous *Pax6* mutant mice (*Sey*), which exhibit a noticeable phenotype (Hill et al., 1991), the concentration of functional Pax6 protein is reduced by half. Although not directly comparable, it can generally be stated that in both cases, the regulatory effect of Pax6 transcription factor on gene expression is partially impaired, though not completely abolished. The heterozygous mutation in mice leads to abnormal development of the central nervous system, affecting neuron growth and differentiation in the telencephalon, diencephalon, and metencephalon (Schmahl et al., 1993). In amphioxus mutants, we observed disorganization of gene expression patterns in various regions of the brain (Figure 5A).

In *Xenopus*, *Pax6* mutant embryos demonstrate changes in the expression of marker genes responsible for telencephalon regionalization, and similar effects have been demonstrated in mice (van Heyningen and Williamson, 2002; Carney et al., 2009). It is suggested that *Pax6* plays a crucial role in the regionalization of the telencephalon and diencephalon divisions (Grindley et al., 1997; Manuel and Price, 2005). In homozygote *Pax6* mutant mouse embryos, the molecular patterning of the diencephalic regions is compromised, affecting the boundary between the mesencephalon and pretectum, and ZLI (Mastick et al., 1997; M Caballero et al., 2014). The molecular markers of the mesencephalon expand into pretectum and the identity of the pretectum is partially shifted towards that of the mesencephalon (Mastick et al., 1997). Additionally, the expression markers of the thalamus are downregulated, and genes normally confined to the ZLI are ectopically expressed in the surrounding regions (Warren and Price, 1997; Pratt et al., 2000; M Caballero et al., 2014).

In amphioxus, we observed distinct changes in the expression of individual genes in the posterior frontal eye, proto-tectum and in the primary motor center (the presumed counterparts of the vertebrate diencephalon/eyes, pretectum, and mesencephalon). Most of the examined genes that were expressed in these territories either lost their expression or were significantly downregulated, with the exception of Brn1/2/4, which expanded into the anterior region of the frontal eye. Additionally, we observed molecular disorganization in the border region between the frontal eye and the proto-tectum, which is presumed to be the ZLI-like region in amphioxus.

Interestingly, the pattern of molecular changes was different from the changes observed in the proto-tectum and primary motor center. Notably, the expression of Otx, which is required for the formation of the ZLI in zebrafish and the ZLI-like region in hemichordates, was severely diminished in the border region between the frontal eye and the proto-tectum in Pax6ΔQL mutants at the four-day-larva stage. Furthermore, Lhx1 expression expanded into the dorsal domain at the anterior border of this region, while its expression was reduced in the proto-tectum. In vertebrates, *Lhx1* is expressed in the ZLI, ventral thalamus, and pretectum (Bachy et al., 2001). In *Pax6* mutant mice, its expression expands into the dorsal thalamus but is reduced in the pretectum (Pratt et al., 2000). Additionally, in *Pax6* mutant mice, the expression of *Shh* and *Ptch* is expanded in the regions around ZLI (M Caballero et al., 2014). In Pax6ΔQL mutants, the restricted elevated expression of *Ptch* disappears in the presumptive ZLI-like region at the T0 and two-day-old larva (Figure 6C a–d'). By the four-day-larva, we did not observe the expression in the border region between the frontal eye and the proto-tectum (Figure 6C e–e'). Furthermore, FoxA1, orthologous to FoxA expressed in the ZLI-like region of hemichordates (Pani et al., 2012), was severely diminished in the presumptive ZLI-like region of amphioxus Pax6ΔQL mutants at both the two-day-old and four-day-old larva stages (Figure 6C f–j'). Combined, these results further support our observation that the border between the frontal eye and the proto-tectum can be recognized as a distinct molecular entity and could thus be homologized to the vertebrate *zona limitans intrathalamica* (ZLI) (Holland, 2020; Lacalli, 2022).

In summary, our data suggest that the role of *Pax6* gene in the brain patterning is conserved in the chordate lineage and support the hypothesis of the evolutionary continuity of the ZLI-like region in deuterostomes (Figure 6B c).

Materials and methods

Amphioxus husbandry

Amphioxus husbandry followed previously published protocols (Carvalho et al., 2017; Yong et al., 2019; Kozmikova and Kozmik, 2020). In brief, *B. floridae* adults were housed in seawater at a temperature of 28°C and were fed with algae daily. To induce spawning, the animals were transferred to a temperature of 18°C for at least 6 weeks before being exposed to a heat shock induced by elevating the temperature to 28°C for 24 h. Following *in vitro* fertilization at room temperature the embryos were raised at a temperature of 25°C.

Oligonucleotides

Oligonucleotides used for the generation of sgRNA and expression constructs, site-directed mutagenesis, and genotyping are shown in Supplementary Table S1.

Genome editing

Oligonucleotides zk1770A/B used to make sgRNA constructs were cloned into BsaI site of pDR274 (Hwang et al., 2013) (pDR274 was a gift from Keith Joung, Addgene plasmid # 42250). Cas9 mRNA was prepared using mMESSAGE mMACHINE T7 ULTRA Kit (Ambion) using plasmid pCS2-nCas9n (Jao et al., 2013) (pCS2-nCas9n was a gift from Wenbiao Chen, Addgene plasmid # 47929). The sgRNAs were transcribed using MEGAshortscript kit (Ambion). A mixture of Cas9 mRNA (100 ng/μL) and sgRNA (25 ng/μL) was injected into amphioxus eggs, eggs were fertilized, and the developing F0 embryos maintained at 25°C. The adult mature F0 animals were crossed with wild-type animals and the F1 progeny was assayed for mutations by DNA sequencing. Genetic crosses with Pax6ΔQL F1 heterozygotes were used to establish mutant line. Embryos of F2 or F3 generations were used for gene expression analysis. Amphioxus embryos were genotyped using primers zk2059/zk1989QL2/zk614 to distinguish wild type, heterozygotes, and homozygotes, respectively.

Reporter gene assays and Western blotting

Site-directed mutagenesis of *B. floridae* Pax6 cDNA cloned in pKW mammalian expression vector was performed by the QuickChange kit (Stratagene) using primers zk 2027A/zk 2027B to generate Pax6ΔQL. The cell culture and transient cell transfection was performed as previously described (Klimova et al., 2015). Expression vectors encoding either wild type Pax6 or mutant Pax6ΔQL were co-transfected with Pax6-resposive reporter gene [-350GluLuc (Schwaninger et al., 1993)] and the β-galactosidase expression plasmid serving to normalize the transfection efficiency. Graph and statistical analysis of triplicate biological assays were generated in GraphPad Prism software. Western blotting was performed as previously described (Vopalensky et al., 2012).

In situ hybridization of amphioxus embryos

In situ hybridization followed the protocols described previously (Kozmikova et al., 2013). After being fixed overnight at 4°C with 4% PFA/MOPS solution [0.1M 3-(N-morpholino) propanesulfonic acid, 2 mM MgSO4, 1 mM EGTA, 0.5M NaCl, pH 7.5], the embryos were transferred to 70% ethanol with DEPC-treated water and stored at −20°C. To generate construct for *Ptch in situ* hybridization probe primers zk 1979C/D were used.

The color development was achieved through incubation in Vector blue solution from Vector Laboratories. Images of the embryos were captured using confocal microscopy. The embryos were mounted in glycerol on glass depression slides. Z-stack imaging was conducted using a Leica SP8 confocal microscopes, and analysed with FIJI image analysis software.

Immunohistochemistry of amphioxus embryos

Antibodies recognizing Pax6, Six3/6, Otx, Brn1/2/4, Brn3, FoxA, Lhx1, and Lhx3 were previously used (Vopalensky et al., 2012; Bozzo et al., 2017; Pergner et al., 2020). Antibody recognizing amphioxus Otp was prepared as described in Bozzo et al. (2017). To generate construct for over-expression of Otp protein fragment primers zk1361A/B were used. Embryos for immunohistochemistry were fixed and processed as described in detail before (Pergner et al., 2020). The embryos were imaged with Leica SP8 confocal microscope and processed with Fiji ImageJ analysis software. Cells positive for individual markers were counted in wild type and Pax6 mutant embryos. GraphPad Prism software was used to generate individual graphs and analyze statistical significance using Mann-Whitney two tailed test.

Data availability statement

The original contributions presented in the study are included in the article/Supplementary Material, further inquiries can be directed to the corresponding author.

Ethics statement

The manuscript presents research on animals that do not require ethical approval for their study.

Author contributions

ZK: Writing–review and editing, Conceptualization, Data curation, Formal Analysis, Funding acquisition, Investigation, Methodology, Resources, Validation, Visualization. IK: Writing–original draft, Writing–review and editing, Conceptualization, Data curation, Formal Analysis, Investigation, Methodology, Validation, Visualization.

Funding

The author(s) declare that financial support was received for the research, authorship, and/or publication of this article. This work was supported by Czechia Science Foundation grant 20-25377S awarded to ZK.

Acknowledgments

We thank Gaspar Jekely for the constructive criticism of an earlier version of the manuscript, Halyna Klymets for technical assistance, Anna Zitova and Veronika Noskova for animal husbandry, Walter Knepel for −350GluLuc, Keith Joung for pDR274 (Addgene plasmid # 42250), and Wenbiao Chen for pCS2-nCas9n (Addgene plasmid # 47929). We acknowledge the Light Microscopy Core Facility, IMG CAS, Prague, Czechia Republic, supported by MEYS (LM2018129, CZ.02.1.01/0.0/0.0/18_046/0016045) and RVO: 68378050-KAV-NPUI, for their support with the microscopy presented herein.

Conflict of interest

The authors declare that the research was conducted in the absence of any commercial or financial relationships that could be construed as a potential conflict of interest.

Publisher's note

Supplementary material

The Supplementary Material for this article can be found online at: https://www.frontiersin.org/articles/10.3389/fcell.2024.1431337/full#supplementary-material

References

Albuixech-Crespo, B., López-Blanch, L., Burguera, D., Maeso, I., Sánchez-Arrones, L., Moreno-Bravo, J. A., et al. (2017). Molecular regionalization of the developing amphioxus neural tube challenges major partitions of the vertebrate brain. *PLoS Biol.* 15 (4), e2001573. doi:10.1371/journal.pbio.2001573

Arendt, D. (2003). Evolution of eyes and photoreceptor cell types. *Int. J. Dev. Biol.* 47 (7-8), 563–571.

Arendt, D., Musser, J. M., Baker, C. V. H., Bergman, A., Cepko, C., Erwin, D. H., et al. (2016). The origin and evolution of cell types. *Nat. Rev. Genet.* 17 (12), 744–757. doi:10.1038/nrg.2016.127

Bachy, I., Vernier, P., and Retaux, S. (2001). The LIM-homeodomain gene family in the developing Xenopus brain: conservation and divergences with the mouse related to the evolution of the forebrain. *J. Neurosci.* 21 (19), 7620–7629. doi:10.1523/JNEUROSCI.21-19-07620.2001

Berson, D. M., Dunn, F. A., and Takao, M. (2002). Phototransduction by retinal ganglion cells that set the circadian clock. *Science* 295 (5557), 1070–1073. doi:10.1126/science.1067262

Bopp, D., Burri, M., Baumgartner, S., Frigerio, G., and Noll, M. (1986). Conservation of a large protein domain in the segmentation gene paired and in functionally related genes of Drosophila. *Cell.* 47 (6), 1033–1040. doi:10.1016/0092-8674(86)90818-4

Bozzo, M., Pergner, J., Kozmik, Z., and Kozmikova, I. (2017). Novel polyclonal antibodies as a useful tool for expression studies in amphioxus embryos. *Int. J. Dev. Biol.* 61 (10-11-12), 793–800. doi:10.1387/ijdb.170259ik

Callaerts, P., Halder, G., and Gehring, W. (1997). PAX6 in development and evolution. *Annu. Rev. Neurosci.* 20, 483–532. doi:10.1146/annurev.neuro.20.1.483

Carney, R. S., Cocas, L. A., Hirata, T., Mansfield, K., and Corbin, J. G. (2009). Differential regulation of telencephalic pallial-subpallial boundary patterning by Pax6 and Gsh2. *Cereb. Cortex* 19 (4), 745–759. doi:10.1093/cercor/bhn123

Carriere, C., Plaza, S., Martin, P., Quatannens, B., Bailly, M., Stehelin, D., et al. (1993). Characterization of quail Pax-6 (Pax-QNR) proteins expressed in the neuroretina. *Mol. Cell. Biol.* 13 (12), 7257–7266. doi:10.1128/mcb.13.12.7257

Carvalho, J. E., Lahaye, F., and Schubert, M. (2017). Keeping amphioxus in the laboratory: an update on available husbandry methods. *Int. J. Dev. Biol.* 61 (10-11-12), 773–783. doi:10.1387/ijdb.170192ms

Cvekl, A., and Callaerts, P. (2017). PAX6: 25th anniversary and more to learn. *Exp. Eye Res.* 156, 10–21. doi:10.1016/j.exer.2016.04.017

Czerny, T., Halder, G., Kloter, U., Souabni, A., Gehring, W. J., and Busslinger, M. (1999). Twin of eyeless, a second Pax-6 gene of Drosophila, acts upstream of eyeless in the control of eye development. *Mol. Cell.* 3 (3), 297–307. doi:10.1016/s1097-2765(00)80457-8

Del Giacco, L., Sordino, P., Pistocchi, A., Andreakis, N., Tarallo, R., Di Benedetto, B., et al. (2006). Differential regulation of the zebrafish orthopedia1 gene during fate determination of diencephalic neurons. *BMC Dev. Biol.* 6 (1), 50. doi:10.1186/1471-213X-6-50

Fernandes, A. M., Beddows, E., Filippi, A., and Driever, W. (2013). Orthopedia transcription factor otpa and otpb paralogous genes function during dopaminergic and neuroendocrine cell specification in larval zebrafish. *PLoS One* 8 (9), e75002. doi:10.1371/journal.pone.0075002

Gehring, W. J., and Ikeo, K. (1999). Pax 6: mastering eye morphogenesis and eye evolution. *Trends Genet.* 15 (9), 371–377. doi:10.1016/s0168-9525(99)01776-x

Glardon, S., Holland, L. Z., Gehring, W. J., and Holland, N. D. (1998). Isolation and developmental expression of the amphioxus Pax-6 gene (AmphiPax-6): insights into eye and photoreceptor evolution. *Development* 125 (14), 2701–2710. doi:10.1242/dev.125.14.2701

Glasgow, E., Karavanov, A. A., and Dawid, I. B. (1997). Neuronal and neuroendocrine expression oflim3,a LIM class homeobox gene, is altered in mutant zebrafish with axial signaling defects. *Dev. Biol.* 192 (2), 405–419. doi:10.1006/dbio.1997.8761

Gotz, M., and Huttner, W. B. (2005). The cell biology of neurogenesis. *Nat. Rev. Mol. Cell. Biol.* 6 (10), 777–788. doi:10.1038/nrm1739

Goulding, M. D., Lumsden, A., and Gruss, P. (1993). Signals from the notochord and floor plate regulate the region-specific expression of two Pax genes in the developing spinal cord. *Development* 117 (3), 1001–1016. doi:10.1242/dev.117.3.1001

Grindley, J. C., Davidson, D. R., and Hill, R. E. (1995). The role of Pax-6 in eye and nasal development. *Development* 121 (5), 1433–1442. doi:10.1242/dev.121.5.1433

Grindley, J. C., Hargett, L. K., Hill, R. E., Ross, A., and Hogan, B. L. M. (1997). Disruption of PAX6 function in mice homozygous for the Pax6Sey-1Neu mutation produces abnormalities in the early development and regionalization of the diencephalon. *Mech. Dev.* 64 (1), 111–126. doi:10.1016/S0925-4773(97)00055-5

Halluin, C., Madelaine, R., Naye, F., Peers, B., Roussigné, M., and Blader, P. (2016). Habenular neurogenesis in zebrafish is regulated by a hedgehog, Pax6 proneural gene cascade. *PLoS One* 11 (7), e0158210. doi:10.1371/journal.pone.0158210

Hattar, S., Liao, H. W., Takao, M., Berson, D. M., and Yau, K. W. (2002). Melanopsin-containing retinal ganglion cells: architecture, projections, and intrinsic photosensitivity. *Science* 295 (5557), 1065–1070. doi:10.1126/science.1069609

Haubst, N., Berger, J., Radjendirane, V., Graw, J., Favor, J., Saunders, G. F., et al. (2004). Molecular dissection of Pax6 function: the specific roles of the paired domain and homeodomain in brain development. *Development* 131 (24), 6131–6140. doi:10.1242/dev.01524

Hill, R. E., Favor, J., Hogan, B. L., Ton, C. C., Saunders, G. F., Hanson, I. M., et al. (1991). Mouse small eye results from mutations in a paired-like homeobox-containing gene. *Nature* 354 (6354), 522–525. doi:10.1038/354522a0

Hirsch, N., and Harris, W. A. (1997). Xenopus Pax-6 and retinal development. *J. Neurobiol.* 32 (1), 45–61. doi:10.1002/(sici)1097-4695(199701)32:1<45::aid-neu5>3.0.co;2-e

Hogan, B. L., Hirst, E. M., Horsburgh, G., and Hetherington, C. M. (1988). Small eye (Sey): a mouse model for the genetic analysis of craniofacial abnormalities. *Development* 103 (Suppl. l), 115–119. doi:10.1242/dev.103.Supplement.115

Hogan, B. L., Horsburgh, G., Cohen, J., Hetherington, C. M., Fisher, G., and Lyon, M. F. (1986). Small eyes (Sey): a homozygous lethal mutation on chromosome 2 which affects the differentiation of both lens and nasal placodes in the mouse. *J. Embryol. Exp. Morphol.* 97, 95–110. doi:10.1242/dev.97.1.95

Holland, L. Z. (2009). Chordate roots of the vertebrate nervous system: expanding the molecular toolkit. *Nat. Rev. Neurosci.* 10 (10), 736–746. doi:10.1038/nrn2703

Holland, L. Z. (2020). “"chapter 4 - invertebrate origins of vertebrate nervous systems,” in *Evolutionary neuroscience*. Editor J. H. Kaas (London: Academic Press), 51–73.

Holland, L. Z., Carvalho, J. E., Escriva, H., Laudet, V., Schubert, M., Shimeld, S. M., et al. (2013). Evolution of bilaterian central nervous systems: a single origin? *Evodevo* 4 (1), 27. doi:10.1186/2041-9139-4-27

Hu, G., Li, G., Wang, H., and Wang, Y. (2017). Hedgehog participates in the establishment of left-right asymmetry during amphioxus development by controlling Cerberus expression. *Development* 144 (24), 4694–4703. doi:10.1242/dev.157172

Huang, S. (2012). The molecular and mathematical basis of Waddington’s epigenetic landscape: a framework for post-Darwinian biology? *Bioessays* 34 (2), 149–157. doi:10.1002/bies.201100031

Hwang, W. Y., Fu, Y., Reyon, D., Maeder, M. L., Tsai, S. Q., Sander, J. D., et al. (2013). Efficient genome editing in zebrafish using a CRISPR-Cas system. *Nat. Biotechnol.* 31 (3), 227–229. doi:10.1038/nbt.2501

Jao, L. E., Wente, S. R., and Chen, W. (2013). Efficient multiplex biallelic zebrafish genome editing using a CRISPR nuclease system. *Proc. Natl. Acad. Sci. U. S. A.* 110 (34), 13904–13909. doi:10.1073/pnas.1308335110

Klimova, L., Antosova, B., Kuzelova, A., Strnad, H., and Kozmik, Z. (2015). Onecut1 and Onecut2 transcription factors operate downstream of Pax6 to regulate horizontal cell development. *Dev. Biol.* 402 (1), 48–60. doi:10.1016/j.ydbio.2015.02.023

Klimova, L., and Kozmik, Z. (2014). Stage-dependent requirement of neuroretinal Pax6 for lens and retina development. *Development* 141 (6), 1292–1302. doi:10.1242/dev.098822

Kobayashi, M., Toyama, R., Takeda, H., Dawid, I. B., and Kawakami, K. (1998). Overexpression of the forebrain-specific homeobox gene six3 induces rostral forebrain enlargement in zebrafish. *Development* 125 (15), 2973–2982. doi:10.1242/dev.125.15.2973

Kozmik, Z. (2005). Pax genes in eye development and evolution. *Curr. Opin. Genet. Dev.* 15 (4), 430–438. doi:10.1016/j.gde.2005.05.001

Kozmik, Z., Daube, M., Frei, E., Norman, B., Kos, L., Dishaw, L. J., et al. (2003). Role of Pax genes in eye evolution: a cnidarian PaxB gene uniting Pax2 and Pax6 functions. *Dev. Cell.* 5 (5), 773–785. doi:10.1016/s1534-5807(03)00325-3

Kozmikova, I., Candiani, S., Fabian, P., Gurska, D., and Kozmik, Z. (2013). Essential role of Bmp signaling and its positive feedback loop in the early cell fate evolution of chordates. *Dev. Biol.* 382 (2), 538–554. doi:10.1016/j.ydbio.2013.07.021

Kozmikova, I., and Kozmik, Z. (2020). Wnt/β-catenin signaling is an evolutionarily conserved determinant of chordate dorsal organizer. *Elife* 9, e56817. doi:10.7554/eLife.56817

Lacalli, T. (2022). An evolutionary perspective on chordate brain organization and function: insights from amphioxus, and the problem of sentience. *Philos. Trans. R. Soc. Lond B Biol. Sci.* 377 (1844), 20200520. doi:10.1098/rstb.2020.0520

Lacalli, T. C., Holland, N., and West, J. (1994). Landmarks in the anterior central nervous system of amphioxus larvae. *Philosophical Trans. R. Soc. Lond. Ser. B Biol. Sci.* 344 (1308), 165–185. doi:10.1098/rstb.1994.0059

Liu, W., Khare, S. L., Liang, X., Peters, M. A., Liu, X., Cepko, C. L., et al. (2000). All Brn3 genes can promote retinal ganglion cell differentiation in the chick. *Development* 127 (15), 3237–3247. doi:10.1242/dev.127.15.3237

Manuel, M., and Price, D. J. (2005). Role of Pax6 in forebrain regionalization. *Brain Res. Bull.* 66 (4), 387–393. doi:10.1016/j.brainresbull.2005.02.006

Mastick, G. S., Davis, N. M., Andrews, G. L., and Easter Jr, S. S. (1997). Pax-6 functions in boundary formation and axon guidance in the embryonic mouse forebrain. *Development* 124 (10), 1985–1997. doi:10.1242/dev.124.10.1985

Matsunaga, E., Araki, I., and Nakamura, H. (2000). Pax6 defines the di-mesencephalic boundary by repressing En1 and Pax2. *Development* 127 (11), 2357–2365. doi:10.1242/dev.127.11.2357

M Caballero, I., Manuel, M., Molinek, M., Quintana-Urzainqui, I., Mi, D., Shimogori, T., et al. (2014). Cell-autonomous repression of Shh by transcription factor Pax6 regulates diencephalic patterning by controlling the central diencephalic organizer. *Cell. Rep.* 8, 1405–1418. doi:10.1016/j.celrep.2014.07.051

McLean, C. Y., Reno, P. L., Pollen, A. A., Bassan, A. I., Capellini, T. D., Guenther, C., et al. (2011). Human-specific loss of regulatory DNA and the evolution of human-specific traits. *Nature* 471 (7337), 216–219. doi:10.1038/nature09774

Nakayama, T., Fisher, M., Nakajima, K., Odeleye, A. O., Zimmerman, K. B., Fish, M. B., et al. (2015). Xenopus pax6 mutants affect eye development and other organ systems, and have phenotypic similarities to human aniridia patients. *Dev. Biol.* 408 (2), 328–344. doi:10.1016/j.ydbio.2015.02.012

Pan, Q., Lu, K., Luo, J., Jiang, Y., Xia, B., Chen, L., et al. (2023a). Japanese medaka Olpax6.1 mutant as a potential model for spondylo-ocular syndrome. *Funct. Integr. Genomics* 23 (2), 168. doi:10.1007/s10142-023-01090-4

Pan, Q., Luo, J., Jiang, Y., Wang, Z., Lu, K., and Chen, T. (2023b). Medaka (*Oryzias latipes*) Olpax6.2 acquires maternal inheritance and germ cells expression, but functionally degenerate in the eye. *Gene* 872, 147439. doi:10.1016/j.gene.2023.147439

Pani, A. M., Mullarkey, E. E., Aronowicz, J., Assimacopoulos, S., Grove, E. A., and Lowe, C. J. (2012). Ancient deuterostome origins of vertebrate brain signalling centres. *Nature* 483 (7389), 289–294. doi:10.1038/nature10838

Pergner, J., and Kozmik, Z. (2017). Amphioxus photoreceptors - insights into the evolution of vertebrate opsins, vision and circadian rhythmicity. *Int. J. Dev. Biol.* 61 (10-11-12), 665–681. doi:10.1387/ijdb.170230zk

Pergner, J., Vavrova, A., Kozmikova, I., and Kozmik, Z. (2020). Molecular fingerprint of amphioxus frontal eye illuminates the evolution of homologous cell types in the chordate retina. *Front. Cell. Dev. Biol.* 8, 705. doi:10.3389/fcell.2020.00705

Pratt, T., Vitalis, T., Warren, N., Edgar, J. M., Mason, J. O., and Price, D. J. (2000). A role for Pax6 in the normal development of dorsal thalamus and its cortical connections. *Development* 127 (23), 5167–5178. doi:10.1242/dev.127.23.5167

Quiring, R., Walldorf, U., Kloter, U., and Gehring, W. J. (1994). Homology of the eyeless gene of Drosophila to the Small eye gene in mice and Aniridia in humans. *Science* 265 (5173), 785–789. doi:10.1126/science.7914031

Schmahl, W., Knoedlseder, M., Favor, J., and Davidson, D. (1993). Defects of neuronal migration and the pathogenesis of cortical malformations are associated with Small eye (Sey) in the mouse, a point mutation at the Pax-6-locus. *Acta Neuropathol.* 86 (2), 126–135. doi:10.1007/bf00334879

Scholpp, S., Foucher, I., Staudt, N., Peukert, D., Lumsden, A., and Houart, C. (2007). Otx1l, Otx2 and Irx1b establish and position the ZLI in the diencephalon. *Development* 134 (17), 3167–3176. doi:10.1242/dev.001461

Schubert, M., Holland, L. Z., Panopoulou, G. D., Lehrach, H., and Holland, N. D. (2000). Characterization of amphioxus AmphiWnt8: insights into the evolution of patterning of the embryonic dorsoventral axis. *Evol. Dev.* 2 (2), 85–92. doi:10.1046/j.1525-142x.2000.00047.x

Schwaninger, M., Blume, R., Oetjen, E., Lux, G., and Knepel, W. (1993). Inhibition of cAMP-responsive element-mediated gene transcription by cyclosporin A and FK506 after membrane depolarization. *J. Biol. Chem.* 268 (31), 23111–23115. doi:10.1016/s0021-9258(19)49433-7

Simpson, T. I., and Price, D. J. (2002). Pax6; a pleiotropic player in development. *Bioessays* 24 (11), 1041–1051. doi:10.1002/bies.10174

Somorjai, I. M. L., Marti-Solans, J., Diaz-Gracia, M., Nishida, H., Imai, K. S., Escriva, H., et al. (2018). Wnt evolution and function shuffling in liberal and conservative chordate genomes. *Genome Biol.* 19 (1), 98. doi:10.1186/s13059-018-1468-3

Spradling, A. C., Stern, D., Beaton, A., Rhem, E. J., Laverty, T., Mozden, N., et al. (1999). The Berkeley Drosophila Genome Project gene disruption project: single P-element insertions mutating 25% of vital Drosophila genes. *Genetics* 153 (1), 135–177. doi:10.1093/genetics/153.1.135

St Johnston, D. (2002). The art and design of genetic screens: *Drosophila melanogaster*. *Nat. Rev. Genet.* 3 (3), 176–188. doi:10.1038/nrg751

Stoykova, A., Gotz, M., Gruss, P., and Price, J. (1997). Pax6-dependent regulation of adhesive patterning, R-cadherin expression and boundary formation in developing forebrain. *Development* 124 (19), 3765–3777. doi:10.1242/dev.124.19.3765

Su, L., Shi, C., Huang, X., Wang, Y., and Li, G. (2020). Application of CRISPR/Cas9 nuclease in amphioxus genome editing. *Genes. (Basel)* 11 (11), 1311. doi:10.3390/genes11111311

Swanhart, L., Takahashi, N., Jackson, R., Gibson, G., Watkins, S., Dawid, I., et al. (2010). Characterization of an *lhx1a* transgenic reporter in zebrafish. *Int. J. Dev. Biol.* 54 (4), 731–736. doi:10.1387/ijdb.092969ls

Tautz, D. (1998). Evolutionary biology. Debatable homologies. *Nature* 395 (6697), 17, 19–19. doi:10.1038/25604

Tosches, M. A., and Arendt, D. (2013). The bilaterian forebrain: an evolutionary chimaera. *Curr. Opin. Neurobiol.* 23 (6), 1080–1089. doi:10.1016/j.conb.2013.09.005

van Heyningen, V., and Williamson, K. A. (2002). PAX6 in sensory development. *Hum. Mol. Genet.* 11 (10), 1161–1167. doi:10.1093/hmg/11.10.1161

von Salvini-Plawen, L., and Mayr, E. (1977). *On the evolution of photorecptors and eyes.* USA: Plenum Press.

Vopalensky, P., Pergner, J., Liegertova, M., Benito-Gutierrez, E., Arendt, D., and Kozmik, Z. (2012). Molecular analysis of the amphioxus frontal eye unravels the evolutionary origin of the retina and pigment cells of the vertebrate eye. *Proc. Natl. Acad. Sci. U. S. A.* 109 (38), 15383–15388. doi:10.1073/pnas.1207580109

Wagner, G. P., and Zhang, J. (2011). The pleiotropic structure of the genotype-phenotype map: the evolvability of complex organisms. *Nat. Rev. Genet.* 12 (3), 204–213. doi:10.1038/nrg2949

Walther, C., and Gruss, P. (1991). Pax-6, a murine paired box gene, is expressed in the developing CNS. *Development* 113 (4), 1435–1449. doi:10.1242/dev.113.4.1435

Wang, W., and Lufkin, T. (2000). The murine Otp homeobox gene plays an essential role in the specification of neuronal cell lineages in the developing hypothalamus. *Dev. Biol.* 227 (2), 432–449. doi:10.1006/dbio.2000.9902

Warren, N., and Price, D. J. (1997). Roles of Pax-6 in murine diencephalic development. *Development* 124 (8), 1573–1582. doi:10.1242/dev.124.8.1573

Wilkie, A. O. (1994). The molecular basis of genetic dominance. *J. Med. Genet.* 31 (2), 89–98. doi:10.1136/jmg.31.2.89

Wray, G. A., and Abouheif, E. (1998). When is homology not homology? *Curr. Opin. Genet. Dev.* 8 (6), 675–680. doi:10.1016/s0959-437x(98)80036-1

Xu, H. E., Rould, M. A., Xu, W., Epstein, J. A., Maas, R. L., and Pabo, C. O. (1999). Crystal structure of the human Pax6 paired domain-DNA complex reveals specific roles for the linker region and carboxy-terminal subdomain in DNA binding. *Genes. Dev.* 13 (10), 1263–1275. doi:10.1101/gad.13.10.1263

Yong, L. W., Kozmikova, I., and Yu, J. K. (2019). Using amphioxus as a basal chordate model to study BMP signaling pathway. *Methods Mol. Biol.* 1891, 91–114. doi:10.1007/978-1-4939-8904-1_8

frontiers | Frontiers in Cell and Developmental Biology

TYPE Original Research
PUBLISHED 09 October 2024
DOI 10.3389/fcell.2024.1434168

OPEN ACCESS

EDITED BY
Donald T. Fox,
Duke University, United States

REVIEWED BY
Carlos Andres Oliva,
Pontificia Universidad Católica de Chile, Chile
Paul Marshall,
Australian National University, Australia

*CORRESPONDENCE
Thomas Raabe,
✉ thomas.raabe@uni-wuerzburg.de

RECEIVED 17 May 2024
ACCEPTED 26 September 2024
PUBLISHED 09 October 2024

CITATION
Barthel L, Pettemeridi S, Nebras A, Schnaidt H, Fahland K, Vormwald L and Raabe T (2024) The transcription elongation factors Spt4 and Spt5 control neural progenitor proliferation and are implicated in neuronal remodeling during *Drosophila* mushroom body development. *Front. Cell Dev. Biol.* 12:1434168. doi: 10.3389/fcell.2024.1434168

The transcription elongation factors Spt4 and Spt5 control neural progenitor proliferation and are implicated in neuronal remodeling during *Drosophila* mushroom body development

Lea Barthel, Stefani Pettemeridi, Ali Nebras, Hayley Schnaidt, Karoline Fahland, Lea Vormwald and Thomas Raabe*

Department Molecular Genetics of the Faculty of Medicine, Biocenter, University of Würzburg, Würzburg, Germany

Spt4 and Spt5 form the DRB sensitivity inducing factor (DSIF) complex that regulates transcription elongation at multiple steps including promotor-proximal pausing, processivity and termination. Although this implicated a general role in transcription, several studies pointed to smaller sets of target genes and indicated a more specific requirement in certain cellular contexts. To unravel common or distinct functions of Spt4 and Spt5 *in vivo*, we generated knock-out alleles for both genes in *Drosophila melanogaster*. Using the development of the mushroom bodies as a model, we provided evidence for two common functions of Spt4 and Spt5 during mushroom body development, namely control of cell proliferation of neural progenitor cells and remodeling of axonal projections of certain mushroom body neurons. This latter function is not due to a general requirement of Spt4 and Spt5 for axon pathfinding of mushroom body neurons, but due to distinct effects on the expression of genes controlling remodeling.

KEYWORDS

***Drosophila*, DSIF complex, mushroom bodies, neuroblast, neuronal remodeling**

Introduction

Transcription by RNA Polymerase II (Pol II) is a multi-step process that involves the assembly of distinct protein complexes to control transcription initiation, pausing, elongation, and termination. One of these transcription-regulating factors is Spt5. It was initially identified in *Saccharomyces cerevisiae* in a genetic screen as a mutation that suppresses the phenotype of a Ty insertion mutation in the 5′ noncoding region of the HIS4 gene (Winston et al., 1984). Spt5 proteins (NusG in bacteria) are found in all three domains of life and share a single N-terminal NusG (NGN) and at least one KOW domain, with eukaryotic Spt5 proteins containing up to seven KOW domains (KOW1-7), a N-terminal acidic region and a C-terminal repeat region (CTR). Except for bacteria, Spt5 dimerizes through its NGN domain with the zinc-finger protein Spt4 to form a complex called DRB sensitivity-inducing factor (DSIF). DSIF fulfills multiple functions during transcription. It stabilizes Pol II and promotes promotor-proximal pausing of Pol II.

Pol II together with Spt4 and the Spt5 NGN and KOW1 domains form the DNA exit tunnel. The RNA exit site is formed by Pol II and Spt5 KOW4 and 5 domains. The paused state is stabilized by Negative Elongation Factor (NELF), which contacts Spt4 and the Spt5 NGN domain at the DNA exit tunnel and also extends to Spt5 KOW 1–4 (Decker, 2021; Dollinger and Gilmour, 2021; Song and Chen, 2022). The structural and biochemical data were complemented by structure-function analyses in *Drosophila* showing that transgenes with deletion or mutations in KOW1, 4, 5 or the NGN domain failed to complement loss of endogenous Spt5 function (Qiu and Gilmour, 2017; Dollinger et al., 2023). One major regulatory mechanism for release of paused Pol II and transcription elongation is phosphorylation of NELF, Pol II and Spt5, which results in phase transition of Spt5 and Pol II from pausing clusters into liquid-like elongation droplets (Guo et al., 2023). This is accompanied by conformational changes of the KOW domains contacting DNA and RNA. Spt4 and Spt5 interact with elongation factors to increase processivity of transcription and promote elongation through nucleosomes. Through less clarified mechanisms, Spt5/DSIF are also involved in Pol II transcription termination. In addition to their function in Pol II transcription, Spt4 and Spt5 interact with RNA polymerase I for ribosomal RNA synthesis (Decker, 2021; Song and Chen, 2022).

Whereas the molecular properties of DISF are well studied, its role in the context of cell type specific functions during development or disease processes in multicellular organisms is less clear. Although mainly considered as a general transcriptional regulator, there are examples of more gene specific functions. Decreasing expression of Spt4 or its interaction with Spt5 selectively lowers the transcription of genes with long tri-or hexanucleotide repeats associated with Huntington disease (Htt, (Liu et al., 2012; Cheng et al., 2015; Deng et al., 2022)), amyotrophic lateral sclerosis/frontotemporal dementia (C9orf72, (Kramer et al., 2016)) and spinocerebellar atrophy type 36 (Nop56, (Furuta et al., 2019)).

Mimicking the effects of Spt5 knock-down with small-molecule inhibitors identified target genes that responded with diverse kinetics and uncovered Spt5 regulatory roles in metabolism and processing of histone genes (Bahat et al., 2019). In zebrafish, complete loss of Spt5 had far-reaching effects on embryonic development (Keegan et al., 2002). Comparative expression profiling of wild-type and Spt5 mutant zebrafish embryos showed that only 5% of genes are differentially expressed (Krishnan et al., 2008). A single amino acid substitution in zebrafish Spt5 resulted in reduction in the number of dopaminergic neurons and a corresponding surplus of serotoninergic neurons (Guo et al., 2000).

In *Drosophila*, Spt5 is located at sites of active transcription on polytene chromosomes and becomes recruited to heat-shock induced genes (Andrulis et al., 2000; Kaplan et al., 2000), but also controls transcriptional activation and repression of specific genes during embryogenesis (Jennings et al., 2004). Spt5 is also required for gene dosage compensation in male flies by promoting X-chromosomal gene expression (Prabhakaran and Kelley, 2012). In a *Drosophila* brain tumor model, knock-down of Spt5 impaired proliferation of tumor inducing neural progenitor cells, delayed tumor formation in the adult and increased lifespan (Hofstetter et al., 2024).

Available data indicated the essential requirement of Spt4 and Spt5 for viability, which hampered the phenotypic analysis of complete loss-of-function alleles at late development stages or in the adult. Mutational analysis of both genes in the context of a specific developmental process should provide information about identical or distinct cellular phenotypes. To address these points, we generated Spt4 and Spt5 knock-out flies and analyzed the phenotypic consequences using the well-studied mushroom body (MB) development in the fly brain as a model (Lin, 2023). Briefly, three major classes of MB neurons (Kenyon cells, KCs) are generated from four equipotent neural progenitor cells (mushroom body neuroblasts, MBNB) in one brain hemisphere in a chronological order; γ-KCs are generated from embryonic stages until early third instar larvae, followed by α´/β´-KCs until late third instar larvae and finally α/β-KCs are born until MBNB terminate proliferation around mid-pupal stage (Ito et al., 1997; Lee et al., 1999). KCs are named according to their axonal projections in the adult brain; α´/β′-and α/β-KCs bifurcate their axons to form the vertical α´-/α-lobes and the medial β´-/β-lobes, respectively. While the axonal projections of α´/β′- and α/β-KCs are maintained throughout life, axons from γ-KCs undergo developmental remodeling at the transition from larval to pupal stage. The initial bifurcated axonal branches are pruned and regrow only into medial direction to form the adult-specific γ-lobe. De-and regeneration of γ-KC axons has been studied in detail and depends on cell intrinsic and extrinsic mechanisms including glia-neuron interactions and signaling, engulfment of axonal debris by infiltrating glial cells, upregulation of protein degradation pathways, transcriptional changes induced by the steroid hormone 20-hydroxyecdysone (Ecdysone), upregulation of growth promoting pathways and re-organization of the actin cytoskeleton (Yaniv and Schuldiner, 2016; Furusawa and Emoto, 2021; Boulanger and Dura, 2022; Truman and Riddiford, 2023).

In this study we show that Spt4 and Spt5 are required for MBNBs proliferation and we uncover a novel function of both proteins in controlling remodeling of γ -KC axons through differential effects on gene expression.

Materials and methods

General fly work

Flies were maintained at 25°C on standard cornmeal food in a 12-h dark-light cycle. The following fly strains were obtained from Bloomington *Drosophila* Stock Center (IN, United States): *ey^{OK107}-Gal4* (BL#854), *UAS-mCD8::GFP* (BL#5130 and 5137), *$P[w^{+}$; FRT] G13 (FRT42B)* (Bl#1956), *heat-shock promotor* (*hsP*)*-Flp; FRT 42B, UAS-mCD8::GFP* (Bl#5131), *FRT 42B, tubulin promotor (tubP)-Gal80* (Bl#5140), *UAS-shRNA-Spt5* (Bl#34837), H24-Gal4 (Bl#51632) and worniu (wor)-Gal4 (BL#56553). The *hs-Flp, UAS-mCD8::GFP* fly line was a kind gift from P. Gallant, the combined tubP-Gal80 (ts); GMR-71G10-Gal4 fly stock was generously provided by Oren Schuldiner. For MARCM analysis (Lee et al., 1999), mitotic recombination between *FRT* sites was induced in first instar larvae by a 2-h heat shock (37°C) and animals of the genotype *hsP-Flp, UAS-mCD8::GFP; FRT42B, $Spt5^{\Delta}$ (or $Spt4^{\Delta}$)/FRT42B, tubulin promotor (tubP)-Gal80; ey^{OK107}-Gal4* were selected for further analysis. In control animals, *UAS-mCD8::GFP* localizes on the second chromosome. Homozygous MBNB clones were detected by mCD8::GFP expression in third instar larval or adult brains.

Generation of Spt4 and Spt5 CRISPR alleles

gRNA cloning

CRISPR/Cas9 cutting sites within the *Spt4* and *Spt5* transcription units were identified with the *CRISPR Optimal Target Finder*. Complementary 5′-phosphorylated oligonucleotides with target-specific sequences for Spt4 gRNAs (gRNA1: 5′-GGCCTTTGACGCGATACCCA-3´; gRNA2: 5′-TACGTGACATGAAGAATCGT-3´; sequences are in 5′–3′ order of the transcript) or Spt5 gRNAs (gRNA1: 5′-AACGTGGGTAATCTTCGGAT-3´; gRNA2: 5′-GTTGGTTACATGAACACTCC-3′) were synthesized with matching overhangs for directional cloning into the BbsI cut *pU6-BbsI-chiRNA* vector (Gratz et al., 2015).

Generation of HDR donor plasmids

As template DNA for homology arm cloning for Spt5 we used the P[acman] BAC clone CH321-94A4 (Venken et al., 2009) obtained from BACPAC Resources Center (Oakland, CA, United States). A 1 kb ´fragment encoding the 3′-homology arm was amplified with forward primer 5′-GTTACATGAACACTCCGTCG-3′ and reverse primer 5′- AAGAAGGAAAGGATAGTGTG-3′, both containing overhangs for directional cloning after SapI digestion into the pHD-DsRed-attP vector (Gratz et al., 2015). This construct was digested with AarI and the 5′-homology arm (1 kb) amplified with forward primer 5′ AATATGTCGGATAGTGGCTC-3′ and reverse primer 5′-CGAAGATTACCCACGTTATC-3′ was inserted after digestion of the flanking AarI linker. For generation of the Spt4 HDR donor plasmid, we followed the same strategy but used genomic DNA isolated from w^{1118} flies as template for amplification of the 0.86 kb 5′-homology arm (AarI forward primer: 5′-CTGAGTGCATAGCAAACGGAG-3′, AarI reverse primer: 5′-CGCGTCAAAGGCCATATTTAC-3′) and the 0.91 kb 3′-homology arm (Sap forward primer: 5′-GACATGAAGAATCGTGGAATTGTC-3, Sap reverse primer: 5′-CAGGTGCAGGTAGACAGCC-3′). The two gRNA constructs and the HDR donor construct for Spt4 or Spt5 were co-injected by Bestgene Inc. (Chino Hills, CA, United States) or FlyORF Injection Service (Zürich, CH) into embryos carrying a *nos-Cas9* or *vas-Cas9* source resulting in $Spt4^{\Delta,\ DsRed+}$ and $Spt5^{\Delta,\ DsRed+}$ flies. Correct gene targeting was confirmed by sequencing of PCR fragments amplified from genomic DNA of adult flies using primers which bind outside the homology arm sequences and pHD-DsRed-attP specific primers. For MARCM analysis, the mutant alleles were recombined onto a *FRT42B* chromosome (*FRT42B*, $Spt4^{\Delta,\ DsRed+}$ and *FRT42B*, $Spt5^{\Delta,\ DsRed+}$). Finally, the 3xP3-DsRed marker was removed by expressing a germline Cre source to establish *FRT42B*, $Spt4^{\Delta,\ DsRed-}$ (named $Spt4^{\Delta}$) and *FRT42B*, $Spt5^{\Delta,\ DsRed-}$ (named $Spt5^{\Delta}$) fly stocks, again verified by sequencing (see Supplementary Figure S1).

Expression constructs for S2R cells and transgenesis

For expression of Myc-tagged Spt5 in S2R cells, the coding sequence of Spt5 was amplified by linker PCR from an existing Spt5 plasmid kindly provided by P. Gallant and cloned into a modified pAC5.1 vector 3′ to the 6xMyc-tag sequences. This construct was used for further subcloning by linker PCR into the pUASTattB vector for transgenesis. HA::Spt4 was synthesized by Invitrogen (Thermo Fisher Scientific, Waltham, MA, United States) and inserted into a pcDNA3.1 vector before subcloning by linker PCR into pUASTattB. The E265K substitution in Spt5 and the S69F substitution in Spt4 were introduced with the Q5 Site directed mutagenesis kit (NEB, Ipswich, MA, United States) using the NEBaseChanger tool for mutagenesis primer design. Transgenic flies were generated by PhiC31 -mediated integration into the third chromosomal attP landing site of fly strain ZH-86Fb loxP (FlyORF Injection Service, Zürich, CH).

Immunohistochemistry

For immunostainings, brains from late third instar larvae or adults were dissected in PBS (10 mM Na_2HPO_4, 2 mM KH_2PO_4, 2.7 mM KCl, 137 mM NaCl) and fixed on ice for 25 min in PLP solution (4% paraformaldehyde, 10 mM $NaIO_4$, 75 mM lysine, 30 mM sodium phosphate buffer, pH 6.8). After blocking in PBT (PBS plus 0.3% Triton X-100) containing 5% normal donkey serum for 1 h, brains were incubated overnight at 4°C with combinations of the following primary antibodies: rat anti-Chinmo (1:500, N. Sokol, Bloomington, IN, United States), rabbit anti-cleaved Dcp-1 (1:100, # 9578, Cell Signaling Techn., Danvers, MA, United States), mouse anti-Dachshund (1:15, clone mABdac2-3, Developmental Studies Hybridoma Bank (DSHB), Iowa City, IA, United States), mouse anti-EcR B1 (1:25, clone AD4.4, DSHB), mouse anti-Fasciclin II (1:10, clone 1D4, DSHB), chicken anti-GFP (1:1,500; #ab13970, abcam, Cambridge, United Kingdom), rabbit-anti-HA-tag (1:800, #3724, Cell Signaling Techn.), rabbit anti-Imp (1:1,500, F. Besse, Nice, FR), rabbit anti-Mef2 (1:750, H. T. Nguyen, Erlangen, DE), mouse anti-Myc-tag (1:100, sc-40, Santa Cruz Biotechn., Dallas, TX, United States), rabbit anti-Retinal homeobox (1:750, U. Walldorf, Homburg, DE), guinea pig anti-Sox14 (1:30, S. Rumpf, Münster, DE). Samples were washed 4 times for 1 h in PBT followed by overnight incubation with secondary antibodies conjugated with AlexaFluor 488, Cy3 or Cy5 (Dianova, Hamburg, DE), and at least 4 washes in PBT for 1 h before embedding in Vectashield (Vector Laboratories, Newark, CA, United States). Confocal images were collected with a Leica SPE or SP8 microscope (Leica Microsystems, Wetzlar, DE). Image processing was carried out with the ImageJ distribution Fiji (Schindelin et al., 2012).

For 5-ethynyl-2′-deoxyuridine (EdU) labeling, brains from third instar larvae were dissected in PBS and incubated with 20 µM EdU in PBS for 90 min. Fixation in 4% paraformaldehyde for 15 min was followed by immunostaining as described before, before EdU incorporation into replicating DNA was detected with the Click-iT® Alexa Fluor 647 EdU imaging kit (Invitrogen, Thermo Fisher Scientific).

Quantification and statistics

For quantification of antibody stainings, signal intensities of 10 randomly selected KCs within GFP labelled control, $Spt4^{\Delta}$ or

Spt5$^{\Delta}$ MBNB clones in one brain were measured with an ImageJ macro (kindly provided by Nils Reinhardt) and averaged. The same was done with 10 non-clonal KCs in close proximity in the same focal planes and then the signal intensity ratio was calculated. Cells from six individual brains per genotype were measured. Distributions of data did not deviate significantly from normality (Kolmogorov-Smirnov test; $P > 0.2$). A one-way analysis of variance (ANOVA) was performed for statistical analysis. The ratio between clonal/non-clonal cells was considered as dependent variables, and the strain (control versus mutant lines) was considered as an independent variable. For multiple testing within one data set, the level of significance was adjusted with the Bonferroni correction factor. Graphs are presented as Box Plots generated with GraphPad Prism 6. Asterisks depict the level of statistical significance $^{****}p \leq 0.00001$.

Proximity ligation assay (PLA)

Third instar larval brains were fixed and incubated with anti-GFP, anti-HA and anti-Myc antibodies as described before. Incubation with an Alexa488-conjugated antibody for detection of GFP and DNA with Hoechst 33342 (1:2000, Thermo Fisher Scientific) were done for 3 h. The PLA assay was done according to the manufacturer's operating instructions (Duolink^{R}, Sigma-Aldrich, Merck, Burlington, MA, United States) with extended times for the Plus and Minus PLA probes incubation (90 min), ligation (60 min) and amplification (120 min) steps.

Cell culture, immunoprecipitation and western blot analysis

Drosophila S2R cells were maintained at 25°C in Schneider's *Drosophila* Medium (Gibco, Thermo Fisher Scientific) supplemented with 10% fetal bovine serum (Biochrom, Berlin, DE) and 1% penicillin/streptomycin (Merck, Darmstadt, DE). 2×10^{6} cells were seeded on 60 mm dishes and after overnight incubation, transfections with combinations of pAC5.1-Myc::Spt5, pAC5.1-Myc::Spt5^{E265K}, UAS-HA::Spt4, UAS-HA::Spt4^{S69F} and tubP-Gal4 plasmids were done with the Effectene Reagent (Qiagen, Hilden, DE) according to manufacturer's protocol. Cells were collected 24–36 h after transfection in lysis buffer (25 mM Tris pH 7.4, 150 mM NaCl 1 mM EDTA, 1% NP-40, 5% glycerol) and after removal of cell debris by centrifugation (13.000 g for 10 min at 4°C), proteins from the same preparation were either first immunoprecipitated with anti-Myc coupled agarose beads (Pierce, Thermo Fisher Scientific) or directly separated by SDS-PAGE followed by Western blot transfer. Nitrocellulose membranes were incubated overnight at 4°C with rabbit-anti-HA-tag (1: 800, #3724, Cell Signaling Techn.) or mouse anti-Myc-tag (1:1,000, sc-40, Santa Cruz Biotech.) antibodies. Following incubation with HRP-coupled secondary antibodies, signal detection was done with the ECL Plus detection reagents (GE Healthcare Life Science, Buckinghamshire, United Kingdom) and a ChemoCam ECL Imager equipped with a 16bit camera (Intas, Göttingen, DE).

Results

Drosophila Spt5 binds to and retains Spt4 in the nucleus

In a previous work, Guo et al. determined the crystal structure of *S. cerevisiae* Spt4 complexed with the NGN domain of Spt5 and identified critical amino acids for this interaction, which are highly conserved in eukaryotes (Guo et al., 2008). We introduced corresponding amino acid substitutions into full-length *Drosophila* Spt5 (E265K) and Spt4 (S69F). Non-mutated and mutated versions were co-expressed as HA- (HA::Spt4, HA::Spt4^{S69F}) and Myc-tagged proteins (Myc::Spt5, Myc::Spt5^{E265K}) in *Drosophila* S2R cells. Co-immunoprecipitation demonstrated binding of wild-type Spt4 to Spt5, whereas the S69F substitution in Spt4 and the E265K substitutions in Spt5 disrupted this interaction (Figure 1A). For further analysis, we generated transgenic flies expressing HA::Spt4, HA::Spt4^{S69F}, Myc::Spt5 and Myc::Spt5^{E265K} under UAS control. Transgenes were expressed with the neuroblast specific driver line worniu-Gal4 in combination with UAS-mCD8::GFP as a marker. In accordance with their function as transcriptional co-regulators, non-mutated HA::Spt4 and Myc::Spt5 co-localized in the nuclei of neuroblasts and their progenies (Figure 1B, top row). The S69F substitution in Spt4 resulted in re-distribution of the protein throughout the cell without affecting nuclear localization of Myc::Spt5 (Figure 1B, middle row). The uniform localization of Spt^{S69F} might be a consequence of passive diffusion. Alternatively, the N-terminal sequence (L-X_2-L-X_3-L-X_3-L) of Spt4 closely conforms to the consensus nuclear export signal sequence (L-$X_{2\text{-}3}$-L-$X_{2\text{-}3}$-L-X-L).

The E265K substitution in Spt5 had no effect on its own nuclear localization. HA::Spt4 localization was only partially altered, probably because endogenous Spt5 captured HA::Spt4 at least to some degree in the nucleus (Figure 1B, bottom row). To verify that the S69F and the E265K substitutions disrupt association of Spt4 with Spt5 in flies, we performed proximity ligation assays (PLA). Nuclear PLA signals were seen upon co-expression of non-mutated Spt4 and Spt5 (Figure 1C), whereas in case of co-expression of HA::Spt4^{S69F} with Myc::Spt5 or HA::Spt4 with Myc::Spt5^{E265K} no or very few background signals were evident (Figure 1C). These results allowed us to conclude that Spt4-Spt5 complex formation takes place in the nucleus. This interaction is necessary to retain Spt4 in the nucleus, whereas Spt5 localization is independent of Spt4.

Generation of Spt 4 and Spt5 knock-out flies

Previously we have shown that cell-type specific knock-down of Spt5 by RNAi delays tumor growth by reducing neuroblast proliferation (Hofstetter et al., 2024). However, this analysis was restricted to Spt5 and some phenotypes might not be expressed because of incomplete gene silencing. Therefore, we generated Spt4 and Spt5 deletion alleles (*Spt4*$^{\Delta}$ and *Spt5*$^{\Delta}$) by CRISPR mediated HDR. The *Spt4*$^{\Delta}$ deletion encompasses nearly the complete open reading frame, whereas *Spt5*$^{\Delta}$ removes part of the NGN domain, KOW domains 1-5 and the CTR (Supplementary Figure S1). As mentioned, the NGN domain and KOW domains 1, 4 and 5 are essential for the *in vivo* function of Spt5. *Spt4*$^{\Delta}$ and *Spt5*$^{\Delta}$ cause homozygous lethality at late embryonic/early first instar larval stages.

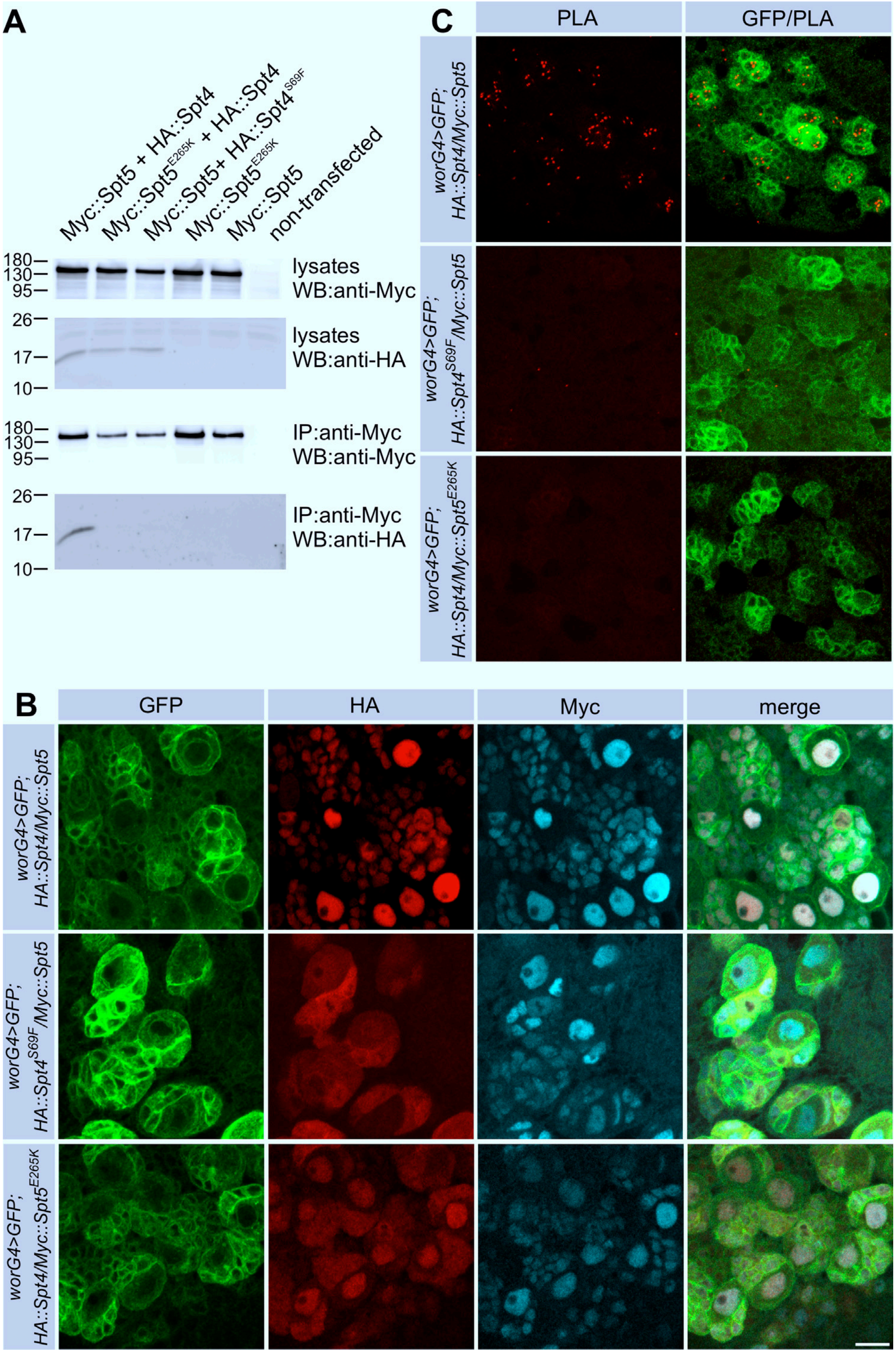

FIGURE 1
Interaction of Spt4 with Spt5. **(A)** Myc-tagged Spt5 and Spt5^{E265K} were transiently expressed in S2R cells alone or in combination with HA-tagged Spt4 or Spt4^{S69F}. Cell lysates were tested for protein expression by Western blot (WB) using anti-HA and anti-Myc-antibodies. For co-immunprecipitation (IP), lysates were first incubated with immobilized anti-Myc antibodies, and after elution, proteins were detected with anti-Myc and anti-HA antibodies. Molecular weight markers (in kD) are indicated. **(B)** Spt4 localization depends on interaction with Spt5. Combinations of UAS-Myc::Spt5, UAS-Myc::Spt5^{E265K}, UAS-HA::Spt4 and UAS-HA::Spt4^{S69F} were expressed with worniu-Gal4 (worG4) in neuroblast lineages in larval brains, which in addition were labeled with UAS-mCD8::GFP. Immunohistochemistry was done with anti-Myc (cyan), anti-HA (red) and anti-GFP (green) antibodies. Scale bar: 10 µm. **(C)** Close association of Spt4 and Spt5. PLA signals (red) in neuronal cells indicating interaction are only detected by co-expression of the non-mutated versions of UAS-Myc::Spt5 and UAS-HA::Spt4 with worG4 in combination with UAS-mCD8::GFP (green). Scale bar: 10 µm.

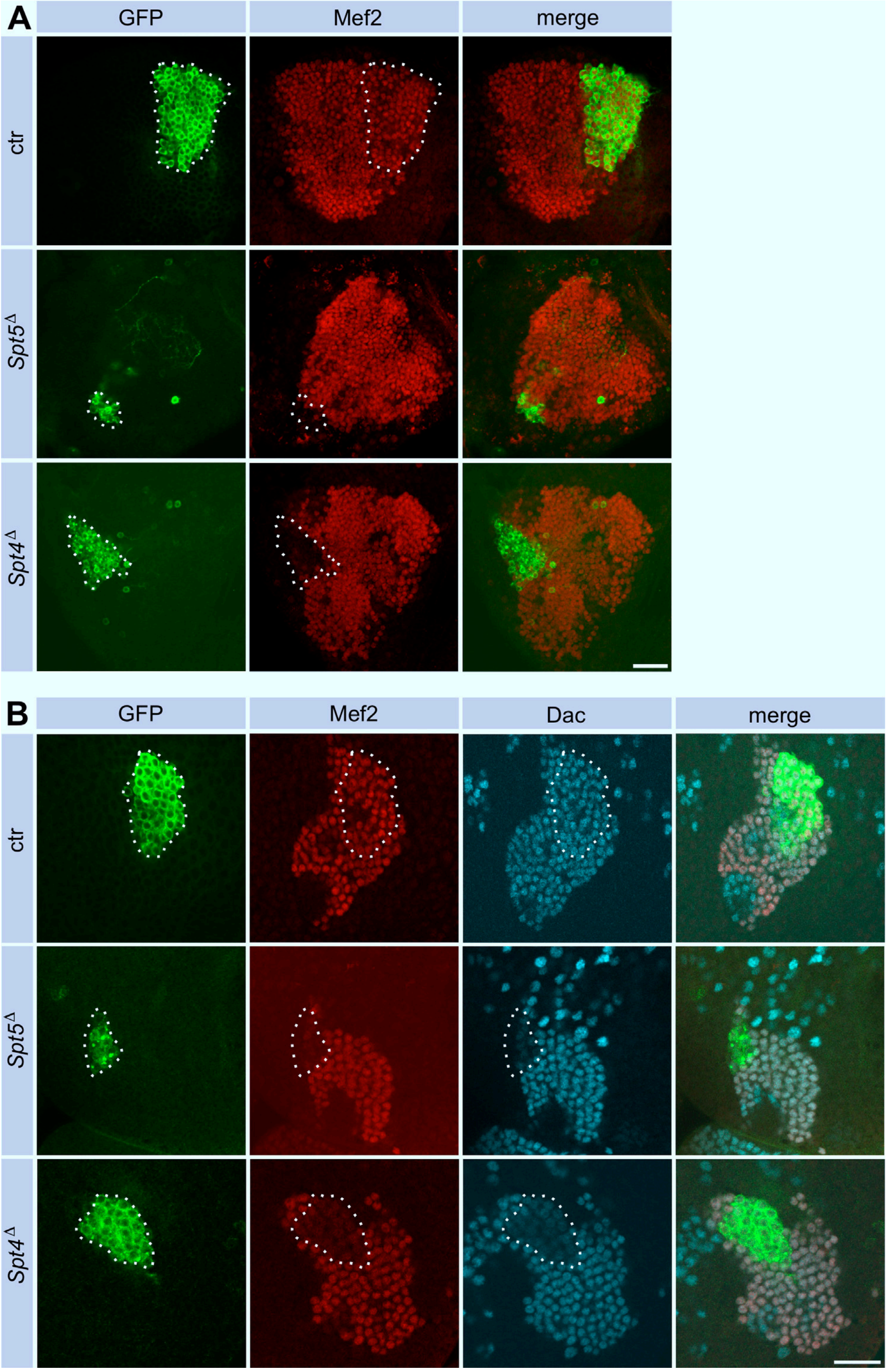

FIGURE 2
Spt5 and Spt4 deletion reduce Kenyon cell number. Control, *Spt5*$^{\Delta}$ and *Spt4*$^{\Delta}$ MBNB clones were induced in first instar larvae and analyzed in the adult **(A)** or in third instar larvae **(B)**. Clonal cells (encircled) were detected with an anti-GFP antibody (green), co-staining with antibodies against Myocyte enhancing factor 2 (Mef2, red) and Dachshund (Dac, cyan) labeled KC nuclei. For quantitative analysis see Supplementary Figure S2 (cell number), Supplementary Figure S4A (Dac) and Supplementary Figure S4B (Mef2). Scale bar: 20 µm.

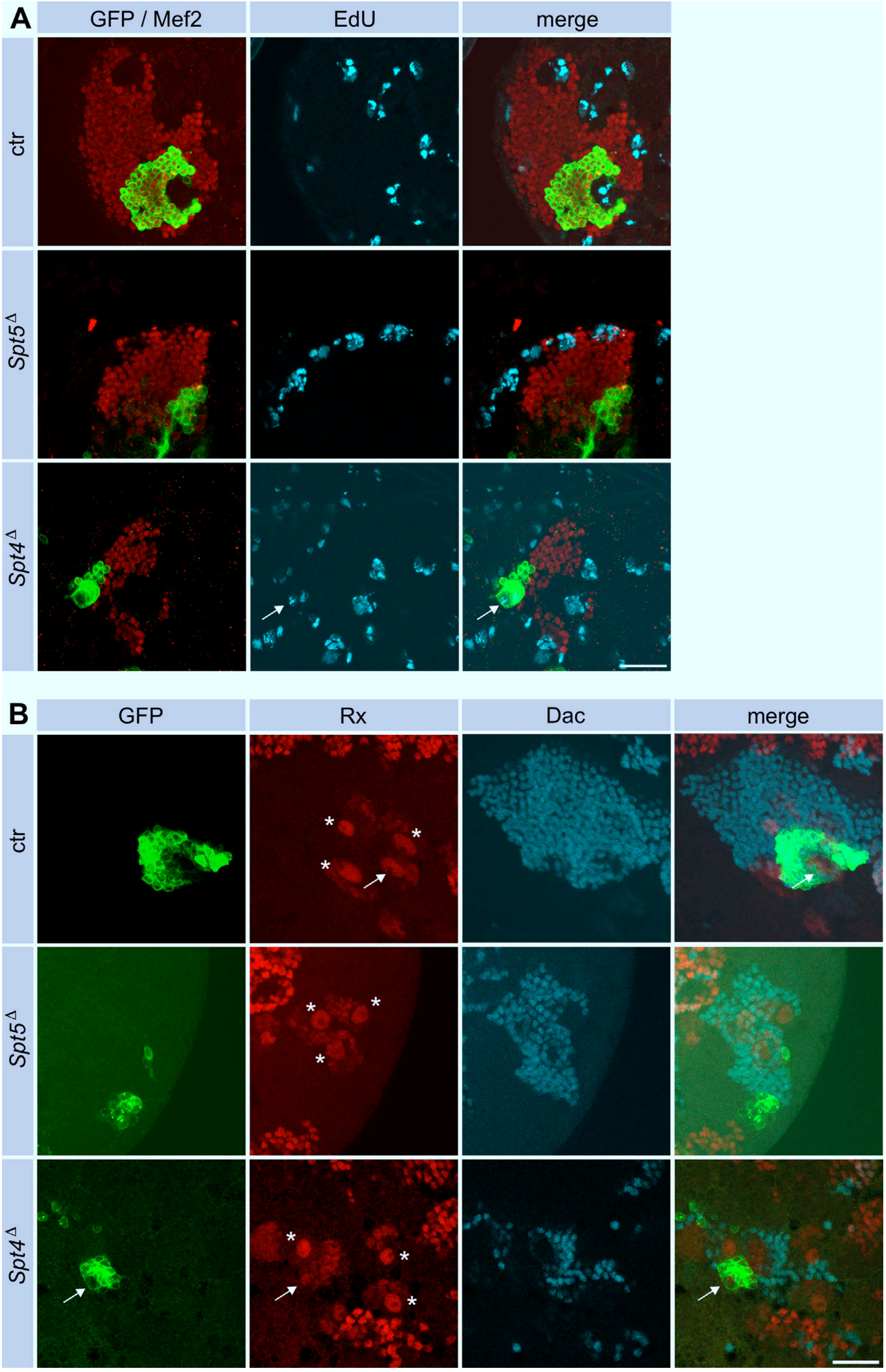

FIGURE 3
Spt5 and Spt4 deletion impair MBNB proliferation. **(A)** Control, *Spt5*$^{\Delta}$ and *Spt4*$^{\Delta}$ MBNB clones were induced in first instar larvae. At third larval instar, brains were dissected and replicating DNA was labeled with EdU for 90 min (cyan). Antibody stainings labeled clonal cells (GFP, green) and KC nuclei (Mef2, red). Scale bar: 20 µm. **(B)** In third instar larval brains from control animals, Rx staining labeled the four large MBNBs (stars and arrow) and associated smaller GMCs within the KC cell body layer (Mef2, red). A single MBNB (arrow) localizes within clonal cells (GFP, green). No Rx signal associated with clonal cells is seen for *Spt5*$^{\Delta}$, faint Rx expression is evident in a smaller *Spt4* mutant MBNB (arrow). Dac was used as a general marker for KC nuclei. Scale bar: 20 µm.

Spt4$^{\Delta}$ and *Spt5*$^{\Delta}$ impair mushroom body neuroblast proliferation

As a model system to study the phenotypic consequences of Spt4 and Spt5 deletion, we used the bilateral arranged mushroom bodies in the central brain. The sequential generation of γ-, α′/β′- and α/β-neurons (Kenyon cells, KCs) from four equipotent mushroom body neuroblasts (MBNB) and their defined axonal projection patterns into a system of lobes allowed us to determine effects of *Spt4*$^{\Delta}$ and *Spt5*$^{\Delta}$ both on MBNB proliferation and differentiation of neurons using the clonal MARCM system to label individual MBNBs and their progenies (Lee et al., 1999). Induction of single MBNB clones in first instar larvae from control animals resulted in labeling of large KC clusters in adult brains (Figure 2A, for quantification see Supplementary Figure S2). In comparison, *Spt5*$^{\Delta}$ mutant clones comprised only very few KCs (Figure 2A; Supplementary Figure S2). A less pronounced decrease in KC number was observed for *Spt4*$^{\Delta}$ MBNB clones (Figure 2A; Supplementary Figure S2). Analysis of MBNB clones in third instar larval brains provided the same result with the strongest reduction in clone size seen for *Spt5*$^{\Delta}$ (Figure 2B; Supplementary Figure S2). As MBNBs proliferate into mid-pupal stage, there is a corresponding increase in KC number in control clones from third instar larvae to the adult. Strikingly, *Spt4*$^{\Delta}$ and *Spt5*$^{\Delta}$ mutant clones not only contained fewer KCs, but also did not show the increase in KC number between larval and adult stages (Supplementary Figure S2). Both phenotypes indicated impaired and premature stop of cell proliferation of *Spt4*$^{\Delta}$ and *Spt5*$^{\Delta}$ mutant MBNB. In addition, survival of generated KCs could be affected.

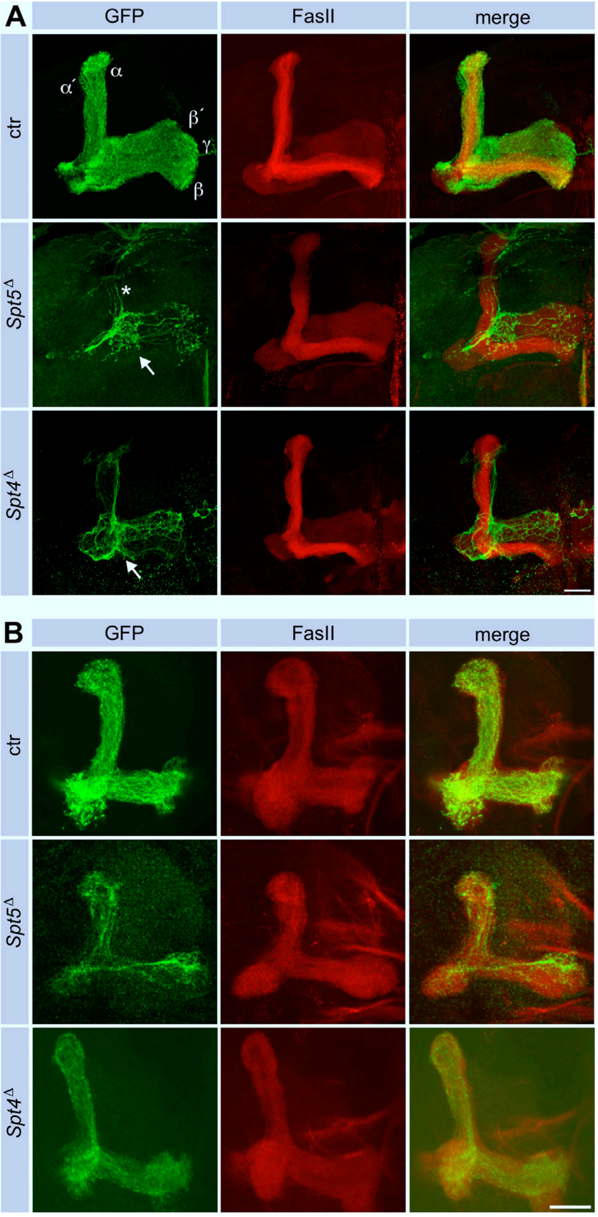

FIGURE 4
Spt5 and Spt4 are required for neuronal remodeling. Control, *Spt5*$^{\Delta}$ and *Spt4*$^{\Delta}$ MBNB clones were induced in first instar larvae and analyzed in adult **(A)** or in third instar larval brains **(B)**. Fasciclin II (FasII, red) labels the mushroom body lobe system (α/β, α´/β′and γ), with prominent staining of the adult α/β-lobes. GFP (green) labels the axons from clonal KCs, which project in all lobes in control animals, reflecting the ability of a single MBNB to sequentially generate all KC subtypes. In case of *Spt5*$^{\Delta}$ and *Spt4*$^{\Delta}$, most axons stopped before entering the lobe system (arrows), only few reached the γ-lobe. In *Spt5*$^{\Delta}$, some remnants of dorsal projections are visible (star), in case of *Spt4*$^{\Delta}$, these projections follow the α´/β′-lobe. Scale bar: 20 µm. **(B)** Deletion of either Spt4 or Spt5 had no effect on projection of KC axons into the larval lobe system stained for FasII. Projections are sparser because of the proliferation defect of the mutant MBNBs. Scale bar: 20 µm.

To investigate these phenotypes in more detail, we induced *Spt4*$^{\Delta}$ or *Spt5*$^{\Delta}$ mutant MBNB clones in first instar larvae and analyzed brains from third instar larvae, a developmental stage when MBNB are still proliferating. Staining for the pro-apoptotic protein Dcp-1 provided no evidence for enhanced neuronal cell death upon Spt4 or Spt5 deletion (Supplementary Figure S3). Proliferation was assayed by pulse labeling of S-phase cells with the base analogue EdU. In control animals, EdU signals were seen throughout the brain, corresponding to continuously dividing neuroblasts and derived ganglion mother cells (GMCs), which divide only once to generate a pair of neurons. This also includes the four MBNB (and associated GMCs), one of which generates the GFP-labeled cell clone (Figure 3A). Within *Spt5*$^{\Delta}$ mutant cell clones (Figure 3A), no EdU signals could be detected (0 out of 9 brains analyzed). In case of *Spt4*$^{\Delta}$ mutant cell clones (Figure 3A), EdU incorporation was evident in most cases (7 out of 11 brains analyzed) in a single larger cell, which we consider as the neuroblast, and in some surrounding smaller cells corresponding to GMCs. These results indicated that between the time point of clone induction in first instar larvae and analysis in third instar larvae, MBNBs and/or GMCs stopped proliferation in case of deletion of Spt5, whereas removal of Spt4 function only impaired mitotic activity based on the smaller overall clone size. To directly monitor the presence of MBNBs and GMCs in the absence of Spt5 or Spt4 function, we performed stainings against Roughex (Rx), a transcription factor expressed among others in the nuclei of MBNBs and derived GMCs (Kraft et al., 2016). Four large Rx-positive signals representing the 4 MBNB nuclei surrounded by smaller labeled GMCs nuclei are seen in control brains with one Rx cluster localized in the GFP-marked clone (Figure 3B). In contrast, in 10 out of 12 brains analyzed, no Rx signal was associated with GFP labeled *Spt5*$^{\Delta}$ cell clones (Figure 3B), only in two cases, we observed weak Rx expression in a small GFP-positive cell. In 7 out of 8 *Spt4*$^{\Delta}$ mutant cell clones, Rx signals were evident. However, the single larger Rx signal belonging to the MBNB within the clone has a much smaller diameter than in the remaining 3 MBNBs outside of the clone (Figure 3B). Since decrease in neuroblast size correlates with the end of neurogenesis, this indicated an impairment of *Spt4*$^{\Delta}$ mutant MBNBs to maintain proliferation.

In summary, Spt5 and, to a lesser extent, Spt4 are required for continuous cell division of MBNB. The results are consistent with our previous findings showing a negative effect of Spt5 knock-down on proliferation in a brain tumor model (Hofstetter et al., 2024).

Spt4$^{\Delta}$ and *Spt5*$^{\Delta}$ show defects in γ-neuron remodeling

Since MBNB clones were induced at first instar larvae, GFP labeled cells in adult control brains belong to the sequentially generated γ-, α′/β′- and α/β-KCs with their axonal projections into the corresponding lobes (Figure 4A). The finding that *Spt5*$^{\Delta}$ mutant MBNB stopped proliferation already in third instar larvae predicted that the few neurons generated by such a neuroblast should mainly belong to the γ-KC class forming the medial γ-lobe. These neurons are unique in terms of their differentiation as they remodel their axonal projections during metamorphosis. Larval γ-neuron axons project through the peduncle and then branch into a medial and dorsal lobe. With beginning of metamorphosis, the axonal branches are pruned, and single projections regrow to form the medial γ-lobe of the adult mushroom body. In case of Spt5 deletion, adult axonal projections follow the peduncle but then most of them remain confined there and only some project into the γ-lobe (Figure 4A). Very few thin dorsal projections were also visible (Figure 4A, star in middle row); these might be the remains of larval γ -KC axons which failed pruning or rare α′/β′-KCs still produced by the mutant MBNB.

We could not distinguish between these possibilities because usage of two γ-KC specific driver lines (*H24-Gal4* and *GMR71G10-Gal4*) instead of the pan-KC driver line *ey*^{OK107}-*Gal4* labeled no cells in Spt5 MBNB clones (data not shown). This indicated a general requirement of Spt5 for normal γ-neuron differentiation. Indeed, Spt5 deletion caused downregulation of two transcription factors involved in KC differentiation, Dachshund (Dac) (Martini et al., 2000) and Myocyte enhancing factor 2 (Mef2) (Crittenden et al., 2018) in larval (Figure 2B, for quantification see Supplementary Figures S4A, SB) and adult brains (Figure 2A). To confirm or exclude a general differentiation defect as the cause for proper axon outgrowth of γ-neurons in adult brains, we performed two experiments. First, when *Spt5*$^{\Delta}$ mutant clones were induced in first instar larvae and analyzed in third instar larvae, the few generated γ-KCs had a normal projection pattern with a vertical and a medial branch (Figure 4B), which argues against a general function of Spt5 in γ-KC specification and in initial outgrowth of their axons. On the other hand, conditional knock-down of Spt5 with a *UAS-shRNA-Spt5* construct expressed in γ-KCs only in the time frame of neuronal remodeling using the *H24-Gal4* or *GMR71G10-Gal4* driver lines in combination with a temperature sensitive *Gal80* transcriptional repressor line (shifted to the restrictive temperature from late third instar larval stage onwards) resulted in no reproducible axon outgrowth phenotype (data not shown). We do not know whether this failure is due to inefficient Spt5 knock-down, perdurance of existing Spt5 protein or indeed reflects an earlier function of Spt5 in γ-neuron differentiation required for subsequent remodeling.

Performing the same experiments with *Spt4*$^{\Delta}$ re-capitulated the phenotypes of *Spt5*$^{\Delta}$, but some defects were not as pronounced. Dac and Mef2 expression were decreased to a similar degree in clonal cells (Figure 2B; Supplementary Figures S4A, SB). As shown, Spt4 deficient MBNBs generated less KCs (Supplementary Figure S2). Most of them project into the γ-lobe and only few into the α′/β′-lobe (Figure 4A), again reflecting impaired proliferation and precocious termination of neurogenesis before α/β-KCs are born. Larval γ-KC axons branched normally into the vertical and medial lobe (Figure 4B), but after pruning, minor projection defects into the adult γ-lobe were observed (Figure 4A).

Spt4$^{\Delta}$ and *Spt5*$^{\Delta}$ affect expression of genes required in neuronal remodeling

Pruning and regrowth of γ-KC axons correlate with significant changes in the transcriptional program (Alyagor et al., 2018). Given the role of Spt4 and Spt5 as transcriptional co-regulators and the central role of Ecdysone-triggered transcriptional changes during remodeling (Yaniv and Schuldiner, 2016; Furusawa and Emoto, 2021; Truman and Riddiford, 2023), we evaluated changes in the expression level of the relevant Ecdysone receptor isoform B1 (EcR B1) and one of its targets, the transcription factor Sox14. Both proteins were reduced in Spt5 and Spt4 depleted KCs (Figures 5A, B, for quantification see Supplementary Figures S4C, SD). These observations correlated with previous findings that knock-down of EcR and Sox14 resulted in remodeling defects (Alyagor et al., 2018). We also noticed that EcR B1 was more evenly distributed in mutant cells, in contrast to its co-localization with nuclear Mef2 in non-mutant cells. This might indicate a failure in ligand mediated EcR B1 activation and its subsequent translocation into the nucleus to drive transcription of target genes.

Since Spt4 and Spt5 mutant MBNBs precociously terminate proliferation, the question remained, whether Spt4 and Spt5 are required for specification and normal axonal differentiation of later born KCs. Therefore, Spt4 and Spt5 depleted MBNB clones were induced in late third instar larvae, the time from which the last born α/β-KCs are generated. In both mutant cases, α/β-KCs showed a wild-type axonal projection pattern (Figure 6), but projections were sparser reflecting the reduced number of generated neurons. These results again confirmed a function of Spt4 and Spt5 in cell proliferation and indicated that both proteins are not required for KC subtype specification. Further support for the latter notion came from the analysis of transcription factor Chronologically inappropriate morphogenesis (Chinmo) and its upstream posttranscriptional regulator IGF-II mRNA-binding protein (Imp). The progressive decline of Chinmo and Imp expression triggers the sequential generation and specification of γ-, α′/β′- and α/β-KCs (Zhu et al., 2006; Liu et al., 2015). In addition, Chinmo acts as one of the upstream regulators of EcR B1 expression (Marchetti and Tavosanis, 2017). Looking in third instar larval brains, Spt4 and Spt5 deletion had no effect on Imp (Supplementary Figures S3A, S4E for quantification) and Chinmo (Supplementary Figures S3B, S4F for quantification) expression

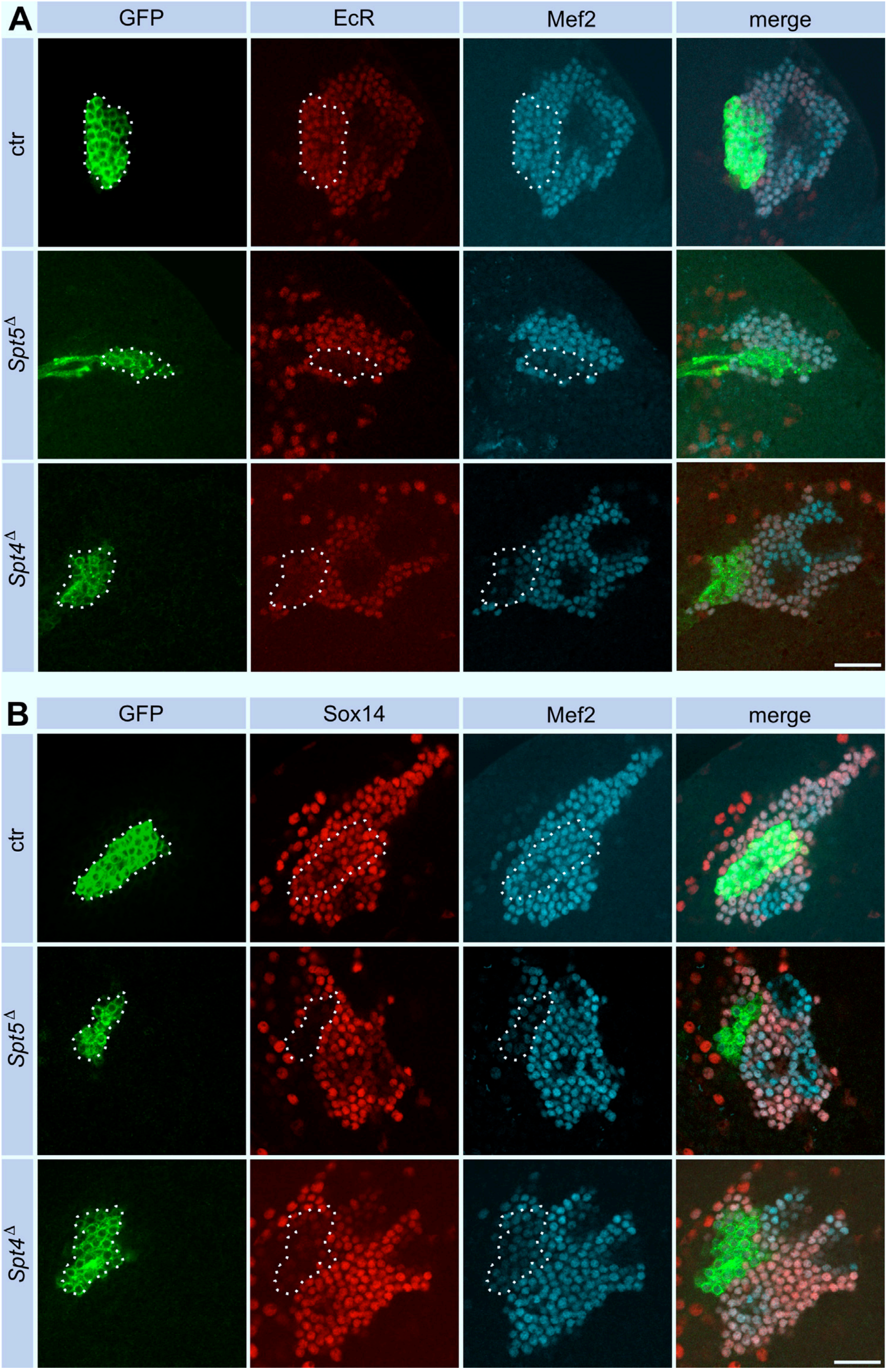

FIGURE 5
Spt5 and Spt4 deletion interferes with Ecdysone signaling. Control, *Spt5*$^{\Delta}$ and *Spt4*$^{\Delta}$ MBNB clones were induced in first instar larvae and brains were analyzed at third larval instar for expression of EcR B1 (A, red) and Sox14 (B, red). Co-staining for GFP (green) labeled clonal cells (encircled), Mef2 **(A)** and Dac **(B)** were used as nuclear KC markers (cyan). For quantitative analysis see Supplementary Figure S4C (EcR) and Supplementary Figure S4D (Sox14). Scale bar: 20 μm.

levels. Although we did not analyze the decline in expression of Chinmo and Imp at later developmental stages, these findings support the hypothesis that Spt5 and Spt4 are not required for Imp-Chinmo dependent specification of KC subtypes. Furthermore, the observed decrease in EcR B1 levels upon Spt4 and Spt5 deletion (Figure 5A) is not caused by loss of Chinmo expression.

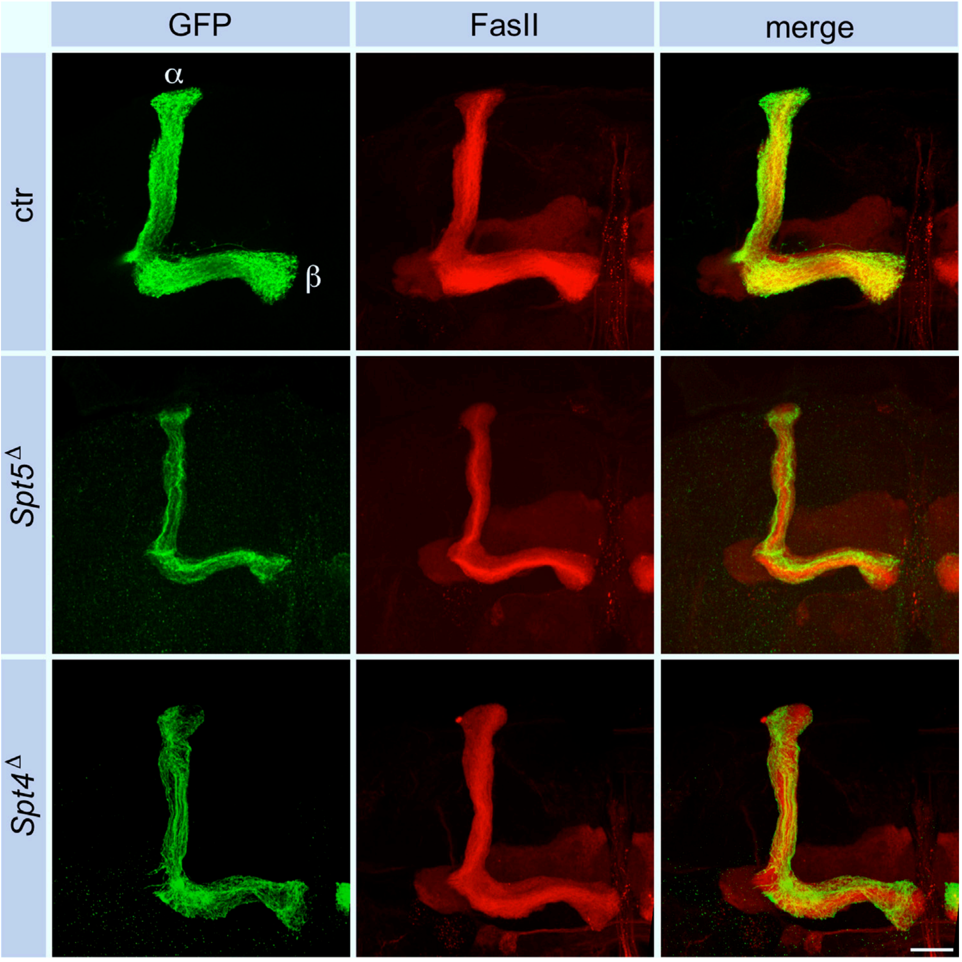

FIGURE 6
Spt5 and Spt4 deletion has no influence on axonal projections of α/β-KCs. Control, *Spt5*^{Δ} and *Spt4*^{Δ} MBNB clones were induced in late third instar larvae and the axonal projection pattern of clonal KCs (GFP, green) into the adult lobe system labeled for FasII (red) was analyzed. Because of the proliferation defect of the mutant MBNBs, the projections into the α/β-lobes were sparser but otherwise unaffected. Scale bar: 20 μm.

Taken together, Spt5 and Spt4 are required for proper expression of proteins involved in remodeling of γ-KC axons during metamorphosis rather than being generally required in axonal pathfinding.

Discussion

As mentioned in the introduction, only in few cases, Spt4 or Spt5 were associated with specific developmental processes or diseases. The aim of this study was to perform a comparative phenotypic analysis of Spt4 and Spt5 knock-out alleles using the *Drosophila* mushroom body development as a model to address two main questions. First, in this specific cellular context, do Spt4 and Spt5 always act together, or do they also fulfill independent functions? Second, does deletion of either gene globally disturb mushroom body development or only specific aspects? In summary, all Spt5 mutant phenotypes were also observed in case of Spt4 deletion, although they were generally less pronounced. This includes the precocious termination of MBNB proliferation, the distinct effects on gene expression and the neuronal remodeling defect.

One explanation for the slightly different phenotypes could be found in the molecular properties of the two proteins. The large Spt5 protein plays a central role in transcription by making multiple contacts with DNA, RNA, Pol II and regulatory proteins, thereby controlling pausing, elongation and termination. Together with Spt5 and Pol II, the small Spt4 protein forms the DNA exit tunnel. In contrast to Spt5, Spt4 is not required for Pol II stability. Spt4 also facilitates transcription through nucleosomal barriers (Decker, 2021; Song and Chen, 2022). Although both proteins are essential for viability, their contribution to efficient and regulated transcription might be different. For example, the functional relevance of Spt4 seems to depend on the genomic context as it selectively regulates expression of genes with expanded hexanucleotide repeats (Cheng et al., 2015; Kramer et al., 2016; Furuta et al., 2019; Deng et al., 2022).

Which role could Spt5 and Spt4 play in maintaining continuous MBNB proliferation from embryogenesis until end of neurogenesis at mid-pupal stages? Spt5 depletion commenced at the onset of larval development resulted in loss of MBNB in third instar larvae. Proliferating Spt4 mutant MBNBs were still present at this developmental stage, but their cell size was much smaller compared to wildtype. Previous studies demonstrated a positive correlation between cell size and neuroblast proliferation. Regrowth after each cell division maintains the proliferation potential until the end of neurogenesis, where neuroblasts reduce size followed by terminal differentiation or, in case of MBNBs, cell death (Maurange et al., 2008; Siegrist et al., 2010; Homem et al., 2014). Cell growth requires ribosome biogenesis and protein synthesis, and one major regulator for expression of the corresponding genes is the transcriptions factor Myc (Grewal et al., 2005). Mutations in *Drosophila* Myc (dMyc) show profound growth defects at the organismal and cellular level, including neuroblasts (Song and Lu, 2011; Gallant, 2013; Rust et al., 2018). Compared to other brain neuroblasts, MBNBs are larger and have elevated dMyc levels, which contribute to their extended proliferation period (Samuels et al., 2020). The RNA binding protein Imp controls dMyc levels by stabilizing *dMyc* mRNA. The progressive decline of Imp levels not only regulate neuronal temporal fate but also decommissioning of neuroblasts (Liu et al., 2015; Yang et al., 2017; Samuels et al., 2020). Since Spt5 or Spt4 deletion did not influence Imp protein levels at least in third instar brains (Supplementary Figure S3A), we consider a more direct involvement of both proteins in Myc-mediated transcription as a likely explanation. Recent studies in human cell lines showed that Myc recruits Spt5 and hands it over to RNA Polymerase II to promote processive transcription elongation (Baluapuri et al., 2019). In cell culture experiment, we confirmed interaction of *Drosophila* Spt5 and dMyc (T.R., data not shown). Thus, in the absence of Spt5/Spt4, growth signals mediated by dMyc might not be efficiently translated into productive transcription to maintain proper neuroblast size.

Finally, our analysis implicated a function of Spt4 and Spt5 in neuronal remodeling of γ-KC. However, the failure to reproduce the phenotype caused by Spt5 and Spt4 deletion alleles by conditional Spt5 knock-down specifically in the time frame of remodeling leaves open the question, whether knock-down was inefficient or whether Spt5 has an impact on proper γ-KC differentiation before remodeling is initiated. There are arguments for both scenarios. The initial elaboration of γ-KC axons was normal but then they failed after pruning to regrow into the adult γ-lobe. Also, loss of Spt4 or Spt5 function has no influence on the establishment and maintenance of the axonal projection patterns of α′/β′-and α/β-KCs. This would argue for proper initial differentiation of all KC and a requirement of Spt4 and Spt5 at the time point of axonal re-organization of γ-KC. On the other hand, expression of two transcription factors required for KC differentiation, Dachshund (Dac) (Martini et al., 2000) and Myocyte enhancing factor 2 (Mef2) (Crittenden et al., 2018), are prominently reduced already in L3 larvae and this might in turn influence expression of genes required for neuronal remodeling at the onset of pupal stage.

Looking for a molecular explanation we found out that expression of two components of the Ecdysone signaling pathway required for neuronal remodeling, the receptor EcR B1 and its transcriptional target Sox 14, were reduced in their expression. Spt5 and Spt4 could either directly regulate EcR B1 gene expression or indirectly by influencing transcription of upstream regulators of EcR B1 expression, also before remodeling in initiated. EcR expression is under control of several systems: TGF-β signaling, the orphan nuclear receptor FTZ-F1, the cohesion complex, micro-RNAs (Yaniv and Schuldiner, 2016; Furusawa and Emoto, 2021) and the transcription factor Chinmo (Marchetti and Tavosanis, 2017). So far, we could only exclude a major influence of Spt4 and Spt5 on expression of Chinmo and its upstream regulator Imp. A related question remains open for Sox14. Reduced Sox 14 expression could be a consequence of decreased EcR B1 signaling. Alternatively, a direct influence of Spt4 and Spt5 on Sox 14 transcription is possible.

Even though a systematic analysis of the transcriptional targets of Spt4 and Spt5 in the context of mushroom body neurogenesis is still pending, our results support the idea both proteins work together to control differential gene expression and thereby elicit cell-type specific responses.

Data availability statement

The raw data supporting the conclusions of this article will be made available by the authors, without undue reservation.

Ethics statement

The animal study was approved by Regierung von Unterfranken, Bavaria, Germany. The study was conducted in accordance with the local legislation and institutional requirements.

Author contributions

LB: Investigation, Visualization, Writing–review and editing. SP: Investigation, Visualization, Writing–review and editing. AN: Investigation, Writing–review and editing. HS: Investigation, Visualization, Writing–review and editing. KF: Investigation, Visualization, Writing–review and editing. LV: Investigation, Writing–review and editing. TR: Conceptualization, Data curation, Funding acquisition, Investigation, Project administration, Supervision, Validation, Visualization, Writing–original draft, Writing–review and editing.

Funding

The author(s) declare that financial support was received for the research, authorship, and/or publication of this article. This work was supported by basic funding of the University of Wuerzburg and its publication by the Open Access Publication Fund of the University of Wuerzburg.

Acknowledgments

We would like to thank Florence Besse, Nicholas Sokol, Hanh Nguyen, Sebastian Rumpf, Oren Schuldiner, Uwe Walldorf and Lesley Weaver for the generous provision of valuable antibodies and fly lines. Further antibodies were obtained from the Developmental Studies Hybridoma Bank, created by the NICHD of the NIH and maintained at The University of Iowa, Department of Biology, Iowa City. Fly stocks obtained from the Bloomington *Drosophila* Stock Center (NIH

P40OD018537) were used in this study. We like to thank Nils Reinhard for an Image J macro used for protein quantifications, Anna Hovhanyan for help in data analysis, and Peter Gallant for stimulating discussions. Eda Kutluyuva and Anna Marlene Nietz contributed to this work as part of an internship. This work was intended to teach undergraduate students in neurobiology research and was supported by basic funding from the University of Wuerzburg.

Conflict of interest

The authors declare that the research was conducted in the absence of any commercial or financial relationships that could be construed as a potential conflict of interest.

Publisher's note

Supplementary material

The Supplementary Material for this article can be found online at: https://www.frontiersin.org/articles/10.3389/fcell.2024.1434168/full#supplementary-material

References

Alyagor, I., Berkun, V., Keren-Shaul, H., Marmor-Kollet, N., David, E., Mayseless, O., et al. (2018). Combining developmental and perturbation-seq uncovers transcriptional modules orchestrating neuronal remodeling. *Dev. Cell* 47 (1), 38–52. doi:10.1016/j.devcel.2018.09.013

Andrulis, E. D., Guzman, E., Doring, P., Werner, J., and Lis, J. T. (2000). High-resolution localization of Drosophila Spt5 and Spt6 at heat shock genes *in vivo*: roles in promoter proximal pausing and transcription elongation. *Genes Dev.* 14 (20), 2635–2649. doi:10.1101/gad.844200

Bahat, A., Lahav, O., Plotnikov, A., Leshkowitz, D., and Dikstein, R. (2019). Targeting spt5-pol II by small-molecule inhibitors uncouples distinct activities and reveals additional regulatory roles. *Mol. Cell* 76 (4), 617–631. doi:10.1016/j.molcel.2019.08.024

Baluapuri, A., Hofstetter, J., Dudvarski Stankovic, N., Endres, T., Bhandare, P., Vos, S. M., et al. (2019). MYC recruits SPT5 to RNA polymerase II to promote processive transcription elongation. *Mol. Cell* 74 (4), 674–687. doi:10.1016/j.molcel.2019.02.031

Boulanger, A., and Dura, J. M. (2022). Neuron-glia crosstalk in neuronal remodeling and degeneration: neuronal signals inducing glial cell phagocytic transformation in Drosophila. *Bioessays* 44 (5), e2100254. doi:10.1002/bies.202100254

Cheng, H. M., Chern, Y., Chen, I. H., Liu, C. R., Li, S. H., Chun, S. J., et al. (2015). Effects on murine behavior and lifespan of selectively decreasing expression of mutant huntingtin allele by supt4h knockdown. *PLoS Genet.* 11 (3), e1005043. doi:10.1371/journal.pgen.1005043

Crittenden, J. R., Skoulakis, E. M. C., Goldstein, E. S., and Davis, R. L. (2018). Drosophila mef2 is essential for normal mushroom body and wing development. *Biol. Open* 7 (9), bio035618. doi:10.1242/bio.035618

Decker, T. M. (2021). Mechanisms of transcription elongation factor DSIF (Spt4-Spt5). *J. Mol. Biol.* 433 (14), 166657. doi:10.1016/j.jmb.2020.09.016

Deng, N., Wu, Y. Y., Feng, Y., Hsieh, W. C., Song, J. S., Lin, Y. S., et al. (2022). Chemical interference with DSIF complex formation lowers synthesis of mutant huntingtin gene products and curtails mutant phenotypes. *Proc. Natl. Acad. Sci. U. S. A.* 119 (32), e2204779119. doi:10.1073/pnas.2204779119

Dollinger, R., Deng, E. B., Schultz, J., Wu, S., Deorio, H. R., and Gilmour, D. S. (2023). Assessment of the roles of Spt5-nucleic acid contacts in promoter proximal pausing of RNA polymerase II. *J. Biol. Chem.* 299 (9), 105106. doi:10.1016/j.jbc.2023.105106

Dollinger, R., and Gilmour, D. S. (2021). Regulation of promoter proximal pausing of RNA polymerase II in metazoans. *J. Mol. Biol.* 433 (14), 166897. doi:10.1016/j.jmb.2021.166897

Furusawa, K., and Emoto, K. (2021). Spatiotemporal regulation of developmental neurite pruning: molecular and cellular insights from Drosophila models. *Neurosci. Res.* 167, 54–63. doi:10.1016/j.neures.2020.11.010

Furuta, N., Tsukagoshi, S., Hirayanagi, K., and Ikeda, Y. (2019). Suppression of the yeast elongation factor Spt4 ortholog reduces expanded SCA36 GGCCUG repeat aggregation and cytotoxicity. *Brain Res.* 1711, 29–40. doi:10.1016/j.brainres.2018.12.045

Gallant, P. (2013). Myc function in Drosophila. *Cold Spring Harb. Perspect. Med.* 3 (10), a014324. doi:10.1101/cshperspect.a014324

Gratz, S. J., Rubinstein, C. D., Harrison, M. M., Wildonger, J., and O'Connor-Giles, K. M. (2015). CRISPR-Cas9 genome editing in Drosophila. *Curr. Protoc. Mol. Biol.* 111, 31. doi:10.1002/0471142727.mb3102s111

Grewal, S. S., Li, L., Orian, A., Eisenman, R. N., and Edgar, B. A. (2005). Myc-dependent regulation of ribosomal RNA synthesis during Drosophila development. *Nat. Cell Biol.* 7 (3), 295–302. doi:10.1038/ncb1223

Guo, C., Zhang, Y., Shuai, S., Sigbessia, A., Hao, S., Xie, P., et al. (2023). The super elongation complex (SEC) mediates phase transition of SPT5 during transcriptional pause release. *EMBO Rep.* 24 (3), e55699. doi:10.15252/embr.202255699

Guo, M., Xu, F., Yamada, J., Egelhofer, T., Gao, Y., Hartzog, G. A., et al. (2008). Core structure of the yeast spt4-spt5 complex: a conserved module for regulation of transcription elongation. *Structure* 16 (11), 1649–1658. doi:10.1016/j.str.2008.08.013

Guo, S., Yamaguchi, Y., Schilbach, S., Wada, T., Lee, J., Goddard, A., et al. (2000). A regulator of transcriptional elongation controls vertebrate neuronal development. *Nature* 408 (6810), 366–369. doi:10.1038/35042590

Hofstetter, J., Ogunleye, A., Kutschke, A., Buchholz, L. M., Wolf, E., Raabe, T., et al. (2024). Spt5 interacts genetically with Myc and is limiting for brain tumor growth in Drosophila. *Life Sci. Alliance* 7 (1), e202302130. doi:10.26508/lsa.202302130

Homem, C. C., Steinmann, V., Burkard, T. R., Jais, A., Esterbauer, H., and Knoblich, J. A. (2014). Ecdysone and mediator change energy metabolism to terminate proliferation in Drosophila neural stem cells. *Cell* 158 (4), 874–888. doi:10.1016/j.cell.2014.06.024

Ito, K., Awano, W., Suzuki, K., Hiromi, Y., and Yamamoto, D. (1997). The Drosophila mushroom body is a quadruple structure of clonal units each of which contains a virtually identical set of neurones and glial cells. *Development* 124, 761–771. doi:10.1242/dev.124.4.761

Jennings, B. H., Shah, S., Yamaguchi, Y., Seki, M., Phillips, R. G., Handa, H., et al. (2004). Locus-specific requirements for Spt5 in transcriptional activation and repression in Drosophila. *Curr. Biol.* 14 (18), 1680–1684. doi:10.1016/j.cub.2004.08.066

Kaplan, C. D., Morris, J. R., Wu, C., and Winston, F. (2000). Spt5 and spt6 are associated with active transcription and have characteristics of general elongation factors in *D. melanogaster*. *Genes Dev.* 14 (20), 2623–2634. doi:10.1101/gad.831900

Keegan, B. R., Feldman, J. L., Lee, D. H., Koos, D. S., Ho, R. K., Stainier, D. Y., et al. (2002). The elongation factors Pandora/Spt6 and Foggy/Spt5 promote transcription in the zebrafish embryo. *Development* 129 (7), 1623–1632. doi:10.1242/dev.129.7.1623

Kraft, K. F., Massey, E. M., Kolb, D., Walldorf, U., and Urbach, R. (2016). Retinal homeobox promotes cell growth, proliferation and survival of mushroom body neuroblasts in the Drosophila brain. *Mech. Dev.* 142, 50–61. doi:10.1016/j.mod.2016.07.003

Kramer, N. J., Carlomagno, Y., Zhang, Y. J., Almeida, S., Cook, C. N., Gendron, T. F., et al. (2016). Spt4 selectively regulates the expression of C9orf72 sense and antisense mutant transcripts. *Science* 353 (6300), 708–712. doi:10.1126/science.aaf7791

Krishnan, K., Salomonis, N., and Guo, S. (2008). Identification of Spt5 target genes in zebrafish development reveals its dual activity *in vivo*. *PLoS One* 3 (11), e3621. doi:10.1371/journal.pone.0003621

Lee, T., Lee, A., and Luo, L. (1999). Development of the Drosophila mushroom bodies: sequential generation of three distinct types of neurons from a neuroblast. *Development* 126 (18), 4065–4076. doi:10.1242/dev.126.18.4065

Lin, S. (2023). The making of the Drosophila mushroom body. *Front. Physiol.* 14, 1091248. doi:10.3389/fphys.2023.1091248

Liu, C. R., Chang, C. R., Chern, Y., Wang, T. H., Hsieh, W. C., Shen, W. C., et al. (2012). Spt4 is selectively required for transcription of extended trinucleotide repeats. *Cell* 148 (4), 690–701. doi:10.1016/j.cell.2011.12.032

Liu, Z., Yang, C. P., Sugino, K., Fu, C. C., Liu, L. Y., Yao, X., et al. (2015). Opposing intrinsic temporal gradients guide neural stem cell production of varied neuronal fates. *Science* 350 (6258), 317–320. doi:10.1126/science.aad1886

Marchetti, G., and Tavosanis, G. (2017). Steroid hormone Ecdysone signaling specifies mushroom body neuron sequential fate via Chinmo. *Curr. Biol.* 27 (19), 3017–3024. doi:10.1016/j.cub.2017.08.037

Martini, S. R., Roman, G., Meuser, S., Mardon, G., and Davis, R. L. (2000). The retinal determination gene, dachshund, is required for mushroom body cell differentiation. *Development* 127 (12), 2663–2672. doi:10.1242/dev.127.12.2663

Maurange, C., Cheng, L., and Gould, A. P. (2008). Temporal transcription factors and their targets schedule the end of neural proliferation in Drosophila. *Cell* 133 (5), 891–902. doi:10.1016/j.cell.2008.03.034

Prabhakaran, M., and Kelley, R. L. (2012). Mutations in the transcription elongation factor SPT5 disrupt a reporter for dosage compensation in Drosophila. *PLoS Genet.* 8 (11), e1003073. doi:10.1371/journal.pgen.1003073

Qiu, Y., and Gilmour, D. S. (2017). Identification of regions in the Spt5 subunit of DRB sensitivity-inducing factor (DSIF) that are involved in promoter-proximal pausing. *J. Biol. Chem.* 292 (13), 5555–5570. doi:10.1074/jbc.M116.760751

Rust, K., Tiwari, M. D., Mishra, V. K., Grawe, F., and Wodarz, A. (2018). Myc and the Tip60 chromatin remodeling complex control neuroblast maintenance and polarity in Drosophila. *EMBO J.* 37 (16), e98659. doi:10.15252/embj.201798659

Samuels, T. J., Jarvelin, A. I., Ish-Horowicz, D., and Davis, I. (2020). Imp/IGF2BP levels modulate individual neural stem cell growth and division through myc mRNA stability. *Elife* 9, e51529. doi:10.7554/eLife.51529

Schindelin, J., Arganda-Carreras, I., Frise, E., Kaynig, V., Longair, M., Pietzsch, T., et al. (2012). Fiji: an open-source platform for biological-image analysis. *Nat. Methods* 9 (7), 676–682. doi:10.1038/nmeth.2019

Siegrist, S. E., Haque, N. S., Chen, C.-H., Hay, B. A., and Hariharan, I. K. (2010). Inactivation of both foxo and reaper promotes long-term adult neurogenesis in Drosophila. *Curr. Biol.* 20, 643–648. doi:10.1016/j.cub.2010.01.060

Song, A., and Chen, F. X. (2022). The pleiotropic roles of SPT5 in transcription. *Transcription* 13 (1-3), 53–69. doi:10.1080/21541264.2022.2103366

Song, Y., and Lu, B. (2011). Regulation of cell growth by Notch signaling and its differential requirement in normal vs. tumor-forming stem cells in Drosophila. *Genes Dev.* 25 (24), 2644–2658. doi:10.1101/gad.171959.111

Truman, J. W., and Riddiford, L. M. (2023). Drosophila postembryonic nervous system development: a model for the endocrine control of development. *Genetics* 223 (3), iyac184. doi:10.1093/genetics/iyac184

Venken, K. J., Carlson, J. W., Schulze, K. L., Pan, H., He, Y., Spokony, R., et al. (2009). Versatile P[acman] BAC libraries for transgenesis studies in *Drosophila melanogaster*. *Nat. Methods* 6 (6), 431–434. doi:10.1038/nmeth.1331

Winston, F., Chaleff, D. T., Valent, B., and Fink, G. R. (1984). Mutations affecting Ty-mediated expression of the HIS4 gene of *Saccharomyces cerevisiae*. *Genetics* 107 (2), 179–197. doi:10.1093/genetics/107.2.179

Yang, C. P., Samuels, T. J., Huang, Y., Yang, L., Ish-Horowicz, D., Davis, I., et al. (2017). Imp and Syp RNA-binding proteins govern decommissioning of Drosophila neural stem cells. *Development* 144 (19), 3454–3464. doi:10.1242/dev.149500

Yaniv, S. P., and Schuldiner, O. (2016). A fly's view of neuronal remodeling. *Wiley Interdiscip. Rev. Dev. Biol.* 5 (5), 618–635. doi:10.1002/wdev.241

Zhu, S., Lin, S., Kao, C. F., Awasaki, T., Chiang, A. S., and Lee, T. (2006). Gradients of the Drosophila Chinmo BTB-zinc finger protein govern neuronal temporal identity. *Cell* 127 (2), 409–422. doi:10.1016/j.cell.2006.08.045

Frontiers in Cell and Developmental Biology

TYPE Original Research
PUBLISHED 24 October 2024
DOI 10.3389/fcell.2024.1448773

Check for updates

OPEN ACCESS

EDITED BY
Michael Schubert,
UMR7009 Laboratoire de Biologie du Développement de Villefranche sur Mer, France

REVIEWED BY
Uwe Strähle,
Karlsruhe Institute of Technology (KIT), Germany
Issam Al Diri,
University of Pittsburgh, United States
Tudor Constantin Badea,
Transilvania University of Brașov, Romania

*CORRESPONDENCE
Zbynek Kozmik,
✉ kozmik@img.cas.cz

RECEIVED 13 June 2024
ACCEPTED 18 September 2024
PUBLISHED 24 October 2024

CITATION
Mikula Mrstakova S and Kozmik Z (2024) Genetic analysis of medaka fish illuminates conserved and divergent roles of Pax6 in vertebrate eye development.
Front. Cell Dev. Biol. 12:1448773.
doi: 10.3389/fcell.2024.1448773

Genetic analysis of medaka fish illuminates conserved and divergent roles of Pax6 in vertebrate eye development

Simona Mikula Mrstakova and Zbynek Kozmik*

Laboratory of Transcriptional Regulation, Institute of Molecular Genetics of the Czech Academy of Sciences, Prague, Czechia

Landmark discovery of eye defects caused by Pax6 gene mutations in humans, rodents, and even fruit flies combined with Pax6 gene expression studies in various phyla, led to the master control gene hypothesis postulating that the gene is required almost universally for animal visual system development. However, this assumption has not been broadly tested in genetically trackable organisms such as vertebrates. Here, to determine the functional role of the fish orthologue of mammalian Pax6 in eye development we analyzed mutants in medaka Pax6.1 gene generated by genome editing. We found that transcription factors implicated in vertebrate lens development (Prox1a, MafB, c-Maf, FoxE3) failed to initiate expression in the presumptive lens tissue of Pax6.1 mutant fish resulting in aphakia, a phenotype observed previously in Pax6 mutant mice. Surprisingly, the overall differentiation potential of Pax6.1-deficient retinal progenitor cells (RPCs) is not severely compromised, and the only cell types affected by the absence of Pax6.1 transcription factor are retinal ganglion cells. This is in stark contrast to the situation in mice where the Pax6 gene is required cell-autonomously for the expansion of RPCs, and the differentiation of all retina cell types. Our results provide novel insight into the conserved and divergent roles of Pax6 gene orthologues in vertebrate eye development indicating that the lens-specific role is more evolutionarily conserved than the role in retina differentiation.

KEYWORDS

lens, retina, eye evolution, vision, gene expression, Pax6

Introduction

Landmark discovery of *Pax6* gene mutations in humans, rodents and fruit fly *Drosophila melanogaster* (Hill et al., 1991; Ton et al., 1991; Glaser et al., 1992; Quiring et al., 1994; Czerny et al., 1999), which all lead to defects in eye development, challenged the contemporary view that widely different anatomical designs arose independently during evolution. Since then, more evidence, mostly based on gene expression studies, has emerged in favour of the redeployment of *Pax6* genes within the genetic program underlying eye formation throughout the animal kingdom (Kozmik, 2005; Cvekl and Callaerts, 2017). In model organisms allowing genetic approaches such as the laboratory mouse or fruit fly we begin to understand function of *Pax6* during animal eye development at mechanistic level, by defining its role in cell proliferation, in cell type differentiation, and in participation in complex gene regulatory networks (Shaham et al., 2012; Cvekl and Callaerts, 2017). Phenotypic studies of *Pax6* mutants performed in selected vertebrate species, such as zebrafish (Kleinjan et al., 2008; Takamiya et al., 2015; Takamiya et al., 2020), mouse (Hill et al., 1991; Ashery-Padan et al., 2000; Marquardt et al., 2001; Klimova and Kozmik, 2014), rat (Matsuo et al., 1993) or *Xenopus* (Nakayama et al., 2015) provided key insight into the role of *Pax6* in visual system development. The vertebrate eye is predominantly composed of the derivatives of neural ectoderm that form the optic vesicle (i.e., optic stalk, neural retina, and retinal pigment epithelium) and surface ectoderm (i.e., lens and cornea). Eye development in mammals begins with evagination of the optic vesicles toward the lens-competent head surface ectoderm (also called presumptive lens ectoderm). As the optic vesicle contacts surface ectoderm, a series of reciprocal inductive signals elicit formation of the lens placode and subsequent invagination of both lens placode and optic vesicle to form a two-layered optic cup with retinal pigmented epithelium surrounding the retina (reviewed by (Fuhrmann, 2010)). Using conditional gene targeting in mice it was established that *Pax6* is cell-autonomously required for lens placode formation (Ashery-Padan et al., 2000). An evolutionary conserved mechanism was identified by which Pax6 controls the downregulation of multiple genes (such as Sox11) through direct upregulation of miR-204 (Shaham et al., 2013).

In addition to the cell-autonomous role of *Pax6* in the lens compartment *Pax6* appears to be required for lens development also non-autonomously in the optic vesicle (Klimova and Kozmik, 2014). When *Pax6* is eliminated from optic vesicle before its transition to the optic cup then the lens is not formed (Klimova and Kozmik, 2014). Interestingly, Pax6 is required for lens formation only before the transition of optic vesicle into optic cup. Once the lens pit starts to emerge from the lens placode, lens development is no longer dependent on Pax6 being expressed in the neural retina. At the time the lens placode is formed, the dorsal region of the optic vesicle becomes specified to the retina populated with mitotically active retinal progenitor cells (RPCs) (Levine and Green, 2004). Lineage tracing studies have shown that RPCs are multipotent with a single progenitor cell competent to give rise to all retinal neuron and glia cell types (Turner and Cepko, 1987; Holt et al., 1988; Turner et al., 1990). The defining feature of RPCs is co-expression of transcription factors Rx, Pax6, Lhx2, Meis1/Meis2, Six3/Six6, Vsx2, and Hes1, which are expressed prior to the activation of neurogenic program and contribute to the proliferative and retinogenic potential of RPCs (Oliver et al., 1995; Burmeister et al., 1996; Tomita et al., 1996; Mathers et al., 1997; Porter et al., 1997; Marquardt et al., 2001; Liu et al., 2010; Klimova and Kozmik, 2014; Liu and Cvekl, 2017; Diacou et al., 2018; Dupacova et al., 2021). In a defined birth order, RPCs differentiate into seven retinal cell types: retinal ganglion cells, horizontal cells and cone photoreceptors differentiate first, followed by amacrine cells and rod photoreceptors, bipolar cells, and finally Muller glia cells (Young, 1985). As retinogenesis proceeds, RPCs are exposed to the changing environment of extrinsic cues (Cepko, 1999). These, in cooperation with intrinsic factors represented by transcription factors, most prominently of the basic helix-loop-helix (bHLH) and homeodomain class, regulate progenitor proliferation and operate to direct the bias towards particular cell types (reviewed in (Cepko, 1999; Hatakeyama and Kageyama, 2004; Zagozewski et al., 2014)). At the time of neuronal differentiation, the subpopulation of progenitors undergoes transition from the proliferative stage towards the lineage-restricted neurogenic stage, when it withdraws from the cell cycle to take up neuronal or glial fate. The proper balance between the cell cycle exit and re-entry is required to ensure temporal generation of all retinal cell types (reviewed in (Agathocleous and Harris, 2009)).

Teleost fish have become popular to study various aspects of developmental biology and genetics of the eye. Teleost eye shows a high degree of similarity to that of mammals including human (Richardson et al., 2017). As in mammals, the retina of zebrafish and medaka possesses six types of neurons and one type of glia arranged into three nuclear layers. Moreover, in all vertebrates analyzed (mammals and fish included), the generation of neuronal and non-neuronal retinal cell types follows the same stereotyped birth order. Retinal ganglion cells are generated first, whereas bipolar cells and Muller glia are the last cell types to be born (Cepko et al., 1996; Livesey and Cepko, 2001). Although the duration of eye development in human, mouse, chick, zebrafish or medaka is vastly different, the sequence of events, the type of embryonic tissues involved, and spatiotemporal expression of key regulatory genes is remarkably similar. Not only the global eye 'organ plan' is largely comparable across vertebrate species, but also the gene regulatory network that is involved in orchestrating eye development is supposed to be mostly conserved (Zhang et al., 2023). Medaka (*Oryzias latipes*) is a small freshwater fish of the family Adrianichthyidae. It is closely related to pufferfish or stickleback and is more distant to the most widely used teleost model organism, zebrafish (*Danio rerio*) (Furutani-Seiki and Wittbrodt, 2004; Signore et al., 2009). Developmental stages of medaka and corresponding morphological characteristics have been described in detail by Iwamatsu (2004). In comparison to zebrafish, medaka embryonic development, including the eye, is slower (Tena et al., 2014). Eye development in medaka is initiated by the specification of the retina anlage in the anterior neural plate at late gastrula stages (stage 15, 16 h post fertilization, hpf). Next the presumptive retina evaginate laterally to form the optic vesicles and contacts the surface ectoderm cells. At the 6-somite stage (stage 21, 28 hpf) the optic cup contains two layers: an inner pseudostratified neuroepithelium from which the neural retina will form, and a thin layer of pigment cells. Retina differentiation is initiated at the 22-somite stage (stage 26, 54 hpf) in the central retina. As in other vertebrates the first neurons to be born are the ganglion cells. The basic helix-loop-helix transcription factor ath5 is first expressed at 54 hpf, marking the onset of ganglion cell differentiation. Morphologically, the three layers of the neural retina appear by 70 hpf (stage 29) and a fully patterned retina is formed by 9 days post fertilization (9 dpf) (Kitambi and Malicki, 2008). Retina differentiation and layer formation in medaka (and zebrafish) progress from the center towards the periphery. The edges of mature fully functional fish retina, the ciliary marginal zone (CMZ), remain undifferentiated and contain retinal progenitor cells (stem cells) that continue to proliferate during the entire adulthood (Perron et al., 1998). Unlike mammals, fish are therefore able to continuously grow their retinas throughout life. In addition to the retinal stem cells present in CMZ there is another population of proliferating cells in postembryonic fish retina. These are Muller glia, which are localized throughout the entire differentiated fish retina. Unlike in mammals, Muller glia in fish is able to produce rod photoreceptors during normal homeostasis and, upon injury, also other neuronal cell types of

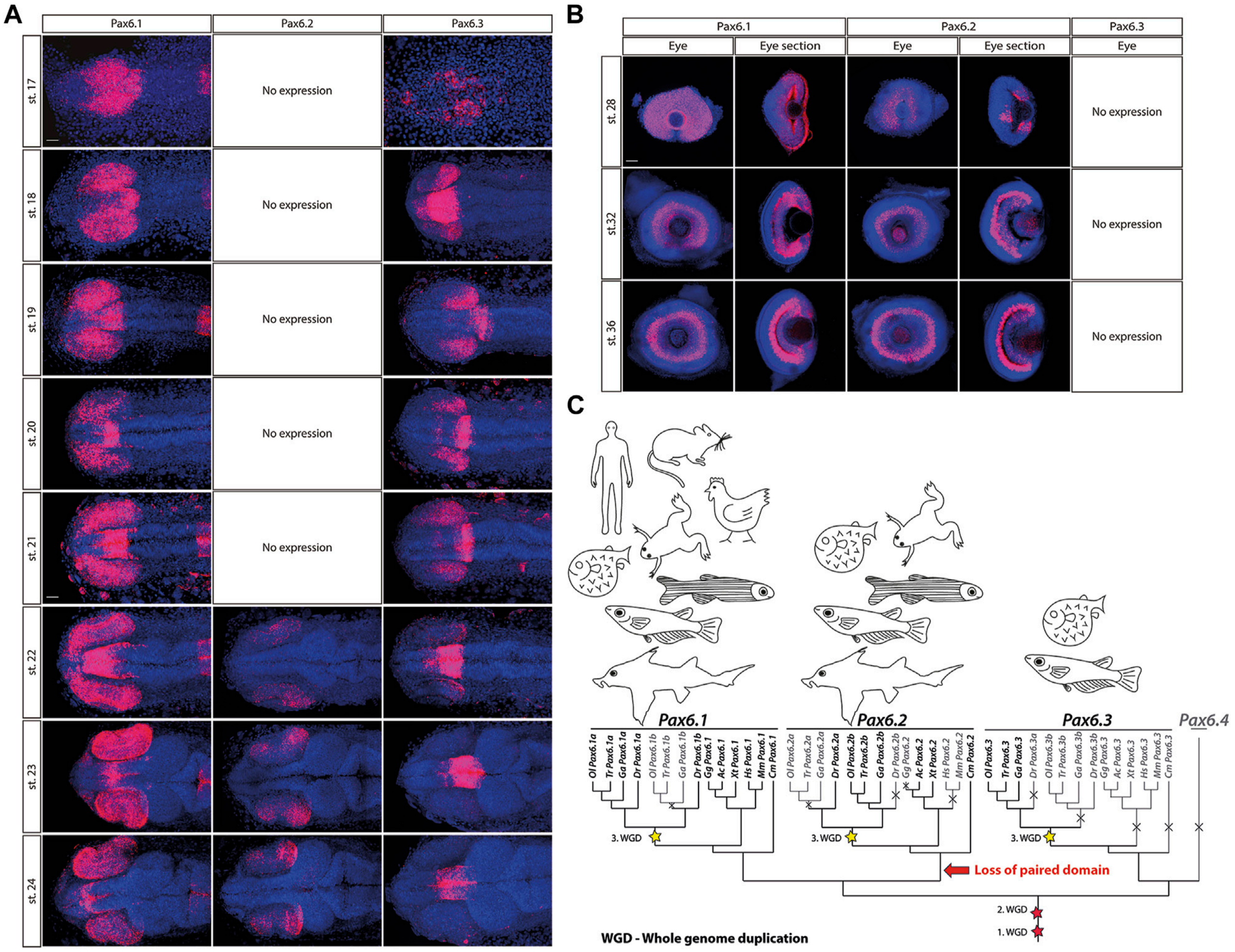

FIGURE 1
The expression patterns of the *Pax6.1*, *Pax6.2* and *Pax6.3* genes during embryonic development of medaka at stages 17–24 **(A)**, stage 28, 32 and 36 **(B)**. Scale bar: 50 µm. **(C)** The evolutionary trajectories of *Pax6.1*, *Pax6.2*, and *Pax6.3* in vertebrates. Gene losses are depicted by crosses and greyed-out branches/labels. The three WGD events are highlighted with stars. Hs, *Homo sapiens* (human); Mm, *Mus musculus* (mouse); Ga, *Gasterosteus aculeatus* (three-spined stickleback); Gg, *Gallus gallus* (chicken); Ac, *Anolis carolinensis* (lizard); Xt, *Xenopus tropicalis* (frog); Dr, *Danio rerio* (zebrafish); Ol, *Oryzias latipes* (medaka); Tr, *Takifugu rubripes* (fugu); Cm, *Callorhinchus milii* (elephant shark).

the retina (Wan and Goldman, 2016; Lust and Wittbrodt, 2018). The gene regulatory networks controlling Müller glia reprogramming upon injury have recently been elucidated (Hoang et al., 2020; Lyu et al., 2023).

Gene and genome duplications are thought to be the driving force of animal evolution. A genome duplication generates paralogous groups of duplicated genes. Being free from selective pressure, paralogous genes undergo neo-functionalization (acquire new function), sub-functionalization (specialize), or one of the paralogs may become extinguished from the genome (Force et al., 1999). After the initial genome duplication, the genomes of different teleost lineages evolved independently. It has become apparent that due to their independent subsequent evolution different fish species show notable differences with respect to the fate of duplicated genes. Medaka and zebrafish are separated from each other by about 110 million years of independent lineage evolution (Wittbrodt et al., 2002; Furutani-Seiki and Wittbrodt, 2004). As a result, medaka possesses a single orthologue of the mammalian *Pax6* gene while zebrafish genome contains two paralogous genes, namely *Pax6.1a* (also referred to as *Pax6a* and *Pax6.1b* (*Pax6b*), respectively (Ravi et al., 2013). Here we investigated the functional role of medaka *Pax6.1* gene in eye development.

Results

Expression of Pax6 gene family in medaka embryos and generation of Pax6.1 mutants

The evolutionary history of the *Pax6* gene family in vertebrates has been elucidated by Ravi et al. (2013). As a result of two rounds of vertebrate-specific and one round of teleost-specific whole genome duplication followed by lineage specific gene losses, Acanthopterygians (e.g. medaka, stickleback, pufferfish) retained three genes, namely *Pax6.1*, *Pax6.2*, and *Pax6.3*, respectively. *Pax6.1* and *Pax6.3* genes are structurally similar, and encode both paired domain and homeodomain. In contrast, *Pax6.2* lacks the paired domain, which is a critical DNA-binding domain of Pax family of

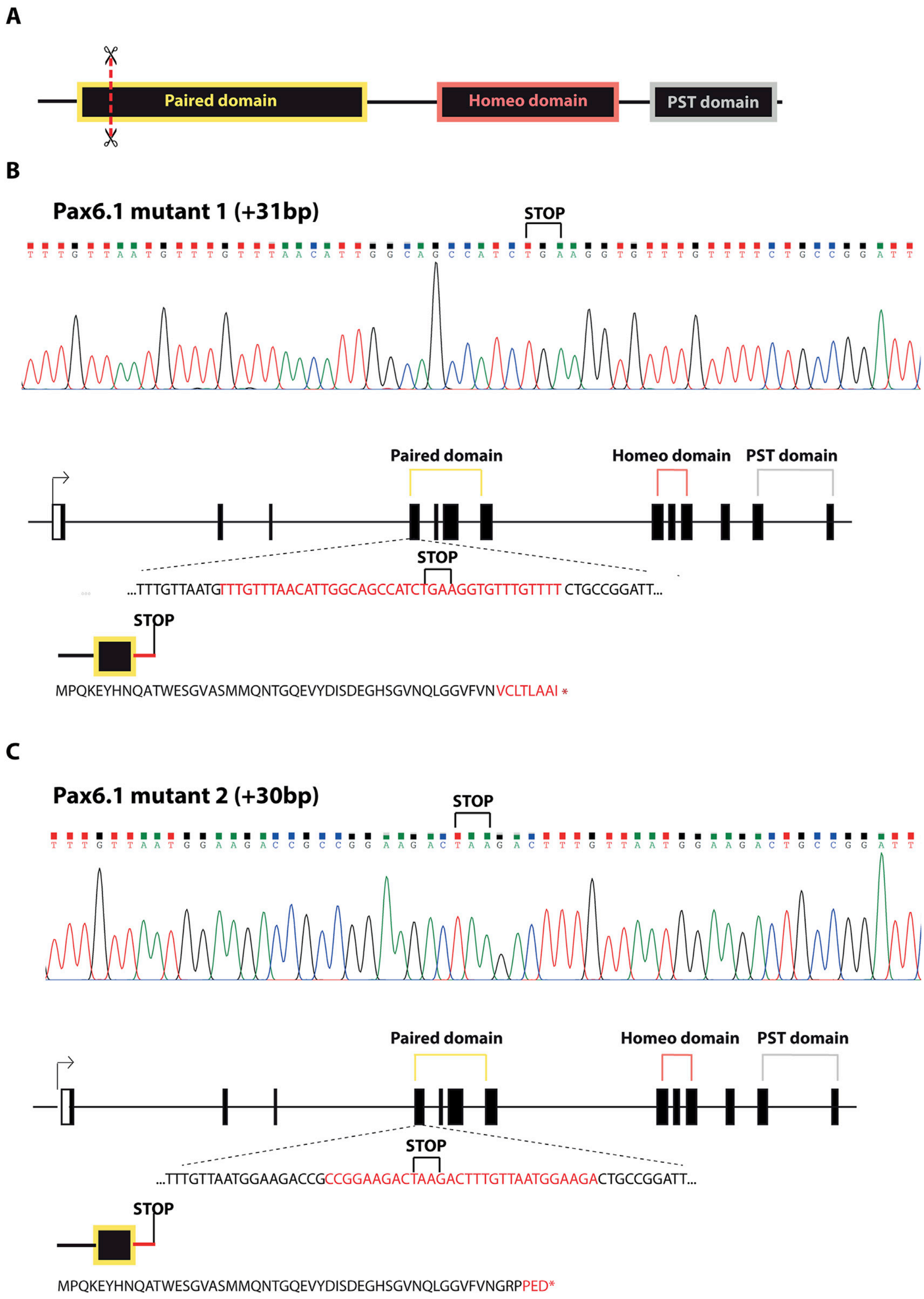

FIGURE 2
Schematic representation of *Pax6.1* gene editing resulting in the two lines carrying frameshift mutations in the paired domain. **(A)** Schematic diagram of the domain structure of Pax6.1 indicating the position of genome editing tools (scissors). **(B, C)** DNA sequencing and the associated protein sequences for alleles corresponding to Pax6.1 mutant1 and mutant2, respectively.

transcription factors, and thus functionally falls into a large group of paired-type homeodomain proteins. Gene expression analysis in medaka embryos supports previous phylogenetic analysis (Ravi et al., 2013) in assigning *Pax6.1* as a true orthologue of mammalian *Pax6* (Figure 1; (Ravi et al., 2013)). Like its mouse orthologue, *Pax6.1* is strongly expressed throughout the developing optic vesicle from the onset of eye formation. It also appears to be expressed from stage 21 and more conspicuously from stage 22 in the forming lens (Figure 1A). Expression of *Pax6.1* remains high throughout the neural retina and CMZ at later stages when differentiation is initiated (Figure 1B) and coincides with markers of ganglion and amacrine cells in the central retina at stage 32 (Supplementary Figure S1).

In contrast, the eye-specific expression of *Pax6.3* is limited to the posterior part of the optic vesicle at stages 18–22. Next, by stage 23 *Pax6.3* gene becomes sharply downregulated and its expression is completely absent from retina at later developmental stages. The two-color whole mount *in situ* hybridization confirmed that *Pax6.3* expression is clearly distinct from that of *Pax6.1* (Supplementary Figure S2). Finally, paired domain-less *Pax6.2* gene only becomes expressed in developing neural retina from stage 22 onwards (Figures 1A, B).

Pax6.1, Pax6.2, and *Pax6.3* genes have distinct evolutionary trajectories (Figure 1C). The subfunctionalization of the two *Pax6.1* paralogs in zebrafish was documented by Kleinjan et al. (2008), where both genes retained seemingly identical and redundant expression in the eye, while the *Pax6.1a* paralog lost its expression in the pancreas. In medaka, the evolutionary trajectory of the *Pax6.1* paralogs following the teleost-specific whole genome duplication led to the loss of one copy.

To determine the functional role of *Pax6.1* gene in eye development we analyzed medaka mutants generated by genome editing. Two independent frameshift alleles of *Pax6.1* were generated by targeting 5′end of the exon encoding the N-terminal half of paired domain thus producing a complete loss-of-function genotypes (designated *Pax6.1* KO mutant 1 and mutant 2; Figure 2). Viable adult homozygotes for *Pax6.1* mutant lines were not recovered (mutants die around hatching) and so the genetic crosses using heterozygotes were established in order to produce embryos for subsequent anatomical and gene expression. To confirm that no functional Pax6.1 paired domain-containing protein product is produced from the genetically manipulated alleles we analyzed RNAs products. It is well established that Pax6 orthologues undergo alternative splicing within paired domain encoding exons leading to either inclusion or exclusion of exon 5a (Kozmik et al., 1997; Fabian et al., 2015). As shown in Supplementary Figure S3, by analyzing RNA products from wild type and mutant alleles we have indeed detected both +5a and −5a variants (+5a variant labeled by asterisk). While the mutant 2 allele produced only the predicted products, the mutant 1 allele generated, in addition to the prediced product, an aberrant variant (designated X in Supplementary Figure S3). DNA sequencing revealed that the mutant1X RNA results from 91bp deletion effectively leading to the frameshift and a truncated Pax6.1 protein.

Combined, phylogenetic and expression data show that medaka *Pax6.1* gene is the true orthologue of *Pax6* in mammals. To study function of medaka *Pax6.1* we produced null alleles suitable for functional analysis.

Pax6.1 is required for lens placode induction in medaka

We first noted that approximately 25% of stage 28 embryos from *Pax6.1* mutant heterozygote crosses did not contain lenses. Since those embryos were genotyped as *Pax6.1* mutant homozygotes we next aimed to determine if lens induction step was affected in the absence of *Pax6* gene function as is the case in mice (Ashery-Padan et al., 2000). We were unable to detect lens placode marker gene expression prior to stage 21 (Supplementary Figure S4). However, by stage 21 a suite of genes encoding transcription factors implicated in vertebrate lens development (*Prox1a*, *MafB*, *c-Maf*, *FoxE3*) comenced expression in lens placode of wild type and *Pax6.1* mutant heterozygote fish (Pax6.1 HET) but not in *Pax6.1* mutant homozygotes (Pax6.1 KO) (Figure 3). Expression of *Prox1a*, *MafB*, *c-Maf*, *FoxE3*, and *Nrl* remained high in wild type and *Pax6.1* mutant heterozygotes but was not detectable in *Pax6.1* mutant homozygotes at stage 23 (Figure 3) consistent with the appearent absence of lens tissue.

Combined, our data show that *Pax6.1* mutants do not develop ocular lens.

Ectoderm enhancer (EE) is dispensable for lens development in medaka

We have previously shown that lens-specific expression in the mouse is achieved by the concerted action of two redundant (shadow) regulatory regions, EE and SIMO enhancers (Antosova et al., 2016). Simulatneous deletion of EE and SIMO phenocopies *Pax6* loss-of-function alleles (Ashery-Padan et al., 2000; Antosova et al., 2016). Although both of those shadow enhancers are evolutionarily conserved in zebrafish (Antosova et al., 2016) we were only able to identify EE but not SIMO in acanthopterygian lineage (medaka, stickleback, pufferfish) indicating either loss of the SIMO enhancer or significant sequence divergence. It is likely that EE plays a more dominant role over SIMO in regulating lens-specific expression of Pax6 in mice as smaller lenses are ocasionally observed in EE but not in SIMO homozygotes (Dimanlig et al., 2001; Antosova et al., 2016). This notion, together with the appearent absence of SIMO prompted us to genetically ablate EE in medaka in order to achieve tissue-specific (lens-restricted) knockout of *Pax6.1.* Unexpectedly, medaka fish carrying a homozygous deletion of EE presented a fully developed lens Figure 4).

Taken together, genetic ablation of EE, the evolutionarily conserved lens-specific enhancer in medaka, does not abrogate lens development.

Pax6.1 is required for the differentiation of retinal ganglion cells

We have previously shown that in mice *Pax6* gene is required cell-autonomously for the expansion of RPCs, and for the differentiation of all retina cell types (Klimova and Kozmik, 2014). Hence we first investigated whether retinal progenitor characteristics were maintained in *Pax6.1* mutants. We assessed the expression of known markers such as *Rx3* at stage 20, as well as *Rx1, Rx2, Sox2, Six3, Meis1, Meis2,* and *Mab21l2* at stage 22. However, the expression of none of these factors was significantly changed (Figure 5) indicating a normal emergence of RPC fate. The proliferative capacity of *Pax6.1*-deficient RPCs as assessed by the phospho-histone H3 marker immunohistochemistry also appeared normal (Supplementary Figure S5). We next tested the differentiation potential of *Pax6.1*-deficient RPCs by the whole-mount *in situ* hybridization at stage 28, stage32, and

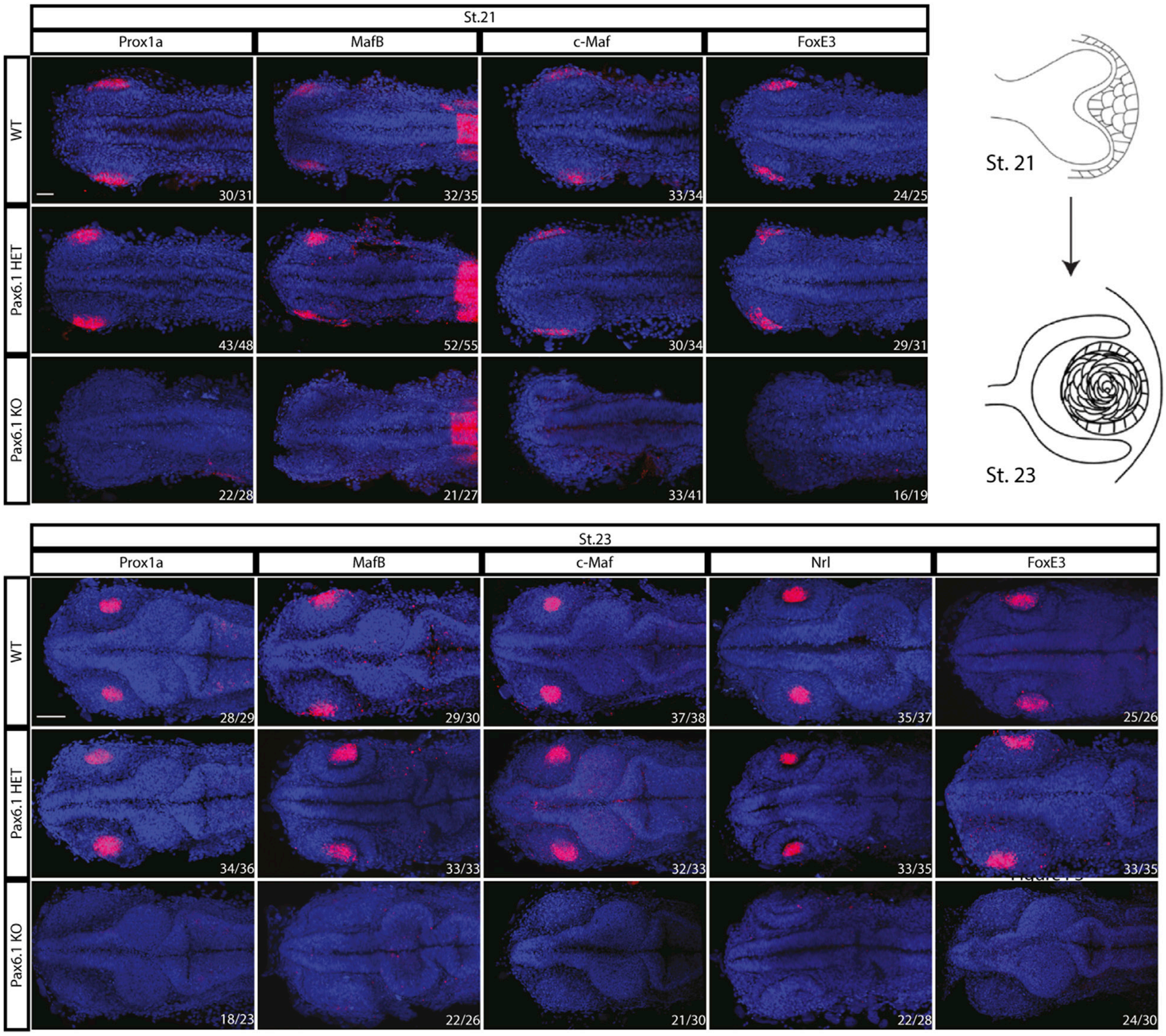

FIGURE 3
Comparison of the initiation of lens formation by *in situ* hybridization for selected lens markers at stage 21 (*Prox1a*, *MafB*, c-*Maf,* and *FoxE3*) and stage 23 (*Prox1a*, *MafB*, c-*Maf*, *Nrl,* and *FoxE3*). Signal in the presumptive lens region is present in the wildtype and *Pax6.1* heterozygote but not in the *Pax6.1* homozygote embryos. Scale bar: 50 μm.

stage 36 respectively, using a panel of specific markers (Figure 6; Supplementary Figure S6; Supplementary Figure S7). Expression of photoreceptor markers (such as *Otx1*, *Otx2, Crx, Nrl, NeuroD1, Nr2e3*, and *Rhodopsin*) confirmed the presence of this cell type in *Pax6.1* mutant retina (Figure 6). Likewise, the expression of markers typical for horizontal cells (*Prox1a*), amacrine cells (*Meis2*), bipolar cells (*Vsx2*), and Muller glia (*Sox2*) was detected in *Pax6.1* mutant retina at levels comparable to wild type fish (Figure 6). In contrast, retinal ganglion markers *Ath5*, *Brn3c*, and *Isl2* were completely absent from *Pax6.1*-deficient retina at stage 32 (Figure 7). Unlike the situation in mammals, fish retina grows continuously due to retinal stem cells located at CMZ. These cells actively migrate towards the middle part of retina and differentiate into any retinal cell type. To exclude the formal possibility that the lack of a more profound phenotype in Pax6.1-deficient retina is due to CMZ-derived differentiation program we analyzed specific markers in stage 28, i.e. before the cells from CMZ start to migrate. However, marker gene expression at stage 28 corroborated our conclusion that retinal ganglion cell marker is the only affected one when wild type and Pax6.1-deficient retinae are compared (Supplementary Figure S7).

Taken together, these results indicate that the overall differentiation potential of Pax6.1-deficient RPCs is not severely compromised, and the only cell type affected by the absence of Pax6.1 transcription factor are retinal ganglion cells.

Mild phenotype in Pax6.1-deficient retina is not due to the compensatory effects caused by *Pax6.3* paralogue

Pax6.1 and *Pax6.3* paralogues are structurally similar and encode transcription factors with similar properties when tested

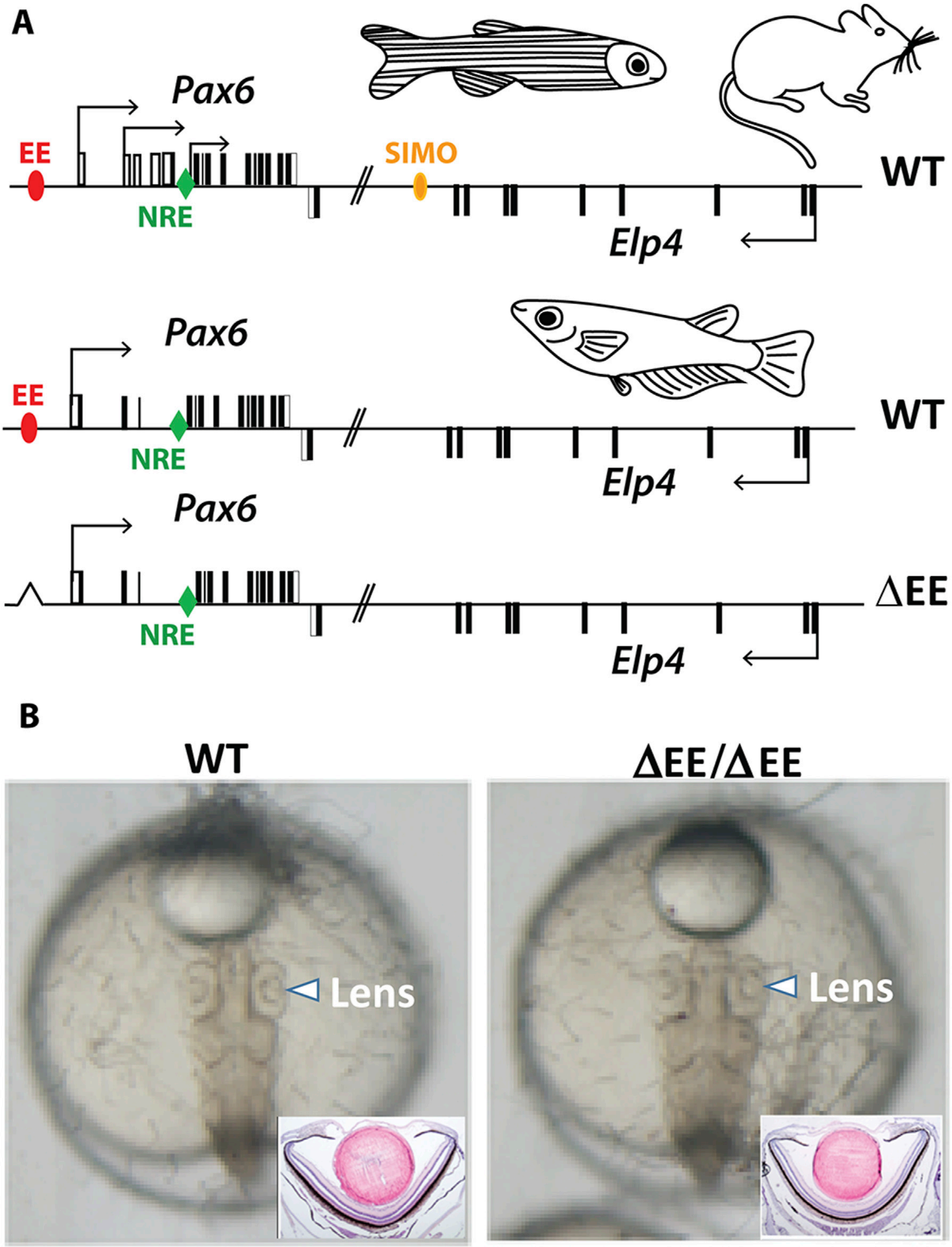

FIGURE 4
Genome editing of medaka ectoderm enhancer (EE). **(A)** Schematic view of Pax6 locus in mouse, zebrafish, and medaka. The position of the shadow enhancers EE and SIMO is shown by red and yellow ovals, respectively. The position of the evolutionarily conserved retina-specific enhancer NRE (aka α-enhancer) is shown by green rhomb. **(B)** Lens development proceeds normally in the fish containing EE homozygote deletion.

using Pax-responsive luciferase reporter gene *in vitro* (Supplementary Figure S8). To determine, if the deletion of *Pax6.1* gene caused compensatory upregulation of *Pax6.3* expression we analyzed its expression from stage 18 through stage 24. As shown in Supplementary Figure S9 the expression of *Pax6.3* was not enhanced but rather reduced in the *Pax6.1*-deficient retina as compared to the wild type. To examine a possible genetic redundancy of *Pax6.1* and *Pax6.3* we used genome editing to

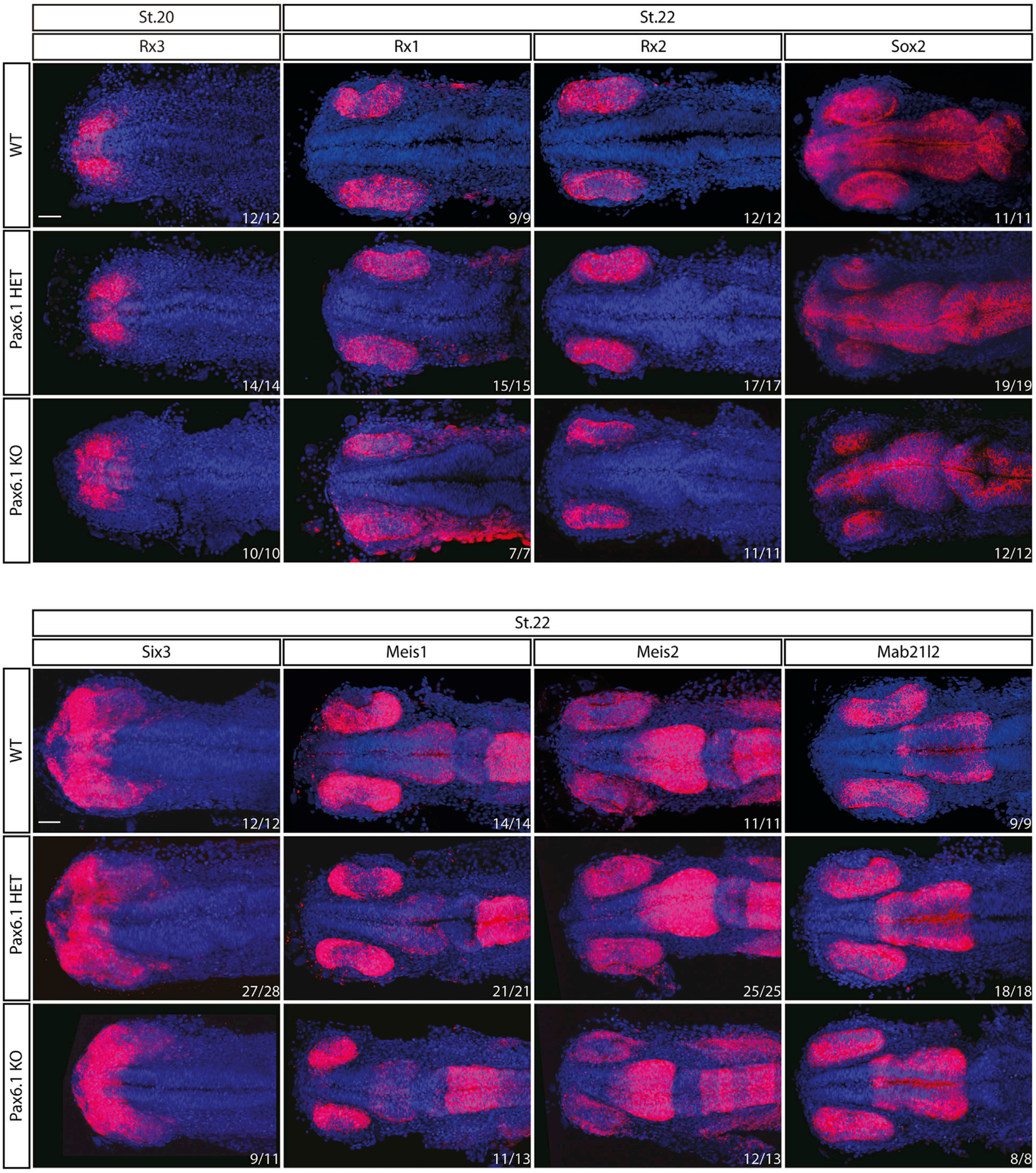

FIGURE 5
In situ hybridization analysis of *Rx3, Rx1, Rx2, Sox2, Six3, Meis1, Meis2,* and *Mab21l2* gene expression during the early retina development (stage 20 and stage 22). The expression pattern of none of the genes is changed in *Pax6.1* homozygote mutant as compared to wildtype or *Pax6.1* heterozygote. Scale bar: 50 μm.

mutagenize *Pax6.3* gene (Supplementary Figure S10). We next analyzed a general morphology (Supplementary Figure S11) and marker gene expression in the developing retina of single *Pax6.3* mutant (Supplementary Figure S12) and of *Pax6.1/Pax6.3* double mutant (Figure 8). We have observed that the lens was present in the *Pax6.3* single mutants and that the overal retina size has not changed in *Pax6.1/Pax6.3* double mutants as compared to the *Pax6.1* single mutants (Supplementary Figure S11). All markers interrogated in the *Pax6.3* mutant retina were expressed including retinal ganglion cell-specific *Brn3c* (Supplementary Figure S12). Finally, retinal ganglion cells were the only cell type conspicuously absent in the *Pax6.1/Pax6.3* double mutant retina (Figure 8).

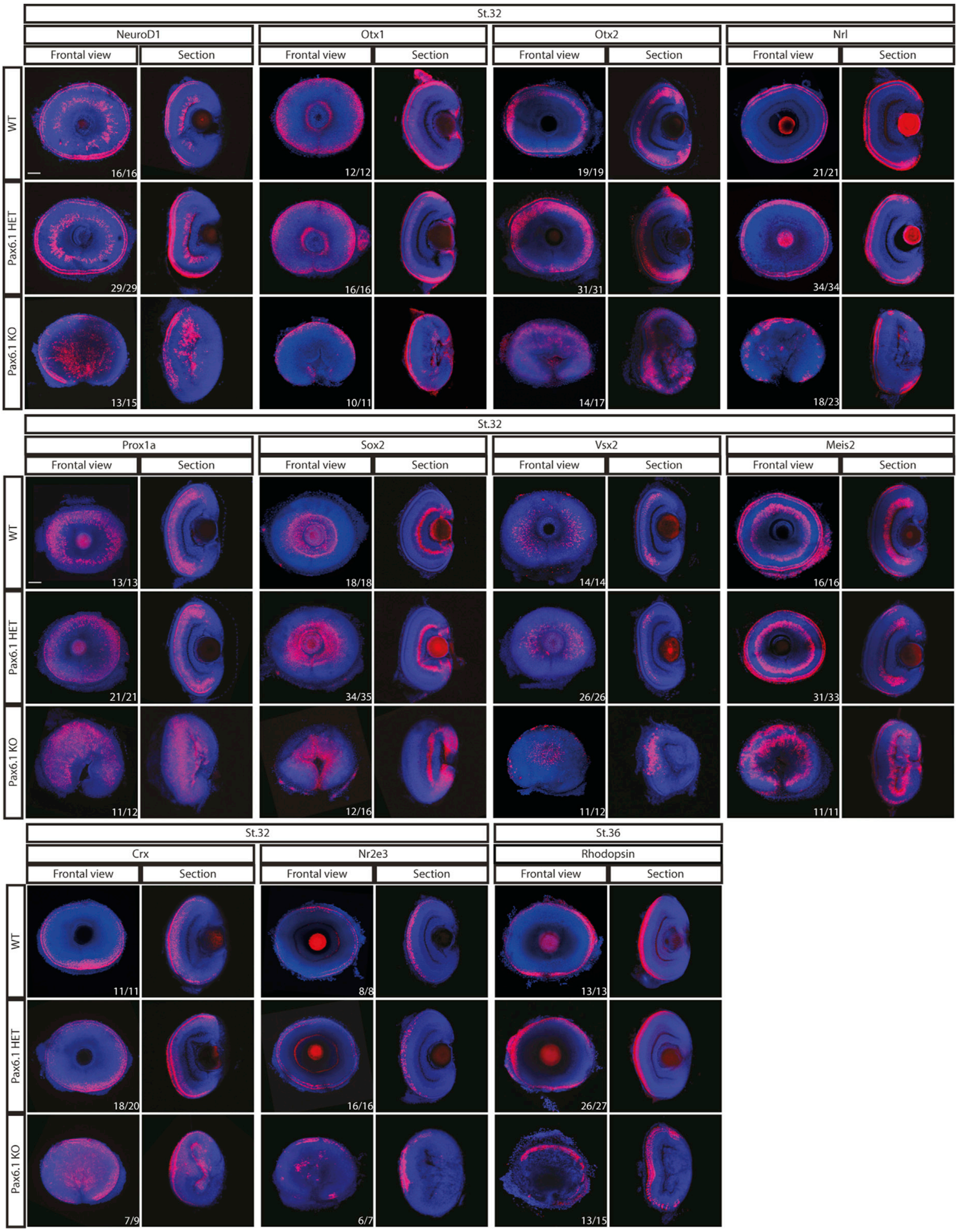

FIGURE 6
In situ hybridization analysis of gene expression in the differentiated retina (stage 32 and stage 36). Comparison of expression patterns of markers for specific retina cell types (*Prox1a*–horizontal cells; *Meis2* – amacrine cells; *Vsx2*-bipolar cells; *Sox2* - Muller glia cells; *Otx1*, *Otx2*, *Nrl*, *Rx2*, *NeuroD1*, *Crx*, *Nr2e3*, and *Rhodopsin* - photoreceptors) in the wild type, *Pax6.1* heterozygotes, and homozygotes, respectively. The expression of markers was not conspicuously altered in the *Pax6.1*-deficient retina as compared to the wild type. Scale bar: 50 μm.

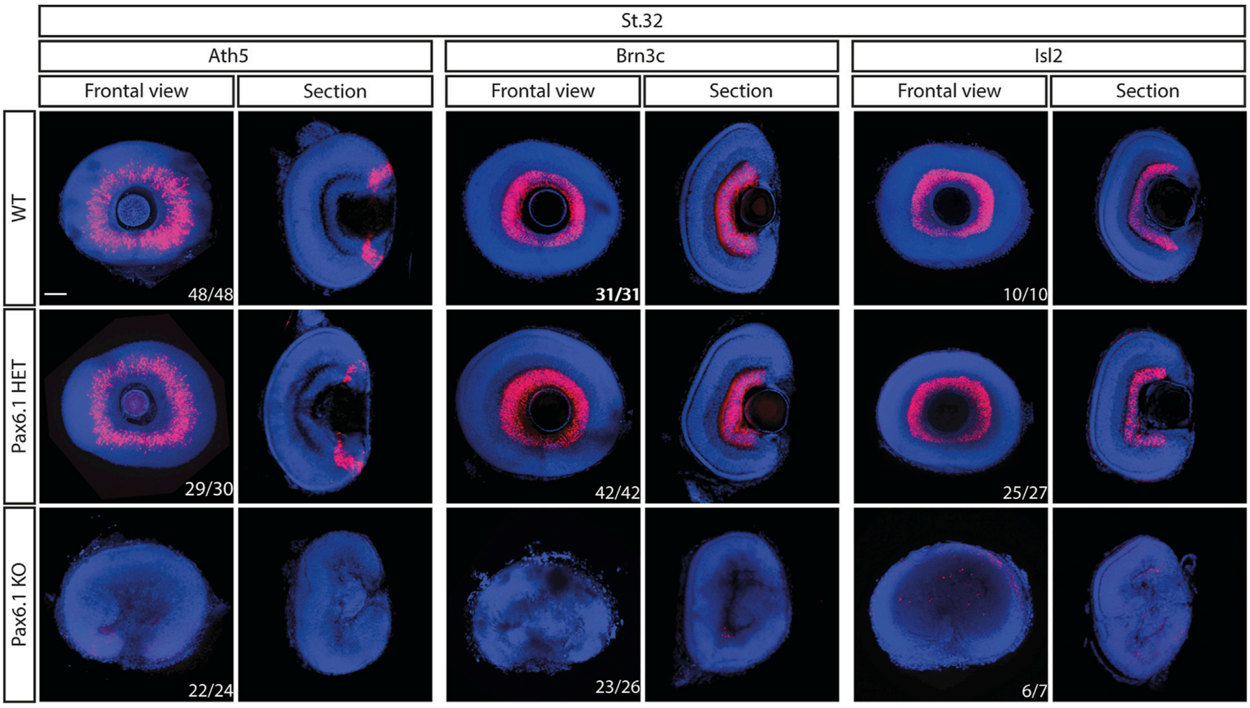

FIGURE 7
Comparison of expression patterns of retinal ganglion cell markers *Ath5*, *Brn3c*, and *Isl2* in the wild type, *Pax6.1* heterozygotes, and homozygotes at stage 32. None of the retinal ganglion cell markers shown here is expressed in *Pax6.1*-deficient retina Scale bar: 50 μm.

Combined, our data strongly suggest that the relatively mild retina phenotype observed in Pax6.1 medaka mutant is not due to (i) compensatory mechanisms occuring at the transcriptional level or (ii) the genetic redundancy.

Discussion

Our genetic study, capitalizing on the reduced *Pax6* gene complement in medaka fish, illuminates conserved and divergent roles of *Pax6* orthologues in vertebrate eye development. Somewhat counterintuitively we found that lens-specific role of Pax6 is more evolutionarily conserved among vertebrates than the role of *Pax6* in retina development (Figure 9A). Ocular lens is an upgrade of the animal visual system that occured multiple times during animal evolution (Jonasova and Kozmik, 2008). The vertebrate camera eyes have been acquired independently to other phyla with image-forming vision. The lens acquisition seems to have occurred in the earliest period of the vertebrate lineage, because the fossil stem vertebrates appear to have possessed eyes with lenses (Shu et al., 1999; Shu et al., 2003; Morris and Caron, 2014). Extant representatives of basal vertebrate lineages (cyclostomes) either do not have lenses due to the presumed degeneration as in hagfish, or in the case of lampreys possess flattened immature lenses at the larval stages that develop into fully functional lens only after metamorphosis (Suzuki and Grillner, 2018).

The nature of the possible conserved role of *Pax6* in vertebrate lens formation is currently enigmatic. For example, there is a clear distinction in lens morphogenesis among present-day vertebrates - lens development procceeds via delamination in fish but through invagination in mammals or birds. *Pax6* appears to be a critical gene for shroom-mediated lens invagination of mammalian lens (Plageman et al., 2010), a role clearly not needed in fish lens development. Furthermore, the well-established role of *Pax6* in lens crystallin gene regulation (Cvekl and Piatigorsky, 1996; Cvekl et al., 2015; Cvekl et al., 2017) represents the case of convergent evolution since the crystallin genes are often taxon specific, and Pax6 transcription factor has been therefore independently co-opted in different lineages.

Medaka and zebrafish lineages have undergone an estimated 110 million years of independent evolution (Wittbrodt et al., 2002; Furutani-Seiki and Wittbrodt, 2004) which in medaka apparently lead to the loss of one of the *Pax6.1* copies produced by teleost-specific whole genome duplication. The presence of two *Pax6.1* paralogous in zebrafish genome, *Pax6.1a* and *Pax6.1b* hampers genetic analysis. Furthermore, the duplicated zebrafish *Pax6.1* genes have subfunctionalized by cis-regulatory divergence (Kleinjan et al., 2008) which further complicates interpretation of *Pax6* gene function in the main fish model organism. Missense mutation (L244P) in the homeodomain of zebrafish *Pax6.1b* gene in *sunrise* mutant causes anterior chamber defects (Kleinjan et al., 2008; Takamiya et al., 2015). However, the true genetic loss-of function mutants of both *Pax6a* and *Pax6b* in zebrafish have not been described. However, Takamiya et al. (2020) used *Pax6.1a*/*Pax6.1b*^{sunrise} double mutants to demonstrate the role of *Pax6.1* gene in the control of neural crest cells during development of the anterior segment. The severe anterior segment dysgenesis phenotype in *Pax6.1a*/*Pax6.1b*^{sunrise} homozygote mutants was

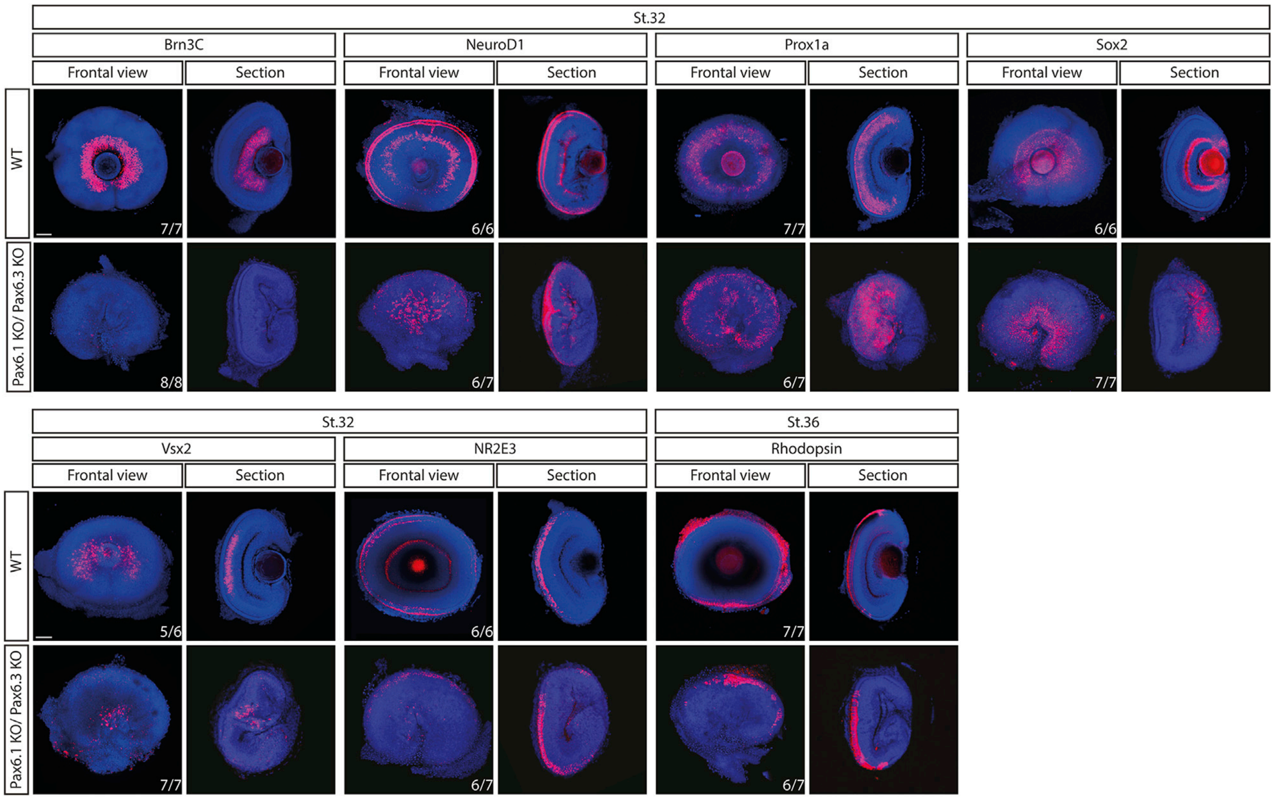

FIGURE 8
Comparison of expression patterns of *Brn3c, NeuroD1, Prox1a, Sox2, Vsx2, Nr2e3,* and *Rhodopsin* marker genes in the wild type and *Pax6.1/Pax6.3* double homozygote mutants. The retinal ganglion cell-specific expression of *Brn3c* is lost while the expression of the remaining markers is preserved in *Pax6.1/Pax6.3*-deficient retina. Scale bar: 50 µm.

characterized by the absence of the lens, corneal endothelium, and vasculature. The iridocorneal angle were missing in the compound *Pax6.1a/Pax6.1b*^{sunrise} mutants and the eye structure was filled with abnormal ocular mesenchymal cells. The results indicated that *Pax6.1* paralogs facilitate the expression of guidance molecules in the optic cup and its surrounding mesenchymal cells. Some defects in the anterior segment of *Pax6.1a/Pax6.1b*^{sunrise} homozygote mutants were at least partially due to the absence of the lens, which serves as a crucial source of further signaling molecules, such as TGFβ. Severe anterior segment dysgenesis in *Pax6.1a/ Pax6.1b*^{sunrise} homozygous mutants could in fact be alleviated by transplantation of a wild type lens. We have observed that the lack of lens in Pax6.1 medaka mutants causes a structural collapse of the anterior chamber (Supplementary Figure S13). It is of note that even though a full-length Pax6.1b protein is made from *sunrise* allele, the compound *Pax6.1a/Pax6.1b*^{sunrise} homozygotes did not appear to possess a conspicuous ganglion cell layer indicating an extreme sensitivity of this cell type to *Pax6* gene function.

Previous study describing the loss of lens structure in medaka *Pax6.1* mutant lacked molecular characterization of the observed phenotype such as marker gene expression or description of the onset of the defect (Pan et al., 2023). Likewise, no characterization of the retina tissue in *Pax6.1* mutant medaka was performed (Pan et al., 2023). We found that lens development in *Pax6.1* mutant medaka is arrested at the onset of lens specification since even the earliest lens markers that we used were not expressed in the homozygote mutant. It is well established that *Pax6* is required cell autonomously for lens development in mice (Ashery-Padan et al., 2000; Antosova et al., 2016). In addition, it was shown using tissue-specific ablation in mice that expression of *Pax6* in the retina compartment at the optic vesicle stage is required for lens placode induction and subsequent lens development (Klimova and Kozmik, 2014).

Conditional ablation of genes using Cre/loxP methodology used routinely in the mouse model is not available in medaka. Hence, realizing that SIMO shadow enhancer is not present in medaka (and in other Acanthopterygii fish), and EE appears to be the sole lens placode enhancer of *Pax6.1* gene, we attempted to generate lens-specific knockout of *Pax6.1* by deleting EE enhancer region. This experiment would allow to bypass lethality of *Pax6.1* whole-body knockout, and would help to define if *Pax6.1* is required for lens induction in fish in a cell-autonomous manner. The lack of lens phenotype in EE mutant medaka has two possible explanations that are not necesarilly mutually exclusive. First of all, it is possible that retina-derived *Pax6.1* is required for lens induction in fish as is the case in the mouse (Klimova and Kozmik, 2014). Another possibility is that another shadow enhancer evolved within Acanthopterygii fish to replace SIMO which has deteriorated.

The basic cellular composition of retina of vertebrates is highly conserved (Lamb, 2013). The adult lamprey, a representative of Agnathans, already contains all types of retinal cells found in jawed vertebrates, distributed into three main nuclear layers and two plexiform layers (Lamb, 2013; Suzuki and Grillner, 2018).

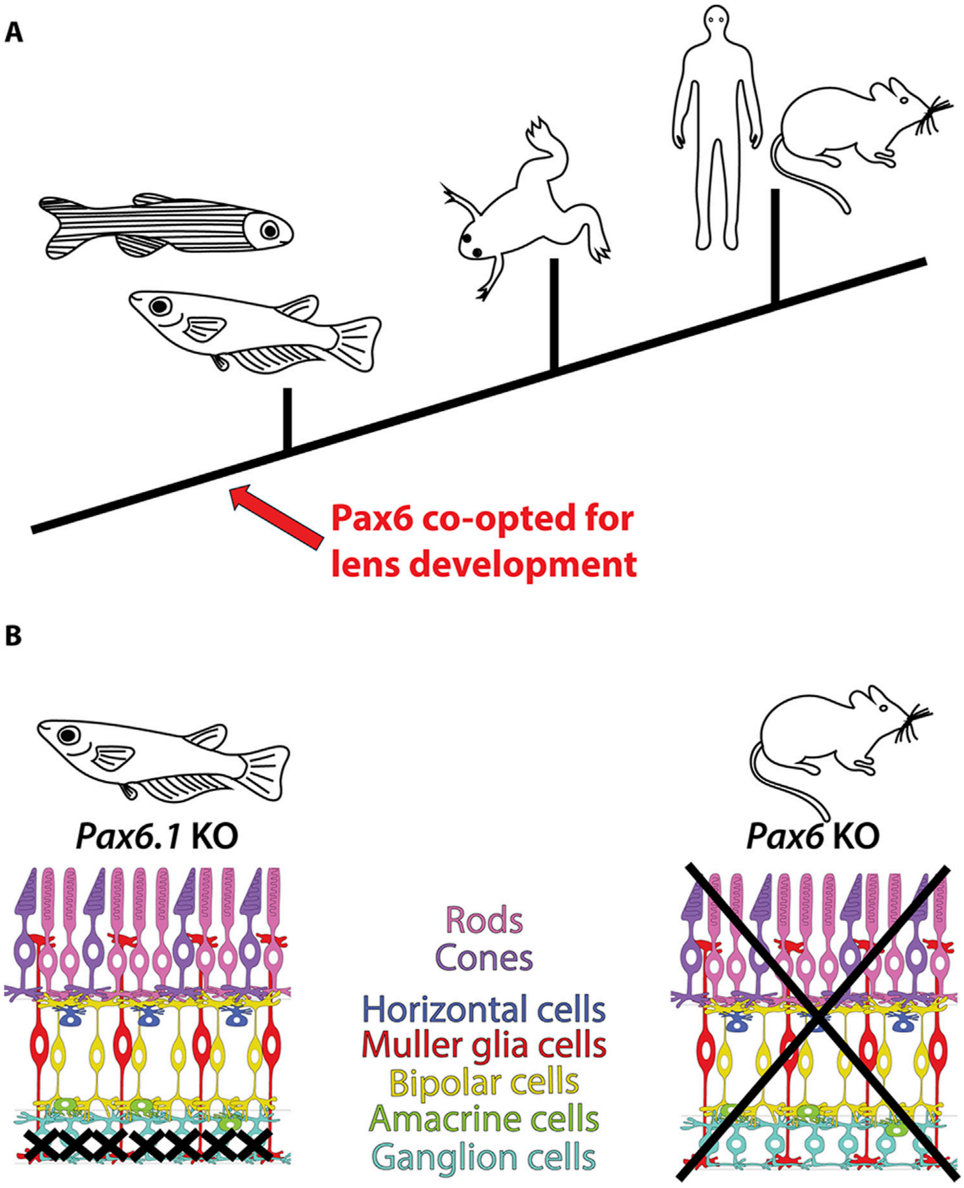

FIGURE 9
Conserved and divergent roles of Pax6 in vertebrate eye development. **(A)** The lens-specific function of Pax6 seems to be evolutionarily conserved among jawed vertebrates, as evidenced by data from fish (this study and (Kleinjan et al., 2008; Takamiya et al., 2020)), frog (Nakayama et al., 2015), mouse (Hill et al., 1991; Ashery-Padan et al., 2000; Antosova et al., 2016), and human (Glaser et al., 1992). **(B)** Divergent roles of *Pax6* in retinal development in mice and medaka fish. In mice, Pax6 is essential for the formation of all retinal cell types (Klimova and Kozmik, 2014), whereas in medaka fish, only retinal ganglion cells are critically dependent on Pax6 gene function (this study).

Moreover, in all vertebrates analyzed so far the generation of retinal cell types follows the same stereotyped birth order. Since the spatiotemporal expression of the key regulatory genes is remarkably similar among model vertebrates, it is generally assumed that the gene regulatory networks involved in the orchestrating eye development may be largely conserved (Zhang et al., 2023). Given the prominent role of *Pax6* in mouse retina development (Marquardt et al., 2001; Klimova and Kozmik, 2014) the relatively mild phenotype observed in medaka *Pax6.1* mutant is intriguing. We have previously found that the first manifestation of abnormal retina development in *Pax6* mutant mice is hypocelularity caused by the loss of RPC proliferation and extended cell cycle length leading to the complete absence of retina tissue by birth (Klimova and Kozmik, 2014). This is clearly distinct from the situation in the medaka fish (Figure 9B). Based on phospho-histone H3 immunostaining *Pax6.1*-deficient RPCs appear to proliferate normally, and as a result the relatively normal size retina is present in the *Pax6.1* mutant larvae. The most striking result of our study was the strict dependance of the Ath5/Brn3c retinal ganglion cell lineage on *Pax6.1* function combined with the fact that differentiation into all other retinal cell types was able to procceed in *Pax6.1* mutants. It is worth noting that transcriptional regulation of *Ath5* in retinal ganglion cells is so far the best example of the evolutionarily conserved mechanism by which *Pax6* operates in the vertebrate retina (Riesenberg et al., 2009; Willardsen et al., 2009). We consider it unlikely that the absence of an effect on non-RGC cell differentiation in *Pax6.1* mutant is due to redundancy with *Pax6.2* gene, given (i) its limited expression pattern and (ii) the absence of the paired domain, which is crucial for retinal differentiation in mice. Nonetheless, the potential redundant roles of *Pax6.2* and *Pax6.1* in medaka retina development merit further investigation. It remains to be determined what adaptive changes were aquired in the teleost and mammalian lineages that are responsible for the distinct requirements for *Pax6* function in RPC expansion and execution of the complete retinal differentiation program. In *Xenopus*, mutations producing truncated Pax6 proteins disrupt forebrain regionalization but do not entirely eliminate eyes. Instead, they result in the development of eye-like structures lacking lenses (Nakayama et al., 2015). It was hypothesized by Nakayama et al. that an additional *Pax6* gene (*Pax6.2*) plays a role in mitigating the degree of the retinal phenotype. Given the results of our study, it is however plausible that *Pax6* gene in *Xenopus* is to some extent not needed for normal retina development indicating that the strict requirement for *Pax6* in retinogenesis arose only after the split of the amphibians from amniots.

Materials and methods

Animal husbandry

Oryzias latipes (medaka) embryos of the Cab inbred strain (Loosli et al., 2000) were used for all experiments. Embryos were collected daily immediately after spawning. Embryonic stages were determined according to Iwamatsu (2004). Housing of animals and *in vivo* experiments were performed after approval by the Animal Care Committee of the Institute of Molecular Genetics (study ID#84/2014 and ID#14/2017) and in compliance with the European Communities Council Directive of 24 November 1986 (86/609/EEC).

Genome editing

TALEN- and CRISPR-based tools were designed and prepared as described previously (Antosova et al., 2016). Polyadenylated TALEN mRNA was prepared using mMESSAGE mMACHINE T7 ULTRA Kit (Ambion) and was injected into one-cell stage medaka. Oligonucleotides used to make sgRNA constructs were cloned into pT7-gRNA (pT7-gRNA was a gift from Wenbiao Chen, Addgene plasmid # 46759). Cas9 mRNA was prepared using mMESSAGE mMACHINE T7 ULTRA Kit (Ambion) using plasmid pCS2-nCas9n (pCS2-nCas9n was a gift from Wenbiao Chen, Addgene plasmid # 47929). The sgRNAs were transcribed using MEGAshortscript kit (Ambion). A mixture of Cas9 mRNA (100 ng/μL) and specific sgRNAs (25 ng/μL each) was injected into one-cell stage medaka. Pax6.1 and Pax6.3 TALENs targeted the sequence TTGGTGGCGTGTTTGTTAAtggaagaccgctgccGGATTCCACCAGGCAGAAAA and TGGGAGACCTCTGCCCGACTccaccaggcagaagaTCGTGGAGCTGGCCCACA, respectively. Pax6.1 sgRNA used to generate line 2 targeted the sequence TGTTAATGGAAGACCGCTGCCGG (PAM sequence underlined). Medaka ectoderm enhancer (EE) was deleted using sgRNAs targeting the sequences CGAACTGCATCTGAAAGTGCAGG and TAATGTCTCGATCCAGGGCCAGG (PAM sequence underlined). The injecting setup was as follows: pressure injector Femtojet (Eppendorf), micromanipulator TransferMan NK (Eppendorf), borosilicate glass capillaries (GC100F10, Harward Apparatus), stereomicroscopes (Olympus SZX7, SZX9). The mature F0 fish were crossed with wild-type fish, and their F1 progeny was assayed for mutations by DNA sequencing. Stable lines of mutagenized fish were established and the subsequent generations were genotyped by PCR. To identify transcripts generated from mutated Pax6.1 alleles the total RNA was isolated using TRIZOL reagent from eye-containing head region of medaka larvae. The single stranded cDNA produced by SuperScript VILO cDNA synthesis kit was subjected to PCR amplification using forward primer ACCACAGGCGAAAGCCTACAT located in the 5′UTR and reverse primers Rev1 ATCTTGCTCACGCAGCCGTT or Rev2 CTGTCCTGGCACTGATGTT. The products were cloned into TOPO vector and sequenced.

Whole-mount RNA *in situ* hybridization

Embryos were fixed overnight at 21°C with fixative solution (4% formaldehyde/PBS + 0.1% Tween), dechorionated and stored in methanol at −20°C. During the experiment, samples were rehydrated and treated with Proteinase K to increase penetration (timing was adjusted according to embryonic stage). After refixation with fixative solution, embryos were further processed for overnight hybridization with digoxigenin (DIG) and/or fluorescein (FITC) labelled antisense riboprobes on 65°C. Next day, samples were incubated with anti-DIG or FITC-Fab fragments (Roche) conjugated with alkaline phosphatase or peroxidase, respectively. The coloring reaction was carried out by either VectorBlue (VECTOR Laboratories) or TSA™ Plus Fluorescein System (PerkinElmer). All samples were stained with DAPI and afterward mounted in 86% glycerol/1.5% low gelling point agarose (Serva) for imaging or 4% low gelling point agarose (Serva) for vibratome sectioning.

Immunohistochemistry

Embryos were fixed overnight at 21°C with fixative solution (4% formaldehyde/PBS + 0.1% Tween) and afterwards dechorionated. Dechorionation was followed by immediate whole-mount immunohistochemistry procedure: Embryos were treated with ice-cold acetone for 7 min, afterwards washed with PBT (PBS + 0.1% Tween) and blocked overnight at 4°C with the Phosphorylated histone H3 (PH3) antibody (Merck) diluted in 10% BSA/PBS + 0.1% Tween (1:500). Next morning, samples were washed several times with PBT and incubated with the Alexa647 antibody (ThermoFisher) for 1.5 h. Subsequently, samples were stained with DAPI and sectioned on a vibratome machine (Leica). Sectioned samples were assessed by light microscopy (high-speed confocal dragonfly spinning disc microscope (Andor)). Total number of cells (stained by DAPI) as well as the number of proliferating cells (stained by PH3) in the retina of 8 wild type and 8 Pax6.1 knock out embryos was calculated manually using ImageJ software (Schindelin et al., 2012). A percentage score was obtained by dividing the number of proliferating cells by the total number of cells for each sample.

Cell nucleus staining

Embryos at selected stages were fixed overnight at 21°C with fixative solution (4% formaldehyde/PBS + 0.1% Tween) and afterwards dechorionated. Cell nucleus staining was achieved by overnight DAPI (Roche, 1:1,000) staining. Stained embryos were stored in 86% glycerol or embedded in 4% low gelling point agarose (Serva).

Vibratome sectioning

Embryos after the *in situ* hybridization, immunohistochemistry staining or cell nucleus (DAPI) staining were sectioned using a vibratome machine (Leica). 50 µm thick sections were obtained and mounted in 86% glycerol on slides.

Imaging

All samples were photographed on a high-speed confocal dragonfly spinning disc microscope (Andor). Pictures were processed by ImageJ software (Schindelin et al., 2012).

Reporter gene assays

The cell culture and transient cell transfection was performed as previously described (Klimova et al., 2015). CMV-based expression vectors encoding either Pax6.1, Pax6.2, or Pax6.3 were co-transfected with Pax6-resposive reporter gene (−350GluLuc (Schwaninger et al., 1993)) and the β-galactosidase expression plasmid serving to normalize the transfection efficiency. Graph and statistical analysis of triplicate biological assays were generated in GraphPad Prism software.

Data availability statement

The raw data supporting the conclusions of this article will be made available by the authors, without undue reservation.

Ethics statement

The animal study was approved by Animal Care Committee of the Institute of Molecular Genetics. The study was conducted in accordance with the local legislation and institutional requirements.

Author contributions

SM: Data curation, Formal Analysis, Investigation, Methodology, Validation, Visualization, Writing–review and editing. ZK: Conceptualization, Data curation, Formal Analysis, Funding acquisition, Investigation, Methodology, Project administration, Resources, Supervision, Validation, Writing–original draft, Writing–review and editing.

Funding

The author(s) declare that financial support was received for the research, authorship, and/or publication of this article. This work was supported by Czech Science Foundation grant 21-27364S awarded to Z.K.

Acknowledgments

We thank Wenbiao Chen for pT7-gRNA (Addgene plasmid # 46759) and pCS2-nCas9n (Addgene plasmid # 47929), and Walter Knepel for −350GluLuc. We thank F. Weisz and P. Kasparek for help and advice during preparation of TALEN constructs. We acknowledge IMG institutional support RVO: 68378050-KAV-NPUI, the Electron Microscopy Core Facility and the Light Microscopy Core Facility, IMG, Prague, Czech Republic, supported by grants “National Infrastructure for Biological and Medical Imaging” (MEYS–LM2023050) and “Modernization of the national infrastructure for biological and medical imaging Czech-BioImaging” (MEYS–CZ.02.1.01/0.0/0.0/18_046/0016045, for their support with the microscopy data presented herein.

Conflict of interest

The authors declare that the research was conducted in the absence of any commercial or financial relationships that could be construed as a potential conflict of interest.

Publisher’s note

Supplementary material

The Supplementary Material for this article can be found online at: https://www.frontiersin.org/articles/10.3389/fcell.2024.1448773/full#supplementary-material

References

Agathocleous, M., and Harris, W. A. (2009). From progenitors to differentiated cells in the vertebrate retina. *Annu. Rev. Cell Dev. Biol.* 25, 45–69. doi:10.1146/annurev.cellbio.042308.113259

Antosova, B., Smolikova, J., Klimova, L., Lachova, J., Bendova, M., Kozmikova, I., et al. (2016). The gene regulatory network of lens induction is wired through meis-dependent shadow enhancers of Pax6. *PLoS Genet.* 12 (12), e1006441. doi:10.1371/journal.pgen.1006441

Ashery-Padan, R., Marquardt, T., Zhou, X., and Gruss, P. (2000). Pax6 activity in the lens primordium is required for lens formation and for correct placement of a single retina in the eye. *Genes Dev.* 14 (21), 2701–2711. doi:10.1101/gad.184000

Burmeister, M., Novak, J., Liang, M. Y., Basu, S., Ploder, L., Hawes, N. L., et al. (1996). Ocular retardation mouse caused by Chx10 homeobox null allele: impaired retinal progenitor proliferation and bipolar cell differentiation. *Nat. Genet.* 12 (4), 376–384. doi:10.1038/ng0496-376

Cepko, C. L. (1999). The roles of intrinsic and extrinsic cues and bHLH genes in the determination of retinal cell fates. *Curr. Opin. Neurobiol.* 9 (1), 37–46. doi:10.1016/s0959-4388(99)80005-1

Cepko, C. L., Austin, C. P., Yang, X., Alexiades, M., and Ezzeddine, D. (1996). Cell fate determination in the vertebrate retina. *Proc. Natl. Acad. Sci. U. S. A.* 93 (2), 589–595. doi:10.1073/pnas.93.2.589

Cvekl, A., and Callaerts, P. (2017). PAX6: 25th anniversary and more to learn. *Exp. Eye Res.* 156, 10–21. doi:10.1016/j.exer.2016.04.017

Cvekl, A., McGreal, R., and Liu, W. (2015). Lens development and crystallin gene expression. *Prog. Mol. Biol. Transl. Sci.* 134, 129–167. doi:10.1016/bs.pmbts.2015.05.001

Cvekl, A., and Piatigorsky, J. (1996). Lens development and crystallin gene expression: many roles for Pax-6. *Bioessays* 18 (8), 621–630. doi:10.1002/bies.950180805

Cvekl, A., Zhao, Y., McGreal, R., Xie, Q., Gu, X., and Zheng, D. (2017). Evolutionary origins of Pax6 control of crystallin genes. *Genome Biol. Evol.* 9 (8), 2075–2092. doi:10.1093/gbe/evx153

Czerny, T., Halder, G., Kloter, U., Souabni, A., Gehring, W. J., and Busslinger, M. (1999). Twin of eyeless, a second Pax-6 gene of Drosophila, acts upstream of eyeless in the control of eye development. *Mol. Cell* 3 (3), 297–307. doi:10.1016/s1097-2765(00)80457-8

Diacou, R., Zhao, Y., Zheng, D., Cvekl, A., and Liu, W. (2018). Six3 and Six6 are jointly required for the maintenance of multipotent retinal progenitors through both positive and negative regulation. *Cell Rep.* 25 (9), 2510–2523. doi:10.1016/j.celrep.2018.10.106

Dimanlig, P. V., Faber, S. C., Auerbach, W., Makarenkova, H. P., and Lang, R. A. (2001). The upstream ectoderm enhancer in Pax6 has an important role in lens induction. *Development* 128 (22), 4415–4424. doi:10.1242/dev.128.22.4415

Dupacova, N., Antosova, B., Paces, J., and Kozmik, Z. (2021). Meis homeobox genes control progenitor competence in the retina. *Proc. Natl. Acad. Sci. U. S. A.* 118 (12), e2013136118. doi:10.1073/pnas.2013136118

Fabian, P., Kozmikova, I., Kozmik, Z., and Pantzartzi, C. N. (2015). Pax2/5/8 and Pax6 alternative splicing events in basal chordates and vertebrates: a focus on paired box domain. *Front. Genet.* 6, 228. doi:10.3389/fgene.2015.00228

Force, A., Lynch, M., Pickett, F. B., Amores, A., Yan, Y. L., and Postlethwait, J. (1999). Preservation of duplicate genes by complementary, degenerative mutations. *Genetics* 151 (4), 1531–1545. doi:10.1093/genetics/151.4.1531

Fuhrmann, S. (2010). Eye morphogenesis and patterning of the optic vesicle. *Curr. Top. Dev. Biol.* 93, 61–84. doi:10.1016/B978-0-12-385044-7.00003-5

Furutani-Seiki, M., and Wittbrodt, J. (2004). Medaka and zebrafish, an evolutionary twin study. *Mech. Dev.* 121 (7-8), 629–637. doi:10.1016/j.mod.2004.05.010

Glaser, T., Walton, D. S., and Maas, R. L. (1992). Genomic structure, evolutionary conservation and aniridia mutations in the human PAX6 gene. *Nat. Genet.* 2 (3), 232–239. doi:10.1038/ng1192-232

Hatakeyama, J., and Kageyama, R. (2004). Retinal cell fate determination and bHLH factors. *Semin. Cell Dev. Biol.* 15 (1), 83–89. doi:10.1016/j.semcdb.2003.09.005

Hill, R. E., Favor, J., Hogan, B. L., Ton, C. C., Saunders, G. F., Hanson, I. M., et al. (1991). Mouse small eye results from mutations in a paired-like homeobox-containing gene. *Nature* 354 (6354), 522–525. doi:10.1038/354522a0

Hoang, T., Wang, J., Boyd, P., Wang, F., Santiago, C., Jiang, L., et al. (2020). Gene regulatory networks controlling vertebrate retinal regeneration. *Science* 370 (6519), eabb8598. doi:10.1126/science.abb8598

Holt, C. E., Bertsch, T. W., Ellis, H. M., and Harris, W. A. (1988). Cellular determination in the Xenopus retina is independent of lineage and birth date. *Neuron* 1 (1), 15–26. doi:10.1016/0896-6273(88)90205-x

Iwamatsu, T. (2004). Stages of normal development in the medaka *Oryzias latipes*. *Mech. Dev.* 121 (7-8), 605–618. doi:10.1016/j.mod.2004.03.012

Jonasova, K., and Kozmik, Z. (2008). Eye evolution: lens and cornea as an upgrade of animal visual system. *Semin. Cell Dev. Biol.* 19 (2), 71–81. doi:10.1016/j.semcdb.2007.10.005

Kitambi, S. S., and Malicki, J. J. (2008). Spatiotemporal features of neurogenesis in the retina of medaka, *Oryzias latipes*. *Dev. Dyn.* 237 (12), 3870–3881. doi:10.1002/dvdy.21797

Kleinjan, D. A., Bancewicz, R. M., Gautier, P., Dahm, R., Schonthaler, H. B., Damante, G., et al. (2008). Subfunctionalization of duplicated zebrafish pax6 genes by cis-regulatory divergence. *PLoS Genet.* 4 (2), e29. doi:10.1371/journal.pgen.0040029

Klimova, L., Antosova, B., Kuzelova, A., Strnad, H., and Kozmik, Z. (2015). Onecut1 and Onecut2 transcription factors operate downstream of Pax6 to regulate horizontal cell development. *Dev. Biol.* 402 (1), 48–60. doi:10.1016/j.ydbio.2015.02.023

Klimova, L., and Kozmik, Z. (2014). Stage-dependent requirement of neuroretinal Pax6 for lens and retina development. *Development* 141 (6), 1292–1302. doi:10.1242/dev.098822

Kozmik, Z. (2005). Pax genes in eye development and evolution. *Curr. Opin. Genet. Dev.* 15 (4), 430–438. doi:10.1016/j.gde.2005.05.001

Kozmik, Z., Czerny, T., and Busslinger, M. (1997). Alternatively spliced insertions in the paired domain restrict the DNA sequence specificity of Pax6 and Pax8. *EMBO J.* 16 (22), 6793–6803. doi:10.1093/emboj/16.22.6793

Lamb, T. D. (2013). Evolution of phototransduction, vertebrate photoreceptors and retina. *Prog. Retin Eye Res.* 36, 52–119. doi:10.1016/j.preteyeres.2013.06.001

Levine, E. M., and Green, E. S. (2004). Cell-intrinsic regulators of proliferation in vertebrate retinal progenitors. *Semin. Cell Dev. Biol.* 15 (1), 63–74. doi:10.1016/j.semcdb.2003.09.001

Liu, W., and Cvekl, A. (2017). Six3 in a small population of progenitors at E8.5 is required for neuroretinal specification via regulating cell signaling and survival in mice. *Dev. Biol.* 428 (1), 164–175. doi:10.1016/j.ydbio.2017.05.026

Liu, W., Lagutin, O., Swindell, E., Jamrich, M., and Oliver, G. (2010). Neuroretina specification in mouse embryos requires Six3-mediated suppression of Wnt8b in the anterior neural plate. *J. Clin. Invest.* 120 (10), 3568–3577. doi:10.1172/JCI43219

Livesey, F. J., and Cepko, C. L. (2001). Vertebrate neural cell-fate determination: lessons from the retina. *Nat. Rev. Neurosci.* 2 (2), 109–118. doi:10.1038/35053522

Loosli, F., Koster, R. W., Carl, M., Kuhnlein, R., Henrich, T., Mucke, M., et al. (2000). A genetic screen for mutations affecting embryonic development in medaka fish (*Oryzias latipes*). *Mech. Dev.* 97 (1-2), 133–139. doi:10.1016/s0925-4773(00)00406-8

Lust, K., and Wittbrodt, J. (2018). Activating the regenerative potential of Muller glia cells in a regeneration-deficient retina. *Elife* 7, e32319. doi:10.7554/eLife.32319

Lyu, P., Iribarne, M., Serjanov, D., Zhai, Y., Hoang, T., Campbell, L. J., et al. (2023). Common and divergent gene regulatory networks control injury-induced and developmental neurogenesis in zebrafish retina. *Nat. Commun.* 14 (1), 8477. doi:10.1038/s41467-023-44142-w

Marquardt, T., Ashery-Padan, R., Andrejewski, N., Scardigli, R., Guillemot, F., and Gruss, P. (2001). Pax6 is required for the multipotent state of retinal progenitor cells. *Cell* 105 (1), 43–55. doi:10.1016/s0092-8674(01)00295-1

Mathers, P. H., Grinberg, A., Mahon, K. A., and Jamrich, M. (1997). The Rx homeobox gene is essential for vertebrate eye development. *Nature* 387 (6633), 603–607. doi:10.1038/42475

Matsuo, T., Osumi-Yamashita, N., Noji, S., Ohuchi, H., Koyama, E., Myokai, F., et al. (1993). A mutation in the Pax-6 gene in rat small eye is associated with impaired migration of midbrain crest cells. *Nat. Genet.* 3 (4), 299–304. doi:10.1038/ng0493-299

Morris, S. C., and Caron, J. B. (2014). A primitive fish from the Cambrian of North America. *Nature* 512 (7515), 419–422. doi:10.1038/nature13414

Nakayama, T., Fisher, M., Nakajima, K., Odeleye, A. O., Zimmerman, K. B., Fish, M. B., et al. (2015). Xenopus pax6 mutants affect eye development and other organ systems, and have phenotypic similarities to human aniridia patients. *Dev. Biol.* 408 (2), 328–344. doi:10.1016/j.ydbio.2015.02.012

Oliver, G., Mailhos, A., Wehr, R., Copeland, N. G., Jenkins, N. A., and Gruss, P. (1995). Six3, a murine homologue of the sine oculis gene, demarcates the most anterior border of the developing neural plate and is expressed during eye development. *Development* 121 (12), 4045–4055. doi:10.1242/dev.121.12.4045

Pan, Q., Lu, K., Luo, J., Jiang, Y., Xia, B., Chen, L., et al. (2023). Japanese medaka Olpax6.1 mutant as a potential model for spondylo-ocular syndrome. *Funct. Integr. Genomics* 23 (2), 168. doi:10.1007/s10142-023-01090-4

Perron, M., Kanekar, S., Vetter, M. L., and Harris, W. A. (1998). The genetic sequence of retinal development in the ciliary margin of the Xenopus eye. *Dev. Biol.* 199 (2), 185–200. doi:10.1006/dbio.1998.8939

Plageman, T. F., Jr., Chung, M. I., Lou, M., Smith, A. N., Hildebrand, J. D., Wallingford, J. B., et al. (2010). Pax6-dependent Shroom3 expression regulates apical constriction during lens placode invagination. *Development* 137 (3), 405–415. doi:10.1242/dev.045369

Porter, F. D., Drago, J., Xu, Y., Cheema, S. S., Wassif, C., Huang, S. P., et al. (1997). Lhx2, a LIM homeobox gene, is required for eye, forebrain, and definitive erythrocyte development. *Development* 124 (15), 2935–2944. doi:10.1242/dev.124.15.2935

Quiring, R., Walldorf, U., Kloter, U., and Gehring, W. J. (1994). Homology of the eyeless gene of Drosophila to the Small eye gene in mice and Aniridia in humans. *Science* 265 (5173), 785–789. doi:10.1126/science.7914031

Ravi, V., Bhatia, S., Gautier, P., Loosli, F., Tay, B. H., Tay, A., et al. (2013). Sequencing of Pax6 loci from the elephant shark reveals a family of Pax6 genes in vertebrate genomes, forged by ancient duplications and divergences. *PLoS Genet.* 9 (1), e1003177. doi:10.1371/journal.pgen.1003177

Richardson, R., Tracey-White, D., Webster, A., and Moosajee, M. (2017). The zebrafish eye-a paradigm for investigating human ocular genetics. *Eye (Lond)* 31 (1), 68–86. doi:10.1038/eye.2016.198

Riesenberg, A. N., Le, T. T., Willardsen, M. I., Blackburn, D. C., Vetter, M. L., and Brown, N. L. (2009). Pax6 regulation of Math5 during mouse retinal neurogenesis. *Genesis* 47 (3), 175–187. doi:10.1002/dvg.20479

Schindelin, J., Arganda-Carreras, I., Frise, E., Kaynig, V., Longair, M., Pietzsch, T., et al. (2012). Fiji: an open-source platform for biological-image analysis. *Nat. Methods* 9 (7), 676–682. doi:10.1038/nmeth.2019

Schwaninger, M., Blume, R., Oetjen, E., Lux, G., and Knepel, W. (1993). Inhibition of cAMP-responsive element-mediated gene transcription by cyclosporin A and FK506 after membrane depolarization. *J. Biol. Chem.* 268 (31), 23111–23115. doi:10.1016/s0021-9258(19)49433-7

Shaham, O., Gueta, K., Mor, E., Oren-Giladi, P., Grinberg, D., Xie, Q., et al. (2013). Pax6 regulates gene expression in the vertebrate lens through miR-204. *PLoS Genet.* 9 (3), e1003357. doi:10.1371/journal.pgen.1003357

Shaham, O., Menuchin, Y., Farhy, C., and Ashery-Padan, R. (2012). Pax6: a multi-level regulator of ocular development. *Prog. Retin Eye Res.* 31 (5), 351–376. doi:10.1016/j.preteyeres.2012.04.002

Shu, D., Luo, H. L., Conway-Morris, S., Zhang, X., Hu, S., Han, J., et al. (1999). Lower Cambrian vertebrates from south China. *Nature* 402, 42–46. doi:10.1038/46965

Shu, D. G., Morris, S. C., Han, J., Zhang, Z. F., Yasui, K., Janvier, P., et al. (2003). Head and backbone of the early cambrian vertebrate haikouichthys. *Nature* 421 (6922), 526–529. doi:10.1038/nature01264

Signore, I. A., Guerrero, N., Loosli, F., Colombo, A., Villalon, A., Wittbrodt, J., et al. (2009). Zebrafish and medaka: model organisms for a comparative developmental approach of brain asymmetry. *Philos. Trans. R. Soc. Lond B Biol. Sci.* 364 (1519), 991–1003. doi:10.1098/rstb.2008.0260

Suzuki, D. G., and Grillner, S. (2018). The stepwise development of the lamprey visual system and its evolutionary implications. *Biol. Rev. Camb Philos. Soc.* 93 (3), 1461–1477. doi:10.1111/brv.12403

Takamiya, M., Stegmaier, J., Kobitski, A. Y., Schott, B., Weger, B. D., Margariti, D., et al. (2020). Pax6 organizes the anterior eye segment by guiding two distinct neural crest waves. *PLoS Genet.* 16 (6), e1008774. doi:10.1371/journal.pgen.1008774

Takamiya, M., Weger, B. D., Schindler, S., Beil, T., Yang, L., Armant, O., et al. (2015). Molecular description of eye defects in the zebrafish Pax6b mutant, sunrise, reveals a Pax6b-dependent genetic network in the developing anterior chamber. *PLoS One* 10 (2), e0117645. doi:10.1371/journal.pone.0117645

Tena, J. J., Gonzalez-Aguilera, C., Fernandez-Minan, A., Vazquez-Marin, J., Parra-Acero, H., Cross, J. W., et al. (2014). Comparative epigenomics in distantly related teleost species identifies conserved cis-regulatory nodes active during the vertebrate phylotypic period. *Genome Res.* 24 (7), 1075–1085. doi:10.1101/gr.163915.113

Tomita, K., Ishibashi, M., Nakahara, K., Ang, S. L., Nakanishi, S., Guillemot, F., et al. (1996). Mammalian hairy and Enhancer of split homolog 1 regulates differentiation of retinal neurons and is essential for eye morphogenesis. *Neuron* 16 (4), 723–734. doi:10.1016/s0896-6273(00)80093-8

Ton, C. C., Hirvonen, H., Miwa, H., Weil, M. M., Monaghan, P., Jordan, T., et al. (1991). Positional cloning and characterization of a paired box- and homeobox-containing gene from the aniridia region. *Cell* 67 (6), 1059–1074. doi:10.1016/0092-8674(91)90284-6

Turner, D. L., and Cepko, C. L. (1987). A common progenitor for neurons and glia persists in rat retina late in development. *Nature* 328 (6126), 131–136. doi:10.1038/328131a0

Turner, D. L., Snyder, E. Y., and Cepko, C. L. (1990). Lineage-independent determination of cell type in the embryonic mouse retina. *Neuron* 4 (6), 833–845. doi:10.1016/0896-6273(90)90136-4

Wan, J., and Goldman, D. (2016). Retina regeneration in zebrafish. *Curr. Opin. Genet. Dev.* 40, 41–47. doi:10.1016/j.gde.2016.05.009

Willardsen, M. I., Suli, A., Pan, Y., Marsh-Armstrong, N., Chien, C. B., El-Hodiri, H., et al. (2009). Temporal regulation of Ath5 gene expression during eye development. *Dev. Biol.* 326 (2), 471–481. doi:10.1016/j.ydbio.2008.10.046

Wittbrodt, J., Shima, A., and Schartl, M. (2002). Medaka--a model organism from the far East. *Nat. Rev. Genet.* 3 (1), 53–64. doi:10.1038/nrg704

Young, R. W. (1985). Cell differentiation in the retina of the mouse. *Anat. Rec.* 212 (2), 199–205. doi:10.1002/ar.1092120215

Zagozewski, J. L., Zhang, Q., Pinto, V. I., Wigle, J. T., and Eisenstat, D. D. (2014). The role of homeobox genes in retinal development and disease. *Dev. Biol.* 393 (2), 195–208. doi:10.1016/j.ydbio.2014.07.004

Zhang, X., Leavey, P., Appel, H., Makrides, N., and Blackshaw, S. (2023). Molecular mechanisms controlling vertebrate retinal patterning, neurogenesis, and cell fate specification. *Trends Genet.* 39 (10), 736–757. doi:10.1016/j.tig.2023.06.002

Frontiers in Cell and Developmental Biology

TYPE Brief Research Report
PUBLISHED 08 January 2025
DOI 10.3389/fcell.2024.1514553

OPEN ACCESS

EDITED BY
Michael Schubert,
UMR7009 Laboratoire de Biologie du Développement de Villefranche sur Mer, France

REVIEWED BY
Pedro Martinez,
University of Barcelona, Spain
Lukasz F. Sobala,
Polish Academy of Sciences, Poland

*CORRESPONDENCE
Daria Y. Romanova,
darjaromanova@gmail.com

‡These authors have contributed equally to this work

RECEIVED 22 October 2024
ACCEPTED 11 December 2024
PUBLISHED 08 January 2025

CITATION
Romanova DY, Povernov AA, Nikitin MA, Borman SI, Frank YA and Moroz LL (2025) Long-term dynamics of placozoan culture: emerging models for population and space biology.
Front. Cell Dev. Biol. 12:1514553.
doi: 10.3389/fcell.2024.1514553

Long-term dynamics of placozoan culture: emerging models for population and space biology

Daria Y. Romanova[1*‡], Alexander A. Povernov[1‡], Mikhail A. Nikitin[1‡], Simkha I. Borman[2], Yana A. Frank[1] and Leonid L. Moroz[3,4]

[1]Lab of Cellular Neurobiology of Learning, Institute of Higher Nervous Activity and Neurophysiology of RAS, Moscow, Russia, [2]Koltzov Institute of Developmental Biology of Russian Academy of Sciences, Moscow, Russia, [3]Departments of Neuroscience and McKnight Brain Institute, University of Florida, Gainesville, FL, United States, [4]Whitney Laboratory for Marine Bioscience, University of Florida, Gainesville, FL, United States

As the simplest free-living animal, *Trichoplax adhaerens* (Placozoa) is emerging as a powerful paradigm to decipher molecular and cellular bases of behavior, enabling integrative studies at all levels of biological organization in the context of metazoan evolution and parallel origins of neural organization. However, the progress in this direction also depends on the ability to maintain a long-term culture of placozoans. Here, we report the dynamic of *Trichoplax* cultures over 11 years of observations from a starting clonal line, including 7 years of culturing under antibiotic (ampicillin) treatment. This study revealed very complex population dynamics, with seasonal oscillation and at least partial correlations with the solar radio emission flux and the magnetic field disturbance parameters. Notable, the analysis of the distribution of Fe^{2+} in living animals revealed not only its high abundance across most cells but also asymmetric localizations of Fe^{2+} in unidentified cells, suggesting that these Fe^{2+} intracellular patterns might be coupled with the animal's bioenergetics. We hypothesize that placozoans might have magnetoreception, which can be experimentally tested in future studies. In sum, *Trichoplax*, in particular, and Placozoa, in general, can be viewed as prospective reference species in traditional evolutionary and system biology but have the yet unexplored potential for planetary ecology and space biomedicine.

KEYWORDS

Placozoa, *Trichoplax*, long-term culturing, aging of culture, behavior, space biology

1 Introduction

Placozoans are one of the most ancient branches of metazoans. These animals have a simple bodyplan with a dozen of cell types (Smith et al., 2014). The phenotypic similarity of placozoan haplotypes and species provides the dissonance between nearly identical morphological architectures and substantial genetic distances when comparing their genomes (Srivastava et al., 2008) and transcriptomes. Mechanisms of complex behavior repertoirs with elements of social interactions between individuals (Kuhl and Kuhl, 1963; Kuhl and Kuhl, 1966; Seravin and Karpenko, 1987; Seravin and Gudkov, 2005a; Seravin and Gudkov, 2005b; Eitel and Schierwater, 2010; Eitel et al., 2013; Smith et al., 2015; Senatore et al., 2017; Armon et al., 2018; Zuccolotto-Arellano and Cuervo-González, 2020; Zhong et al., 2023) requires a detailed comparative analysis of cellular and system features, ideally for all proposed placozoan species/haplotypes (Miyazawa et al., 2012; Eitel, 2010; Eitel et al., 2013; Aleshin et al., 2004; Miyazawa et al., 2021; Schierwater and DeSalle, 2018; Tessler et al., 2022). However, whether there are species-specific growth dynamics is still an open question; and this information can be essential for taxonomy and speciation.

Placozoa inhabit temperate to tropical latitudes (Ueda et al., 1999; Signorovitch et al., 2006; Pearse and Voigt, 2007; Eitel and Schierwater, 2010; Nakano, 2014), preferring calm coastal waters over a wide range of salinities (Pearse, 1989), depths (Eitel et al., 2013), pH (Schleicherová et al., 2017; Schierwater, 2005; Schierwater et al., 2010), and temperatures (Pearse, 1989). The animals are bottom dwellers on substrates of a mixture of bacteria and algae (Grell, 1972; Ruthmann, 1977; Signorovitch et al., 2006; Seravin and Gerasimova, 1998; Jackson and Buss, 2009; Smith et al., 2014). At present, the ecological niches and exact food sources for Placozoa are only loosely defined. Pearse and Voigt (2007) suggested that Placozoa in tropical and subtropical areas feed by consuming organic detritus, as well as algae and bacteria that form biofilms on corals and rocky bottoms.

Today, most experimental work on Placozoa is carried out under conditions of culturing, comparable to their natural microenvironments in biotopes: photoperiod or climate control at 6:18 h, temperature of 22–24° Celsius in Petri dishes (Heyland et al., 2014; Romanova et al., 2022; Romanova et al., 2024). Since *in situ* observations on placozoans are difficult to perform, there are small numbers of identified environmental parameters in their natural habitats.

It has been shown that, depending on the quality and quantity of the substrate, animals can exhibit three patterns of population dynamics under cultured conditions (Romanova et al., 2022): 1) with a sufficient density of microalgae, animals are capable of dividing once a day or two, 2) with a lack of food substrate, a decrease in the animal biomass and body sizes had been observed, and asexual reproduction might be suppressed, 3) a significant increase in the biomass of animals and the appearance of aggregations of animals in Petri dishes occurred on a thick substrate of green algae *T. marina*, as the primary food source.

Assessing the population size is straightforward since animals reproduce asexualy, gaining biomass in cell culture (Okshtein, 1987). Sexual reproduction in laboratory conditions has been rarely observed, and only early stages of development (up to 128 cells) have been reported (Eitel et al., 2011). Given a high animal density and food scarcity as possibe indictor of embryo formation (Eitel et al., 2011), sexual reproduction may not contribute to population growth in laboratory conditions.

Long-term culturing in laboratory conditions, as well as field observations, have shown that there is a seasonal dependence on the number of individuals in populations over the years (Ueda et al., 1999; Maruyama, 2004; Pearse and Voigt, 2007), related to changes in illumination, temperature, and chemical parameters of the environment such as acidity (Schleicherová et al., 2017). And in natural conditions population dynamics might be associated with complex biofilm dynamics, light and temperature gradients, as well as tides and hydodynamics (Pearse and Voigt, 2007).

Here, we report the seasonal changes in population growth rates of *Trichoplax adhaerens* (Placozoa) under constant temperature conditions over an 11-year observation period from January 2014 to December 2024.

2 Material and methods

2.1 Culturing of placozoans

We used axenic clonal cultures of the major placozoan reference species: *Trichoplax adhaerens* (Grell's strain H1, from the Red Sea). We maintained all populations in culture for 11 years (2014–2024), allowing long-term observations and adjustments of culture conditions (Romanova et al., 2022; Romanova et al., 2024).

A suspension of the green alga *Tetraselmis marina* (WoRMS Aphia, ID 376158) was added to the culture dishes. When the biofilm of microalgae became thinner or depleted, freshly prepared 1–2 mL suspension of *T. marina* could be added to the culture dishes weekly (~6.5×10^6 cells of *T. marina* per 1 μL). H1 haplotype was maintained at the two environmental chambers. The first option is a room with controlled ventilation, constant temperature (24°), and humidity (~70%), natural light (comes from windows). The second option is a climate chamber (#B3, Europolitest), with a photoperiod of 6:18, lighting of 400 lux, and temperature of 24°C.

Under long-term culturing, animals usually divided every 1–2 days without signs of sexual reproduction (Malakhov, 1990; Zuccolotto-Arellano and Cuervo-González, 2020).

2.2 Individual treatment with antibiotics

Trichoplax might contain potentially symbiotic bacteria in fiber cells (Driscoll et al., 2013; Kamm et al., 2019). To control levels of potential bacterial endosymbionts and their effect on culturing dynamics, we used treatment with different antibiotics [ampicillin (5 μg/mL), doxycycline (1.25 μg/mL)]. Three groups are: control clonal line (CCL), ampicillin clonal line (ACL), and doxycycline clonal line (DCL).

To control the efficiency of antibiotic treatments, total DNA from individual animals was extracted using a silica-based DiaTom DNAprep 100 kit (Isogene, Moscow, Russia) according to the manufacturer's protocol. Amplification was performed using EncycloPlus PCR kit (Evrogen, Moscow, Russia) with the following program: 95°C – 3 min, 35 cycles of PCR (95°C – 20 s, 50°C – 20s, 72°C – 1 min), and 72°C – 5 min. We have used universal forward primer 27F (AGA GTT TGA TCM TGG CTC AG) and specific reverse primer 449R (ACC GTC ATT ATC TTC YCC AC). The reverse primer was designed against 16S RNA of *Rickettsia belli* (NR_074484.2) and sequences from *Trichoplax* DNA were obtained through NCBI Trace Archive Blast using NR_074484.2 as the query. After 6 months of ampicillin treatment, the markers of *Rickettsia* were not detected.

2.3 F10.7 and ap indices

The solar activity index is the radio emission flux F10.7 with a wavelength of 10.7 cm (2,800 MHz). It is measured in solar flux units: 1 s.f.u. = 10^{-22} W/(m^2*Hz). The data are presented as observed values measured by a solar radio telescope (https://www.ngdc.noaa.gov/stp/solar/solar-indices.html).

The Kp index characterizes the global disturbance of the Earth's magnetic field in a three-hour time interval. The Kp index is defined as the average value of the disturbance levels of two horizontal components of the geomagnetic field observed at 13 selected magnetic observatories located in the subauroral zone between 48 and 63° north and south geomagnetic latitudes. The ap index is calculated from the Kp index values and represents the change in the most disturbed element of the magnetic field D or H in a three-hour time interval at mid-latitude stations. The ap index is called the planetary amplitude in a three-hour interval. The ap index varies in the range from 0 to 400 and represents the Kp values converted to a linear scale in nanoteslas (nT), which shows the equivalent amplitude disturbance at the station.

The correlation results presented in this paper rely on geomagnetic indices made available by ISGI Collaborating Institutes from data collected at magnetic observatories. We thank the involved national institutes, the INTERMAGNET network and ISGI (isgi.unistra.fr).

2.4 Statistical analysis

For population growth rate (PGR) experiments, we cultured axenic lines of H1 haplotype at constant temperature (24°C) and natural light in environmental chambers for 11 years. PGR, locomotion, number of individuals, and occurrences of aggregates were monitored every third day at the same time as counts of animals.

We used the Statistica software 7.0 (Afifi et al., 2003). The Kolmogorov-Smirnov criterion was used to test a hypotheses about cut belongings of parameter samples. The Spearman rank correlation test and the Pearson goodness-of-fit test were used to study the correlation between samples. These methods were applied both to cut samples as a whole and their grouping for animals of control, ampicillin, and doxycycline clonal lines. To detect differences between groups, Kruskall-Wallis ANOVA was used to compare all three samples simultaneously, and Mann-Whitney U-test was used to compare pairwise samples.

To make cut lines on the graph smoother and easier to perceive, as well as to show longer trends in cut changes in number of animals, ap and F10.7 indices, a moving average over a fixed number of observations of size 5 for each cup was shown. This number was chosen for the reason that a smaller window size did not significantly change the resulting image, and larger sizes had a noticeable effect on the amount of total displayed data. To find confidence intervals, the variance and standard deviation in numbers of animals, ap and F10.7 indices over a 5-day interval for each cup were calculated, and median values were found. The boundaries of the confidence interval were calculated as the sum and difference of the median and the standard deviations.

For visualizing and plotting, we used Pandas, Matplotlib, and Seaborn in a Python environment by Anaconda-Navigator (JupiterLab).

2.5 Staining

Before fixation, a dozen of individuals were allowed to settle on the bottom for one hour in 35 mm Petri dish. Then we add 0.5–1 μL of 1 mM HMRhoNox-M dye (#3317-50 μg, LumiProbe, Russia) in one hour. Fixation was achieved by gently adding 30 μL of 0.25% glutaraldehyde in artificial seawater (ASW) at room temperature for 10 min. Next, preparations were washed in phosphate buffer solution (0.1 M, pH = 7.4) three times (20 min) and mounted on a slide using Prolong gold antifade reagent with DAPI, and stored in the dark at 4°C. The samples were examined using a laser confocal Cerna-based microscope (Thorlabs, United States). Image processing was carried out using ImageJ software.

3 Results

3.1 Long-term culturing for eleven years

The analysis of animal population growth rates (PGR) from 2014 to 2024 showed unspecified oscillation in the dynamics of *Trichoplax* populations for the optimized culture protocol (Figure 1A; Supplementary Table S1). Weekly, freshly prepared 1–2 mL suspension of *T. marina* was be added to the culture dishes. Throughout the observation period, animals were kept under uniform conditions: constant temperature of 24°C, natural illumination, shaded from direct sunlight, regular change of artificial seawater (twice a week). Population dynamics showed repetitive changes for annual (Figure 2A) and monthly (Figure 2B) intervals.

3.2 Antibiotic clonal lines

Antibiotic tests were chosen as additional parameters to detect long-term changes in the PGR dynamics of *Trichoplax* relative to the external and internal microbiomes, and theirs potential impacts on structures of placozoan's populations. Long-term observation data for the test groups with ampicillin and doxycycline showed an increase in the growth of the number of animals relative to the control (Figure 2).

There is a statistically significant difference both for the sampling over all years ($p < 0.001$ in K-W ANOVA, $p < 0.001$ in M-W U-test between all groups) and for each year separately: from 2018 to 2023 between the control and ampicillin groups ($p < 0.001$ in M-W U-test), between the control and doxycycline groups in 2017 ($p = 0.011$) and 2018 ($p < 0.001$), as well as between the ampicillin and doxycycline groups in 2018 ($p = 0.017$). In 2017 and 2024, no statistically significant differences were found between the number of animals in the control and ampicillin groups ($p = 0.665$, $p = 0.767$, respectively). Statistically significant mounthly differences between the control and ampicillin were found in 53 months out of 85 (Supplementary Table S2): 3 out of 4 months in 2017, 9 out of 12 months in 2018, 5 out of 12 months in 2019 and 2020, 8 out of 12 months in 2021, 7 out of 12 in 2022, 9 out of 12 in 2023, 7 out of 9 in 2024 ($p < 0.05$, M-W U-test). The descriptive statistics parameters (Median, [LQ, UQ]) for animals in the control group are 52, [23; 112], while for animals of the ampicillin

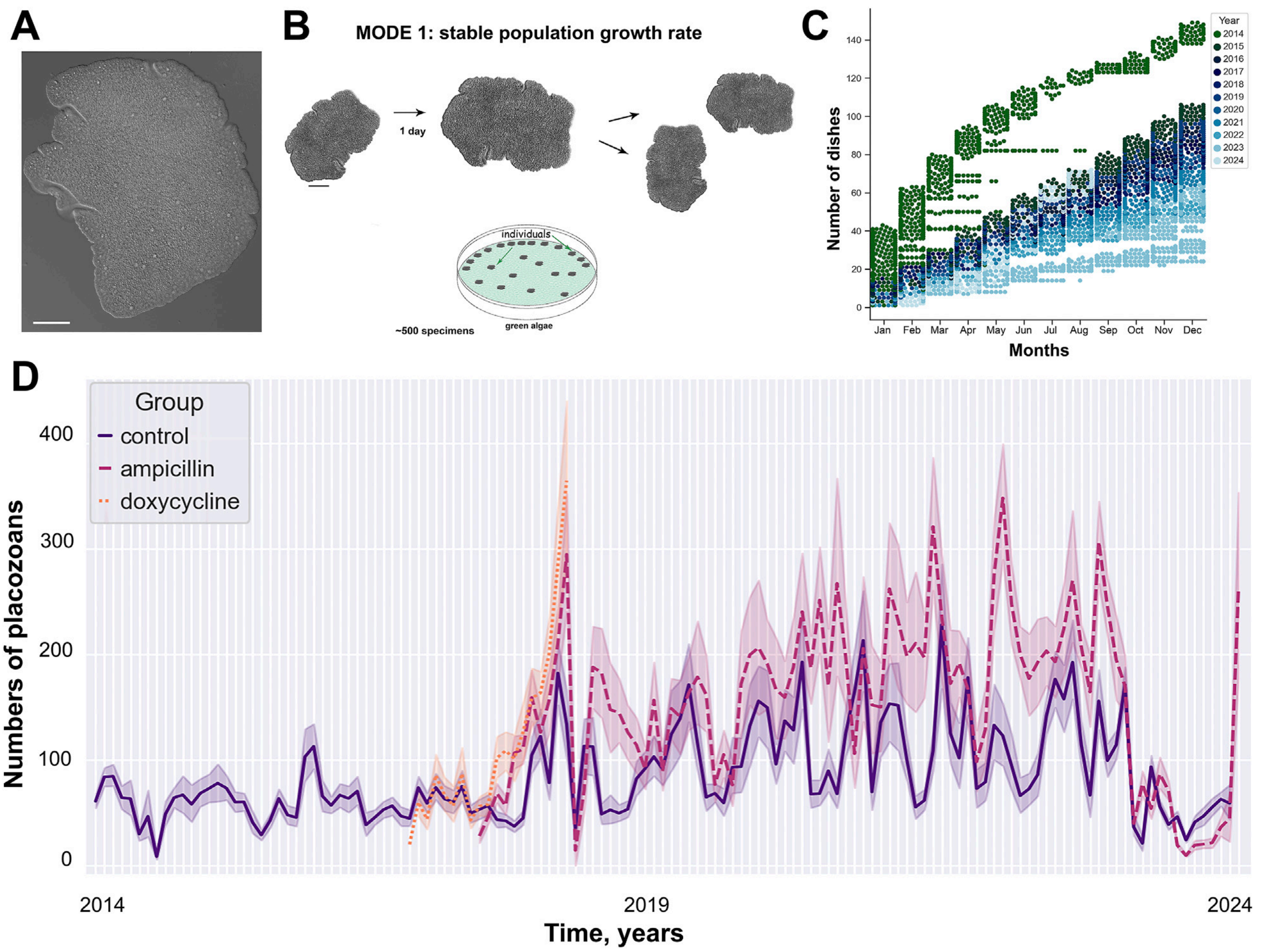

FIGURE 1
11 years of long-term culturing of placozoans. **(A)** Photo of Trichoplax adhaerens, H1 haplotype **(B)** Mode 1: stable population growth rate under culture condition. **(C)** The number of Petri dishes (earch dot represents one dish, colors mark different years) as used in the study. **(D)** Oscillations of the population growth (meant +/− standard errors) under three exparimental conditions (control/CCL, ampicillin/ACL, and doxycycline/DCL). See details in Supplementary Table S1. **(B)** modified from Romanova et al. (2022).

group – 95, [30; 220] with the number of observations being 9203 and 4419, respectively.

Based on the fact that the groups with ampicillin and doxycycline have an increase in the growth compare to the control group, combined with the presence of statistically significant differences between the groups, we can assume that populations treated with ampicillin and doxycycline are more stable, due to the suppression of both external microbiomes and symbionts.

3.3 Potential planetary-scale factors and population dynamics

Here, we noted potential correlations of the observed long-term culture dynamics with the intensity of solar activity factors and disturbance of the magnetic field of Earth (i.e., the ap and F10.7 indices) similar to reports on other organisms (Häder, 2000; Deng et al., 2018; Neale and Thomas, 2016). According to the Kolmogorov-Smirnov criterion, the values of PGR data and the ap and F10.7 indices are not normally distributed at a significance level of <0.01. The Pearson correlation coefficient between the ap and F10.7 indices was equal to 0.27 at a significance level of $p < 0.001$, which hints a potential tendency for a joint increase or decrease in the values of these parameters (Figure 3).

Pearson correlation coefficients between the number of animals and the ap and F10.7 indices were equal to −0.05 ($p< 0.001$) and −0.03 ($p = 0.004$), which indicates a statistically significant weak negative effect of high values of these parameters on the number of animals. Spearman correlation coefficient between the total number for 11 years and the F10.7 index was equal to −0.06 ($p < 0.001$), which also indicates a statistically significant weak negative effect of high values of this parameter on the growth of the number of animals, while the correlation coefficient of the ap index is equal to 0.014 ($p = 0.193$). The values of the correlation coefficients between the number of animals and the ap index in the annual analysis have low levels of reliability. However, when comparing data by months and weeks of observation between groups, statistical reliability has a support at the corridor of values of $p < 0.05–0.001$. The low levels of reliability of the

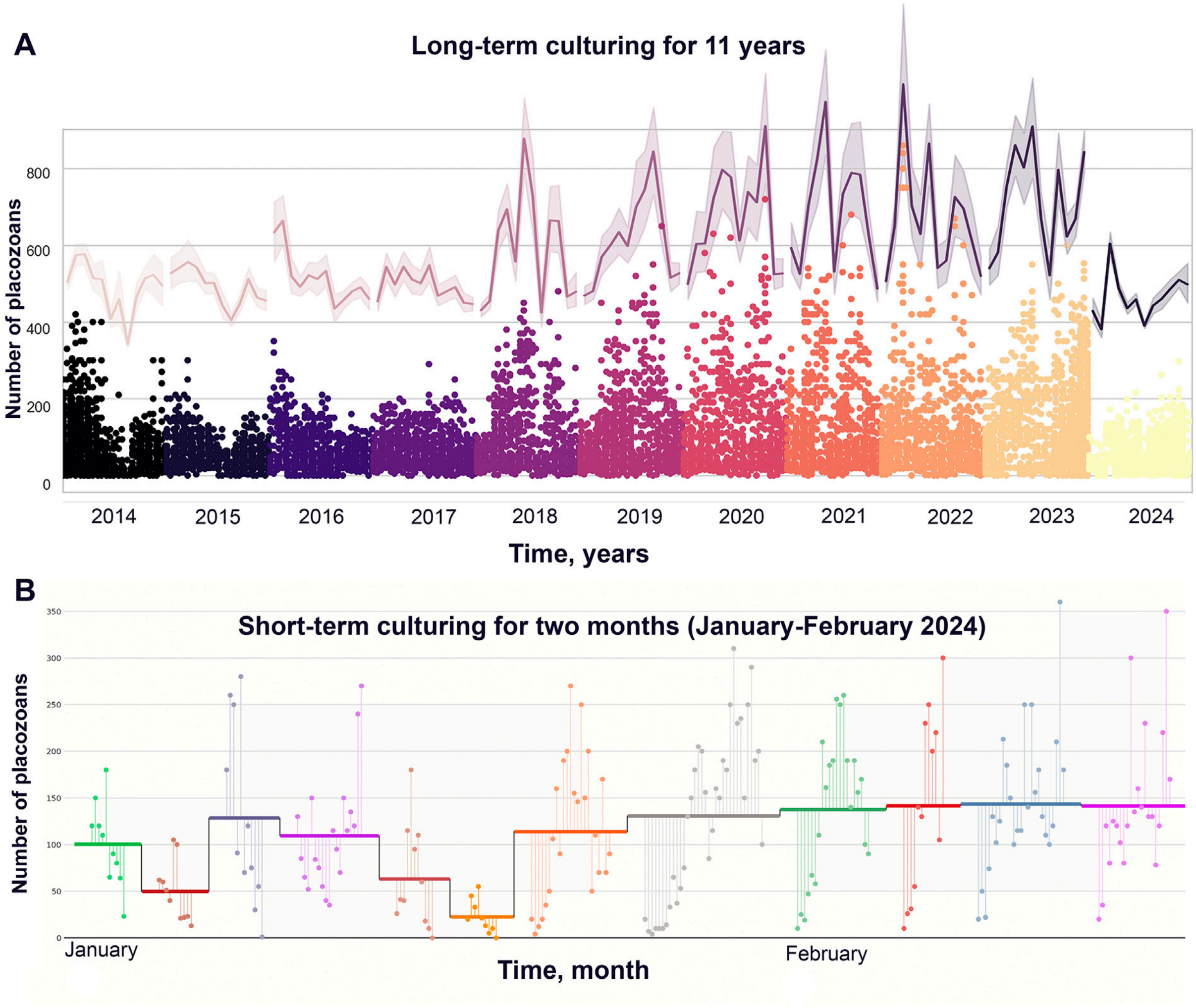

FIGURE 2
Annual and monthly population dynamics during long-term cultivation of *Trichoplax adhaerens*. **(A)** Long-term culturing from 2014 to 2024 (up to December). Oscillations of the population growth (meant +/− standard errors); continuous error bands are a graphical representation of error or uncertainty shown as a shaded region around a main trace (upper purple line in the gradient graph (the same in in Figure 1D) in gradient graph). **(B)** Dynamic of culturing during January-February 2024. On the graph: all colors−sequential Petri dishes, horizontal line for every dish is mean values of animals' count (mean +/− standard error).

correlation coefficients between the number of animals and the ap index in the annual analysis and the levels in the study by month and weeks might be observed due to the fact that the values of the ap index differ greatly between years of observation, and slightly differ between weeks and months.

When we grouped the datasets by the ap index, the influence of the F10.7 index on the number of animals changes from negative to positive with an increase in the ap index values: the Pearson correlation coefficient is −0.112 ($p = 0.116$) for the range of 0–2 nT; −0.12 ($p < 0.001$) for the range of 2–4 nT; −0.11 ($p < 0.001$) for the range of 4–6 nT; −0.115 ($p < 0.001$) for the range of 6–8 nT; −0.043 ($p = 0.113$) for the range of 8–10 nT; 0.088 ($p = 0.024$) for the range of 10–12 nT; 0.129 ($p = 0.007$) for the range 12–14 nT and 0.049 ($p = 0.112$) for the range >14 nT. This implies a statistically significant negative correlation of solar activity at low values of the ap index, and a possible positive impact at average values.

The effect of the ap index on animal abundance also varies, showing a negative impact at low and high values of the radiation flux and a positive one at medium values: at solar activity values equal to 60–80 s.f.u. (−0.061 at $p < 0.001$), 80–100 s.f.u. (−0.116 at $p < 0.001$), 100–120 s.f.u. (−0.075 at $p = 0.026$) and 200–220 s.f.u. (−0.075 at $p = 0.797$). For the range of radiation flux values of 120–140 s.f.u. (Pc = 0.002 at $p = 0.955$), 140–160 s.f.u. (Pc = 0.086 at $p = 0.003$), 160–180 s.f.u. (Pc = 0.336 at $p< 0.001$) and 180–200 s.f.u. (Pc = 0.042; $p < 0.001$), the Pearson correlation coefficients were calculated. This can be infered as statistically significant negative correlation of magnetic field disturbances at low and high values of the solar radio flux, as well as a positive effect at average values.

The Spearman correlation coefficient for groupings between the number of animals and solar activity for grouping geomagnetic activity was −0.048 ($p = 0.502$) for the 0–2 nT group, −0.137 ($p < 0.001$) for the 2–4 nT group, −0.141 ($p < 0.001$) for the 4–6 nT group, −0.079 ($p = 0.001$) for the 6–8 nT group, −0.031 ($p = 0.254$)

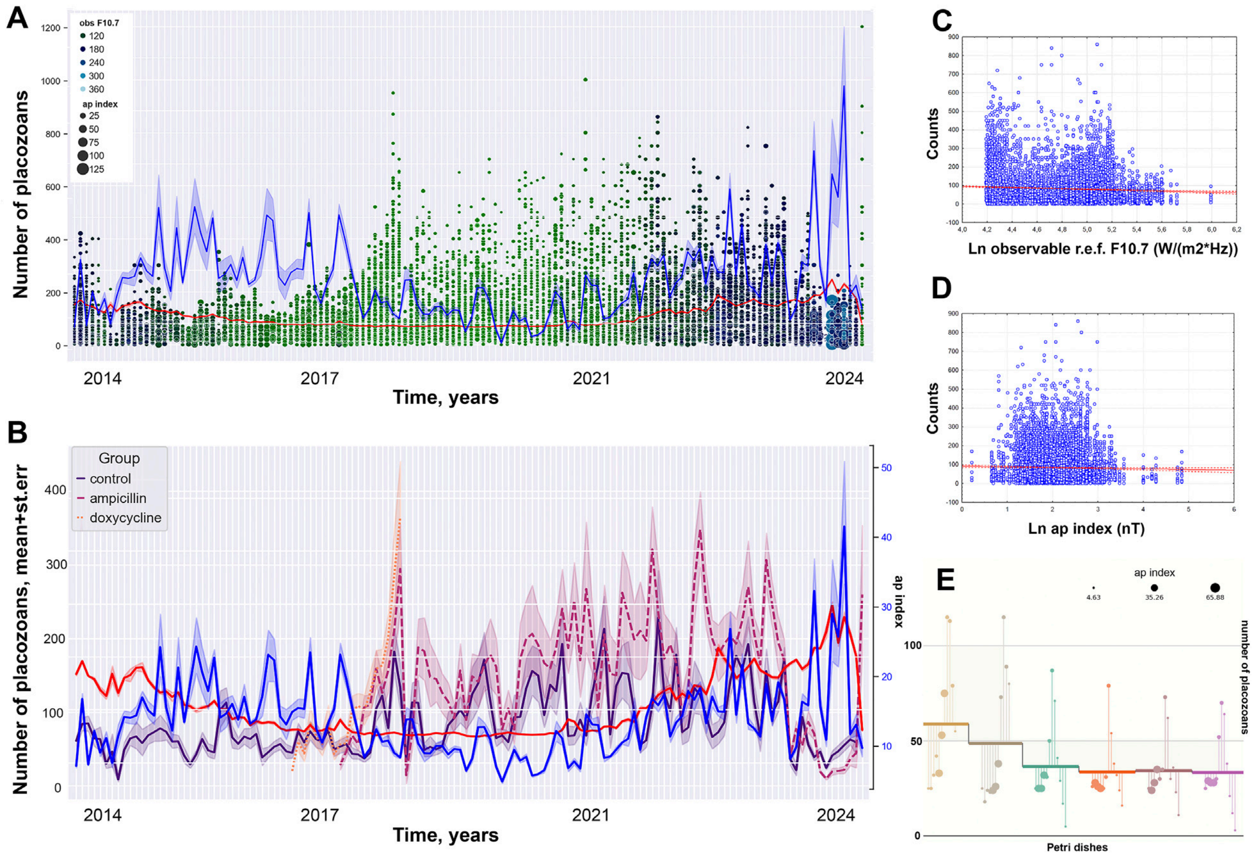

FIGURE 3
Decade of oscillation in population growth rate (PGR) (control group). **(A)** Long-term culturing of control clonal individuals for 11 years (dot represent numbers of animal per a dish). **(B)** Dynamic of PGR for normal clonal live and antibiotic treatment groups with ap and F10.7 indices (blue and red lines respectively). **(C)** Pearson scatterplot for the observable solar F10.7 index versus numbers of placozoans. **(D)** Pearson scatterplot for the ap index versus numbers of placozoans. **(E)** Numbers of animals in the individual Petri dishes during 2024 overlaped with data of ap index for the current period.

for the 8–10 nT group, 0.086 (p = 0.028) for the 10–12 nT group, 0.193 ($p < 0.001$) for the 12–14 nT group, and 0.039 (p = 0.209) for the >14 nT group. This implies a statistically significant negative correlation of solar activity at low values of the ap index, and a positive correlation at average values.

The Spearman correlation coefficient for groupings between the number of animals and the ap index with the grouping index F10.7 was −0.033 (p = 0.055) for the 60–80 s.f.u. group, −0.118 ($p < 0.001$) for the 80–100 s.f.u. group, 0.023 (p = 0.499) for the 100–120 s.f.u. group, 0.042 (p = 0.192) for the 120–140 s.f.u. group, 0.09 (p = 0.002) for the 140–160 s.f.u. group, 0.393 ($p < 0.001$) for the 160–180 s.f.u. group, 0.136 (p = 0.007) for the 180–200 s.f.u., 0.35 ($p < 0.001$) for the 200–220 s.f.u. group and 0.055 (p = 0.55) for the >220 s.f.u. group. This suggests negative correlation of magnetic field disturbances at low values of the solar radio flux, as well as a positive correlation at average values. Thus, we can hypothesize that there is a negative correlation of low values of the F10.7 index on population growth in *Trichoplax*, and a positive correlation at average values, and the correlation of the ap index is positive at average values, and negative at low and high values.

When studying the scatter diagrams, two peaks in the number of animals are observed—at low and medium-high values of the F10.7 index: 60–80 s.f.u. (Sp. R = −0.044 (p = 0.012)) and 140–160 s.f.u. (Sp. R = −0.067 (p = 0.021)); and a sharp decline at very high values of the F10.7 index: 200–220 s.f.u. (Sp. R = −0.108 (p = 0.096)) and >220 s.f.u. (Sp. R = −0.06 (p = 0.479)). For the ap index, the peak in abundance is observed at its average values: 8–10 nT (Sp. R = 0.026 (p = 0.304)), 10–12 nT (Sp. R = -0.043 (p = 0.22)), 12–14 nT (Sp. R = 0.126 (p = 0.001)) and 12–14 nT (Sp. R = 0.215 ($p < 0.001$); declines in abundance occur at very low and very high values: <2 nT (Sp. R = −0.014 (p = 0.939)), 2–4 nT (Sp. R = −0.002 (p = 0.937)), >20 nT (Sp. R = −0.1 (p = 0.059)).

Based on the results obtained, we can suggest that the influence of the F10.7 index on population growth in *Trichoplax* would be negative at low values and positive at average values, and the influence of the ap index is negative at low and high values and positive at average values. Therefore, we can hypothesize that an optimal range of values of the F10.7 and ap indices potentially contributing to population growth in *Trichoplax*, and the values of the indices are approximately as follows: F10.7–140–200 s.f.u., ap – 10–16 nT.

3.4 Fe^{2+}-selective staining of individuals

To initially assess the cellular bases of possible geomagnetic effects, we used a Fe^{2+}-selective fluorescent indicator to visualize the

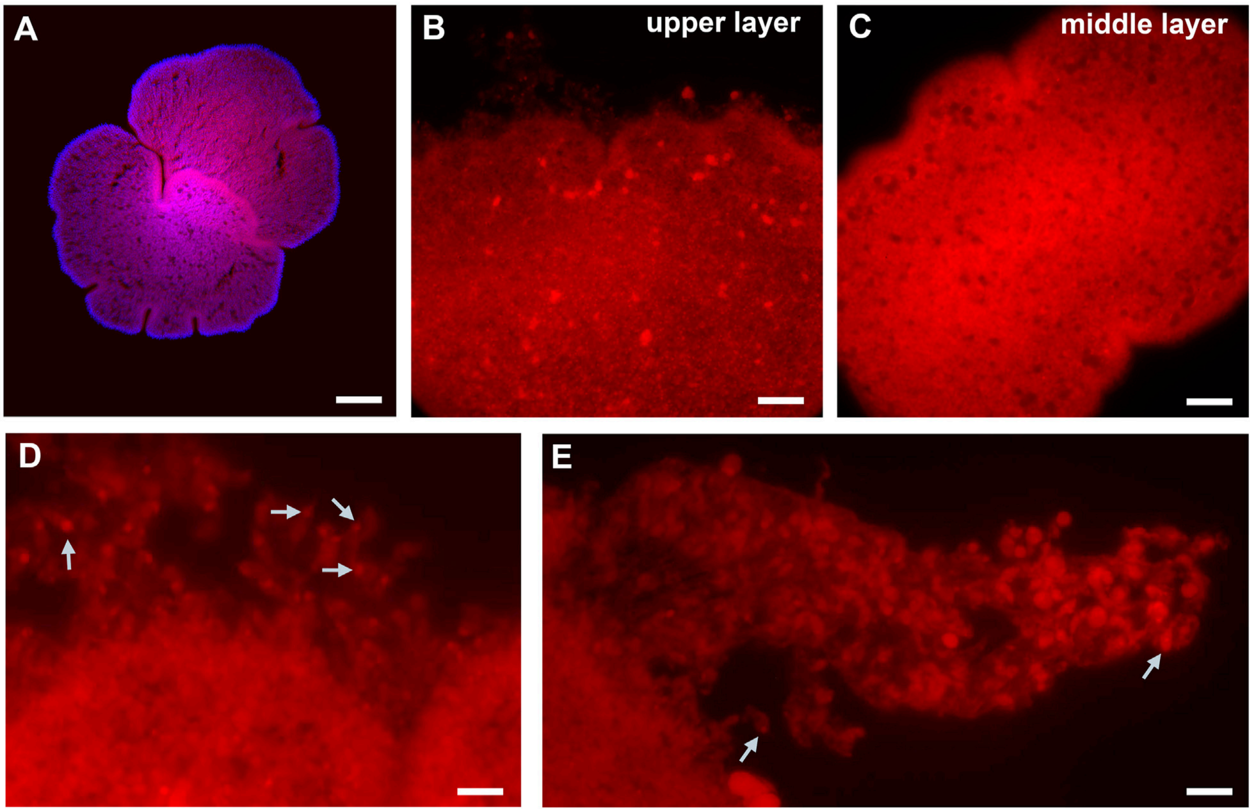

FIGURE 4
Fe^{2+}-selective staining in Trichoplax. **(A)** Top view Red: HMRhoNox-M, blue−DAPI. **(B)** Focus on upper epithelia with large inclusions, and damaged rim [high magnification, see **(D)**]. **(C)** Middle layer focus with microcavities. **(D)** Rim area: epithelial cells with fluorescent signal inside. **(E)** The part of damaged rim epithelium: some cells show assymetric distribution of fluorescent signal location. White arrows point to areas of inclusions presumably enriched in Fe^{2+}. Scale bar: **(A)**-100 μm, **(B)**-20 μm, **(C)**-50 μm, **(D, E)** – 10 μm.

distribution of iron ions in lysosomes (Lv and Shang, 2018; Hirayama et al., 2019). Figure 4 shows widespread labeling with the dye, suggesting the abundant and broad distribution of Fe^{2+} across most cell types. The most intense labeling was observed in the “digestive” zone, where lipophilic, secretory, and glandular cell types, involved in the nutrition process, are located. The edge of the epithelium zone was stained significantly less than the “digestive” zone. Finally, for large, unidentified cell types, we detected asymmetrical localization of Fe^{2+} (Figure 4B); labeling occurred outside nuclei as an organelle-like localization, similar to the morphology of crystal cells (although these were not crystal cells).

4 Discussion

Since placozoans are an integral part of marine ecosystems (Schierwater et al., 2010; Schierwater et al., 2021; Nakano, 2014) and involved in benthic food chains, it is important to assess the parameters associated with the growth of animal populations. Any population has internal and external factors that impact its structure and survival, such as seasonal temperature fluctuations, oceanic currents, dynamics of biogenic micro- and macroelements, and even solar activity (Chizhevsky, 1976; Ranta et al., 1997; Kravchenko et al., 2006). It was also reported that temperature and pH could significantly affect the physiology of placozoans (Schleicherová et al., 2017; Schierwater, 2005; Schierwater et al., 2010), and algal substrates can modulate the behavior of both individual animals and the population as a whole (Romanova et al., 2022).

Under favorable conditions, animals divide every 1–2 days (Heyland et al., 2014; Romanova et al., 2024; Okshtein, 1987). Such a steady increase in cell numbers (due to mitosis) and size of *Trichoplax* following subsequent asexual reproduction by division is an excellent model for assessing the growth of an animal population under long-term influences influence of external factors. Here, the use of standardized, well-controlled parameters allowed us to reveal complex oscillations in population growth, with potentially dynamic regulation of the number of individuals during monthly, seasonal, and annual observation periods over eleven years (2014–2024, Supplementary Figures S1, S2, S4). Notable, the evident correlation between the population growth in placozoans and solar activity can be depicted from long-term observations independently performed by Maruyama (Maruyama, 2004); see Supplementary Figure S3 for details.

Wave-like dynamics of the number of *Trichoplax* under constant cultivation conditions allowed us to consider additional external factors potentially influencing the animal population growth. We hypothesize that two external factors have effects on the PGR - the solar radio emission flux with a wavelength of 10.7 cm/ 2,800 MHz (by index F10.7) and the magnetic field disturbance parameter in a three-hour time interval (by ap index) with a degree of reliability when analyzing the studied groups within each year of observation. This should be a subject of careful future investigations. Ideal controls, in the future, can be performed in magnetic chambers or as another long-term project at different geographic locations, ideally with international collaboration.

In the quest for the potential presence and mechanisms of magnetoreception in placozoans, we found that the highly selective indicator for Fe^{2+} revealed the abundance of iron in nearly every placozoan cell, with the predominant localization in the digestive zone. Some links to the physiology of Placozoa might be associated with endosymbiotic bacteria (Kamm et al., 2019), again to be investigated in the future.

It is known that bacterial cells can have magnetosomes, which are organelles made of magnetite (Fe_3O_4) or greigite (Fe_3S_4) with a phospholipid bilayer and associated proteins MamK/MamY, Ccfm (Pfeiffer et al., 2020; Liu et al., 2024). According to this hypothesis about the nature of magnetosomes, they might be associated with vesicles as a storage system for ferrous iron ions (Lv and Shang, 2018) and serve as a potential exaptation to sense magnetic fields. Whether such a system exists in endosymbiotic bacteria or specialized cells of placozoans needs to be determined in future studies.

5 Conclusions and future directions

We report the complex oscillations within *Trichoplax* populations during over 11 years of culturing. This study also implies a very complex population dynamics and likely partial correlations with the solar radio emission flux and the magnetic field disturbance parameters.

Notable, the analysis of the distribution of Fe^{2+} in living placozoans illuminated not only its high abundance across most cells but also asymmetric localizations of Fe^{2+} in large unidentified cell types (Figure 4B), suggesting that these Fe^{2+} intracellular patterns might be coupled with the animal's bioenergetics and magnetoreception, potentially affecting mucus associated feeding behaviors which can be experimentally tested in future research. It might not be an overstatement that this research direction on placozoans could be relevant to better understanding systemic adaptations to microgravity and animal health under stress factors.

In sum, *Trichoplax*, in particular, and Placozoa, in general, can be viewed as prospective reference species in traditional evolutionary and system biology but have the yet unexplored potential for planetary ecology and space biomedicine (Romanova and Moroz, 2024). Additional long-term observations of population dynamics, and ideally at different geographic locations both in laboratory culture conditions and natural habitats are needed.

Data availability statement

The original contributions presented in the study are included in the article/Supplementary Material, further inquiries can be directed to the corresponding author.

Ethics statement

The manuscript presents research on animals that do not require ethical approval for their study.

Author contributions

DR: Conceptualization, Data curation, Formal Analysis, Funding acquisition, Investigation, Methodology, Project administration, Resources, Supervision, Validation, Visualization, Writing–original draft, Writing–review and editing. AP: Formal Analysis, Investigation, Data curation, Methodology, Writing–review and editing. MN: Formal Analysis, Investigation, Supervision, Writing–review and editing, Data curation, Methodology. SB: Writing–review and editing, Investigation, Methodology. YF: Writing–review and editing, Methodology, Visualization. LM: Writing–review and editing.

Funding

The author(s) declare that financial support was received for the research, authorship, and/or publication of this article. This work was supported in part by the Russian Science Foundation grant (23-14-00050) to DR.

Acknowledgments

The authors thank students Kololeeva V. S. and Allyamova M. T. for help in short-term maintaining cultural dishes, Aseev N. A. for helping with microscopy. We thank the involved national institutes, the INTERMAGNET network and ISGI (isgi.unistra.fr).

Conflict of interest

The authors declare that the research was conducted in the absence of any commercial or financial relationships that could be construed as a potential conflict of interest.

Generative AI statement

The author(s) declare that no Generative AI was used in the creation of this manuscript.

Publisher's note

Supplementary material

The Supplementary Material for this article can be found online at: https://www.frontiersin.org/articles/10.3389/fcell.2024.1514553/full#supplementary-material

SUPPLEMENTARY MATERIAL S1
Statistical analysis.

SUPPLEMENTARY TABLE S1
Original datasets for statistical analyses.

SUPPLEMENTARY TABLE S2
Mann-Whitney U-test by months for all investigated groups (CCL, ACL, DCL).

SUPPLEMENTARY FIGURE S1
Analysis of population growth data of *Trichoplax* with the ap index during 2024 (original file).

SUPPLEMENTARY FIGURE S2
Analysis of population growth data on placozoans.

SUPPLEMENTARY FIGURE S3
Comparisons of the present datasets with previously published data from (Maruyama, 2004).

SUPPLEMENTARY FIGURE S4
Comparison of standard plots (left) and sliding windows for 5 observations (right). The upper plot includes all groups of animals, CCL, control; ACL, ampicillin-treated animals; DCL, doxycyclin-treated animals.

References

Afifi, A., May, S., and Clark, V. A. (2003). *Computer-aided multivariate analysis*. Boca Raton: CRC Press.

Aleshin, V. V., Konstantinova, A. V., Nikitin, M. A., and Okstein, I. L. (2004). On the genetic uniformity of the genus *Trichoplax* (Placozoa). *Genetika* 40 (12), 1714–1716. (in Russ).

Armon, S., Bull, M. S., Aranda-Diaz, A., and Prakash, M. (2018). Ultrafast epithelial contractions provide insights into contraction speed limits and tissue integrity. *Proc. Natl. Acad. Sci. U. S. A.* 115 (44), E10333–E10341. doi:10.1073/pnas.1802934115

Chizhevsky, A. L. (1976). *Earthly echo of solar storms*. Moscow: Ripol Classic. (in Russ).

Deng, J., Zhang, W., Qin, B., Zhang, Y., Paerl, H. W., and Salmaso, N. (2018). Effects of climatically-modulated changes in solar radiation and wind speed on spring phytoplankton community dynamics in Lake Taihu, China. *PloS One* 13 (10), e0205260. doi:10.1371/journal.pone.0205260

Driscoll, T., Gillespie, J. J., Nordberg, E. K., Azad, A. F., and Sobral, B. W. (2013). Bacterial DNA sifted from the *Trichoplax adhaerens* (Animalia: Placozoa) genome project reveals a putative rickettsial endosymbiont. *Genome Biol. Evol.* 5 (4), 621–645. doi:10.1093/gbe/evt036

Eitel, M., Guidi, L., Hadrys, H., Balsamo, M., and Schierwater, B. (2011). New insights into placozoan sexual reproduction and development. *PloS ONE* 6 (5), e19639c. doi:10.1371/journal.pone.0019639

Eitel, M., Osigus, H. J., DeSalle, R., and Schierwater, B. (2013). Global diversity of the Placozoa. *PloS ONE* 8 (4), e57131c. doi:10.1371/journal.pone.0057131

Eitel, M. S. (2010). *Phylogenetic position, biodiversity, phylogeography and biology of the Placozoa*.

Eitel, M., and Schierwater, B. (2010). The phylogeography of the Placozoa suggests a taxon-rich phylum in tropical and subtropical waters. *Mol. Ecol.* 19 (11), 2315–2327. doi:10.1111/j.1365-294X.2010.04617.x

Grell, K. G. (1972). Eibildung und furchung von *Trichoplax adhaerens* FE Schulze (Placozoa). *Zoomorphology* 73 (4), 297–314. doi:10.1007/bf00391925

Häder, D. P. (2000). Effects of solar UV-B radiation on aquatic ecosystems. *Adv. Space Res.* 26 (12), 2029–2040. doi:10.1016/s0273-1177(00)00170-8

Heyland, A., Croll, R., Goodall, S., Kranyak, J., and Wyeth, R. A. (2014). *Trichoplax adhaerens*, an enigmatic basal metazoan with potential. *Methods Mol. Biol.* 1128, 45–61. doi:10.1007/978-1-62703-974-1_4

Hirayama, T., Inden, M., Tsuboi, H., Niwa, M., Uchida, Y., Naka, Y., et al. (2019). A Golgi-targeting fluorescent probe for labile Fe (ii) to reveal an abnormal cellular iron distribution induced by dysfunction of VPS35. *Chem. Sci.* 10 (5), 1514–1521. doi:10.1039/c8sc04386h

Jackson, A. M., and Buss, L. W. (2009). Shiny spheres of placozoans (*Trichoplax*) function in anti-predator defense. *Invertebr. Biol.* 128 (3), 205–212. doi:10.1111/j.1744-7410.2009.00177.x

Kamm, K., Osigus, H. J., Stadler, P. F., DeSalle, R., and Schierwater, B. (2019). Genome analyses of a placozoan rickettsial endosymbiont show a combination of mutualistic and parasitic traits. *Sci. Rep.* 9 (1), 17561. doi:10.1038/s41598-019-54037-w

Kravchenko, K. L., Grechany, G. V., and Gadjiev, G. D. (2006). Correlation between *Drosophila* population sizes and solar activity parameters. *Biophysics* 51, 466–470. doi:10.1134/s0006350906030201

Kuhl, W., and Kuhl, G. (1963). Bewegungsphysiologische untersuchungen an *Trichoplax adhaerens* F.E.schulze. *Zool. Anz. Suppl.* 26, 460–469.

Kuhl, W., and Kuhl, G. (1966). Untersuchungen uber das Bewegungsverhalten von *Trichoplax adhaerens* F.E.Schulze (Zeittransformation: Zeitranffung). *Z. Morph. Okol. Tiere.* 5, 417–435.

Liu, L., Huang, B., Lu, Y., Zhao, Y., Tang, X., and Shi, Y. (2024). Interactions between electromagnetic radiation and biological systems. *Iscience* 27, 109201. doi:10.1016/j.isci.2024.109201

Lv, H., and Shang, P. (2018). The significance, trafficking and determination of labile iron in cytosol, mitochondria and lysosomes. *Metallomics* 10 (7), 899–916. doi:10.1039/c8mt00048d

Malakhov, V. V. (1990). *Enigmatic groups of marine invertebrates: Trichoplax, Orthonectida, Dicyemida, Porifera*.

Maruyama, Y. K. (2004). Occurrence in the field of a long-term, year-round, stable population of placozoan. *Biol. Bull.* 206 (1), 55–60.

Miyazawa, H., Osigus, H. J., Rolfes, S., Kamm, K., Schierwater, B., and Nakano, H. (2021). Mitochondrial genome evolution of placozoans: gene rearrangements and repeat expansions. *Genome Biol. Evol.* 13 (1), evaa213. doi:10.1093/gbe/evaa213

Miyazawa, H., Yoshida, M. A., Tsuneki, K., and Furuya, H. (2012). Mitochondrial genome of a Japanese placozoan. *Zool. Sci.* 29 (4), 223–228. doi:10.2108/zsj.29.223

Nakano, H. (2014). Survey of the Japanese coast reveals abundant placozoan populations in the Northern Pacific Ocean. *Sci. Rep.* 4, 5356. doi:10.1038/srep05356

Neale, P. J., and Thomas, B. C. (2016). Solar irradiance changes and phytoplankton productivity in Earth's ocean following astrophysical ionizing radiation events. *Astrobiology* 16 (4), 245–258. doi:10.1089/ast.2015.1360

Okshtein, I. L. (1987). On the biology of *Trichoplax* sp. (Placozoa). *Zool. Zh.* 66 (3), 339.

Pearse, V. B. (1989). Growth and behavior of *Trichoplax adhaerens*: first record of the phylum Placozoa in Hawaii.

Pearse, V. B., and Voigt, O. (2007). Field biology of placozoans (*Trichoplax*): distribution, diversity, biotic interactions. *Integr. Comp. Biol.* 47 (5), 677–692. doi:10.1093/icb/icm015

Pfeiffer, D., Toro-Nahuelpan, M., Awal, R. P., Müller, F. D., Bramkamp, M., Plitzko, J. M., et al. (2020). A bacterial cytolinker couples positioning of magnetic organelles to cell shape control. *Proc. Natl. Acad. Sci.* 117 (50), 32086–32097. doi:10.1073/pnas.2014659117

Ranta, E., Lindstrom, J., Kaitala, V., Kokko, H., Linden, H., and Helle, E. (1997). Solar activity and hare dynamics: a cross-continental comparison. *Am. Nat.* 149 (4), 765–775. doi:10.1086/286019

Romanova, D. Y., and Moroz, L. L. (2024). Parallel evolution of gravity sensing. *Front. Cell Dev. Biol.* 12, 1346032. doi:10.3389/fcell.2024.1346032

Romanova, D. Y., Nikitin, M. A., Shchenkov, S. V., and Moroz, L. L. (2022). Expanding of life strategies in Placozoa: insights from long-term culturing of *Trichoplax* and *Hoilungia*. *Front. Cell Dev. Biol.* 10, 823283. doi:10.3389/fcell.2022.823283

Romanova, D. Y., Varoqueaux, F., Eitel, M., Yoshida, M. A., Nikitin, M. A., and Moroz, L. L. (2024). "Long-term culturing of placozoans (*Trichoplax* and *Hoilungia*)," in *Ctenophores: methods and protocols* (New York, NY: Springer US), 509–529.

Ruthmann, A. (1977). *Cell differentiation, DNA content and chromosomes of Trichoplax adhaerens FE Schulze*.

Schierwater, B. (2005). My favorite animal, *Trichoplax adhaerens*. *BioEssays* 27 (12), 1294–1302. doi:10.1002/bies.20320

Schierwater, B., and DeSalle, R. (2018). Placozoa. *Cur. Biol.* 28 (3), R97–R98. doi:10.1016/j.cub.2017.11.042

Schierwater, B., Eitel, M., Osigus, H. J., von der Chevallerie, K., Bergmann, T., Hadrys, H., et al. (2010). *Trichoplax* and Placozoa: one of the crucial keys to understanding metazoan evolution. *Key transitions animal Evol.* 289, 326. doi:10.1201/b10425-16

Schierwater, B., Osigus, H. J., Bergmann, T., Blackstone, N. W., Hadrys, H., Hauslage, J., et al. (2021). The enigmatic Placozoa part 1: exploring evolutionary controversies and poor ecological knowledge. *BioEssays* 43 (10), 2100080.

Schleicherová, D., Dulias, K., Osigus, H. J., Paknia, O., Hadrys, H., and Schierwater, B. (2017). The most primitive metazoan animals, the placozoans, show high sensitivity to increasing ocean temperatures and acidities. *Ecol. Evol.* 7 (3), 895–904. doi:10.1002/ece3.2678

Senatore, A., Reese, T. S., and Smith, C. L. (2017). Neuropeptidergic integration of behavior in *Trichoplax adhaerens*, an animal without synapses. *J. Exp. Biol.* 220 (18), 3381–3390.

Seravin, L. N., and Gerasimova, Z. P. (1998). Features of the fine structure of *Trichoplax adhaerens* trichoplax, feeding on dense plant substrates. *Cytologiya* 30, 1188–1193. (in Russ).

Seravin, L. N., and Gudkov, A. V. (2005a). Ameboid properties of cells in the process of early morphogenesis and the nature of a possible protozoal ancestor of Metazoa. *Zh. Obsh. Biol.* 66 (3), 212–223. (in Russ).

Seravin, L. N., and Gudkov, A. V. (2005b). *Trichoplax adhaerens (type Placozoa) - one of the most primitive multicellular animals*. St. Peterburg: SPb.: TESSA. (in Russ).

Seravin, L. N., and Karpenko, A. A. (1987). Features of orientation of invertebrates in three-dimensional space. *Zool. Zh.* 66 (9), 1285–1292. (in Russ).

Signorovitch, A. Y., Dellaporta, S. L., and Buss, L. W. (2006). Caribbean placozoan phylogeography. *Biol. Bull.* 211 (2), 149–156. doi:10.2307/4134589

Smith, C. L., Pivovarova, N., and Reese, T. S. (2015). Coordinated feeding behavior in *Trichoplax*, an animal without synapses. *PLoS One* 10, e0136098. doi:10.1371/journal.pone.0136098

Smith, C. L., Varoqueaux, F., Kittelmann, M., Azzam, R. N., Cooper, B., Winters, C. A., et al. (2014). Novel cell types, neurosecretory cells, and body plan of the early-diverging metazoan *Trichoplax adhaerens*. *Cur. Biol.* 24 (14), 1565–1572. doi:10.1016/j.cub.2014.05.046

Srivastava, M., Begovic, E., Chapman, J., Putnam, N. H., Hellsten, U., Kawashima, T., et al. (2008). The *Trichoplax* genome and the nature of placozoans. *Nature* 454 (7207), 955–960. doi:10.1038/nature07191

Tessler, M., Neumann, J. S., Kamm, K., Osigus, H. J., Eshel, G., Narechania, A., et al. (2022). Phylogenomics and the first higher taxonomy of Placozoa, an ancient and enigmatic animal phylum. *Front. Ecol. Evol.* 10, 1016357. doi:10.3389/fevo.2022.1016357

Ueda, T., Koya, S., and Maruyama, Y. K. (1999). Dynamic patterns in the locomotion and feeding behaviors by the placozoan *Trichoplax adhaerence*. *Biosystems* 54 (1-2), 65–70. doi:10.1016/s0303-2647(99)00066-0

Zhong, G., Kroo, L., and Prakash, M. (2023). Thermotaxis in an apolar, non-neuronal animal. *J. R. Soc. Interface* 20 (206), 20230279. doi:10.1098/rsif.2023.0279

Zuccolotto-Arellano, J., and Cuervo-González, R. (2020). Binary fission in *Trichoplax* is orthogonal to the subsequent division plane. *Mech. Dev.* 162, 103608. doi:10.1016/j.mod.2020.103608

Frontiers in Cell and Developmental Biology

TYPE Review
PUBLISHED 09 January 2025
DOI 10.3389/fcell.2024.1531560

OPEN ACCESS

EDITED BY
Michael Schubert,
UMR7009 Laboratoire de Biologie du Développement de Villefranche sur Mer, France

REVIEWED BY
Marco Gerdol,
University of Trieste, Italy
Charles Bradley Shuster,
New Mexico State University, United States

*CORRESPONDENCE
Andreas Wanninger,
andreas.wanninger@univie.ac.at

RECEIVED 22 November 2024
ACCEPTED 16 December 2024
PUBLISHED 09 January 2025

CITATION
Wanninger A and Schwarze G (2025) The quagga mussel, *Dreissena rostriformis*: a novel model for EcoEvoDevo, environmental research, and the applied sciences.
Front. Cell Dev. Biol. 12:1531560.
doi: 10.3389/fcell.2024.1531560

The quagga mussel, *Dreissena rostriformis*: a novel model for EcoEvoDevo, environmental research, and the applied sciences

Andreas Wanninger* and Gudrun Schwarze

Department of Evolutionary Biology, Unit for Integrative Zoology, University of Vienna, Vienna, Austria

Bivalve mollusks are globally distributed in marine and freshwater habitats. While exhibiting a relatively uniform bodyplan that is characterized by their eponymous bivalved shell that houses the soft-bodied animal, many lineages have acquired unique morphological, physiological, and molecular innovations that account for their high adaptability to the various properties of aquatic environments such as salinity, flow conditions, or substrate composition. This renders them ideal candidates for studies into the evolutionary trajectories that have resulted in their diversity, but also makes them important players for research concerned with climate change-induced warming and acidification of aquatic habitats. Some species, such as the blue and Mediterranean as well as the zebra and quagga mussels, form biodegradable fibers, the byssus threads. These have significant potential for biomimetic approaches by aiding in developing sustainable textiles and other fiber-based fabrics. Despite this broad span of scientific relevance, bivalves remain dramatically understudied and key resources such as high-quality genomes and developmental transcriptomes in combination with established laboratory protocols to carry out state-of-the-art molecular and morphological studies are only available for less than a handful of species. Here, we report on one of the best-investigated bivalves in this respect, the quagga mussel, *Dreissena rostriformis*, an invasive freshwater species. We summarize the current state of knowledge and available resources that make the quagga mussel highly amenable for studying adaptive mechanisms for life in hypoosmotic environments, biomineralization, biomimetics, and evolutionary developmental biology. We argue that the unique combination of biological features and the broad relevance of the quagga mussel for the basic and the applied sciences as well as for biomonitoring and conservation biology measures call for intensified research efforts using *Dreissena rostriformis* as a model.

KEYWORDS

bivalve, mollusk, evolution, development, evodevo, invasive species, hox, biomineralization

1 Introduction

The phylum Mollusca boasts approximately 120.000 extant species, which makes it the second-most speciose phylum after Arthropoda (Ponder et al., 2019). Its eight class-level taxa, the vermiform, cylindrical Neomeniomorpha (Solenogastres) and Chaetodermomorpha (Caudofoveata), the dorso-ventrally flattened Polyplacophora with eight dorsal shell plates, the univalved Monoplacophora with a cap-like shell, the dorsoventrally elongated Scaphopoda with a calcareous tube, as well as the more commonly known Gastropoda (snails and slugs), Bivalvia (mussels, clams, oysters, scallops, among others), and Cephalopoda (nautiluses, squids, octopuses) exhibit a vast diversity of phenotypes with adaptations to virtually all terrestrial and aquatic habitats. As a consequence of this morphological and ecological plasticity, numerous features of a proposed ancestral mollusk have either been modified (e.g., the foot, which may function as a creeping, attachment, burrowing, or swimming organ), were entirely lost (e.g., the radula in bivalve mollusks or the shell in various lineages), or have secondarily acquired considerable complexity (e.g., the brain in cephalopods) in a number of representatives (Wanninger and Wollesen, 2019). Accordingly, these morphological variations and the multiple conquest of various habitats render mollusks an ideal group for comparative studies into the developmental and molecular mechanisms that underlie the establishment of these features on a micro- and macro-evolutionary scale.

Despite this huge potential, relatively little is known concerning the evolutionary transitions that have occurred between (and along) the various molluscan class-level lineages. This is partly due to the still poorly resolved interrelationships of the various classes, but even more so, because well-established model systems are scarce and largely lacking for most clades, including prominent representatives such as the gastropods, cephalopods, and bivalves. However, an increasing number of genomic resources have become available across Mollusca over the past few years, which may form an important base for future evolutionary studies (see, e.g., Wollesen and Wanninger, 2023).

Among the shelled groups (Conchifera), Bivalvia constitutes a taxon of particular wide distribution in freshwater and marine habitats. Several bivalve representatives are of outstanding economic importance as source of protein (food) or jewelry (pearls), and are thus prominently featured in aquaculture systems worldwide. On the other hand, being capable of attaching themselves, during settlement and metamorphosis, to hard substrates, either reversibly via so-called organic byssus threads (e.g., blue mussels, zebra and quagga mussels) or permanently via calcareous secretions (e.g., oysters), they constitute major biofouling organisms that pose technical and/or economical problems by, e.g., clogging water pipes or by increasing the water resistance of ship bodies, thereby causing excess fuel expenditure (Inoue et al., 2021; Karatayev and Burlakova, 2022; McCartney et al., 2022; Simmons et al., 2023). Some species (shipworms) may bore into wooden structures and thus contribute to severe damage to estuarine plants as well as manmade constructions including underwater archeological sites (Paalvast and van der Velde, 2011; Hernández and Angelini, 2019).

The bivalve adult bodyplan is unique insofar as bivalves have evolved a number of unique morphological features. Their body is encased by a bipartite shell that is underlain by the mantle epithelium in which the visceral organs of the animal are housed. Studies into the morphogenesis and gene expression during shell formation have found that in the earliest phases of the process the primordial bivalve shell (the protoconch I or embryonic shell) forms from a single shell field, similar to their conchiferan kin. Ontogenetically, the protoconch I is followed by the protoconch II (the larval shell) that, similar to its successor, the teleoconch (adult shell), is formed after metamorphosis by continuous secretion from cells of the mantle margin. Accordingly, the larval and adult shells often show growth patterns, and especially the latter may exhibit highly elaborated ornamentation and coloration (Wanninger and Wollesen, 2019).

In bivalve shells, both lateral halves (valves) are interconnected dorsally by a hinge-like structure and, importantly, by the so-called ligament that is of organic composition. The kinetic energy, that is generated when the animal closes its valves by means of contraction of its prominent adductor muscles, is released upon adductor relaxation, thereby opening the shell passively.

A number of bivalve internal features are characterized by having a more “simple” morphology than the respective counterparts of their conchiferan relatives. A distinct “head” is missing, alongside with the mollusk-specific radula, a rasping tongue that is otherwise present in almost all mollusk species. The nervous system shows some degree of ganglionization along the pedal and visceral nerve cords, but is much less elaborated as, e.g., in gastropods or cephalopods (Ponder et al., 2019).

The bivalve life cycle usually begins with shedding of the male and female gametes into the water column where fertilization occurs (but brooding is also common in some groups). Subsequent development often includes a (usually short-lived and non-feeding, i.e., lecithotrophic) trochophore-type larva that is followed by a planktotrophic veliger larva that may live in the plankton for months. The veliger larva gradually forms most internal organ systems also present in the adult animal (heterochrony). Thus, upon settlement and metamorphosis, where larval features such as the ciliated swimming and feeding device (the velum) and excretory system (protonephridia) are reduced, the young bivalve is immediately ready to commence its benthic lifestyle. Deviations from this ancestral life cycle are found in, e.g., some freshwater taxa (e.g., unionids) that brood their larvae which, upon release and a short swimming period, parasitize on fish skin and gills to which they attach by specific devices such as hooks and threads (Ponder et al., 2019; Wanninger and Wollesen, 2019).

While the vast majority of bivalve species are marine, several lineages have independently ventured into the freshwater realm, the majority of which belonging to the Paleoheterodonta. Some species have shown an astounding capability to cope with fluctuations in salinity values and thus are found in marine/brackish as well as freshwater environments. One such group are the dreissenids, in particular two congeners, *Dreissena polymorpha* (the zebra mussel) and *Dreissena rostriformis* (the quagga mussel), that have an origin in the brackish waters of the eastern European Ponto-Caspian region (Heiler et al., 2013; Aldridge et al., 2014; Calcino et al., 2019; Karatayev and Burlakova, 2022). From there, they spread into the Great Lakes of North America and towards middle and northern Europe from the 1980s onwards, probably by originally travelling with the ballast water of cargo ships (Dahlberg et al., 2023). Once introduced into a new ecosystem, both species may spread rapidly. This is due to the particularly high number of eggs (hundreds of thousands) that may be produced by gravid females and that are released into the water column, where they are fertilized and commence their ancestral, indirect life cycle via free-swimming trochophore and veliger larvae. In favorable conditions, these may stay in the plankton for several weeks and may thus travel considerable distances before they eventually settle and start their benthic lifestyle. Once metamorphosed into a juvenile, dreissenids are high-throughput filter feeders that remove considerable amounts of organic matter, in particular phytoplankton, from the water column, thus impoverishing the food supply for other consumers such as fish and crustacean larvae (Dahlberg et al., 2023). Lacking these primary producers, the water becomes more transparent and penetrable for light, resulting in enhanced growth of submerged plants including algae, thereby significantly impacting the ecosystem's nutrient and energy fluxes and, ultimately, its species composition. Accordingly, *Dreissena polymorpha* and *Dreissena rostriformis* can be regarded as major "ecosystem engineers", also because they may form dense aggregates, so-called mussel beds, that serve as habitat for other invertebrate species. In order to minimize their impact on the native freshwater fauna and flora, millions of dollars are invested annually in the United States in various projects that aim at monitoring and controlling the dispersal of these species (Dahlberg et al., 2023).

In addition to their high filtration capacity and reproduction as well as dispersal rate, the zebra and quagga mussel have evolved physiological and cellular mechanisms that allow them to rapidly adapt to salinity conditions that are significantly below that of their region of origin (Calcino et al., 2019). All these factors, that act in favor of *Dreissena*, have contributed to a severe decline of the native freshwater bivalve fauna, particularly of unionids (e.g., the alewife floater, *Anodonta implicata*, its congener, *Anodonta anatina*, the Eastern pearl mussel, *Margaritifera margaritifera*, or the tidewater mucket, *Atlanticoncha* (formerly *Leptodea*) *ochracea*) in North American and European freshwater systems. This has pushed dreissenid bivalves into the limelight of conservation biologists, but up to now, efforts to control these invasive species have proven only little successful.

Given the combination of conserved (typical bivalve bodyplan with shells, filter feeding, reversible attachment mechanisms, free spawning, indirect development in the water column) and derived, i.e. *de novo* evolved ("innovative") features (e.g., rapid adaptation to low salinity levels), the common zebra mussel (*Dreissena polymorpha*) and quagga mussel (*Dreissena rostriformis*) are prime candidates for research into various biological disciplines including evolutionary developmental biology (evodevo), physiology (adaptation to changes in osmolarity), ecology (invasiveness), and biomineralization, also in the light of climate change scenarios with increased water temperatures and decreased pH values and associated impacts on biocalcification (Calcino et al., 2019; McCartney et al., 2022; Zieger et al., 2022; Simmons et al., 2023).

In the past decade, significant progress in our understanding of dreissenid ontogeny on the morphological and the molecular level has been made. This includes the establishment of protocols for immunofluorescence staining, gene expression studies, and single cell RNA sequencing, as well as the production of a high quality genome and a series of transcriptomes for all key developmental stages of the quagga mussel, *Dreissena rostriformis* (Pavlicek et al., 2018; Calcino et al., 2019; Salamanca-Diaz et al., 2021; Salamanca-Diaz et al. 2022a; Salamanca-Diaz et al. 2022b; Schulreich et al., 2022; Zieger et al., 2022). These resources form an ideal base for tackling biological questions using the quagga mussel for studies from the molecular through the cellular to the organismal and ecosystem scale. Accordingly, topics relevant for the basic sciences (evolutionary biology) as well as applied disciplines (avoidance of biofouling, ecosystem protection) can be addressed using this system. Here, we highlight the state-of-the-art of dreissenid research using the quagga mussel, *Dreissena rostriformis*, as a model, with a focus on its bearing on ecoevodevo studies, summarize and discuss recent findings, and provide an outline for future research paths. We also point out how such data may prove relevant for research into the applied sciences, ecosystems research, climate change, and aquatic pest management.

2 *Dreissena* as a model for evodevo research: morphological and molecular aspects of bivalve bodyplan and life cycle evolution

Mollusca is a member of the superclade Lophotrochozoa and its members are characterized by having derived from a last common ancestor with a spiral cleavage pattern (Spiralia). Spiral cleavage has been conserved in most early branching lineages of the various mollusk subclades including Bivalvia. This mode of cleavage is highly determinate, i.e., the fate of each blastomere is predictable, defined early on in development, and conserved across closely related species (Wanninger and Wollesen, 2015; Wanninger and Wollesen, 2019). As such, comparative analyses into the contributions of each blastomere lineage to individual morphological traits allows for insights into the shared ancestry (homology) of given characters, such as ciliated swimming/feeding structures (e.g., prototroch, velum, telotroch), neural and sensory systems (e.g., the larval apical organ), or the shell (see below).

Similar to many of their marine kin, *Dreissena* species have a conserved life cycle during which mature egg and sperm are shed freely into the water column where fertilization takes place. Cleavage is spiral and embryos start to actively swim by means of their cilia as early as in their gastrula stage (Meisenheimer, 1899; Meisenheimer, 1901; Pavlicek et al., 2018; Salamanca-Diaz et al., 2021). This stage is characterized by two ectodermal invaginations, the blastopore (the future mouth) that marks the ventral region, and the more prominent shell field that is part of the dorsal ectoderm (Figure 1). Subsequently, a short-lived planktonic trochophore larva is formed, followed by a veliger larva that may reside in the plankton for several weeks. Development of serotonin-like immunoreactive compounds of the nervous system starts with one flask-like receptor cell in the apical organ of early trochophore larvae (Figure 1; Pavlicek et al., 2018). In the veliger stage, this number increases to four. At the same time, the neurons of the paired visceral cord form, together with receptor cells of the posterior sense organ, a structure that is typical for some larval bivalves, and subsequently the first cells of the future cerebral ganglion emerge. Prior to metamorphosis the apical tuft and the underlying flask cells are gradually lost, as is the posterior sense organ, while the cerebral ganglion is continuously elaborated (Figure 1; Pavlicek et al., 2018).

Similar to neurogenesis, muscle formation starts in the trochophore stage, but elaborate and functional muscles are first found in the veliger larva. The larval myoarchitecture of *Dreissena* is highly complex and includes a number of retractor muscles that enable retraction of the larval body including the velum into the shell. Except for parts of the adductor system, that start forming in

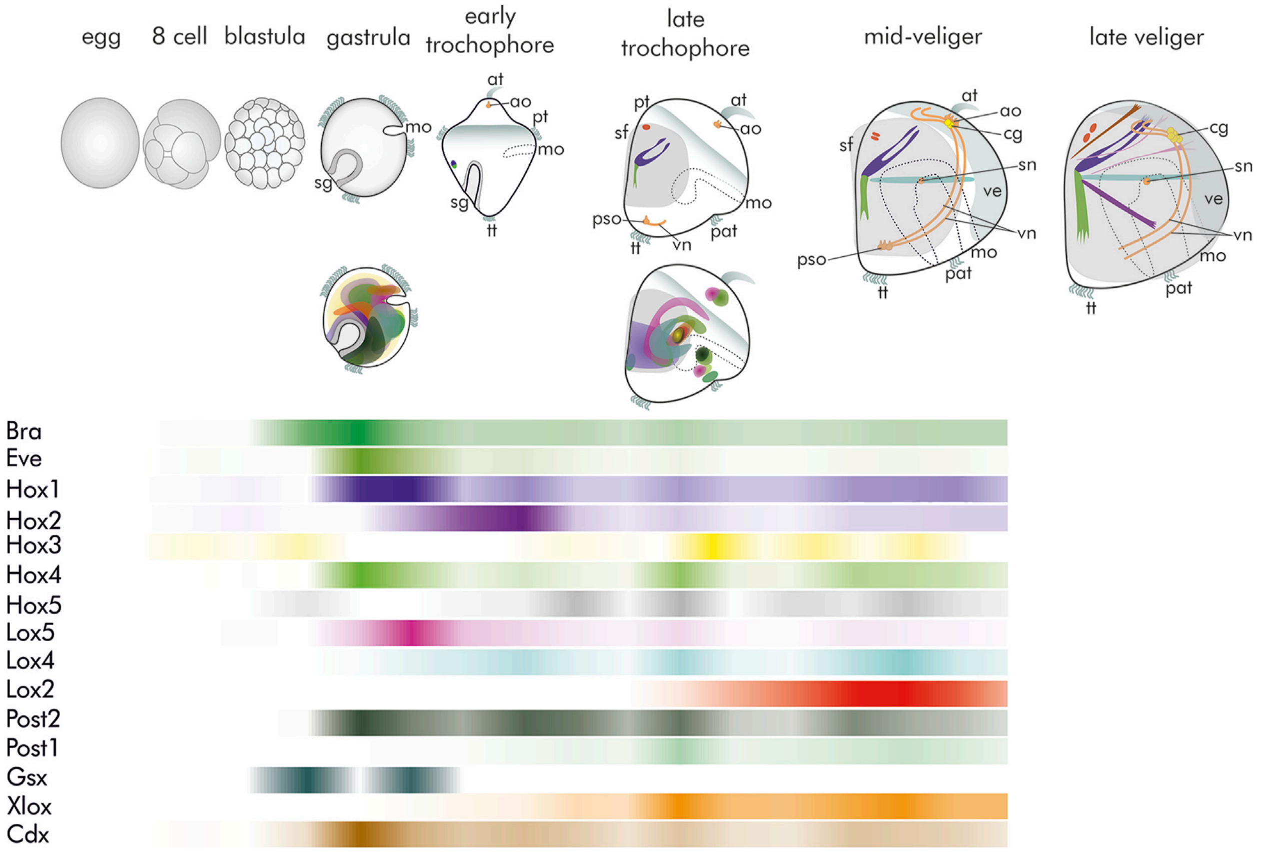

FIGURE 1
Schematic summary of morphogenesis, gene expression domains, and relative quantitative occurrence of transcripts of *brachyury*, *even-skipped*, as well as the genes of the Hox and ParaHox cluster in *Dreissena*. Data from Salamanca-Díaz et al. (2021) and Schulreich et al. (2022). Top row: Morphogenesis with developing nervous system and musculature. All images are in lateral view with apical facing upwards. (at) apical tuft, (ao) apical organ, (cg) anlagen of the future cerebral ganglion, (mo) mouth opening, (pat) pre-anal tuft, (pso) posterior larval sensory organ, (pt) prototroch, (sf) shell field, (sg) shell gland, (sn) stomatogastric nerve cell, (tt) telotroch, (ve) velum, (vn) ventral neurites. Grey surfaces mark the developing shell and prototroch/velum, respectively. The first serotonin-like immunoreactive (lir) flask-shaped apical cell (orange) appears in the trochophore stage. Myogenesis (green/blue) starts in close proximity to the shell gland. In the late trochophore, two serotonin-lir flask-shaped cells are present in the apical organ, together with the first-formed serotonin-lir flask-shaped cell of the posterior larval sensory organ and the anlage of the ventral neurites. In addition, the dorsal velum retractor (blue), larval retractor (green), and anterior adductor anlage (red) emerge. Four flask-shaped cells form the apical organ in the D-shaped mid-veliger stage, while two roundish, non-sensory cells (yellow) form the anlage of the future cerebral ganglia. In the posterior larval sensory organ, a third flask-shaped cell emerges. A stomatogastric nerve cell is present. The larval retractor (green), the two-partite anterior adductor (red), the dorsal velum retractor (blue), and the ventral velum retractor (turquoise) are present. The immunoreactive cells of the posterior larval sensory organ have disappeared, and the anlage of the future cerebral ganglion has enlarged. Additional muscles of the late veliger larva include two mantle retractors (pink), a foot retractor (purple), and an accessory velum retractor (brown). Middle: Schematic representation of gene expression domains of *brachyury* (*bra*), *even-skipped* (*eve*), Hox, and ParaHox genes. Most genes are expressed in the gastrula and late trochophore stage. Note the overlapping, non-staggered (non-collinear) mode of expression of Hox genes. For color code see bars in relative expression timeline chart below. Bottom: Schematic representation of relative quantitative abundance of *brachyury* (*bra*), *even-skipped* (*eve*), Hox, and ParaHox gene transcripts.

the veliger stage, all these larval muscle systems are lost during metamorphic body plan remodelling and all adult systems arise *de novo* (Figure 1; Schulreich et al., 2022).

Data on developmental gene expression are scarce for bivalves, with *Dreissena rostriformis* being one of the best-investigated species today. Ten of the 11 predicted molluscan Hox genes are present in the *Dreissena rostriformis* genome (*Hox-7* appears to be absent). The three bilaterian ParaHox genes were also found (Salamanca-Diaz et al., 2021). Both, the proposed Hox and the ParaHox cluster appear to be broken in *Dreissena*. Compared to other mollusks, Hox gene expression appears unique in the quagga mussel in that no traces of a staggered mode of expression is present. Instead, Hox gene expression, that starts already in the gastrula stage for most genes, shows significant overlap of their expression domains (Figure 1; Salamanca-Diaz et al., 2021). These become largely confined to mesodermal regions, but, again different to other conchiferans, their spatial expression cannot be assigned to any specific developing morphological structures. *Hox-1* is one of the very few exceptions, as it is expressed in the shell field, similar to all other conchiferans investigated so far (Salamanca-Diaz et al., 2021). Since Hox genes are key players in anterior-posterior patterning, the compact, widely overlapping domains in *Dreissena* may be a result of the low degree of longitudinal regionalization of bivalves, whose bodyplan is characterized by the loss of regionally specific traits such as a head or radula. To this end, comparative data on distant but also close dreissenid (marine) relatives within Imparidentia such as myoid, venerid or cardiid representatives would be useful to further assess this hypothesis. However, since protocols to perform functional genetic studies such as RNAi (gene knockdown), gene targeting (gene knockout), or gene editing (using the CRISPR/Cas system) are currently not available for *Dreissena* or any other bivalve, a final argument concerning the function of specific genes remain speculative at present. Yet, the great variety of expression domains of Hox genes across conchiferan representatives suggests that these developmental transcription factors may have been co-opted independently into different functions in the various molluscan lineages, an exciting hypothesis that remains to be tested employing functional genetic methods.

3 Biomineralization and the evolution of mollusk skeletal hardparts

Numerous mollusks are characterized by the possession of external armor that my come in spicules (in the aplacophorans), plates (polyplacophorans), or shells (conchiferans). Reductions and modifications of the ancestral conchiferan single-partite, external shell have occurred multiple times along various lineages, having led to complete loss (e.g., in interstitial or terrestrial slugs), internalization (coleoid cephalopods), or bipartioning (some sacoglossan gastropods, most bivalves) in certain representatives (Wanninger and Wollesen, 2019; Ponder et al., 2019).

In taxa that exhibit the ancestral, indirect life cycle, the shell field, that in bivalves may develop as early as in the gastrula stage, initially invaginates (see above and Figure 1). Subsequently, the shell field evaginates (“flattens”) and secretes the organic matrix (the periostracum) that serves as a scaffold for the calcification process during which calcium carbonate molecules are deposited to eventually produce the embryonic shell (protoconch I) (Wanninger and Wollesen, 2015). The protoconch I appears to calcify from two centers of the originally single shell field, thereby establishing the bipartite condition of the bivalve shell. Calcification of the protoconch I is rapid, resulting in the smooth appearance of its surface. In some long-lived planktonic gastropod larvae and numerous bivalves (including *Dreissena*), an intermediate larval shell (protoconch II) is formed that, similar to its successor, the teleoconch (the adult shell), is continuously secreted from cells of the mantle margin. Thus, while the larval shell (where present) forms an ontogenetic continuum with the adult shell, the fundamentally different mode of embryonic shell formation calls into question the putative homology of the latter with the former two shell types (Salamanca-Diaz et al., 2022a).

Recent studies employing singe cell RNA sequencing have shown that the gene complement of both, embryonic and adult shells, in bivalves include a large number of (taxonomically restricted?) genes that show no ortholog match with other metazoans (Salamanca-Diaz et al., 2022a). Accordingly, these genes may thus be prone to high mutation rates over short periods of time, a characteristic of so-called “rapidly evolving” morphological features (Jackson et al., 2006; Kocot et al., 2016; Aguilera et al., 2017; Clark et al., 2020; Yarra et al., 2021; Salamanca-Diaz et al., 2022a). A comparison of the genes expressed during embryonic and larval shell secretion further revealed that both ontogenetic shell types differ greatly in the suite of genes expressed during their secretion, lending support to the hypothesis that the first-formed embryonic shell is not homologous to the larval shell (and thus likely neither to the adult shell; Salamanca-Diaz et al., 2022a). However, the comparative database of gene expression during the formation of all three bivalve shell types is very scant, thus hampering well-founded conclusions into the evolutionary relatedness of these three shell types to each other.

The plasticity of bivalve skeletogenesis is not only manifested by the highly diverging genes that appear to be involved in the process, but also by the morphological properties exhibited by their shells. Accordingly, these may come in various, differing layers that build the shells in the respective lineages, variations in their colors and color patterns, and, most strikingly, in innumerous modifications of their calcareous surface that may include various ornamentation such as ribs, spines, and the like (Ponder et al., 2019). A particularly striking example includes the teredinids (shipworms) that have secondarily transformed their shell valves from a protective apparatus into a drill-like boring device. Given the fact that all bivalves derive from a last common ancestor with a bivalved, most likely small, simple, and little elaborated shell, further comparative analyses into the molecular and genetic toolkit on the DNA (genes), RNA (gene expression), proteome (shell matrix components), and biomineralization (e.g., ions incorporated in the various shell layers) level will offer a wealth of opportunities to assess evolutionary processes and key drivers on a (micro)evolutionary level - also outside Bivalvia, Mollusca, or even Bilateria, since the ability to form mineralized exo- or endoskeletal features dates back well into the Pre-Cambrian (Murdock, 2020).

In addition to research agendas revolving around evolutionary questions, the analysis of biomineralization processes, particularly in aquatic representatives, has become increasingly popular over the past decades because it provides the possibility to directly observe putative consequences of various issues dealing with the topic of climate change impact on living organisms. As one of the most abundant and ecologically as well as economically important biomineralizing marine animals with billions of offspring produced yearly, bivalves are ideally suited for research into the consequences that, e.g., lower pH values (acidification) may have on the process of producing mineralized skeletal elements using standardized laboratory settings. Numerous studies have proven that continued acidification of aquatic environments may severely impact the vital process of biomineralization in various marine and freshwater invertebrates, particularly gastropods and bivalves, thereby posing significant threats to the survival of species that rely on functional processes to build their skeletal features (e.g., Fabry et al., 2008; Lombardi et al., 2011; Bray et al., 2014). However, despite these well-known negative consequences of acidified habitats for their inhabitants, very little is known about the molecular and genetic mechanisms underlying these processes. To this end, high-quality genomes in combination with tight series of developmental transcriptomes by RNA sequencing hold a strong potential to gain insights into the dynamics and key mediators of biomineralization, since such resources can be specifically mined for suspected candidate genes. Potential hits can then be further analyzed using *in situ* hybridization to assess the tempo-spatial expression of these genes in the organism of interest across its developmental timescale

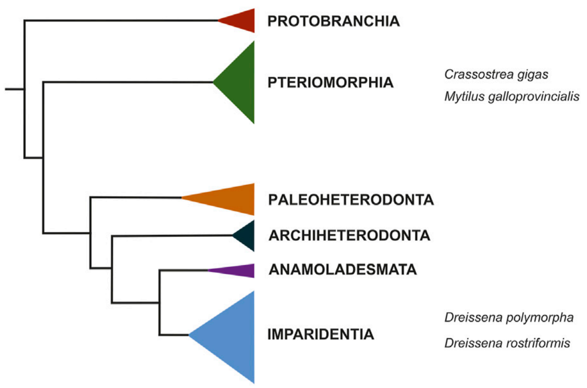

FIGURE 2
Condensed phylogeny of Bivalvia based on a supermatrix composed of 47 molluscan taxa. Modified after Calcino et al. (2019). The quagga mussel, *Dreissena rostriformis*, together with its congener *Dreissena polypmorpha*, the zebra mussel, is nested within Imparidentia. The only two other bivalve species for which comparable genomic and transcriptomic resources are available, the Pacific oyster, *Crassostrea gigas*, and the Mediterranean mussel, *Mytilus galloprovincialis*, are marine species and are phylogenetically distant to the quagga mussel, residing within Pteriomorphia.

and verify if the respective gene is indeed active in tissue with biomineralization properties. Such tight series of developmental transcriptomes do exist for only a few bivalve species, e.g., the quagga mussel, *Dreissena rostriformis* (Calcino et al., 2019), the Mediterranean mussel, *Mytilus galloprovincialis* (Gerdol et al., 2020; Miglioli et al., 2024), and the Pacific oyster, *Crassostrea gigas* (Zhao et al., 2018; Peñaloza et al., 2021). While the latter two belong to the Pteriomorphia, *Dreissena* species are part of a distant bivalve lineage, the Imparidentia (Figure 2), and thus are key for comparative evolutionary studies, including those that aim at reconstructing the processes and players behind the formation of mineralized hardparts. Such data should render more reliable predictions as to how further (anthropogenically induced) environmental change may have a negative bearing on animals that rely on the formation of skeletal elements, thereby aiding in enforcing protection measures in the future (see below).

4 The molecular and cellular foundations of freshwater adaptation in the quagga mussel

There is little doubt that life on Earth evolved in marine environments. From there, animals have ventured onto land and into freshwater numerous times independently. These transitions evoked dramatic physiological adaptations with respect to change in diets, metabolism, excretion, and osmoregulation. In particular, desiccation and osmoregulatory issues need to be overcome when exchanging the high osmotic marine for the hypoosmotic freshwater or the dry terrestrial realm.

Bivalves have invaded freshwater habitats independently on numerous occasions (Calcino et al., 2019). How do they cope with the dramatic osmoregulatory challenges? In adults, excess water is expelled via distinct, multicellular organ systems such as the nephridia. Water removal mechanisms, however, are far less well understood for the early ontogenetic (cleavage) stages, that mark the most vulnerable phase during animal development. It had long been known that *Dreissena* and other freshwater species form large, rhythmically contracting, fluid-filled cavities during early cleavage stages, features that have been attributed to mechanisms of water expulsion in order to avoid cell rupture (Allen, 2000; Tani et al., 2002; Datta et al., 2011; Calcino et al., 2019). Recent combined genomic, cell biological, and developmental studies have shown that a vacuolar ATPase subunit, a sodium/hydrogen exchanger, and a lophotrochozoan-specific aquaporin water channel are involved in the process of water ejection via these cleavage cavities (Calcino et al., 2019). Thereby, a maternally inherited, *Dreissena rostriformis*-specific aquaporin accumulates at the so-called cytokinetic bridge, an arrangement of centrally-located microtubules that forms in the region of the midbody during the process of cell division (Figure 3A; Zieger et al., 2022). During cleavage cavity expansion, the concentration of this aquaporin in the midbody increases (Figure 3B). After cleavage cavity collapse (and extrusion of the contained liquid) as well as separation of the two daughter cells from each other, the midbody and its associated aquaporin is inherited by one of these two cells (Figure 3C). Thereafter, a new cycle of aquaporin recruitment into the midbody region in association with vacuole formation commences once the next generation of cleavage cycles is initiated (Figure 3D; Zieger et al., 2022). While the exact cytological and molecular mechanisms involved in cellular water extrusion remain elusive, these findings on *Dreissena rostriformis* form an important base for future (comparative) research into this matter. The independent multiplication of aquaporin-coding genes in various freshwater bivalve lineages suggests high selective pressures on freshwater-conquering mussels, and putatively also other free-spawning invertebrates, in adopting such an aquaporin-mediated system of water excretion during embryogenesis for survival in hypoosmotic habitats.

5 Discussion

5.1 Available *Dreissena rostriformis* resources for EcoEvoDevo studies

Alongside *Mytilus galloprovincialis* and *Crassostrea gigas*, *Dreissena rostriformis* is one of the very few bivalve species that are currently at the forefront of becoming “true” model systems in ecological and evolutionary developmental biology. For *Dreissena rostriformis*, a series of developmental transcriptomes from the unfertilized, freshly spawned egg through late larval stages is available, as is a high quality genome (Calcino et al., 2019). Reliable protocols for immunofluorescence staining, electron microscopy, histology, and gene expression analyses are well established for *Dreissena* (Pavlicek et al., 2018; Calcino et al., 2019; Salamanca-Diaz et al., 2021; Salamanca-Diaz et al. 2022a; Salamanca-Diaz et al. 2022b; Schulreich et al., 2022; Zieger et al., 2022), and the cell lineage of key organ systems has long been described (Meisenheimer, 1899; 1901). At least in Central Europe, the reproductive period is long, spanning at least from April through

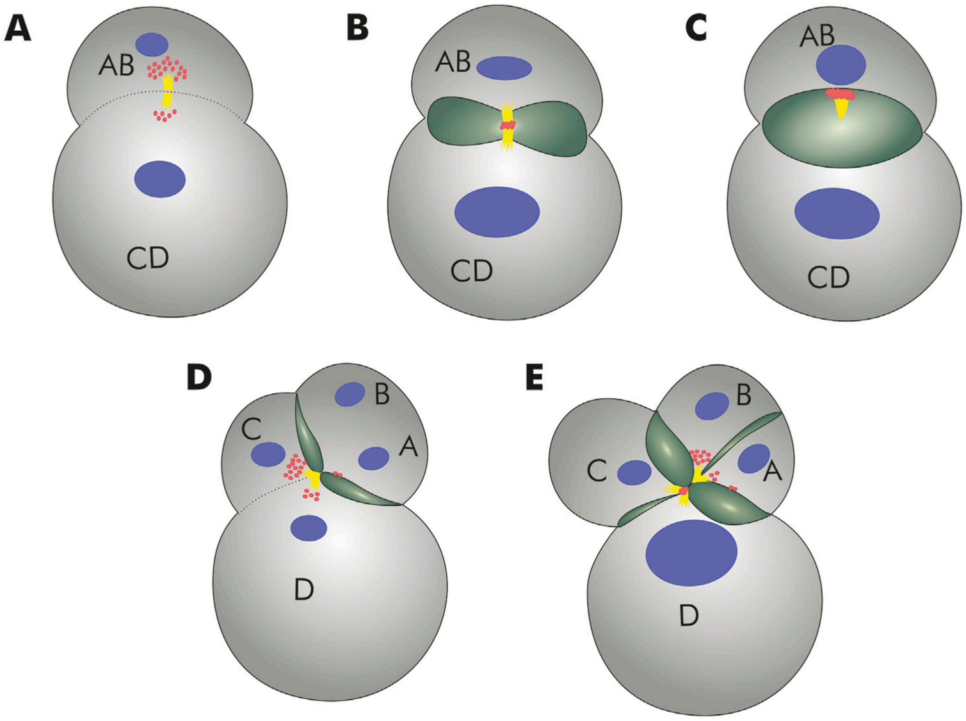

FIGURE 3
Schematic representation of lumen formation during *Dreissena rostriformis* cleavage as proposed by Zieger et al. (2022). **(A)** Aquaporin (red) accumulation at the cytokinetic bridge (yellow). Cell nuclei in blue. **(B)** Aquaporin is recruited to the midbody during cleavage. Cleavage cavity (green) formation is initiated. **(C)** Expansion of the cleavage cavity and separation of the blastomeres AB and CD. One of the two daughter cells inherits the aquaporin immunoreactive midbody remnant. **(D)** The larger CD blastomere divides slightly earlier than the smaller AB blastomere, giving rise to a transient three-cell stage. Note the aquaporin accumulation prior to formation of the second midbody between blastomeres C and D. Two additional cytokinetic bridges are produced by the second round of cleavages; these bridges are displaced towards the interface between the A/D and B/C blastomeres in the middle of the embryo. **(E)** Subsequent cleavages result in additional cavities along the cleavage furrows of forming blastomeres with aquaporin remaining accumulated along the cavity membranes.

October. Spawning can be induced artificially by the addition of serotonin, and hundreds of thousands of offspring can be harvested per individual spawn. Both, adults and developmental stages are easily kept in the laboratory, thus keeping costs and required manpower for animal care low (Pavlicek et al., 2018; Calcino et al., 2019). However, further research should be dedicated to increase the yield of postmetamorphic individuals. Metamorphosis is a key step in the life cycle of indirect developing animals, and in aquatic invertebrates this process often fails in laboratory cultures, resulting in a high percentage of loss of individuals before the juvenile stage is achieved. While this undoubtedly reflects the condition in the wild (producing thousands of offspring is a strategy to cope with high mortality rates prior to adulthood), research should strive towards establishing laboratory conditions to close the life cycle from gametes to adult to gametes as reliably as possible. This is still in its infancy for bivalves in general, because larval phases are often several weeks long, their optimal diet is still unknown, and the mediators of larval metamorphosis - as for almost all aquatic invertebrates - remain elusive. However, for many ecological, developmental, and evolutionary, as well as applied research agendas, the quagga mussel already today offers a wide range of possibilities that are worth exploring. This is particularly true since, within Bivalvia, *Dreissena* species reside within Imparidentia, a lineage that diverged early from the Pteriomorphia to which the two other promising bivalve models, *Crassostrea* and *Mytilus* belong (Figure 2). Due to this early phylogenetic split, the genetic distance of dreissenids to pteriomorphs is relatively large, an important prerequisite for evolutionary studies on broader scales and across long geological timescales.

With both the quagga and the zebra mussel genomes available (Calcino et al., 2019; McCartney et al., 2022), microevolutionary processes can be studied using both dreissenid congeners in comparative approaches. Both species often co-occur alongside each other, with *Dreissena polymorpha* usually being the primary colonizer of a given habitat. However, despite rapidly forming large and stable cultures, several reports have shown that in some habitats *Dreissena polymorpha* may be outcompeted over time by the quagga mussel, *Dreissena rostriformis*, which may lead to partial or full replacement of the former by the latter (Karatayev and Burlakova, 2022). Since both species strikingly resemble each other with respect to size, morphology, life cycle, ecological, and physiological needs, the drivers that render *Dreissena rostriformis* ecologically more competitive than its congener remain largely elusive. A first step towards answering such questions may lie in in-depth comparative genomic analysis of both species, which may reveal potential differences in genes encoding for metabolic pathways, efficient usage of food resources, adaptive capacities to life in freshwater, or higher tolerance to environmental factors including those related to climate change issues.

5.2 Under pressure: the quagga mussel in a changing world

Due to their rather non-selective filter-feeding lifestyle, bivalves in general, and those that form large colonies such as dreissenids in particular, have long been recognised as good candidates to monitor nutrition intake and degrees of pollution, including the accumulation of microplastics, in aquatic environments (Inoue et al., 2021). In the age of genomics, the impact of habitat changes can now be monitored not only on the macroscopic level, but also on the level of genes and signaling cascades that are involved in producing key morphological features throughout the life cycle of the respective species. Accordingly, research into the genetic basis of biomineralization is a field that has received considerable attention over the past decades, and the dramatic consequences of human-made impacts on pH decrease (acidification) on aquatic organisms that depend on forming mineralized hardparts has been widely reported (Fabry et al., 2008; Lombardi et al., 2011; Bray et al., 2014). As important ecosystem engineers, the decline of bivalve populations due to failures in the process of biocalcification, particularly in the vulnerable larval stages, will have strong impacts on limnic ecosystems with significant bivalve (including dreissenid) populations (see above). Direct consequences of dramatically reduced population densities will include decrease in microscopic phytoplankton, the major food source of these efficient filter feeders, ultimately leading to lower yield of commercial fish. The increased transparency of the water column after removal of major parts of the phytoplankton may increase growth rates and depth distribution of aquatic macrophytes, which in turn may lead to greater organic waste production and increased oxygen-poor regions at greater depths. In a way, these processes may (partially) reverse those originally imposed on limnic ecosystems by introduction of these invasive species since the 1980s, but if such impact is desired is a matter of discussion in a larger bioconservation context. In any case, close monitoring of putative defects in larval and embryonic shell formation of dreissenid bivalves will allow for predictions of their putative decrease in a given habitat and associated potential environmental impact.

Aside from calcareous exoskeletal elements, dreissenids, as well as other bivalves, e.g., mytilids, have evolved additional, organic biomaterials that are prone to suffer defects from increased CO2 and thus decreased pH levels. These are the byssus threads, that serve for firm but reversible attachment to hard substrates, allowing the animals to withstand currents or other forms of mechanical displacement. Byssus threads are secreted from the byssus gland in the foot as a liquid proteinaceous substance that hardens once in contact with water. The composition and biomechanical properties of bivalve byssus threads have been a matter of research for some time (see below), and recent data indicate that their functional performance suffers from acidification, just like their calcareous shells (O'Donnell et al., 2013). As such, it has been shown for marine *Mytilus* mussels that, if exposed to higher CO2 regimes that resulted in a change in pH from 8 to 7.5 during secretion, the tenacity of their byssus threads was decreased by 40% (O'Donnell et al., 2013). This occurred largely in the distal-most region of the byssus, where a so-called plaque is formed that attaches to the substrate. Interestingly, these negative effects on byssus performance occurred rapidly in short-time exposure experiments, during which shell and tissue growth as well as other physiological processes remained unaffected, indicating that these attachment structures may suffer faster from acidification events than mineralized structures (O'Donnell et al., 2013). In addition, byssus produced under heat stress have likewise proven to be less stable and exhibit slower secretion rates in marine species (Xu et al., 2023). Whether dreissenid byssus would suffer similar weakened performances in waters with climate change-induced increased temperatures remains unknown, but if so, this might have dramatic effects on their ability to manifest themselves and form stable colonies, particularly in habitats with temporary or permanent turbulence such as smaller streams or rivers, where attachment to the substrate is key to survival of these benthic animals. Accordingly, research focussing on the performance of *Dreissena* byssus threads under predicted future increasingly acidic and higher temperature regimes will allow for modelling the potential of *de novo* colonialization events as well as the stability of existing colonies in given freshwater habitats. Obviously, such environmentally caused reduced tenacity of *Dreissena* byssus threads will also affect the biofouling capacities of these bivalves, and survival rates may generally be significantly lowered due to defects in shell formation.

5.3 Use me: *Dreissena* as a model for applied research

Byssus threads have been used by humans for centuries, primary as textiles of the privileged (Ehrlich, 2019). More recently, the ability of bivalve byssus to adhere to substances in wet environments has resulted in the development of a number of synthetic polymers, particularly for biomedical applications, with anchoring, adhesive, and sealing properties (Lee et al., 2011).

While the molecular nature of the *Mytilus* byssus has been known for some time, the detailed protein composition that makes up the dreissenid byssus, in particular that of the quagga mussel, *Dreissena rostriformis* (aka *Dreissena bugensis*), was only recently revealed (Simmons et al., 2023). This study showed that byssus threads of the quagga and zebra mussel are stronger and more resistant than those of *Mytilus* (Brazee and Carrington, 2006). This is probably due to several unique properties of the dreissenid byssus which include the lack of collagen (present in all other bivalve byssi investigated so far) and the addition of a β-sheet crystalline structure that is also found in spider silk (Simmons et al., 2023). In spiders, these β-crystallites contribute to silk strength, and its deployment into the dreissenid byssus may thus be key to producing particularly tenacious threads. A significant drawback in artificial synthesis of such β-crystalline-containing fibers inspired by spider silk has so far been the complex biochemical process by which these fibers are formed, requiring a combination of acidification, ion exchange, applied sheer force, and water removal in the spider (Rising and

Harrington, 2023; Simmons et al., 2023). This process, however, appears to be simplified in dreissenid bivalves, since it seems to only depend on mechanical forces generated by the moving foot that houses the secretory byssus gland, rather than additional molecular mechanisms (Simmons et al., 2023). Accordingly, in addition to the biomedical applications based on mytilid byssus components such as aided wound healing, artificially produced fibers employing the unique properties of dreissenid byssus threads will open a whole new dimension of applications for resistant, protein-based, biodegradable and thus environmentally friendly polymer fibers. To this end, artificially produced fibers that mimic *Mytilus* byssus have been shown to be able to replace non-degradable synthetic fibers used in marine applications for, e.g., building enclosures for commercial seaweed and fish farming as well as nets for the fishing industry (Hong et al., 2024). These biomimetic fibers degrade in marine environments by bacterial activity, and thus are highly promising candidates to reduce the waste of nylon and other synthetic plastics in human applications on oceanic systems. Interestingly, byssus-producing mussels are themselves able to displace these fibers in order to move away from their attachment area, but the underlying molecular mechanisms and the genes involved in breaking down these fibers in the mussel remain unknown (Giraldes et al., 2019). It must, however, be assumed that this process is bacteria-independent and rather caused by enzymes produced by the bivalve itself. Accordingly, enhanced research into the molecular pathways underlying not only the secretion, but also the (enzymatic) degradation of bivalve byssus threads using the transcriptomic and genomic resources available for the quagga mussel appears highly promising for developing more sustainable textile production.

5.4 The quagga mussel in future EcoEvoDevo research

As pointed out above, the quagga mussel, *Dreissena rostriformis*, holds a large potential for future studies in the applied, environmental, and evolutionary sciences. With the bulk of transcriptomic, genomic, morphological, and developmental data available and their amenities as laboratory system (inducible spawning, large number of offspring), a wealth of questions revolving around the field of evolutionary developmental biology can be approached. For example, the evolution of asymmetry in primarily bilaterian animals is one of the current hot topics in EvoDevo (e.g., Namigai et al., 2014). Several bivalves (e.g., oysters) show strong tendency towards an asymmetric bodyplan morphology, while others, such as the dreissenids, do not. Accordingly, comparison of up- and downregulation of candidate (or novel) genes during establishment of morphological asymmetries with the behavior of the respective homologs in symmetrical reference species such as the quagga mussel can provide important insights into how the deviation from a once common developmental scheme (bilaterality) evolved to eventually produce non-symmetrical offspring.

For assessing the plasticity of gene expression signatures in various shell types within and across molluscan lineages, the database from *Dreissena rostriformis* forms an ideal reference for future comparative research. Likewise, the bivalve attachment system, the byssus, has been shown to show considerable variation with respect to their protein composition, whereby oysters form superhelical nanofibrils (Pasche et al., 2018), the giant clam uses tetrameric coiled coils, and mytilids form their threads from collagen precursors (Waite et al., 1998). Collagen appears to be absent in *Dreissena* species; instead, it seems that dreissenids have acquired gene(s) encoding for the predecessor(s) of the α-helical coiled coils used in their byssus by horizontal gene transfer from associated bacteria (Simmons et al., 2023). These coiled coils may have significantly contributed to the extraordinary tenacity of the *Dreissena* byssus (Simmons et al., 2023). Despite this progress, the detailed gene regulatory networks underlying bivalve byssus formation - and thus the putative convergent evolution of this system along various lineages - remains obscure.

As outlined above, formation of both the biocalcified exoskeletal hardparts and their adhesive threads are key to the success of dreissenids as invasive species. With *Dreissena rostriformis* as a powerful model at hand, there is hope that research into the mechanisms that govern crucial developmental processes such as shell and byssus formation as well as the transition from the larval to the juvenile phase (settlement and metamorphosis) may soon provide us with tools that help to reduce the fouling capacities and the spreading of these animals in non-native waterways and will lessen their negative impact on human-made constructions.

There is a lot to explore using bivalve evolution using the emerging triumvirate of the Mediterranean mussel, *Mytilus galloprovincialis*, the Pacific oyster, *Crassostrea gigas*, and the quagga mussel, *Dreissena rostriformis*, as models. As with every study that aims at decoding evolutionary phenomena, comparative analyses are pivotal in this endeavor. With the quagga mussel as the only freshwater bivalve currently at hand that is amenable for large-scale developmental studies, conventional evodevo research programmes, that are mainly concerned with questions of bodyplan evolution, can now be expanded and broadened towards topics such as the evolution of invasiveness and the adaptation to freshwater environments including the underlying molecular, cellular, developmental, and physiological processes.

Author contributions

AW: Conceptualization, Formal Analysis, Funding acquisition, Investigation, Project administration, Resources, Supervision, Validation, Writing–original draft, Writing–review and editing. GS: Visualization, Writing–review and editing.

Funding

The author(s) declare that financial support was received for the research, authorship, and/or publication of this article. This work was funded by grant P29455-B29 of the Austrian Science Fund (FWF) to AW.

Acknowledgments

We thank all members of the Wanninger Lab who contributed to research on the quagga mussel over the past decade.

Conflict of interest

The authors declare that the research was conducted in the absence of any commercial or financial relationships that could be construed as a potential conflict of interest.

The author(s) declared that they were an editorial board member of Frontiers, at the time of submission. This had no impact on the peer review process and the final decision.

Generative AI statement

The author(s) declare that no Generative AI was used in the creation of this manuscript.

Publisher's note

References

Aguilera, F., McDougall, C., Degnan, B. M., and Irwin, D. (2017). Co-option and *de novo* gene evolution underlie molluscan shell diversity. *Mol. Biol. Evol.* 34, 779–792. doi:10.1093/molbev/msw294

Aldridge, D. C., Ho, S., and Froufe, E. (2014). The Ponto-Caspian quagga mussel, *Dreissena rostriformis bugensis* (Andrusov, 1897), invades Great Britain. *Aquat. Invasions.* 9, 529–535. doi:10.3391/ai.2014.9.4.11

Allen, R. D. (2000). The contractile vacuole and its membrane dynamics. *BioEssays* 22, 1035–1042. doi:10.1002/1521-1878(200011)22:11<1035::AID-BIES10>3.0.CO;2-A

Bray, L., Pancucci-Papadopoulou, M., and Hall-Spencer, J. M. (2014). Sea urchin response to rising pCO2 shows ocean acidification may fundamentally alter the chemistry of marine skeletons. *Mediterr. Mar. Sci.* 15, 510–519. doi:10.12681/mms.579

Brazee, S. L., and Carrington, E. (2006). Interspecific comparison of the mechanical properties of mussel byssus. *Biol. Bull.* 211, 263–274. doi:10.2307/4134548

Calcino, A. D., De Oliveira, A. L., Simakov, O., Schwaha, T., Zieger, E., Wollesen, T., et al. (2019). The quagga mussel genome and the evolution of freshwater tolerance. *DNA Res.* 26, 411–422. doi:10.1093/dnares/dsz019

Clark, M. S., Peck, L. S., Arivalagan, J., Backeljau, T., Berland, S., Cardoso, J. C. R., et al. (2020). Deciphering mollusc shell production: the roles of genetic mechanisms through to ecology, aquaculture and biomimetics. *Biol. Rev.* 95, 1812–1837. doi:10.1111/brv.12640

Dahlberg, A. D., Waller, D. L., Hammond, D., Lund, K., and Phelps, N. B. D. (2023). Open water dreissenid mussel control projects: lessons learned from a retrospective analysis. *Sci. Rep.* 13, 10410. doi:10.1038/s41598-023-36522-5

Datta, A., Bryant, D. M., and Mostov, K. E. (2011). Molecular regulation of lumen morphogenesis. *Curr. Biol.* 21, R126–R136. doi:10.1016/j.cub.2010.12.003

Ehrlich, H. (2019). "Byssus: from inspiration to development of novel composites," in *Marine biological materials of invertebrate origin. Biologically-inspired systems*. Editor H. Ehrlich (Cham: Springer), 13, 211–224. doi:10.1007/978-3-319-92483-0_16

Fabry, V. J., Seibel, B. A., Feely, R. A., and Orr, J. C. (2008). Impacts of ocean acidification on marine fauna and ecosystem processes. *ICES J. Mar. Sci.* 65, 414–432. doi:10.1093/icesjms/fsn048

Gerdol, M., Moreira, R., Cruz, F., Gómez-Garrido, J., Vlasova, A., Rosani, U., et al. (2020). Massive gene presence-absence variation shapes an open pan-genome in the Mediterranean mussel. *Genome Biol.* 21, 275. doi:10.1186/s13059-020-02180-3

Giraldes, B. W., Leitão, A., and Smyth, D. (2019). The benthic sea-silk-thread displacement of a sessile bivalve, *Pinctada imbricata radiata* (Leach, 1819) in the Arabian-Persian Gulf. *PLoS ONE* 14, e0215865. doi:10.1371/journal.pone.0215865

Heiler, K. C. M., de Vaate, A. B., Ekschmitt, K., von Oheimb, P. V., Albrecht, C., and Wilke, T. (2013). Reconstruction of the early invasion history of the quagga mussel (*Dreissena rostriformis bugensis*) in Western Europe. *Aquat. Invasions* 8, 53–57. doi:10.3391/ai.2013.8.1.06

Hernández, A. B., and Angelini, C. (2019). Wood traits and tidal exposure mediate shipworm infestation and biofouling in southeastern U.S. estuaries. *Ecol. Eng.* 132, 1–12. doi:10.1016/j.ecoleng.2019.03.008

Hong, Y., Yang, H.-S., Lee, M. H., Kim, S., Park, S. B., Hwang, S. Y., et al. (2024). Fishing gear with enhanced drapability and biodegradability: artificial, eco-friendly fibers inspired by the mussel byssus. *J. Chem. Eng.* 489, 151388. doi:10.1016/j.cej.2024.151388

Inoue, K., Onitsuka, Y., and Koito, T. (2021). Mussel biology: from the byssus to ecology and physiology, including microplastic ingestion and deep-sea adaptations. *Fish. Sci.* 87, 761–771. doi:10.1007/s12562-021-01550-5

Jackson, D. J., McDougall, C., Green, K., Simpson, F., Wörheide, G., and Degnan, B. M. (2006). A rapidly evolving secretome builds and patterns a sea shell. *BMC Biol.* 4, 40. doi:10.1186/1741-7007-4-40

Karatayev, A. Y., and Burlakova, L. E. (2022). What we know and don't know about the invasive zebra (*Dreissena polymorpha*) and quagga (*Dreissena rostriformis bugensis*) mussels. *Hydrobiologia*, 1–74. doi:10.1007/s10750-022-04950-5

Kocot, K. M., Aguilera, F., McDougall, C., Jackson, D. J., and Degnan, B. M. (2016). Sea shell diversity and rapidly evolving secretomes: insights into the evolution of biomineralization. *Front. Zool.* 13, 23. doi:10.1186/s12983-016-0155-z

Lee, B. P., Messersmith, P. B., Israelachvili, J. N., and Waite, J. H. (2011). Mussel-inspired adhesives and coatings. *Annu. Rev.Mater. Res.* 41, 99–132. doi:10.1146/annurev-matsci-062910-100429

Lombardi, C., Cocito, S., Gambi, M. C., Cisterna, B., Flach, F., Taylor, P. D., et al. (2011). Effects of ocean acidification on growth, organic tissue and protein profile of the Mediterranean bryozoan *Myriapora truncata*. *Aquat. Biol.* 13, 251–262. doi:10.3354/ab00376

McCartney, M. A., Auch, B., Kono, T., Mallez, S., Zhang, Y., Obille, A., et al. (2022). The genome of the zebra mussel, *Dreissena polymorpha*: a resource for comparative genomics, invasion genetics, and biocontrol. *G3* 12, jkab423. doi:10.1093/g3journal/jkab423

Meisenheimer, J. (1899). Entwicklungsgeschichte von *Dreissensia polymorpha* Pall. I. Bis zur Ausbildung der jungen Trochophoralarve. *Sitzungsberichte Ges. zur Beförderung gesamten Naturwissenschaften Marbg.* 1899, 1–43. 1 plate.

Meisenheimer, J. (1901). Entwicklungsgeschichte von *Dreissensia polymorpha* Pall. *Z. Wiss. Zool.* 69, 1–137. pls. 1-13.

Miglioli, A., Tredez, M., Boosten, M., Sant, C., Carvalho, J. E., Dru, P., et al. (2024). The Mediterranean mussel *Mytilus galloprovincialis*: a novel model for developmental studies in mollusks. *Development* 151, dev202256. doi:10.1242/dev.202256

Murdock, D. J. E. (2020). The "biomineralization toolkit" and the origin of animal skeletons. *Biol. Rev.* 95, 1372–1392. doi:10.1111/brv.12614

Namigai, E. K. O., Kenny, N. J., and Shimeld, S. M. (2014). Right across the tree of life: the evolution of left–right asymmetry in the Bilateria. *Genesis* 52, 458–470. doi:10.1002/dvg.22748

O'Donnell, M., George, M., and Carrington, E. (2013). Mussel byssus attachment weakened by ocean acidification. *Nat. Clim. Change* 3, 587–590. doi:10.1038/nclimate1846

Paalvast, P., and van der Velde, G. (2011). New threats of an old enemy: the distribution of the shipworm *Teredo navalis* L. (Bivalvia: teredinidae) related to climate change in the Port of Rotterdam area, The Netherlands. *Mar. Pollut. Bull.* 62, 1822–1829. doi:10.1016/j.marpolbul.2011.05.009

Pasche, D., Horbelt, N., Marin, F., Motreuil, S., Macías-Sánchez, E., Falini, G., et al. (2018). A new twist on sea silk: the peculiar protein ultrastructure of fan shell and pearl oyster byssus. *Soft Matter* 14, 5654–5664. doi:10.1039/C8SM00821C

Pavlicek, A., Schwaha, T., and Wanninger, A. (2018). Towards a ground pattern reconstruction of bivalve nervous systems: neurogenesis in the zebra mussel *Dreissena polymorpha*. *Org. Divers. Evol.* 18, 101–114. doi:10.1007/s13127-017-0356-0

Peñaloza, C., Gutierrez, A. P., Eöry, L., Wang, S., Guo, X., Archibald, A. L., et al. (2021). A chromosome-level genome assembly for the Pacific oyster *Crassostrea gigas*. *Gigascience* 10, giab020. doi:10.1093/gigascience/giab020

Ponder, W. F., Lindberg, D. R., and Ponder, J. M. (2019). *Biology and evolution of the Mollusca*. Boca Raton: CRC Press. Vols. 1 and 2.

Rising, A., and Harrington, M. J. (2023). Biological materials processing: time-tested tricks for sustainable fiber fabrication. *Chem. Rev.* 123, 2155–2199. doi:10.1021/acs.chemrev.2c00465

Salamanca-Díaz, D. A., Calcino, A. D., De Oliveira, A. L., and Wanninger, A. (2021). Non-collinear Hox gene expression in bivalves and the evolution of morphological novelties in mollusks. *Sci. Rep.* 11, 3575. doi:10.1038/s41598-021-82122-6

Salamanca-Díaz, D. A., Ritschard, E. A., Schmidbaur, H., and Wanninger, A. (2022a). Comparative single-cell transcriptomics reveals novel genes involved in bivalve embryonic shell formation and questions ontogenetic homology of molluscan shell types. *Front. Cell. Dev. Biol.* 10, 883755. doi:10.3389/fcell.2022.883755

Salamanca-Díaz, D. A., Schulreich, S. M., Cole, A. G., and Wanninger, A. (2022b). Single-Cell RNA sequencing atlas from a bivalve larva enhances classical cell lineage studies. *Front. Ecol. Evol.* 9, 783984. doi:10.3389/fevo.2021.783984

Schulreich, S. M., Salamanca-Díaz, D. A., Zieger, E., Calcino, A. D., and Wanninger, A. (2022). A mosaic of conserved and novel modes of gene expression and morphogenesis in mesoderm and muscle formation of a larval bivalve. *Divers. Evol.* 22, 893–913. doi:10.1007/s13127-022-00569-5

Simmons, M., Horbelt, N., Sverko, T., Scoppola, D., Jackson, D. J., and Harrington, M. J. (2023). Invasive mussels fashion silk-like byssus via mechanical processing of massive horizontally acquired coiled coils. *Proc. Natl. Acad. Sci. U.S.A.* 120, e2311901120. doi:10.1073/pnas.2311901120

Tani, T., Tominaga, T., Allen, R. D., and Naitoh, Y. (2002). Development of periodic tension in the contractile vacuole complex membrane of *Paramecium* governs its membrane dynamics. *Cell Biol. Int.* 26, 853–860. doi:10.1006/cbir.2002.0937

Waite, J. H., Qin, X. X., and Coyne, K. J. (1998). The peculiar collagens of mussel byssus. *Matrix Biol.* 17, 93–106. doi:10.1016/S0945-053X(98)90023-3

Wanninger, A., and Wollesen, T. (2015). "Mollusca," in *Evolutionary developmental biology of invertebrates 2: Lophotrochozoa (spiralia)*. Editor A. Wanninger (Springer), 103–153. doi:10.1007/978-3-7091-1871-9_7

Wanninger, A., and Wollesen, T. (2019). The evolution of molluscs. *Biol. Rev.* 94, 102–115. doi:10.1111/brv.12439

Wollesen, T., and Wanninger, A. (2023). "Chapter 8: Hox genes in Mollusca," in *Hox modules in evolution and development*. Editor D. E. K. Ferrier (Boca Raton: CRC Press), 161–175. doi:10.1201/9781003057215

Xu, X., Yang, K., Liu, Y., Deng, Y., and Zhao, L. (2023). Heatwaves hinder mussel invasion by weakening byssus production. *Front. Mar. Sci.* 10, 1239801. doi:10.3389/fmars.2023.1239801

Yarra, T., Blaxter, M., and Clark, M. S. (2021). A bivalve biomineralization toolbox. *Mol. Biol. Evol.* 38, 4043–4055. doi:10.1093/molbev/msab153

Zhao, R., Takeuchi, T., Luo, Y.-J., Ishikawa, A., Kobayashi, T., Koyanagi, R., et al. (2018). Dual gene repertoires for larval and adult shells reveal molecules essential for molluscan shell formation. *Mol. Biol. Evol.* 35, 2751–2761. doi:10.1093/molbev/msy172

Zieger, E., Schwaha, T., Burger, K., Bergheim, I., Wanninger, A., and Calcino, A. D. (2022). Midbody-localized aquaporin mediates intercellular lumen expansion during early cleavage of an invasive freshwater bivalve. *Front. Cell. Dev. Biol.* 10, 894434. doi:10.3389/fcell.2022.894434

Frontiers in Cell and Developmental Biology

TYPE Original Research
PUBLISHED 06 February 2025
DOI 10.3389/fcell.2025.1528797

The lamprey habenula provides an extreme example for the temporal regulation of asymmetric development

Lucile Guichard[1‡], Ronan Lagadec[1‡], Léo Michel[1†], Hélène Mayeur[1], Michaël Fuentès[1], Jordan Pain[1], Noah Heier[1], Quentin Rougemont[2], Maria Celina Rodicio[3], Antón Barreiro-Iglesias[3,4], Patrick Blader[5], Michael Schubert[6] and Sylvie Mazan[1]*

[1]CNRS, UMR7232-Biologie Intégrative des Organismes Marins (BIOM), Observatoire Océanologique, Sorbonne Université, Banyuls-sur-Mer, France, [2]CNRS, AgroParisTech, Laboratoire Ecologie Systématique et Evolution, Université Paris-Saclay, Gif-sur-Yvette, France, [3]Departamento de Bioloxía Funcional, Facultade de Bioloxía, Universidade de Santiago de Compostela, Santiago de Compostela, Spain, [4]Aquatic One Health Research Center (ARCUS), Universidade de Santiago de Compostela, Santiago de Compostela, Spain, [5]Molecular, Cellular and Developmental Biology (MCD, UMR5077), Centre de Biologie Intégrative (CBI, FR3743), Université de Toulouse, CNRS, UPS, Toulouse, France, [6]Laboratoire de Biologie du Développement de Villefranche-sur-Mer, Institut de la Mer de Villefranche, Sorbonne Université, CNRS, Villefranche-sur-Mer, France

OPEN ACCESS

EDITED BY
Timothy Petros,
Eunice Kennedy Shriver National Institute of Child Health and Human Development (NIH), United States

REVIEWED BY
Eduardo Puelles,
Miguel Hernández University of Elche, Spain
Edra London,
Eunice Kennedy Shriver National Institute of Child Health and Human Development (NIH), United States

*CORRESPONDENCE
Sylvie Mazan,
mazan@obs-banyuls.fr

†PRESENT ADDRESS
Léo Michel, The Department of Fundamental Neuroscience, The University of Lausanne, Lausanne, Switzerland

‡These authors have contributed equally to this work

RECEIVED 15 November 2024
ACCEPTED 20 January 2025
PUBLISHED 06 February 2025

CITATION
Guichard L, Lagadec R, Michel L, Mayeur H, Fuentès M, Pain J, Heier N, Rougemont Q, Rodicio MC, Barreiro-Iglesias A, Blader P, Schubert M and Mazan S (2025) The lamprey habenula provides an extreme example for the temporal regulation of asymmetric development. *Front. Cell Dev. Biol.* 13:1528797. doi: 10.3389/fcell.2025.1528797

By their phylogenetic position and their marked epithalamic asymmetries, lampreys are relevant models for understanding the formation and evolution of this trait across vertebrates. In this study, we use a transcriptomic approach to identify novel signature markers to characterize the highly asymmetric, bipartite organization of habenulae in lampreys. Lamprey habenulae are subdivided into two complementary subdomains related, respectively, to the lateral/ventral and the medial/dorsal habenulae of jawed vertebrates: a dorsal, right-restricted subdomain and a bilateral subdomain that includes the left habenula as well as its ventral right counterpart. Analysis of the formation of the lamprey habenula at prolarval and larval stages using a combination of morphological, immunohistochemical, and *in situ* hybridization approaches highlights a marked asymmetric temporal regulation. The dorsal right subdomain forms and already expresses all identified signature markers in prolarval stages. In contrast, the left and ventral right subdomain appears significantly later, with the first indication of neuronal identity elaboration in these territories being observed in larval stages. As in gnathostomes, Wnt signaling may be involved in the regulation of this unique, asymmetric mode of development, since β-catenin shows asymmetric and highly dynamic nuclear distributions both in neural progenitors and differentiated neuronal precursors of the two habenular subdomains. These data confirm the importance of lampreys to unravel the developmental logic underlying the recurrence and variation of habenular asymmetries in vertebrates and pave the way for future functional analyses.

KEYWORDS

habenula, asymmetry, lamprey, temporal regulation, Wnt signaling

1 Introduction

The habenula is a bilateral epithalamic structure that forms a key node in neuronal circuits connecting the basal forebrain with different midbrain and brainstem nuclei (Ables et al., 2023; Beretta et al., 2012). Based on projection analyses and molecular characterizations in different vertebrate taxa, including mammals and teleosts, but also cyclostomes (or jawless vertebrates) and chondrichthyans (or cartilaginous fishes), vertebrate habenulae have been shown to share a conserved bipartite organization (medial/lateral or dorsal/ventral in jawed vertebrates) (Amo et al., 2010; Grillner et al., 2018; Stephenson-Jones et al., 2012). A remarkable feature of this structure in humans and many other vertebrates is that it displays asymmetries between the left and right sides (Abuduaini et al., 2023; Ahumada-Galleguillos et al., 2016; Concha and Wilson, 2001; Hitti et al., 2022). The biological functions of these asymmetries have been assessed in the zebrafish, where they regulate the integration of sensory cues and adaptive responses to the environment (Chen et al., 2019; Dreosti et al., 2014; Duboué et al., 2017; Facchin et al., 2015). As expected from structures processing input from different ecological contexts, habenular asymmetries vary considerably across vertebrates not only in their degree but also in their nature, with variations reported in neuronal identities and projections, as well as in the broad organization of habenular subdomains (Concha and Wilson, 2001; Stephenson-Jones et al., 2012). Despite their biological relevance, the evolutionary origin of habenular asymmetries in vertebrates and the ontogenetic variations underlying their diversification have remained for long largely unexplored, with most studies focusing on teleosts, primarily the zebrafish (Michel et al., 2022; Roussigné et al., 2012; Signore et al., 2009; Villalón et al., 2012). Recently, however, a transcriptomic characterization of habenular asymmetries and an analysis of the mechanisms underlying their formation in a cartilaginous fish (or chondrichthyan), the small spotted catshark *Scyliorhinus canicula*, provided new insights into the evolution of habenular development (Lanoizelet et al., 2024). A systematic comparison of the catshark with species occupying key phylogenetic positions in the vertebrate tree suggested an ancient origin of asymmetries in the lateral habenula. This study also highlighted Wnt signaling as a candidate mechanism involved in both asymmetry formation and diversification across vertebrates. As in the zebrafish, a left repression of Wnt activity is thus observed in the catshark, in line with the hypothesis of an ancient involvement of Wnt signaling in habenular asymmetry formation (Guglielmi et al., 2020; Hüsken et al., 2014; Lanoizelet et al., 2024). However, ancestral Wnt-dependent cellular mechanisms and regulatory programs remain unclear in view of major differences between the zebrafish and the catshark. Wnt signaling thus operates in different cellular contexts (lateral habenula in the catshark, dorsal habenula in the zebrafish), via distinct cellular mechanisms (neuronal identity choices in post-mitotic precursors in the catshark, control of neurogenesis timing in neural progenitors in the zebrafish), and downstream of different developmental regulations (Nodal- and parapineal-dependent, respectively, in the catshark and the zebrafish) (Guglielmi et al., 2020; Lagadec et al., 2015; Lanoizelet et al., 2024; Powell et al., 2024).

Genome-wide characterizations of habenular asymmetries and detailed analyses of their mechanisms of formation are required in a broader sampling of species to obtain a comprehensive picture of their nature in ancestral vertebrates and to clarify the functional evolution of Wnt signaling in their formation. Lampreys are crucial species in this respect. As members of the cyclostomes, the sister group of gnathostomes, they occupy an important phylogenetic position to reconstruct ancestral vertebrate states (Shimeld and Donoghue, 2012). They are also endowed with marked habenular asymmetries that exhibit both conserved and divergent features when compared to gnathostomes, which makes lampreys a relevant model for studying the evolution of these asymmetries. Analyses of efferent projection patterns, supported by expression profiles of a limited number of subdomain markers, suggest that the right lateral habenula of the catshark corresponds to the right dorsal habenula of the river lamprey. This work has also pointed to a complete absence of a lateral component in the lamprey left habenula, a characteristic never observed in gnathostomes (Grillner et al., 2018; Stephenson-Jones et al., 2012). The molecular mechanisms underlying the formation of habenular asymmetries during lamprey development remain largely elusive. The only study on this subject revealed an ancestral dependence on Nodal signaling, shared by the river lamprey and the catshark, but absent in zebrafish (Lagadec et al., 2015). Genome-wide characterizations of habenular asymmetries as well as cellular and molecular analyses of their mechanisms of formation in the lamprey are important to establish the lamprey as a reference for comparisons with gnathostome model organisms and thus to reconstruct ancestral vertebrate traits. As a first step towards further functional analyses of habenular asymmetry formation in lampreys, we have used a transcriptomic approach to provide an unbiased identification of habenular asymmetries in the river lamprey (*Lampetra fluviatilis*). Using asymmetric markers identified in our transcriptomic screen, we describe the elaboration of habenula subdomain organization in lampreys at prolarval and larval stages. Our results provide a refined view of the subdomain organization of the lamprey habenula and highlight a remarkable asymmetry in the temporal regulation of its formation.

2 Materials and methods

2.1 Animals and tissue collection

Adult river lamprey (*L. fluviatilis*) specimens, collected during their upstream migratory phase in the Dordogne river, were purchased from professional fishermen. The animals were transported to the Observatoire Océanologique in Banyuls-sur-Mer, France, and maintained at 12°C in oxygenated, filtered fresh water until sexual maturation. Oocytes and sperm were obtained from mature animals by gentle stripping and mixed in Petri dishes for fertilization. Embryos and prolarvae were maintained at 12°C in oxygenated fresh water and staged according to (Tahara, 1988). Young river lamprey larvae with sizes between 0.8 and 1.3 cm were maintained under the same conditions and fed by addition of Tetra Micro Granules (Tetra, Blacksburg, VA, United States). Older larvae (sizes between 3.5 and 7.0 cm) from two other lamprey species, the sea lamprey *Petromyzon marinus* and the brook lamprey *Lampetra*

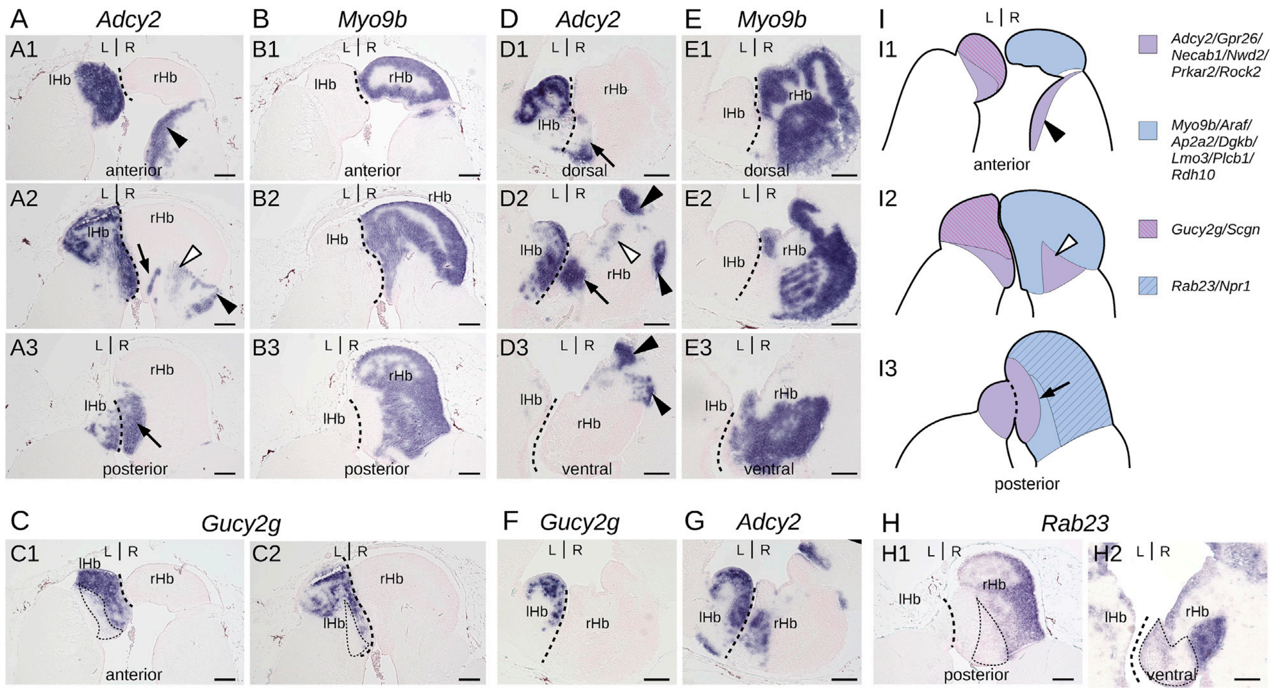

FIGURE 1
Subdomain organization of adult lamprey habenulae. **(A–C,H1)** show transverse sections and **(D–G,H2)** horizontal sections of adult river lamprey habenulae after *in situ* hybridization with probes for *Adcy2* **(A,D, G)**, *Myo9b* **(B, E)**, *Gucy2g* **(C, F)**, and *Rab23* **(H)**. **(A–C,H1)** are sections from the same specimen, same for **(D–G,H2)**. **(A1–A3)** show successive sections from anterior to posterior, same for **(B1–B3)**. **(D1–D3)** show successive sections from dorsal to ventral, same for **(E1–E3)**. **(A1, B1, C1)** are adjacent sections, same for **(A2, B2, C2)**, for **(B3)** and **(H1)**, for **(D2)**, **(F)**, and **(G)** as well as for **(E3)** and **(H2)**. Dashed lines show the boundary between left and right habenulae. Thin dotted lines in **(C1, C2)** and in **(H1, H2)** respectively delimit a *Adcy2*-positive subdomain negative for *Gucy2g* and a *Myo9b*-positive subdomain negative for *Rab23*. Thin arrows as well as black and white arrowheads point to discrete ventral subterritories expressing *Adcy2* in the right habenula. **(I)** are schemes showing the subdomain organization of habenulae as observed on transverse sections from anterior **(I1)** to posterior **(I3)**. Signature genes for each color are shown on the right based on profiles shown in this figure and in Supplementary Figure S1B-X. Abbreviations: L, left; R, right; lHb, left habenula; rHb, right habenula. Scale bar = 100 µm.

planeri, were, respectively, collected in the river Ulla (Galicia, Spain) with permission from the Xunta de Galicia and in the river Oir (Normandie, France) with permission from the préfecture de la Manche. Ethical review and agreement were not required for analyses of these specimens according to national and European regulations because their study only involved analyses of non-feeding prolarvae or brain tissue collection from euthanized adults and larvae. All prolarvae, larvae, and adults were euthanized by immersion in an overdose of buffered tricaine solution (>1 g/L).

2.2 RNA isolation, library construction, and sequencing

Left and right habenula explants were manually dissected from brains collected from euthanized adult river lampreys and stored in TRI reagent (T9424, Sigma-Aldrich, Saint-Louis, MO, United States) at −20°C until RNA extraction. Three left pools, each containing 4 left habenulae from two females and two males and three right pools, containing the corresponding 4 right habenulae, were prepared from these explants. Total RNA was isolated using the NucleoSpin RNA Clean-up XS kit (740903, Macherey-Nagel, Düren, Germany). RNA quantities and integrity indexes (RINs) were assessed prior to Illumina library construction using a Bioanalyzer 2100 (Agilent Technologies, Santa Clara, CA, United States). For each pool analyzed, the smallest RIN measured was 9.9. Subsequently, 50 ng of total RNA from each pool was used to isolate mRNAs using the NEBNext Poly(A) mRNA Magnetic Isolation Module (E7490, NEB, Ipswich, MA, United States). Libraries were then prepared using the NEBNext Ultra II RNA Library Prep kit for Illumina (E7770, NEB, Ipswich, MA, United States). Each library was validated using a Bioanalyzer 2100, quantified using the QuantiFluor dsDNA system with a Quantus Fluorometer (E2670, Promega, Madison, WI, United States), and equal amounts of each library were pooled. Paired-end 100 base-pair sequencing was performed on a DNBSEQ-T7 (Shenzhen, Guangdong, China) generating about 1 billion reads (The NCBI identifier for this dataset is SRS233376, as indicated in Supplementary Table S2).

2.3 Read mapping and statistical analysis

In the absence of an annotated genome of the river lamprey, we generated a reference database for read mapping (Supplementary Table S1). This was done by clustering of the datasets listed in Supplementary Table S2. To do so, we used the DRAP 1.92 runDrap pipeline (Cabau et al., 2017). The pipeline used Trinity (Grabherr et al., 2011) for normalization and Oases (Schulz et al., 2012) with

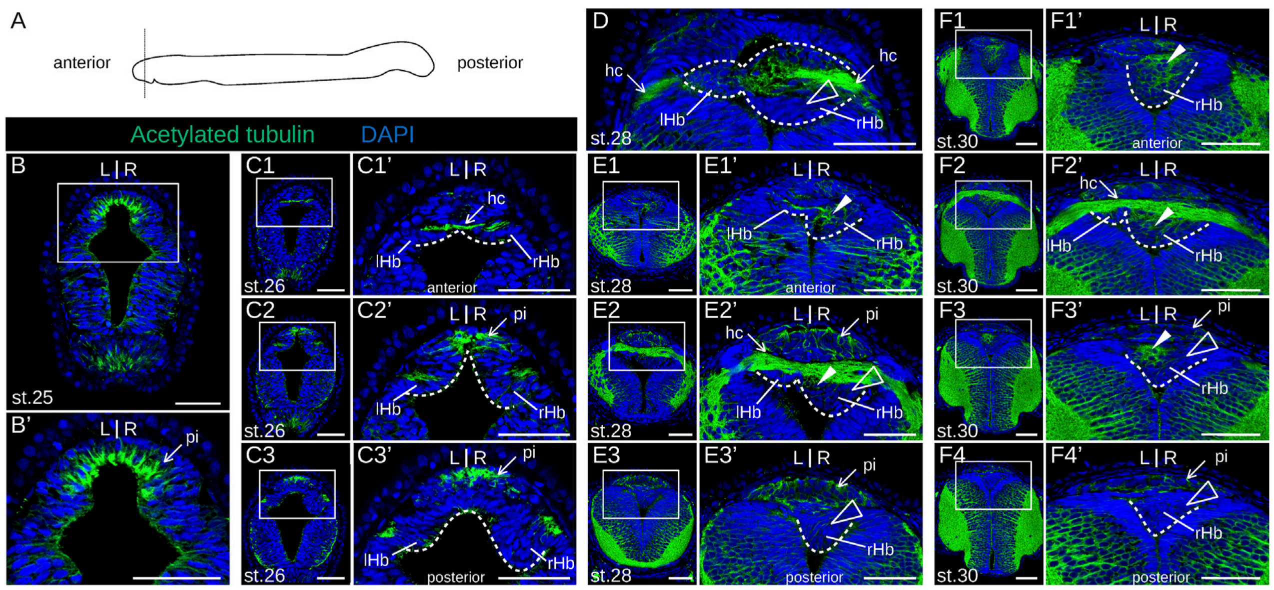

FIGURE 2
Morphology of lamprey developing habenulae at prolarval stages. **(A)** is a scheme showing the section plane used, orthogonal to the anterior-posterior axis. **(B)**, **(C1-3)**, **(E1-3)**, and **(F1-4)** show transverse sections of developing river lamprey habenulae at prolarval stages 25, 26, 28, and 30, respectively, after immunohistochemistry with an antibody directed against acetylated tubulin (green) and DAPI staining (blue). **(D)** is a horizontal section at stage 28 with the same labeling. **(C1–C3)** show successive sections of the same specimen from anterior to posterior, same for **(E1–E3)**, and for **(F1–F4)**. **(B′,C1′–C3′,E1′–E3′,F1′–F4′)** show higher magnifications of the habenula region boxed respectively in **(B,C1–C3,E1–E3,F1–F4)**. Dashed lines delimit the forming habenulae, the left one being restricted to a thin cell population in contact with the habenular commissure at these stages. White arrowheads point to neuropil-rich territories in the right habenula, as assessed from acetylated tubulin signals. Empty arrowheads point to territories devoid of acetylated tubulin labeling. Abbreviations: L, left; R, right; lHb, left habenula; rHb, right habenula; hc, habenular commissure; pi, pineal field; st., stage. Scale bar = 50 µm.

kmers 37, 47, 57, and 63 for assembly, with subsequent merging using the DRAP runMeta pipeline. We mapped the original reads onto the resulting assembly using bowtie2 (Langmead and Salzberg, 2012) and used Corset (Davidson et al., 2014) and SuperTranscripts (Davidson et al., 2017) on the resulting alignment file to merge putatively redundant transcripts and putative splice site variants, yielding transcripts representative of all splicing variants of their corresponding genes. For the transcriptomic analysis of asymmetries, reads were pseudo-mapped onto this database of reference gene models and pseudo-counted using a k-mer quantification method, kallisto (Bray et al., 2016). Contigs exhibiting statistically significant count differences between the left and the right habenulae were identified using the Wald test (q-value threshold 5E-02) implemented in sleuth (Pimentel et al., 2017) and annotated by similarity search against cyclostome sequences from Swissprot. We refer to the corresponding genes as left- or right-enriched.

2.4 *In situ* hybridization (ISH) of sections

Whole lamprey specimens (prolarvae and 0.8–1.3 cm larvae) or dissected brains (3.5–7.0 cm larvae and adults) were fixed, dehydrated, and stored at −20°C until paraffin embedding and sectioning (section thickness: 5–10 µm). ISH of paraffin sections was carried out using digoxigenin-labeled antisense RNA probes, transcribed *in vitro* from synthetic gene fragments using a standard protocol (Derobert et al., 2002). Following ISH, nuclei were counterstained using Nuclear Fast Red solution (N3020, Sigma-Aldrich, Saint-Louis, MO, United States) and mounted in Eukitt (03989, Sigma-Aldrich, Saint-Louis, MO, United States). Brain sections were imaged with a Zeiss Axioscope 5 (Carl Zeiss Microscopy, Germany) equipped with a ZEISS Axiocam 208 color camera and the Zeiss ZEN Blue software (version 3.7.4). Probe sequences are listed in Supplementary Table S3. They were inferred from river lamprey sequences but also used for ISH of sections from sea lamprey and brook lamprey, the high level of sequence similarity between the three species allowing extensive cross-hybridizations, as previously reported (Lagadec et al., 2015).

2.5 Immunohistochemistry (IHC) of sections

After epitope unmasking, paraffin sections were subjected to fluorescent IHC as previously described (Lagadec et al., 2018), with the following modification: for the detection of β-catenin antibody, an additional signal amplification was conducted using the TSA plus Cyanine 5 kit (NEL745001KT, Akoya Biosciences, Menlo Park, CA, United States) following the supplier's instructions. Antibodies and the concentrations used in this study are listed in Supplementary Table S4. Brain sections were imaged with an inverted Leica SP8 microscope (Leica Microsystems Inc., Wetzlar, Germany) equipped with a SuperK EXTREME white laser source (NKT Photonics A/S, Birkerød, Denmark) and a Leica Hybrid Detector. Images were processed using ImageJ.

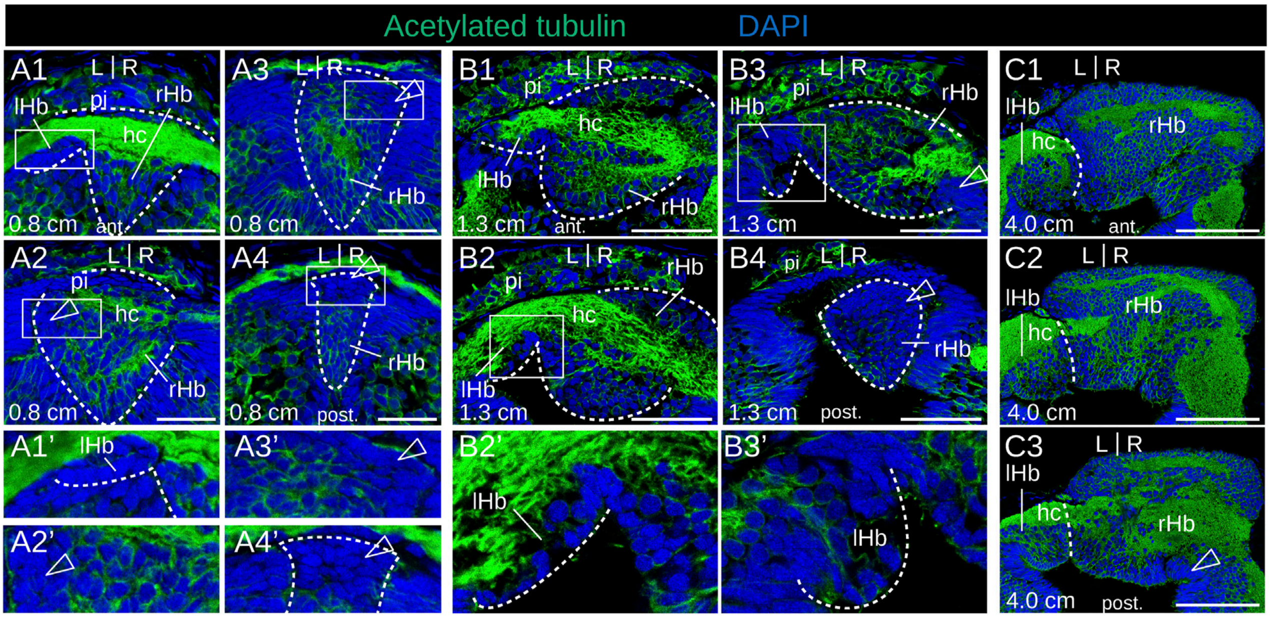

FIGURE 3
Morphology of lamprey developing habenulae at larval stages. **(A1–4)**, **(B1–4)**, and **(C1–3)** are transverse sections of developing habenulae in 0.8 cm, 1.3 cm and 4.0 cm larvae, respectively, after immunohistochemistry with an antibody directed against acetylated tubulin (green) and DAPI staining (blue). **(A1–4)** and **(B1–4)** were obtained from river lamprey larvae, while **(C1–3)** were obtained from a brook lamprey larva. **(A1–A4)** show successive sections of the same specimen from anterior to posterior, same for **(B1–B4)**, and for **(C1–C3)**. **(A1′–A4′,B2′–B3′)** show higher magnifications of the habenula region boxed respectively in **(A1–A4,B2–B3)**. Dashed lines delimit the forming habenulae in **(A1–A4,A1′,A4′,B1–B4)** and show the boundary between left and right habenulae in **(C1–C3)**. Empty arrowheads point to territories devoid of acetylated tubulin labeling. Abbreviations: L, left; R, right; lHb, left habenula; rHb, right habenula; hc, habenular commissure; pi, pineal field; ant., anterior; post., posterior. Scale bar = 25 µm in **(A1–4)**, 50 µm in **(B1–4)**, and 100 µm in **(C1–3)**.

2.6 TUNEL assays on sections

Apoptosis was assessed on paraffin-embedded sections with the *In Situ* Cell Death Detection kit (11684809910, Roche, Basel, Switzerland) as previously described (Lagadec et al., 2018). Briefly, slides were pretreated in 0.1 M citrate buffer (pH6.0) with a 350 W microwave irradiation for 5 min and incubated in the TUNEL reaction mixture for 1 h at 37°C prior to DAPI nuclear staining. For positive controls, a DNase I treatment (1000 U/mL) was carried out for 10 min at room temperature prior to the labeling procedure. For negative controls, slides were treated as described above, except that terminal transferase was omitted in the reaction.

3 Results

3.1 Transcriptomic analysis of asymmetries in river lamprey habenulae

To obtain an unbiased characterization of asymmetries in river lamprey habenulae, we carried out a transcriptomic comparison between their right and left moieties. To do so, we constructed barcoded Illumina libraries using total RNA extracted from pools of manually dissected left and right habenula explants. Library sequencing from three replicates for each side led to a total of 994 million reads, which were mapped against an annotated reference gene model database (Supplementary Table S1). Their statistical analysis resulted in the identification of 11799 contigs differentially expressed between the left and the right sides, 6174 left-enriched and 5625 right-enriched (Supplementary Figure S1A; Supplementary Table S5). Genes previously shown to be asymmetrically expressed, such as *Prox1a* (Cluster-16156.0; q-value = 5.9e-50; fold change = 26.8 to the right), *Prox1b* (Cluster-16156.1; q-value = 3.0e-62; fold change = 7.73 to the right) or *Kctd12* (Cluster-4041.6113; q-value = 1.0e-33; fold change = 3.03 to the left) were retrieved in this analysis, with the expected laterality. To obtain a spatial characterization of asymmetries, we conducted ISH analyses on adult habenula sections for a total of 29 genes (15 left-enriched and 14 right-enriched), selected among those exhibiting the highest statistical support for left- or right-enrichment in the transcriptomic analysis (Supplementary Figure S1A). Regionalized asymmetric profiles were obtained in all cases except for 6 genes (Supplementary Table S3), and they confirmed the expression laterality predicted by the transcriptomic analysis (Supplementary Figure S1B–X). All left-enriched genes exhibiting a regionalized expression share a broad territory in the left habenula (Supplementary Figures S1B–L), with two of them being only expressed in a dorso-anterior subdomain (*Gucy2g* and *Scgn*) (Supplementary Figure S1C,D) and with six of them exhibiting additional right-sided ventral territories (*Rock2*, *Nwd2*, *Necab1*, *Prkar2a*, *Adcy2*, and *Gpr26*) (Supplementary Figures S1F,G,H,I,J,L). Similarly, all right-enriched genes with a regionalized expression show largely overlapping, right-restricted expression territories (Supplementary Figures S1M–X).

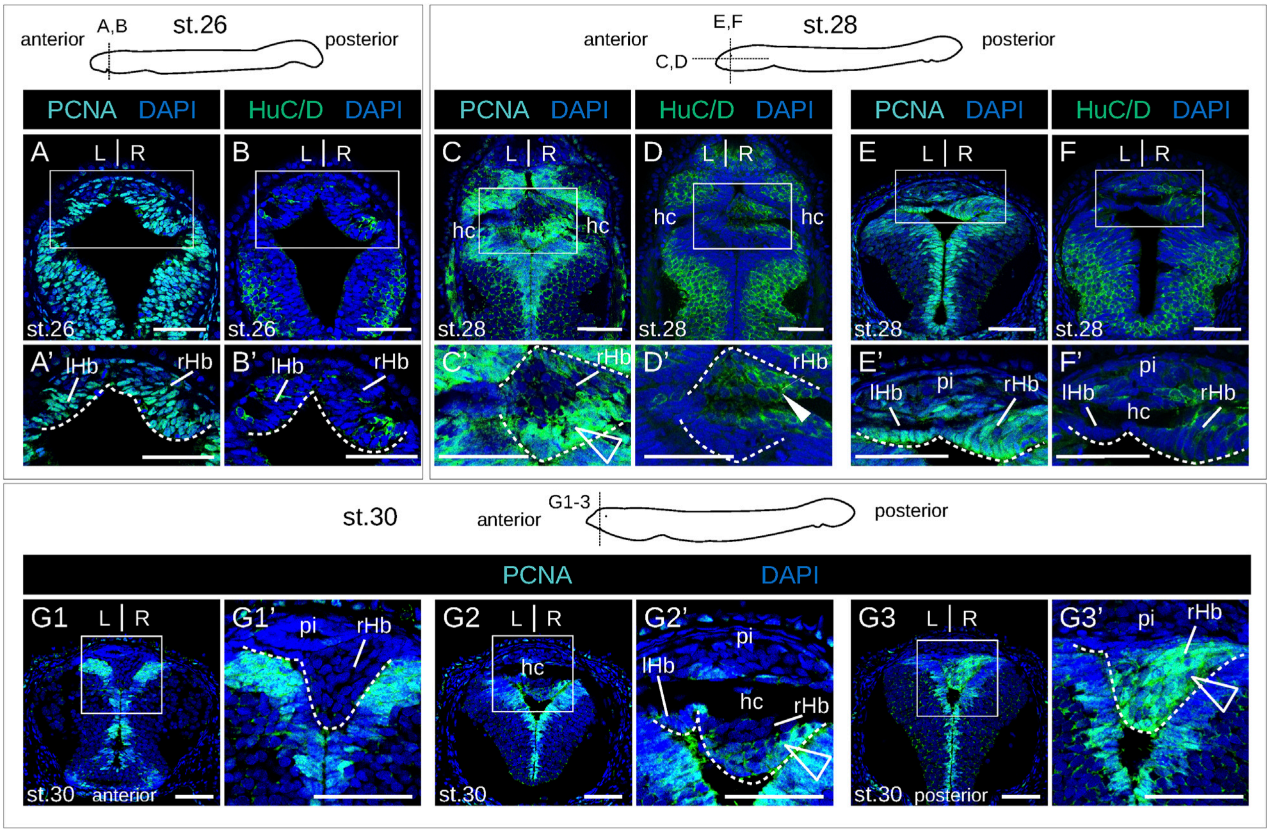

FIGURE 4
Proliferation-differentiation pattern in developing lamprey habenulae at prolarval stages. **(A,C,E,G1-3)** and **(B,D,F)** are sections of developing river lamprey habenulae at prolarval stages 26 **(A, B)**, 28 **(C–F)**, and 30 **(G1–G3)**, after immunohistochemistry with antibodies directed against either PCNA (green) **(A,C,E,G1–G3)** or HuC/D (green) **(B,D, F)** and DAPI staining (blue). Section planes are shown on schemes above the photographs **(A,B,E,F,G1-3)**: transverse planes; **(C, D)**, horizontal planes. **(G1–G3)** show sections of the same specimen from anterior to posterior. **(A′–F′, G1′–G3′)** are higher magnifications of the habenula region boxed respectively in **(A–F, G1–G3)**. White arrowheads point to anterior HuC/D-positive territories, empty arrowheads highlight posterior PCNA-positive territories in right habenulae at stages stage 28–30. Abbreviations: L, left; R, right; lHb, left habenula; rHb, right habenula; hc, habenular commissure; pi, pineal field; st., stage. Scale bar = 50 µm.

3.2 Subdomain organization of adult river lamprey habenulae

To more precisely describe the subdomain organization of lamprey habenulae, we focused on four markers exhibiting distinct territories with sharp expression boundaries, *Gucy2g*, *Adcy2*, *Myo9b,* and *Rab23*. The relative organization of their respective territories was examined on adjacent sections of the same specimens, along transverse and horizontal planes (Figure 1; Supplementary Figure S2). *Adcy2* and *Myo9b* show mutually exclusive, complementary territories, altogether spanning the whole left and right habenulae (compare Figures 1A,B,D,E; Supplementary Figures S2B,C). *Myo9b* is strictly restricted to the right habenula, with a broad expression territory located dorsally at anterior levels and laterally at posterior ones. This territory excludes three well-delimited, right-sided *Adcy2*-positive cell populations, occupying, respectively, a ventro-lateral position (Figures 1A1,D2,D3; Supplementary Figures S2B1–3), a ventro-medial location in a tract-rich zone (Figures 1A2,D2; Supplementary Figures S2B2–4), and a medial position, adjacent to the midline, at posterior levels (Figures 1A3,D1–3; Supplementary Figures S2B4,5). *Adcy2* expression spans the whole left habenula in addition to these three right-sided cell populations. Analysis of *Gucy2g* and *Rab23* highlight further partitioning of the left habenula and of the *Myo9b*-positive territory in the right habenula. *Gucy2g* marks a dorso-anterior subdomain of the left habenula (Figures 1C,F; Supplementary Figure S2A). The *Rab23* territory is superimposable on that of *Myo9b* in the right habenula, excepting a medial posterior subdomain that is devoid of *Rab23* expression (Figure 1H; Supplementary Figures S2,D5).

3.3 Major morphological asymmetries in developing lamprey habenulae

We next addressed the developmental sequence leading to the elaboration of asymmetries in the river lamprey. To do so, we first generated a morphological reference, using IHC on serial sections with an antibody directed against acetylated tubulin (Figure 2). Habenular evaginations first become visible at stage 25, as previously described (Lagadec et al., 2015), ventral to an acetylated tubulin-positive, neuropil-rich zone corresponding, by its location, to the pineal field (Figure 2B1,B1′). At this stage, the right evagination already appears larger than the left one. At stage 26, the habenular commissure becomes visible (Figure 2C1,C1′). The difference in size between left and right habenulae is more

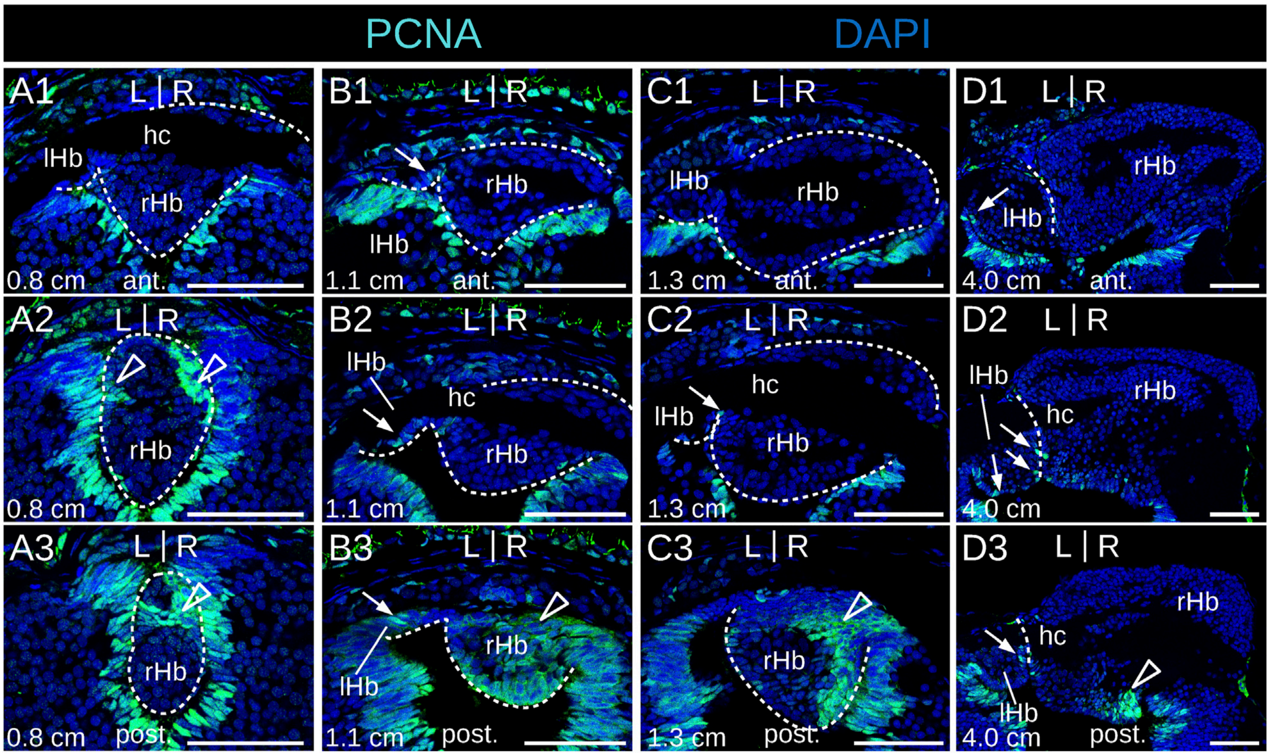

FIGURE 5
Identification of neural progenitors in developing lamprey habenulae at larval stages. **(A1-3)**, **(B1-3)**, **(C1-3)**, and **(D1-3)** are transverse sections of developing habenulae in respectively 0.8 cm, 1.1 cm, 1.3 cm, and 4.0 cm larvae, after immunohistochemistry with an antibody directed against PCNA (green) and DAPI staining (blue). **(A1–A3)** show sections of the same specimen from anterior to posterior, same for (B1–**B3)**, for **(C1–C3)**, and for **(D1–D3)**. Sections were obtained from river lamprey specimens in **(A1–A3,B1–B3,C1–C3)** and from a brook lamprey specimen in **(D1–D3)**. Empty arrowheads point to posterior PCNA-positive territories in the right habenula, thin arrows point to dispersed PCNA-positive cells in the left habenula. Abbreviations: L, left; R, right; lHb, left habenula; rHb, right habenula; hc, habenular commissure; ant., anterior; post., posterior. Scale bar = 50 µm.

conspicuous in the posterior part of the structure (Figures 2C2,C2′,C3,C3′). Acetylated tubulin signals are maintained in the pineal field but are undetectable in the habenula, except at the level of the habenular commissure. At stage 28, the left habenula is restricted to a thin layer of cells, located ventrally to the habenular commissure (Figure 2E1’,E2′), while the right habenula expands towards the left side, occupying most of the neural tube lumen posteriorly (Figures 2E1’–E3′). At this stage, acetylated tubulin is detected anteriorly in the right habenula, with the neuropil being completely absent from the posterior part of the right habenula (Figures 2D,E1’–E3′). These broad characteristics are maintained at stage 30, with a clear partitioning of the right habenula into an expanding anterior, neuropil-rich territory (Figures 2F1′,F2′,F3′) and a posterior territory devoid of acetylated tubulin signal (Figures 2F3′,F4′). Of note, at the level of the habenular commissure, most of the right habenula is located ventrally to the commissure with the exception of a few dorsal cells adjacent to the morphologically distinct pineal rudiment (Supplementary Figures S3A,A1). A change in morphology and size of the left habenula was only observed at the earliest larval stage analyzed (in 0.8 cm larvae). At this stage, dispersed inner cells accumulate between the habenular commissure and the ventricular cell layer (Figure 3A1,A1′). The whole right habenula exhibits acetylated tubulin labeling, except at a posterior dorsal level at the transition to the adjacent thalamus (Figures 3A3,A3′,A4,A4′). In 1.3–6.2 cm larvae, the left habenula has grown posteriorly and ventrally relative to the habenular commissure (Figures 3B2,B3,B2′,B3′; Supplementary Figures S3B–D). On the right, two ventral lobes, separated by a constriction most visible anteriorly, and distinct cell populations, differing by the density of their nuclei, become detectable in 4.0–6.2 cm larvae (Figures 3C1–C3; Supplementary Figures S3B–D). As observed in adults (Lanoizelet et al., 2024), a dense cell organization prevails dorsally in the right habenula of 6.2 cm larvae. In contrast, at ventral levels, cells appear more dispersed and are characterized by larger nuclei, similar to the cell organization observed in the left habenula (Supplementary Figures S3B1–B3,C1). Cells devoid of acetylated tubulin signal with a neuroepithelial organization are restricted to a small lateral and ventral territory of the right habenula in 1.3–6.2 cm larvae (Figures 3B4,C3; Supplementary Figures S3B–D).

3.4 Highly asymmetric proliferation-differentiation patterns in developing lamprey habenulae

No evidence of apoptosis was observed using a TUNEL assay at prolarval stages (Supplementary Figure S4). To identify neural

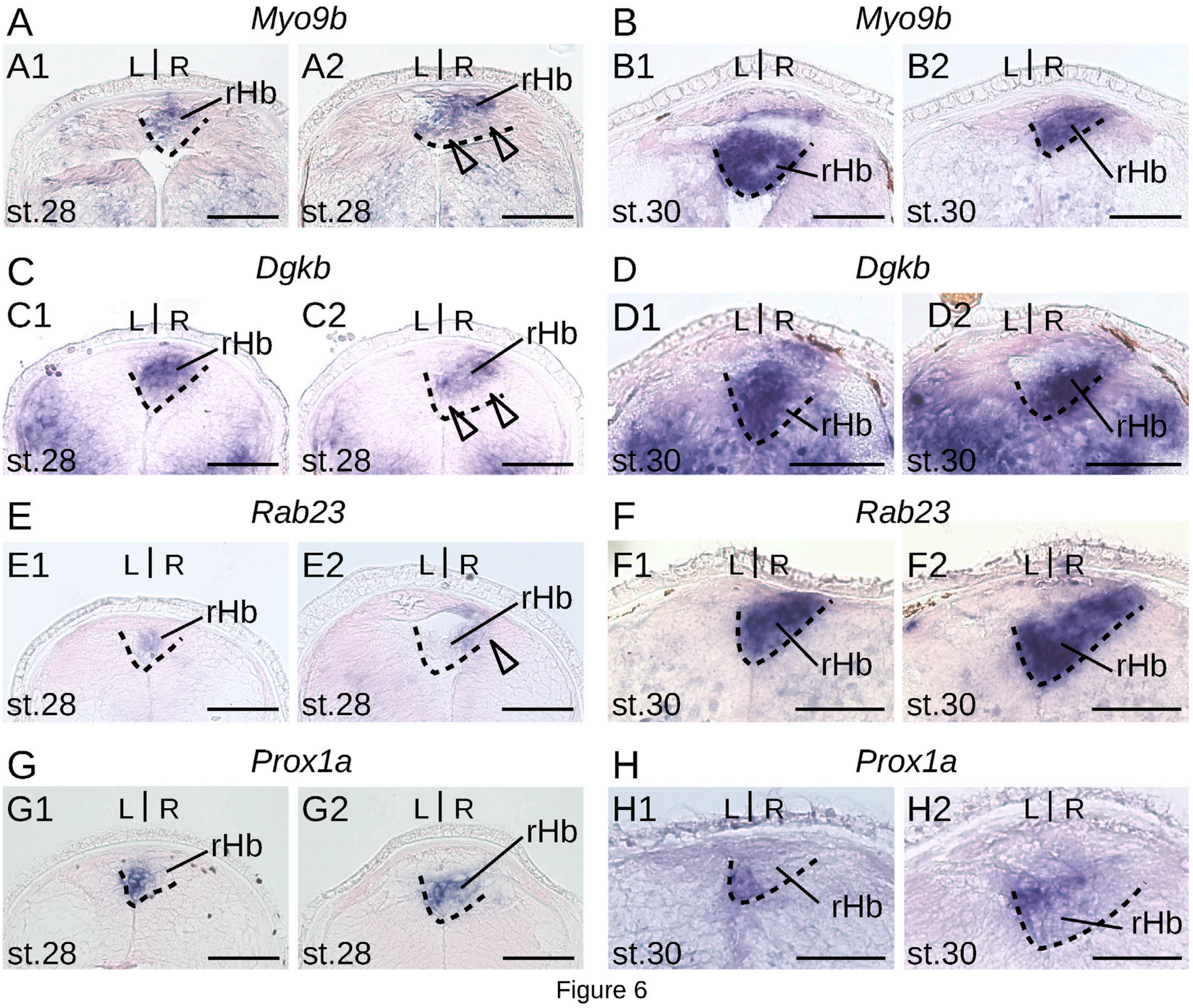

FIGURE 6
Expression of markers of the dorsal right habenula during lamprey prolarval stages. **(A,C,E, G)** and **(B,D,F, H)** are transverse sections of developing habenulae in respectively stage 28 and stage 30 river lamprey prolarvae, after *in situ* hybridization with probes for *Myo9b* **(A, B)**, *Dgkb* **(C, D)**, *Rab23* **(E, F)** and *Prox1a* **(G, H)**. **(A1–H1)** are from the same specimen as **(A2–H2)** and are located anterior to **(A2–H2)**. Dashed lines delimit the right habenula. Empty arrowheads point to negative territories for the gene analyzed, corresponding by their location to PCNA-positive cell populations. Abbreviations: L, left; R, right; lHb, left habenula; rHb, right habenula; st., stage. Scale bar = 50 µm.

progenitors and gain insights into the mode of habenula growth, we used IHC with an antibody directed against PCNA (proliferating cell nuclear antigen). IHC using an antibody directed against HuC/D (RNA-binding proteins of the Elav family) was also carried out at prolarval stages to identify newborn neurons. At stage 26, most habenular cells show nuclear signals for PCNA (Figure 4A), but only a few cells are positive for HuC/D, which is more abundant on the right than on the left side and more consistently observed at lateral locations (Figure 4B; Supplementary Figure S5). Very different PCNA profiles are observed between left and right habenulae at subsequent stages. In the right habenula, at stage 28, PCNA nuclear signals become restricted to ventral and posterior territories (Figures 4C,C′) and correlate with those devoid of neuropil as assessed by acetylated tubulin labeling. HuC/D-positive cells are preferentially located anteriorly, at the same location as the neuropil-rich territories expressing acetylated tubulin (Figures 4D,D′). In stage 30 prolarvae, a dense population of PCNA-positive nuclei in territories devoid of neuropil is maintained in the posterior part of the right habenula (Figures 4G1–G3,G1′-G3′). In the left habenula, most cells show nuclear PCNA signals and are negative for HuC/D at stage 28 (Figures 4E,E’,F,F′). At stages 29–30, HuC/D-expressing cells become visible medially at the level of the habenular commissure, concomitantly with a loss of nuclear signals of PCNA at this location (Figure 4G2,G2′; Supplementary Figure S6A-C). Concerning larval stages, in 0.8 cm larvae, a strong nuclear PCNA signal is observed posteriorly and dorsally, at the level of the transition to presumptive thalamic territories (Figures 5A1–A3). This dense population is gradually displaced laterally in the right habenula during larval growth (Figures 5B1–B3,C1-C3) and only occupies a restricted posterior ventral territory of the right habenula in 4.0 cm larvae (Figure 5D3). At later larval stages, PCNA-positive nuclei are

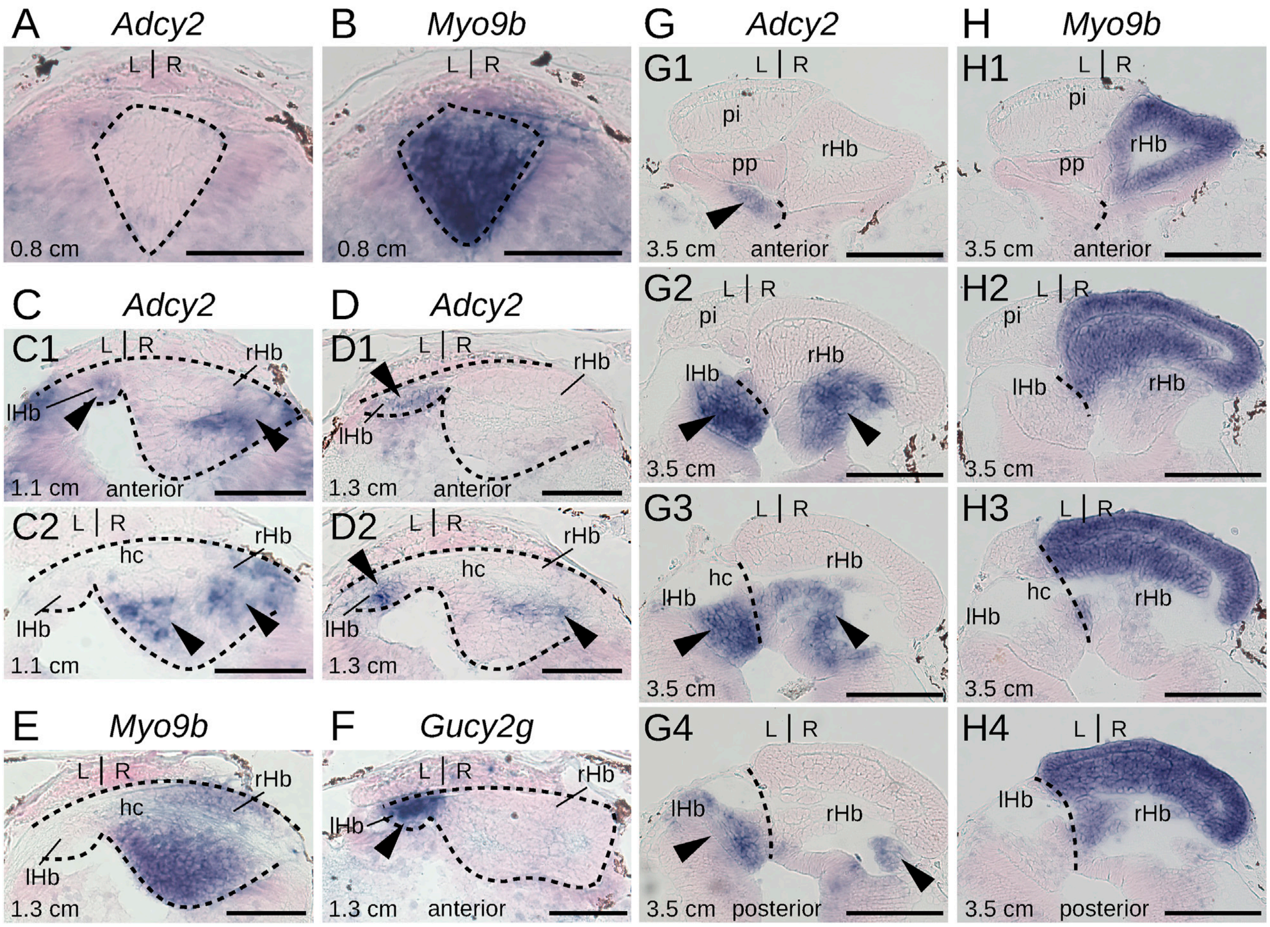

FIGURE 7
Elaboration of habenula subdomain organization during lamprey larval stages. **(A–H)** are transverse sections of developing habenulae in respectively 0.8 cm, 1.1 cm, 1.3 cm, and 3.5 cm lamprey larvae, after *in situ* hybridization with probes for *Adcy2* **(A,C,D, G)**, *Myo9b* **(B,E, H)** and *Gucy2g* **(F)**. **(A–F)** are from river lamprey specimens, **(G, H)** are from a sea lamprey specimen. **(A, B)** are from the same specimen, same for **(G, H)**. **(C1,D1,F)** are located anterior to the habenular commissure, **(C2,D2,E)** are located at the level of the anterior commissure **(E)** or immediately posterior to it **(C2,D2)**. **(G1–G4)** show successive sections from anterior to posterior, same for **(H1–H4)**. Dashed lines delimit habenulae in **(A–D)**. They delineate the boundary between left and right habenulae in **(G, H)**. Black arrowheads point to territories expressing *Gucy2g*- **(F)** and *Adcy2* **(C,D, G)**. Abbreviations: L, left; R, right; lHb, left habenula; rHb, right habenula; hc, habenular commissure. Scale bar = 50 μm in **(A–F)** and 100 μm in **(G, H)**.

maintained at this level but become interspersed with PCNA-negative nuclei (Supplementary Figures S6D1–3,D5,E1–3). In the left habenula, at all larval stages examined, ventricular expression of PCNA in left habenulae is generally weak and restricted to dispersed nuclei (Figures 5B1–3,C2,D1-3; Supplementary Figures S6D1–4,E2–3).

3.5 Expression timing of subdomain markers in developing lamprey habenulae

To gain insights into the timing of neuronal identity elaboration in different habenular subdomains in the river lamprey, we analyzed the expression dynamics of four genes defining distinct territories of the dorsal right habenula (*Myo9b*, *Dgkb*, *Rab23* and *Prox1a*) and of two genes expressed, respectively, in the whole left and the ventral right habenula (*Adcy2*) and in a dorso-anterior subdomain of the left habenula (*Gucy2g*). ISH analysis of expression profiles was first carried out at prolarval stages (stages 26, 28, and 30) (Figure 6). No signal was observed for any of these markers at stage 26. At stage 28, all right-restricted markers show very similar signals in the right habenula, excluding ventral and posterior-most territories corresponding, by their location, to those of PCNA-positive neural progenitors (Figures 6A,C,E,G). These expression territories are maintained at stage 30 (Figures 6B,D,F,H). In contrast, no signal was detectable for either *Adcy2* or *Gucy2g* at these stages (not shown). Furthermore, no evidence for prolarval expression was obtained by analysis of a broader range of left-enriched genes (*Prkar2*, *Nwd2*, *Rock2*, and *Scgn*) (not shown). At larval stages, analysis was restricted to three gene markers, *Myo9b*, *Adcy2*, and *Gucy2g*. While *Adcy2* and *Gucy2g* expression is undetectable in 0.8 cm larvae, a major *Myo9b* signal is observable in the right habenula (Figures 7A,B). In contrast, *Gucy2g* and *Adcy2* expression is detectable in 1.1–1.3 cm larvae, in the left habenula anteriorly to the habenular commissure, with *Adcy2* being further expressed in the right habenula posteriorly to the habenular commissure (Figures 7C,D,F). In these larvae, *Myo9b* is broadly expressed in the right habenula (Figure 7E). In 3.5 cm larvae, the

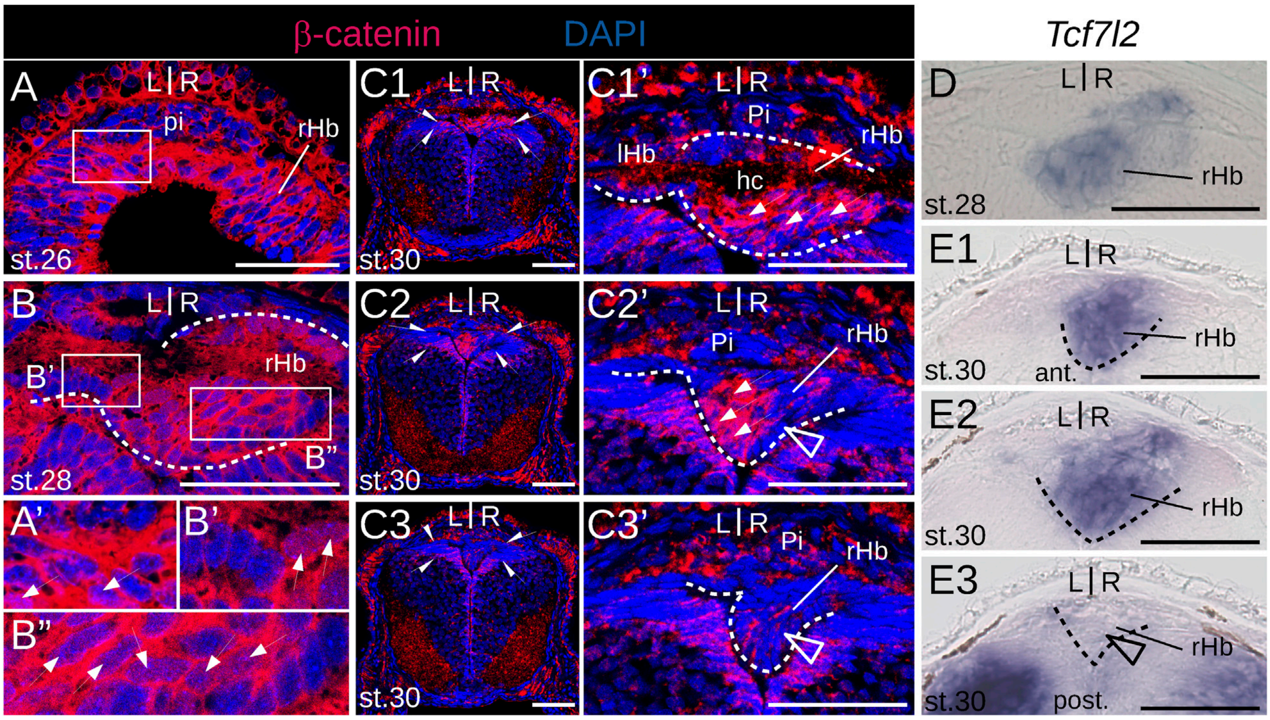

FIGURE 8
β–catenin and *Tcf7l2* expression in developing lamprey habenulae at prolarval stages. **(A, B)** and **(C1–C3)** are transverse sections of developing river lamprey habenulae at prolarval stages 26 **(A)**, 28 **(B)**, and 30 **(C1–C3)**, after immunohistochemistry with an antibody directed against β-catenin (red) an,d DAPI staining (blue). **(D)** and **(E1–E3)** are transverse sections of developing river lamprey habenulae at prolarval stages 28 **(A)** and 30 **(E1–E3)**, after *in situ hybridization* with a probe for *Tcf7l2*. **(C1–C3)** show sections of the same specimen from habenular commissure to posterior levels, **(E1–E3)** show sections of the same specimen from anterior to posterior. **(A′)**, **(B′,B′′)**, **(C1′, C3′)** are higher magnifications of the habenula region boxed respectively in **(A, B)**, **(C1–C3)**. Dashed lines delimit habenulae. Thin arrows point to nuclei positive for β-catenin. Empty arrowheads point to territories corresponding by their location to populations of PCNA-positive neural progenitors. Half-arrows in **(C1–C3)** delimit a thalamic neuroepithelial territory negative for β-catenin. Abbreviations: L, left; R, right; ant., anterior; post., posterior; lHb, left habenula; rHb, right habenula; hc, habenular commissure; pi, pineal field; ant., anterior; post., posterior; st., stage. Scale bar = 50 μm.

complementarity between the expression domains of *Myo9b* (dorsal) and *Adcy2* (ventral) becomes evident in the right habenula and *Adcy2* is detectable in the whole left habenula (Figures 7G,H). These expression characteristics are maintained in 7.0 cm larvae, which exhibit cell populations related, by their location, to those observed in adults (Supplementary Figures S7B,C). Thus, at this stage, the right ventral *Adcy2* territory, although continuous, contains both dense and more dispersed cell populations at locations comparable to those of the three *Adcy2*-positive subdomains in right adult habenulae (Supplementary Figures S7B1–4). In addition, expression of *Gucy2g* in 7.0 cm larvae becomes restricted to an anterior subdomain of the left habenula, as observed in adults (Supplementary Figure S7A).

3.6 Dynamics of Wnt activity in developing lamprey habenulae

Since Wnt signaling has been involved in the formation of habenulae asymmetry in catshark and zebrafish, we analyzed the activity profile of the Wnt pathway in developing lamprey habenulae at prolarval and larval stages, using IHC with an antibody directed against β–catenin (Figures 8A,B,C1–C3; Figure 9). An ISH analysis of *Tcf7l2*, whose expression is restricted to the right dorsal habenula in adults (Supplementary Figure S1M) was also included at prolarval stages (Figures 8DE1–E3). When habenulae become morphologically visible at stage 26, faint nuclear signals of β–catenin can be detected at dorsal habenula levels, but they remain absent from the adjacent pineal field (Figures 8A,A′). At stage 28, stronger nuclear signals are present in the right habenula, completely excluding the left habenula as well as ventral and posterior territories expressing PCNA-positive signals (Figures 8B,B′,B″). A similar profile is observed at stage 30, with widespread nuclear expression of β–catenin in the right habenula, except in neural progenitors, and with a total absence of nuclear signals in the left habenula (Figures 8C1–C3,C1′-C3′). Of note, at this stage, a sharp boundary demarcates territories either positive or negative for nuclear β–catenin in the ventricular pseudostratified neuroepithelium, which delimits the site of habenula formation (Figures 8C1–C3,C1′–C3′). No *Tcf7l2* signal is detected at stage 26 but a very specific expression is established at stages 28–30, in the same territories as those expressing other right dorsal markers and positive for nuclear β–catenin (Figures 8D,E1–E3). A related profile of β–catenin distribution is observed in 0.8 cm larvae, with strong nuclear signals in the right habenula, excluding PCNA-positive zones, and with an absence in the left habenula (Figures 9A1–A3). Two changes are observed in 1.1–1.3 cm larvae. While most nuclei maintain a strong

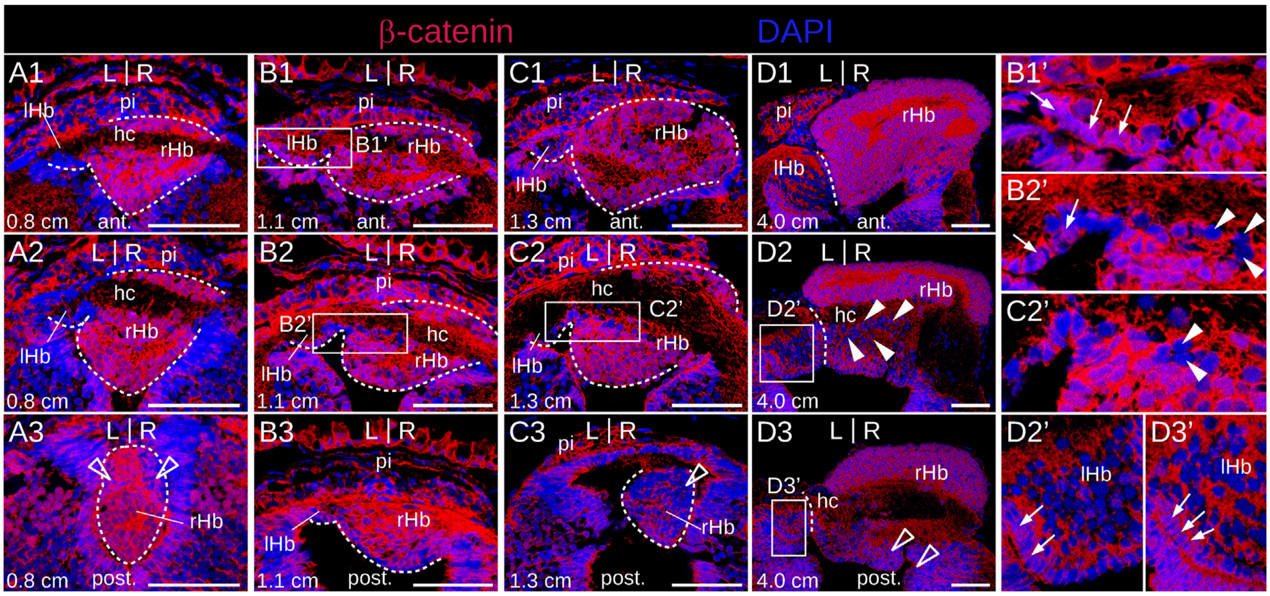

FIGURE 9
β–catenin and *Tcf7l2* expression in developing lamprey habenulae at larval stages. **(A1–A3)**, **(B1–B3)**, **(C1–C3)**, and **(D1–D3)** are transverse sections of developing habenulae in 0.8 cm, 1.1 cm, 1.3 cm and 4.0 cm lamprey larvae, after immunohistochemistry with an antibody directed against β-catenin (red) and DAPI staining (blue). **(A1–A3,B1–B3,C1–C3)** and **(D1–D3)** were from river lamprey and brook lamprey specimens respectively. **(A1–A3)** show sections of the same specimen from anterior to posterior, same for **(B1–B3)**, **(C1–C3)** and **(D1–D3)**. Dashed lines delimit habenulae in **(A1–A3)**, **(B1,B3)** and **(C1–C3)**. They delineate the boundary between left and right habenulae in **(D1–D3)**. **(B1′, B2′)**, **(C2′)**, **(D2′, D3′)** are higher magnifications of the habenula region boxed respectively in **(B1, B2)**, **(C2)**, **(D2, D3)**. Thin arrows point to nuclei positive for β-catenin in the ventricular zone of the left habenula. Empty arrowheads point to territories corresponding by their location to populations of PCNA-positive neural progenitors. White arrowheads point to nuclei negative for β-catenin, observed ventrally to the habenular commissure in 1.1–1.3 cm larvae. Abbreviations: L, left; R, right; ant., anterior; post., posterior; lHb, left habenula; rHb, right habenula; hc, habenular commissure; pi, pineal field; ant., anterior; post., posterior; st., stage. Scale bar = 50 μm.

β–catenin expression in the right habenula except at the posterior-most levels, that are positive for PCNA, a dispersed population of negative nuclei appears, ventrally to the habenular commissure (Figures 9B2,B2′,C2,C2′). In addition, while no nuclear β–catenin signal is detected in the left habenula at the prolarval stage 30 and in 0.8 cm larvae, some positive nuclei, interspersed with negative ones, are now present in ventricular cells (Figures 9B1–B3,C1–C3,B1′,B2′). These changes are confirmed in 4.0 cm larvae. In the right habenula, almost all cells exhibit strong nuclear β–catenin signals in dorsal *Myo9b*-positive territories. In contrast, the proportion of β–catenin-negative nuclei markedly increases in right ventral territories excluding ventricular zones, with a distribution reflecting *Adcy2*-positive territories (Figures 9D1–D3). In the left habenula, most nuclei are negative for β–catenin, except in the ventricular cell population, where nuclear PCNA signals are detectable (Figures 9D1–D3). In summary, we observe highly dynamic, asymmetric profiles of nuclear β–catenin localization both in neural progenitors and neuronal precursor subdomains.

4 Discussion

In this study, we have carried out an unbiased characterization of habenular asymmetries in lampreys and have compiled a detailed description of their formation during prolarval and larval stages. Our work provides strong support for the existence of a bipartite organization of the lamprey habenula, similar to that previously proposed based on a candidate gene approach with the catshark as reference (Lanoizelet et al., 2024). While the previously used gene markers (*Kctd12b* and *Prox1a/b*) showed overlapping territories of expression in the lamprey habenula, ISH analyses of genes retrieved from our transcriptomic analysis provide a much more detailed picture, as exemplified by the mutually exclusive expression patterns of *Myo9b* in the dorsal right habenula and of *Adcy2* in the left plus ventral right habenula, which, when taken together, cover the whole habenula. In line with an analysis of efferent projections from the lamprey habenula (Stephenson-Jones et al., 2012), our previous molecular characterization suggested that the partitioning observed in the lamprey reflects the organization into two subdomains of gnathostome habenulae (medial/lateral or dorsal/ventral in actinopterygians). The present analysis, which expands the set of territory markers available in the lamprey, allowed us to identify additional genes that further support the evolutionary relationship between the left plus ventral right habenulae of lampreys and the medial habenulae of jawed vertebrates (Table 1). Of the 8 lamprey genes with broad expression in these territories, 4 (*LfNecab1*, *Prkar2a*, *Gpr26*, and *Nwd2*) possess one ohnolog in the mouse with expression that is largely restricted to the medial habenula (Chen et al., 2022; Lein et al., 2007; London et al., 2020): *MmNecab2*, *MmPrkar2a*, *MmGpr26*, and *MmNwd2* (Supplementary Figure S8). These genes may therefore correspond to ancient and highly conserved markers of the medial habenular territory. We also identified novel habenular

TABLE 1 Dynamics of expression of subdomain markers in lamprey habenulae at prolarval and larval stages. For each of the three markers analyzed (*Myo9b*, *Adcy2*, and *Gucy2g*) and at each stage studied, "–" and "+" respectively indicate the absence and presence of expression in developing habenulae. When expression was detected, the labeled territory is indicated. Abbreviations: lHb, left habenula; rHb, right habenula; st., stage.

	Prolarva			Larva			
	st.26	st.28	st.30	0.8 cm	1.1 cm	1.3 cm	3.5–7.0 cm
Myo9b	-	+ rHb	+ rHb	+ rHb	+ rHb	+ rHb	+ dorsal rHb
Adcy2	-	-	-	-	+ lHb, rHb	+ lHb, rHb	+ lHb, ventral rHb
Gucy2g	-	-	-	-	+ lHb	+ lHb	+ anterior lHb

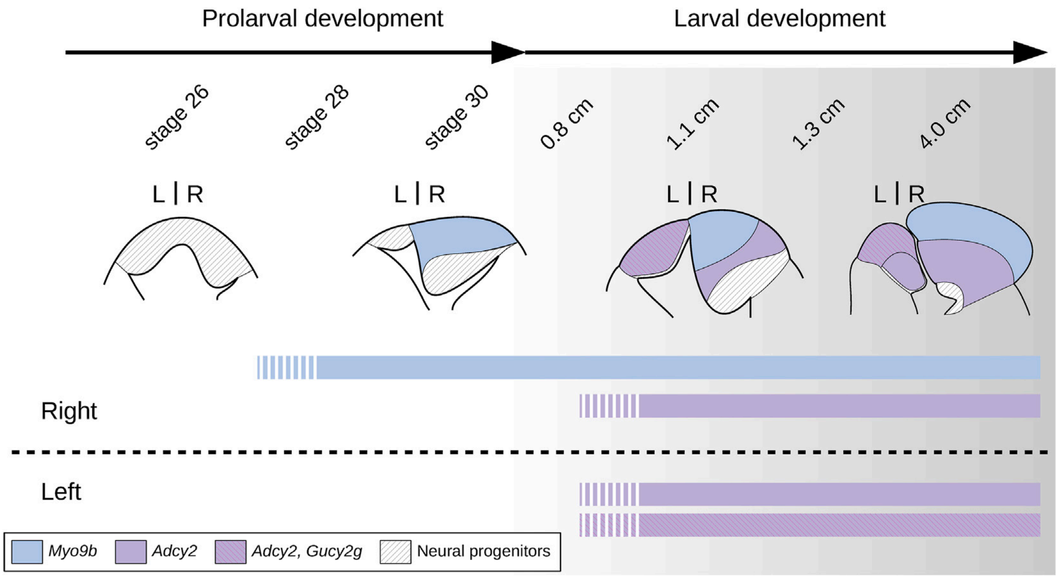

FIGURE 10
Scheme showing major changes in the organization of lamprey habenulae during prolarval and larval development. Broad transitions in the general organization of habenulae are shown with the *Myo9b*-positive right dorsal habenula in blue and with the bilateral, *Adcy2*-positive territory spanning both the left and ventral right habenula in purple, and its *Gucy2g*-positive subdomain hatched (magenta lines on purple background). Territories of neural progenitors are shown hatched (black lines on white background). The developmental stages shown in the diagram do not show a homogeneous developmental progression but have been chosen based on the progression of habenula formation and of the establishment of habenular asymmetries. At stage 26, no indication of neuronal identity elaboration is observed. Starting from prolarval stage 28 and until at least early larval stages (0.8 cm in the river lamprey), the right habenula expands and expresses neuronal signatures of the adult dorsal right habenula. In contrast, the left and ventral right habenulae do not markedly expand and exhibit no indication of neuronal identity elaboration until significantly later larval stages (1.1 cm in the river lamprey). At the temporal resolution of our analysis, the expression initiation of *Gucy2g*, a marker for a dorso-anterior subdomain of the left habenula, was synchronous with that of *Adcy2* in ventral territories of left and right habenulae. However, we cannot exclude differential temporal regulations of neuronal identity elaboration between these *Gucy2g*-positive and negative subdomains.

subdomains, both on the left and on the right side. While the left and the ventral right habenulae appear molecularly related, the left habenula contains a dorsal and anterior subdomain expressing at least two genes (*Gucy2g* and *Scgn*), whose expression is undetectable on the right side. Such an asymmetric partitioning of the medial habenula has previously been reported both in the zebrafish and the catshark (Aizawa et al., 2007; deCarvalho et al., 2014; Gamse et al., 2005; 2003; Lanoizelet et al., 2024; Pandey et al., 2018), but the limited number of markers available does not allow any firm conclusions as to possible cross-species relationships. Similarly, in the dorsal right habenula, *Rab23* defines a lateral subdomain without any clear correspondence in other species. These difficulties to detect cross-species similarities in subdomain architecture and asymmetry of habenulae may be related to lineage-specific diversifications, as recently reported in teleosts and tetrapods (Lanoizelet et al., 2024), or simply due to the scarcity of available data, precluding a robust phylogenetic approach. Spatially-resolved, genome-wide characterizations of habenulae from a variety of different species will thus be crucial for obtaining a more comprehensive view of the conservation and divergence of habenular organization across vertebrates.

From a developmental perspective, we previously reported major size differences between the left and the right habenulae of lampreys, starting from the earliest stages of habenula formation (Lagadec et al., 2015). The availability of subdomain markers leads to a more comprehensive picture of these size asymmetries and provides new insights into the mode of habenula development in the lamprey (Figure 10). We found that the first habenula subdomain to form, during prolarval and the earliest larval stages, is the dorsal right one, and that this right-restricted process is mainly responsible for shaping the left/right size asymmetry we previously observed. Based on the temporal resolution of our analysis, the left plus ventral right habenulae form simultaneously, and significantly later (in larvae larger than 1.0 cm in size) as molecularly related bilateral territories. However, a more extensive sampling of time points during the prolaval-to-larval transition will be necessary to more precisely define the progression of habenular development during this period. In the absence of such data, a preliminary conclusion is that the temporal regulation of subdomain formation in the lamprey habenula is reminiscent of the successive formation, in the catshark, of territories respectively related to the lateral and medial habenulae on the right side (Lanoizelet et al., 2024). A major difference between the two species is the absence, in the lamprey, of a habenular territory of lateral identity on the left side, an asymmetry established at early stages of habenula formation in the catshark. The underlying cellular mechanisms remain to be assessed. We found no evidence for apoptosis at the prolarval stages studied, but we cannot exclude that some apoptotic cells may have escaped detection, either in micro-domains or at time points not included in this study. Newly born, HuC/D-positive neurons were detected both on the right and the left sides starting from early stages of habenula formation, without clear evidence for an asymmetric temporal regulation of cell cycle exits (Aizawa et al., 2007; Guglielmi et al., 2020; Lagadec et al., 2018; Powell et al., 2024; Lagadec et al., 2024) or for an earlier onset of neuronal differentiation on the left as observed in gnathostomes (Roussigné et al., 2009). However, the involvement of an asymmetric regulation of neurogenesis should be further assessed and quantified using analyses of cell cycle exits during the elaboration of habenular subdomains. Finally, an asymmetric regulation of cell proliferation, as reported in the catshark (Lagadec et al., 2018), may be a major factor in the development of size asymmetries in lamprey habenulae. In line with this hypothesis, only dispersed PCNA-positive cells were observed on the left side from late prolarval stages (stage 29) to relatively advanced larval stages, while a dense posterior population of neuroepithelial cells was maintained on the right side, evoking a major, localized proliferation center. Quantitative analyses of proliferation rates will be crucial to test this possibility. Concerning the *Adcy2*-positive left and ventral right subdomains, the similar timing of their formation does not seem to translate into a symmetry of their neuronal identities, as shown by the presence of a left-restricted *Gucy2g*-positive anterior subterritory. In the zebrafish, the asymmetric partitioning of the medial habenula, their putative gnathostome counterpart, results from an asymmetric temporal regulation of neurogenesis, also described in the developing medial habenula of the catshark, although a causal relationship between the processes observed in zebrafish, catshark, and lamprey remains to be demonstrated (Aizawa et al., 2007; Guglielmi et al., 2020; Lagadec et al., 2018; Powell et al., 2024; Lagadec et al., 2024). Detailed analyses of the timing of subterritory-specific cell cycle exits will have to be carried out in the lamprey left habenula to address the possible conservation of this process. As in the zebrafish (Concha et al., 2003; Gamse et al., 2003; Lekk et al., 2019), it might involve spatial, left- and anterior-restricted cues, possibly resulting from interactions with the parapineal, which, in the lamprey, is located in close proximity to the initial expression domain of *Gucy2g*.

We previously proposed an ancient involvement of Wnt signaling in habenular asymmetry formation based not only on the role of the Wnt pathway in the catshark and in the zebrafish, but also on asymmetric profiles of nuclear β−catenin distribution in habenulae at advanced stage of differentiation in a broad sampling of species, including the river lamprey (Lanoizelet et al., 2024). The dynamic and highly asymmetric profiles of nuclear β−catenin in developing lamprey habenulae confirm and extend this hypothesis. They indeed suggest that asymmetric Wnt activity concerns PCNA-positive neural progenitors, as well as neuronal subdomain precursors, as identified by signature markers. The strong nuclear β−catenin signals, initiated in the *Myo9b-/Prox1a/b*-positive right dorsal habenula concomitantly with the onset of *Myo9b-/Prox1a/b* expression and maintained throughout development, evoke a conserved role for Wnt signaling in promoting the corresponding neuronal identity: lateral right in ancestral gnathostomes, as exemplified in the catshark (Lanoizelet et al., 2024), dorsal right in the lamprey. The absence of nuclear β−catenin in neural progenitors of the right habenula of prolarvae and early larvae is also consistent with a regulation operating in post-mitotic precursors, as reported in the catshark (Lanoizelet et al., 2024). In contrast, the nuclear distribution of β−catenin signals appeared highly dynamic in the left habenula, with positive signals coinciding with PCNA-positive cell populations in larvae larger than 1.1 cm in size. This is consistent with an involvement of Wnt signaling in the control of neurogenesis, as demonstrated in the zebrafish (Guglielmi et al., 2020; Powell et al., 2024). Altogether, these data suggest that the lamprey may have retained distinct, ancient roles of Wnt signaling in habenular asymmetry formation, which remain to be directly addressed using experimental perturbations of Wnt activity. Pharmacological approaches combined with CRISPR-Cas9 inactivation of genes coding for Wnt pathway components and regulators as reported in the lamprey (Square et al., 2015) will thus be crucial to test this hypothesis and to obtain a comprehensive view of the evolution of Wnt functions during habenular asymmetry formation. In conclusion, the unique characteristics of habenula asymmetry formation in lampreys, together with the rise of advanced technologies applicable to these species such as spatial transcriptomics and gene editing, substantiate the interest of this taxon for comparative studies and allow new perspectives on the developmental logic underlying the recurrence and variation of habenular asymmetries across vertebrates.

Data availability statement

The datasets presented in this study can be found in online repositories (NCBI). The names of the repository/repositories and accession number(s) can be found in the article/Supplementary Material (Supplementary Table S2, S3).

Ethics statement

Ethical approval was not required for the study involving animals in accordance with the local legislation and institutional requirements because All animal manipulations were carried out in compliance with validated veterinary practices. The work involved analyses of non-mammalian, non-feeding prolarvae and organ (brain) collections from euthanized animals (larvae and adults).

Animals were euthanized under anesthesia. As such, the experiments did not require an ethical validation and license following French and European regulations.

Author contributions

LG: Writing–review and editing. RL: Writing–review and editing. LM: Writing–review and editing. HM: Writing–review and editing. MF: Writing–review and editing. JP: Writing–review and editing. NH: Writing–review and editing. QR: Writing–review and editing. MR: Writing–review and editing. AB-I: Writing–review and editing. PB: Writing–review and editing. MS: Writing–review and editing. SM: Writing–original draft, Writing–review and editing.

Funding

The author(s) declare that financial support was received for the research, authorship, and/or publication of this article. The work was funded by Agence Nationale de la Recherche contract n° ANR-16-CE13-0013-02 to SM and PB, and by a Ph.D. fellowship to LM (Ministère de la Recherche, ED515). MS is supported by the Centre National de la Recherche Scientifique and by Agence Nationale de la Recherche contract n° ANR-21-CE340006-02.

Acknowledgments

We thank Michaël Fuentès, Pascal Romans, and the Aquariology Service of the Observatoire Océanologique in Banyuls-sur-Mer, France, for help in obtaining, transporting and maintaining lamprey specimens, Guillaume Evanno, INRAE, UMR1037 LPGP, Fish Physiology and Genomics, Rennes, France, for giving access to brook lamprey specimens, EMBRC-France for support to local marine infrastructures, David Pecqueur and the BioPic imaging platform for access to confocal microscopy, Nyree West and the Bio2Mar service for access to the molecular biology platform, and the Service de Bio-Informatique BSBII for HM's support.

Conflict of interest

The authors declare that the research was conducted in the absence of any commercial or financial relationships that could be construed as a potential conflict of interest.

The author(s) declared that they were an editorial board member of Frontiers, at the time of submission. This had no impact on the peer review process and the final decision.

Generative AI statement

The author(s) declare that no Generative AI was used in the creation of this manuscript.

Publisher's note

Supplementary material

The Supplementary Material for this article can be found online at: https://www.frontiersin.org/articles/10.3389/fcell.2025.1528797/full#supplementary-material

References

Ables, J. L., Park, K., and Ibañez–Tallon, I. (2023). Understanding the habenula: a major node in circuits regulating emotion and motivation. *Pharmacol. Res.* 190, 106734. doi:10.1016/j.phrs.2023.106734

Abuduaini, Y., Pu, Y., Thompson, P. M., and Kong, X. (2023). Significant heterogeneity in structural asymmetry of the habenula in the human brain: a systematic review and meta-analysis. *Hum. Brain Mapp.* 44, 4165–4182. doi:10.1002/hbm.26337

Ahumada-Galleguillos, P., Lemus, C., Díaz, E., Osorio-Reich, M., Härtel, S., and Concha, M. (2016). Directional asymmetry in the volume of the human habenula. *Brain Struct. Funct.* 222, 1087–1092. doi:10.1007/s00429-016-1231-z

Aizawa, H., Goto, M., Sato, T., and Okamoto, H. (2007). Temporally regulated asymmetric neurogenesis causes left-right difference in the zebrafish habenular structures. *Dev. Cell.* 12, 87–98. doi:10.1016/j.devcel.2006.10.004

Amo, R., Aizawa, H., Takahoko, M., Kobayashi, M., Takahashi, R., Aoki, T., et al. (2010). Identification of the zebrafish ventral habenula as a homolog of the mammalian lateral habenula. *J. Neurosci. official J. Soc. Neurosci.* 30, 1566–1574. doi:10.1523/JNEUROSCI.3690-09.2010

Beretta, C. A., Dross, N., Guiterrez-Triana, J. A., Ryu, S., and Carl, M. (2012). Habenula circuit development: past, present, and future. *Front. Neurosci.* 6, 51–10. doi:10.3389/fnins.2012.00051

Bray, N. L., Pimentel, H., Melsted, P., and Pachter, L. (2016). Near-optimal probabilistic RNA-seq quantification. *Nat. Biotechnol.* 34, 525–527. doi:10.1038/nbt.3519

Cabau, C., Escudié, F., Djari, A., Guiguen, Y., Bobe, J., and Klopp, C. (2017). Compacting and correcting trinity and Oases RNA-seq *de novo* assemblies. *PeerJ* 5, e2988. doi:10.7717/peerj.2988

Chen, W., Peng, X., Deng, Q., Chen, M., Du, J., and Zhang, B. (2019). Role of olfactorily responsive neurons in the right dorsal habenula–ventral interpeduncular nucleus pathway in food-seeking behaviors of larval zebrafish. *Neuroscience* 404, 259–267. doi:10.1016/j.neuroscience.2019.01.057

Chen, Z., Long, H., Guo, J., Wang, Y., He, K., Tao, C., et al. (2022). Autism-risk gene necab2 regulates psychomotor and social behavior as a neuronal modulator of mGluR1 signaling. *Front. Mol. Neurosci.* 15, 901682. doi:10.3389/fnmol.2022.901682

Concha, M. L., Russell, C., Regan, J. C., Tawk, M., Sidi, S., Gilmour, D. T., et al. (2003). Local tissue interactions across the dorsal midline of the forebrain establish CNS laterality. *Neuron* 39, 423–438. doi:10.1016/S0896-6273(03)00437-9

Concha, M. L., and Wilson, S. W. (2001). Asymmetry in the epithalamus of vertebrates. *J. Anat.* 199, 63–84. doi:10.1046/j.1469-7580.2001.19910063.x

Davidson, N. M., Hawkins, A. D. K., and Oshlack, A. (2017). SuperTranscripts: a data driven reference for analysis and visualisation of transcriptomes. *Genome Biol.* 18, 148. doi:10.1186/s13059-017-1284-1

Davidson, N. M., and Oshlack, A. (2014). Corset: enabling differential gene expression analysis for de novoassembled transcriptomes. *Genome Biol.* 15, 410. doi:10.1186/s13059-014-0410-6 deCarvalho, T. N., Subedi, A., Rock, J., Harfe, B. D., Thisse, C., Thisse, B., et al. (2014). Neurotransmitter map of the asymmetric dorsal habenular nuclei of zebrafish. *Genesis* 52, 636–655. doi:10.1002/dvg.22785

Derobert, Y., Plouhinec, J.-L., Sauka-Spengler, T., Le Mentec, C., Baratte, B., Jaillard, D., et al. (2002). Structure and expression of three Emx genes in the dogfish *Scyliorhinus canicula*: functional and evolutionary implications. *Dev. Biol.* 247, 390–404. doi:10.1006/dbio.2002.0700

Dreosti, E., Vendrell Llopis, N., Carl, M., Yaksi, E., and Wilson, S. W. (2014). Left-right asymmetry is required for the habenulae to respond to both visual and olfactory stimuli. *Curr. Biol.* 24, 440–445. doi:10.1016/j.cub.2014.01.016

Duboué, E. R., Hong, E., Eldred, K. C., and Halpern, M. E. (2017). Left habenular activity attenuates fear responses in larval zebrafish. *Curr. Biol.* 27, 2154–2162.e3. doi:10.1016/j.cub.2017.06.017

Facchin, L., Duboué, E. R., and Halpern, M. E. (2015). Disruption of epithalamic left–right asymmetry increases anxiety in zebrafish. *J. Neurosci.* 35, 15847–15859. doi:10.1523/JNEUROSCI.2593-15.2015

Gamse, J. T., Kuan, Y.-S., Macurak, M., Brösamle, C., Thisse, B., Thisse, C., et al. (2005). Directional asymmetry of the zebrafish epithalamus guides dorsoventral innervation of the midbrain target. *Development* 132, 4869–4881. doi:10.1242/dev.02046

Gamse, J. T., Thisse, C., Thisse, B., and Halpern, M. E. (2003). The parapineal mediates left-right asymmetry in the zebrafish diencephalon. *Development* 130, 1059–1068. doi:10.1242/dev.00270

Grabherr, M. G., Haas, B. J., Yassour, M., Levin, J. Z., Thompson, D. A., Amit, I., et al. (2011). Full-length transcriptome assembly from RNA-Seq data without a reference genome. *Nat. Biotechnol.* 29, 644–652. doi:10.1038/nbt.1883

Grillner, S., Von Twickel, A., and Robertson, B. (2018). The blueprint of the vertebrate forebrain – with special reference to the habenulae. *Seminars Cell. and Dev. Biol.* 78, 103–106. doi:10.1016/j.semcdb.2017.10.023

Guglielmi, L., Bühler, A., Moro, E., Argenton, F., Poggi, L., and Carl, M. (2020). Temporal control of Wnt signaling is required for habenular neuron diversity and brain asymmetry. *Development* 147, dev182865. doi:10.1242/dev.182865

Hitti, F. L., Parker, D., Yang, A. I., Brem, S., and Verma, R. (2022). Laterality and sex differences of human lateral habenula afferent and efferent fiber tracts. *Front. Neurosci.* 16, 837624. doi:10.3389/fnins.2022.837624

Hüsken, U., Stickney, H. L., Gestri, G., Bianco, I. H., Faro, A., Young, R. M., et al. (2014). Tcf7l2 is required for left-right asymmetric differentiation of habenular neurons. *Curr. Biol.* 24, 2217–2227. doi:10.1016/j.cub.2014.08.006

Lagadec, R., Laguerre, L., Menuet, A., Amara, A., Rocancourt, C., Péricard, P., et al. (2015). The ancestral role of nodal signalling in breaking L/R symmetry in the vertebrate forebrain. *Nat. Commun.* 6, 6686. doi:10.1038/ncomms7686

Lagadec, R., Lanoizelet, M., Sánchez-Farías, N., Hérard, F., Menuet, A., Mayeur, H., et al. (2018). Neurogenetic asymmetries in the catshark developing habenulae: mechanistic and evolutionary implications. *Sci. Rep.* 8, 4616. doi:10.1038/s41598-018-22851-3

Langmead, B., and Salzberg, S. L. (2012). Fast gapped-read alignment with Bowtie 2. *Nat. Methods* 9, 357–359. doi:10.1038/nmeth.1923

Lanoizelet, M., Michel, L., Lagadec, R., Mayeur, H., Guichard, L., Logeux, V., et al. (2024). Analysis of a shark reveals ancient, Wnt-dependent, habenular asymmetries in vertebrates. *Nat. Commun.* 15, 10194. doi:10.1038/s41467-024-54042-2

Lein, E. S., Hawrylycz, M. J., Ao, N., Ayres, M., Bensinger, A., Bernard, A., et al. (2007). Genome-wide atlas of gene expression in the adult mouse brain. *Nature* 445, 168–176. doi:10.1038/nature05453

Lekk, I., Duboc, V., Faro, A., Nicolaou, S., Blader, P., and Wilson, S. W. (2019). Sox1a mediates the ability of the parapineal to impart habenular left-right asymmetry. *eLife* 8, e47376. doi:10.7554/eLife.47376

London, E., Wester, J. C., Bloyd, M., Bettencourt, S., McBain, C. J., and Stratakis, C. A. (2020). Loss of habenular Prkar2a reduces hedonic eating and increases exercise motivation. *JCI Insight* 5, e141670. doi:10.1172/jci.insight.141670

Michel, L., Palma, K., Cerda, M., Lagadec, R., Mayeur, H., Fuentès, M., et al. (2022). Diversification of habenular organization and asymmetries in teleosts: insights from the Atlantic salmon and European eel. *Front. Cell. Dev. Biol.* 10, 1015074. doi:10.3389/fcell.2022.1015074

Pandey, S., Shekhar, K., Regev, A., and Schier, A. F. (2018). Comprehensive identification and spatial mapping of habenular neuronal types using single-cell RNA-seq. *Curr. Biol.* 28, 1052–1065.e7. doi:10.1016/j.cub.2018.02.040

Pimentel, H., Bray, N. L., Puente, S., Melsted, P., and Pachter, L. (2017). Differential analysis of RNA-seq incorporating quantification uncertainty. *Nat. Methods* 14, 687–690. doi:10.1038/nmeth.4324

Powell, G. T., Faro, A., Zhao, Y., Stickney, H., Novellasdemunt, L., Henriques, P., et al. (2024). Cachd1 interacts with Wnt receptors and regulates neuronal asymmetry in the zebrafish brain. *Science* 384, 573–579. doi:10.1126/science.ade6970

Roussigné, M., Bianco, I. H., Wilson, S. W., and Blader, P. (2009). Nodal signalling imposes left-right asymmetry upon neurogenesis in the habenular nuclei. *Development* 136, 1549–1557. doi:10.1242/dev.034793

Roussigné, M., Blader, P., and Wilson, S. W. (2012). Breaking symmetry: the zebrafish as a model for understanding left-right asymmetry in the developing brain. *Dev. Neurobiol.* 72, 269–281. doi:10.1002/dneu.20885

Schulz, M. H., Zerbino, D. R., Vingron, M., and Birney, E. (2012). *Oases:* robust *de novo* RNA-seq assembly across the dynamic range of expression levels. *Bioinformatics* 28, 1086–1092. doi:10.1093/bioinformatics/bts094

Shimeld, S. M., and Donoghue, P. C. J. (2012). Evolutionary crossroads in developmental biology: cyclostomes (lamprey and hagfish). *Development* 139, 2091–2099. doi:10.1242/dev.074716

Signore, I. A., Guerrero, N., Loosli, F., Colombo, A., Villalón, A., Wittbrodt, J., et al. (2009). Zebrafish and medaka: model organisms for a comparative developmental approach of brain asymmetry. *Philosophical Trans. R. Soc. Lond. Ser. B, Biol. Sci.* 364, 991–1003. doi:10.1098/rstb.2008.0260

Square, T., Romášek, M., Jandzik, D., Cattell, M. V., Klymkowsky, M., and Medeiros, D. M. (2015). CRISPR/Cas9-mediated mutagenesis in the sea lamprey, *Petromyzon marinus*: a powerful tool for understanding ancestral gene functions in vertebrates. *Dev. Dev.* 125609, 4180–4187. doi:10.1242/dev.125609

Stephenson-Jones, M., Floros, O., Robertson, B., and Grillner, S. (2012). Evolutionary conservation of the habenular nuclei and their circuitry controlling the dopamine and 5-hydroxytryptophan (5-HT) systems. *Proc. Natl. Acad. Sci. U.S.A.* 109, E164–E173. doi:10.1073/pnas.1119348109

Tahara, Y. (1988). Normal stages of development in lamprey, Lampetra reissneri (dybowski). *Zoological Sci.* 5, 109–118.

Villalón, A., Sepúlveda, M., Guerrero, N., Meynard, M. M., Palma, K., and Concha, M. L. (2012). Evolutionary plasticity of habenular asymmetry with a conserved efferent connectivity pattern. *PLoS ONE* 7, e35329. doi:10.1371/journal.pone.0035329

frontiers | Frontiers in Cell and Developmental Biology

TYPE Original Research
PUBLISHED 06 February 2025
DOI 10.3389/fcell.2025.1496298

OPEN ACCESS

EDITED BY
Denhi Schnabel,
National Autonomous University of México,
Mexico

REVIEWED BY
Alfredo Varela-Echavarria,
National Autonomous University of Mexico,
Mexico
Iris Martínez-Rodero,
Vall d'Hebron University Hospital, Spain

*CORRESPONDENCE
Xinrong Peng,
pengxinronglinda@126.com
Chenxi Liu,
chenxi_4000@163.com

†These authors share first authorship

RECEIVED 14 September 2024
ACCEPTED 15 January 2025
PUBLISHED 06 February 2025

CITATION
An L, Zhang L, Wu Y, Teng Y, Liu Z, Ma M, Li M, Peng X and Liu C (2025) Gene expression changes in blastocyst hatching affect embryo implantation success in mice.
Front. Cell Dev. Biol. 13:1496298.
doi: 10.3389/fcell.2025.1496298

Gene expression changes in blastocyst hatching affect embryo implantation success in mice

Liyou An[1]†, Liang Zhang[1]†, Yulin Wu[1], Yadi Teng[1], Zihan Liu[1], Meixiang Ma[1], Miaolong Li[1], Xinrong Peng[2]* and Chenxi Liu[2]*

[1]Xinjiang Key Laboratory of Biological Resources and Genetic Engineering, College of Life Science and Technology, Xinjiang University, Urumqi, China, [2]Institute of Animal Biotechnology, Xinjiang Academy of Animal Science, Urumqi, China

In mammalian embryonic development, blastocyst hatching is essential for normal implantation and development of the fetus. We reported previously that blastocysts hatching out of the zona pellucida (ZP) exhibited site preferences that were associated with pregnancy outcomes. To characterize these site differences, we analyzed the transcriptomes in the following developing mouse blastocysts within 16 h of hatching: expanding (E), hatching from the A-site (A), B-site (B), and C-site (C), hatched (H), and non-hatching (N). By principal component analysis and hierarchical cluster analysis, we determined that the gene expression profiles of A and B blastocysts, which resulted in good fertility, clustered closely. C and N blastocysts, which resulted in poor fertility, clustered closely, but distantly from A and B. Embryos hatched at B- vs. C-sites, with good vs. poor pregnancy, showed 178 differentially expressed genes (DEGs), mainly involved in immunity, which correlated positively with birth rate. These DEGs were primarily regulated by transcription factors TCF24 and DLX3. During blastocyst hatching, immune-related genes were regulated, such as *Ptgs1, Lyz2, Il-α, Cfb* (upregulated) and *Cd36* (downregulated). By immunofluorescence staining, we found C3 and IL-1β on the extra-luminal surface of the trophectoderm of the hatched blastocyst, suggesting that they play a role in maternal-fetal interactions. As the blastocysts developed from the expanding to the fully hatched state, 307 DEGs were either upregulated by transcription factor ATOH8 or downregulated by SPIC to switch on immune pathways. Based on the hatching outcome, we identified three transcription patterns in developing blastocysts, with complex changes in the transcriptional regulation network of failed hatched blastocysts vs. successfully hatched blastocysts. We developed a LASSO regression-based model using DEGs *Lyz2, Cd36, Cfb*, and *Cyp17a1* to predict implantation success. This study revealed the diverse, multidimensional developmental fates of blastocysts during short-term hatching and indicated that the immune properties of the embryo had a major effect on blastocyst hatching outcomes. We suggest that transcriptional changes and their regulation during the development of the preimplantation blastocyst affect implantation. This study contributes to our understanding of the role of transcriptional changes in mammalian embryonic development during hatching and their effect on maternal-fetal interactions.

KEYWORDS

mouse blastocyst, hatching, gene expression, implantation, cell fate

1 Introduction

Mammalian embryonic development begins with fertilization, which is followed by cell proliferation and differentiation, forming the blastocyst that is surrounded by the trophectoderm (TE) and the inner cell mass (ICM). As the blastocyst cavity expands, the embryo hatches from the zona pellucida (ZP), directly contacts the uterine endometrium, initiating embryo implantation and pregnancy, and develops into a fetus (Terakawa et al., 2012; Ma et al., 2024). Blastocyst hatching is a consequence of elevated osmotic pressure due to active Na^+/K^+ ion transporters in TE cells and proteases produced by TE that hydrolyze the ZP (Leonavicius et al., 2018). Blastocyst hatching is an essential preimplantation event that promotes physiological/molecular embryo-uterine crosstalk to initiate embryo implantation. During hatching, there are changes in the blastocyst phenotype, including where the TE initially hatches out of the ZP, the outcome of hatching, and the molecules involved in hatching (Liu et al., 2022). In blastocyst hatching, steroid hormones, growth factors, cytokines, enzymes, and transcription factors coordinately regulate the development of preimplantation embryos and create a favorable environment for embryo implantation (Leonavicius et al., 2018; Wang and Dey, 2006). Successful hatching and implantation involve specific spatiotemporal patterns and dynamic expression of many factors (Ma et al., 2024; Ma et al., 2019); however, the process is not well understood. As previous studies have focused on blastocyst cell-lineage differentiation and regulation of blastocysts and post-implantation development (Leonavicius et al., 2018; Wang et al., 2023; Arutyunyan et al., 2023), it is unclear how the fate of preimplantation embryos is determined and how it affects embryo implantation. In assisted reproductive technology (ART) practice, we cannot predict whether a blastocyst will develop normally after transfer and implant successfully (Rienzi et al., 2017; Knudtson et al., 2017).

There are few studies on the role of blastocyst hatching in implantation. Liu et al. reported a preference for certain hatching sites in mouse blastocysts (Liu et al., 2020), and we also demonstrated site preferences for blastocyst hatching, which determine the efficiency of implantation and pregnancy outcomes (An et al., 2021). With the ICM at the 12 o'clock position, blastocyst hatching is classified into five patterns: O-site (12 o'clock), A-site (1–2 o'clock), B-site (3 o'clock), C-site (4–5 o'clock), and D-site (6 o'clock). We found that 81.8% of blastocysts hatched from near or beside the ICM (A-site and B-site, respectively), whereas 15.6% hatched opposite the ICM (C-site and D-site). After embryo transfer, the birth rate was highest for blastocysts that hatched from the B-site (65.6%), higher than for the C-site (21.3%) or the control group (expanding blastocysts, 41.3%), with no significant difference compared to the A-site (55.6%). The failure of blastocyst hatching results in a birth rate of only 5.1% following embryo transfer (An et al., 2021). In ART, the ZP usually hardens as a result of *in vitro* culture, embryo cryopreservation, or artificial embryo manipulations (Rienzi et al., 2017). Assisted hatching techniques are commonly used in clinical ART To facilitate embryo hatching, but their efficacy is controversial (Knudtson et al., 2017; Kissin et al., 2014). Blastocyst hatching shows site preference, and embryos hatched from the vicinity of the ICM have a higher implantation efficiency and birth rate; therefore, we developed a modified assisted hatching technique that treated the ZP at the specified site, resulting in a birth rate of 77.1% for treated B-site blastocysts after embryo transfer and confirmed the importance of the hatching site on implantation (An et al., 2021).

Although blastocyst hatching affects embryo implantation, the molecular aspects of development in blastocyst hatching are poorly understood (Liu et al., 2022; Ilina et al., 2021). In this study, we performed a multi-level molecular analysis incorporating RNA-seq, RT-qPCR and immunofluorescence to characterize transcriptional changes during embryo hatching. Additionally, we aimed to explore the differential development of hatching blastocysts that may influence hatching site preferences, hatching outcomes and implantation. Furthermore, we developed a predictive model for blastocyst pregnancy outcomes. This study provides new insights into blastocyst development and cell fate that may lead to new methods to optimize ART.

2 Materials and methods

2.1 Animal care and ethical approval

All animal care and use procedures were approved by the Animal Care and Use Committee of Xinjiang University (IACUC-20210709) and performed according to the guidelines of the U.S. National Institutes of Health. Female CD-1 mice (6–8 weeks old) and male CD-1 mice (8–9 weeks old) were purchased from the Animal Resource Centre of Xinjiang Medical University and housed in a specific pathogen-free facility of Xinjiang University under a standard 12-h light/12-h dark cycle with free access to food and water.

2.2 Reagents

Reverse transcription reagents and qPCR reagents were purchased from Applied Biological Materials Inc (abm, Richmond, Canada). Unless otherwise specified, other reagents were purchased from Sigma-Aldrich (MO, United States).

2.3 Mouse treatments and embryo collection

Female mice were treated with pregnant mare serum gonadotropin (PMSG) and human chorionic gonadotropin (high) to induce superovulation and were mated with male mice as previously described (Wu et al., 2013). With the observation of a copulatory plug the next morning, the pregnancy stage was considered 0.5 days post-coitus (dpc). The uterus with a short Fallopian tube was recovered at 3.5 dpc. Subsequently, a blunt 30-gauge needle was inserted into the Fallopian tube, and expanding blastocysts were flushed from the uterus using 200 μL of M2 medium. Embryos were collected and cultured in KSOM medium under mineral oil. After culture for 6–8 h, blastocyst hatching was classified based on the hatching site (A-site, B-site, or C-site) (An et al., 2021). After 16 h of culture, blastocysts were divided into hatched and hatching failure groups (hatching embryos, H; non-hatching embryos, N; Figure 1A).

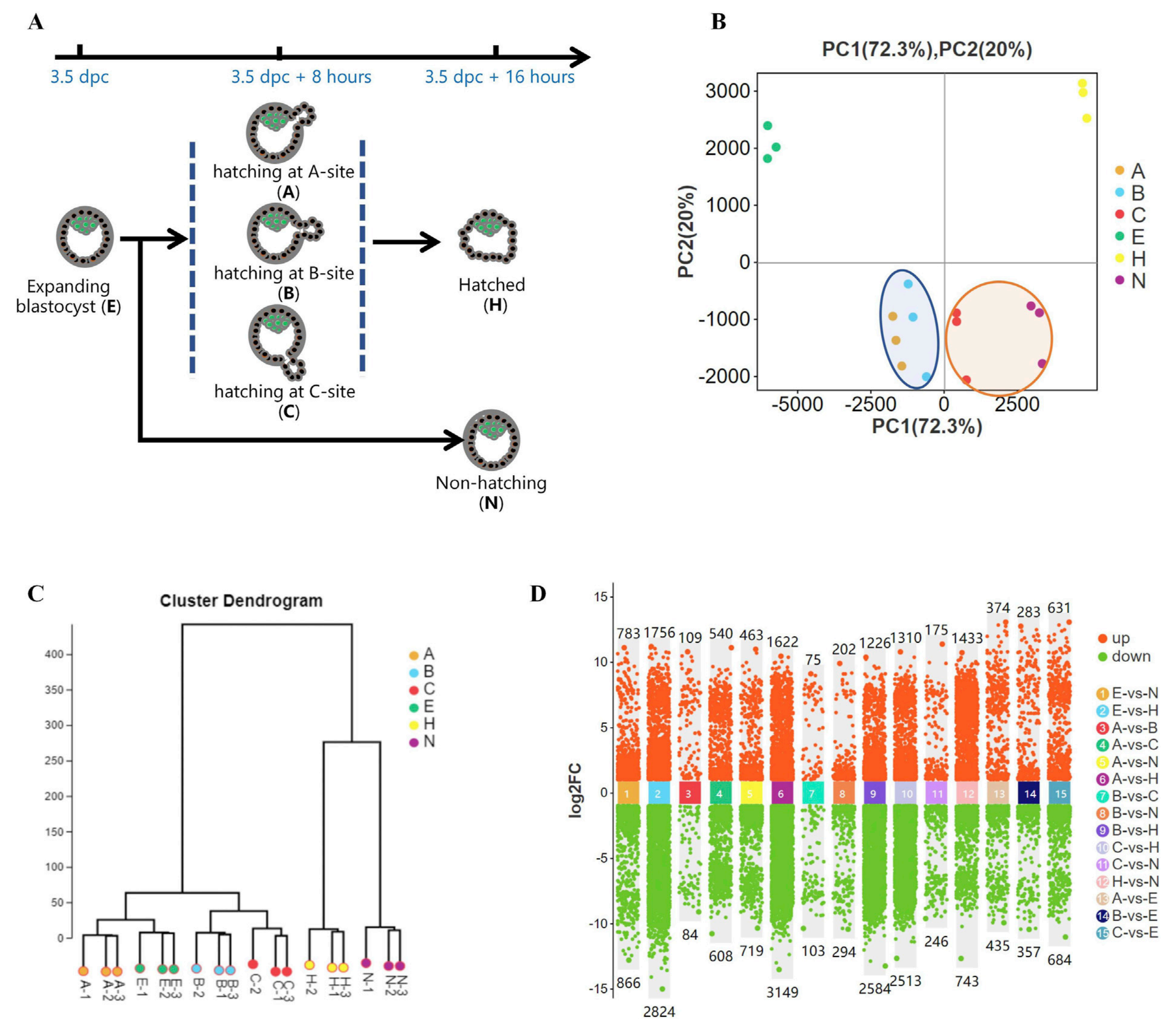

FIGURE 1
Gene expression differences during blastocyst hatching and development. **(A)** Most expanding blastocysts (3.5 dpc) developed to the hatching state at about 8 h (3.5 dpc +8 h) and hatched at about 16 h (3.5 dpc +16 h). The remaining blastocysts failed to hatch (3.5 dpc +16 h). Blastocysts were classified into five groups according to their hatching states, including expanding (E), hatching at A-site (A), hatching at B-site (B), hatching at C-site (C), hatched (H), and non-hatching/hatching failure (N) and analyzed by Smart-Seq. **(B)** Global gene expression was analyzed by principal component analysis (PCA). It showed that the gene expression profiles of A and B blastocysts, which resulted in good fertility, clustered closely (circled in blue). C and N blastocysts, which resulted in poor fertility, clustered closely (circled in yellow). **(C)** Hierarchical cluster analysis revealed two main clusters of gene expression in developing blastocysts. One cluster comprised expanding blastocysts and those hatching at A, B, and C, and the other comprised blastocysts hatched and non-hatched blastocysts. **(D)** Comparison of differentially expressed genes (DEGs) for each blastocyst group.

2.4 RNA sequencing (Smart-Seq)

Total RNA extracted from embryos using TRIzol method. Expanding blastocysts (E), blastocysts with A-site, B-site, or C-site hatching sites (A, B, C), hatched blastocysts (H), and non-hatching embryos (N) were analyzed by RNA sequencing (Figure 1A). In each group, a panel of 30 embryos was collected and stored in 100 μL of TRIzol (Thermo Fisher Scientific, MA, United States) with three replicates (total 90 embryos). Transcriptome sequencing with Smart-Seq (Goetz and Trimarchi, 2012) was conducted by the Guangzhou GENE DENOVO Company. Differentially expressed genes (DEGs) were analyzed by EdgeR and normalized in fragments per kilobase of transcript per million mapped reads (FPKM, see Supplementary Table 1). DEGs and gene sets were analyzed using Gene Ontology (GO) term enrichment and Kyoto Encyclopedia of Genes and Genomes (KEGG) analysis using the online analysis system (Guangzhou GENE DENOVO Company, Guangzhou, China). In transcription factor-target gene regulatory network analysis, transcription factors (TFs) were identified in the selected gene set, the JASPAR database was used to obtain transcription factor binding motifs, and MEME FIMO software was used to predict the transcription target genes in the selected set. A transcription factor targeting network showed the association between TFs and target genes.

2.5 Single-blastocyst reverse transcriptase-qPCR

A pool of 10 embryos in each group was collected, and cDNA was synthesized by All-In-One 5 × RT MasterMix according to the manufacturer's instructions (abm). For single embryo measurements, we lysed one embryo for cDNA synthesis using a scaled-down reaction based on the manufacturer's instructions (abm). Simply, cDNA synthesis was modified by treating an embryo in a micro-drop (5 μL) scaled-down reaction solution on a plastic dish covered with mineral oil to prevent evaporation of fluids. The cDNA was stored at −20°C for qPCR. Through transcriptome analysis we identified ten key genes (*Cd36*, *Ccl9*, *C3*, *Cyp17al*, *Il-1a*, *Ccl5*, *Susd4*, *Cfb*, *Ptgs1*, and *Lyz2*) for analysis and designed qPCR primers for them (primer sequence see Supplementary Table 2). Those 10 key genes selected from GO and KEGG enrichment in immunity and with relatively high expression (FPKM>1). The housekeeping gene *Gapdh* was used for RNA normalization. The 20-μL qPCR reaction comprised 10 μL of Blasaq 2 × qPCR Master Mix (abm), 0.5 μL of each upstream and downstream primer, and 2 μL of cDNA. The products were electrophoresed on a 2% agarose gel to confirm amplification. For RT-qPCR analysis, data were obtained from three technical replicates in each experiment and three biological replicates in each blastocyst group.

2.6 Immunofluorescence analysis

Expression of the protein products of *C3, Cdx2, Il-1β, Lyz2,* and *Plac1* was determined using immunofluorescence (IF) as previously described (An et al., 2021). Briefly, the embryos were washed three times in 0.1% polyvinyl alcohol (PVA) for 3–5 min, fixed in 4% paraformaldehyde buffer for 20 min, followed by three washes with 0.1% PVA. Embryos were permeabilized with 0.5% Triton X-100 at room temperature for 15 min, washed three times with 0.1% PVA, and blocked in 4% fetal bovine serum at room temperature for 1 h. Embryos were incubated with the primary antibody C3, Cdx2, IL-1β, Lyz2 and Plac1 respectively (diluted 1:200 in 2% phosphate-buffered saline, Abcam, Cambridge, United Kingdom), at 37°C for 1 h or at 4°C overnight. Embryos were washed with 0.1% PVA and incubated in the corresponding secondary antibody (goat anti-rabbit IgG AF488, Abcam) in the dark at 37°C for 1 h, washed three times with 0.1% PVA, and stained with 4′,6-diamidino-2-phenylindole (DAPI) for 5 min. Images were acquired using a laser-scanning confocal microscope (Nikon, Japan).

2.7 Development of a prediction model by least absolute shrinkage and selection operator regression analysis

Using the R language survival and glmnet package, we prepared the input data and then built the LASSO regression model. We selected the appropriate λ value and remodeled the data using this λ value. We performed cross-validation on the LASSO analysis results to determine the gene data to be included in the model, ensuring a rational and effective model.

2.8 Experimental design

Blastocysts were classified into five groups according to their hatching status, including expanding blastocysts (E), hatching blastocysts with A-site (1-2 o'clock), B-site (3 o'clock), C-site (4-5 o'clock) hatching sites (A, B, C), hatched blastocysts (H) and non-hatching embryos (N). Blastocysts hatching at O-site (12 o'clock) and D-site (6 o'clock) were excluded due to the rarity of hatching events and the difficulty of collecting enough embryos for analysis. First, gene expression profiles were analyzed to describe the general state of development during blastocyst hatching. Then, to explain how blastocyst hatching determines its implantation, a comparative analysis was performed in blastocysts hatching from the B-site (good pregnancy outcome) vs. the C-site (poor pregnancy outcome). To reveal how hatching occurs and is achieved, blastocysts were analyzed at the stages from expansion to hatching and hatched. To reveal the intrinsic determinants of different hatching outcomes, hatched and non-hatched blastocysts were analyzed comparatively. Based on the above data analysis, a predictive model of implantation success was developed. A modified single blastocyst gene expression detection approach was established to confirm the expression profiles of key genes in the prediction model.

2.9 Statistical analysis

The data obtained for RT-qPCR and IF are presented as mean ± standard error of the mean (SEM). One-way analysis of variance with a *post hoc* two-sided Sidak *t*-test was used to determine differences between treatment groups. All statistical analyses were performed using GraphPad Prism 9.01 for Windows, version 24.0 software (GraphPad Software, La Jolla, CA, United States). A $p < 0.05$ difference between groups was considered significant.

3 Results

3.1 Gene expression profiles during blastocyst hatching and development

We previously found a strong association between the birth rate and the hatching states in mice (An et al., 2021). To further investigate this, we performed Smart-Seq on pre-hatching or expanding blastocysts at 3.5 dpc (E); blastocysts hatching from A-site (A), B-site (B), and C-site (C) at 3.5 dpc plus 8 h; and hatched blastocysts (H) as well as non-hatching blastocysts (N) at 3.5 dpc plus 16 h (Figure 1A),consistent with research groups as previous study (An et al., 2021). Global gene expression, analyzed by principal component analysis (PCA), showed distinct groups based on hatching states (Figure 1B). A and B, which resulted in higher embryo implantation (55.6%, 65.6%) (An et al., 2021), clustered closely at the left side of the plot, whereas C and N, with very low birth rates of 21% and 5.2%, respectively, clustered closely. In addition, fully hatched blastocysts formed a distinct cluster. Hierarchical cluster analysis of gene expression segregated the developing blastocysts into a cluster that comprised expanding blastocysts and hatching A, B and C blastocysts. The other

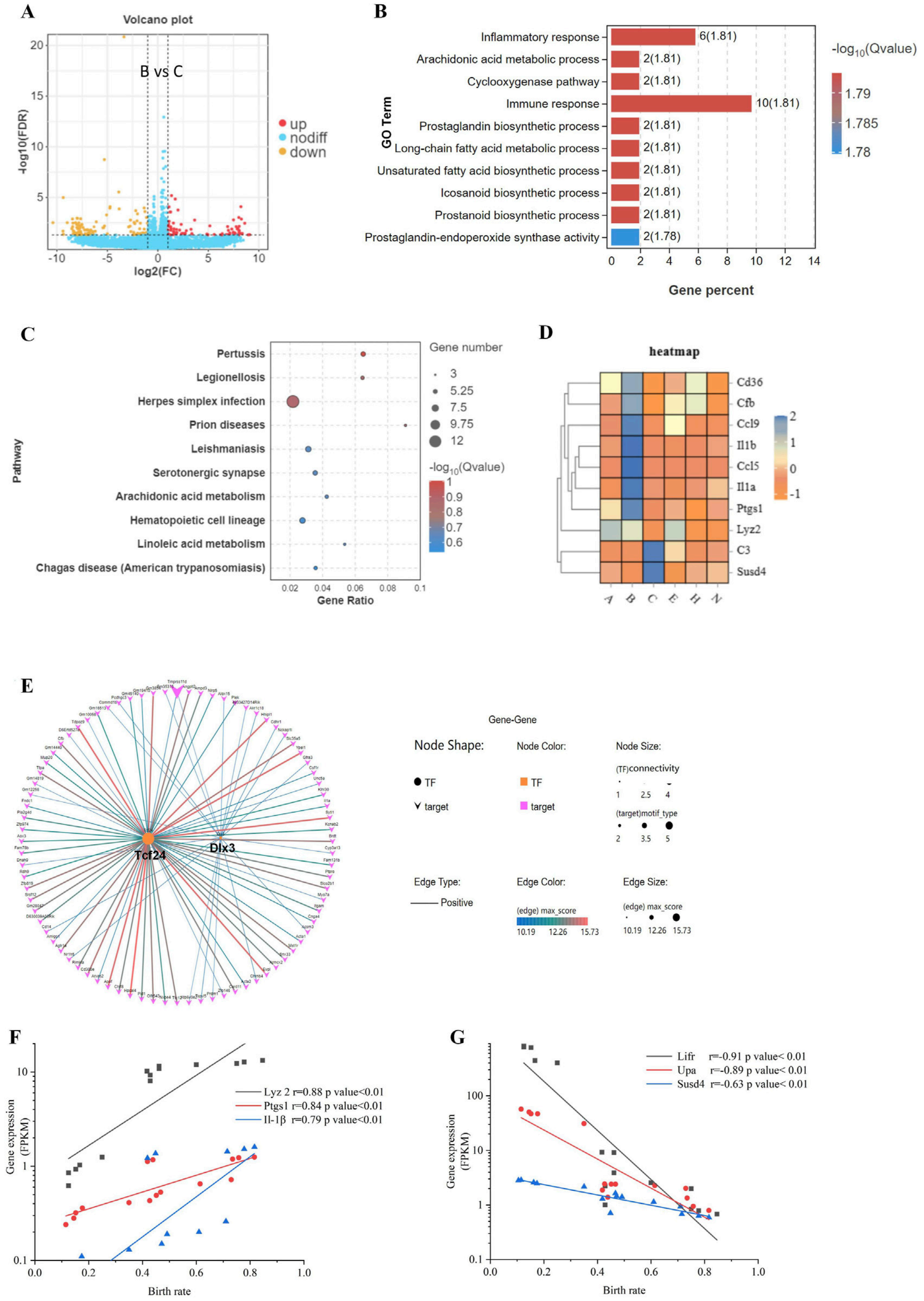

FIGURE 2
Differences in gene expression during blastocyst hatching and development that affect pregnancy success. **(A)** The differential gene expression between B and C blastocysts, which had the greatest difference in birth rates (65.6% vs. 21.3%), was analyzed and visualized as a volcano map. **(B)** DEGs were analyzed by Gene Ontology (GO) functional enrichment for the top 10 significant biological events. **(C)** The top 10 GO signaling pathways were enriched by the Kyoto Encyclopedia of Genes and Genomes (KEGG) analysis. **(D)** Expression patterns of immune-related genes, enriched in GO and KEGG, visualized as a heatmap for each blastocyst state. **(E)** Transcription factor-target gene regulatory network analysis of DEGs identified enriched TFs as *Tcf24* and *Dlx3.* The expression of three upregulated DEGs **(F)** and three downregulated DEGs **(G)** was analyzed for correlation with the birth rate.

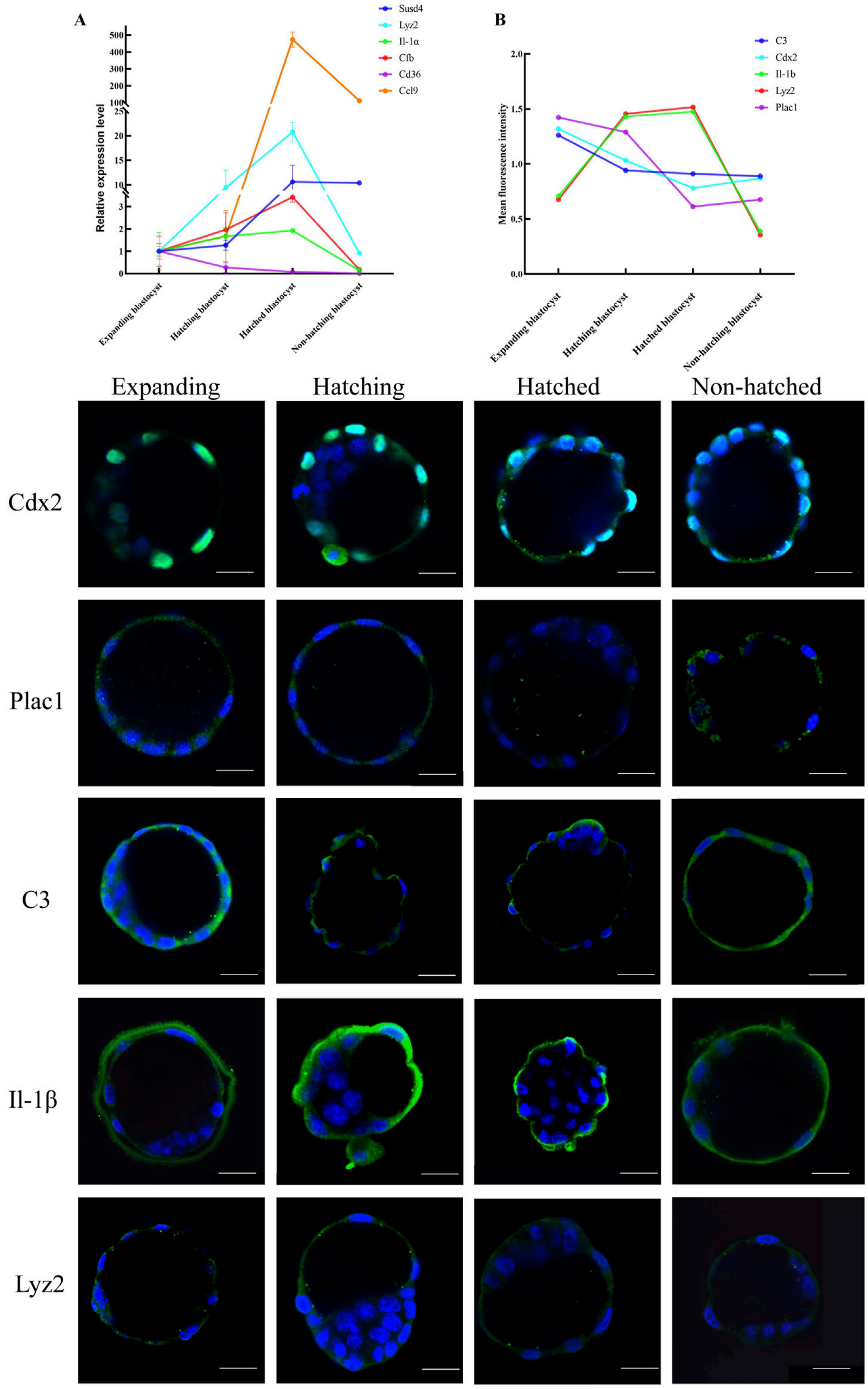

FIGURE 3
Expression patterns of key genes in embryo hatching. **(A)** Relative expression of the immune-related genes enriched in KEGG was measured by RT-qPCR expressed as the fold change determined by $2^{-\Delta\Delta CT}$ normalized the housekeeping gene *Gapdh*. **(B)** Protein expression for CDX2, PLAC1, C3, IL-1β, and LYZ2 was determined by green IF staining in embryos imaged by confocal microscopy during the blastocyst hatching process expressed as relative mean fluorescence intensity. All nuclei were labeled with DAPI (blue). Scale bar, 20 μm.

cluster comprised H and N blastocysts (Figure 1C). Thus, blastocysts with different pregnancy outcomes had marked differences in gene expression profiles. Moreover, as a blastocyst developed from expanding to hatching to hatched, its gene expression profile changed dramatically (Figure 1D), reflecting blastocyst development during this process.

3.2 Differences in gene expression during blastocyst hatching and development affect pregnancy success

Comparing the blastocysts hatching from the B-site (65.6% birth rate) vs. the C-site (21.3% birth rate) (An et al., 2021), we found that 75 genes were upregulated, and 103 genes were downregulated (Figure 2A). Among DEGs, 1) biology process of inflammatory response and immune response, and 2) pathway of infectious disease were highly enriched by GO and KEGG analysis (Figures 2B, C). As immune genes *Cd36, Cfb, Ccl9, Il-1β, Ccl5, Il-1α, Ptgs1, Lyz2, C3,* and *Susd4* showed significant differences between B-site and C-site blastocysts (Figure 2D), immunological changes in the hatching blastocyst likely allow it to recognize the endometrium at embryo implantation.

For B-site and C-site hatching blastocysts, DEGs fell into groups with > 5-fold change or < 5-fold change (Figure 2A), suggesting that genes with a > 5-fold change may be transcriptionally coregulated during the 8 h of blastocyst hatching. Indeed, we found by transcription factor-target gene regulatory network analysis that 2 TFs, TCF24 and DLX3, controlled over 82 out of 178 DEGs (46%) (Figure 2E). We selected four DEGs, *Lyz2*, *Ptgs1*, *Il-1β, and Susd4*, and two previously investigated genes significantly correlating with implantation, *Lifr* and *Upa* (An et al., 2021), and analyzed the correlation of their expression level with birth rate. *Lyz2*, *Ptgs1*, and *Il-1β* were positively correlated with birth rate, whereas *Lifr*, *Upa*, and *Susd4* were negatively correlated with birth rate (Figures 2F, G). Differentiation genes coordinate and determine developmental fate during blastocyst hatching. Therefore, these gene products may be involved in maternal-fetal interactions during implantation, which helps to determine pregnancy outcomes.

3.3 mRNA and protein expression of key genes in embryo hatching

We used RT-qPCR to measure transcription of immune-related genes *Ptgs1*, *Lyz2*, *Il-α*, *Cfb*, *Ccl9*, *Cd36*, *Ccl5*, *C3*, *Cyp17 al*, and *Susd4* in five blastocysts each from expanding, hatching, hatched, and non-hatching groups. We found upregulation of *Lyz2*, *Il-α*, *Cfb, Ccl9* and *Susd4,* and downregulation of *Cd36* expression during blastocyst hatching (Figure 3A). *Ccl5*, *C3, Cyp17al*, and *Ptgs1* exhibited low expression levels or were undetectable. There was a different level of gene expression in the non-hatching blastocyst. The RT-qPCR gene expression patterns were consistent with the transcriptome analysis.

We used immunofluorescence (IF) microscopy to measure genes Cdx2 and Plac1 (regulating trophoblast differentiation), C3, IL-1β, and Lyz2 (immune-relative genes) in each hatching state (Figure 3). IF signals for Plac1, C3, IL-1β, and Lyz2 were mainly in the cytoplasm of trophoblast cells, whereas Cdx2 was expressed in the nuclei of trophoblast cells (Figure 3). Notably, C3 and IL-1β were expressed on the extra-luminal surface of the TE of the hatched blastocysts, implying that these proteins play a role in maternal-fetal interactions when the embryo comes into contact with the endometrium. However, in non-hatched blastocysts, this protein translocation was not detected. Based on mean fluorescence intensity, we found a decrease in the expression of Plac1, Cdx2, and C3 and an increase in the expression of Lyz2 and IL-1β from expanding to hatching blastocysts (Figure 3B) consistent with the transcriptomic and RT-qPCR results. Non-hatching blastocysts had lower levels of Lyz2 and IL-1β compared to hatched blastocysts, showing a dysregulation of these proteins.

3.4 Differential gene expression and associated processes that regulate development during blastocyst hatching

We analyzed the DEG expression patterns during the hatching process for E, B, and C blastocysts by Venn diagrams (Figures 4A, B) and found that the expression of 307 genes correlated with blastocyst hatching, thereby determining blastocyst development from expanding to hatching (A-site, B-site, and C-site). By trend analysis, the 307 DEGs showed four significant gene expression patterns, with 141 genes in profiles 6 and 7 showing an upregulated trend and 133 genes in profiles 0 and 1 showing a downregulated trend (Figure 4C). Thus, there were two dominant sets of DEGs that were associated with blastocyst development during hatching. By transcription factor-target gene regulatory network analysis, we found that 1) TF ATOH8 regulated 41.8% of DEGs with an upregulated trend (59/141, Figure 4D), 2) TFs SPIC, GM9044, GM9046 and GM9040 regulated 97% of DEGs with a downregulated trend (129/133, Figure 4E), and 3) SPIC was a major regulator of coregulated *Gm9044, Gm9046 and Gm9040*.

By GO analysis of DEGs, the top 10 enriched terms included the regulation of cell differentiation, cell proliferation, and developmental and apoptotic processes (Figure 4F). In the KEGG analysis, the top 10 enriched signaling pathways included cytokine-cytokine receptor interaction, viral infection, and a Toll-like receptor signaling pathway (Figure 4G). Thus, remodeling of cell processes and the shaping of immunological properties were the major developmental events during blastocyst hatching.

3.5 Biological processes associated with changes in transcriptional profiles during development of blastocysts with various hatching outcomes

PCA analysis of DEGs for E, H, and N blastocysts revealed clear clusters for E, H, and N blastocysts, showing a low correlation between hatched and non-hatched blastocysts (Figure 5A). In non-hatched blastocysts, 1,433 genes were upregulated, and 743 genes were downregulated compared with hatched blastocysts (Figure 5B). Venn diagram analysis of DEGs for E, N, and H blastocysts showed that 3,428 genes correlated with differential hatching outcomes (Figure 5C), thereby determining whether blastocysts hatched. By trend analysis, we determined that 1) 868 genes showed a decreasing trend, 2) 1,217 genes showed a V-shape trend, and 3) 821 genes showed an inverted V-shaped trend (Figure 5D). For these three trends, transcription factor-target gene regulatory network analysis identified 17 TFs (852 target genes), 8 TFs (472 target genes) and 10 TFs (668 target genes) (Figure 5E), indicating complex patterns of transcriptional gene regulation that determine whether the blastocyst will hatch. Changes in the expression of these genes,

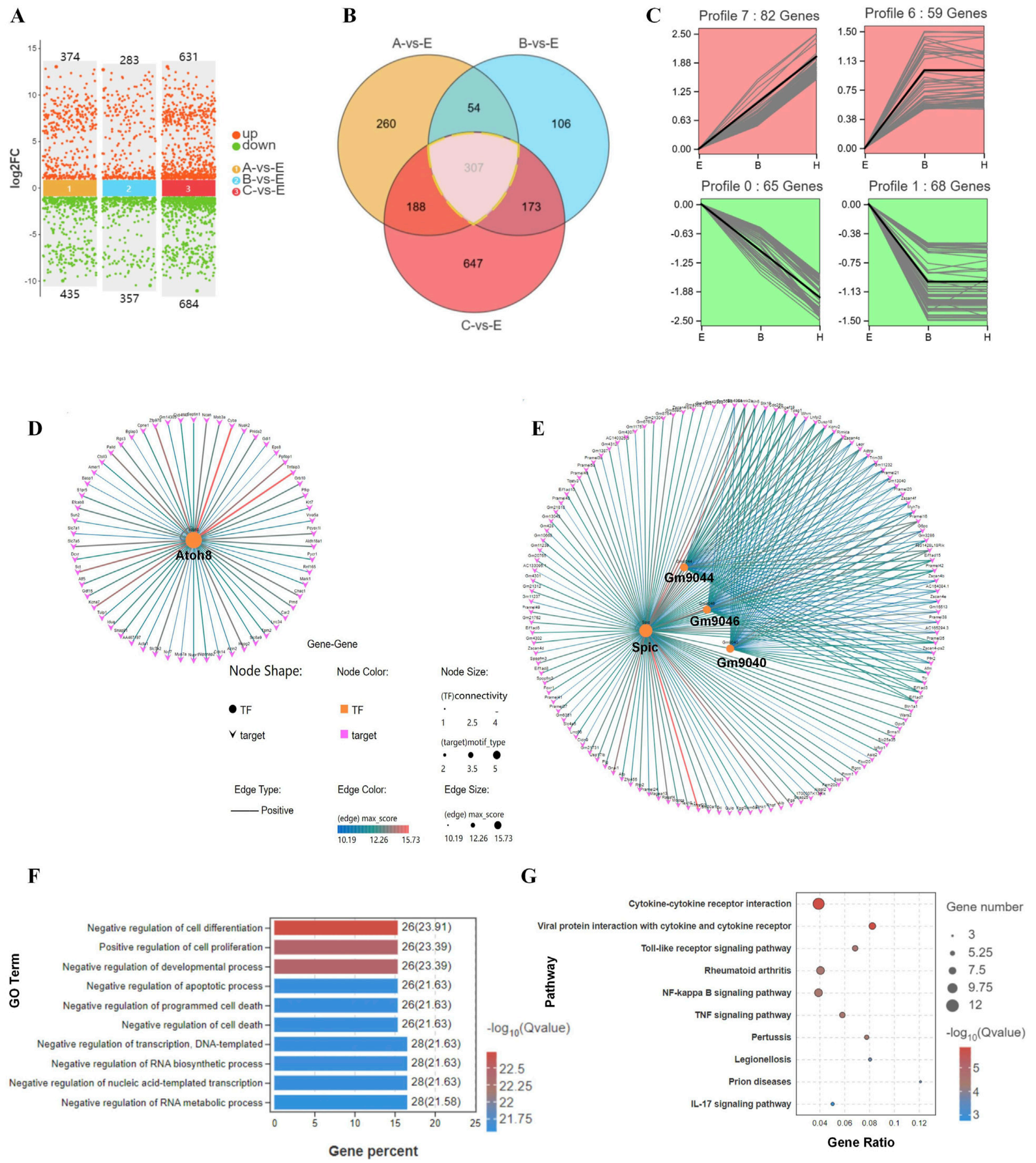

FIGURE 4
Differential gene expression and their associated processes regulate differentiation during blastocyst hatching. **(A)** DEGs were compared in E, A, B, and C blastocysts. **(B)** DEGs were analyzed by Venn diagram, and 307 genes were common to all comparisons of blastocyst hatching (circled by a dotted line). **(C)** Trend analysis identified genes with various types of expression profile changes from blastocyst expanding to hatching and hatched. These genes were analyzed by transcription factor-target gene regulatory network analysis, which identified TFs ATOH8 in profiles 6 and 7 **(D)**, and SPIC, GM9044, GM9046 and GM9040 in profiles 0 and 1 **(E)**. The genes identified by trend analysis were analyzed by GO functional enrichment for the top 10 significant biological processes **(F)** and KEGG pathway enrichment for the top 10 significant signaling pathways **(G)**.

which were enriched in processes related to cell surface receptor signaling, binding, and the plasma membrane (Figure 5F), affect the hatching outcome. KEGG analysis showed that the top enriched signaling pathways were related to cancer, phenylalanine metabolism, and the cAMP signaling pathway (Figure 5G). These GO and KEGG results demonstrate that during hatching, these molecular events and their transcriptional regulation control the processes that lead to blastocyst development.

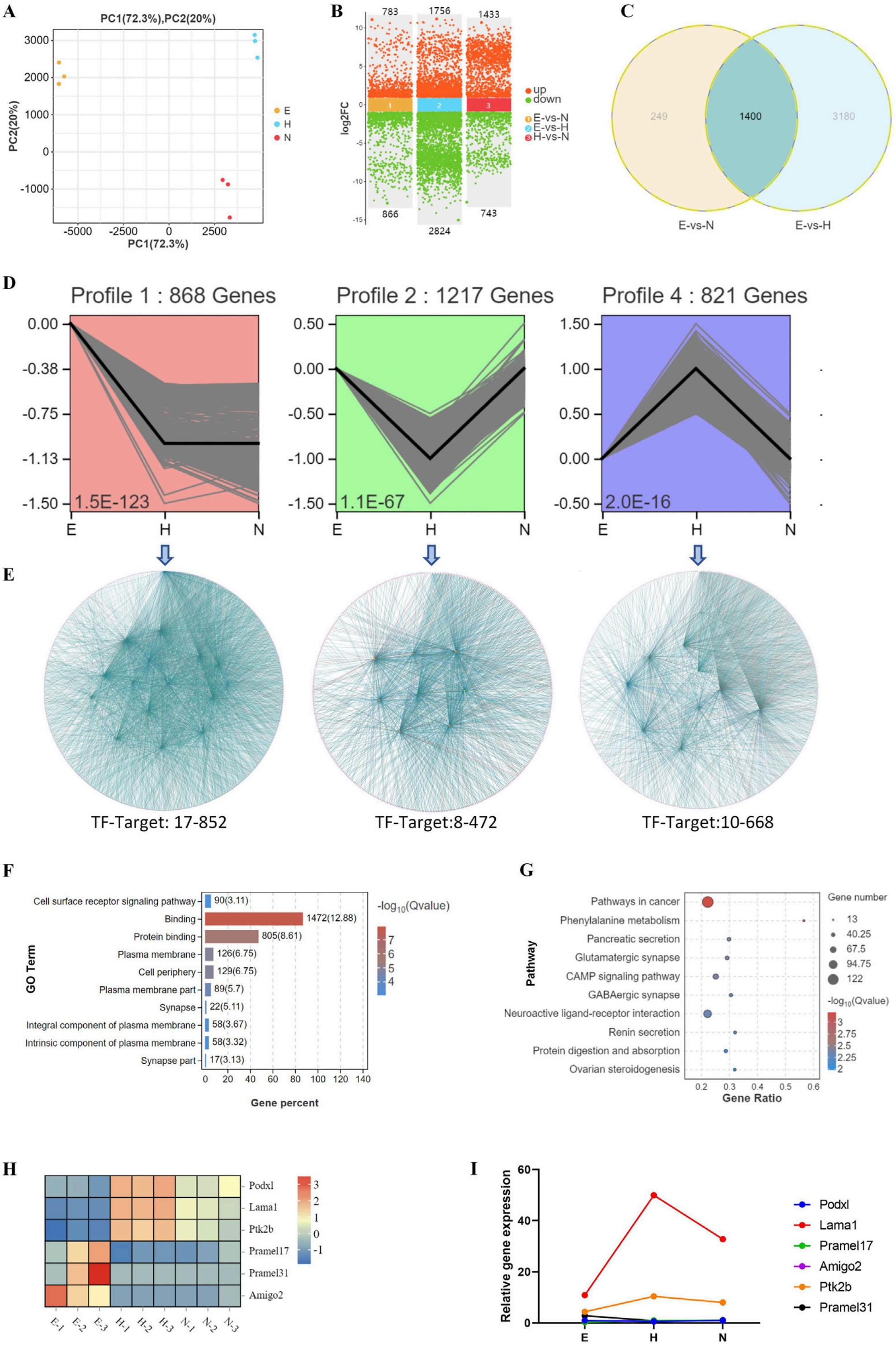

FIGURE 5
Biological processes associated with changes in transcriptional profiles during development of blastocysts with various hatching outcomes. **(A)** DEGs were analyzed by PCA in blastocysts with different hatching outcomes. **(B)** DEGs were compared in hatching blastocysts and non-hatched blastocysts. **(C)** DEGs were analyzed by Venn diagram among E (expanding), H (hatched), and N (non-hatched) blastocyst; 3,428 genes correlated with different hatching outcomes (circled by dotted line). **(D)** Trend analysis identified genes with three types of expression profile changes for blastocysts with different hatching outcomes. **(E)** The genes identified by trend analysis were further analyzed by transcription factor-target gene regulatory network analysis. The genes identified by trend analysis were analyzed by GO functional enrichment for the top 10 significant biological processes **(F)** and by KEGG pathway enrichment for the top 10 significant signaling pathways **(G)**. **(H)** The expression patterns of selected genes identified by trend analysis are shown in a heatmap. **(I)** Transcription of these genes was confirmed by RT-qPCR. The relative expression level shown as fold changes was calculated by $2^{-\Delta\Delta CT}$, normalized to the housekeeping gene *Gapdh*.

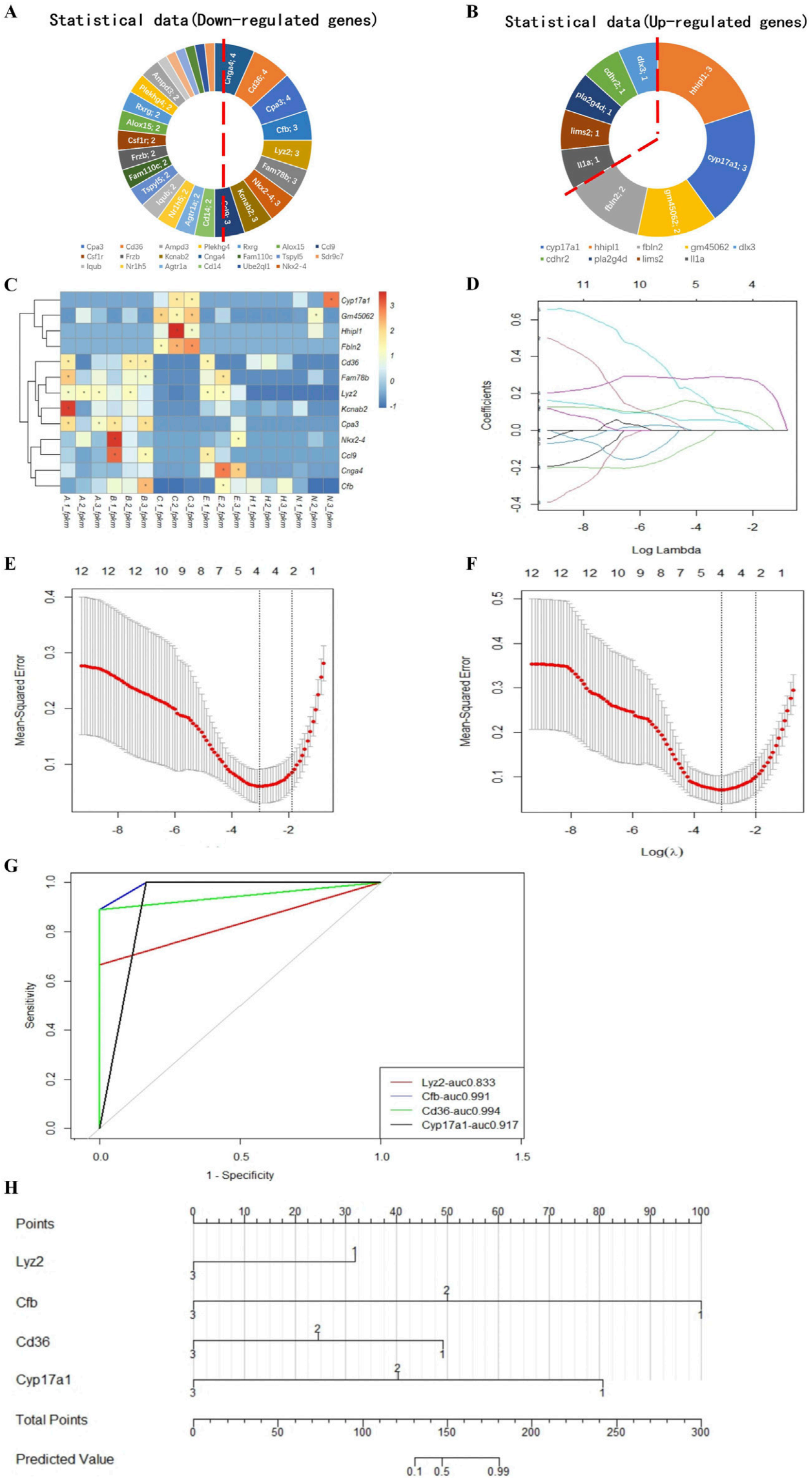

FIGURE 6
Model for predicting the implantation success for hatching blastocysts. Nine downregulated candidate genes from the expression trends **(A)** and four upregulated genes **(B)** are shown in a heatmap **(C)**. These genes were analyzed using the LASSO regression model. **(D)** Each curve represents a coefficient, and the *x*-axis represents the regularization penalty parameter. As the tuning parameter (λ) changes, a coefficient that becomes non-zero enters the LASSO regression model. **(E, F)** Cross-validation to select the optimal λ. The red dotted vertical line crosses over the optimal log λ, which corresponds to the minimum value for multivariate Cox modeling. The two dotted lines represent one standard deviation from the minimum value. **(G)** The predictive performance of the model was evaluated by receiver operating characteristic curve analysis. The evaluated variables (genes) were used to construct an implantation potential prediction model by nomogram graph **(H)**. In this predictive model, gene expression levels corresponded to a score. The scores for each gene were added to obtain the total points, which corresponded to the predicted values that specify the risk/potential for implantation outcomes.

We used RT-qPCR to measure the transcription of genes associated with these trends, including *Podxl*, *Lama1*, *Ptk2b*, *Pramel17*, *Pramel31*, and *Amigo2*. *Lama1* and *Ptk2b* were upregulated, whereas expression of *Pramel17*, *Amigo2, Pramel31*, and *Podxl* was low or undetectable in blastocyst hatching (Figure 5I), consistent with their transcriptomic expression patterns (Figure 5H).

3.6 A model to predict implantation success for hatching blastocysts

We ranked the DEGs associated with blastocyst development from the transcriptome analysis and identified 13 candidate genes to develop a model to predict blastocyst implantation success. The nine DEGs that were downregulated in three out of four measurements and the four DEGs that were upregulated in two out of three measurements (Figures 6A, B) are shown in a heatmap (Figure 6C). Predictive aggregate effects were identified using LASSO regression (Figure 6D). To determine the gene variables to include in the model and to ensure a rational, effective model, we used LASSO regression analysis using the R language survival and glmnet package, followed by cross-validation of the LASSO analysis results (Figures 6D–F). We screened *Lyz2*, *Cd36*, *Cfb*, and *Cyp17a1* as variables using LASSO regression and determined by LASSO Cox regression analysis that these four genes, the minimum value for multivariate Cox modeling, were statistically significant. To determine the predictive performance of the model, we evaluated these genes using receiver operating characteristic (ROC) curve analysis, which showed that they made a significant contribution to the prediction of the model, with area under the ROC curve values generally greater than 0.8 (Figure 6G).

Using these validated genes as the variables, we plotted a nomogram graph based on the LASSO regression and cross-validation data (Figure 6H) to produce a predictive model of implantation success for hatching blastocysts. In this predictive model, the level of expression corresponded to the score for each gene. For example, if the relative expression level of *Lyz2* was 1, this gene was given a score of 32. The scores for each gene were added together to produce a total score, which corresponded to the predicted value, which indicated the potential implantation outcome for a blastocyst.

3.7 Expression of genes used in the prediction model

We measured the expression of the genes in the prediction model in single blastocysts by RT-qPCR. For a single blastocyst hatching at the B- and C-sites, we found that the expression of *Lyz2* and *Cfb* was consistent with data obtained from pooled blastocyst RT-qPCR, confirming the validity of the single-blastocyst technique (Figures 7A, B). Differences in the expression of *Lyz2* were observed across 27 populations of expanding blastocysts, suggesting that the expression of *Lyz2* is regulated by the intrinsic programming fate before hatching (Figure 7C). PCA analysis of *Lyz2* expression profiles in blastocyst populations from the expanding, hatching, hatched, and non-hatched stages showed strong clustering for blastocysts in the expanding state, weaker clustering for blastocysts at the hatching state, and poor clustering for cells at the hatched stage (Figure 7D). However, based on *Lyz2* expression, blastocysts that failed to hatch were dispersed (Figure 7D).

4 Discussion

We found previously that the hatching site affects blastocyst implantation and a successful pregnancy (An et al., 2021). In this study, we determined the role of changes in gene expression in blastocyst development during the short-term hatching process to identify the key proteins and pathways that influence implantation outcomes.

Embryo implantation, which requires close contact between a developmentally competent blastocyst and a receptive uterus, includes blastocyst localization, adhesion and invasion, as well as placenta formation (Wang and Dey, 2006; Matsumoto, 2017). Blastocyst hatching, which is the emergence of the embryo from the ZP, is critical for successful implantation in mammalian embryos (Leonavicius et al., 2018). Any factors adversely affecting blastocyst hatching can lead to implantation failure (Zhan et al., 2018). Hatching plays a critical role in the interaction between the embryo and the maternal environment, determining whether the embryo implants, producing a successful fetus (Wang et al., 2023; Cheng et al., 2023). The relationship between embryonic development during hatching and maternal recognition in mammals is unknown. Previously, we reported site preferences in blastocyst hatching, which determines the pregnancy outcome of embryos (An et al., 2021). In this study, we found that blastocysts that differ in their various pregnancy outcomes had marked differences in gene expression profiles, indicating differences in blastocyst development. The DEGs between blastocysts hatched at the B- and C-sites were mainly related to immune function. We found that most DEGs were regulated by common TFs, suggesting that the implantation fate of blastocysts is regulated during hatching. Implantation requires dynamic bidirectional communication between the blastocyst and the uterine endometrium (Jones-Paris et al., 2017). Maternal immune cells recognize embryonic signals, inducing an immune tolerance that aids in embryo implantation (Fujiwara et al., 2016). However, the immune signals produced by the embryo during hatching that induce the uterine response are poorly understood.

In embryonic development, heterogeneity of cell division is important in determining cell fate at the 2-cell stage, whereas cell position is critical for lineage differentiation at the 8-cell stage. In the morula stage, multiple embryonic layers are differentiated, followed by germ layer differentiation at the blastocyst stage (Zhang et al., 2013; Hernandez Mora et al., 2023; Dang et al., 2023). Previous studies on cell fate have not found a correlation between early embryo differentiation and implantation potential (Clyde, 2022). However, blastocyst hatching is a critical juncture in the transition from early embryo development to implantation (Tvergaard et al., 2021). We found that blastocyst hatching determines implantation and pregnancy outcomes (An et al., 2021), suggesting that within the short hatching period, changes in embryonic development lead to different implantation fates. Here, we showed that gene expression patterns in blastocysts as they proceeded from expanding to hatching were characterized by upregulated and downregulated DEGs regulated by TFs. The DEGs were mainly related to

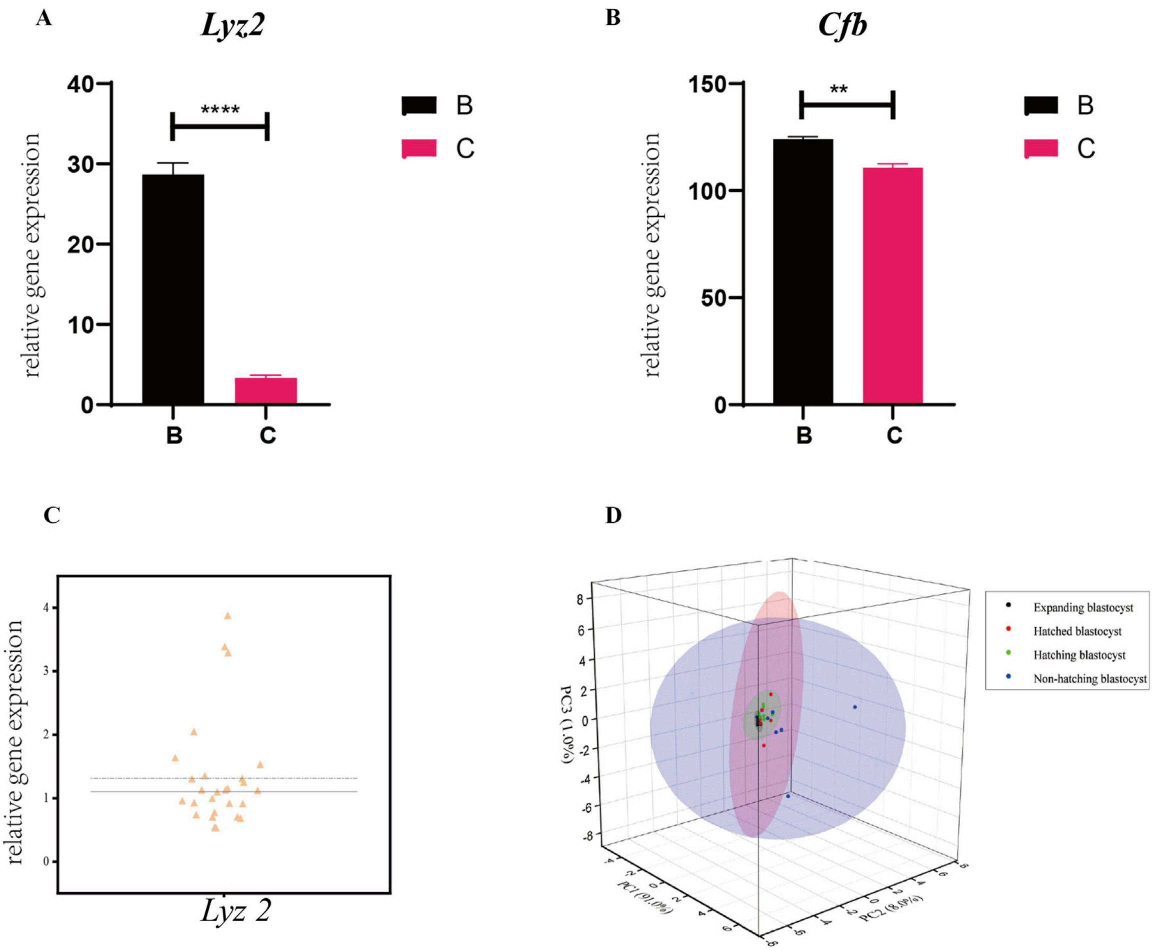

FIGURE 7
Expression of the genes in the prediction model in single blastocysts. Expression of *Lyz2* **(A)** and *Cfb* **(B)** was measured by RT-qPCR in single blastocysts hatching at B- and C-sites. All data are represented as mean ± SEM (n = 3). Asterisk denotes statistically significant differences $*p < 0.05$; $**p < 0.01$; $***p < 0.001$; $****p < 0.0001$. **(C)** Variability in the expression of *Lyz2* was observed in different populations of pre-hatching/expanding blastocysts. **(D)** *Lyz2* expression profiles in blastocyst populations at the expanding, hatching, hatched, and non-hatched stages were analyzed by PCA.

immunity and inflammation, such as *Ptgs1*, *Lyz2*, *Il-α*, *Cfb*, *Ccl9*, *Cd36*, *Ccl5*, and *C3*. Chemokine genes *Ccl9* and *Ccl5* were highly expressed in hatching blastocysts. The *Ccl5* chemokine receptor CCR1 induces myeloid-derived suppressor cell recruitment (He et al., 2016). The balance between proinflammatory factors and the anti-inflammatory cytokine CCL9 ensures effective embryo-uterus recognition with a tolerable immune response (Robertson et al., 2018). There are many studies of the immunological processes during embryo implantation; however, specific cellular and molecular interactions are poorly characterized (Oghbaei et al., 2022). We found that a non-hatched blastocyst resulted from complex perturbations in the regulation of transcription. A-site and B-site hatching embryos, which hatch at the vicinity of the ICM, had a similar rate of implantation but presented different expression profiles. It implies that the multidimensional development of embryos is controlled by ICM, allowing animals to maintain reproduction and continuation of populations. The gene expression profiles in C-site and non-hatched blastocysts clustered together, suggesting that errors made during the blastocyst hatching can completely reverse the developmental fate of the embryo. It may involve the same mechanism for identifying and eliminating abnormalities in the female uterus. Understanding the transcriptional changes from preimplantation to post-implantation embryo development will reveal the implantation mechanism and improve the efficiency of ART.

The study of peri-implantation embryonic development has increased our understanding of embryonic developmental events. Single-cell RNA sequencing of the ovine conceptus and the corresponding endometrium at pre- and peri-implantation stages revealed that an elongated conceptus differentiated into 17 cell types, indicating dramatic cell fate specification (Jia et al., 2023). In the cow, Scatolin et al. defined the cellular composition and gene expression profiles of the embryonic disc, hypoblast, and trophoblast lineages in bovine peri-implantation embryos using single-cell transcriptomes, and compared embryonic peri-implantation lineage programs between bovine and other mammalian species (Scatolin et al., 2024). However, there is much to learn as it is still not possible to predict implantation results by screening an embryo for transfer (Yao et al., 2019). Embryos are usually selected for transfer based on morphological criteria such as the integrity of the blastocyst cavity and the number of inner cell mass/trophectoderm cells (Alegre et al., 2019; Huyen et al., 2018). Even with fresh embryo transfers, the pregnancy rate is less than 54% in humans (Boylan et al., 2020). New technologies combining artificial intelligence with morphokinetic parameters have been developed to screen embryos (Zaninovic and Rosenwaks, 2020), as well as omics-based approaches (Poh et al., 2023). Although these approaches have identified many candidate biomarkers, there is no evidence that they can be used to accurately screen embryos for implantation potential (Aguilera et al., 2024). Here, using key genes involved in blastocyst hatching and hatching outcomes that represent implantation potential, we developed a predictive model for implantation potential for expanding blastocysts. This model, which was weighted using secretory proteins as biomarkers, could provide a non-invasive approach to select embryos for transfer. We are working hard to develop a single embryo detection method that can detect 5 μL culture medium after 2 h embryo culture. Through retrospective study after the delivery of transferred embryos, the embryo culture medium can be detected to validate the effect of this predictive model. With a prospective randomized trial before embryo transfer, embryos with good implantation potential can be selected for transfer to improve the birth rate. As developmental genes are functionally conserved in mammals, this mouse model may be useful for breeding in animals and assisted reproduction in humans.

In conclusion, we analyzed the gene expression profiles of blastocysts during hatching and found changes in transcription patterns that likely determine the hatching phenotype, the hatching process, and hatching outcomes, revealing the molecular changes that prepare blastocyst hatching for implantation. We established a predictive model for implantation success for blastocyst screening. We suggest that transcriptional changes during the development of the preimplantation blastocyst affect its implantation. This study contributes to our understanding of mammalian embryo development during hatching, allowing us to improve our practice in ART.

Data availability statement

The datasets presented in this study can be found in online repositories. The names of the repository/repositories and accession number(s) can be found in the article/Supplementary Material.

Ethics statement

The animal study was approved by the Animal Care and Use Committee of Xinjiang University. The study was conducted in accordance with the local legislation and institutional requirements.

Author contributions

LA: Funding acquisition, Investigation, Project administration, Writing–original draft. LZ: Conceptualization, Investigation, Visualization, Writing–original draft. YW: Formal Analysis, Investigation, Visualization, Writing–original draft. YT: Formal Analysis, Investigation, Visualization, Writing–original draft. ZL: Formal Analysis, Investigation, Visualization, Writing–original draft. MM: Formal Analysis, Investigation, Visualization, Writing–original draft. ML: Formal Analysis, Investigation, Visualization, Writing–original draft. XP: Funding acquisition, Project administration, Supervision, Writing–review and editing. CL: Funding acquisition, Project administration, Supervision, Writing–review and editing.

Funding

The author(s) declare that financial support was received for the research, authorship, and/or publication of this article. This study was supported in part by Natural Science Foundation of Xinjiang (2022D01E09), Project of Science Fund for Tianchi Distinguished Young Scholars of Xinjiang, and Central Guided Local Science and Technology Development Project (ZYYD2024ZY03) to LA, Key R&D Project of Xinjiang to XP and CL.

Conflict of interest

The authors declare that the research was conducted in the absence of any commercial or financial relationships that could be construed as a potential conflict of interest.

Publisher's note

Supplementary material

The Supplementary Material for this article can be found online at: https://www.frontiersin.org/articles/10.3389/fcell.2025.1496298/full#supplementary-material

References

Aguilera, C., Wong, Y. S., Gutierrez-Reinoso, M. A., Velásquez, A. E., Melo-Báez, B., Cabezas, J., et al. (2024). Embryo-maternal communication mediated by extracellular vesicles in the early stages of embryonic development is modified by *in vitro* conditions. *Theriogenology* 214, 43–56. doi:10.1016/j.theriogenology.2023.10.005

Alegre, L., Del Gallego, R., Arnal, L. B., Muñoz, M., Pellicer, A., and Meseguer, M. (2019). A massive embryo morphokinetics comparison system is able to select embryos with high implantation potential enhancing single embryo transfer policy. *Fertil. Steril.* 112 (Suppl. 3), e274. doi:10.1016/j.fertnstert.2019.07.811

An, L., Liu, Y., Li, M., Liu, Z., Wang, Z., Dai, Y., et al. (2021). Site specificity of blastocyst hatching significantly influences pregnancy outcomes in mice. *FASEB J.* 35 (9), e21812. doi:10.1096/fj.202100653R

Arutyunyan, A., Roberts, K., Troule, K., Wong, F. C. K., Sheridan, M. A., Kats, I., et al. (2023). Spatial multiomics map of trophoblast development in early pregnancy. *Nature* 616 (7955), 143–151. doi:10.1038/s41586-023-05869-0

Boylan, C., Kanter, J. R., Koelper, N. C., Mersereau, J., and Berger, D. S. (2020). Equivalent biochemical pregnancy rate between fresh and frozen embryo transfers. *Fertil. Steril.* 114 (Suppl. 3), e165. doi:10.1016/j.fertnstert.2020.08.472

Cheng, J., Sha, Z., Li, J., Li, B., Luo, X., Zhang, Z., et al. (2023). Progress on the role of estrogen and Progesterone signaling in mouse embryo implantation and decidualization. *Reprod. Sci.* 30 (6), 1746–1757. doi:10.1007/s43032-023-01169-0

Clyde, D. (2022). DNA methylation and cell fate in mouse embryos. *Nat. Rev. Genet.* 23 (12), 713. doi:10.1038/s41576-022-00542-0

Dang, Y., Zhu, L., Yuan, P., Liu, Q., Guo, Q., Chen, X., et al. (2023). Functional profiling of stage-specific proteome and translational transition across human pre-implantation embryo development at a single-cell resolution. *Cell Discov.* 9 (1), 10. doi:10.1038/s41421-022-00491-2

Fujiwara, H., Araki, Y., Imakawa, K., Saito, S., Daikoku, T., Shigeta, M., et al. (2016). Dual positive regulation of embryo implantation by endocrine and immune systems – Step-by-step maternal recognition of the developing embryo. *Am. J. Reprod. Immunol.* 75 (3), 281–289. doi:10.1111/aji.12478

Goetz, J. J., and Trimarchi, J. M. (2012). Transcriptome sequencing of single cells with Smart-Seq. *Nat. Biotechnol.* 30 (8), 763–765. doi:10.1038/nbt.2325

He, Y. Y., Li, D. J., Li, M. Q., and Sun, Y. (2016). Myeloid-derived suppressor cells (MDSCs) recruited and activated by chemokine CCL5 and its receptor CCR1 is crucial for pathogenic progression of endometriosis. *J. Reprod. Immunol.* 115, 28. doi:10.1016/j.jri.2016.04.032

Hernandez Mora, J. R., Buhigas, C., Clark, S., Del Gallego Bonilla, R., Daskeviciute, D., Monteagudo-Sánchez, A., et al. (2023). Single-cell multi-omic analysis profiles defective genome activation and epigenetic reprogramming associated with human pre-implantation embryo arrest. *Cell Rep.* 42 (2), 112100. doi:10.1016/j.celrep.2023.112100

Huyen, N. T. T., Vinh, D. Q., Toan, P. D., and Huyen, N. T. T. (2018). Comparison of clinical outcome of frozen embryo transfer after embryo selection based on morphokinetic versus morphologic criteria for freezing. *Biomed. Res. Ther.* 5 (12), 2910–2917. doi:10.15419/bmrat.v5i12.510

Ilina, I. V., Khramova, Y. V., Ivanova, A. D., Filatov, M. A., Silaeva, Y. Y., Deykin, A. V., et al. (2021). Controlled hatching at the prescribed site using femtosecond laser for zona pellucida drilling at the early blastocyst stage. *J. Assisted Reprod. Genet.* 38 (2), 517–529. doi:10.1007/s10815-020-01998-x

Jia, G. X., Ma, W. J., Wu, Z. B., Li, S., Zhang, X. Q., He, Z., et al. (2023). Single-cell transcriptomic characterization of sheep conceptus elongation and implantation. *Cell Rep.* 42 (8), 112860. doi:10.1016/j.celrep.2023.112860

Jones-Paris, C. R., Paria, S., Berg, T., Saus, J., Bhave, G., Paria, B. C., et al. (2017). Embryo implantation triggers dynamic spatiotemporal expression of the basement membrane toolkit during uterine reprogramming. *Matrix Biol.* 57-58, 347–365. doi:10.1016/j.matbio.2016.09.005

Kissin, D. M., Kawwass, J. F., Monsour, M., Boulet, S. L., Session, D. R., Jamieson, D. J., et al. (2014). Assisted hatching: trends and pregnancy outcomes, United States, 2000-2010. *Fertil. Steril.* 102 (3), 795–801. doi:10.1016/j.fertnstert.2014.06.013

Knudtson, J. F., Failor, C. M., Gelfond, J. A., Goros, M. W., Chang, T. A., Schenken, R. S., et al. (2017). Assisted hatching and live births in first-cycle frozen embryo transfers. *Fertil. Steril.* 108 (4), 628–634. doi:10.1016/j.fertnstert.2017.07.011

Leonavicius, K., Royer, C., Preece, C., Davies, B., Biggins, J. S., and Srinivas, S. (2018). Mechanics of mouse blastocyst hatching revealed by a hydrogel-based microdeformation assay. *Proc. Natl. Acad. Sci. U. S. A.* 115 (41), 10375–10380. doi:10.1073/pnas.1719930115

Liu, S. J., Sun, J. B., Hao, X., Han, Z., Wen, X., Wang, X. Y., et al. (2020). Blastocyst hatching site is regularly distributed and does not influence foetal development in mice. *Sci. Rep.* 10 (1), 2475. doi:10.1038/s41598-020-59424-2

Liu, Y., Jones, C., and Coward, K. (2022). An investigation of mechanisms underlying mouse blastocyst hatching: a ribonucleic acid sequencing study. *F S Sci.* 3 (1), 35–48. doi:10.1016/j.xfss.2021.12.003

Ma, M., Zhang, L., Liu, Z., Teng, Y., Li, M., Peng, X., et al. (2024). Effect of blastocyst development on hatching and embryo implantation. *Theriogenology* 214, 66–72. doi:10.1016/j.theriogenology.2023.10.011

Ma, N., Mochel, N. R. d., Pham, P. D., Yoo, T. Y., Cho, K. W. Y., and Digman, M. A. (2019). Label-free assessment of pre-implantation embryo quality by the Fluorescence Lifetime Imaging Microscopy (FLIM)-phasor approach. *Sci. Rep.* 9 (1), 13206. doi:10.1038/s41598-019-48107-2

Matsumoto, H. (2017). Molecular and cellular events during blastocyst implantation in the receptive uterus: clues from mouse models. *J. Reprod. Dev.* 63 (5), 445–454. doi:10.1262/jrd.2017-047

Oghbaei, F., Zarezadeh, R., Jafari-Gharabaghlou, D., Ranjbar, M., Nouri, M., Fattahi, A., et al. (2022). Epithelial-mesenchymal transition process during embryo implantation. *Cell Tissue Res.* 388 (1), 1–17. doi:10.1007/s00441-021-03574-w

Poh, Q. H., Rai, A., Salamonsen, L. A., and Greening, D. W. (2023). Omics insights into extracellular vesicles in embryo implantation and their therapeutic utility. *Proteomics* 23 (6), e2200107. doi:10.1002/pmic.202200107

Rienzi, L., Gracia, C., Maggiulli, R., LaBarbera, A. R., Kaser, D. J., Ubaldi, F. M., et al. (2017). Oocyte, embryo and blastocyst cryopreservation in ART: systematic review and meta-analysis comparing slow-freezing versus vitrification to produce evidence for the development of global guidance. *Hum. Reprod. Update* 23 (2), 139–155. doi:10.1093/humupd/dmw038

Robertson, S. A., Care, A. S., and Moldenhauer, L. M. (2018). Regulatory T cells in embryo implantation and the immune response to pregnancy. *J. Clin. Investig.* 128 (10), 4224–4235. doi:10.1172/JCI122182

Scatolin, G. N., Ming, H., Wang, Y., Iyyappan, R., Gutierrez-Castillo, E., Zhu, L., et al. (2024). Single-cell transcriptional landscapes of bovine peri-implantation development. *iScience* 27 (4), 109605. doi:10.1016/j.isci.2024.109605

Terakawa, J., Watanabe, T., Obara, R., Sugiyama, M., Inoue, N., Ohmori, Y., et al. (2012). The complete control of murine pregnancy from embryo implantation to parturition. *Reproduction* 143 (3), 411–415. doi:10.1530/REP-11-0288

Tvergaard, V., Needleman, D., and Needleman, A. (2021). A mechanical model of blastocyst hatching. *Extreme Mech. Lett.* 42, 101132. doi:10.1016/j.eml.2020.101132

Wang, H., and Dey, S. K. (2006). Roadmap to embryo implantation: clues from mouse models. *Nat. Rev. Genet.* 7 (3), 185–199. doi:10.1038/nrg1808

Wang, H. Q., Liu, Y., Li, D., Liu, J. Y., Jiang, Y., He, Y., et al. (2023). Mate rnal and embryonic signals cause functional differentiation of luminal epithelial cells and receptivity establishment. *Dev. Cell* 58 (21), 2376–2392 e6. doi:10.1016/j.devcel.2023.08.004

Wu, B.-j., Xue, H.-y., Chen, L.-p., Dai, Y. f., Guo, J. t., and Li, X. h. (2013). Effect of PMSG/hCG superovulation on mouse embryonic development. *J. Integr. Agric.* 12 (6), 1066–1072. doi:10.1016/s2095-3119(13)60485-2

Yao, C., Zhang, W., and Shuai, L. (2019). The first cell fate decision in pre-implantation mouse embryos. *Cell Regen.* 8 (2), 51–57. doi:10.1016/j.cr.2019.10.001

Zaninovic, N., and Rosenwaks, Z. (2020). Artificial intelligence in human *in vitro* fertilization and embryology. *Fertil. Steril.* 114 (5), 914–920. doi:10.1016/j.fertnstert.2020.09.157

Zhan, S., Cao, S., Du, H., Sun, Y., Li, L., Ding, C., et al. (2018). Parental genetic material and oxygen concentration affect hatch dynamics of mouse embryo *in vitro*. *Reprod. Biol. Endocrinol.* 16 (1), 39. doi:10.1186/s12958-018-0356-8

Zhang, S., Lin, H., Kong, S., Wang, S., Wang, H., Wang, H., et al. (2013). Physiological and molecular determinants of embryo implantation. *Mol. Asp. Med.* 34 (5), 939–980. doi:10.1016/j.mam.2012.12.011

frontiers | Frontiers in Cell and Developmental Biology

TYPE Original Research
PUBLISHED 11 March 2025
DOI 10.3389/fcell.2025.1540212

OPEN ACCESS

EDITED BY
Michael Schubert,
UMR7009 Laboratoire de Biologie du Développement de Villefranche sur Mer, France

REVIEWED BY
David Ellard Keith Ferrier,
University of St Andrews, United Kingdom
Shigeki Fujiwara,
Kōchi University, Japan

*CORRESPONDENCE
Chiara Anselmi,
✉ chiara.anselmi@unipd.it

†These authors have contributed equally to this work

RECEIVED 05 December 2024
ACCEPTED 11 February 2025
PUBLISHED 11 March 2025

CITATION
Anselmi C, Ishizuka KJ, Palmeri KJ, Burighel P, Voskoboynik A, Hotta K and Manni L (2025) Speed vs completeness: a comparative study of solitary and colonial tunicate embryogenesis. *Front. Cell Dev. Biol.* 13:1540212.
doi: 10.3389/fcell.2025.1540212

Speed vs completeness: a comparative study of solitary and colonial tunicate embryogenesis

Chiara Anselmi[1]*, Katherine J. Ishizuka[2], Karla J. Palmeri[2], Paolo Burighel[1], Ayelet Voskoboynik[2,3], Kohji Hotta[4]† and Lucia Manni[1]†

[1]Department of Biology, Padova University, Padua, Italy, [2]Department of Biology, Stanford University, Palo Alto, CA, United States, [3]Institute for Stem Cell Biology and Regenerative Medicine, Stanford University, Stanford, CA, United States, [4]Department of Biosciences and Informatics, Keio University, Minato, Japan

Solitary ascidians, such as *Ciona robusta*, have been used for over a century as model systems for embryological studies. These species are oviparous, producing many relatively small and transparent eggs, which are released and fertilized outside the parent body. Embryos develop rapidly in a stereotyped manner and reach the larva stage in less than 1 day (at 20°C). The larvae then settle and metamorphose into sessile juveniles in approximately 2 days. On the other hand, colonial ascidians are ovoviviparous, with heavily yolked eggs that develop inside the parent body. In the colonial *Botryllus schlosseri*, embryos are connected to the parental body via a cup-like placenta and develop into larvae within a week (at 20°C). These larvae, which possess both typical larval organs and prospective juvenile organs, are released into seawater, where they settle very rapidly, sometimes after only 15 minutes of free swimming. Then, they metamorphose into juvenile oozooids. The ability to study embryo development in colonial ascidians within the parent body is limited. To address this, we developed a method for *in vitro* culturing *B. schlosseri* embryos outside the parental body and combined it with time-lapse and confocal microscopy to describe the embryonic developmental stages. Moreover, we used histological analysis based on serial sections to investigate late-stage development, when embryo opacity made other techniques ineffective. We identified 19 stages of development, from the fertilized egg to the swimming larva, and described the stage of organ appearance and differentiation. Comparing the embryonic development timeline of *B. schlosseri* with that of *C. robusta*, we found heterochrony in development, particularly in the timing of organ appearance and growth rate. We hypothesize that this difference in maturation timing between solitary and colonial ascidians reflects a shift in the regulation of key developmental pathways that contributed to ascidian diversification. This heterochronic evolution likely facilitated a significant (approximately four-fold) shortening of the metamorphosis time in *B. schlosseri* by allowing embryos to remain in a safe ovoviviparous environment five times longer than those in *C. robusta* before hatching.

KEYWORDS

adultation, *Ciona robusta*, *Botryllus schlosseri*, colonial, evo-devo, heterochrony, solitary, tunicate

1 Introduction

Within chordates, tunicates exhibit the widest range of reproductive strategies. These marine invertebrates are considered the sister group of vertebrates (Delsuc et al., 2018), sharing several chordate features with them, such as the notochord, segmented musculature, pharyngeal pockets, endostyle/thyroid gland, and dorsal hollow neural tube. In colonial tunicates, some of these structures, like the endostyle and pharyngeal pockets, develop not only by passing through the typical pharyngula phylotypic stage (He et al., 2020) but also via stem cell-mediated processes during asexual reproduction or in whole-body regeneration (Laird et al., 2005; Voskoboynik et al., 2008; Alié et al., 2018; Manni et al., 2019). Other shared features between tunicates and vertebrates include secondary hair cell-like mechanoreceptors, neural crest-like cells, and embryonic proto-placodal areas (Patthey et al., 2014; Manni and Pennati, 2015; Anselmi et al., 2024; Todorov et al., 2024).

Within ascidians, the main tunicate taxon, solitary species, such as *Ciona robusta*, are oviparous, producing large numbers of small, transparent eggs (140 μm in diameter), which are ovulated and fertilized by heterologous sperm in seawater, giving rise to embryos that develop autonomously from the parents (Figure 1A). These embryos rapidly (less than 1 day) reach the free-swimming tadpole larval stage (Hotta et al., 2007; Hotta et al., 2020). After swimming for several hours, the larvae adhere to a suitable substrate and undergo extensive metamorphosis, a process lasting a couple of days. During metamorphosis, prospective juvenile organs become recognizable, the body axis rotates 90°, and they complete their development, while larval tissues, including the tail and the brain, are resorbed. The resulting juvenile is a sessile, filter-feeding animal, which will continue to grow and increase in size throughout its entire life. In some species (the Enterogona ones), such as *C. robusta*, juveniles complete their development with the fusion of the two atrial siphon rudiments in a single dorsal structure during the post-metamorphosis period, 7 days after fertilization (Hotta et al., 2020). Generally, solitary ascidians have regenerative abilities restricted to the apical structures, such as the siphons and the brain (Vanni et al., 2022b). However, the Red Sea ascidian *Polycarpa mytiligera* is an exception; when a single individual is cut into three parts, each can regenerate into a whole body (Gordon et al., 2021). Due to *in vitro* fertilization and embryo culture, solitary ascidians have become model organisms to investigate cell lineage, blastomere determination, and morphogenesis. The ontology of anatomy and development is now available for *C. robusta*, standardizing developmental studies (Hotta et al., 2020). Ascidian embryogenesis is characterized by stereotyped development based on invariant early cell lineages and a remarkably small cell number (Kumano and Nishida, 2007). These unique features allow the study of chordate developmental programs at the cellular or even subcellular level using a variety of molecular tools, including CRISPR/Cas9 (Kogure et al., 2022; Pennati et al., 2024).

In contrast, colonial ascidians also reproduce asexually by budding (blastogenesis), producing zooids (blastozooids) through the involvement of pluripotent/multipotent stem cells (Alié et al., 2018; Manni et al., 2019, p. 20; Vanni et al., 2022a). These blastozooids form colonies of clonal individuals, all derived from cycles of blastogenesis originating from an individual (oozooid), which emerges from the metamorphosis of a larva and is considered the founder of the colony (Figure 1). Colonial ascidians exhibit extensive regenerative abilities (Vanni et al., 2022b). For example, in *Botryllus schlosseri* (Manni et al., 2014; Brunetti et al., 2017), which can be easily cultured on glass slides, whole-body regeneration is triggered when all the zooids are surgically removed from a colony due to pluripotent and/or multipotent stem and progenitor cells that initiate budding (Sabbadin et al., 1975; Voskoboynik et al., 2007; Tiozzo et al., 2008; Manni et al., 2019; Scelzo et al., 2019; Ricci et al., 2022; Vanni et al., 2022c).

Sexual reproduction in colonial ascidians occurs concomitantly with the asexual one. Typically, colonial species produce a few yolky eggs (in *B. schlosseri*, 1–3 eggs per zooid; Gasparini et al., 2015), which are larger and more opaque than those produced by solitary ascidians (Manni et al., 1993; Manni et al., 1994; Zaniolo et al., 1994b). Moreover, in colonial ascidians, both fertilization and embryogenesis occur within the parental zooids, with minimal or no parental nutrient contribution to the embryonic development (Zaniolo et al., 1987), except in rare viviparous species (*Botrylloides violaceus*, *Botrylloides lenis*, and *Hypsistozoa fasmeriana*) that develop from yolkless eggs and, therefore, rely on parental sustenance (reviewed in Zaniolo et al., 1998). In colonial ascidians, gestation lasts several days, and the resulting larvae are usually bigger than those produced by solitary ascidians. Moreover, they also display a variable level of adultation, *i.e.*, the early development of rudimentary adult organs, making them more complex than the larvae of solitary species. In *B. schlosseri*, for example, hatched larvae show open siphons, perforated protostigmata, the heart, the rudiment of the adult nervous system, and two buds (Kowarsky et al., 2021; Manni et al., 2022). Typically, in solitary ascidians, these structures (except buds) develop in the juvenile after the larva adhesion to the substrate. Therefore, there is heterochrony, *i.e.*, a change in the timing of developmental events (Keyte and Smith, 2014; Iwata and Vanderhaeghen, 2024), when comparing the embryonic and post-embryonic (*i.e.*, the post-metamorphic) development of colonial vs. solitary ascidians. This reflects a shift in the onset of growth and possibly the growth rate of some organs.

In *B. schlosseri*, attempts to fertilize isolated eggs (removed from the parent zooid) with isolated sperm and track their development *in vitro* were made in the past (Milkman and Borgmann, 1963; Milkman, 1967). However, their internal development and larval complexity hindered embryonic study, so a comprehensive description of whole-embryo development and cell lineage in a colonial ascidian is not yet available. Therefore, despite their heterochronic development, ascidians represent a valuable model for understanding the links between development and evolution, although comparative studies between solitary and colonial species development have been limited to detailed observations regarding specific organs (Manni et al., 2022). Nonetheless, due to the contemporary presence of different developmental strategies, *i.e.*, embryogenesis, blastogenesis, and whole-body regeneration, all resulting in similar individuals, colonial ascidians such as *B. schlosseri* provide an opportunity to investigate, from an evo-devo perspective, how different developmental trajectories generate the same adult form (Tiozzo et al., 2005; Manni and Burighel, 2006; Gasparini et al., 2011; Kowarsky et al., 2021).

This work aims to bridge the knowledge gap by presenting the first comprehensive description of the development and anatomy of

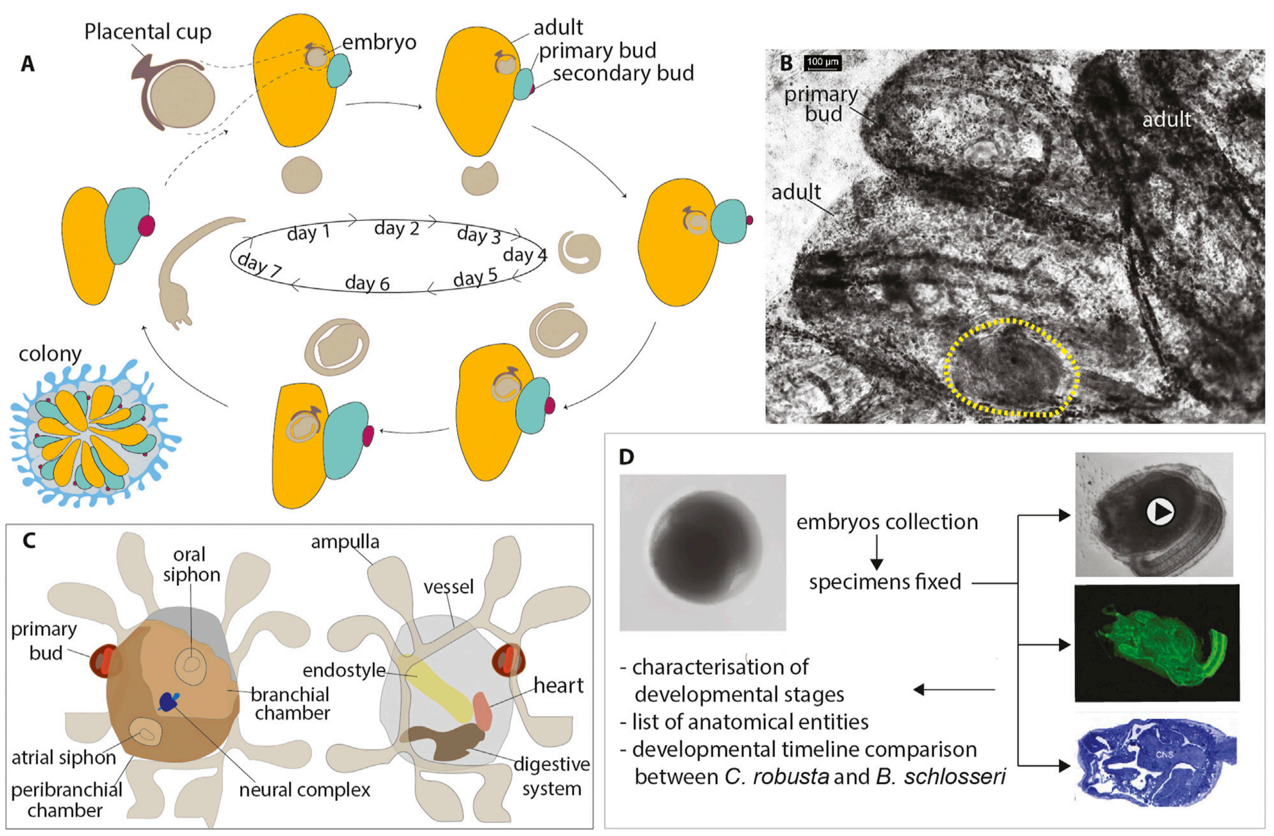

FIGURE 1
(A) *B. schlosseri* life cycle. A colony shows weekly (at 20°C) synchronized waves of budding accompanied by the regression and reabsorption of filtering adults (Manni et al., 2014). Blastozooids are organized in star-shaped systems embedded in a common tunic; a colonial circulatory system of vessels joins all the blastozooids, present in three generations: the adults, the primary buds growing on adults, and the secondary buds developing on the primary buds. Sexual and asexual cycles coincide: the embryo stage of development and the day of larval hatching in a colony are closely related to the colonial blastogenetic phase, so larvae are released before their parent resorption (Manni et al., 2007). **(B)** Details of an adult zooid (in ventral view) with an embryo (yellow dashed line) developing within the peribranchial chamber. Whole-mount colony. **(C)** Illustration of an oozooid in dorsal (left) and ventral (right) views showing main organs **(D)**. Methodological procedure followed to describe the development of *B. schlosseri*. Fertilized eggs and embryos across different developmental stages were gently removed from the parental peribranchial chamber. Samples were observed using a stereomicroscope, photographed, and fixed for CLSM and histology. Data analyses included the characterization of developmental stages, the list of anatomical entities and their definition, and the developmental timeline comparison between *C. robusta* and *B. schlosseri*.

a colonial ascidian embryo in *B. schlosseri*. These new data update previous observations on *B. schlosseri* embryogenesis, dating back a century (Scott, 1934; Grave, 1934; Grave and Woodbridge, 1924), and integrate information on the development of specific territories, such as the larval and adult nervous system, papillae, protostigmata, endostyle, heart, and hemocytes (Manni et al., 1999; Manni et al., 2004; Manni et al., 2022; Sorrentino et al., 2000; Tiozzo et al., 2005; Degasperi et al., 2009; Caicci et al., 2010; Gasparini et al., 2011; Gasparini et al., 2013; Kowarsky et al., 2021; Cima, 2023). Additionally, a comparative analysis of the developmental timing between *C. robusta* and *B. schlosseri* embryos reveals that heterochrony impacts not only alterations in the timing of development of some organs but also their rate of development.

2 Materials and methods

For *in vivo* observations and confocal imaging, mature *B. schlosseri* colonies were collected from piers at the Monterey Marina (CA, United States), close to the Hopkins Marine Station of Stanford University. The colonies were then attached to a glass slide and placed into an aquarium at 20°C (Boyd et al., 1986). Mature colonies for histological analysis were collected from floating blades of the marine plant *Zostera marina* in the Lagoon of Venice, near the Hydrobiological Station of the University of Padova (Chioggia, Italy). The colonies were removed from their natural substratum, made to adhere to glass slides, and maintained at 20°C (Sabbadin, 1955).

2.1 Preparation of embryos for time-lapse imaging

Embryos and developing larvae, which are visible inside the parental body and are individually suspended in a placental cup within the peribranchial chamber (Zaniolo et al., 1987), were removed using a thin needle. Embryos in a colony develop at the same rate. Therefore, multiple synchronized embryos were obtained from a single colony; however, several mature colonies at different blastogenetic phases were necessary to obtain embryos at different stages. After carefully removing the embryos from the parental organism with an insulin needle, they were transferred using a P200 pipette into Petri dishes containing filtered seawater. To optimize the development of each embryo, a maximum of 25 embryos were placed at the center of each dish. This approach ensured that the embryos had sufficient space for growth while minimizing interference between them. The seawater was filtered using a Millipore syringe filter (pore size 0.22 μm) to maintain a clean and contaminant-free environment, which was essential for the embryos' healthy development. The water in the Petri dishes was changed daily using a glass pipette, which allowed for the precise removal of waste products and the addition of fresh, filtered seawater, ensuring a stable and optimal culture medium. The embryos were reared at a constant temperature of 23°C, which was determined by the environmental conditions of the BZ-9000 Keyence Microscope used for observation. Due to technical limitations, the temperature could not be independently adjusted from the microscope setting. Throughout the developmental process, the embryos were closely monitored under the microscope, which provided high-resolution imaging for detailed observation of their growth and developmental stages.

2.2 Image acquisition at confocal scanning laser microscopy

Embryos were fixed for 30 min at room temperature with 4% paraformaldehyde in MOPS buffer (0.1 M 3-(N-morpholino) propane sulfonic acid), adjusted to a pH value of 7.5, and washed in PBT two times. Fixed samples were stained for 30 min in 1/1,000 diluted cell mask orange for staining cytoplasm. After three washes with PBT, Alexa phalloidin 546 was used for actin staining overnight at 4°C. Samples were made transparent by dehydrating them with a series of solutions of 2-propanol in PBT, followed by treatment with BABB (benzyl alcohol (Sigma B-1042)/benzyl benzoate (Sigma B-6630) in a 1:2 ratio). For nuclear staining, embryos were fixed, stained with DAPI (Vector Laboratories), and mounted in a mounting medium (VECTASHIELD). Stained samples were observed using a confocal laser microscope (Olympus FV1000) under a ×10–×40 oil objective lens. Three-dimensional images were reconstructed from stack images (interval 1–3 μm) using Imaris software. Several dozen embryos were collected for each stage, and representative embryos were selected for imaging.

2.3 Histology

Five embryos, both in the tailbud and larva periods, were fixed for 2 h in 1.5% glutaraldehyde in 0.2 M sodium cacodylate and 1.6% NaCl buffer. After three washes in 0.2 M sodium cacodylate and 1.6% NaCl buffer, samples were post-fixed for 30 min in 1% OsO_4 in 0.2 M cacodylate buffer at 4°C. The samples were dehydrated and subsequently soaked in Epon and propylene solution. They were then embedded in resin at 37°C, 45°C, and 60°C, oriented, and sectioned using a Leica Ultramicrotome. Sections, 1-μm-thick, were stained with toluidine blue.

2.4 Whole-mount preparations

Colonies adhering to glass slides were anesthetized with MS 222, fixed in Bouin's fluid, washed in PBS, and stained with Mayer's hemalum (Sigma-Aldrich, MHS32). After washing in distilled water, the colonies were dehydrated in ethanol, cleared in xylene, and mounted with Technovit 8100 (EMS cat. no. 14,654).

3 Results

3.1 Embryo development in *B. schlosseri*

3.1.1 *B. schlosseri* embryos can survive and develop outside the parental body

To study embryogenesis in *B. schlosseri*, we analyzed the development of embryos *in vitro* by dissecting them from the parental colony (Figure 1B; Table 1). We successfully cultured these embryos and tracked their development until the oozooid stage (Kowarsky et al., 2021). Unlike solitary ascidians, where stages can be easily defined based on *in vivo* imaging due to embryo transparency (Hotta et al., 2007), *B. schlosseri* required additional imaging techniques to observe its development. Using a combination of *in vivo* imaging (observations and movies) and confocal scanning laser microscopy (CLSM) (virtual sections and 3D reconstructions), we were able to define the stages of embryogenesis, from the zygote to the swimming larva. These stages correspond to the meta-periods "Pre-embryonic development" and "Embryonic development, pre-metamorphosis" (Table 2; Figures 2, 3; Supplementary Video S1) (Hotta et al., 2007). This combination of methods allowed us to identify a higher number of stages compared to our previous study (Kowarsky et al., 2021).

In general, embryos removed at early developmental stages (up to the neurula period) had a lower survival rate through metamorphosis than those removed at later stages. For example, only 20% of embryos removed during the gastrula period (stages E2.1–E2.3 in Table 2) reached the oozooid stage and opened their siphons. In contrast, 68% of embryos removed during the tailbud period (Stage E6 in Table 2) completed development normally. However, in several cases, oozooids died soon after metamorphosis, largely due to abnormal ampulla (Figure 1C) development and the inability to adequately attach to the substrate. Therefore, the final number of healthy oozooids was significantly lower than the total number of oozooids obtained from metamorphosed larvae.

3.1.2 Timetable and description of *B. schlosseri* embryonic development

To describe the meta-periods "Pre-embryonic development" and "Embryonic development, pre-metamorphosis," we estimated the timing of development based on the colonial blastogenetic phases (Scott, 1934; Manni et al., 2007) as we were unable to determine the exact time of fertilization, which occurs inside the parental body shortly after siphon opening (Milkman, 1967). Since the adult life span is 6–7 days at 20°C (the same as embryonic development until larval hatching; Manni et al., 2007), we referred to the development stages using the formula "E.1," "E.2," and so on,

TABLE 1 Number of reared embryos per stage and percentage of embryos completing development. The "total number of oozooids" indicates the number of embryos that passed through the metamorphosis stage becoming filter-feeding oozooids, even if not normal.

Colony ID	Developmental period/stage of embryo removal from colony	Number of removed embryos	Total number of oozooids	Number of normal oozooids	% of embryos completing development	% of embryos with normal development
2.0	2 cells	16	5	3	31.25%	18.75%
2.1	2 cells	18	4	2	22.2%	11.1%
7	16 cells	25	20	2	80%	8%
3	After 16 cells until early gastrula	3	2	0	66.67%	0
6	Early gastrula	10	4	2	40%	20%
9	Early neurula	18	8	2	44.4%	11.1%
1	Early neurula	11	7	2	63.6%	18.1%
4	Tailbud late 1 wrap	25	10	3	40%	12%
5	Tailbud late 1 wrap	25	20	17	80%	68%
12	Tailbud late 1 wrap	20	10	3	50%	15%

where E stands for embryo and the number following it indicates the day of development, following the approach of Kowarsky et al. (2021). Without precise reference to the time of fertilization, the hatching could occur after 6 or 7 days of larval development. It is also to be considered that the larval swimming phase in *B. schlosseri* is very short, and settling occurs, on average, after a couple of hours of free swimming (sometimes, even after only 15 minutes of free swimming, according to Grave and Woodbridge, 1924). For these reasons, the start and duration of the larva period were defined as "E.6–7.1" and "E.6–7.2" in this study.

The *in vitro* development was faster than the *in vivo* one since it occurred at a higher temperature (23°C, Table 2); this is consistent with previous observations comparing the duration of the blastogenetic cycle at different temperatures (Gasparini et al., 2015).

The subdivision into periods and stages is in line with the developmental ontology published for *C. robusta* (Hotta et al., 2007). Only early development up to the 32-cell stage (cleavage period) was easily identifiable *in vivo*. After this stage, the presence of yolk within blastomeres rendered embryos opaque, making it difficult to track each mitosis. Gastrulation was identified by the appearance of the blastopore, while neurulation was marked by the presence of the neural plate and the forming neural tube. During the tailbud period, the main parameter used to define the stages was the length of the tail, which grows on the left around the trunk at its equatorial level beneath the chorion and, at maximum extension, wraps around the trunk 1.5 times (Manni et al., 1999; Kowarsky et al., 2021). These stages deeply differ from those described in *C. robusta* (Hotta et al., 2007).

The detailed description of tailbud and larva periods is primarily based on histological analysis of serial sections of whole embryos sectioned according to different planes as the opacity of the late embryo also prevented deep laser penetration at CLSM. The list of the anatomical entities peculiar to *B. schlosseri* recognized in this study, along with their definitions, is provided in Supplementary Table S1; it represents a revision of the anatomical entity list published for the juvenile of *C. robusta* (Hotta et al., 2020).

3.1.3 Meta-period: pre-embryonic development

3.1.3.1 Period: pre-fertilization

Stage: Unfertilized egg (Figure 2A', Figure 3A-A′). The ovulated egg contains densely packed yolk globules and measures approximately 250–300 µm in diameter. A continuous thin layer of inner follicular cells, which collaborate with the oviduct cells to form the placental cup, covers it (Zaniolo et al., 1987). The inner follicle cells lie on the acellular vitelline coat (or chorion). Within the perivitelline space, (individuated between the oolemma and the vitelline coat), several test cells are present. The outer follicle cells that surrounded the oocyte during oogenesis were discharged at ovulation, remaining in the mantle as a sort of *corpus luteum* (Zaniolo et al., 1987).

3.1.3.2 Meta-period: embryonic development, pre-metamorphosis

3.1.3.2.1 I period: zygote. *Stage E1.0* (Stage 1, day 1 of development). The zygote (1-cell embryo) consists of a single fertilized cell. The stage extends from fertilization to the completion of the first mitotic cycle.

3.1.3.2.2 II period: cleavage. *Stage E1.1* (Stage 2, day 1 of development) (Figures 2B, 3B): 2-cell embryo. The first division separates the left and right halves of the embryo.

Stage E1.2 (Stage 3, day 1 of development) (Figures 2C, 3C): 4-cell embryo. The second cleavage plane is determined by the embryos dividing into anterior and posterior halves.

Stage E1.3 (Stage 4, day 1 of development) (Figures 2D, 3D): 8-cell embryo. The third cleavage plane is horizontal and separates the animal from the vegetal blastomeres. At this stage, the four founder lineages are defined as follows: A, anterior vegetal; B, posterior vegetal; a, anterior animal; b, posterior animal (Conklin, 1905).

Stage E1.4 (Stage 5, day 1 of development) (Figures 2E, 3E'): 16-cell embryo. The embryo possesses groups of cells of different sizes that are clearly recognizable. The animal and vegetal cells have undergone the fourth cleavage, and blastomeres show bilateral

TABLE 2 Timetable of the development of *B. schlosseri* embryo referred to the meta-period "Embryonic development, pre-metamorphosis". "Stage (20°C)" refers to the stage nomenclature proposed in Kowarsky et al. (2021): E indicates the embryonic development; the number following it (1–7) indicates the day of the blastogenetic cycle in which the stage was found; the last number (separated by dot from the previous one), when present, numbers the embryo stage in that day. The stages E6–E7.1 and E6–E7.2 last approximately 2 h and depend on colony takeover onset; they occur after 6–7 days from the oral siphon aperture in adults, event allowing the fertilization of ovulated eggs. *, new stages with respect to Kowarsky et al. (2021). "Stage N" indicates the progressive stage number according to the practice used for solitary ascidians (Hotta et al., 2007; Hotta et al., 2020). Hpf, hours post fertilization. Note that the *in vitro* development was faster than *in vivo* since it occurred at a higher temperature. The percentage of development is calculated referring to the *in vitro* development at 23°C, with 0% of development occurring at day 1 (zygote) and 100% at day 4.5 (108 hpf) (hatched larva).

Stage (20°C)	Stage N°	Stage name	Definition	Hpf *in vitro* development (23°C)	% of development
I. Zygote period					
E1.0	1	1 cell	Zygote, fertilized egg	0–1 h	0
II. Cleavage period					
E1.1	2	2 cells	Two-cell stage embryo	1 hpf	0.9
E1.2	3	4 cells	Four-cell stage embryo	2 hpf	1.8
E1.3	4	8 cells	Eight-cell stage embryo	4 hpf	3.7
E1.4	5	16 cells	16 cells of different sizes	6 hpf	5.5
E1.5	6	32 cells	32-cell stage embryo, blastula as hollow sphere of cells	8 hpf	7.4
III. Gastrula period					
E2.1*	7	Early gastrula	Sinking of the embryo vegetal side; large blastopore	16 hpf	14.8
E2.2*	8	Mid gastrula	Invagination of mesodermal tissue occurring and blastopore with triangle shape	18 hpf	16.6
E2.3*	9	Late gastrula	Closing blastopore	23 hpf	21.3
IV. Neurula period					
E3.1*	10	Early neurula	Neuropore (blastopore) halfway in embryo; notochord cells recognizable but not yet in convergent extension	25 hpf	23.1
E3.2*	11	Late neurula	Pear-shaped embryo with anterior neuropore. Embryo elongating	29 hpf	26.8
V. Tailbud period					
E3.3*	12	Initial tailbud	Initial separation between tail and trunk. Neural tube cylindrical	31 hpf	28.7
E3.4*	13	Tailbud ¼ wrap	Tail circumscribing ¼ of the trunk; embryo resembling a comma	35 hpf	32.4
E3.5*	14	Tailbud ½ wrap	Tail circumscribing half of the trunk. Notochord cells at the end of convergent extension movement	39 hpf	36.1
E4	15	Tailbud ¾ wrap	Tail circumscribing ¾ of the trunk	40 hpf	37
E5	16	Tailbud early 1 wrap	Tail making one complete turn around the trunk	44 hpf	40.7
E6	17	Tailbud late 1 wrap	Tail encircling the trunk more than 1 wrap (maximum extension: 1.5 wrap). Trunk ovoidal and increased in size; papillae recognizable	66 hpf	61.1
VI. Larva period					
E6–E7.1*	St. 18	Hatched larva	Larva swimming upward, attracted toward light sources	4–5 days	100
E6–E7.2*	St. 19	Swimming larva	Larva first indifferent to light, then negative to light, and touching the substrate repeatedly, before attaching permanently to the substrate and beginning to metamorphose	4–5 days	

symmetry in their arrangements. During these early stages, embryos are characterized by a spherical shape and pink color (brown under a stereomicroscope).

Stage E1.5 (Stage 6, day 1 of development) (Figures 2F, 3F): 32-cell embryo, blastula. The embryo is a hollow sphere of cells. From this stage until gastrulation, blastomeres continue

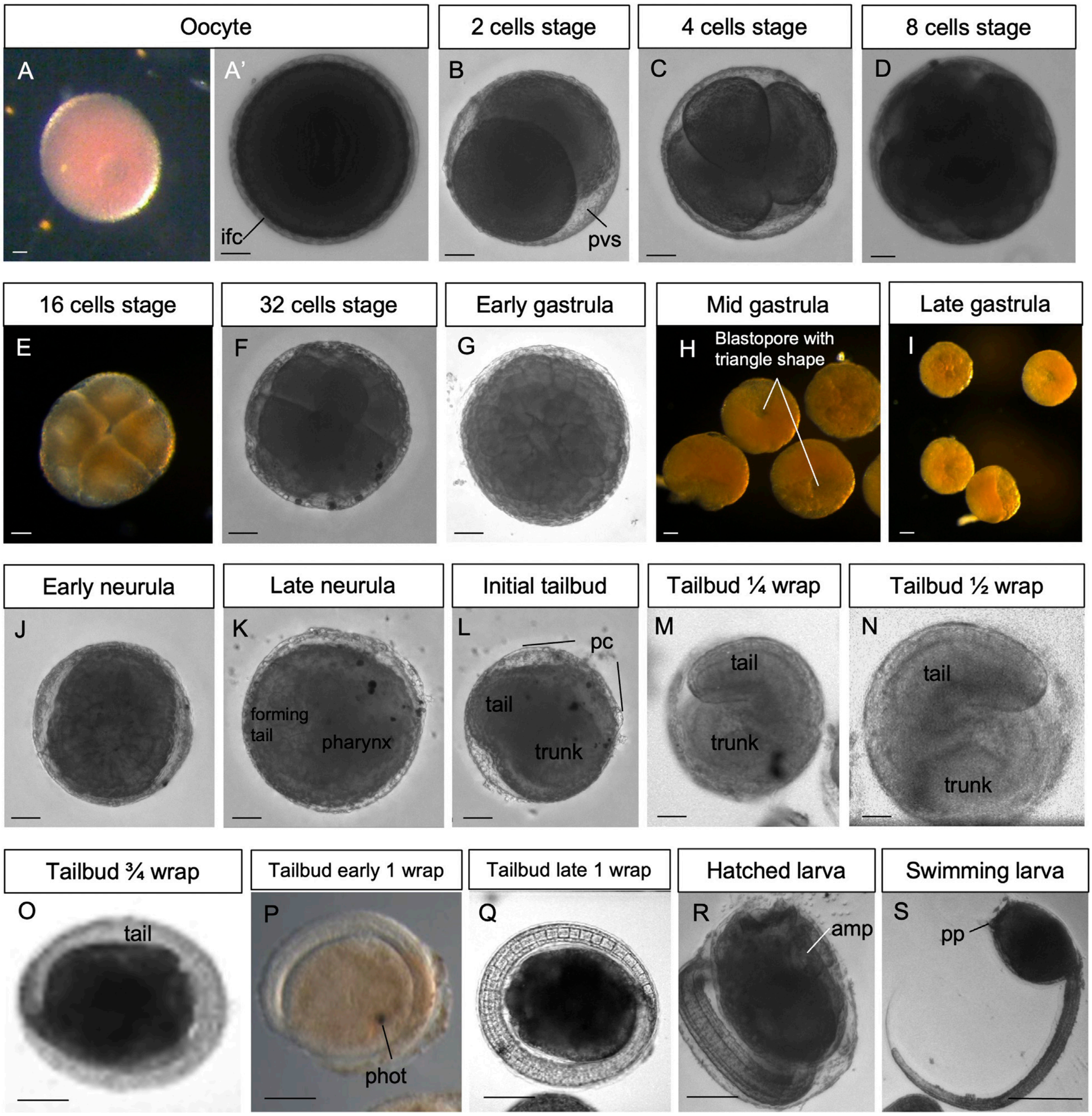

FIGURE 2
(A–S) *In vivo* embryos at stages 1–19. Stereomicroscopy. Scale bar, 100 µm. amp, ampullae; ifc, inner follicles cells; pc, placental cup; phot, photolite; pp, papilla; pvs, perivitelline space. See list of abbreviations in Supplementary Table S1.

dividing, but the number of cell divisions is no longer detectable through *in vivo* observations under a stereomicroscope.

3.2 Period: gastrula

Stage E2.1 (Stage 7, day 2 of development) (Figures 2G, 3G): early gastrula stage. The invagination of the endodermal layer begins, and a large blastopore is recognizable.

Stage E2.2 (Stage 8, day 2 of development) (Figures 2H, 3H): mid gastrula stage. Gastrulation continues with the involution of mesodermal cells. The blastopore has a triangle shape.

Stage E2.3 (Stage 9, day 2 of development) (Figures 2I, 3I): late gastrula stage. The blastopore is closing, and the neural plate is forming.

3.2.1 Period: neurula

Stage E3.1 (Stage 10, day 3 of development) (Figures 2J, 3J): early neurula stage. The larval neural plate forms the neural fold; the

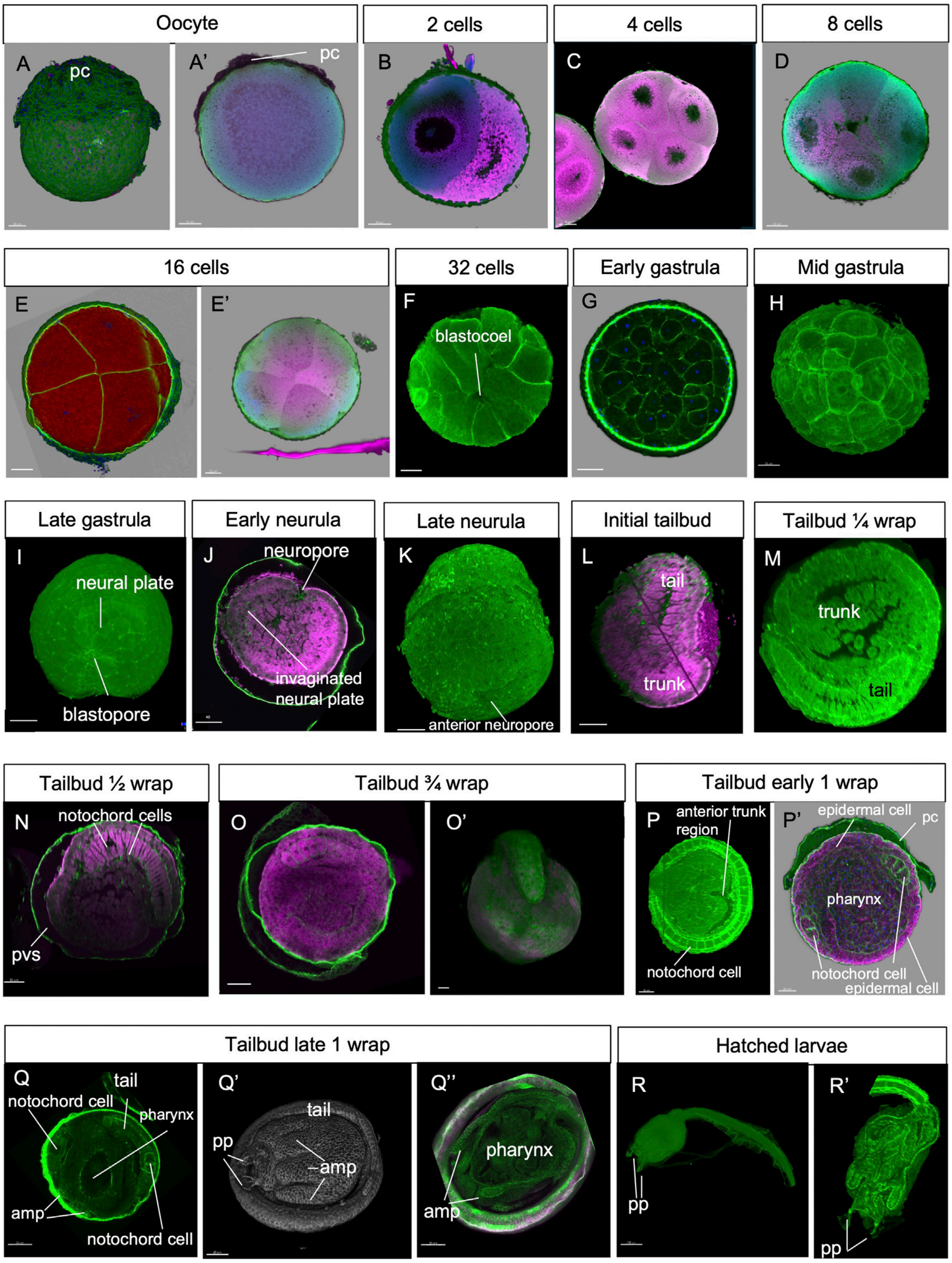

FIGURE 3
(A–R) Confocal laser scanning microscopy of embryos at stages 1–19 (green: Alexa phalloidin; pink: cell mask orange). amp, ampullae; pc, placental cup; pp, papilla; pvs, perivitelline space.

nervous system closes, and the anterior neuropore (blastopore) is open in the embryo. The notochord has not yet started the process of convergent extension.

Stage E3.2 (Stage 11, day 3 of development) (Figures 2K, 3K): late neurula stage. The embryo is oval. The neural tube is closed. The pharynx has an oval lumen delimited by endodermal cells. In the forming tail, the endodermal strand is recognizable ventral to the notochord, which is oval. Small mesodermal cells, representing the muscle cell precursors, flank the notochord cells.

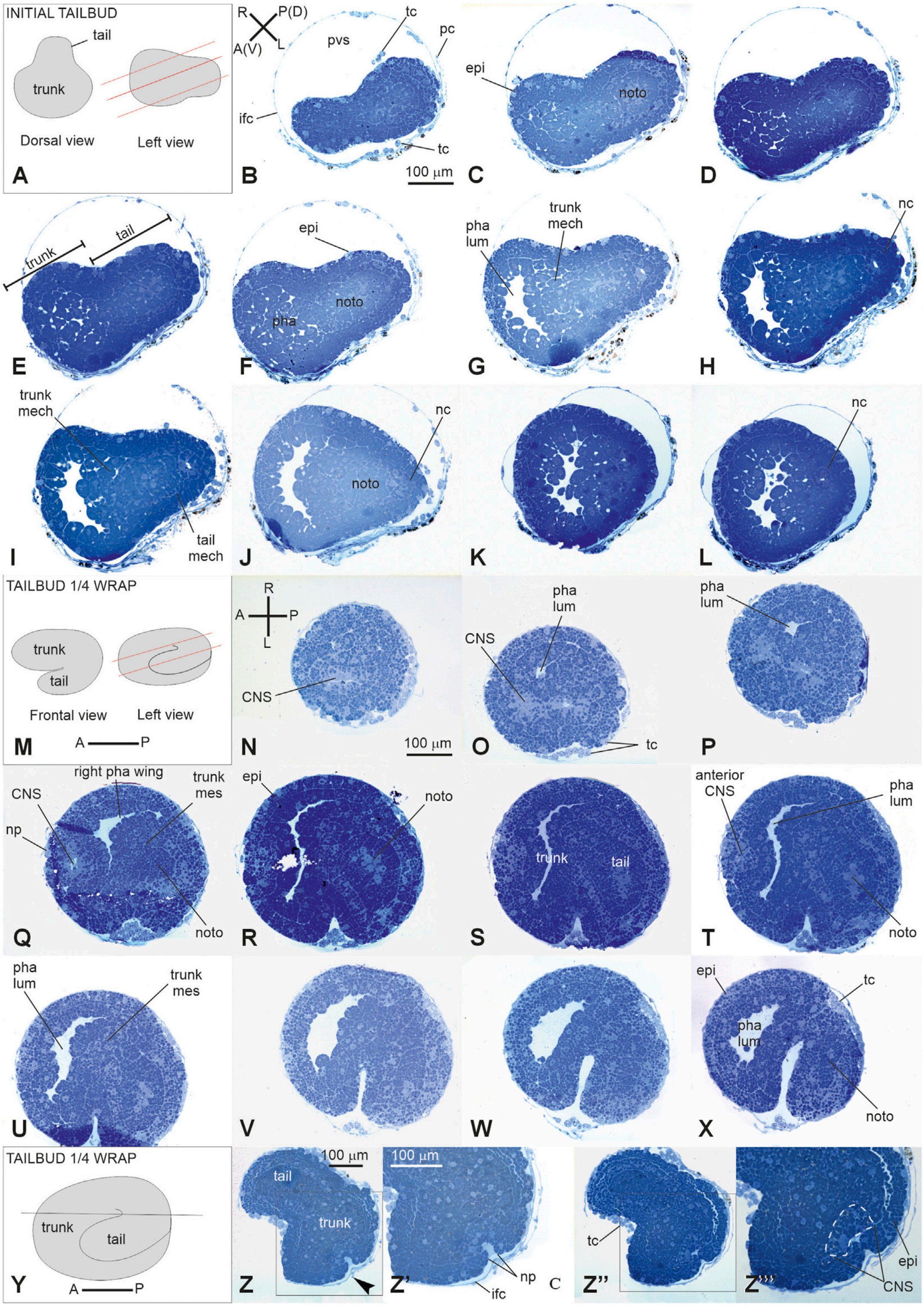

FIGURE 4

V period. **(A–L)** tailbud. Stage E3.3 (Stage 12, day 3 of development). Initial tailbud **(M–Z‴)**: *Stage E3.4* (Stage number 13, day 3 of development). Tailbud ¼ wrap **(A)**. Dorsal and lateral illustrations of embryos at the initial tailbud stage. Red lines indicate the cut planes in lateral view **(B–L)**. Frontal-transverse sections selected from a complete series of the same embryo cut from the posterior **(P)** side to the anterior **(A)** one, slightly tilted dorso **(D)**-ventrally **(V, M)**. Frontal and lateral illustrations of embryos at tailbud ¼ wrap. Red lines indicate the cut planes in lateral view **(N–X)**. Frontal serial sections selected from a complete series of the same embryo cut from the dorsal-right side **(N)** to the ventral-left one **(X, Y)**. Illustration of an embryo at tailbud ¼ wrap; the red line indicates the cut planes in left view **(Z-Z‴)**. Two frontal sections **Z,** one more dorsal than the **(Z″)** selected from a complete series of the same embryo at the neuropore level. **(Z′)** and **(Z‴)** represent enlargements of the square areas shown in **(Z)** and in **(Z′)**, respectively. White dotted line in **(Z‴)** represent the central nervous system. **(A–P)** and **(R–L)** Illustrations of anterior–posterior and right-left axes, respectively; CNS, central nervous system; epi, epidermis; ifc, inner follicle cell; mech, mesenchyme cell; nc, nerve cord; noto, notochord; np, neuropore; pc, placental cup; pha, pharynx; pha lum, pharynx lumen; pvs, perivitelline space; righ pha wing, right wing of the pharynx; tc, test cell; trunk mes, trunk mesenchyme. Enlargement is the same in **(B–L)**, **(N–X)**, **(Z, Z′)**, and **(Z′, Z‴)**. Toluidine blue.

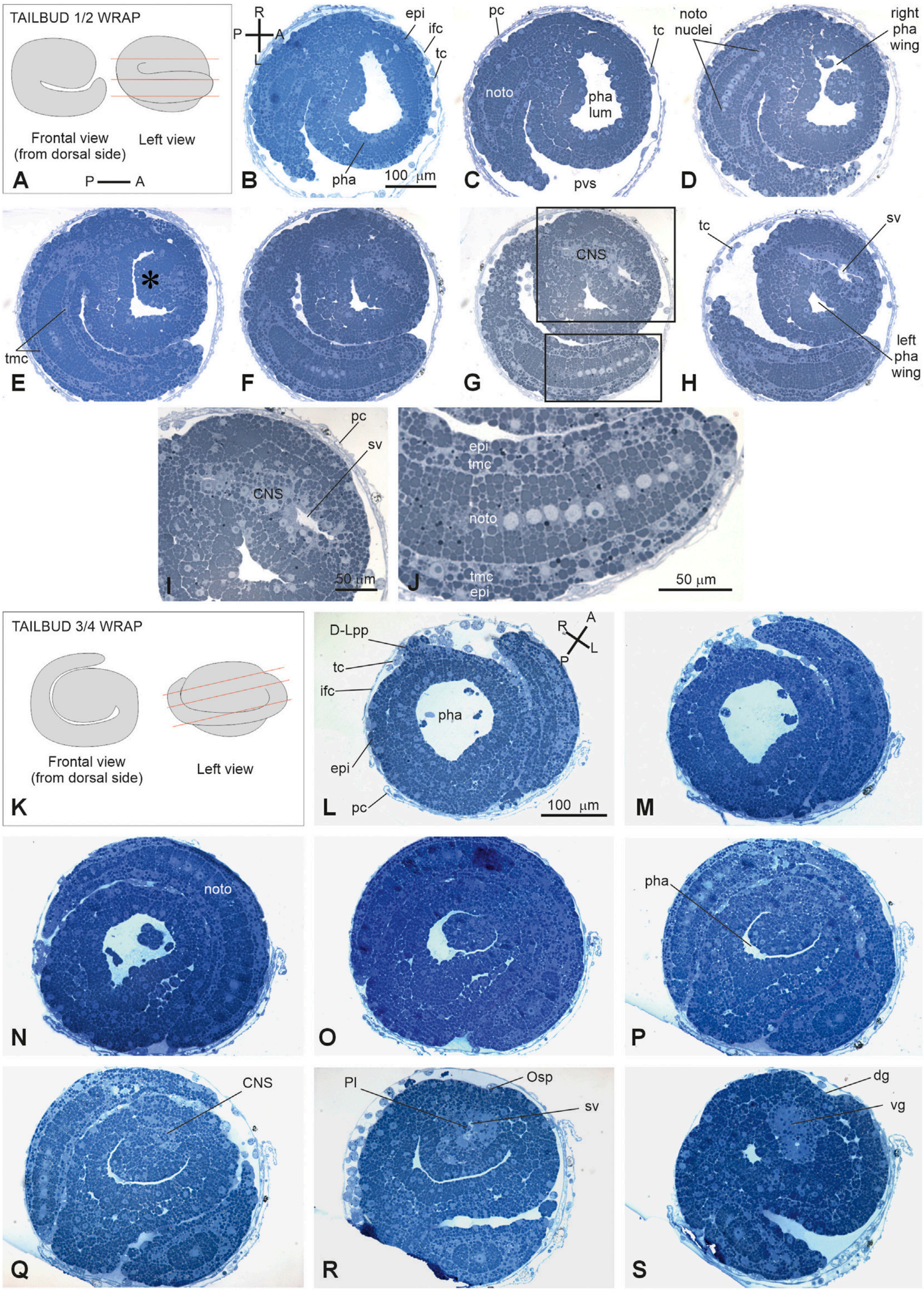

FIGURE 5
(A–H): V period. Tailbud 1/2 wrap. Stage E3.5 Stage 14, day 3 of development A. Frontal and left illustrations of embryos. Red lines indicate the cut planes in lateral view **(B–J)**. Sagittal-oblique serial sections selected from a complete series of the same embryo cut from the dorsal-right side to the ventral-left side. **(E)** Wide depression on the pharynx roof (asterisk) caused by the sensory vesicle expansion. Squared areas in G are enlarged in I and J to show details of the sensory vesicle and of the tail **(K–S)**: V period. Tailbud ¾ wrap. Stage E4 (Stage 15, day 4 of development). Frontal and left illustrations of embryos. Red lines indicate the cut planes in lateral view **(K)**. Frontal and left illustrations of embryos. Red lines indicate the cut planes in lateral view **(L–O)**. Frontal-oblique sections selected from a complete series of the same embryo cut from the ventral-left-anterior side to the dorsal-right-posterior side. In **(B, L)**, **(A–P)** and **(R–L)** show the anterior–posterior and right–left axes, respectively; CNS, central nervous system; dg, dorsal groove; **(D–L)** pp, dorsal left papilla; epi, epidermis; ifc, inner follicle cells; left pha wing, left wing of the pharynx; nc, nerve cord; noto, notochord; Osp, oral siphon primordium; pc, placental cup; pha, pharynx; pha lum, pharynx lumen; Pl, photolith; pvs, perivitelline space; right pha wing, right wing of the pharynx; sv, sensory vesicle; tc, test cell; tmc, tail muscle cell precursor; vg, visceral ganglion. Enlargement is the same in **(B–H)**, **(I–J)**, and **(L, S)**. Toluidine blue.

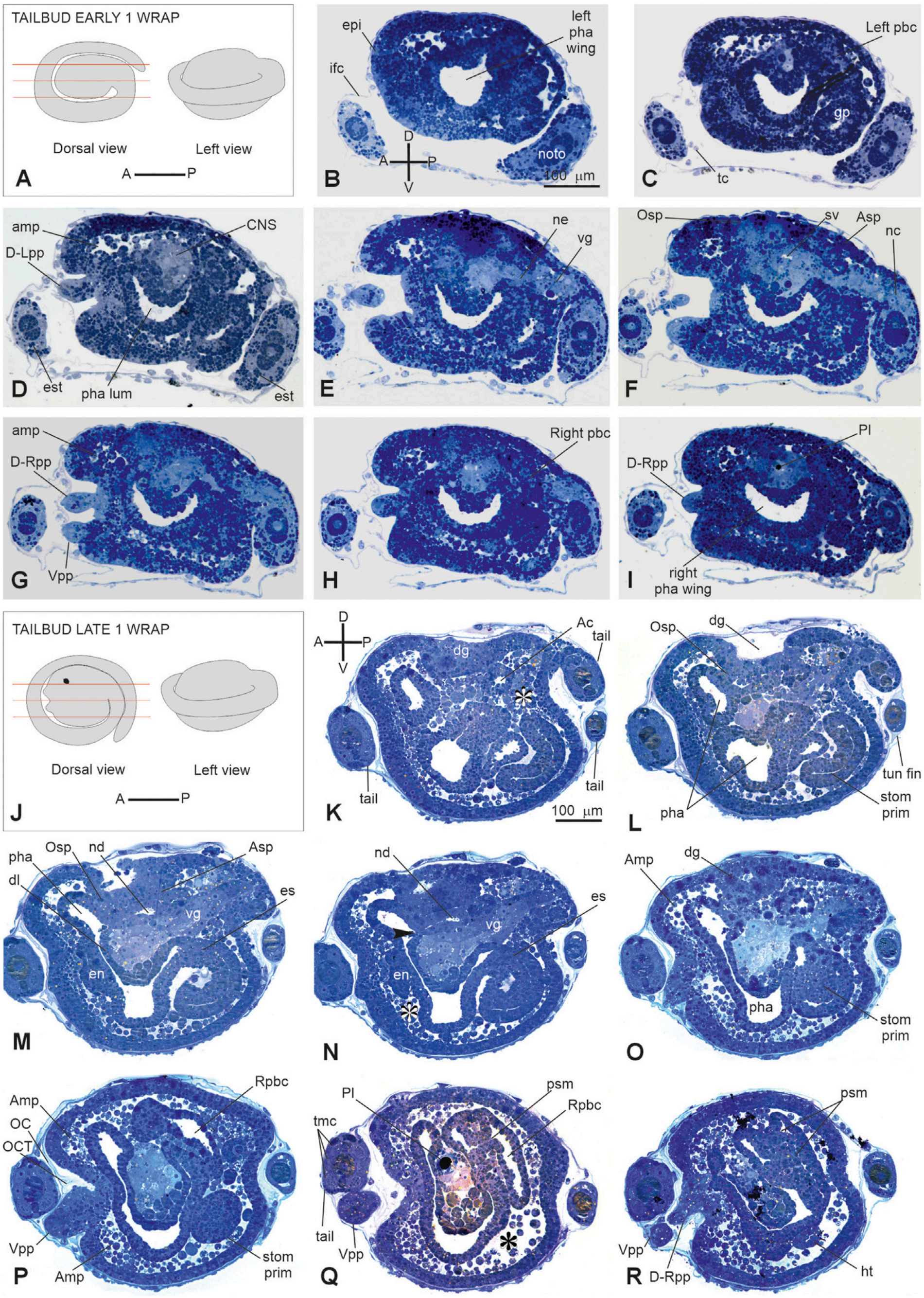

FIGURE 6
(A–I): V period. Tailbud early one wrap. Stage E 5 Stage 16, day 5 of development. A. Frontal and left illustrations of embryos. Red lines indicate the cut planes in dorsal view **(B–I)**. Sagittal serial sections selected from a complete series of the same embryo cut from the left side to the right side. **(F)** Areas individuating the oral (Osp) and atrial (Asp) siphon primordia. Both the ampullae (amp in **D**, **G**) and the papillae (D-Rpp and Vpp in G) protrude from the anterior epidermis **(J–R)**: V period. Tailbud late one wrap. Stage E6 (Stage 17, day 6 of development). **(J)** Frontal and left illustrations of embryos. Red lines indicate the cut planes in the dorsal view **(K–R)**. Sagittal sections selected from a complete series of the same embryo cut from the left side to the right side. The dorsal groove (dg in **H–O**), the neurohypophyseal duct (nd in **M–N**), and the oral (Osp in **L**) and atrial (Asp in **M**) siphon primordia are well-recognizable. In B and K, **(A–P)** and **(D–V)** show the anterior–posterior and dorsal-ventral axes, respectively; asterisks in (**K**, **N**, and **Q**) represent blood lacuna; arrowhead in N represents neurohypophyseal duct aperture in the pharynx lumen. Ac, atrial cavity; Amp, ampulla; Asp, atrial siphon primordium; CNS, central nervous system; dg, dorsal groove; D-Lpp, dorsal left papilla; D-Rpp, dorsal right papilla; en, endostyle primordium; epi, epidermis; es, esophagus; est, endodermal strand; ht, heart; ifc, inner follicle cells; left pbc, left peribranchial chamber; left pha wing, left wing of the pharynx; nc, nerve cord; ne, neck; noto, notochord; OC, outer cuticular layer of tunic; OCT, outer compartment of tunic; Osp, oral siphon primordium; pha, pharynx; pha lum, pharynx lumen; Pl, photolith; psm, protostigma; Rpbc, right peribranchial chamber; righ pha wing, right wing of the pharynx; stom prim, stomach primordium; sv, sensory vesicle; tmc, tail muscle cell precursors; tun fin, tunic fin; vg, visceral ganglion; Vpp, ventral papilla. Enlargement is the same in **(B–I)**, and in **(K, R)**. Toluidine blue.

3.2.2 Period: tailbud

Stage E3.3 (Stage 12, day 3 of development) (Figures 2L, 3L, 4A–L): initial tailbud. The embryo is pear-shaped, and the first separation between the tail and the trunk appears. Different embryonic tissues are progressively recognizable at the histological level due to the different cell shapes, sizes, and arrangements, as well as their spatial relationships. Epithelia are monolayers. The entire embryo is covered by small epidermal cells (Figure 4F). In the trunk, the nervous system is in its typical dorsal position (Figure 4H); it has cells that are smaller than the endodermal ones. The anterior neuropore is present. In the tail, which is straight, the nerve cord elongates dorsal to the notochord (Figure 4J). The latter is ovoid, and 2–4 cells can be recognized in the same cross section. Endodermal cells are very rich in yolk and form the pharynx rudiment (branchial chamber rudiment) in the trunk, which is more recognizable in the anterior trunk than in the posterior trunk. The pharynx exhibits a small, oval lumen (Figure 4G). Mesenchyme cells occupy spaces between the epidermal and endodermal leaflets in the ventral and lateral trunks (Figure 4G). The yolk is distributed in all the embryo cells, decreasing in quantity from the notochord and endodermal cells to mesenchymal cells and nervous system cells.

Stage E3.4 (Stage 13, day 3 of development) (Figures 2M, 3M, 4M–Z”‘): tailbud ¼ wrap. A thick tail circumscribes ¼ of the trunk equatorially on its left side, and the embryo resembles a comma (Figure 4S). The tail, pressing against the trunk’s left side, slightly deforms the pharynx lumen, posteriorly wider on the right side than on the left side. The anterior neuropore is closed (Figure 4Z”); its position is marked by a slight ectodermal depression.

Stage E3.5 (Stage 14, day 3 of development) (Figures 2N, 3N, 5A–J): tailbud ½ wrap. The tail, now thinner than in the previous stage, circumscribes half of the trunk (Supplementary Figure S5). A total of 36 notochord cells are in convergent extensions, assuming a disc shape and arranging in a single line (Figure 5J). Three symmetrical lines of muscle cell precursors flank them. The nervous system begins to expand anteriorly in the sensory vesicle (identifiable due to its lumen) (Figure 5H) that presses on the pharynx roof (Figure 5E), narrowing the pharynx lumen on its right side. The pharynx is also deformed on its left side by the tail and posteriorly by mesenchymal cells in the ventral right trunk.

Stage E4 (Stage 15, day 4 of development) (Figures 2O, 3O’, Figure 5K–O): tailbud ¾ wrap (tail circumscribing ¾ of the trunk (less than one complete wrap)). Three small anterior papillae, two dorsal and one ventral, protrude anteriorly (Figure 5L). The sensory vesicle with the photolith (the pigmented organ responding to both gravity and light; Sorrentino et al., 2000; Figure 5N), the visceral ganglion (Figure 5O), the neck, and the nerve cord are recognizable. Dorsally, the ectoderm deepens in the dorsal groove (Figure 5O), extending antero-posteriorly in the middle ectoderm: initially, it is in the form of a wide depression. The pharynx is larger than in the previous stage; it is depressed dorsally by the sensory vesicle and on the left by the growing tail. In the tail, the notochord cells are located in a single line, ventral to the nerve cord. Muscle cell precursors (still without evident myofibrils) are organized in three symmetric lines of cells flanking the notochord.

Stage E5 (Stage 16, day 5 of development) (Figures 2P, 3P’, Figure 6A–I; Supplementary Figure 2A–C): tailbud early one wrap. The embryo trunk maintains a relatively circular shape, and the tail makes one complete turn around the trunk. The three papillae are well evaginated, without a cavity (Figures 6D, G); the interpapillary region is depressed. Close to the papillae, a ring of eight ampulla rudiments is present. Anteriorly, the pharynx rises in front of the sensory vesicle, toward the dorsal ectodermal invagination of the dorsal groove, representing the oral siphon primordium (stomodeum) (Supplementary Figure 2A); posteriorly, the pharynx extends into the esophagus and the stomach. The atrial chamber rudiment is in the form of a single dorsal ectodermal invagination in communication with the outside (Supplementary Figure 2B). In the brain, a small sensory vesicle, containing the forming photolith, is recognizable. The neurohypophyseal duct, representing the rudiment of the oozooid neural complex (Manni et al., 1999), is open into the pharynx. The heart is in the form of a compact mass of mesodermal cells. In the hemocoel, hemoblasts (lymphocyte-like cells) and morula cells can be detected (Supplementary Figure 2B–C; Kowarsky et al., 2021).

Stage E6 (Stage 17, day 6 of development) (Figures 2Q, 3Q-Q″, Figure 6K–R): tailbud late one wrap. The tail encircles the trunk more than one wrap; it will continue growing to reach its maximum extension, making 1.5 wraps. The trunk is ovoid and progressively increases in size. Wide blood lacuna and sinuses are recognizable since epithelia are thinning for yolk consumption and the trunk is enlarging. The body wall (Supplementary Table S1) is rich in hemocytes. Phagocytic cells (hyaline amebocytes) and pigment cells can be detected. The larval tunic (outer cuticular layer and outer compartment), which constitutes the larval fins and will be lost at metamorphosis, is present around the trunk and the tail. The three papillae are more protruded anteriorly than in the previous stage, and their receptor end-organs are forming (Supplementary Figure 2D–E). The eight blood ampullae are well expanded. Dorsally, the dorsal groove occupies approximately 1/3 of the trunk length, and the tunic fills it; at this stage, the oral and the atrial siphons are developing (Figure 6M). The atrial chamber rudiment loses its communication with the outside at the end of this stage. Later, it elongates posteriorly in two wide invaginations, assuming a horseshoe shape; these invaginations descend, flanking the neural tube. Their bottom, on the right and left, represents the rudiments of the peribranchial chambers, which are derived from the uneven atrial chamber rudiment. A small left ganglionic vesicle is in continuity with the neurohypophyseal duct (Figures 6M, N; Manni et al., 1999). Its anterior-most part is in the form of a small duct opening into the pharynx. The neurohypophyseal region, posterior to the duct, is involved in the delamination of neuroblasts to form the adult cerebral ganglion (Manni et al., 1999; Sorrentino et al., 2000). The sensory vesicle is on the right of the visceral ganglion and contains an evident photolith (Figure 6Q; Manni et al., 1999). The branchial chamber is more deformed than in the previous stage. It exhibits a flat endostyle primordium on its floor, with two lateral–dorsal wings embracing the visceral ganglion. Two to three protostigmata are perforated, following an anterior–posterior pattern that allows the communication between the pharynx lateral–dorsal wings and the posterior descending peribranchial chambers. After the larva adhesion, the oozooid will exhibit five long protostigmata, dorsoventrally oriented. The peribranchial chambers are ventrally elongated; on the left, the peribranchial chamber is close to the stomach to form the perivisceral epithelium surrounding the gut. The latter grows

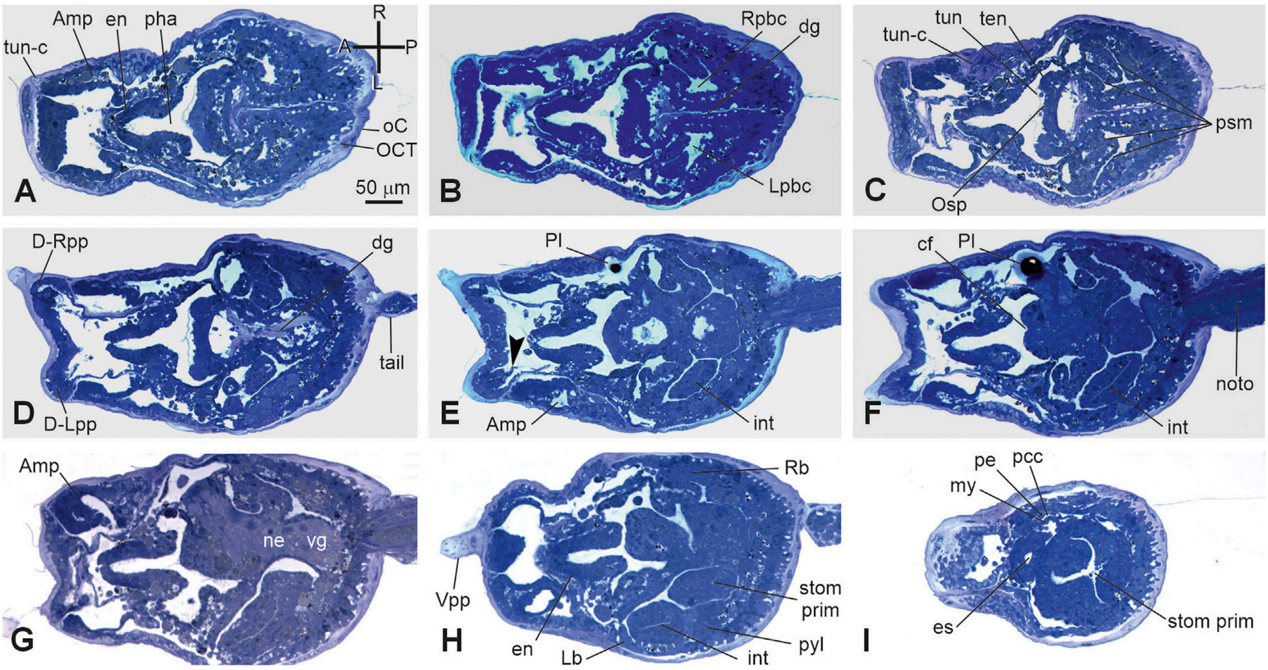

FIGURE 7
(A-I) VI period. Swimming larva. Stage E.6–E7.1 (Stage 18, day 6–7 of development). Frontal serial sections selected from a complete series of the same embryo cut from the dorsal side to the ventral side; E, and H are enlarged in Supplementary Figure 2G, H, respectively. Note that in H, the right bud is in the form of thickening of the peribranchial epithelium (stage 1); both the heart **(I)** and the intestine **(E–H)** are well-recognizable. The outer compartment of the tunic is populated by tunic cells **(A)**. Arrowhead in E, papillary neuron; A-P and R-L, anterior–posterior and right-left axes, respectively; Amp, ampulla; cf, ciliated funnel; dg, dorsal groove D-Lpp, dorsal left papilla; D-Rpp, dorsal right papilla; en, endostyle; int: intestine; Lb, left bud; Lpbc, left peribranchial chamber; my, myocardium; ne, neck; noto, notochord; es, esophagus; Osp, oral siphon primordium; pe, pericardium; pcc, pericardial cavity; pha, pharynx; Pl, photolith; psm, protostigma; pyl, pyloric cecum; Rb, right bud; Rpbc, right peribranchial chamber; stom prim, stomach primordium; ten, oral tentacle rudiment; tun, tunic; tun-c, tunic cell; vg, visceral ganglion; Vpp, ventral papilla. Enlargement is the same in A–I. Toluidine blue.

dorsally and closes the dorsal groove in the region where the atrial siphon is opening. The heart is a hollow vesicle that begins to invaginate along its raphe (Figure 6R). As this stage progresses, an additional layer of the tunic is also recognizable around the trunk: the inner compartment of the tunic, with its cuticle (inner cuticular layer) representing the definitive tunic of the post-metamorphosing oozooid (Supplementary Figure 2D–F). The sensory vesicle sits on the right of the visceral ganglion. The neurohypophyseal duct parallels the dorsal groove and separates from the left ganglionic vesicle. The dorsal lamina (Figure 6M) is recognizable on the roof of the pharynx. The left peribranchial epithelium follows the gut growth, enveloping it as perivisceral epithelium; the gut is completely formed.

3.2.2.1 Period: swimming larva

This period lasts 2 hours on average (Grave and Woodbridge, 1924) and is divided into two short stages. These stages are characterized by different larval behaviors and different conformations of the anterior papillae (Grave and Woodbridge, 1924; Caicci et al., 2010).

Stage E6–E7.1 (Stage 18, day 6–7 of development) (Figures 2R, 3R', Figure 7; Supplementary Figure 2G): hatched larva. The larva has a 400 mµ-long trunk and a 1 mm-long tail; it swims upward (negative to gravity) and is attracted toward light sources. Its anterior region is expanded in the eight ampullae, surrounding a central protruding area with the three papillae. Here, the receptor end-organs of the papillary neurons elongate in the anterior tunic. The eight endostyle zones differentiate (Supplementary Figure 2G; Kowarsky et al., 2021). Both the rudiments of the oral and atrial siphons face the dorsal groove; they are occluded by the tunic and will definitely open during metamorphosis. Some of the eight stomach folds are recognizable. The gut is completely enveloped by the perivisceral epithelium (Supplementary Figure 2H). The pyloric cecum is well-formed (Figure 7H). Both the left and right buds are recognizable as thickened discs of the peribranchial epithelium; the right one is wider than the left one. The pericardium and the myocardium are well-separated and delimit a narrow pericardial cavity. The larval brain is organized in a large sensory vesicle, the visceral ganglion, the neck, and the nerve cord. The adult neural complex, derived from the neurohypophyseal duct, is composed of the differentiating cerebral ganglion and neural gland complex. The yolk globules are no longer easily recognizable in the cells.

Stage E6–E7.2 (Stage 19, day 6–7 of development) (Supplementary Figure S2): swimming larva. The larva goes through a short period of indifference to light, then, just before metamorphosis, becomes negatively photo tactic, and repeatedly touches the substrate. The receptor end-organs of the papillary neurons pass through small fenestrations in the anterior tunic protruding outside in the environment; the cells of the interpapillary region release secretions that change the properties

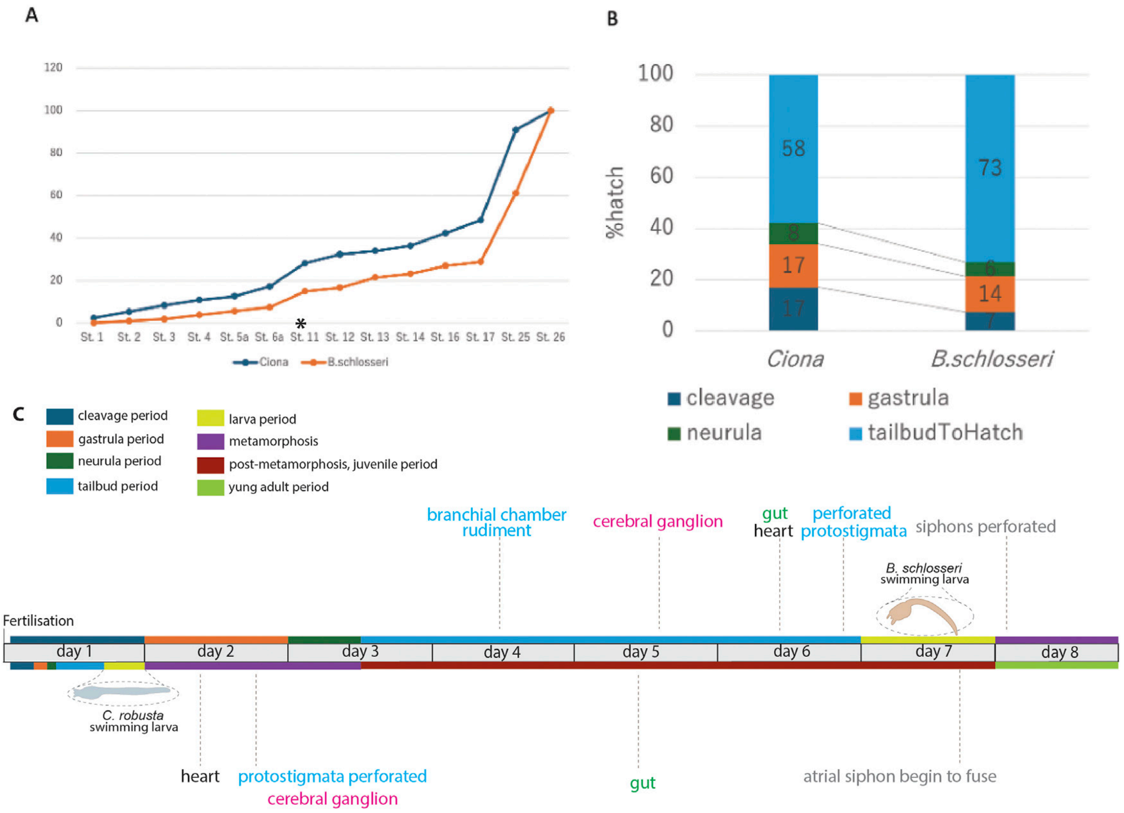

FIGURE 8
Comparison between embryonic development in *B. schlosseri* and *C. robusta*. Based on Table 2 and from the fingings of Hotta et al. (2007) and Hotta et al. (2020), **(A)** relative developmental progress of *C. robusta* and *B. schlosseri* from the cleavage stage to hatching, shown as a percentage of total time to hatching. *C. robusta* progresses through developmental stages at a much faster rate than *B. schlosseri*, particularly after the tailbud stage (start indicated with an asterisk and end corresponding to stage 26). **(B)** Percentage of total time spent at each major developmental period (cleavage, gastrula, neurula, and tailbud) in *C. robusta* and *B. schlosseri*, illustrating extended tailbud development in *B. schlosseri* compared to *C. robusta*. **(C)** Developmental timeline of *B. schlosseri* and *C. robusta*, including key anatomical milestones and periods. The colored bars represent major developmental periods/meta-periods: cleavage (blue), gastrula (orange), neurula (green), tailbud (light blue), larva (yellow), metamorphosis (purple), post-metamorphosis (brown), and young adult (olive). The timing of specific organ development such as the formation of the cerebral ganglion, heart, branchial chamber rudiment, and perforated protostigmata are indicated along the timeline.

of the tunic layers, favoring the next adhesion of the larva to the substrate.

The metamorphosing larva will definitely open the siphons after approximately 1.5 days from its adhesion (at approximately 18°C (Brunetti et al., 2017)), beginning its filtering activity. However, the oozooid morphogenesis will not be complete, and only the right bud will develop. The latter will substitute the oozooid in the filtering activity approximately 7 days from settlement and will represent the zooid (blastozooid) of the first blastogenetic generations (Brunetti et al., 2017). Gonads will mature after some blastogenetic generations (Gasparini et al., 2015), but functional germline progenitors are specified during embryogenesis (Brown et al., 2009).

3.3 Compared to *C. robusta*, *B. schlosseri* enhances organ development by prolonging the tailbud stages

The identification of embryonic development stages, along with the description of organ appearance and differentiation, allows for a comparison between developmental events in *B. schlosseri* and *C. robusta* (Hotta et al., 2007; Hotta et al., 2020). The two pathways differ in terms of the time taken for larval development, the relative duration of some developmental periods, the complexity of hatched larvae, and the timing of organ appearance (Figure 8).

A comparison between the percentage of time spent at each developmental stage relative to the total time from fertilization to hatching in the two species shows that the overall trend of the developmental progress from fertilization to the tailbud period is strikingly similar (Figure 8A; Table 2). However, from the tailbud period, the developmental trend between the two species diverges (Figure 8B). When examining the proportion of time spent in each developmental period (cleavage, gastrula, neurula, and tailbud periods), it was found that the tailbud period in *B. schlosseri* lasts relatively longer than the other periods.

The complexity of *B. schlosseri* larva reflects 1) the absolute extension in time of the developmental phases: at 20°C, the “Embryonic development, pre-metamorphosis” meta-period lasts 6–7 days in *B. schlosseri* and 17 h 30 min in *C. robusta* (Hotta et al., 2007; Hotta et al., 2020). Although metamorphosis and post-metamorphosis have not been yet described in detail in *B. schlosseri*, data from the literature show that these phases last

1.5 days at 18°C (Brunetti et al., 2017). In contrast, the "Metamorphosis" and "Post-metamorphosis" meta-periods in *C. robusta* last 6 days at the same temperature. 2) The relative extension in time of the tailbud period, during which the main organogenesis events occur.

Considering the larval complexity, in *B. schlosseri*, we identified 116 anatomical entities in embryos and larvae (Supplementary Table S1); only 30 of them are also exhibited by *C. robusta* during embryogenesis (Hotta et al., 2007; Hotta et al., 2020). It is notable that the anatomical ontology of *C. robusta* includes some entities not present in *B. schlosseri*, such as those related to atrium formation (atrial siphon primordia, left atrial siphon, and right atrial siphon) and sensory organs (ocellus and otolith) in the brain. These additional entities are related to anatomical differences between the two larvae and cannot be attributed to higher larval complexity in *C. robusta*. The latter also displays some larval epidermal neurons (apical trunk epidermal neurons, dorsal caudal epidermal neurons, rostral trunk epidermal neurons, and ventral caudal epidermal neurons) not described in *B. schlosseri*.

Specifically, the *B. schlosseri* embryo possesses an ectodermal dorsal groove where both the siphons open at the larval stage (although still occluded by the tunic). In particular, the atrial chamber originates from a single ectodermal mid-dorsal rudiment, as typical in Pleurogona ascidians (Manni et al., 2022; Lin et al., 2023). In contrast, *C. robusta* does not show a dorsal groove, and the oral siphon rudiment and the paired atrial siphon rudiments open independently at metamorphosis.

A photolith characterizes the larval sensory vesicle of *B. schlosseri*, as is typical for Styelidae, to which *B. schlosseri* belongs; in contrast, in most ascidian larvae, including *C. robusta*, feature a sensory vesicle containing an otolith and an ocellus. An additional vesicle, the left ganglionic vesicle, which contains a possible residuum of a primitive photoreceptor organ (Sorrentino et al., 2000), characterizes *B. schlosseri* with respect to *C. robusta*. Finally, in the tailbud period, eight ectodermal ampullae evaginate from the anterior epidermis in *B. schlosseri* for the stable adhesion of the metamorphosing larva; in *C. robusta*, a basal stalk, elongating during the "Metamorphosis" meta-period, represents the holdfast (Hotta et al., 2020).

The larval complexity, during the "Embryonic development, pre-metamorphosis" meta-period, in *B. schlosseri* is mainly due to the development of 43 prospective juvenile organs, which are absent in *C. robusta,* in addition to 73 transitory larval structures (Figure 8C; Supplementary Table S1). Organs such as the branchial chamber with perforated protostigmata, the cerebral ganglion, the heart, and the gut are recognizable in all their main subcomponents during the tailbud and larva periods in *B. schlosseri*, but these organs become recognizable only during the metamorphosis and/or the post-metamorphosis periods in *C. robusta*.

4 Discussion

4.1 Embryonic development in *B. schlosseri*

Combining complementary information from *in vivo*, CLSM, and histological analyses, our data on *B. schlosseri* embryogenesis provide insights into the species' developmental biology, highlighting both similarities to and differences from solitary ascidians, particularly in terms of developmental timelines, features for stage identification, and anatomical structures. Moreover, these analyses offer the most accurate description of embryogenesis in a colonial ascidian so far available.

This description aligns with previous reports on *B. schlosseri* embryogenesis, which, however, only referred to a few stages or reported synthetic descriptions (Grave and Woodbridge, 1924; Grave, 1934; Scott, 1934; Manni et al., 1999; Sorrentino et al., 2000). With respect to the more recent report on *B. schlosseri* embryogenesis by Kowarsky et al. (2021), we describe a higher number of stages in this study: three gastrula period stages (E2.1, E2.2, and E2.3) instead of one (E2); two neurula period stages (E3.1 and E3.2) instead of one (E3.1); and six tailbud period stages (E3.2, E3.3, E3.4, E4, E5, and E6) instead of four (E3.2, E4, E5, and E6). The larva period, previously including one "swimming larva" stage (E6–E7), is subdivided into two stages in this study, namely, the "hatched larva" stage (E6–E7.1) and the "swimming larva" stage (E6–E7.2). Although this timeline is not precisely defined, it updates the morphogenetic atlas *Tabula compositi chordati Botrylli*, facilitating a better comprehension of the molecular signature of *B. schlosseri* embryogenesis (Kowarsky et al., 2021). Moreover, it represents a base for the future elaboration of a canonical developmental and anatomical ontology of the embryonic development in *B. schlosseri* that will complement the available ontology of blastogenetic development (Manni et al., 2014; Kowarsky et al., 2021).

Our study demonstrates that *B. schlosseri* embryos can survive and develop *ex vivo*, successfully progressing through embryonic stages to the oozooid stage when cultured outside the parental body. However, embryonic survival and development completion rates significantly varied depending on the developmental stage at the time of removal, with higher success rates observed when embryos were excised at later stages (*e.g.*, tailbud period) than earlier stages (*e.g.*, gastrula period). These findings indicate that the parental environment may play a crucial role in the early stages of embryogenesis and may become less essential as development progresses, making *ex vivo* culturing more reliable in the later stages. It is, however, notable that in *B. schlosseri*, a nutrient transfer from the parent to the developing embryo through the placental cup has not been evidenced (Zaniolo et al., 1987), in contrast to closely related species such as *Botrylloides leachii* and *B. violaceus* (Zaniolo et al., 1994a; Zaniolo et al., 1998). Additionally, the differences in the developmental rate and progression of *ex vivo* embryos, particularly the accelerated development at higher temperatures (23°C), align with those of prior studies on temperature-dependent growth in *B. schlosseri* (Gasparini et al., 2015). This observation is valuable for understanding how environmental factors may impact embryogenesis and larval release timing, especially in controlled experimental settings.

Our approach to staging the *B. schlosseri* embryonic development using meta-periods, periods, and stages based on "Embryo Day" notation (*e.g.*, E.1 and E.2) provides a practical framework that compensates for the inability to accurately track the fertilization time. Although the precise timing of fertilization remains a challenge, this framework provides a reliable and consistent means of both tracking development in relation to the blastogenetic cycle and comparing embryonic progress across different species and environmental conditions. In particular, our success in culturing embryos enabled us to observe and analyze developmental processes in detail outside the parental body, overcoming the limitations posed by studying embryos solely within the protective confines of the colony. This will open new perspectives in the study of this species since some tools, such as *in vitro* embryo manipulation and transgenesis, so far not possible, could be finely tuned in the near future, allowing the advancement of comparative, developmental, and evolutionary studies. Including a high-resolution atlas of *B. schlosseri* embryonic anatomical structures, this study offers an in-depth examination of key morphological features across developmental stages, providing valuable insights into species-specific traits. Considering that in *B. schlosseri*, some developmental genes have been co-opted from embryogenesis and redeployed in the blastogenetic development (Alié et al., 2018; Kowarsky et al., 2021), this anatomical atlas will open the door to further investigations on commonalities and differences between embryogenesis, blastogenesis, and possibly regeneration.

The *B. schlosseri* larva also displays two early buds, evidencing the precocity of asexual reproduction as crucial for colony success. This highlights the presence of restricted pluripotent epithelial areas in the larva's lateral peribranchial chamber leaflets, which are involved in budding. Stem cells in the larva may also contribute to blastogenesis as hemoblasts, *i.e.*, candidate stem cells, are detectable in the embryo, with their appearance coinciding with the high expression of hematopoietic stem cell genes (Voskoboynik et al., 2008; Rinkevich et al., 2013; Rosental et al., 2018; Kowarsky et al., 2021). Additionally, germline precursors, identified by *vasa* expression in *B. schlosseri* embryos, circulate in the colonial circulatory system for several generations before contributing to the gonad niche (Brown et al., 2009). In the larva, the right bud is more developed than the left one, evidencing the early onset of the asymmetry in the blastogenic power of the lateral body walls, as long recognized in blastozooids (Gasparini et al., 2015). Only the right bud will continue its development during the Metamorphosis and Post-Metamorphosis Periods, as typically occurs in the blastogenetic cycle when colony energy does not support bilateral growth of its buds.

4.2 Coloniality, heterochrony, and reproductive strategies

Allowing a direct comparison with the established developmental ontologies of *C. robusta*, this timeline bridges the gap between solitary and colonial ascidians, allowing evolutionary consideration (Hotta et al., 2007; Hotta et al., 2020).

The distinct heterochrony observed between *B. schlosseri* and *C. robusta* at both temporal (time taken to larval development and relative extension in time of some periods) and anatomical (complexity of hatched larvae and timing of organ appearance) levels underscores the evolutionary divergence within ascidians, providing clues about the adaptive significance of extended periods in *B. schlosseri*. These may be extended to other colonial ascidians, considering the unique requirements of a colonial life cycle, such as budding and colony establishment.

Although embryogenesis is not known in detail in other colonial ascidians, these species share long gestation periods coupled with high larval complexity compared to solitary ascidians (see Burighel et al. (1997) for review). This suggests that the evolution of the colonial habitus is associated with the reproductive strategy, *i.e.*, it needed a shift from oviparity to ovoviviparity/viviparity, from the external fertilization of tiny eggs to the internal fertilization of yolked eggs and from the development of orphan embryos to gestation. Coloniality in ascidians manifests in different modalities across different species and has been proposed to be the result of multiple independent acquisitions and subsequent diversifications (Alié et al., 2018). Accordingly, the variety of reproductive solutions exhibited by colonial ascidians suggests that the passage from oviparity to ovoviviparity/viviparity evolved in different ways, resulting in morpho-functional modifications of gametes (such as increased yolk amount in eggs, egg envelopes participating in the formation of placental cups/brood pouches, and specialized sperm equipped with apical structures for reaching the ovulated egg for internal fertilization), gonads (producing very few eggs per individual), oviducts (usually very short, with openings located far from the atrial aperture to facilitate the retention of embryos, and in some cases involved in the formation of the placental cups or capable of storing sperms for internal fertilization), and parent structures for housing the developing embryos (such as particular regions of the oviduct or tunic and chambers exposed to seawater) (Berrill, 1950; Zaniolo et al., 1987; Zaniolo et al., 1994a; Zaniolo et al., 1994b; Zaniolo et al., 1998; Martinucci et al., 1988; Manni et al., 1994; Burighel and Martinucci, 2000; Kawamura et al., 2011). Further comparative investigations into the morpho-functional features driving ascidian heterochrony could offer deeper insights into the evolutionary underpinnings of these developmental adaptations.

The contrasting developmental strategies of solitary and colonial tunicates, exemplified by *C. robusta* and *B. schlosseri*, offer intriguing insights into the evolutionary trade-offs between producing many larvae for open-water development and a few larvae by brooding. Although *C. robusta* prioritizes rapid development, reaching the competent larval stage within a day, its larvae hatch with less developed organs, a likely adaptation for pursuing speed and shortening the open-ocean life to avoid predation. In contrast, *B. schlosseri* larvae, protected within the parent colony, undergo slower development but hatch with more advanced organ systems, suggesting a prioritization of developmental completeness. Notably, *B. schlosseri* significantly shortens the next developmental meta-period (metamorphosis) by shifting the time normally required for the maturation of adult organs in solitary ascidians (*i.e.*, after metamorphosis) to the tailbud period. Although *C. robusta* requires only 18 h to hatch, its metamorphosis and post-metamorphosis periods extend over 6 days, allowing the organogenesis to be completed after hatching. Conversely, *B. schlosseri* spends approximately 96 h (4 days) in protected development due to ovoviviparity, hatching with mature organs and requiring only 1.5 days for metamorphosis and post-metamorphosis, a four-fold acceleration compared to *C. robusta*. These divergent strategies highlight the diverse evolutionary paths that tunicates have taken to optimize their reproductive success in different ecological contexts.

In summary, our comparative analyses of *B. schlosseri* development contribute to a deeper understanding of tunicate biology by evidencing both conserved and divergent aspects of ascidian embryogenesis. These insights also offer a framework for understanding the evolution of animal morphology and life history strategies, ultimately enhancing our comprehension of the diversity and adaptability of animal life.

Data availability statement

The datasets presented in this article are not readily available because NA. Requests to access the datasets should be directed to chiara.anselmi@unipd.it.

Ethics statement

The manuscript presents research on animals that do not require ethical approval for their study.

Author contributions

CA: conceptualization, data curation, investigation, and writing–original draft. KI: data curation and writing–review and editing. KP: data curation and writing–review and editing. PB: data curation and writing–review and editing. AV: writing–review and editing, data curation, and investigation. KH: conceptualization, data curation, investigation, and writing–review and editing. LM: conceptualization, data curation, investigation, and writing–original draft.

Funding

The author(s) declare that financial support was received for the research, authorship, and/or publication of this article. This work was supported by the Seal of Excellence@UNIPD, ANARCHORD and funded by the European Union_NextGenerationEU to CA, Keio Gijuku Academic Development/KLL Funds and JSPS KAKENHI (grant numbers JP16H01451/JP16K07426) to KH, the grant "Iniziative di Cooperazione Universitaria 2016," University di Padova, to LM, and NIH (grant RO1AG076908) to AV and ILW. Open Access funding provided by Università degli Studi di Padova | University of Padua, Open Science Committee.

Acknowledgments

The authors thank Yutaka Satou Lab at Kyoto University, Manabu Yoshida at the University of Tokyo, and Yasunori Sasakura at the University of Tsukuba for their support to the National Bio-Resource Project of AMED, Japan.

Conflict of interest

The authors declare that the research was conducted in the absence of any commercial or financial relationships that could be construed as a potential conflict of interest.

Generative AI statement

The author(s) declare that no Generative AI was used in the creation of this manuscript.

Publisher's note

Supplementary material

The Supplementary Material for this article can be found online at: https://www.frontiersin.org/articles/10.3389/fcell.2025.1540212/full#supplementary-material

References

Alié, A., Hiebert, L. S., Simion, P., Scelzo, M., Prünster, M. M., Lotito, S., et al. (2018). Convergent acquisition of nonembryonic development in styelid ascidians. *Mol. Biol. Evol.* 35, 1728–1743. doi:10.1093/molbev/msy068

Anselmi, C., Fuller, G. K., Stolfi, A., Groves, A. K., and Manni, L. (2024). Sensory cells in tunicates: insights into mechanoreceptor evolution. *Front. Cell Dev. Biol.* 12, 1359207. doi:10.3389/fcell.2024.1359207

Berrill, N. J. (1950). "The Tunicata with an account of the British species," in *Ray soc.* Available at: https://cir.nii.ac.jp/crid/1571980074761186432 (Accessed November 26, 2024).

Boyd, H. C., Brown, S. K., Harp, J. P., and Weissman, I. L. (1986). Growth and sexual maturation of laboratory-cultured Monterey botryllus schlosseri. *The Biolo. Bulle.* 170 (1), 91–109. doi:10.2307/1541383

Brown, F. D., Tiozzo, S., Roux, M. M., Ishizuka, K., Swalla, B. J., and De Tomaso, A. W. (2009). Early lineage specification of long-lived germline precursors in the colonial ascidian Botryllus schlosseri. *Development* 136, 3485–3494. doi:10.1242/dev.037754

Brunetti, R., Manni, L., Mastrototaro, F., Gissi, C., and Gasparini, F. (2017). Fixation, description and DNA barcode of a neotype for botryllus schlosseri (pallas, 1766) (tunicata, ascidiacea). *Zootaxa* 4353, 29–50. doi:10.11646/zootaxa.4353.1.2

Burighel, P., Cloney, R. A., and Cloney, B. (1997). Microscopic anatomy of invertebrates, *Microsc. Anat. Invertebr.*; 15: 221–347.

Burighel, P., and Martinucci, G. B. (2000). Urochordata. *Reprod. Biol. Invertebr.* 9, 261–298.

Caicci, F., Zaniolo, G., Burighel, P., Degasperi, V., Gasparini, F., and Manni, L. (2010). Differentiation of papillae and rostral sensory neurons in the larva of the ascidian Botryllus schlosseri (Tunicata). *J. Comp. Neurol.* 518, 547–566. doi:10.1002/cne.22222

Cima, F. (2023). Larval settlement on marine surfaces: the role of physico-chemical interactions. *J. Mar. Sci. Eng.* 11, 859. doi:10.3390/jmse11040859

Conklin, E. G. (1905). Organ-forming substances in the eggs of ascidians. *Biol. Bull.* 8, 205–230. doi:10.2307/1535879

Delsuc, F., Philippe, H., and Tsagkogeorga, G. (2018). A phylogenomic framework and timescale for comparative studies of tunicates. *BMC Biol.* 16, 39. doi:10.1186/s12915-018-0499-2

Degasperi, V., Gasparini, F., Shimeld, S. M., Sinigaglia, C., Burighel, P., and Manni, L. (2009). Muscle differentiation in a colonial ascidian: organisation, gene expression and evolutionary considerations. *BMC Dev. Biol.* 9, 48. doi:10.1186/1471-213X-9-48

Gasparini, F., Degasperi, V., Shimeld, S. M., Burighel, P., and Manni, L. (2013). Evolutionary conservation of the placodal transcriptional network during sexual and asexual development in chordates. *Dev. Dyn.* 242, 752–766. doi:10.1002/dvdy.23957

Gasparini, F., Manni, L., Cima, F., Zaniolo, G., Burighel, P., Caicci, F., et al. (2015). Sexual and asexual reproduction in the colonial ascidian Botryllus schlosseri. *Genesis* 53, 105–120. doi:10.1002/dvg.22802

Gasparini, F., Shimeld, S. M., Ruffoni, E., Burighel, P., and Manni, L. (2011). Expression of a Musashi-like gene in sexual and asexual development of the colonial chordate Botryllus schlosseri and phylogenetic analysis of the protein group. *J. Exp. Zool. B Mol. Dev. Evol.* 316, 562–573. doi:10.1002/jez.b.21431

Gordon, T., Upadhyay, A. K., Manni, L., Huchon, D., and Shenkar, N. (2021). And then there were three extreme regeneration ability of the solitary chordate Polycarpa mytiligera. *Front. Cell Dev. Biol.* 9, 652466. doi:10.3389/fcell.2021.652466

Grave, C. (1934). The Botryllus type of ascidian larva.

Grave, C., and Woodbridge, H. (1924). Botryllus schlosseri (Pallas): the behavior and morphology of the free-swimming larva. *J. Morphol.* 39, 207–247. doi:10.1002/jmor.1050390107

He, C., Han, T., Liao, X., Guan, R., Chen, J.-Y., Tremblay, K. D., et al. (2020). On the origin of vertebrate body plan: insights from the endoderm using the hourglass model. *Gene Expr. Patterns* 37, 119125. doi:10.1016/j.gep.2020.119125

Hotta, K., Dauga, D., and Manni, L. (2020). The ontology of the anatomy and development of the solitary ascidian Ciona: the swimming larva and its metamorphosis. *Sci. Rep.* 10, 17916. doi:10.1038/s41598-020-73544-9

Hotta, K., Mitsuhara, K., Takahashi, H., Inaba, K., Oka, K., Gojobori, T., et al. (2007). A web-based interactive developmental table for the ascidian *Ciona intestinalis*, including 3D real-image embryo reconstructions: I. From fertilized egg to hatching larva. *Dev. Dyn. Off. Publ. Am. Assoc. Anat.* 236, 1790–1805. doi:10.1002/dvdy.21188

Iwata, R., and Vanderhaeghen, P. (2024). Metabolic mechanisms of species-specific developmental tempo. *Dev. Cell* 59, 1628–1639. doi:10.1016/j.devcel.2024.05.027

Kawamura, K., Tiozzo, S., Manni, L., Sunanaga, T., Burighel, P., and De Tomaso, A. W. (2011). Germline cell formation and gonad regeneration in solitary and colonial ascidians. *Dev. Dyn.* 240, 299–308. doi:10.1002/dvdy.22542

Keyte, A. L., and Smith, K. K. (2014). Heterochrony and developmental timing mechanisms: changing ontogenies in evolution. *Semin. Cell Dev. Biol.* 34, 99–107. doi:10.1016/j.semcdb.2014.06.015

Kogure, Y. S., Muraoka, H., Koizumi, W. C., Gelin-alessi, R., Godard, B., Oka, K., et al. (2022). Admp regulates tail bending by controlling ventral epidermal cell polarity via phosphorylated myosin localization in Ciona. *Development* 149, dev200215. doi:10.1242/dev.200215

Kowarsky, M., Anselmi, C., Hotta, K., Burighel, P., Zaniolo, G., Caicci, F., et al. (2021). Sexual and asexual development: two distinct programs producing the same tunicate. *Cell Rep.* 34, 108681. doi:10.1016/j.celrep.2020.108681

Kumano, G., and Nishida, H. (2007). Ascidian embryonic development: an emerging model system for the study of cell fate specification in chordates. *Dev. Dyn.* 236, 1732–1747. doi:10.1002/dvdy.21108

Laird, D. J., De Tomaso, A. W., and Weissman, I. L. (2005). Stem cells are units of natural selection in a colonial ascidian. *Cell* 123, 1351–1360. doi:10.1016/j.cell.2005.10.026

Lin, B., Shi, W., Lu, Q., Shito, T. T., Yu, H. H., and Dong, B. (2023). Establishment of a developmental atlas and transgenetic tools in the ascidian Styela clava. *Marine. Life. Sci. Techno.* 5 (4), 435–454.

Manni, L., Anselmi, C., Cima, F., Gasparini, F., Voskoboynik, A., Martini, M., et al. (2019). Sixty years of experimental studies on the blastogenesis of the colonial tunicate Botryllus schlosseri. *Dev. Biol.* 448, 293–308. doi:10.1016/j.ydbio.2018.09.009

Manni, L., and Burighel, P. (2006). Common and divergent pathways in alternative developmental processes of ascidians. *BioEssays News Rev. Mol. Cell. Dev. Biol.* 28, 902–912. doi:10.1002/bies.20462

Manni, L., Caicci, F., Anselmi, C., Vanni, V., Mercurio, S., and Pennati, R. (2022). Morphological study and 3D reconstruction of the larva of the ascidian halocynthia roretzi. *J. Mar. Sci. Eng.* 10, 11. doi:10.3390/jmse10010011

Manni, L., Gasparini, F., Hotta, K., Ishizuka, K. J., Ricci, L., Tiozzo, S., et al. (2014). Ontology for the asexual development and anatomy of the colonial chordate Botryllus schlosseri. *Plos One* 9, e96434. doi:10.1371/journal.pone.0096434

Manni, L., Lane, N. J., Joly, J.-S., Gasparini, F., Tiozzo, S., Caicci, F., et al. (2004). Neurogenic and non-neurogenic placodes in ascidians. *J. Exp. Zool. B Mol. Dev. Evol.* 302, 483–504. doi:10.1002/jez.b.21013

Manni, L., Lane, N. J., Sorrentino, M., Zaniolo, G., and Burighel, P. (1999). Mechanism of neurogenesis during the embryonic development of a tunicate. *J. Comp. Neurol.* 412, 527–541. doi:10.1002/(sici)1096-9861(19990927)

Manni, L., and Pennati, R. (2015). "Tunicata," in *Structure and evolution of invertebrate nervous systems* (Oxford University Press), 699–718. doi:10.1093/acprof:oso/9780199682201.001.0001

Manni, L., Zaniolo, G., and Burighel, P. (1993). Egg envelope cytodifferentiation in the colonial ascidian Botryllus schlosseri (Tunicata). *Acta Zool. Stockh. swed.* 74, 103–113. doi:10.1111/j.1463-6395.1993.tb01226.x

Manni, L., Zaniolo, G., and Burighel, P. (1994). Ultrastructural study of oogenesis in the compound ascidian botryllus schlosseri(tunicata). *Acta Zool.* 75, 101–112. doi:10.1111/j.1463-6395.1994.tb01115.x

Manni, L., Zaniolo, G., Cima, F., Burighel, P., and Ballarin, L. (2007). Botryllus schlosseri: a model ascidian for the study of asexual reproduction. *Dev. Dyn.* 236, 335–352. doi:10.1002/dvdy.21037

Martinucci, G. B., Burighel, P., Zaniolo, G., and Brunetti, R. (1988). Ovulation and egg segregation in the tunic of a colonial ascidian, Diplosoma listerianum (Tunicata, Ascidiacea). *Zoomorphology* 108, 219–227. doi:10.1007/BF00312222

Milkman, R. (1967). Genetic and developmental studies on botryllus schlosseri. *Biol. Bull.* 132, 229–243. doi:10.2307/1539891

Milkman, R., and Borgmann, M. (1963). "External fertilization of Botryllus schlosseri eggs," in *Biological bulletin, (MARINE BIOLOGICAL LABORATORY 7 MBL ST, WOODS HOLE, MA 02543)*, 385.

Patthey, C., Schlosser, G., and Shimeld, S. M. (2014). The evolutionary history of vertebrate cranial placodes–I: cell type evolution. *Dev. Biol.* 389, 82–97. doi:10.1016/j.ydbio.2014.01.017

Pennati, A., Jakobi, M., Zeng, F., Ciampa, L., and Rothbächer, U. (2024). Optimizing CRISPR/Cas9 approaches in the polymorphic tunicate *Ciona intestinalis*. *Dev. Biol.* 510, 31–39. doi:10.1016/j.ydbio.2024.03.003

Ricci, L., Salmon, B., Olivier, C., Andreoni-Pham, R., Chaurasia, A., Alié, A., et al. (2022). The onset of whole-body regeneration in botryllus schlosseri: morphological and molecular characterization. *Front. Cell Dev. Biol.* 10, 843775. doi:10.3389/fcell.2022.843775

Rinkevich, Y., Voskoboynik, A., Rosner, A., Rabinowitz, C., Paz, G., Oren, M., et al. (2013). Repeated, long-term cycling of putative stem cells between niches in a basal chordate. *Dev. Cell* 24, 76–88. doi:10.1016/j.devcel.2012.11.010

Rosental, B., Kowarsky, M., Seita, J., Corey, D. M., Ishizuka, K. J., Palmeri, K. J., et al. (2018). Complex mammalian-like haematopoietic system found in a colonial chordate. *Nature* 564, 425–429. doi:10.1038/s41586-018-0783-x

Sabbadin, A. (1955). Osservazioni sullo sviluppo, l'accrescimento e la riproduzione di Botryllus schlosseri (Pallas), in condizioni di laboratorio. *Bolletino Zool.* 22, 243–263. doi:10.1080/11250005509439204

Sabbadin, A., Zaniolo, G., and Majone, F. (1975). Determination of polarity and bilateral asymmetry in palleal and vascular buds of the ascidian Botryllus schlosseri. *Dev. Biol.* 46, 79–87. doi:10.1016/0012-1606(75)90088-3

Scelzo, M., Alié, A., Pagnotta, S., Lejeune, C., Henry, P., Gilletta, L., et al. (2019). Novel budding mode in Polyandrocarpa zorritensis: a model for comparative studies on asexual development and whole body regeneration. *EvoDevo* 10, 7. doi:10.1186/s13227-019-0121-x

Scott, F. M. (1934). "Studies on the later embryonic development of tunicata: botryllus schlosseri and amaroecium constellatum, a dissertation," in *Sister florence marie Scott*. Columbia, Columbia University.

Sorrentino, M., Manni, L., Lane, N. J., and Burighel, P. (2000). Evolution of cerebral vesicles and their sensory organs in an ascidian larva. *Acta Zool.* 81, 243–258. doi:10.1046/j.1463-6395.2000.00054.x

Tiozzo, S., Christiaen, L., Deyts, C., Manni, L., Joly, J.-S., and Burighel, P. (2005). Embryonic versus blastogenetic development in the compound ascidian Botryllus schlosseri: insights from Pitx expression patterns. *Dev. Dyn.* 232, 468–478. doi:10.1002/dvdy.20250

Tiozzo, S., Voskoboynik, A., Brown, F. D., and De Tomaso, A. W. (2008). A conserved role of the VEGF pathway in angiogenesis of an ectodermally-derived vasculature. *Dev. Biol.* 315, 243–255. doi:10.1016/j.ydbio.2007.12.035

Todorov, L. G., Oonuma, K., Kusakabe, T. G., Levine, M. S., and Lemaire, L. A. (2024). Neural crest lineage in the protovertebrate model Ciona. *Nature* 635, 912–916. doi:10.1038/s41586-024-08111-7

Vanni, V., Anselmi, C., Ballarin, L., Drago, L., Gasparini, F., Gordon, T., et al. (2022a). "Current knowledge on stem cells in ascidians," in *Advances in aquatic invertebrate stem cell research*. Editors L. Ballarin, B. Rinkevich, and B. Hobmayer (Basel: MDPI AG), 273–333. doi:10.3390/books978-3-0365-1635-6

Vanni, V., Ballarin, L., Gasparini, F., Peronato, A., and Manni, L. (2022b). "Studying RegenerationRegeneration in AscidiansAscidians: an historical overview," in *Whole-body regeneration: methods and protocols*. Editors S. Blanchoud and B. Galliot (New York, NY: Springer US), 27–48. doi:10.1007/978-1-0716-2172-1_2

Vanni, V., Salonna, M., Gasparini, F., Martini, M., Anselmi, C., Gissi, C., et al. (2022c). Yamanaka factors in the budding tunicate botryllus schlosseri show a shared spatio-temporal expression pattern in chordates. *Front. Cell Dev. Biol.* 10, 782722. doi:10.3389/fcell.2022.782722

Voskoboynik, A., Simon-Blecher, N., Soen, Y., Rinkevich, B., De Tomaso, A. W., Ishizuka, K. J., et al. (2007). Striving for normality: whole body regeneration through a series of abnormal generations. *FASEB J.* 21, 1335–1344. doi:10.1096/fj.06-7337com

Voskoboynik, A., Soen, Y., Rinkevich, Y., Rosner, A., Ueno, H., Reshef, R., et al. (2008). Identification of the endostyle as a stem cell niche in a colonial chordate. *Cell Stem Cell* 3, 456–464. doi:10.1016/j.stem.2008.07.023

Zaniolo, G., Burighel, P., and Martinucci, G. (1987). Ovulation and placentation in Botryllus schlosseri (Ascidiacea): an ultrastructural study. *Can. J. Zool.* 65, 1181–1190. doi:10.1139/z87-183

Zaniolo, G., Manni, L., Brunetti, R., and Burighel, P. (1998). Brood pouch differentiation in Botrylloides violaceus, a viviparous ascidian (Tunicata). *Invertebr. Reprod. Dev.* 33, 11–23. doi:10.1080/07924259.1998.9652338

Zaniolo, G., Manni, L., and Burighel, P. (1994a). Ovulation and embryo-parent relationships in Botrylloides leachi (ascidiacea, tunicata). *Invertebr. Reprod. Dev.* 25, 215–225. doi:10.1080/07924259.1994.9672388

Zaniolo, G., Manni, L., Martinucci, G., and Burighel, P. (1994b). Sexual reproduction in ascidians: comparative aspects of oviduct, ovulation and spawning. *Anim. Biol. Leiden. Neth.* 3, 67–74.

Frontiers in
Cell and Developmental Biology

Explores the fundamental biological processes of life, covering intracellular and extracellular dynamics.

The world's most cited developmental biology journal, advancing our understanding of the fundamental processes of life. It explores a wide spectrum of cell and developmental biology, covering intracellular and extracellular dynamics.

Discover the latest Research Topics

See more →

frontiers

Frontiers in
Cell and Developmental
Biology

Frontiers

Avenue du Tribunal-Fédéral 34
1005 Lausanne, Switzerland
frontiersin.org

Contact us

+41 (0)21 510 17 00
frontiersin.org/about/contact